

Lecture Notes in Mechanical Engineering

Banh Tien Long · Kozo Ishizaki ·  
Hyung Sun Kim · Yun-Hae Kim ·  
Nguyen Duc Toan ·  
Nguyen Thi Hong Minh ·  
Pham Duc An *Editors*

# Proceedings of the 3rd Annual International Conference on Material, Machines and Methods for Sustainable Development (MMMS2022)

Volume 3: Sustainable Approaches in Machine  
Design, Life Cycle Engineering, and Energy  
Management for Manufacturing Processes

 Springer

# Lecture Notes in Mechanical Engineering

## Series Editors


Fakher Chaari, National School of Engineers, University of Sfax, Sfax, Tunisia

Francesco Gherardini , Dipartimento di Ingegneria “Enzo Ferrari”, Università di Modena e Reggio Emilia, Modena, Italy

Vitalii Ivanov, Department of Manufacturing Engineering, Machines and Tools, Sumy State University, Sumy, Ukraine

Mohamed Haddar, National School of Engineers of Sfax (ENIS), Sfax, Tunisia

## Editorial Board

Francisco Cavas-Martínez , Departamento de Estructuras, Construcción y Expresión Gráfica Universidad Politécnica de Cartagena, Cartagena, Murcia, Spain

Francesca di Mare, Institute of Energy Technology, Ruhr-Universität Bochum, Bochum, Nordrhein-Westfalen, Germany

Young W. Kwon, Department of Manufacturing Engineering and Aerospace Engineering, Graduate School of Engineering and Applied Science, Monterey, CA, USA

Tullio A. M. Tolio, Department of Mechanical Engineering, Politecnico di Milano, Milano, Italy

Justyna Trojanowska, Poznan University of Technology, Poznan, Poland

Robert Schmitt, RWTH Aachen University, Aachen, Germany

Jinyang Xu, School of Mechanical Engineering, Shanghai Jiao Tong University, Shanghai, China

**Lecture Notes in Mechanical Engineering (LNME)** publishes the latest developments in Mechanical Engineering—quickly, informally and with high quality. Original research or contributions reported in proceedings and post-proceedings represents the core of LNME. Volumes published in LNME embrace all aspects, subfields and new challenges of mechanical engineering.

To submit a proposal or request further information, please contact the Springer Editor of your location:

**Europe, USA, Africa:** Leontina Di Cecco at [Leontina.dicecco@springer.com](mailto:Leontina.dicecco@springer.com)

**China:** Ella Zhang at [ella.zhang@springer.com](mailto:ella.zhang@springer.com)

**India:** Priya Vyas at [priya.vyas@springer.com](mailto:priya.vyas@springer.com)

**Rest of Asia, Australia, New Zealand:** Swati Meherishi at [swati.meherishi@springer.com](mailto:swati.meherishi@springer.com)

Topics in the series include:

- Engineering Design
- Machinery and Machine Elements
- Mechanical Structures and Stress Analysis
- Automotive Engineering
- Engine Technology
- Aerospace Technology and Astronautics
- Nanotechnology and Microengineering
- Control, Robotics, Mechatronics
- MEMS
- Theoretical and Applied Mechanics
- Dynamical Systems, Control
- Fluid Mechanics
- Engineering Thermodynamics, Heat and Mass Transfer
- Manufacturing Engineering and Smart Manufacturing
- Precision Engineering, Instrumentation, Measurement
- Materials Engineering
- Tribology and Surface Technology

**Indexed by SCOPUS, EI Compendex, and INSPEC.**

All books published in the series are evaluated by Web of Science for the Conference Proceedings Citation Index (CPCI).

To submit a proposal for a monograph, please check our Springer Tracts in Mechanical Engineering at <https://link.springer.com/bookseries/11693>.

Banh Tien Long · Kozo Ishizaki · Hyung Sun Kim ·  
Yun-Hae Kim · Nguyen Duc Toan ·  
Nguyen Thi Hong Minh · Pham Duc An  
Editors

# Proceedings of the 3rd Annual International Conference on Material, Machines and Methods for Sustainable Development (MMMS2022)

Volume 3: Sustainable Approaches  
in Machine Design, Life Cycle Engineering,  
and Energy Management for Manufacturing  
Processes

 Springer



*Editors*

Banh Tien Long  
Vietnam Association for Science Editing  
Hanoi University of Science  
and Technology  
Hanoi, Vietnam

Hyung Sun Kim  
Department of Materials Science  
and Engineering  
Inha University  
Nam-gu, Korea (Republic of)

Nguyen Duc Toan  
School of Mechanical Engineering  
Hanoi University of Science  
and Technology  
Hanoi, Vietnam

Pham Duc An  
Hanoi University of Science  
and Technology  
Hanoi, Vietnam

Kozo Ishizaki  
Nagaoka University of Technology  
Nagaoka, Japan

Yun-Hae Kim  
Department of Ocean Advanced Materials  
Convergence Engineering  
Korea Maritime and Ocean University  
Busan, Korea (Republic of)

Nguyen Thi Hong Minh  
Hanoi University of Science  
and Technology  
Hanoi, Vietnam

ISSN 2195-4356

ISSN 2195-4364 (electronic)

Lecture Notes in Mechanical Engineering

ISBN 978-3-031-57459-7

ISBN 978-3-031-57460-3 (eBook)

<https://doi.org/10.1007/978-3-031-57460-3>

© The Editor(s) (if applicable) and The Author(s), under exclusive license to Springer Nature Switzerland AG 2024

This work is subject to copyright. All rights are solely and exclusively licensed by the Publisher, whether the whole or part of the material is concerned, specifically the rights of translation, reprinting, reuse of illustrations, recitation, broadcasting, reproduction on microfilms or in any other physical way, and transmission or information storage and retrieval, electronic adaptation, computer software, or by similar or dissimilar methodology now known or hereafter developed.

The use of general descriptive names, registered names, trademarks, service marks, etc. in this publication does not imply, even in the absence of a specific statement, that such names are exempt from the relevant protective laws and regulations and therefore free for general use.

The publisher, the authors, and the editors are safe to assume that the advice and information in this book are believed to be true and accurate at the date of publication. Neither the publisher nor the authors or the editors give a warranty, expressed or implied, with respect to the material contained herein or for any errors or omissions that may have been made. The publisher remains neutral with regard to jurisdictional claims in published maps and institutional affiliations.

This Springer imprint is published by the registered company Springer Nature Switzerland AG  
The registered company address is: Gewerbestrasse 11, 6330 Cham, Switzerland

Paper in this product is recyclable.

# Organizing Committee

## Conference Chairs

Prof. Sci. Dr. Banh Tien Long, Vietnam Association for Science Editing, Vietnam;  
Hanoi University of Science and Technology

Prof. Yun-Hae Kim, Professor in Ocean Advanced Materials Convergence Engineering; Ex-Acting President of KMOU; Visiting Professor, Naval Postgraduate School (NPS), USA; Vice President of the Korean Society for Composite Materials; Editor-in-Chief of *Nano Hybrids Composites*

Prof. Hyung Sun Kim, Inha University

Prof. Kozo Ishizaki, Nagaoka University of Technology, Japan

## Conference Co-chairs

Prof. Le Anh Tuan, Hanoi University of Science and Technology, Vietnam, e-mail: [Tuan.LeAnh@hust.edu.vn](mailto:Tuan.LeAnh@hust.edu.vn)

Prof. Nguyen Duc Toan, Hanoi University of Science and Technology, Vietnam, e-mail: [Toan.NguyenDuc@hust.edu.vn](mailto:Toan.NguyenDuc@hust.edu.vn)

Prof. Dinh Van Chien, Vietnam Association for Science Editing, Vietnam, e-mail: [vanchien.dinh@gmail.com](mailto:vanchien.dinh@gmail.com)

Assoc. Prof. Nguyen Thi Hong Minh, Vietnam Association for Science Editing, Vietnam; Hanoi University of Science and Technology, e-mail: [Minh.NguyenThiHong@hust.edu.vn](mailto:Minh.NguyenThiHong@hust.edu.vn)

Dr. Ho Xuan Nang, Phenikaa University, e-mail: [nangvicostone@gmail.com](mailto:nangvicostone@gmail.com)

Dr. Nguyen Tien Dung, Nam Can Tho University

Prof. Kim Kyuman, Kyungpook National University, Korea

Prof. S.-H. Chang, National Kaohsiung University of Science and Technology, Taiwan, ROC

## Contact Persons

Dr. Phan Van Hieu, Hanoi University of Science and Technology, Vietnam, e-mail: [hieu.phanvan@hust.edu.vn](mailto:hieu.phanvan@hust.edu.vn)

Dr. Pham Duc An, Hanoi University of Science and Technology, Vietnam, e-mail: [An.PhamDuc@hust.edu.vn](mailto:An.PhamDuc@hust.edu.vn)

Dr. Hoang Van Quy, Hai Phong University, e-mail: [Quyhv@dhhp.edu.vn](mailto:Quyhv@dhhp.edu.vn)

## Science Secretaries

Dr. Pham Duc An, Hanoi University of Science and Technology, Vietnam, e-mail: [An.PhamDuc@hust.edu.vn](mailto:An.PhamDuc@hust.edu.vn)

Dr. Phan Van Hieu, Hanoi University of Science and Technology, Vietnam, e-mail: [hieu.phanvan@hust.edu.vn](mailto:hieu.phanvan@hust.edu.vn)

Dr. Mac Thi Thoa, Hanoi University of Science and Technology, Vietnam, e-mail: [Thoa.MacThi@hust.edu.vn](mailto:Thoa.MacThi@hust.edu.vn)

## International Organizing Committee

Banh Tien Long, Vietnam Association for Science Editing, Vietnam

Bui The Duy, Ministry of Science and Technology, Vietnam

Hoang Minh Son, Ministry of Education and Training, Vietnam

Nguyen Van Phuc, Ministry of Education and Training, Vietnam

Phan Xuan Dung, Vietnam Union of Science and Technology Associations, Vietnam

Dinh Van Phong, Hanoi University of Science and Technology, Vietnam

Huynh Dang Chinh, Hanoi University of Science and Technology, Vietnam

Hyung Sun Kim, Council of Asian Science Editors, Korea

Kim Kyuman, Kyungpook National University, Korea

Kim Youngsuk, Kyungpook National University, Korea

Kozo Ishizaki, Nagaoka University of Technology, Japan

I. A. Parinov, Southern Federal University, Russia

S.-H. Chang, National Kaohsiung University of Science and Technology, Taiwan

Nobuhiko Azuma, Nagaoka University of Technology, Japan

Nguyen Tien Dung, Nam Can Tho University, Vietnam

Nguyen Van Quang, Nam Can Tho University, Vietnam

Vu Ngoc Pi, Thai Nguyen University, Vietnam

Truong Hoanh Son, Hanoi University of Science and Technology, Vietnam

## **International Advisory Committee**

Chinda Charoenphonphanich, King Mongkut's Institute of Technology Ladkrabang, Thailand

Nguyen Duc Chien, Hanoi University of Science and Technology, Vietnam

Kim Kyuman, Kyungpook National University, Korea

Nguyen Duc Toan, Hanoi University of Science and Technology, Vietnam

Heidy Visbal, Kyoto University, Japan

Holger Kohl, Fraunhofer IPK Berlin, Germany

Hyung Sun Kim, Inha University, Korea

Jong Kyu Ha, Seoul National University, Korea

Jung-II Jin, Korea University, Korea

Kozo Ishizaki, Nagaoka University of Technology, Japan

Makoto Nanko, Nagoya Institute of Technology, Japan

Nobumasa Sekishita, Toyohashi University of Technology, Japan

Nobutaka Ito, Chiang Mai University, Thailand

Ralph J. Hexter, UC Davis, USA

Ramanathan Subramaniam, National Institute of Education, Singapore

Ramesh S. Kanwar, University of Hawaii, USA

Seung-Han Yang, Kyungpook National University, Korea

Soo Wahn Lee, Professor, Sun Moon University, Korea

Takashi Shirai, Kyoto Institute of Technology, Japan

Tetsuro Majima, Osaka University, Japan

Wim Dewulf, Katholieke Universiteit Leuven, Belgium

Worachart Sirawaraporn, Mahidol University, Thailand

Yoshiki Mikami, Nagaoka University of Technology, Japan

Yukari Matsuo, Hosei University, Japan

Bui Van Ga, Da Nang University, Vietnam

Le Anh Tuan, Hanoi University of Science and Technology, Vietnam

Tran Van Nam, Da Nang University, Vietnam

Nguyen Thanh Nam, Ho Chi Minh City University of Technology (HCMUT), Vietnam

Nguyen Hay, Nong Lam University, Vietnam

Nguyen Dinh Tung, Research Institute of Agricultural Machinery, Vietnam

Tran Duc Quy, Hanoi University of Industry, Vietnam

Bui Trung Thanh, Hung Yen University of Technology and Education, Vietnam

Vu Ngoc Pi, Thai Nguyen University, Vietnam

Cao Hung Phi, Vinh Long University of Technology Education, Vietnam

Pham Xuan Duong, Vietnam Maritime University, Vietnam

Nguyen Quoc Hung, Vietnamese-German University, Vietnam

Huynh Trung Hai, Hanoi University of Science and Technology, Vietnam

Truong Hoanh Son, Hanoi University of Science and Technology, Vietnam

Luong Cong Nho, Vietnam Maritime University, Vietnam

Tran Van-Nghia, Ministry of Science and Technology, Vietnam

V. K. Gupta, PDPM-Indian Institute of Information Technology, Design and Manufacturing Jabalpur, India  
 R. Hastijanti, University of 17 Agustus 1945 Surabaya, Indonesia  
 K. Hasyim, University of Darul Ulum, Jombang, Indonesia  
 H.-C. Huang, National Kaohsiung University of Science and Technology, Taiwan, ROC  
 M. A. Jani, University of 17 Agustus 1945 Surabaya, Indonesia  
 V. V. Kalinchuk, Southern Scientific Center of Russian Academy of Sciences, Russia  
 P. K. Kankar, Indian Institute of Technology Indore, India  
 C.-T. Lin, National Kaohsiung University of Science and Technology, Taiwan, ROC  
 M. B. Manuilov, Southern Federal University, Russia  
 A. V. Metelitsa, Southern Federal University, Russia  
 V. I. Minkin, Southern Federal University, Russia  
 E. L. Mukhanov, Southern Federal University, Russia  
 M. Musta'in, University of Darul Ulum, Jombang, Indonesia  
 T. Nakayama, Nagaoka University of Technology, Japan  
 M. Nanko, Nagaoka University of Technology, Japan  
 Nurmawati, University of 45 Surabaya, Indonesia  
 I. Prasetyawan, Lloyd's Register Asia, Malaysia  
 M. A. Rahim, University of 17 Agustus 1945 Surabaya, Indonesia  
 Sajjo, University of 17 Agustus 1945 Surabaya, Indonesia  
 T. Sekino, Osaka University, Japan  
 A. N. Soloviev, Don State Technical University, Russia  
 I. A. Verbenko, Southern Federal University, Russia  
 J.-K. Wu, National Kaohsiung University of Science and Technology, Taiwan, ROC  
 M.-C. Wu, National Tsing Hua University, Taiwan, ROC

## **Local Organizing Committee**

Banh Tien Long, Vietnam Association for Science Editing, Vietnam  
 Dinh Van Chien, Vietnam Association for Science Editing, Vietnam  
 Nguyen Thi Hong Minh, Vietnam Association for Science Editing, Vietnam  
 Nguyen Duc Toan, Vietnam Association for Science Editing, Vietnam  
 Phan Van Hieu, Vietnam Association for Science Editing, Vietnam  
 Mac Thi Thoa, Hanoi University of Science and Technology, Vietnam  
 Pham Duc An, Hanoi University of Science and Technology, Vietnam  
 Nguyen Huu Quang, Vietnam Association for Science Editing, Vietnam  
 Hoang Van Quy, Vietnam Association for Science Editing, Vietnam  
 Bui Van Bien, Haiphong University  
 Hoang Long, Vietnam Association for Science Editing, Vietnam  
 Bui Long Vinh, Hanoi University of Science and Technology, Vietnam  
 Dinh Van Phong, Hanoi University of Science and Technology, Vietnam  
 Le Anh Tuan, Hanoi University of Science and Technology, Vietnam  
 Nguyen Minh Hong, Ministry of Information and Telecommunications, Vietnam

Bui Trung Thanh, Hung Yen University of Technology and Education, Vietnam  
 Tran The Van, Hung Yen University of Technology and Education, Vietnam  
 Do Anh Tuan, Hung Yen University of Technology and Education, Vietnam  
 Nguyen Tien Dung, Nam Can Tho University, Vietnam  
 Nguyen Van Quang, Nam Can Tho University, Vietnam  
 Quach Hoai Nam, Nha Trang University, Vietnam  
 Tran Hung Tra, Nha Trang University, Vietnam  
 Nguyen Van Tuong, Nha Trang University, Vietnam

## **Scientific Committee**

Banh Tien Long, Hanoi University of Science and Technology, Vietnam  
 Bui Van Ga, Da Nang University, Vietnam  
 Le Anh Tuan, Hanoi University of Science and Technology, Vietnam  
 Tran Van Nam, Da Nang University, Vietnam  
 Nguyen Thanh Nam, Ho Chi Minh City University of Technology (HCMUT), Vietnam  
 Nguyen Hay, Nong Lam University, Vietnam  
 Chu Van Dat, Military Technical Institute, Vietnam  
 Nguyen Lac Hong, Le Quy Don University, Vietnam  
 Luong Cong Nho, Vietnam Maritime University, Vietnam  
 Nguyen Tien Dung, Nam Can Tho University, Vietnam  
 Nguyen Van Quang, Nam Can Tho University, Vietnam  
 Nguyen Duc Toan, Hanoi University of Science and Technology, Vietnam  
 Chinda Charoenphonphanich, King Mongkut's Institute of Technology Ladkrabang, Thailand  
 Dao Hong Bach, Hanoi University of Science and Technology, Vietnam  
 Tran Hung Tra, Nha Trang University, Vietnam  
 Dang Xuan Phuong, Nha Trang University, Vietnam  
 Bui Anh Hoa, Hanoi University of Science and Technology, Vietnam  
 Dinh Van Hai, Hanoi University of Science and Technology, Vietnam  
 Truong Hoanh Son, Hanoi University of Science and Technology, Vietnam  
 Phan Van Hieu, Hanoi University of Science and Technology, Vietnam  
 Hoang Hong Hai, Hanoi University of Science and Technology, Vietnam  
 Nguyen Dinh Tung, Research Institute of Agricultural Machinery, RIAM, Vietnam  
 Truong Viet Anh, Hanoi University of Science and Technology, Vietnam  
 Nguyen Phong Dien, Hanoi University of Science and Technology, Vietnam  
 Nguyen Ngoc Trung, Hanoi University of Science and Technology, Vietnam  
 Nguyen Huy Bich, Nong Lam University, Vietnam  
 Erik Bohez, Asian Institute of Technology, Thailand  
 Gyu Man Kim, Kyungpook National University, Korea  
 Jung-II Jin, Korea University, Korea  
 Le Quang, Hanoi University of Science and Technology, Vietnam

Nobuhiko Azuma, Nagaoka University of Technology, Japan  
 Nobumasa Sekishita, Toyohashi University of Technology, Japan  
 Nghiem Trung Dung, Hanoi University of Science and Technology, Vietnam  
 Nguyen Dang Binh, Viet Bac University, Vietnam  
 Nguyen Hong Lanh, Military Technical Institute, Vietnam  
 Nguyen The Mich, Hanoi University of Science and Technology, Vietnam  
 Nguyen Thi Thu Hien, Hanoi University of Science and Technology, Vietnam  
 Nguyen Viet Dung, Hanoi University of Science and Technology, Vietnam  
 Pham Minh Tuan, Hanoi University of Science and Technology, Vietnam  
 Pham Thanh Huy, Hanoi University of Science and Technology, Vietnam  
 Pham Van Hung, Hanoi University of Science and Technology, Vietnam  
 Seung-Han Yang, Kyungpook National University, Korea  
 Soo Wahn Lee, Professor, Sun Moon University, Korea  
 Tran Van Dich, Hanoi University of Science and Technology, Vietnam  
 Truong Ngoc Than, Hanoi University of Science and Technology, Vietnam  
 Vu Duc Lap, Military Technical Institute, Vietnam  
 Vu Quoc Huy, Hanoi University of Science and Technology, Vietnam  
 Wim Dewulf, Katholieke Universiteit Leuven, Belgium  
 Heidy Visbal, Kyoto University, Japan  
 Holger Kohl, Fraunhofer IPK Berlin, Germany  
 Hyung Sun Kim, Inha University, Korea  
 Jong Kyu Ha, Seoul National University, Korea  
 Kozo Ishizaki, Nagaoka University of Technology, Japan  
 Makoto Nanko, Nagoya Institute of Technology, Japan  
 Nobutaka Ito, Chang Mai University, Thailand  
 Ralph J. Hexter, UC Davis, USA  
 Ramanathan Subramaniam, National Institute of Education, Singapore  
 Ramesh S. Kanwar, University of Hawaii, USA  
 Takashi Shirai, Kyoto Institute of Technology, Japan  
 Tetsuro Majima, Osaka University, Japan  
 Worachart Sirawaraporn, Mahidol University, Thailand  
 Yoshiki Mikami, Nagaoka University of Technology, Japan  
 Yukari Matsuo, Hosei University, Japan  
 Nguyen Huy Bich, Nong Lam University, Vietnam  
 Nguyen Van Tuong, Nha Trang University, Vietnam  
 Pham Dinh Tung, Le Quy Don University, Vietnam  
 Tran The Van, Hung Yen University of Technology and Education, Vietnam  
 Do Anh Tuan, Hung Yen University of Technology and Education, Vietnam  
 Nguyen Khac Tuan, Thai Nguyen University, Vietnam  
 Vu Dinh Quy, Hanoi University of Science and Technology, Vietnam  
 Nguyen Duc Nam, Ho Chi Minh University of Industry, Vietnam  
 Ngo Van He, Hanoi University of Science and Technology, Vietnam  
 Nguyen Van-Thien, Hanoi University of Industry, Vietnam  
 Nguyen Tuan Linh, Hanoi University of Industry, Vietnam  
 Nguyen Tien-Han, Hanoi University of Industry, Vietnam

# Welcome Message

On behalf of the Organizing Committee, we are pleased to present the volume of *Lecture Notes in Mechanical Engineering*, which contains a selection of papers from The Third International Conference on Material, Machines, and Methods for Sustainable Development (MMMS2022) held from November 10–13, 2022, in Can Tho, Vietnam. Since 2018, MMMS has been focused on extending overall Sustainable Development Engineering to engage more researchers from different areas and various fields. Building on the success of the 2018 conference in Nalod, Danang, Vietnam, and the 2020 conference in Nha Trang, MMMS2022 aimed to evolve into one of the leading academic conferences in the field of Sustainable Development Engineering, underpinned by insightful lectures and presentations to attract even more attendees.

MMMS2022 is an international symposium hosted by the Vietnam Association of Science Editing (VASE) in collaboration with prestigious institutions such as Hanoi University of Science and Technology (HUST), Nam Can Tho University (NTU), Phenikaa University (PKA), Thai Nguyen University (TNU), Kyungpook National University (KNU-Korea), Nagaoka University of Technology (NUT Japan), Vietnam Federation of Mechanical Engineering Associations (VFMEA), and Council of Asian Science Editors (CASE). The event covers a wide range of topics related to engineering and sustainable manufacturing for the benefit of a global society. Researchers, policymakers, industry professionals, practitioners, and students from all countries are invited to submit papers and participate in various sessions, keynotes, and workshops.

The main objective of the conference is to explore critical aspects of sustainable development, particularly in the areas of materials, machines, and methods. Through interactive sessions, policymakers, researchers, and industry professionals can exchange feedback and inputs on the topics to ensure local technological development toward sustainable development in a global context. Furthermore, networking is promoted between participants through special sessions organized by VASE, including those focusing on improving writing for publishing in advanced international journals, presented by Prof. Hyung Sun Kim, Former President of the Council of Asian Science Editors (CASE).



The purpose of this volume of *Lecture Notes in Mechanical Engineering* is to explore and ensure an understanding of the critical aspects that contribute to sustainable development, particularly materials, machines, and methods. The conference aims to assist policymakers, industries, and researchers at various levels to position local technological development toward sustainable development in the global context and to promote decision-making toward a greener approach, especially for materials, machines, and methods.

We would like to express our gratitude to the members of the International Organizing and Academic Committees of the Conference for their hardwork and advice, which helped to maintain the high level of the conference. We also thank Springer Nature Switzerland AG 2020 for publishing the selected papers in the *Lecture Notes in Mechanical Engineering*. We hope that all the papers will provide valuable information for academics, researchers, engineers, and students.

Prof. Banh Tien Long  
Vietnam Association for Science Editing (VASE)  
Hanoi University of Science and Technology  
Hanoi, Vietnam

Prof. Nguyen Duc Toan  
Hanoi University of Science and Technology  
Hanoi, Vietnam

## Keynote Speakers



### **Prof. Yun-Hae Kim**

**Affiliation:** Korea Maritime and Ocean University, Republic of Korea.

### **Bio Statement:**

Professor Yun-Hae Kim graduated from the Department of Marine Engineering, Korea Maritime and Ocean University in 1983 and received Ph.D. degree from Kyushu University in Mechanical Engineering, Japan. He worked at NIST, USA, as a visiting professor from 1997 to 1998, and his studies focused on the fabrication and evaluation of composite materials. He worked as a research assistant, 1985–1987, at Korea Maritime and Ocean University. He published over 150 papers in international and national journals; He joined over 60 conferences and symposia at international and national levels as a general speaker, invited speaker, or keynote speaker. He founded two international conferences, namely Asian Conference on Engineering Education (ACEE, 2009) and Asian Conference on Campus Sustainability (ACCS, 2015). He was the president of the Korea Association of Green Campus Initiatives (KAGCI). He was the ex-Acting president of Korea Maritime and Ocean University, ex-Dean of Student Affairs, and ex-Dean of Academic Affairs from 2014 to 2016.

He was a conference chair of the Advanced Materials Development and Performance (AMDP 2014). At that time, over 400 delegates participated in this conference. He was the editor of SCI journal, *International Journal of Modern Physics B*. Now, he is working as the Editors-in-Chief of the *Journal of Ocean Engineering and Technology* for 9 years and *Nano Hybrids Composites*. In particular, he joined in the last five years (2013 and 2017) over 20 conferences as Keynote Speaker and Conference Co-Chairs. He is working as Director of Idea Factory Center at KMOU. He received many awards, Ministry of Science and Technology (Jang Young Sil Best Award, Korea), Ministry of Science and Technology, Korea, Distinguished Professor Award, The Korean Society of Engineering Education, Distinguished Service Medal, The Korean Society of Engineering Education, Ministry of Education, Science and Technology (Ministry Award) (Engineering Education Innovation Field), Ministry of Education, Science and Technology, Korea, Best Paper Award, ICPNS, Seattle, USA. His research interests include R&D of novel materials and composites based on polymer materials (in particular, environmental characteristics, fracture mechanics and strength evaluations, ocean applications of advanced materials and composites).

Yun-Hae Kim was chairman and co-chairman of the following International Conferences:

- (i) 1st Asian Conference on Engineering Education (ACEE), ACEE 2009 (October 28–30, 2009, Busan, Korea)
- (ii) Advanced Materials Development and Performance (AMDP), AMDP 2014 (July 17–20, 2014, Busan, Korea)
- (iii) Asian Conference on Campus Sustainability 2015, ACCS 2015 (November 10–11, 2015, Busan, Korea)
- (iv) 6th International Joint Symposium on Engineering Education (IJSEE), IJSEE 2016 (December 23, 2016, Busan, Korea)
- (v) 7th Advanced Materials Development and Performance (AMDP), AMDP 2017 (July 11–15, 2017, Pune, India).

**Gyu Man Kim**

Professor, School of Mechanical Engineering

Kyungpook National University

Micro-System and Nano-Engineering (MSNE) Research Group

<http://msne.knu.ac.kr/>

1370, Sankyuk-Dong, Daegu, Republic of Korea, 702-701

Tel: 82-53-950-7570 Fax: 82-53-950-6550 Cp: 82-10-9902-6755

e-mail: [gyuman.kim@knu.ac.kr](mailto:gyuman.kim@knu.ac.kr)

**Research Interests**

- Research on micro-/nanoscale fabrication
  - microelectromechanical system (MEMS)
  - Micro-/nano-stencil (shadowmask) technology for micro-/nanoscale patterning
  - Soft lithography
  - Self-assembled monolayer for surface modification.
- Research on microtechnology for life science
  - Micropatterned cell culture
  - Preparation of mono-dispersed biopolymer microparticles
  - Lab-on-a-chip (LOC) and bio-sensors.
- Research on precision manufacturing for miniaturized mechanical systems
  - Micro-electro-discharge machining (MEDM)
  - Micro-electro-chemical machining (MECM).

Gyu Man Kim received the B.S., M.S., and Ph.D. degrees in mechanical design and production engineering from the Seoul National University, Seoul, Korea, in 1993, 1995, and 1999, respectively.

Currently, he is an professor at School of Mechanical Engineering, Kyungpook National University, Korea. He has been a postdoctoral research fellow at

MESA+ Research Institute, Twente University, the Netherlands, and at Microsystems Laboratory, Ecole Polytechnique Federale de Lausanne (EPFL).

His recent research works include the formation of hydrogel microdroplet and particles in a microfluidic device, microfabrication using nano- and microstencil, soft lithography, and hybrid technologies of MEMS and precision manufacturing processes. His recent research project includes “Laboratory on microfabrication of enzymatic biofuel cell,” “Fabrication of micro/mesoscale hybrid structures based on porous biopolymer,” “Micropatterned cell culture for stem cell for therapeutic strategies in neurodegenerative disease,” “Inkjetting of biopolymer for Biomedical applications,” and “Nanoparticle and cell-laden microparticle fabrication and its bio application.” He has published over 100 peer-reviewed scientific publications. His research includes micro-/nano-scale fabrication, microfluidics, and miniaturized mechanical systems to be applied to the field of life science, industry, and energy. He is also co-inventor of over 20 patents.

He is member of the KSME, KSPE, and KSMPE. He is an Editor-in-Chief of *International Journal of Precision Engineering and Manufacturing-Green Technology*.

### **Awards**

- Gaheon Award, Gaheon-Sindoh Foundation, 2021
- Best Paper Award, Korean Society for Precision Engineering, 2017
- IJPEM Highly Commended Paper Award, Korean Society for Precision Engineering, 2016
- Best Poster Award, International Symposium on Green Manufacturing and Applications, 2015
- Baek-Am Award, Korean Society for Precision Engineering, 2015
- Best Paper Award, JCK MEMS/NEMS with Nano Korea, 2014
- Best Paper Award, International Symposium on Green Manufacturing and Applications, 2012
- Best Poster Prize, International Conference for Micro- and Nanotechnologies for the Biosciences.

### **Professional Association Activities**

- Editor/Editor-in-Chief *International Journal of Precision Engineering and Manufacturing-Green Technology (IJPEM-GT)*, 2014~
- Editorial committee member/Editor, *International Journal of Precision Engineering and Manufacturing (IJPEM)*, 2009~2017
- Editorial Director, *Korean Society for Precision Engineering (KSPE)*, 2012~
- Member, *Korean Society for Mechanical Engineers (KSME)*, 2003~
- Member, *Korean Society for Precision Engineering (KSPE)*, 2003~

**Makoto Nanko**

Professor, the Department of Mechanical Engineering, Nagaoka University of Technology

1603-1, Kamitomioka, Nagaoka, Niigata 940-2188, Japan

**Education**

Bachelor of Engineering, Nagaoka University of Technology, Japan, 1990

Master of Engineering, Nagaoka University of Technology, Japan, 1992

Doctor of Engineering, Nagaoka University of Technology, Japan, 1995

**Works**

Assistant Professor, Tokyo Institute of Technology, 1995–2001

Associate Professor, Nagaoka University of Technology, 2001–2016

Professor, Nagaoka University of Technology, 2016–Current

Presidential Aide, 2021–Current

**Major**

Materials Science and Engineering, in particular, High-temperature Physical Chemistry

**Publications**

Nine books, 96 journal papers, 32 reviews, 39 proceedings papers, and eight patents

**Awards**

Young Research Award, Japan Institute of Metals (2000)

The Commendation for Science and Technology by the Minister of Education, Culture, Sports, Science and Technology (April 2014)

**Prof. Quang-Cherng Hsu**

Department of Mechanical Engineering

National Kaohsiung University of Science and Technology (NKUST), Taiwan

e-mail: [hsuqc@nkust.edu.tw](mailto:hsuqc@nkust.edu.tw)

**Brief Introduction of Professor Quang-Cherng Hsu**

Dr. Quang-Cherng Hsu currently is a professor of Mechanical Engineering, National Kaohsiung University of Science and Technology (NKUST), Taiwan. He earned his Ph.D. degree in Mechanical Engineering, National Cheng-Kung University in 1981. After two-year service in military, he joined Metal Industries Research and Development Center, a government fund non-profit research organization, in Kaohsiung as a research engineer about two years. Then, he joined the current university. In 2003~2004, he visited Ohio State University, USA, as a visiting scholar for one year. During September 12–30, 2016, he visited Aachen University, German, to study Industry 4.0. From March 3 to 26, 2017, he visited Hung Yen University of Technology and Education, and Hai-Phone University, Vietnam, and gave intensive speeches. Research interests of his include image processing and machine vision, metal forming (forging, extrusion, sheet metal forming), nanoimprint lithography applications, molecular dynamics simulation. He has published 61 referred journal papers, has obtained 14 invention patents, and has attended 77 international conferences among 13 countries to present his research results. He also likes to organize student's handy-team to attend domestic professional competitions including industrial robot competition, computer-aided measurement and verification competition, mold and die industrial application and innovation competition, image servo and precision measurement competition, optical-electronic inspection instrument competition, and precision machinery competition.

**Prof. Chyi-Yeu Lin**

Department of Mechanical Engineering and the founding director of the University Research Center: Center for Intelligent Robotics in National Taiwan University of Science and Technology, Taiwan.

Chyi-Yeu Lin is a distinguished professor in the Department of Mechanical Engineering and the founding director of the university research center: Center for Intelligent Robotics in National Taiwan University of Science and Technology, Taiwan. He was elected as a corresponding member of Russian International Academy of Engineering since 2011. Since 2018, he served as the vice-director of the Center for Cyber-physical System Innovation (CPSi), from the Featured Areas Research Center Program within the framework of the Higher Education Sprout Project by the Ministry of Education (MOE) in Taiwan. The CPSi center is the only center funded by MOE in the area of robotics.

He received his Ph.D. degree from the University of Florida in 1991. His research interests and extensive scientific contributions cover from structural optimization and evolutionary methods before 2005, and since 2005 mostly on intelligent robotics and intelligent manufacturing.

He led a research team to debut the world-first robot theater performance with male and female bipedal androids with facial expression capability and two dual-wheeled robots at NTUST campus theater in December 27, 2008. The performed programs included hand puppet show, real-time music note reading and singing, real-time face portrait painting, the Phantom of the Opera show, and harmonic dance and singing. He made many innovative robots in different application domains.

He published about 100 SCI journal papers and 150 conference papers. He participated in near 80 research projects from government and industry with a total budget of more than 8 million USD.

He also founded a robotics and automation company in Taiwan, providing cutting-edge technologies and systems to industries. He loved to invent and had generated more than 50 invention patents globally.



# Contents

<b>Sustainable Machine Design: Metratronics, Robotics, CAD/CAM/CAE, and Maritime Engineering</b>	
<b>Experimental Study on the Forming Limit Curve of SECC Sheet Material</b> .....	3
The-Thanh Luyen, Minh-Tan Nguyen, Tien-Long Banh, Duc-Toan Nguyen, and Thi-Bich Mac	
<b>Investigation on the Influence of Obstacle Size in Path Planning by a Hybrid Model Combining an Improved A-star Algorithm and Digital Twin</b> .....	11
Doan Thanh Xuan and Vu Toan Thang	
<b>Design and Control of Waterbomb Robot</b> .....	21
Thai Phuong Thao and Nguyen Ngoc Hai	
<b>Analysis SUV Vehicle Structure in Car to Car Frontal Impact</b> .....	29
Nguyen Phu Thuong Luu and Ly Hung Anh	
<b>A New Method to Extend the Measurement Range of a Displacement Measuring Interferometer by Measuring the Modulation Depth</b> .....	37
Hoang Anh Tú, Hoang Trung Kien, Vu Thanh Tùng, Dong Xuan Hieu, Nguyen Thanh Dong, and Vu Van Quang	
<b>Simulation of Aerodynamics for Unmanned Aerial Vehicles with the SolidWorks Platform</b> .....	45
Thi Minh Tu Bui, Quoc Thai Pham, Le Chau Thanh Nguyen, and Tan Thong Ngo	
<b>Spiral Bevel Gear Manufacturing Technology: A Review</b> .....	55
Hoang Thuy Dinh, Van Tuan Pham, and Quoc Hoang Pham	

**Design of a Face Recognition Technique Based MTCNN and ArcFace** ..... 71  
Dang Thai Viet, Phan Van Thien, Nguyen Huu Tu, Hoang Gia Minh, and Ngoc-Tam Bui

**Development of a New Flow-Mode Magneto-Rheological Damper Featuring Tooth-Shaped Duct** ..... 79  
Quoc-Duy Bui, Huu-Quan Nguyen, Long-Vuong Hoang, and Quoc Hung Nguyen

**Design the Abnormal Object Detection System Using Template Matching and Subtract Background Algorithm** ..... 87  
Dang Thai Viet and Ngoc-Tam Bui

**Modeling and Simulation the Drone System Used in the Warehouse** .... 97  
Thi-Dong-Ngan Nguyen, Minh-Tai Le, Thi-Phuong-Truc Vo, and Thanh-Tung Phung

**Research on Capacitive Micromachined Ultrasonic Transducer Array for the Wrist-Type Suspension Control System** ..... 107  
Gia-Thinh Bui

**Optical Recognition of Handwritten by Aiding Computer Vision and Deep Learning** ..... 117  
Anh-Son Tran, Duc-An Pham, and Van-Nghia Le

**Proposing Method to Solve Kinematics Problem of a Lower Limb Rehabilitation Robot** ..... 125  
Tien Nguyen, Trung Nguyen, and Tam Bui

**Applying Dynamic Movement Primitives to Motion Planning and Inverse Kinematics Problems of an Upper Limb Exoskeleton Robot** ..... 135  
Huy Nguyen, Trung Nguyen, Hung Dao, Dung Nguyen, and Ha Pham

**A Study on Building a Motorcycle Finite Element Model for Crashworthiness Base on the Current Transportation in Vietnam** ..... 145  
Nguyen Phu Thuong Luu and Ly Hung Anh

**Simulation and Investigation of the Influence of Pressure on the Stiffness of Air Spring Suspension in Passenger Vehicles Using ABAQUS** ..... 155  
Nguyen Thanh Cong and Pham Duy Binh

**A Study on Humanoid Robot Using Ros** ..... 163  
Xuan-Thuan Nguyen, Huy-Anh Bui, Van-Quy Hoang, and Duc-An Pham

**Design of a Self-Balancing System of Autonomous Underwater Vehicle** ..... 171  
 Ton Thien Phuong, Tran Thien Phuc, and Huynh Manh Dien

**Design of Educational Robot for Multilevel Steam Education** ..... 185  
 Dinh-Ba Bui and Duc An Pham

**A Study on Effects of Design Parameters on Extrusion Product Quality Using Comsol LiveLink for Inventor** ..... 193  
 Van-The Than, Jin H. Huang, Chi-Chang Wang, Tat-Tai Truong, and Thi-Thao Ngo

**The Application of the Reinforcement Learning Method for Mobile Robot Navigation in an Unknown Environment** ..... 201  
 Anh-Tu Nguyen and Hong-Son Nguyen

**Optimisation of Parameters When Polishing Aluminium Cookware Using Wool Felt Wheel** ..... 209  
 Truong Dinh Luan, Nguyen Trong Doanh, and Bui Qui Luc

**Analysis of Pedestrian Head Kinematics During Impact to Car Process Using a Full Deformable Pedestrian Model** ..... 219  
 Van-Luc Ngo, Ngoc-An Tran, and Van-Hai Nguyen

**Development of Point to Point Algorithm AMR Navigation** ..... 227  
 Minh Khong, Van-Luc Ngo, Minh-Hiep Le, Van-Tung Nham, and Quoc-Dat Do

**Systematic Design of a Sitting-Type Lower Limb Rehabilitation Robot for Stroke Patient** ..... 235  
 Duc Luu, Trung Nguyen, and Tam Bui

**Kinematics Analysis of 7-DOF Collaborative Robotic Manipulators with Offsets at Shoulder and Wrist** ..... 247  
 Nguyen Quang Hoang, Do Tran Thang, Dinh Van Phong, and Thai Phuong Thao

**Accumulation of Permanent Deflection of Steel Plates Subjected to Repeated Slamming Impact Loadings** ..... 255  
 Dac Dung Truong, Van Vu Huynh, Sang-Rai Cho, Xuan-Phuong Dang, and Hao Dinh Duong

**Influence of Blank Holder Force and Limiting Drawing Ratio on Fracture Height During Cup—Drawing Process of SECC Sheet Metal** ..... 263  
 Thi-Bich Mac, Ngoc-Quyet Ly, and The-Thanh Luyen

**Automatically Abnormal Detection for Radiator Fans Through Sound Signals Using a Deep Learning Technique** ..... 271  
 Minh-Tuan Nguyen, Tien-Phong Nguyen, and The-Van Tran

**Interference Fit Calculation with Numerical and Simulation Methods** ..... 279  
 Vi Phong Lam and Huu Loc Nguyen

**Analysis and Optimisation of Magnetorheological Dampers Using Ansys Workbench** ..... 287  
 Kim-Thach Tran, Nguyen Van Bien, Quoc Hung Nguyen, and Weihua Li

**Development of the Control Method for AGV to Navigate in the Warehouse** ..... 295  
 Van Hieu Phan

**Structural Topology Optimization of a Large-Sized Link Mechanism in a Radar Antenna Lifting System** ..... 307  
 Van Doan Cao, Duc Dung Le, and Duc Son Hoang

**Optimization of Machining Factors Affects Chip Shrinkage Coefficient, Surface Roughness When High-Speed Milling of Aluminum Alloy A7075** ..... 315  
 Thi-Hoa Pham, Duc-Toan Nguyen, Viet-Hoi Tran, and Dang-Thuc Phan

**Design an Intelligent Braking System Using Ultrasonic Sensors and IR Sensors** ..... 325  
 Vu Hai Quan, Nguyen Anh Ngoc, Le Hong Quan, Nguyen Xuan Khoa, Nguyen Quoc Khanh, and Ngo Quang Tao

**An Investigation of Transverse Shrinkage in Single V and Bevel-Groove Butt Joints Using GMAW Process** ..... 335  
 Thi-Thao Ngo, Jin H. Huang, Chi-Chang Wang, and Van-The Than

**Robotic Bin-Picking System Based on Voice Recognition, Deep Learning, and Point Cloud Processing** ..... 345  
 Van-Dung Tran, Thanh-Hung Nguyen, Dinh-Ba Bui, and Minh-Ha Le

**A Lightweight Design of End Effector for Industrial Robot** ..... 353  
 Giang-Nam Le and Thanh-Xuan Nguyen

**An Integrated Design of Industrial Robots and Machine Vision for Product Sorting System** ..... 363  
 Giang-Nam Le, Ngoc-Sang Vu, and Ngoc-Phu Doan

**Computational Fluid Analysis and Experiment Verification of a Liquid Cooling System for an Array Radar’s Transmit-Receive Module** ..... 373  
 Van Doan Cao, Duc Dung Le, Anh Quang Dang, and Anh Duc Hoang

**Evaluate the 3D Measurement System Accuracy Through 3D Point Cloud Processing Algorithm** ..... 381  
 Nguyen Thi Kim Cuc, Cao Xuan Binh, and Tien Dung Vu

**Study on the Impact of Structural Parameters on the Vibration of Automobiles** ..... 389  
Van Hoang Tran

**A Case Study on Impact of Ethanol-Mixed Gasoline on Exhaust Emissions of Automobile Engines** ..... 399  
Van Hoang Tran, Thanh Huan Nguyen, Trong The Tran, Van Phuong Dinh, and Thanh Binh Nguyen

**Face Recognition and Hand Gesture Control for Tello Drone Navigation** ..... 407  
Huy-Anh Bui, Anh-Tu Nguyen, Thanh-Hung Nguyen, and Xuan-Thuan Nguyen

**Optimization Toolpath Generation for Drill Hole on Three Axes CNC Machine Using Genetic Algorithms** ..... 415  
Van Quy Hoang, Ngoc Tuyen Bui, Xuan Dung Pham, and Gia Hai Vuong

**Kinetic Analysis of a Spatial Structure by Orthographic Projection** .... 427  
Pham Van Son and Van Hieu Phan

**Use Perpendicular Projection to Prove Some Properties of Disphenoid and Some of Its Applications in Engineering** ..... 437  
Manh Hong Do

**Motion and Condition Monitoring of an Industrial Robot Based on Digital Twins** ..... 445  
Nguyen Nguyen, Chu Anh My, Chi Hieu Le, Nikolay Zlatov, Georgi Hristov, James Gao, Ho Quang Nguyen, Jamaluddin Mahmud, Trung Thanh Bui, and Michael S. Packianather

**Novel Exoskeleton Design of Lower Limb Rehabilitation Robot Using Pneumatic Cylinder** ..... 457  
Van-Thuc Tran and Tuan-Anh Bui

**Development of an Automated Electronic Toll Collection System Based on Deep Learning** ..... 465  
Thi Thoa Mac

**6 DOF Robot Control with Object Detection Based on Deep Learning** ..... 473  
Hoang Hong Hai, Nguyen Thanh Hung, Le Sy Dung, and Nguyen Huu Long

**Generative Adversarial Network for Building Large Custom Dataset** ..... 481  
Hoang Hong Hai

**A Robust Robot Correction System Using 6-Axis Force/Torque Sensor** ..... 489  
Chi-Cuong Tran, Syed Humayoon Shah, Chyi-Yeu Lin,  
and Anton Royanto Ahmad

**A Study on YOLOv4 Algorithm for Harvesting Agriculture Robot** ..... 497  
Sy-Tai Nguyen, Hong-Ky Dang, Tien Duc Nguyen, Hai-Le Bui,  
and Thi Thoa Mac

**Design and Simulation of a Scaled Motion Platform System Based Parallel Robot** ..... 505  
Van-Quy Hoang, Do Van, Hoang Manh Hung, Pham Kim Mung,  
Le Van Khanh, and Duc An Pham

**A Multi-Floor Elevator Control Based on Oriented-Object Programming by Using Function Block** ..... 513  
Si-Tuan Hoang and Duc An Pham

**Real-Time Deep Learning-Based Automatic Pill Classification** ..... 521  
Thi Thoa Mac and Minh-Huy Nguyen

**Design and Simulation of a Self-Tuning Fuzzy PID Controller for One Axis bar Model** ..... 529  
Truong Minh Thong and Pham Duc An

**Sustainable Machine Design:  
Metratronics, Robotics, CAD/CAM/CAE,  
and Maritime Engineering**

# Experimental Study on the Forming Limit Curve of SECC Sheet Material



The-Thanh Luyen, Minh-Tan Nguyen, Tien-Long Banh, Duc-Toan Nguyen, and Thi-Bich Mac

**Abstract** Numerical simulation in the sheet metal forming field helps engineers effectively solve various problems in the manufacturing of industrial products. In the forming, necking and fracture can occur on the products. These phenomena are caused by many reasons like the original mold design, technological parameters, and especially the limited forming of the sheet material. In order to accurately simulate the fracture phenomenon during forming, a forming limit curve (FLC) of the material is the most important input data. In this research, to determine the FLC of SECC sheet material by experiment method, a set of molds is first designed and manufactured according to the Nakazima model. Eight samples with various dimensions are then formed and measured major and minor strain points which are near fracture locations. This FLC data is verified through simulation of the forming process of the cup-shaped part. The simulated result of fracture height is compared with the experimental one and shows good agreement.

**Keywords** Forming limit curve (FLC) · Forming limit diagram (FLD) · Nakazima tests · SECC steel sheet

## 1 Introduction

Nowadays, new methods of limited strain detection with digital image correlation (DIC) algorithms have largely used to determine the FLC of sheet metal that interchanged the method of analysis the circular grid of defective specimens. Some of the prominent methods are method is based on the neck strain's acceleration depending

---

T.-T. Luyen · M.-T. Nguyen · T.-L. Banh · T.-B. Mac (✉)

Faculty of Mechanical Engineering, Hungyen University of Technology and Education, Dan Tien, Khoai Chau, Hung Yen, Vietnam  
e-mail: [bich.utehy@gmail.com](mailto:bich.utehy@gmail.com)

T.-L. Banh · D.-T. Nguyen

School of Mechanical Engineering, Hanoi University of Science and Technology, 1A-Dai Co Viet Street, Hai Ba Trung District, Hanoi City, Vietnam



on time [1], method is based on the distribution of strain at fracture (ISO 12004-2) [2], and method is tracking the curvature based on geometry of the necking are [3], etc.

Besides, a method that was the most widely applied for predicting the FLC called the M–K method was established by Marciniak and Kuczynski [4]. This method is based on the development of a localization band because of an imperfect thickness. The M–K method has a strong foundation in physics which is cause to see many extensions for accounting for material's texture [5], stress through thickness [6], shear through thickness [7], and plastic damage in the non-linear strain lines [8].

There were some studies on the FLC [9, 10] applied in numerical simulation to determine the fracture height when stamping cup-shaped products and verified by the corresponding experiment. The aim of this research is constructing the FLC of SECC sheet metal with the experimental model of Nakazima [11]. This experimental FLD data can be applied in numerical simulation software packages to predict the forming ability of different types of products made from SECC.

## 2 Material and Experimental Model

In this study, experiments were carried out on SECC sheet metal with thickness of 0.6 mm. The chemical composition of this material is shown in Table 1.

Requirements of meeting the content of other residual elements: Cu < 0.15%, Ni < 0.15%, Cr < 0.15%, As < 0.05%, Sn < 0.05%.

To determine the FLD data, tests were performed on an experimental mold with the dimensions shown in Fig. 1. The forming mold set was designed according to the Nakazima model standard with a punch of the hemispherical shape, the blank holder, and the die. In which, the die had a lockbead to be fixed when forming as shown in Fig. 2. The experimental process was conducted on a Servo hydraulic multi-function testing machine with a maximum load of 100 tons. In the forming process, the workpiece was fixed between the blank holder and the die while the punch moved from top to bottom at a speed of 60 mm/min. The samples were designed according to the standard with the size as shown in Fig. 3 and printed in a circular mesh with a diameter of 5 mm. The results of the samples when cracking or tearing occurred were shown in Fig. 4.

**Table 1** The chemical composition of SECC steel sheet [12]

Element code	C	Si	Mn	P	S
Content (%)	< 0.12	< 0.05	< 0.50	< 0.025	< 0.025

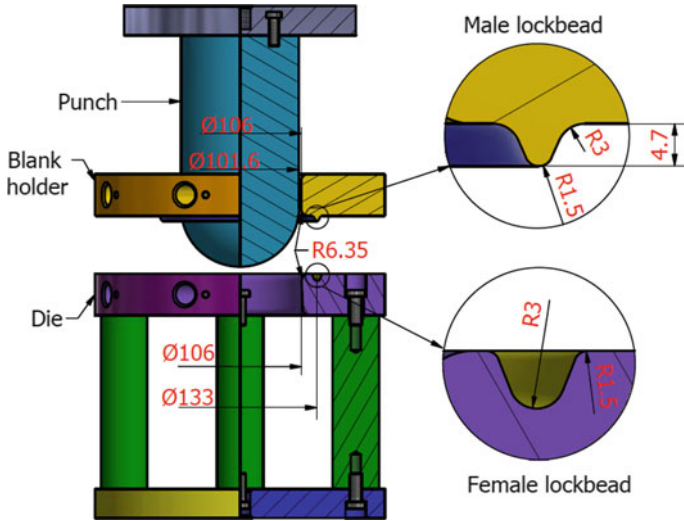


Fig. 1 Nakazima mold set model

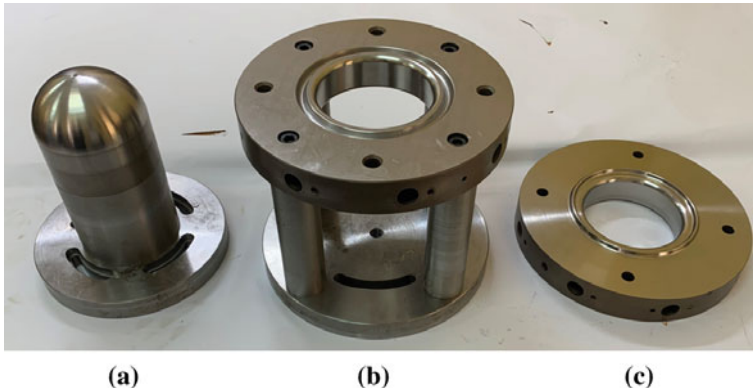
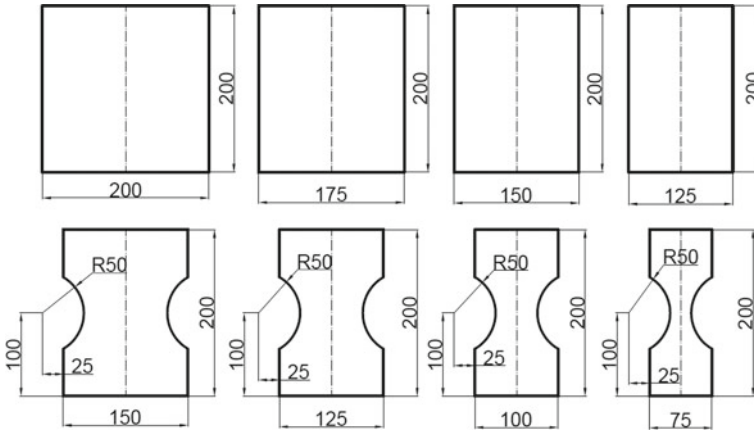


Fig. 2 Experimental mold set including. a Punch; b Die; c Blank holder

### 3 Constructing the FLC of SECC Material by Experimental Method

The samples are printed in a mesh with a circle diameter of 5 mm. After the experiment, the mesh is deformed with major strains ( $\epsilon_1$ ) and minor strains ( $\epsilon_2$ ). To perform strain measurement of experimental samples, a caliper is used to measure the strains at locations near the cracking. The deformations are then determined according to formula (1).



**Fig. 3** Samples dimension

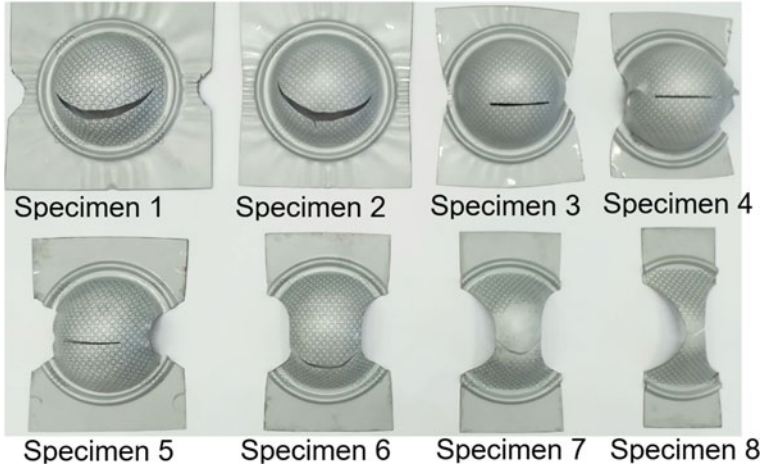


**Fig. 4** Experimental results according to Nakazima model

$$\varepsilon = \frac{d - d_0}{d_0} \quad (1)$$

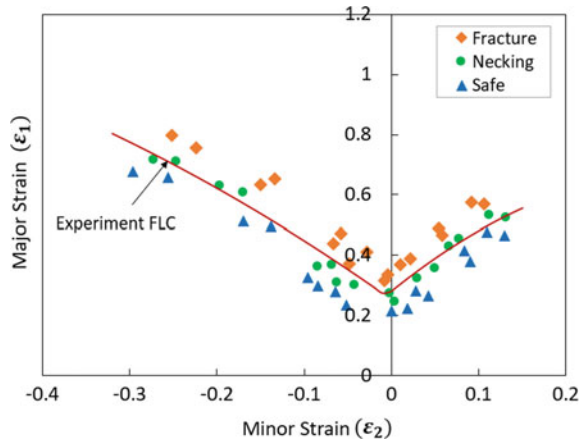
where: +  $d_0$ : original circle diameter

+  $\varepsilon$ : major strain ( $\varepsilon_1$ ) and minor strain ( $\varepsilon_2$ ).

+  $d$ : diameter in the direction of major and minor strain.

The measurement results of deformation points of the eight samples are shown in Fig. 5, and from these points a fitting curve as forming limit curve of the SECC sheet metal is constructed. The results show that, the samples (1–3) have deformation points located on the right side of the graph, and these points tend to deform uniformly

**Fig. 5** The FLC of SECC sheet metal is constructed from experimental data



in both directions. The sample 4 has strain points in the middle position and has flat deformation. The samples (5–8) have strain points on the left side of the graph and tend to have tensile strains. Experimental workpieces as shown in Fig. 4 show that the samples (1, 2, 6, 7) have fracture position tending to the bottom location, while the samples (3, 4, 5, 8) shows the fracture position at the middle of the workpiece.

#### 4 Application of the FLC in Simulation of Cylindrical Cup Stamping Process

In order to evaluate the accuracy of the FLC, the FLC data as Fig. 5 is used in simulating the cup-shaped stamping process with the stamping model as shown in Fig. 6. The resulting product's forming height in simulation is compared with the experimental results to measure the accuracy of FLC. In which, the simulation and experimental model are set up according to a previous study by the authors [9]. The workpiece of SECC material with a diameter of 150 mm is used in this research.

$$\Delta H_S(\%) = \frac{|H_S - H_E|}{H_E} \cdot 100\% \quad (2)$$

The deviation of fracture height between the simulation and experimental method is determined by the formula (2). The fracture height according to the simulation method is 42.86 mm and the experimental one is 41.7 mm. The result shows a good agreement between simulation and experiment with a deviation of 2.78% and are shown in Fig. 7.

**Fig. 6** The stamping mold model for cup-shape samples

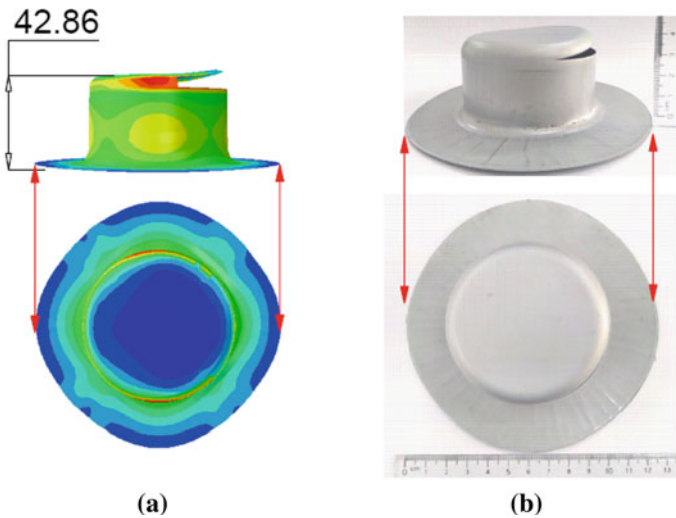
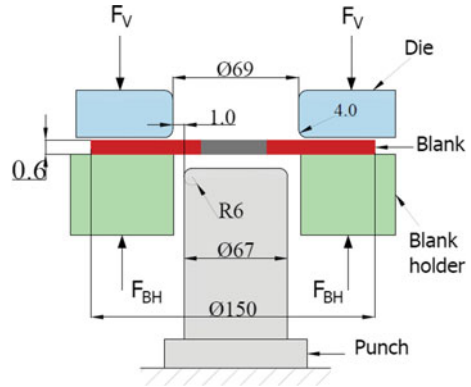


**Fig. 7** The forming height in simulation (a) and experiment (b)

## 5 Conclusion

In this study, to determine the FLC of SECC sheet metal by experiment, the stamping mold as the Nakazima model was designed and manufactured with 8 samples according to the standard. The FLC data of SECC material has been verified through numerical simulation of the stamping process of cylindrical cups. The results showed a good agreement on the fracture height between the simulation and experiment with a deviation of 2.78%.

## References

1. INTERNATIONAL and STANDARD, Metallic Materials Determination of Forming Limit Curves for Sheet and in the Laboratory, vol. 2021 (2021)
2. W. Volk, P. Hora, New algorithm for a robust user-independent evaluation of beginning instability for the experimental FLC determination. *Int. J. Mater. Form.* **4**(3), 339–346 (2011). <https://doi.org/10.1007/s12289-010-1012-9>
3. J. Min, T.B. Stoughton, J.E. Carsley, J. Lin, An improved curvature method of detecting the onset of localized necking in Marciniak tests and its extension to Nakazima tests. *Int. J. Mech. Sci.* **123**, 238–252 (2017). <https://doi.org/10.1016/j.ijmecsci.2017.02.011>
4. Z. Marciniak, K. Kuczyński, Limit strains in the processes of stretch-forming sheet metal. *Int. J. Mech. Sci.* **9**(9), 609–620 (1967). [https://doi.org/10.1016/0020-7403\(67\)90066-5](https://doi.org/10.1016/0020-7403(67)90066-5)
5. K. Inal, K.W. Neale, A. Aboutajeddine, Forming limit comparisons for FCC and BCC sheets. *Int. J. Plast.* **21**(6), 1255–1266 (2005). <https://doi.org/10.1016/j.ijplas.2004.08.001>
6. C.L. Chow, L.G. Yu, W.H. Tai, M.Y. Demeri, Prediction of forming limit diagrams for AL6111-T4 under non-proportional loading. *Int. J. Mech. Sci.* **43**(2), 471–486 (2001). [https://doi.org/10.1016/S0020-7403\(99\)00123-X](https://doi.org/10.1016/S0020-7403(99)00123-X)
7. P. Eyckens, A. Van Bael, P. Van Houtte, Marciniak-Kuczynski type modelling of the effect of through-thickness shear on the forming limits of sheet metal. *Int. J. Plast.* **25**(12), 2249–2268 (2009). <https://doi.org/10.1016/j.ijplas.2009.02.002>
8. F. Zhang, J. Chen, J. Chen, Effect of through-thickness normal stress on forming limits under Yld 2003 yield criterion and M–K model. *Int. J. Mech. Sci.* **89**, 92–100 (2014). <https://doi.org/10.1016/j.ijmecsci.2014.08.024>
9. T.T. Luyen, V.C. Tong, D.T. Nguyen, A simulation and experimental study on the deep drawing process of SPCC sheet using the graphical method. *Alexandria Eng. J.* **61**(3), 2472–2483 (2021). <https://doi.org/10.1016/j.aej.2021.07.009>
10. T.-T. Luyen, Q.-T. Pham, Y.-S. Kim, D.-T. Nguyen, Application/comparison study of a graphical method of forming limit curve estimation for DP590 steel sheets. *J. Korean Soc. Precis. Eng.* **36**(9), 883–890 (2019). <https://doi.org/10.7736/kspe.2019.36.9.883>
11. J. Noder, C. Butcher, A comparative investigation into the influence of the constitutive model on the prediction of in-plane formability for Nakazima and Marciniak tests. *Int. J. Mech. Sci.* **163**, 5138 (2019). <https://doi.org/10.1016/j.ijmecsci.2019.105138>
12. <https://www.cosasteel.com/secc-steel/>

# Investigation on the Influence of Obstacle Size in Path Planning by a Hybrid Model Combining an Improved A-star Algorithm and Digital Twin



Doan Thanh Xuan and Vu Toan Thang

**Abstract** The development of simulation technology has made it possible to create digital copies that are identical to a real system from geometry to dynamics. With reference to this, digital twin technology can help us determine the minimum collision-free distance between a robot and an obstacle on the virtual system, thereby planning the corresponding better path for the real system. In addition, the A-star algorithm was invented and many improvements were made to boost the efficiency of the original A\* path planning algorithm. The advanced method shows the first breakthrough about the local path planning between a goal node and a current node, which has been already planned for the following search in the region of a current node. The local path will be adopted directly if it is safe and collisionless. This method also shows the second breakthrough about the application of the post-processing stage for path planning optimization by aligning the local path to lower a number of local paths along with path length. In this study, a combination of digital twin and an improved A-star algorithm was used for planning the robotic path in a light bulb assembly production line. The influence of obstacle size was also evaluated in terms of the efficiency of either method (i.e. A-star algorithm and digital twin) to further enhance robotic path planning when applied in practice to a system with obstacles of different sizes.

**Keywords** Industrial robotics · A-star algorithm · Digital twin · Path planning · Hybrid model

## 1 Introduction

The aim of emerging the concept of Digital Twins (DT) is to help software users and developers be accessible on digital platforms to physical things and related data sources [1]. For comparable or partly coinciding concepts, the readers can refer to

---

D. T. Xuan · V. T. Thang (✉)

School of Mechanical Engineering, Hanoi University of Science and Technology, Hanoi, Vietnam  
e-mail: [thang.vutoan@hust.edu.vn](mailto:thang.vutoan@hust.edu.vn)

© The Author(s), under exclusive license to Springer Nature Switzerland AG 2024  
B. T. Long et al. (eds.), *Proceedings of the 3rd Annual International Conference on Material, Machines and Methods for Sustainable Development (MMMS2022)*, Lecture Notes in Mechanical Engineering, [https://doi.org/10.1007/978-3-031-57460-3\\_2](https://doi.org/10.1007/978-3-031-57460-3_2)

a series of terms such as digital counterpart, virtual twin, virtual object, product agent, and avatar [2]. A digital replica is a virtual representation that serves as a real-time digital replica of a process or a physical object. Although the concept had been proposed before (by Michael Grieves at first and in 2002 by the University of Michigan), the term “a digital twin” was officially defined by NASA in 2010 for the enhancement of physical model simulation of a spacecraft [3]. Digital twin consists of three components: (i) an object or a physical system, which can be a device, a production line; (ii) a virtual model built from CAD files (computer aided design), an identical simulation of a physical device or system; (iii) a real-time communication connection between the physical system and the virtual system [4]. A\* (as “A-star”) is a graph traversal and path search algorithm, which is frequently employed in many fields of computer science owing to its absoluteness, optimality, and ideal efficiency [5].

## 2 Improved A\* Algorithm

In literature, the query phase of the probabilistic roadmap planner consists of the path planning relied on the improved A\* algorithm [6, 7]. There are two phases in the probabilistic roadmap planner i.e. a pre-processing one and a query one. In the former phase, a random generation of collisionless sampling points occurs in robotic configuration space. The local path planner then builds a collisionless path and a local safety between these points. To check possible collision and path validity, the plans are mapped to robotic joint space by the local path planner and this execution is done by joint space constraints (e.g. velocity, acceleration, and energy optimization). Local safety paths and collisionless sampling points are thus constituents of the probabilistic roadmap. In the latter phase, with the adoption of the improved A\* algorithm the constituted probabilistic roadmap planner searches and acquires a safe path for robotic movement connecting the initial node  $s$  (starting point) and the goal node  $g$  (ending point). There are two stages in the proposed improved A\* algorithm: the pre-processing one and the post-processing one [8].

## 3 Experiments

### 3.1 *The Physical Space*

Testing the proposed method was done for a high-skill preparation of a lamp assembly production line. We set up a station by mounting a Universal Robots’ UR3 on a stand placed on a table. This station works by receiving a sub-assembly from the preceding station, mounting additional parts on it and transferring it to the succeeding station. The UR3 robot lifts alternately a socket and a bulb to put in the punch hole. It is



followed by bringing light bulbs from the conveyor belt and placing sockets in the pallet. After lowering the stamping cylinder to create a force for sticking the socket to the bulb, the UR3 robot lifts and puts the finished product on the conveyor belt to transfer it to the warehouse.

### 3.2 The Digital Space

A simulation model (digital space in digital twin) is a dynamic environment built by incorporating 3D computer-aided design (CAD) objects into Tecnomatix Process Simulate software. Tao and Zhang [9] suggested that the virtual model consists of four layers, i.e. geometry (generating 3D CAD objects), physical location (position of CAD objects in the scene), behavior (robotic kinetics) and rules (sequence of an assembly process). Tecnomatix can import CAD data in JT (Jupiter Tessellation) format. TCP/IP protocol is used to connect real-time communication connection between a real robot and a virtual robot via Ethernet port. The “Live Mode” in Tecnomatix Process Simulate software is used to connect real and virtual robot. The digital twin of the UR3 robot was conceived, where every action in the real robot is instantly reflected in real time on the virtual robot.

## 4 Results

Consider the moving distance of the UR3 robot when it transports (i.e., picks up and places on) an assembled product (i.e., a bulb) from the punching hole to the conveyor belt for warehouse. The obstacle herein is the stamping cylinder. More obstacles are added when measuring the robotic moving time with the digital twin, A\* algorithm and improved A\* algorithm applied. Using digital twins for robotic path planning. Use the collision detection feature in Technomatix software to find a suitable path for robotic movement. According to [10], the robotic path planning was found by the digital twin method as shown in Fig. 1. Durations for robotic movement corresponding to the acceleration speed 500–800–1200 mm/s<sup>2</sup> and the velocity speed 250–500 mm/s at 50-mm/s steps are displayed in the following Table 1.

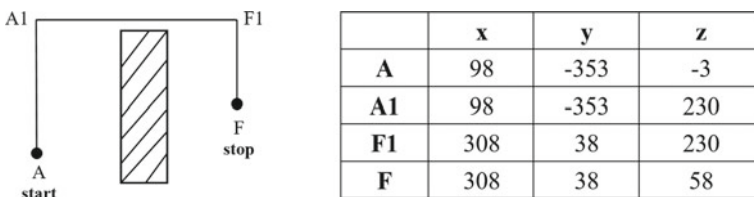


Fig. 1 Robotic path found by the digital twin method

**Table 1** Durations for robotic movement according to AA1F1F

A = 500 mm/s <sup>2</sup>		A = 800 mm/s <sup>2</sup>		A = 1200 mm/s <sup>2</sup>	
V (mm/s)	AA1F1F duration (s)	V (mm/s)	AA1F1F duration (s)	V (mm/s)	AA1F1F duration (s)
250	4.896	250	4.336	250	4.024
300	4.632	300	3.952	300	3.584
350	4.504	350	3.736	350	3.304
400	4.448	400	3.624	400	3.128
450	4.424	450	3.552	450	3.016
500	4.424	500	3.52	500	2.944

**Case 1**

Case 1A: Using the original A\* algorithm, the robotic path planning was shown in Fig. 2 (in the left side) as ABCDEF; according to [10], we have the following data (Table 2).

Case 1B: Using the A\* improved algorithm for robotic path planning, we have the robotic path as ACDF (Fig. 2 in the middle position). This path is 6-points shorter than that obtained by the original A\* algorithm. We have the durations for robotic movement obtained by the improved A\* algorithm in Table 2.

**Case 2:** The improved A\* algorithm with the addition of obstacles of the same height.

Case 2A: adding a 30-mm width obstacle with the same height (Fig. 3 in the left side). Case 2B: adding a 50-mm width obstacle with the same height (Fig. 3 in the middle position), we have the results in Table 2.

**Case 3:** The improved A\* algorithm with placing consecutively pairs of obstacles 1–2 (case 3A), 3–4 (case 3B), 5–6 (case 3C) in a 50-mm decreasing order of height as shown in Fig. 4, we have the results in Table 3.

Measuring the duration for robotic movement with an increasing number of passing points from D3 to D8, we have the results in Table 3.

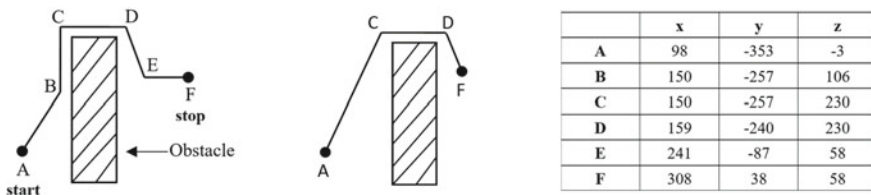


**Fig. 2** Robotic path found by the c A\* algorithm (the left side) and by the improved A\* algorithm (the middle position), coordinate parameters (the right side)

**Table 2** Coordinate parameters and durations for robotic movement according to ABCDEF (case 1A), ACDF (case 1B), ACDIF (case 2A) and ACD2F (case 2B)

A (mm/ s <sup>2</sup> )	V (mm/ s)	ABCDEF-duration (s)	ABCDEF-%	ACDF-duration (s)	ACDF-%	ACDIF-duration (s)	ACDIF-%	ACD2F-duration (s)	ACD2F-%	
500	250	4.808	- 1.80	3.856	- 21.24	3.992	- 18.46	4.056	- 17.16	
	300	4.664	0.69	3.64	- 21.42	3.8	- 17.96	3.88	- 16.23	
	350	4.648	3.20	3.56	- 20.96	3.72	- 17.41	3.816	- 15.28	
	400	4.648	4.50	3.52	- 20.86	3.696	- 16.91	3.8	- 14.57	
	450	4.656	5.24	3.52	- 20.43	3.696	- 16.46	3.8	- 14.10	
	500	4.648	5.06	3.52	- 20.43	3.704	- 16.27	3.808	- 13.92	
	800	250	4.024	- 7.20	3.4	- 21.59	3.488	- 19.56	3.52	- 18.82
		300	3.824	- 3.24	3.112	- 21.26	3.216	- 18.62	3.264	- 17.41
		350	3.704	- 0.86	2.952	- 20.99	3.064	- 17.99	3.12	- 16.49
		400	3.68	1.55	2.856	- 21.19	2.976	- 17.88	3.048	- 15.89
450		3.68	3.60	2.8	- 21.17	2.936	- 17.34	3.008	- 15.32	
1200	500	3.688	4.77	2.792	- 20.68	2.928	- 16.82	3.008	- 14.55	
	250	3.544	- 11.93	3.136	- 22.07	3.184	- 20.87	3.208	- 20.28	
	300	3.304	- 7.81	2.808	- 21.65	2.88	- 19.64	2.904	- 18.97	
	350	3.144	- 4.84	2.6	- 21.31	2.68	- 18.89	2.712	- 17.92	
	400	3.048	- 2.56	2.456	- 21.48	2.552	- 18.41	2.6	- 16.88	
Mean	450	3.024	0.27	2.368	- 21.49	2.472	- 18.04	2.52	- 16.45	
	500	3.008	2.17	2.32	- 21.20	2.424	- 17.66	2.48	- 15.76	
							- 18.07		- 16.44	

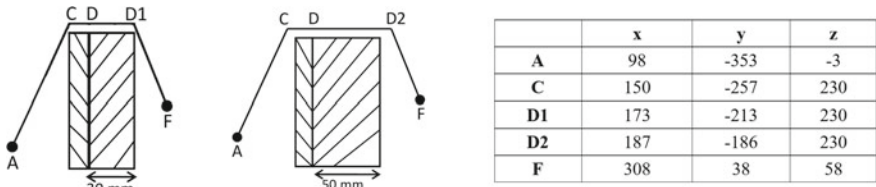


**Fig. 3** Robotic path found by the improved A\* algorithm when a 30-mm obstacle added (in the left side); Robotic path found by the improved A\* algorithm when a 50-mm obstacle added (in the middle position); coordinate parameters (in the right side)

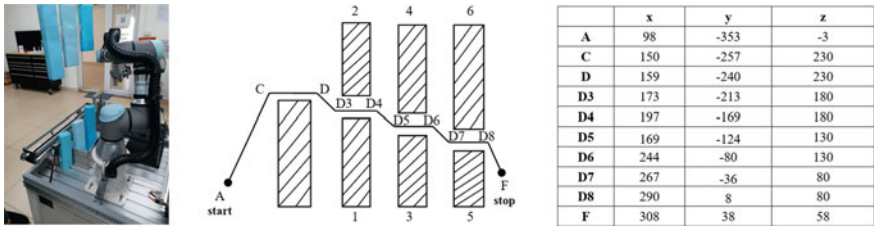


**Fig. 4** Real image of the pairs of obstacles (in the left side); Representation of the pairs of obstacles (in the middle position); coordinate parameters (in the right side)

## 5 Discussion

Consider Case 1 when the A\* algorithm (1A) and improved A\* algorithm (1B) were used. In case 1A, it is shown that the robotic moving time could be shorter or longer when A\* algorithm used in place of digital twin (Table 2). It obviously means that the A\* algorithm is not always better than the digital twin method. We see that in the case of a few obstacles, the duration for robotic movement obtained by the improved A\* algorithm is smaller than that obtained by digital twin method. In contrast, in case 1B the improved A\* algorithm is always better than digital twin method. Consider Case 2 when obstacles with constant height (case 2A: an obstacle with 30-mm larger in width and case 2B: an obstacle with 50-mm larger in width) were added. The improved A\* algorithm reduced the average robotic moving time by  $-18.07\%$  and  $-16.44\%$ , respectively (Table 2). Consider Case 3 when obstacles with varying dimensions were added in pair. It is shown that for obstacles with  $< 50$  mm in height. The improved A\* algorithm using increased the robotic moving time in most cases. In case 3, when the number of obstacles increases with varying heights, leading to an increase in the number of passing points. In Table 3, for case 3A the duration for robotic movement obtained by digital twin method is getting shorter with speeds of 350 mm/s and acceleration of 800 mm/s<sup>2</sup> ( $-0.43\%$ ). When the obstacles 3–4 with  $< 50$  mm in height were added (case 3B), the A\* algorithm using increased the robotic moving time over the range of velocity and acceleration under study (the average robotic moving time is 23.9%). When the obstacles 5–6 with  $< 50$  mm in height were

**Table 3** Durations for robotic movement when more pairs of obstacles added in a 50-mm decreasing order of height

A	V (mm/ s <sup>2</sup> )	ACDD3D4F-duration (s)	ACDD3D4F-%	ACDD3D4D5D6F-duration (s)	ACDD3D4D5D6F-%	ACDD3D4D5D6D7D8F-duration (s)	ACDD3D4D5D6D7D8F-%
500	250	4.792	- 2.12	5.944	21.41	6.792	38.73
	300	4.648	0.35	5.872	26.77	6.720	45.08
	350	4.6	2.13	5.848	29.84	6.696	48.67
	400	4.6	3.42	5.84	31.29	6.696	50.54
	450	4.6	3.98	5.84	32.01	6.696	51.36
	500	4.6	3.98	5.848	32.19	6.704	51.54
800	250	4.064	- 6.27	4.88	12.55	5.504	26.94
	300	3.84	- 2.83	4.728	19.64	5.392	36.44
	350	3.72	- 0.43	4.664	24.84	5.336	42.83
	400	3.656	0.88	4.632	27.81	5.304	46.36
	450	3.632	2.25	4.616	29.95	5.288	48.87
	500	3.64	3.41	4.624	31.36	5.296	50.45
1200	250	3.608	- 10.34	4.216	4.77	4.664	15.90
	300	3.344	- 6.70	4.008	11.83	4.512	25.89
	350	3.176	- 3.87	3.888	17.68	4.424	33.90
	400	3.08	- 1.53	3.824	22.25	4.376	39.90
	450	3.016	0.00	3.792	25.73	4.344	44.03
	500	2.984	1.36	3.776	28.26	4.328	47.01
Mean					23.90		41.36

also added (case 3C), the improved A\* algorithm using further increased the average robotic moving time by (the average robotic moving time is 41.36%). It implies that the digital twin method is better than the improved A\* algorithm when obstacles with varying heights used; whereas the reverse is true when obstacles with constant height used.

## 6 Conclusion

In this study, the experiments have been performed to find robotic path with a difference in size and number of obstacles. Our results show that the applicability of improved A\* algorithm and digital twin method is dependent upon the robotic speed, acceleration, and number of passing points. Although the improved A\* algorithm is always better than the digital twin method in terms of shortening robotic moving distance, the influence of robotic velocity and acceleration on its inertia when changing direction of movement must be taken into account. It results in the fact that the robotic moving time could get shorter by the improved A\* algorithm in the case of adding obstacles with constant height or by the digital twin method in the case of adding obstacles with varying heights. Thus, the application of a robotic path planning method needs to adapt to the characteristics and a number of obstacles in reality.

## References

1. H. Laaki, Y. Miche, K. Tammi, Prototyping a digital twin for real time remote control over mobile networks: application of remote surgery. *IEEE Access* **7**, 20325–20336 (2019)
2. J. Autiosalo, Platform for industrial Internet and digital twin focused education, research, and innovation: ilmatar the overhead crane, in *Proceedings of the IEEE 4th World Forum Internet Things (WF-IoT)* (2018), pp. 241–244
3. E. Negri, A review of the roles of digital twin in CPS-based production systems. *Proced. Manuf.* **11**, 939–948 (2017)
4. E. Glaessgen, D. Starge, The digital twin paradigm for future NASA and U.S. air force vehicles, in *Proceedings of the 53rd AIAA/ASME/ASCE/AHS/ASC Structural Structure Dynamic in Materials Conference, Honolulu, HI, USA* (2012). <https://doi.org/10.2514/6.2012-1818>
5. S. Russell, P. Norvig, *Artificial Intelligence a Modern Approach*, 4th edn. (Pearson, Boston, 2021)
6. G. Sánchez, J.C. Latombe, On delaying collision checking in PRM planning: application to multi-robot coordination. *Int. J. Robot. Res.* **21**(1), 5–26 (2002)
7. C.M. Clark, Probabilistic road map sampling strategies for multi-robot motion planning. *Robot. Auton. Syst.* **53**, 244–264 (2005)
8. B. Fu, L. Chen, Y. Zhou, D. Zheng, Z. Wei, J. Dai, H. Pan, An simproved A\* algorithm for the industrial robot path planning with high success rate and short length. *Robot. Auton. Syst.* **106**, 26–37 (2018)

9. F. Tao, M. Zhang. Digital twin shop-floor: a new shop-floor paradigm towards smart manufacturing. *IEEE Access* **5**, 20418–20427 (2017)
10. Xuan DT, Nam LG, Viet DT, Thang VT (2022) A-star algorithm for robot path planning based on digital twin, in *RCTEMME 2021, LNME*, eds. by A.-T. Le et al., pp. 83–90. [https://doi.org/10.1007/978-981-19-1968-8\\_8](https://doi.org/10.1007/978-981-19-1968-8_8)

# Design and Control of Waterbomb Robot



Thai Phuong Thao and Nguyen Ngoc Hai

**Abstract** Transformable robot nowadays plays an important role in our society as its convenience and application. In this research, a new transformable robot that inspired from the origami pattern is transformable and portable: Waterbomb robot. Waterbomb is a traditional pattern in origami and is applied broadly in technology. This pattern is multiple degree of freedom, however, with symmetrical pattern, it reduces to one. This robot can change shapes between a box shape into 2D configuration by one action. Hence, only one motor is enough to transforming the different shapes of robot, then the robot satisfies the requirement of lightweight and portability. This paper solves the kinematic and dynamic problem of waterbomb linkages and robot's motion is illustrated by MATLAB.

**Keywords** Origami technology · Waterbomb · Transformable robot

## 1 Introduction

Waterbomb is a well-known origami pattern and has various applications, as origami stent [1], worm robot and transformable wheel robot [2]. The waterbomb pattern is often folded on normal paper sheets with zero thickness, just like other origami patterns. Nonetheless, in origami technology with thick panels, the thickness of the folding pattern is considered. There are different solutions for this problem. For example, tapered surfaces were used to fold thick Miura-ori sheet [3], meanwhile in the other, authors created offsets at the edge of the panels to fold thick panels that is used for folding the square-twist origami pattern [4]. Recently, the approach of replacing folds with two parallel ones to manage the thickness of materials has been introduced [5]. In all of the above methods, the origami pattern is considered as a linkage with spherical joints, then the kinematic analysis was carried out. In this paper, the authors of this paper have also introduced an approach in which the

---

T. P. Thao (✉) · N. N. Hai

School of Mechanical Engineering, Hanoi University of Science and Technology, Hanoi, Vietnam  
e-mail: [thao.thaiphuong@hust.edu.vn](mailto:thao.thaiphuong@hust.edu.vn)



creasing are considered as hinges, therefore the fold lines are on the first or the last layer of thick panels due to the mountain or valley folds. As a results, the folding pattern is replaced by a mechanical linkages connected by hinges.

From view of rigid origami, This pattern is multiple degree of freedom, however, with symmetrical pattern, it reduces to one. With this advantage, this paper proposes a new robot that is created: Waterbomb Mobile Robot. This robot can change shapes between a box shape into 2D configuration by one action. Hence, only one motor is enough to transforming the different shapes of robot, then the robot satisfies the requirement of lightweight and portability.

Thre are 5 sections in this paper: The design of the transformable waterbomb robot is given in Sect. 2. The problems of kinematics and dynamics are solved in Sect. 3. Section 3.2 is the analysis of controlling for the waterbomb mobile robot, and the simulations of our concept is given in Sect. 4.

## 2 Design of Transformable Waterbomb Robot

### 2.1 Waterbomb Crease Pattern

Firstly, we consider a traditional waterbomb pattern made by six-crease bases (Fig. 1a). There are two kinds of vertices, valley and mountain vertices (called D and W) (Fig. 1b, c). The thick crease pattern around each kind of vertex is considered kinematically as a linkage, in which the creases are considered as revolute joints and rigid links are made to replace sheets between creases. The number of DOF of spherical 6R linkage is three, but when with the symmetric folding, this number is reduced to one [6].

The traditional waterbomb pattern can be folded with thick panels. The fold lines are placed on top or bottom surfaces of the panel in case of valley or mountain crease. Then, at the vertices of mountain or valley, sixfold-lines still appear, however, they

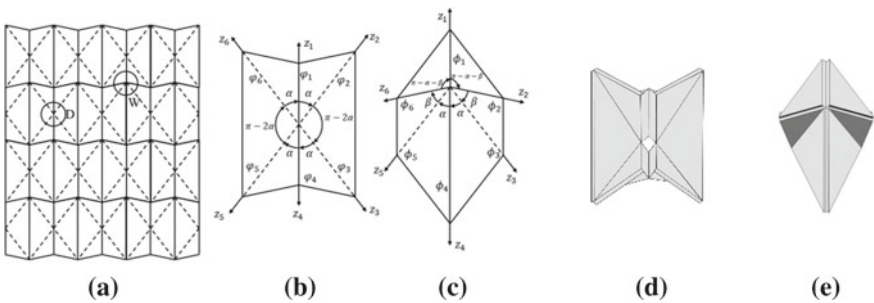


**Fig. 1** Waterbomb pattern. **a** The traditional pattern; **b** valley vertex; **c** mountain vertex; **d** valley vertex in thick panel; **e** mountain vertex in thick panel

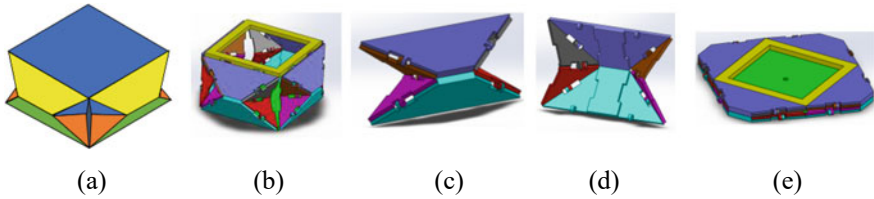


**Fig. 2** Design of waterbomb mobile robot. **a** The tessellation pattern of waterbomb robot, **b** the box structure of the robot; **c** the folding behaviour of one box side; **d** the inner structure of the box; **e** the flat mode of the box

are not intersected at one vertex any more. This means the distances between the adjacent fold lines exist. To analyze the kinematic properties, the spatial 6R linkage is used instead of the spherical 6R linkage. As shown in Fig. 1d and e, the valley and mountain creases are remained, the connection between the creases are almost like hinges.

## 2.2 Conceptual Design of Waterbomb Mobile Robot

Inspired from the Sarrus mobile robot [7] and the application of waterbomb pattern, the new model of box-shaped mobile robot has been created. The tessellation pattern of the robot is given as in Fig. 2a.

In Fig. 2a, there are 6 sides in the box-shaped model. This is a simplified model of waterbomb pattern, only the vertex D and its surrounding creases are used in the new robot model. There are 6 parts for one side of the model, the creases connecting each side with the origami rules [6] can help the model transform 3D shape into 2D shape easily. The thick structure is developed from the tessellation model, the connecting creases used in the thick model are hinges (Fig. 2b). The valley and mountain creases are remained as in the tessellation (Fig. 2c, d). However, the thickness of the big parts (purple and cyan parts) is designed double than 4 four sided parts (brown, pink, red and grey parts). The purpose of making bigger thickness is to create perfect flat shape in sleeping mode of the box shape (Fig. 2d, e).

## 3 Control of Transformable Waterbomb Robot

### 3.1 Kinematics and Kinetics of Waterbomb Mobile Robot

To analyze the kinematic relations of the model, we use Denavit–Hartenberg method. As the symmetric model, we consider only one side of the box. The panel 1 is the bottom part, other parts are numbered clockwise. The geometric parameters and the

joint angles are shown in Fig. 3a. The shapes of different folding way are given in Fig. 3b and c. Other D–H parameters are given in Fig. 3 and shown in Table 1.

Let  $q_i$  be the angle between part  $i$  and  $i + 1$ , therefore, with mountain crease:  $q_i = \pi - \theta_i$ , and with valley crease  $q_i = \pi + \theta_i$ . As the model is symmetric, then  $q_1 = q_6 = q_3 = q_4$ ;  $q_2 = q_5$ . The relation between  $q_1$  and  $q_2$  is given as following

$$\tan \frac{q_2}{2} = \sqrt{2} \tan \frac{q_1}{2} \quad (1)$$

As can be seen in the Fig. 3a, we can derive:

$$h = 2a \sin q_0 \Rightarrow AB = 2a \sin q_0 + 2.2b \cos q_0 \Rightarrow q_2 = 2q_0 \quad (2)$$

The position of mass center is determined as below:

$\mathbf{p}_{c_i}^0 = \mathbf{T}_{01} \mathbf{T}_{12} \dots \mathbf{T}_{i-1,i} = [x_{C_i}, y_{C_i}, z_{C_i}, 1]^T$ , in which  $\mathbf{T}_{ij}$  is the transformation matrix. Let  $\mathbf{r}_{C_i} = [x_{C_i} \ y_{C_i} \ z_{C_i}]$ ,  $\mathbf{q} = [q_0 \ q_1]^T$ .

The kinetic energy of 2 big plates is calculated as following:

$$2T = 2J_{big} \dot{q}_0^2 + \sum_{i=1,4} m_i \dot{\mathbf{r}}_{C_i}^T \dot{\mathbf{r}}_{C_i} = \dot{\mathbf{q}}^T \left( \sum_{i=1,4} m_i \mathbf{J}_{TC_i}^T \mathbf{J}_{TC_i} \right) \dot{\mathbf{q}} + \dot{\mathbf{q}}^T \begin{bmatrix} 2J_{big} & 0 \\ 0 & 0 \end{bmatrix} \dot{\mathbf{q}} \quad (3)$$

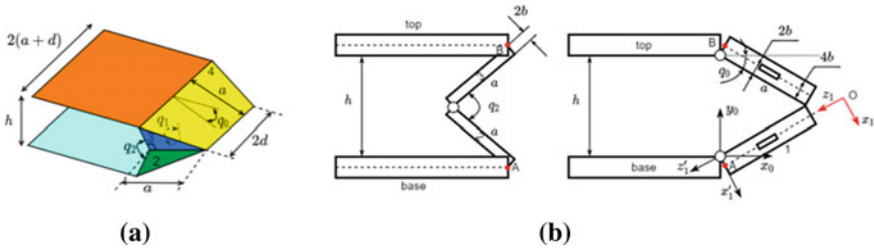


**Fig. 3** Kinematic model of the waterbomb robot. **a** The geometric parameters; **b** the kinematic model of one folding behavior; **c** the kinematic model of other folding behavior

**Table 1** Denavit–Hartenberg parameters of one side of the box-shaped mobile robot

Joint	$\theta_i$	$d_i$	$a_i$	$\alpha_i$
1	$\theta_1$	$d\sqrt{2}$	$2b$	$-\pi/4$
2	$-\theta_2$	0	$-2b$	$-\pi/4$
3	$\theta_3$	$-d\sqrt{2}$	0	$-\pi/2$
4	$\theta_4$	$d\sqrt{2}$	$2b$	$-\pi/4$
5	$-\theta_5$	0	$-2b$	$-\pi/4$
6	$\theta_6$	$-d\sqrt{2}$	0	$-\pi/2$

in which,  $J_{big}$  is the mass moment of inertia of 2 big plates around its shafts.

The kinetic energy of 4 small plates is calculated as following:

$$2T = \sum_{i=2,3,5,6} (m_i \dot{\mathbf{r}}_{Ci}^T \dot{\mathbf{r}}_{Ci} + \mathbf{w}_i^T \mathbf{I}_{Ci} \mathbf{w}_i) \quad (4)$$

with:  $\mathbf{w}_2 = [\omega_{x2}, \omega_{y2}, \omega_{z2}]$ ,  $\mathbf{w}_5 = [-\omega_{x2}, -\omega_{y2}, \omega_{z6}]$ ,  $\mathbf{w}_3 = [\omega_{x3}, \omega_{y3}, \omega_{z3}]$ ,  $\mathbf{w}_6 = [-\omega_{x3}, -\omega_{y3}, \omega_{z3}]$ .

$$\mathbf{I}_{C3} = \mathbf{I}_{C6} = \begin{bmatrix} J_1 & 0 & 0 \\ 0 & J_2 & 0 \\ 0 & 0 & J_3 \end{bmatrix}, \mathbf{I}_{C2} = \mathbf{I}_{C5} = \begin{bmatrix} J_1 & 0 & 0 \\ 0 & (J_2 + J_3)/2 & (J_3 - J_2)/2 \\ 0 & (J_3 - J_2)/2 & (J_2 + J_3)/2 \end{bmatrix} \quad (5)$$

Kinetic energy of 1 side of waterbomb model is derived as followings:

$$T = 0.5 \dot{\mathbf{q}}^T \left( \sum_{i=1,6} m_i \mathbf{J}_{T_{Ci}}^T \mathbf{J}_{T_{Ci}} + \begin{bmatrix} 2I_{big} & 0 \\ 0 & 0 \end{bmatrix} \right) + \sum_{i=2,3,5,6} \mathbf{J}_{Ri}^T \mathbf{I}_{Ci} \mathbf{J}_{Ri} \dot{\mathbf{q}} \quad (6)$$

$$\mathbf{M}_S(\mathbf{q}) = \sum_{i=1,6} m_i \mathbf{J}_{T_{Ci}}^T \mathbf{J}_{T_{Ci}} + \begin{bmatrix} 2I_{big} & 0 \\ 0 & 0 \end{bmatrix} + \sum_{i=2,3,5,6} \mathbf{J}_{Ri}^T \mathbf{I}_{Ci} \mathbf{J}_{Ri},$$

$$\Pi_S(\mathbf{q}) = g \sum_{i=1,6} m_i y_{Ci}; \mathbf{G}_S(\mathbf{q}) = \frac{\partial \Pi_S(\mathbf{q})}{\partial \mathbf{q}}$$

Similarly, we derive for the top part:

$$\mathbf{M}_t(\mathbf{q}) = m_t \begin{bmatrix} (2a \cos q_0 - 4b \sin q_0)^2 & 0 \\ 0 & 0 \end{bmatrix}, \mathbf{G}_t(\mathbf{q}) = m_t g \begin{bmatrix} 2a \cos q_0 - 4b \sin q_0 \\ 0 \end{bmatrix} \quad (7)$$

Then, we derive:  $\mathbf{M}(\mathbf{q}) = 2\mathbf{M}_S + \mathbf{M}_t$ ,  $\mathbf{G}(\mathbf{q}) = 2\mathbf{G}_S + \mathbf{G}_t$ .

The linkage equation is derived from (1).

$$\mathbf{A} = \left[ \tan^2 q_0 + 1 - \frac{\sqrt{2}}{2} (\tan^2 \frac{q_1}{2} + 1) \right], \quad \begin{aligned} &\Rightarrow \mathbf{A} \dot{\mathbf{q}} = 0 \\ &\Rightarrow \mathbf{A} \ddot{\mathbf{q}} + \dot{\mathbf{A}} \dot{\mathbf{q}} = 0 \end{aligned} \quad (8)$$

Then the equation of motion of the robot is derived:

$$\mathbf{M}(\mathbf{q}) \ddot{\mathbf{q}} + \mathbf{C}(\mathbf{q}, \dot{\mathbf{q}}) \dot{\mathbf{q}} + \mathbf{G}(\mathbf{q}) + \mathbf{A}^T \lambda = \mathbf{U}, \quad \mathbf{A} \ddot{\mathbf{q}} + \dot{\mathbf{A}} \dot{\mathbf{q}} = 0$$

From (9) we derive:

$$\dot{q}_1 = \frac{2\dot{q}_0(\tan^2 q_0 + 1)}{\sqrt{2}(\tan^2 q_0 + 1)},$$

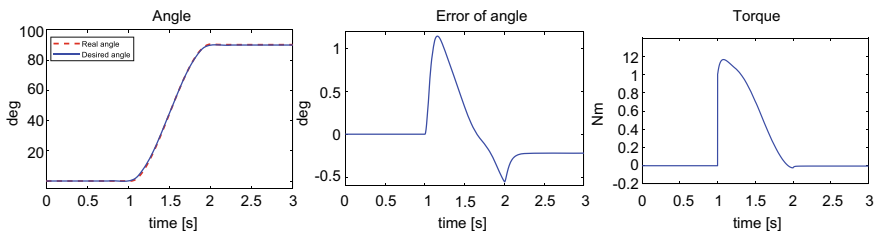


**Fig. 4** Results of PD controlling with trajectory. **a** Result of controlling angle; **b** error of angle during controlling time; **c** result of controlling torque

$$\ddot{q}_1 = \frac{2(\tan^2 q_0 + 1) \left( \begin{array}{c} \ddot{q}_0 \\ +2\dot{q}_0^2 \tan q_0 \end{array} \right) - \frac{\dot{q}_1^2}{2} \tan q_0 (\tan^2 q_0 + 2)}{\sqrt{2}(\tan^2 q_0 + 2)} \quad (9)$$

### 3.2 Control of Waterbomb Robot

The PD control torque is computed as followings:

$$U = M(q)(\ddot{q}_d + K_d \dot{e} + K_p e) + C(q, \dot{q})\dot{q} + G(q) \quad (10)$$

in which,  $e = q - q_d$ ,  $q_d$  is the desired angle. The motion of the desired angle is designed as followings:  $q_d(t) = 0.01 + 269.94(t - 1)^2 - 179.96(t - 1)^3$

The PD control parameters in simulation are given as follows:  $K_p = 900$ ,  $K_d = 60$ . The total mass of the model designed on SolidWorks is 1768 g, the area of the model at flat mode  $0.775 \cdot 10^6$  (mm<sup>2</sup>).

The results of this controllation is calculated in MATLAB [8] and given in Fig. 4. As can be seen in these figure, after 2 s, the constant trajectory is depicted in Fig. 4a. The error of controllation and the computed torque are illustrated in Fig. 4b and c. The figures show that these input actuation histories can be quite large when the gains are large. The reason why we choose the controllation trajectory is the quadratic equation as to form the 3D shape, if we choose the position equation, the singularity may occur and reduce the strength of the mechanism.

## 4 Conclusion

This research aims to apply a new mechanism inspired from origami pattern for mobile box-shaped robot to form 3D shape form from 2D model with only 1 motor. The kinematics and kinetics analysis are completed and applied in the problem of

controlling. The desired 3D shape of the mobile robot is formed after 3 s. The value of driving torque for forming the mechanism has been calculated. This calculation will be necessary for building the real model and future research. This mobile robot has various patterns, so the comparison should be improved and optimizing design is a problem that should be considered carefully.

**Acknowledgements** This research is funded by Hanoi University of Science and Technology (HUST) under project number T2021-SAHEP-010.

## References

1. K. Kuribayashi, K. Tsuchizya, Z. You, D. Tomus, M. Umemoto, T. Ito, M. Sasaki, Self-deployable origami stent grafts as a biomedical application of Ni-rich TiNi shape memory alloy foil. *Mater. Sci. Eng.* **419**(1–2), 131–137 (2006)
2. C.D. Onal, R.J. Wood, D. Rus, An origami-inspired approach to worm robots. *IEEE/ASME Trans. Mechatron.* **18**, 430–438 (2013)
3. T. Tachi, Rigid-foldable thick origami. *Origami* **5**, 253–264 (2011)
4. B.J. Edmondson, R.J. Lang, S.P. Magleby, L.L. Howell, An offset panel technique for thick rigidly foldable origami, in *ASME 5B, 38th Mechanisms and Robotics Conference* (2014)
5. J.S. Ku, E. Demaine, Folding flat crease patterns with thick materials. *J. Mech. Robot.* **8**(3), 031003 (2016)
6. Y. Chen, H. Feng, J. Ma, R. Peng, Z. You, Symmetric waterbomb origami. *Proc. R. Soc. A.* **472**, 20150846 (2016)
7. P.T. Thai, N.H. Nguyen, *Design and Control of a Double-Sarrus Mobile Robot, Mechanisms and Machine Science* (Springer, New York, 2021), p.113
8. <https://www.mathworks.com/help/matlab/>

# Analysis SUV Vehicle Structure in Car to Car Frontal Impact



Nguyen Phu Thuong Luu and Ly Hung Anh

**Abstract** This study provides an analysis of the structural characteristics of an SUV vehicle in the context of a frontal impact. The results of the analysis provide an indication of the deformation magnitude and the capacity of the SUV vehicle structure to absorb the energy of the collision. This paper examines the structural characteristics of an SUV vehicle in the context of a frontal impact. Through simulations of the SUV vehicle structure model colliding with an object at various speed levels, the analysis seeks to identify the frame structures that can absorb the most impact energy and minimize deformation, thus safeguarding the occupants of the vehicle. The results of this study indicate that the A-Pillars and the longitudinal need to be improved to ensure the safety of the passengers.

**Keywords** Analysis · Simulate · SUV · Vehicle structure · Frontal impact

## 1 Introduction

Statistics from the Traffic Police Department of the Ministry of Public Security [1] show that more than 45% of cases involve traffic accidents with passenger cars, taxis, and cars caused by trucks, resulting in 52.1% fatalities and 80.5% injuries. These

---

N. P. T. Luu (✉)

Faculty of Automotive Engineering, School of Technology, Van Lang University, Ho Chi Minh City, Vietnam

e-mail: [luu.npt@vlu.edu.vn](mailto:luu.npt@vlu.edu.vn)

Department of Automotive Engineering, Faculty of Engineering and Technology, Binh Duong Economics and Technology University, Binh Duong City, Vietnam

L. H. Anh

Department of Aerospace Engineering, Faculty of Transportation Engineering, Ho Chi Minh City University of Technology (HCMUT), 268 Ly Thuong Kiet Street, District 10, Ho Chi Minh City, Vietnam

Viet Nam National University Ho Chi Minh City, Linh Trung Ward, Thu Duc District, Ho Chi Minh City, Vietnam

particularly serious traffic accidents are mainly due to drivers' lack of awareness while driving or using a device. The collision process can deform the side of the sport utility vehicle (SUV), putting the occupants in danger. Accidents can be frontal, side, rear, or overturn.

According to US-NCAP (United States New Vehicle Assessment Program), a hard-wall frontal crash test at 64 km/h is same as a car head-on collision at 55 km/h [2]. Some crash studies in Japan show that a head-on collision between two cars with a speed of 48.4–68.6 km/h is considered a speed hazard [3]. In a head-on collision, the height of the chassis greatly affects the deformation of the chassis [4]. The research [5] demonstrates that the impact force is divided, with half being taken up by the chassis and the other half spread across the engine and other parts.

The Insurance Institute for Highway Safety (IIHS) reported that SUVs with a Unibody frame decreasing the mortality risk by 18% compared to Body-on-frame vehicles [6], and that head-on collisions had a 51% risk of death [7]. Additionally, crash tests were conducted to measure the small overlapping collisions that occurred between 120 and 150 ms [8], and a simulated test of a collision between two SUVs and a sedan was conducted by adjusting the height, which resulted in different overlap rates [9].

This paper focuses on crash simulation and analysis of the deformation and collision absorption capacity of the vehicle sidewall. SUV is a sport utility vehicle with a larger size and payload than other large cars, built and simulated entirely on LS-DYNA software [10], in order to analyze and check problems [11, 12].

## 2 The Foundation of Collision Theory

When two moving cars collide with each other (collision at the center), an amount will appear, this is called a quantity and point. Energy and point depend on crash speed, chassis structure and vehicle design structure. With a constant speed, the maximum amount of energy and points when connecting the frame and making the material of absolute rigidity. However, when two vehicles collide, the structure and material manufacture are damaged and absorb some energy. This energy is known as absorbed energy.

Assume that two vehicles are moving on one coordinate axis  $Ox$  (Fig. 1).

$v_1$  is the car 1 speed

$v_2$  is the car 2 speed.

$p$  is the pre-crash relative velocity.

$p'$  is the post-crash relative velocity.

Based on Newton's second law, vehicle A and vehicle B interact with each other by applying forces on each other. These forces are known as relative forces and are equal in magnitude and opposite in direction. The force between car A and car B is denoted as  $F$  and it acts over a specific time interval from  $t$  to  $t'$ . In other words, the



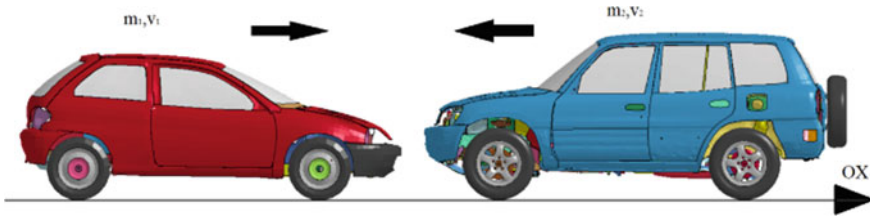


Fig. 1 Two vehicles are moving on one coordinate axis OX

force exerted by vehicle A on vehicle B is equal to the force exerted by vehicle B on vehicle A.

Where:  $t$  is the starting crash time.  
 $t'$  is the end time of crash.  
 Then impulses will be created:

$$I = \int_t^{t'} F(t)dt \tag{1}$$

where:  $I$  is the linear pulse

$F$  is the crash force.

Utilize the concepts of linear impulse and angular momentum to analyze the vehicles pre-crash and post-crash:

$$m_1v_1 - I = m_1v_1' \tag{2}$$

$$m_2v_2 + I = m_2v_2' \tag{3}$$

where:  $v_1, v_2$  are the starting velocities of vehicle A and B,

$v_1', v_2'$  are the post-crash speeds of vehicle A and B.

According to pre-crash and post-crash the conservation of kinetic energy as shown below:

$$\frac{m_1}{2}v_1^2 + m_2v_2 = \frac{m_1}{2}v_1'^2 + \frac{m_2}{2}v_2'^2 + \Delta E \tag{4}$$

From Eqs. (2), (3) and Eq. (4), we rewrite:

$$\frac{m_1}{2}(v_1 - v_1')(v_1 + v_1') = \frac{m_2}{2}(v_2 - v_2')(v_2 + v_2') + \Delta E' \tag{5}$$

From Eqs. (2), (3) and Eq. (4), we rewrite:

$$\frac{I}{2}(v_1 + v_1') = \frac{I}{2}(v_2 + v_2') + \Delta E' \tag{6}$$

**Fig. 2** The height of Car Frame S shape on Toyota RAV4

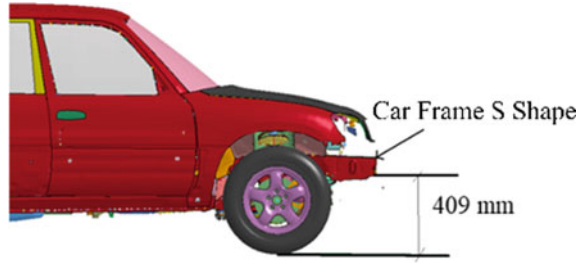


**Table 1** Specifications of Toyota RAV4

Toyota RAV4	
Wheelbase	2410 (mm)
Width	1695 (mm)
Height	1660 (mm)

$$\Rightarrow \Delta E' = \frac{I}{2} [(v_1 - v_2) + (v_1' - v_2')] \tag{7}$$

$$\Rightarrow \Delta E' = \frac{I}{2} (p + p') \tag{8}$$

### 3 Analysis of Frame Structure

The Toyota RAV4 series, an SUV with a Unibody frame, was employed as the model for the study. The National Center for Incident Analysis (NCAC) utilized reverse engineering to construct a finite element (FE) model of the Toyota RAV4 (Fig. 2) based on its actual specifications (Table 1) and assessed by the US National Highway Traffic Safety Administration (NHTSA). The model was then tested in a crash simulation at 64 km/h with a solid barrier, which was enabled by the modeling aspect of the research.

### 4 Simulation

As previously discussed, there are two widely used types of frames for SUVs: Unibody and Body-on-frame. As a result, crashes at 55 km/h will be calculated in this study using 100% frontal collisions in accordance with NHSTA and IIHS guidelines. Create a crash simulation between car A (blue) and car B (red) to find the SUVs weakness areas. For Unibody chassis on Toyota RAV4 examples, adjustment

of two crash models to a frontal collision is displayed [13]. The last case examines the deformation of both types of frames during impact. Set up a simulation using the LS-DYNA software with three collision scenarios (Fig. 3).

Case 1: Simulation of the finite element model (FE) between two Toyota Rav4 (SUV) vehicles in head-on collision with the same speed of 55 km/h, the model is taken from NHSTA and tested according to NCAC, simulating both vehicles collided with a speed of 55 km/h and the collision process on the LS-DYNA software (Fig. 4).

The process in Case 1 shows that both cars collide at the same speed, the chassis at this time is pinched inward and bent at the S position at 65–100 ms. Due to the large volume of the collision, the rear body was pushed up, causing the front of the vehicle to face down, and the frame was found to be bent in the downward direction.

Case 2: Simulation of the finite element model (FE) between two Toyota Rav4 (SUV) cars in 100% head-on collision, car A (blue) moving at 55 km/h and car B

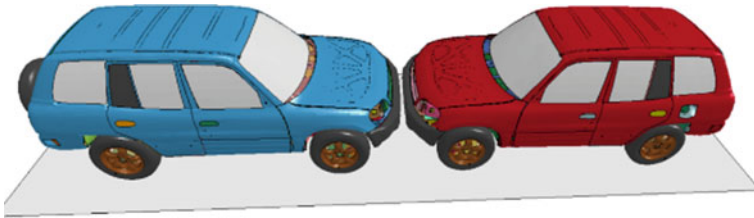


Fig. 3 Simulation of a head-to-head collision between two Toyota Rav4 (SUV) vehicles

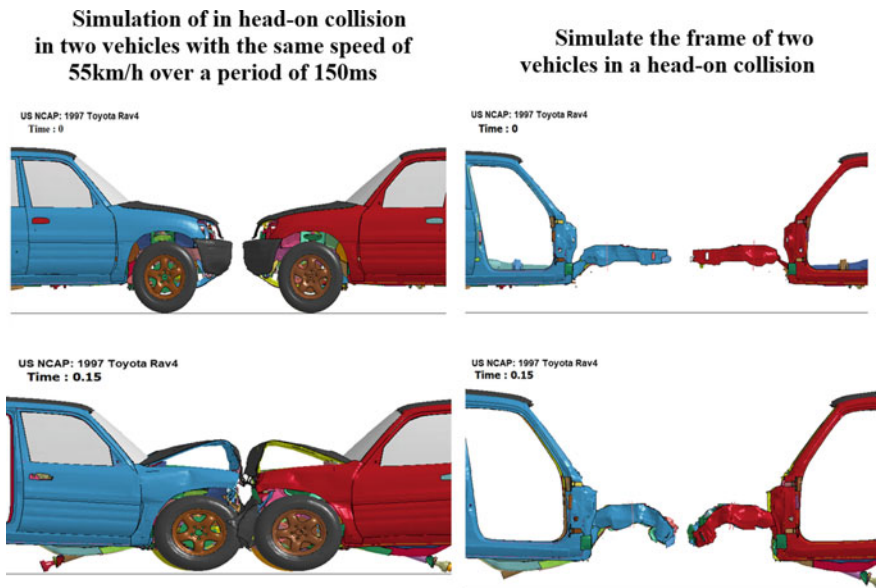


Fig. 4 The simulation a collision between two SUVs at the speed of 55 km/h

(color red) is stationary, simulating both the frontal collision and the collision process on the LS-DYNA software (Fig. 5).

The collision process in Case 2 of a direct collision between vehicle A with a speed of 55 km/h and vehicle B at rest shows that the elements of the front chassis of vehicle A are less deformed, showing that when the collision occurs collision with a stationary vehicle of similar height.

Case 3: Simulation of finite element (FE) between two Toyota Rav4 (SUV) frontal collision 40%, both cars collide at the same speed of 55 km/h, model is taken from NHSTA and tested according to NCAC, simulate both frontal collision (Fig. 6) and crash process on LS-DYNA software (Fig. 7).

Through all 3 cases, it was found that the Toyota Rav4 chassis was pinched if it collided with a vehicle with a horizontal frame size or larger, in Case 3, both the frame and the body were compressed quite a bit. In case of 100% head-on collision at the

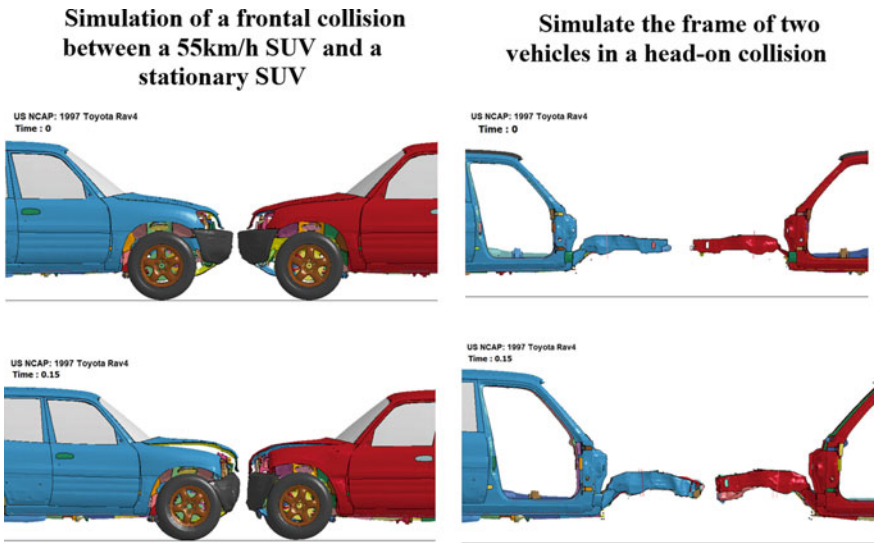
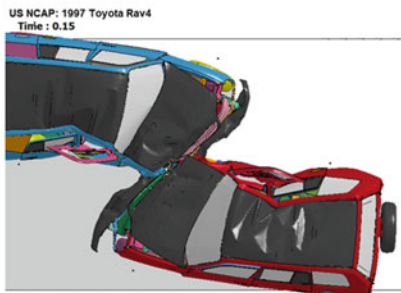
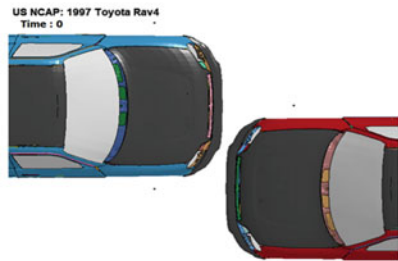


Fig. 5 The simulation a collision between two SUVs with different speeds

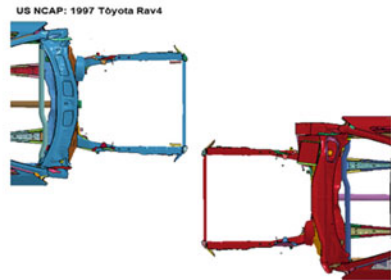


Fig. 6 Simulation of a collision between two SUVs with a 40% deviation

**Simulation of a frontal collision between two vehicles with the same speed of 55km/h for a period of 150ms (Topview)**



**Simulation of two vehicle skeletons in frontal collision 40% (Topview)**



**Fig. 7** The simulated collision process between two SUVs collides with a 40% deviation at a speed of 55 km/h

same or different speeds, the safety of the driver and occupants in the vehicle is still ensured in Case 1 and Case 2. But in Case 3, it is noticed if the collision is deflected. 40% leads to deformation of both the chassis and the passenger compartment (Fig. 7), endangering the occupants on the impact side and the rear passengers.

## 5 Conclusion

In this study, the finite element model (FE), which shows the deformation of the chassis structure of the SUV, uses the unibody frame type on the LS-DYNA software. The car has not yet shown full crash compatibility. Frontal crash simulation focuses on the front frame to improve inadequate energy absorption, while too much penetration into the dashboard easily injures the front occupants. Simulation results only when the collision at the same speed finds that the front frame of the vehicle is bent and pressed inward at the connection position between the frame and the passenger compartment. In a crash simulation that was not representative of actual conditions, the passenger compartment was observed to suffer significant deformation, thus posing a risk to the safety of the passengers. Consequently, it is imperative that the safety features of

SUVs be enhanced in order to guarantee the protection of the driver and passengers in the event of a collision.

**Acknowledgements** The authors express their gratitude to Van Lang University in Vietnam for their invaluable contribution in financing this study.

## References

1. N.P.T. Luu, L.H. Anh, A study on small vehicle structure in rear under-ride impact by using a CAE based methodology. *J. Eng. Technol. Sci.* **54**(5), 1018–1035 (2022)
2. C.A. Hobbs, P.J. McDonough, *Development of the European New Car Assessment Programme (Euro Ncap)*, Transport Research Laboratory United Kingdom Paper Number S11-10-06 (1998)
3. K. Mizuno, J. Kajzer, Compatibility problems in frontal, side, single car collisions and car-to-pedestrian accidents in Japan. *Accid. Anal. Prevent.* **31**, 381–391 (1999)
4. B.C. Baker, J.M. Nolan, B. O’Neill, A.P. Genetos, Crash compatibility between cars and light trucks: benefits of lowering front-end energy-absorbing structure in SUVs and pickups. *Accid. Anal. Prevent.* **40**, 116–125 (2008)
5. W.J. Witteman, *Improved Vehicle Crashworthiness Design by Control of the Energy Absorption for Different Collision Situations* (Technische Universiteit Eindhoven, Eindhoven, 1999)
6. E.M. Ossiander, T.D. Koepsell, B. McKnight, Crash fatality risk and unibody versus body-on-frame structure in SUVs. *Accid. Anal. Prevent.* **70**, 267–272 (2014)
7. S.-W. Hong, C.-K. Park, P. Mohan, R.M. Morgan, C.-D. Kan, K. Lee, et al., *A Study of the IIHS Frontal Pole Impact Test*. SAE Technical Paper Series (2008)
8. C.P. Sherwood, B.C. Mueller, J.M. Nolan, D.S. Zuby, A.K. Lund, Development of a frontal small overlap crashworthiness evaluation test. *Traffic Inj. Prevent.* **14**, S128–S135 (2013)
9. G. Li, J. Yang, Influence of vehicle front structure on compatibility of passenger car-to-SUV frontal crash, in *Third International Conference on Digital Manufacturing and Automation* (2012)
10. J.O. Hallquist, *LS-DYNA Keyword User Manual*, Livermore Software Technology Corporation (2007)
11. P.T.L. Nguyen et al., Analysis of vehicle structural performance during small overlap frontal impact. *IJAT* **16**, 799–805 (2015)
12. P.T.L. Nguyen et al., A study on optimal design of vehicles structure for improving small overlap rating. *IJAT* **16**, 959–965 (2015)
13. D. Marzougui, R.R. Samaha, F. Tahan, C. Cui, C.-D. Kan, *Finite Element Model of Toyota Rav 4. (FHWA/NHTSA) National Crash Analysis Center*

# A New Method to Extend the Measurement Range of a Displacement Measuring Interferometer by Measuring the Modulation Depth



Hoang Anh Tú, Hoang Trung Kien, Vu Thanh Tùng, Dong Xuan Hieu, Nguyen Thanh Dong, and Vu Van Quang

**Abstract** Laser interferometers are widely used for sub-micrometer accuracy of measurements. However, conventional interferometers (homodyne and heterodyne interferometers) can be used to measure the displacement only. Therefore, the measurement signal must be continuous during the measurement process. This is difficult for a long measurement range with the presence of vibrations, misalignment of the optics, and tolerance of sliders. In this paper, a method of retrieving the absolute distance of the measured object by determining the modulation depth was proposed and demonstrated. This was the unique feature of the frequency-modulated interferometer. The modulation index is a function of the modulation excursion, modulation frequency, and the unbalanced length between the two arms of the interferometer. On the other hand, the modulation index can be determined through the Bessel function. Therefore, the absolute position of the target at special values of the modulation depth can be determined. These positions were utilized as markers on the scale to divide a large measuring range into small measuring ranges while ensuring the continuity of the system. Therefore, the proposed method can extend the measuring range of the interferometer even under the influence of vibrations or misalignment systems.

**Keywords** Modulation depth · Laser interferometer · Displacement measurement · Frequency modulated interferometer

---

H. A. Tú · V. T. Tùng (✉) · D. X. Hieu · N. T. Dong · V. Van Quang  
School of Mechanical Engineering, Hanoi University of Science and Technology, No. 1, Dai Co Viet, Hanoi, Vietnam  
e-mail: [tung.vuthanh@hust.edu.vn](mailto:tung.vuthanh@hust.edu.vn)

H. T. Kien  
National Research Institute of Mechanical Engineering, Ministry of Industry and Trade, Hanoi, Vietnam

© The Author(s), under exclusive license to Springer Nature Switzerland AG 2024  
B. T. Long et al. (eds.), *Proceedings of the 3rd Annual International Conference on Material, Machines and Methods for Sustainable Development (MMMS2022)*, Lecture Notes in Mechanical Engineering, [https://doi.org/10.1007/978-3-031-57460-3\\_5](https://doi.org/10.1007/978-3-031-57460-3_5)

## 1 Introduction

Nowadays, ultra-precision machining plays a significant role that belongs with new machining technologies, especially CNC machining centers still account for a considerable proportion of modern machining methods. Therefore, the accuracy of mechanical machining is improved by using CNC machining centers which is always a key direction with many innovative research problems have been conducted [1, 2]. Machining accuracy is fully controlled by drive systems and standard linear translation stages. The accuracy of the standard stage depends on the driven system including shape deviation (straightness, flatness), relative position deviation (parallelism, perpendicularity), and the accuracy of displacement [3, 4]. In working conditions, shear force, friction, and temperature deform material reduce the accuracy of the linear guided stage, so the standard guided stage must be carefully inspected and calibrated. The challenge from the standard measurement system of machining centers or machine tools highly requires accuracy in an enormous range of measurements, under the influence of vibrations from the measuring environment, and a large measuring speed. The precision of mechanical machining is increasing rapidly which makes huge challenges and motivates the field of measurement and calibration. Research articles in this field are diverse, new displacement encoders can achieve the nano-level of accuracy and are less dependent on environmental changes (temperature, refractive index) [5–7]. However, the disadvantage of an encoder that the measuring range is always smaller than the encoder geometrical size. The larger encoder is the more difficult it makes when integrated into a mechanical machining system. In contrast, capacitive sensors are often used in the small displacement range [8–10]. A capacitive sensor has a high resolution, 1 nm/1  $\mu\text{m}$  in measuring range, but the measuring range is small ( $< \pm 3$  mm) and does not suitable for large displacement systems of machine tools, and machining centers. The two-frequency interferometer can achieve 1 nm resolution in an extensive range of measurements [11–15]. The limitation due to this method that system is quite large, is difficult to install in a machining system, and is sensitive to noise and expensive. Currently, we developed a frequency-modulated semiconductor laser to overcome the above disadvantages [16–18].

In this study, the laser diode allows frequency modulation through direct injection current modulation. In the evaluated system, the standard linear stage was calibrated carefully using a laser interferometer. The modulation amplitude was actively controlled so that achieving the high quality of component harmonic signal in different measuring ranges, the influence of vibration and the change from the environmental refractive index was eliminated by the flexible frequency filter. The measurement speed of the system was enhanced by using a higher modulation frequency for the semiconductor laser by modulating the direct injection current of the laser diode. The new idea from this research is the ability to retrieve the absolute distance of the measured object. Therefore, the measurement signal must be continuous and interrupted free. This is difficult to complete in working conditions of machining centers which require a large displacement range, strong vibrations, and



misalignment of the linear guided stage in the drive system, which easily leads to loss of interference signals. In the frequency modulated interferometer, the modulation index is a function of modulated amplitude, modulated frequency, and the difference between the two arms of the interferometer. In addition, the modulation index can be determined by using the Bessel function. In this study, the method of determining the absolute position of measuring objects at critical values of modulation depth was proposed. These known positions function as marker points on the scale. These points were used to divide the large measuring range into small measuring ranges while ensuring the continuity of the measuring system. Therefore, this method can solve important problems such as extending the measuring range of the interferometer even under the influence of vibrations or misalignment from the drive system. In addition, by improving the measuring speed of frequency modulated interferometer so that it can be applied to measure during the machining process and is also an achievement of this study. Furthermore, the proposed interferometer can operate stably in noisy environments like factories and manufacturing plants, under the impact of vibrations and the change of environment refraction index.

## 2 Measurement Principle

The intensity  $I(\tau, t)$  of the interference signal of the frequency modulated interferometer is written as [16–18]

$$\begin{aligned}
 I(\tau, t) = & E_{01}^2 + E_{02}^2 + 2E_{01}E_{02} \cos(\omega_0\tau) J_0(m) \\
 & + 4E_{01}E_{02} \cos(\omega_0\tau) \sum_{n=1}^{\infty} J_{2n}(m) \cos(2n\omega t) \\
 & - 4E_{01}E_{02} \sin(\omega_0\tau) \sum_{n=1}^{\infty} J_{2n-1}(m) \cos[(2n-1)\omega t], \quad (1)
 \end{aligned}$$

where  $\tau$ ,  $m$ ,  $E_{01}$  and  $E_{02}$ ,  $n$ ,  $J_0(m)$ ,  $J_{2n}(m)$ , and  $J_{2n-1}(m)$  are the changes in time between the two arms of the interferometer, the modulation index, the amplitudes of the electric fields in the reference and measurement arms, an integer, and the Bessel functions, respectively. Here,

$$m = \frac{\Delta\omega}{\omega} \sin\left(\frac{\omega\tau}{2}\right) \approx \frac{2\pi\Delta f n_{\text{air}} L}{c} \quad (2)$$

where  $\Delta f$  ( $\Delta\omega = 2\pi\Delta f$ ),  $n_{\text{air}}$ ,  $L$ , and  $c$  are the frequency modulation excursion, the refractive index of air, the unbalance length of the interferometer, and the light velocity in a vacuum. A divider split  $I(\tau, t)$  into two parts, which are coupled into the two purely sinusoidal signals of  $2\omega$  and  $3\omega$  from the function generator. By using the two LIAs, the intensities  $I_{2\omega}$  and  $I_{3\omega}$  of the  $2\omega$  and  $3\omega$  harmonics of  $I(\tau, t)$ ,

respectively, are produced as follows

$$\begin{aligned} I_{2\omega} &= 2E_{01}E_{02}\cos(\omega_0\tau)J_2(m), \\ I_{3\omega} &= -2E_{01}E_{02}\sin(\omega_0\tau)J_3(m). \end{aligned} \tag{3}$$

Here,  $J_2(m)$  and  $J_3(m)$  are the second and third order Bessel functions. By using the Lissajous diagram,  $\omega_0\tau$  is determined. The total phase difference  $\Phi$  between the arms is

$$\Phi = \omega_0\tau = \arctan\left(-\frac{I_{3\omega}}{I_{2\omega}} \cdot \frac{J_2(m)}{J_3(m)}\right). \tag{4}$$

The displacement  $\Delta L$  calculated from the phase shift is given by

$$\Delta L = \frac{\lambda_0}{4\pi n} \arctan\left(-\frac{I_{3\omega}}{I_{2\omega}} \cdot \frac{J_2(m)}{J_3(m)}\right). \tag{5}$$

Figure 1 shows the Bessel functions from  $J_2(m)$  to  $J_4(m)$ . There are some critical points where two consecutive Bessel functions are equal,  $J_1(m) = J_2(m)$  when  $m = 2.63$  rad and  $J_2(m) = J_3(m)$  when  $m = 3.77$  rad. The displacement  $\Delta L$  is independent on the modulation index  $m$  at various specific value of  $m$ , hence Eq. (5) become

$$\Delta L = \frac{\lambda_0}{4\pi n} \arctan\left(-\frac{I_{3\omega}}{I_{2\omega}}\right). \tag{6}$$

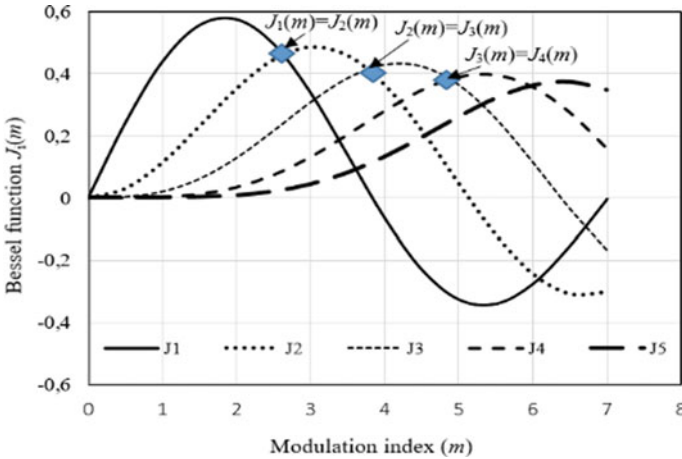


Fig. 1 Bessel function

The measurement uncertainties of modulation index measurement and approximation Bessel function value are removed from uncertainty sources of the proposed interferometer.

In this paper, the modulation index was carefully controlled to reach some special values (2, 63, 3.77...). The modulation index depends on the unbalanced length, and modulation excursion as shown in Eq. (2). Laser diodes offer modulation frequency directly by modulating the injection current. Therefore, the modulation excursion is adjusted to obtain the special values of the modulation index. At the values, the Lissajous diagram generated from two consecutive harmonics is circular. Moreover, Eq. (2) proves that when the modulation excursion  $\Delta f$  and the modulation  $m$  are known, the unbalanced length  $L$  can be determined. It means that the absolute position of the measuring object at critical values of the modulation depth can be determined immediately. These known positions function as markers on the scale and critical points are used to divide the large measuring range into small measuring ranges while ensuring the continuity of the system. This method is immensely helpful to extend the measuring range of the frequency modulated interferometer and limit the effects of vibrations or straightness errors that can lose interference signal during the broad range of measuring displacements.

### 3 Experiment and Discussion

The experiment was designed to verify two characteristics of the proposed method, the controlling of modulation index by adjusting the modulation excursion and the displacement measurement at a critical value of modulation index. The experimental system is shown in Fig. 2. A collimated laser diode (HL6344G, Thorlabs Inc.) at the wavelength of 633 nm was used as a light source for the interferometer. The movement of the reference mirror was sinusoidally modulated by a PZT actuator (PA4FKW, Thorlabs Inc.). The interference signal was detected using a photodetector (PDA36A-EC, Thorlabs Inc.). A signal processing module was built by combining analog lock-in amplifiers and high-resolution data acquisition. The experimental condition was shown in Table 1.

The modulation excursion was adjusted by changing the amplitude of modulation current. When the modulation excursion was equal to 360 MHz the modulation index obtained 2.67. The Lissajour diagram was circle and the displacement measured was independent to the modulation index. The displacement was successfully measured with low noise, Fig. 3. Moreover, the absolute length of 3.489 m can be determined when  $m = 2.63$ .

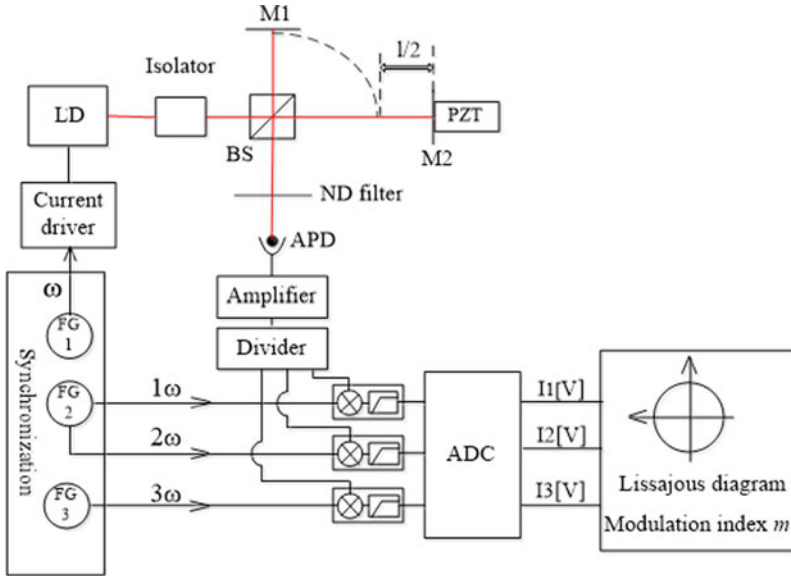


**Fig. 2** Experimental setup for frequency modulated interferometer

**Table 1** The experimental conditions

Frequency modulation for LD	3 MHz
Frequency modulation excursion for LD	360 MHz
Operating frequency of PZT	1 Hz
Amplitude of PZT stage	0.5 $\mu\text{m}$ (0.5 V <sub>pp</sub> )
Wavelength	633 nm
Cut off frequency of low pass filter	1 MHz

## 4 Conclusion

This research was proposed and verified a new method to extend the measurement range of a frequency modulated interferometer. The modulation index was controlled to reach some special values, where two consecutive harmonics have the same Bessel function value. The displacement was measured without any effect of the modulation index. Moreover, the absolute value of length can be determined at the critical value of the modulation index.

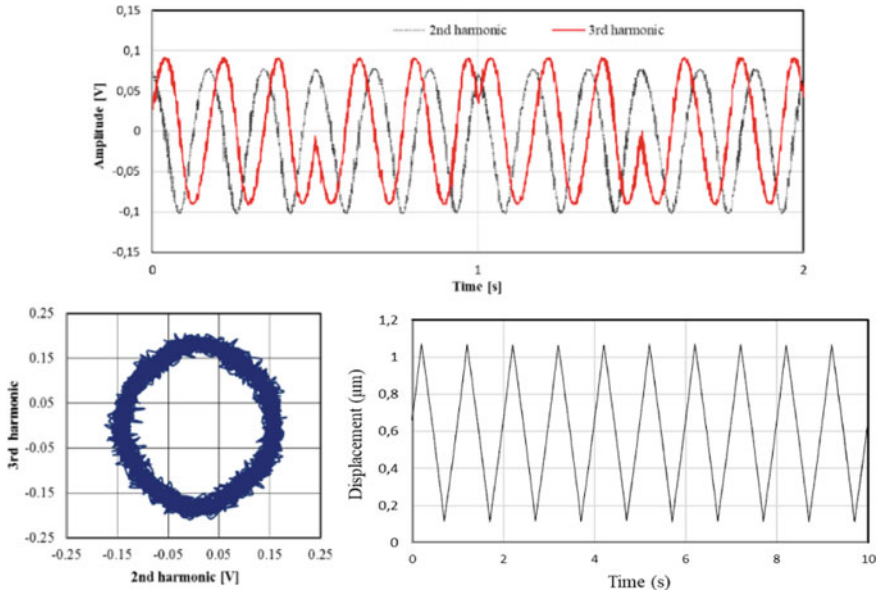


Fig. 3 Lissajous diagram and displacement measurement result

## References

1. Y. Guo, Y. Sun, K. Wu, Research and development of monitoring system and data system and data acquisition of CNC machine tool in intelligent manufacturing. *Int. J. Adv. Robot. Syst.* **17**(2), 1729881419898017 (2020)
2. D. Souza, A. Fagali et al., Development of a mobile application for monitoring and controlling a CNC machine using Industry 4.0 concepts. *Int. J. Adv. Manufact. Technol.* **111**(9), 2545–2552 (2020)
3. S.M. Merghache, A. Hamdi, Numerical evaluation of geometrical errors of three-axes CNC machine tool due to cutting forces—case: milling. *Int. J. Adv. Manufact. Technol.* **111**(5), 1683–1705 (2020)
4. D. Lyu et al., Dynamic error of CNC machine tools: a state-of-the-art review. *Int. J. Adv. Manufact. Technol.* **106**(5), 1869–1891 (2020)
5. Y. Li, M. Zhao, S. Zhou, Servo axis incipient degradation assessment of CNC machine tools using the built-in encoder. *Int. J. Adv. Manufact. Technol.* **106**(9), 4293–4305 (2020)
6. H. Lu et al., A novel geometric error compensation method for gantry-moving CNC machine regarding dominant errors. *Processes* **8**(8), 906 (2020)
7. S. Kidani, *A Study on Identification and Compensation of the Dynamic Behavior of CNC Machine Motion Error*. Diss. UC Berkeley (2020)
8. Y. Shi et al., Design and testing of a linear encoder capable of measuring absolute distance. *Sens. Actuat. A Phys.* **12**, 111935 (2020)
9. N. Bosmans, J. Qian, D. Reynaerts, Design and experimental validation of an ultra-precision Abbe-compliant linear encoder-based position measurement system. *Precis. Eng.* **47**, 197–211 (2017)
10. S. Kumar, A.S. Anil et al., Improved capacitive sensor for combined angular and linear displacement sensing. *IEEE Sens. J.* **19**(22), 10253–10261 (2019)
11. N. Anandan, B. George, A wide-range capacitive sensor for linear and angular displacement measurement. *IEEE Trans. Ind. Electr.* **64**(7), 5728–5737 (2017)

12. K. Xiang et al., A T-type capacitive sensor capable of measuring 5-DOF error motion of precision spindles. *Sensors* **17**(9), 1975 (2017)
13. M. Holub et al., Capability assessment of CNC machining centres as measuring devices. *Measurement* **118**, 52–60 (2018)
14. G. Sun et al., Body diagonal error measurement and evaluation of a multiaxial machine tool using a multibeam laser interferometer. *Int. J. Adv. Manufact. Technol.* **12**, 1–15 (2020)
15. F. Zheng et al., A method for simultaneously measuring 6DOF geometric motion errors of linear and rotary axes using lasers. *Sensors* **19**(8), 1764 (2019)
16. T.T. Vu, Y. Maeda, M. Aketagawa, Sinusoidal frequency modulation on laser diode for frequency stabilization and displacement measurement. *Measurement* **94**, 927–933 (2016)
17. T.T. Vu, M. Higuchi, M. Aketagawa, Accurate displacement-measuring interferometer with wide range using an I2 frequency-stabilized laser diode based on sinusoidal frequency modulation. *Measur. Sci. Technol.* **27**(10), 105201 (2016)
18. Q.A. Duong, T.T. Vu, M. Higuchi, D. Wei, M. Aketagawa, Iodine-frequency-stabilized laser diode and displacement-measuring interferometer based on sinusoidal phase modulation. *Measure. Sci. Technol.* **29**, 065204 (2018)

# Simulation of Aerodynamics for Unmanned Aerial Vehicles with the SolidWorks Platform



Thi Minh Tu Bui, Quoc Thai Pham, Le Chau Thanh Nguyen,  
and Tan Thong Ngo

**Abstract** This paper presents the application of Solidworks Flow Simulation software to support aerodynamic simulation for unmanned aerial vehicles, helping to improve flight conditions during operation under the influence of external aircraft forces. In recent years, many countries have focused on and strongly developed unmanned aerial vehicles (UAV) research and development, especially for agriculture, hydrometeorology, and the military, to improve and enhance the quality of life. Therefore, it is essential to research and calculate to stabilize the ability to fly in the actual conditions of unmanned aerial vehicles. Through the survey, an unmanned aerial vehicle's control includes many factors related to the fields such as mechanics, electricity, electronics, and automation. In building the size parameters of the dynamic model for pesticide spraying drones for agriculture, the authors built the initial size parameters using SolidWorks software to perform the simulation. Aerodynamics acts on the aircraft's rudder to optimize the size parameters suitable for flight conditions when operating by experimenting with the wing flight model by adjusting the parameters and determining the appropriate size parameters for flight conditions with boundary conditions in the flight area for pesticide spraying. It is necessary to have a set of aerodynamic coefficients to determine the aerodynamic forces acting on the aircraft's wing during flight. After setting the basic size parameters, to ensure flight conditions, the set of aerodynamic coefficients is determined by the experimental method and adjusted in actual situations with different boundary conditions. For adjusting the wing size parameters of the flat-wing aircraft, the authors use aerodynamic simulation software with SolidWorks flow simulation modules with the boundary conditions set. Solidwork Flow Simulation using computational fluid dynamics analysis allows us to simulate fluid flow and heat transfer quickly and efficiently through obstruction surfaces. With such requirements, Solidwork software

---

T. M. T. Bui · Q. T. Pham (✉)

The University of Danang-University of Science and Technology, Danang, Vietnam  
e-mail: [pqthai@dut.udn.vn](mailto:pqthai@dut.udn.vn)

L. C. T. Nguyen · T. T. Ngo (✉)

The University of Danang-University of Technology and Education, Danang, Vietnam  
e-mail: [ntthong@ute.udn.vn](mailto:ntthong@ute.udn.vn)

with the Flow Simulation module can effectively support analysis and calculation for designing and manufacturing wing aircraft for agriculture.

**Keywords** Unmanned aerial · Aerodynamics · SolidWorks software · Simulation · Aerodynamic analysis

## 1 Introduction

Present aircraft are constantly evolving and being upgraded. Over the past 20 years, the use of drones in both the public and private (military) sectors. UAV (Unmanned Aerial Vehicles-UAV is a common name for a flying object with no operator). UAVs are autonomous flying objects that can perform many tasks ranging from simple flight operations (such as landing and takeoff) to more complex missions. An operator on the ground usually controls UAVs, but they can also be controlled automatically by systems built into them [1]. Comprehensive development with sophisticated precision sensors and specialized software is also the most challenging area for ordinary people to access. Besides, in agriculture, entertainment is an area that amateurs can access. It can be said that the appearance of unmanned aerial vehicles (UAV) is a revolution in data collection, surveying, monitoring, working, and tracking objects in different areas. In addition, they are used for many other essential purposes in the military, agriculture, and hydrology [1].

Solidwork Flow Simulation using computational fluid dynamics analysis allows us to simulate fluid flow and heat transfer quickly and efficiently through obstruction surfaces. You can easily calculate fluid forces and understand the impact of airflow on vane performance. With such requirements, Solidwork software with a Flow Simulation module can effectively support analysis and calculation for designing and manufacturing wing airplanes for agriculture [2]. Adjusting these wings and the engine's thrust will help the aircraft keep its balance in the air, perform wing tilt, change direction left and right, fly up and down, and change altitude when flying by air [3].

This research focuses mainly on the application of Solidwork software to simulate the aerodynamic impact on the wings of aircraft wings by spraying pesticides. On that basis, it helps us adjust the lift's design to match the actual flight conditions.

## 2 Material and Method

In this chapter, we will investigate the basic parameters and give the aircraft's configuration of the fuselage, wings, and landing gear. The result is a design drawing for a complete UAV. The design configuration will be based on the actual pesticide spraying aircraft model applied today; the survey's reference parameters are the used index, including bevel angle and wing size ratio.



Like other objects, the UAV moving in space is also influenced by Surface Force and Mass Force. Surface force is the total aerodynamic force  $R$ , propulsion of the engine  $P$ ; the mass force is the gravity  $G$  due to the mass of the whole body created by the earth's gravitational force [4].

- Total aerodynamic force  $R$ .
  - Placement point: at the center of gravity  $O$  of the UAV
  - Size:  $R = 1/2 \rho V^2 \cdot C_R \cdot S$
- $C_R$  is the total aerodynamic force coefficient.
- $\rho$  is the density of air.
- $S$  is the wing area of the UAV.

We get the components when projecting  $R$  onto the Oxycyczc speed coordinate system.

- Lifting force  $Y (=Ryc)$ : is the component of the total aerodynamic force projected on the shaft.  $Oyc$ , located at the center of the UAV, has an upward direction, Fig. 1.

Size:  $Y = C_y \frac{\rho V^2}{2} \cdot S = C_y \cdot q \cdot S$  Drag force  $X (= Rxc)$ : is the component of the total aerodynamic force projected on the axis  $Oxc$ , located at the UAV's center of gravity, opposite the flight speed.

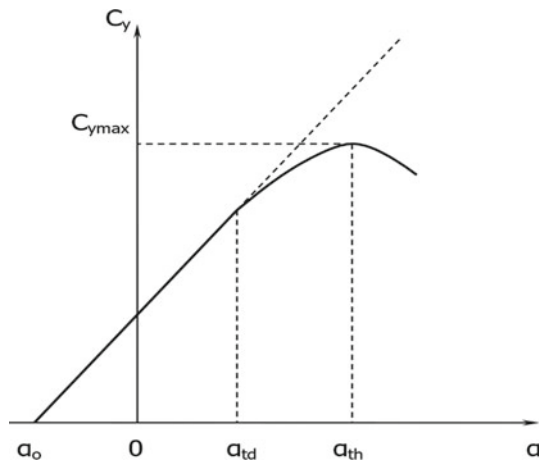
Size:  $X = C_x \cdot \frac{\rho V^2}{2} \cdot S = C_x \cdot q \cdot S$  With small angles of attack  $\alpha$ , we have:

$$C_x = C_{x0} + C_{xi} = C_{x0} + AC_y^2$$

- Edge force  $Z (= Rzc)$ : is the component of the total aerodynamic force projected on the axis.

Size:  $Z = C_z \cdot \frac{\rho V^2}{2} \cdot S = C_z \cdot q \cdot S$

**Fig. 1** Relationship between  $C_y$  and  $\alpha$  angle



When the slope angle ( $\beta$ ) is 0,  $R$  lies in the plane of symmetry. Then  $R_{zc} = 0$  or side force  $Z = 0$ . Usually, when calculating the small angle  $\beta$ , people ignore the side force's effect.

Survey to set the dynamics and optimize the design of the wing lifter to suit the actual conditions for UAV serving pesticide spraying in agriculture; here, the authors used Solidwork software to perform aerodynamic simulations for flat-wing aircraft. Solidwork Flow Simulation using computational fluid dynamics analysis allows us to simulate fluid flow and heat transfer quickly and efficiently through obstruction surfaces. You can easily calculate fluid forces and understand the impact of airflow on vane performance. With such requirements, Solidwork software with a Flow Simulation module can effectively support analysis and calculation for designing and manufacturing wing airplanes for agriculture. Below are the types of objects that Solidwork Flow Simulation software can help for effective analysis and calculation, including liquid, gas, and heat transfer flow; External and internal fluid flow; mixed, turbulent, and transitional flows; Gas mixtures, liquid mixtures, etc. [5, 6].

### 3 Results and Discussion

After designing the profile of the plane lifter, in this problem, we will choose the two best aerodynamic profile samples to bring into the comparison calculation and finally select a profile with the best aerodynamic properties—the best aerodynamics, suitable for the wing-on-body model. Optimization problems can be solved directly in Solidwork Flow Simulation.

Maintain the original alignment of the design and, at the same time, create solutions for the desired shape without having to go back and change the design of the object profile; this process continues until finding the desired shape. The optimal shape when applying boundary conditions [6].

#### 3.1 Build the Main Wing Model

Using the design feature on Solidwork, we can quickly build the main wing profile of Fig. 2, which can be set up on the popular UAV platform today. Figure 3. describes the simulation results of the *Computational domain for 3D wings*.

#### 3.2 Set Input Parameters

From Solidwork software, we set the unit as SI including (m kg s) shown in Fig. 4. Select the type of analysis inside surface or outside surface, Fig. 5

**Fig. 2** Main wing simulation

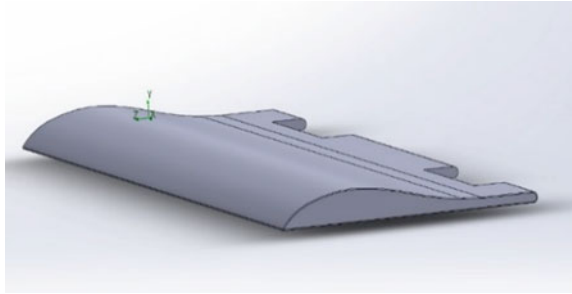


**Fig. 3** Computational domain for 3D wings

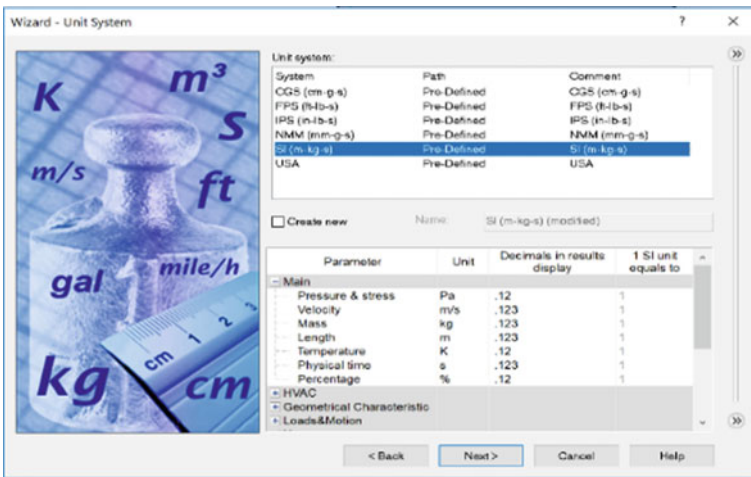
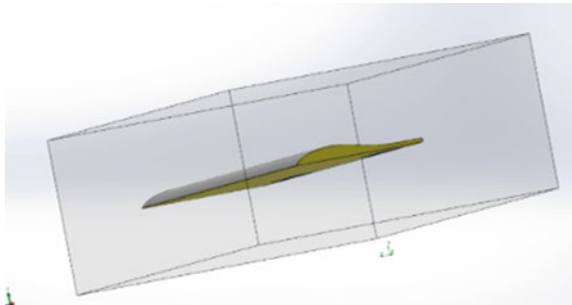


**Fig. 4** Unit setting

- Select the type of surface analysis as external: External.
- Exclusion conditions:

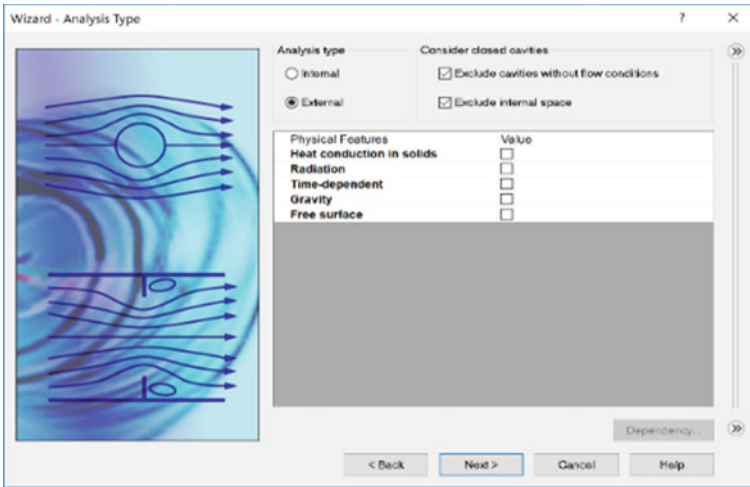


Fig. 5 Select type of analysis surface

- Exclude cavities without flow conditions: Exclude cavities without flow conditions.
- Exclude internal space: exclude the internal space

Set initial conditions and surroundings, boundary conditions [6], Fig. 6.

Gauge pressure.

Velocity = 30 m/s.

Expression of velocity value: Absolute.

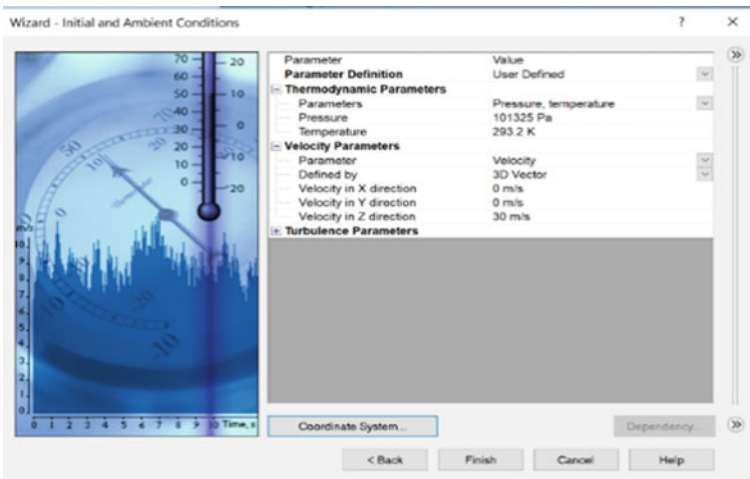


Fig. 6 Set the boundary condition



Fig. 7 The target parameters

Stable flow, independent of time: Steady.

Material: Aluminum Alloy.

Fluid name: Gas.

Fluid type: Ideal gas.

Determine valuable parameters that the target should be considered.

- Total pressure: effective pressure.
- Velocity: speed of action
- Force: the lifting force acting.
- Friction force: frictional force acting.

### 3.3 Carrying Out the Analysis

Performing the convergence analysis after 200 iterations, we get the results as shown in Fig. 7. The graph shows the target parameters. Surface pressure above and below the wing Fig. 8. Pressure distribution on the top and bottom of the wing.

Airflow and wind direction running through the UAV lifters are shown in Fig. 9. Figure 10. describes the simulation of the wind direction acting on the main wing.

## 4 Results

After optimization on Solidwork Flow Simulation software, we obtain the results of the necessary parameters, as shown in Table 1. Target parameter table.

**Fig. 8** Pressure distribution on the top and bottom of the wing

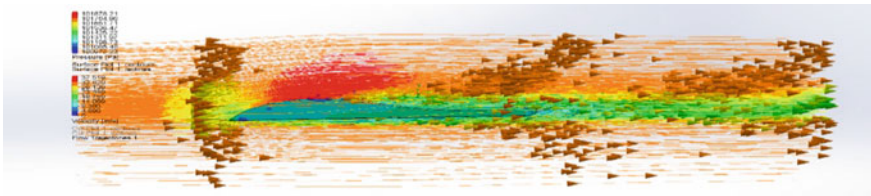
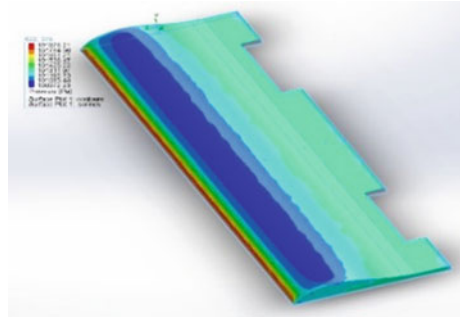


**Fig. 9** Simulate air flow around the wing

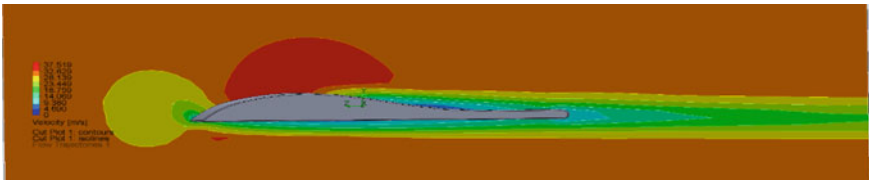


**Fig. 10** Simulation of the wind direction acting on the main wing

**Table 1** Target parameter table

Target parameter	Display value
Lifting force	158.943 (N)
Friction force	1.50715 (N)
Total pressure value	241,722 Pa
Maximum speed	97.96 m/s

At a speed of 30 m/s, the main wing lift meets the requirements of the problem. Analysis and simulation by SoliWworks software bring us an intuitive view of the problem to be solved. Still, the results depend entirely on the operator’s subjectivity from the steps of model building, meshing, setting boundary conditions, and setting up the solution all affect the results of the problem.

Turbulence occurs at the tip of the wing due to a pressure difference on the top and bottom surfaces, creating vortices directed from the bottom to the top, which

**Fig. 11** Prevents eddy currents through the tip of the wing

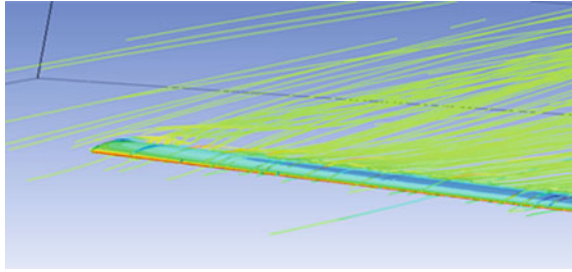
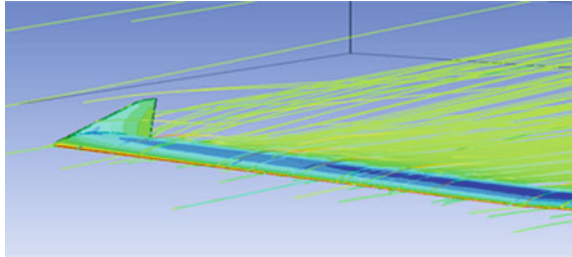


**Fig. 12** Graph of lift coefficient



reduces lift. To overcome this, we make tiny vertical wings at the tips of the wings. Not only does it reduce the effect of turbulence, but it also helps to stabilize the plane. The wingtip helps reduce wingtip spin, provides lateral stability, and improves lift. With the arrow-shaped wing, the advantage of the Wingtip wing will be more clearly expressed [7]. Thus, the final production model will have the use of a wingtip. However, to simplify the model and facilitate the meshing process, survey the aerodynamic characteristics of the wing aircraft by UAV. Figure 11 Prevents eddy currents through the tip of the wing, and Fig. 12. Graph of lift coefficient. Improving the aerodynamic quality factor for 3D wings, the control meshing for 3D wings can show the necessary points for adjusting the size of the UAV wing. Executing the optimization command using the Optimizer menu, we have the results shown in Fig. 13. Dimensions of the forklift.

After running the optimization, the pressure distribution on the surface of the aircraft wing is shown in Table 2, comparing parameters before and after optimization.

From Table 2, we can see the change in the value of lift force, drag force as well as in aerodynamic quality ratio. The software has improved the aerodynamic characteristics of the Airfoil 8414 lift, helping to achieve better aerodynamics. Based on the existing design parameters, we build a UAV model with the size parameters fit.

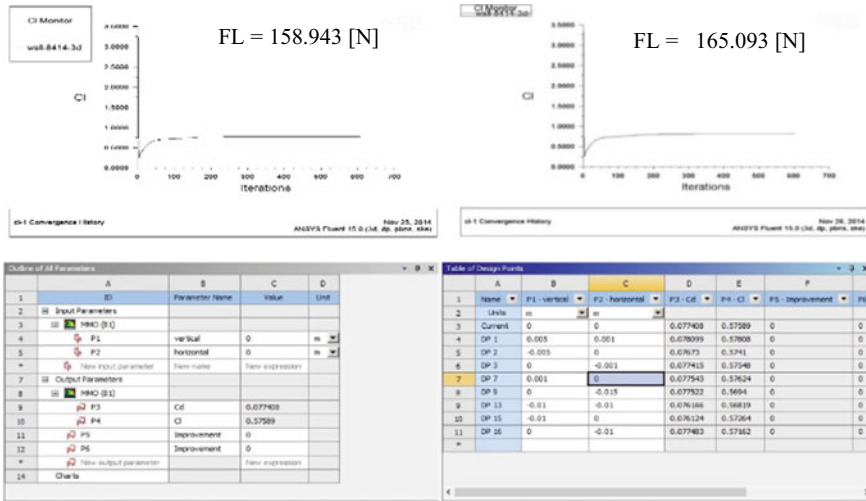


Fig. 13 Dimensions of the fork lift

Table 2 Parameters before and after optimization

	Before optimization	After optimization
Lifting force value (FL)	158.943	161.568
Resistance value (Fd)	18.6505	18.9344
Lift coefficient	0.1696	0.1725
Drag coefficient	0.0225	0.0228
Aerodynamic quality ratio	7.5377	7.5657

## References

1. L. Canh, T.-P.Q. Huy, *Arduino and the Flying Device* (Youth Publishing House, 2020)
2. T.T. Thien, N.T. Nha, T.T. Duong, *Simulation of Mechanical Dynamics of a Solid System Using SolidWorks* (Publishing House of the National University of Ho Chi Minh City, Ho Chi Minh, 2018)
3. T.V. Duc-Nguyen, V. Son-Pham, V. Uy, *Flight Kinematics and Principles of Single-Channel Controlled Flight Instruments* (Science and Technology Publishing House, 2019)
4. N.D. Cuong, *Modeling and Simulating the Motion of an Autopilot, Monographs Center of Science and Technology: Military Technology* (People’s Army Publishing House, Hanoi, 2002)
5. T. Minh, T.-P.Q. Huy, *Solidwork User Manual* (Hanoi Polytechnic Publishing House, 2019)
6. SolidWorks Flow Simulation of the wing profile—YouTube
7. T.H.G. Megson, *Aircraft Structures for Engineering Students* (Edward Arnold (Publisher) Ltd., London, 1972)



# Spiral Bevel Gear Manufacturing Technology: A Review



Hoang Thuy Dinh, Van Tuan Pham, and Quoc Hoang Pham

**Abstract** The research on improving the manufacturing quality of spiral bevel gear transmissions has been widely considered by many researchers worldwide. This study presents a survey of research works published in the past 15 years on the manufacturing technology of spiral bevel gears, including cutting methods, cutting machines, cutting tools, manufacturing error, and measurement. The survey results show that spiral bevel gear manufacturing technology has made many advances in recent years, and the manufacturing quality has been increasingly improved. Many advanced research methods have been applied, such as finite element simulation and loaded and unloaded teeth contact analysis to optimize tooth surfaces. Computer numerical control (CNC) machining machines, coordinate measuring machines, and surface coating cutting tools have improved productivity and machining accuracy. The review results provide a better understanding of the spiral bevel gear manufacturing technology.

**Keywords** Spiral bevel gear · Manufacturing technology · Tooth contact analysis

## 1 Introduction

The spiral bevel gears are commonly used to in various mechanical products such as: mining machinery, vehicles, robot, automation, helicopters and aerospace engineering because of their high strength, high contact ratio and smooth driving [1–3].

Due to the complication of tooth surface and cutting kinematic, machining process of spiral bevel gear becomes difficult to understand and analyze. Therefore, the research on manufacturing technology of spiral bevel gears to improve machining quality is always a topic of interest to many scientists.

---

H. T. Dinh · V. T. Pham · Q. H. Pham (✉)  
Le Quy Don Technical University, Hanoi, Vietnam  
e-mail: [phqhoang@lqdtu.edu.vn](mailto:phqhoang@lqdtu.edu.vn)

© The Author(s), under exclusive license to Springer Nature Switzerland AG 2024  
B. T. Long et al. (eds.), *Proceedings of the 3rd Annual International Conference on Material, Machines and Methods for Sustainable Development (MMMS2022)*, Lecture Notes in Mechanical Engineering, [https://doi.org/10.1007/978-3-031-57460-3\\_7](https://doi.org/10.1007/978-3-031-57460-3_7)

This paper presents an overview of the spiral bevel gear machining methods, machine and cutting tools for processing spiral bevel gear, manufacturing errors and measurement of spiral bevel gear, and research trends in spiral bevel gear.

## 2 Main Cutting Methods

Spiral bevel gears can be manufactured on CNC universal milling machines [4–6]. However, in industry spiral bevel gears are mainly cut on specialized machining machines because of their high productivity. The main cutting methods on these machines are face milling and face hobbing [1, 7–10].

In face milling method, only one slot is machined at a time until the full depth is cut, so it's called the single indexing method. After completing one slot, the workpiece will rotate to the position for machining next slot and the process will be repeated until all tooth spaces are completed. Lengthwise tooth curve of face milled bevel gears is circular. Kinematic of face milling method is shown in Fig. 1.

In face hobbing method, all the tooth spaces are cut at a time, so it's called the continuous indexing method. The cutting system, besides the rotation around its axis, also performs a relative motion with the rotation around axis of the workpiece so that each slot is cut a little until the final requested depth. Face hobbled gears have an extended epicycloid lengthwise tooth curve. Kinematic of face hobbing method is shown in Fig. 2.

The tooth depth and thickness of face milled gears are tapered (the depth and thickness at the toe is usually smaller than at the heel) and slot width may be constant [12] (Fig. 3). Similar to face milled gears, face hobbled gears have tapered tooth thickness but tooth depth is constant and slot width is tapered (Fig. 4).

Regarding the forming method, both generating and non generating (Formate) method can be used for both face milled and face hobbled gears, but the opinion is always cut with the generating method.

**Fig. 1** Kinematic of face milling method [11]

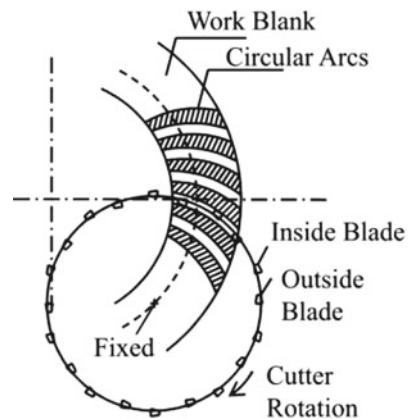


**Fig. 2** Kinematic of face hobbing method [11]

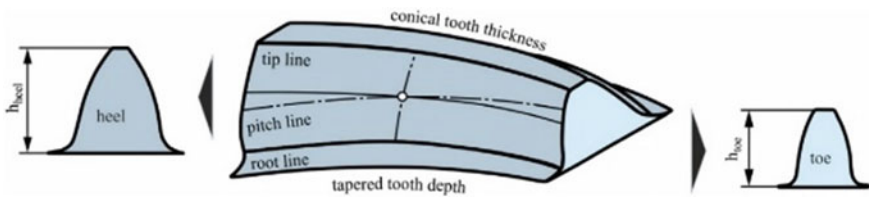
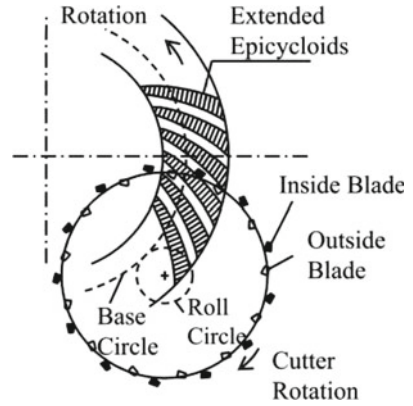


**Fig. 3** Tooth geometry of face milled gears [7]

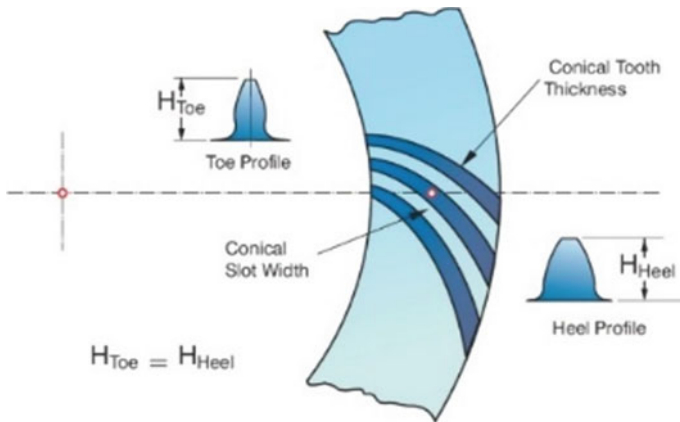


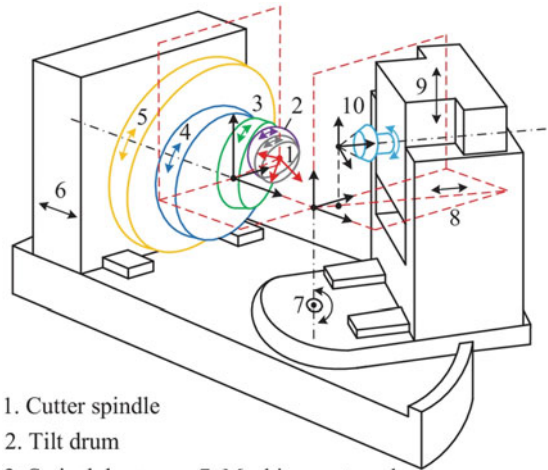
**Fig. 4** Tooth geometry of face hobbed gears [13]

### 3 Cutting Machines

In the early period, the traditional cradle-style machines are used to produce spiral bevel gears. They consisted of many components cutter spindle, tilt drum, swivel drum, eccentric drum, cradle, sliding base, machine root angle, machine center to back, blank offset and work spindle (Fig. 5). The drive trains of these machines is very complex because of using many meshing gear pairs (Fig. 6).

Nowadays, spiral bevel gear cutting machines have been greatly improved from earlier machines. Today’s modern machine is numerically controlled by computers (CNC machine) with direct-drive technology and high-speed spindles for both the

**Fig. 5** Traditional cradle-style spiral bevel gear machine



- 1. Cutter spindle
- 2. Tilt drum
- 3. Swivel drum
- 4. Eccentric drum
- 5. Cradle
- 6. Sliding base
- 7. Machine root angle
- 8. Machine center to back
- 9. Blank offset
- 10. Work spindle

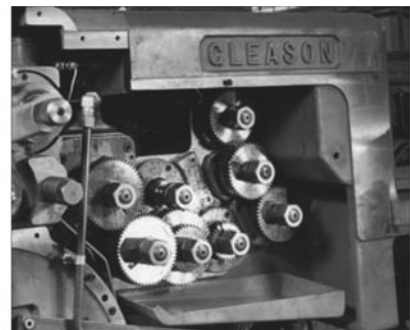
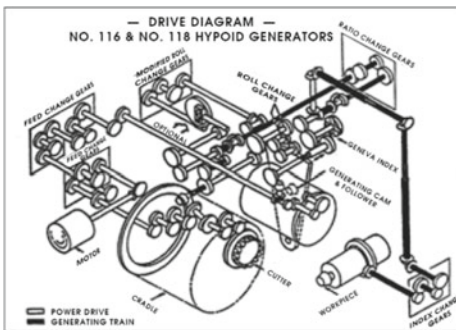


**Fig. 6** A drive system of traditional cradle-style machines [12]

work and cutter. The machine itself may not contain any gears. CNC spiral bevel gear cutting machine is composed of six kinematical components. The cradle motion in the traditional cradle-style cutting machines is replaced by a vertical slider ( $Y$ -axis) and a horizontal slider ( $X$ -axis) in CNC machine (Fig. 7). Figure 8 shows a German spiral bevel gear cutting machine Klingelberg C27.

The traditional cradle-style cutting machines and CNC spiral bevel gear cutting machines have a similar machining principle. The cutting motions of traditional machines can be converted into the motions of CNC generators by computer control.

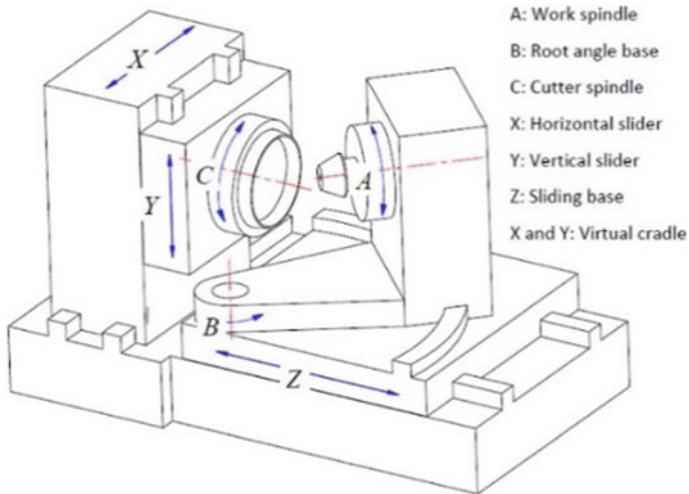


Fig. 7 Six-axis CNC bevel gear cutting machine [14]

Fig. 8 CNC spiral bevel gear cutting machine Klingelberg C27



In CNC generators, the servo motors directly driven six axes so that can implement prescribed motion functions. In comparison with traditional cradle-style machine, the CNC spiral bevel gear cutting machine has outstanding productivity and accuracy because the machine has better stability and solidity, allowing high speed and precision machining.

## 4 Cutting Tools

### 4.1 Cutter Systems

There are different types of cutter system, because each supplier provides its cutter system for different methods of machining gears. In the early days cutters were manufactured in three typical types for machining spiral bevel gears by the face milling method [12]. The first type is integral blade cutter system or solid body cutters, their blades and head are one solid block (Fig. 9). The second type is segmental blade cutter system that has groups of blades fastened to the cutter head by bolts. The last type is inserted blade cutter system, in which individual blades are bolted to slotted heads (Fig. 10).

In the 1970s, a new type of cutter system was invented, that was stick blade cutter system (Fig. 11). In comparison with previous types of cutter system, this type has more blades can be fastened in the cutter head.

In the first three cutter system type, a three-blade configuration was utilized in the blade grouping including an inside, an outer, and a bottom blade. Stick blade cutter systems use only inside blades and outer blades.

**Fig. 9** Integral blade cutter system



**Fig. 10** Inserted blade cutter system



**Fig. 11** Stick blade cutter system



## 4.2 Cutting Tool Materials

From the 1900s–1940s, only one cutting tool material was used that is 18–4–1 high speed steel, which consisted of 18% wolfram, 4% chromium, and 1% vanadium [12]. Today many high-speed steels are used for cutting tool materials as listed in Table 1. These steels are added about 4.5–7.0% molybdenum and 5.0–9.0% cobalt, hardness reaching 64–70 HRC.

Along with developing composite materials, spiral bevel gear cutting tools are also researched and made from composite materials consisting of hard carbide particles bonded together by a cobalt binder. Carbide hardness is more significant than steel (about four times). So the use of composite materials improves cutting speed and does not require the use of coolant to increase productivity and reduce product costs. However, using composite materials as cutting tools has the limitation that carbide particles may shatter the gear surface, increasing the surface roughness.

Nowadays, surface coating technology is increasingly developing, which makes cutting tool manufacturing reach a new step. Cutting tools with coatings are becoming increasingly popular due to their advantages, such as high hardness and good wear

**Table 1** Today's high-speed steel cutting tool materials

	C	Cr	W	Mo	V	Co	HRC
CPM M2	1.0	4.2	6.4	5.0	2.0	–	64
CPM M4	1.4	4.3	5.8	4.5	3.6	–	64
CPM REX 45	1.3	4.1	6.3	5.0	3.1	8.3	66
CPM REX 54	1.45	4.3	5.8	4.5	3.6	5.0	65
CPM REX 76	1.5	3.8	10.0	5.3	3.1	9.0	67
CPM REX 86	2.0	4.0	10.0	5.0	5.0	9.0	68
CPM REX 121	3.3	3.8	10.0	5.3	9.0	9.0	70
CPM T15	1.6	4.0	12.3	–	5.0	5.0	66
ASP 2023	1.3	4.2	6.4	5.0	3.1	–	64
ASP 2030	1.3	4.0	5.0	6.5	3.0	8.0	66
ASP 2060	2.3	4.0	6.5	7.0	6.5	9.0	68
M35V (Conventional)	1.2	4.1	6.0	5.0	3.0	5.0	66

resistance, which increases tool life, machining speed, and accuracy. Some of today's coatings and their the properties are listed in Table 2 [12].

## 5 Manufacturing Error and Measurement

### 5.1 Manufacturing Error

There are two major classes of the manufacturing errors of a spiral bevel gear, such as dimensional (or macrogeometry) errors and microgeometry errors [15]. The most significant macrogeometry error is the tooth thickness error, which is the leading cause of increase or reduction of the backlash between the meshing gears. Increase of the backlash can cause the noise (on reversal) and reduce effective tooth strength.

Microgeometry errors can be divided into two types: form errors and location errors. Form errors include profile errors and lead errors, meanwhile pitch errors and runout are important regarding location errors (Fig. 12). The quality and functional performance of gears are greatly influenced by the number and magnitude of these errors.

Profile error is one of the main sources of the noise of gear transmission and also increases localized contact stress to accelerated gear wear and fatigue. The main causes of profile errors are geometric deviations in cutting tool and mounting errors.

Lead error can cause transmission problems with non-uniform motion, uneven loading, and localized loadbearing leading that make gear wear go faster. Lead error also affects the gear torque transfer capacity.

Pitch errors and runout are causes of problems of structural integrity. Pitch errors lead to non-uniform motion that causes transmission errors. Runout may affect most



**Table 2** Some of today's coatings

	TiN	TiCN	AlNite®	TiAIN-X-CEED	TiAIN- + WC/C	AlCrN	nACo
Hardness	2300	3000	3300	3300	3000	3200	4590
Coefficient of friction	0.4	0.4	0.30-0.35	0.4	0.15-0.20	0.35	0.45
Max. service temp	600 °C	400 °C	900 °C	900 °C	800 °C	1100 °C	1200 °C
Coating color	Gold	Blue-Grey	Violet-Grey	Blue-Grey	Dark Grey	Blue-Grey	Violet-Grey
Coating structure	Mono-layer	Multi-layer	Nano	Mono-layer	Multi-layer	Mono-layer	Nano

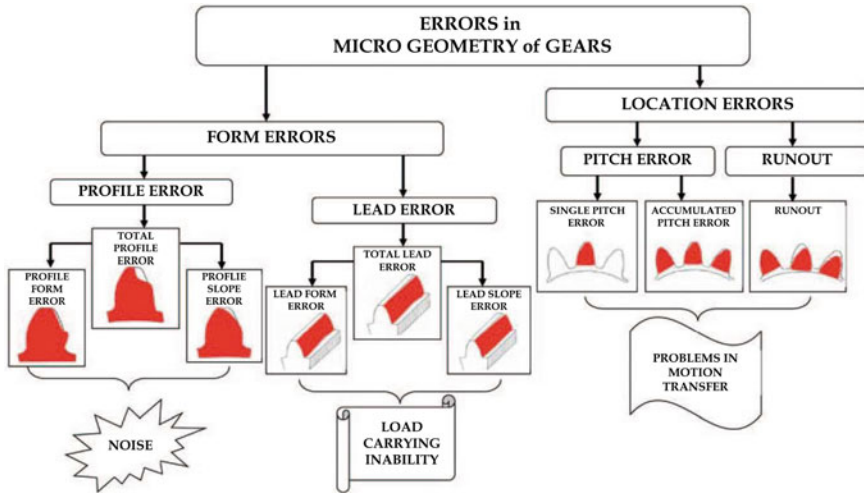


Fig. 12 Microgeometry errors of gears and their effects [15]

other gear quality parameters such as tooth form errors, lead deviation, pitch errors, and noise and vibration. The primary causes of location errors are cutting machine kinematic errors and mounting.

## 5.2 Measurement

Due to the complex geometrical profile, spiral bevel gears are challenging to measure geometrical parameters by traditional mechanical generative instruments. During the spiral bevel gear manufacturing process, the macrogeometry parameter (chordal tooth thickness) is monitored as process control. For measuring chordal tooth thickness, the most frequently used tool is the gear tooth Vernier caliper (Fig. 13). This method has accuracy limitations due to the double Vernier scale reading interrelationship. The most accurate and advanced method to measure the spiral bevel gear microgeometry error is to use a coordinate measuring machine (CMM) (Fig. 14).

The CMM can measure all microgeometry parameters (profile, lead, pitch, and runout) with high accuracy and reliability, thereby determining the manufacturing errors and the accuracy level of the manufactured gears. A typical result of pitch and runout measurement by CMM is shown in Fig. 15, and the profile error is shown in Fig. 16. The inspection results are used to evaluate the quality of the manufactured gear and adjust the manufacturing process parameters to improve machining accuracy.

**Fig. 13** Gear tooth vernier caliper

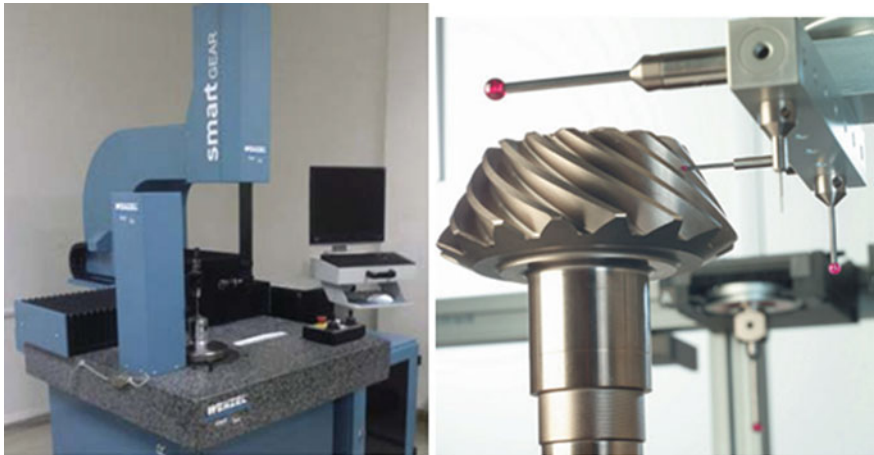
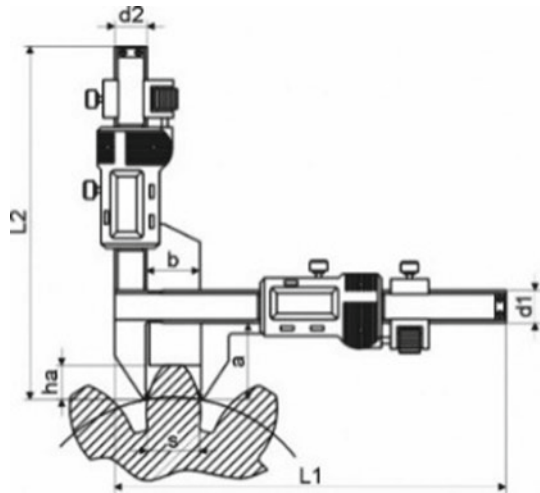


**Fig. 14** Coordinate measuring machine

## 6 Advanced Research Trends

Nowadays, research trends that are concerned too many researchers are optimizing tooth contact area and reducing transmission errors. The transmission errors of gear pair and contact pattern can be determined using a meshing simulation. The purpose of optimizing tooth contact is to adjust the meshing area of the gears to increase load capacity, reduce tooth edge wear and thereby increase gear life. The transmission error is an important cause of the gear noise and vibration. Tooth contact analysis (TCA) technology is an effective tool for gear meshing performance assessment

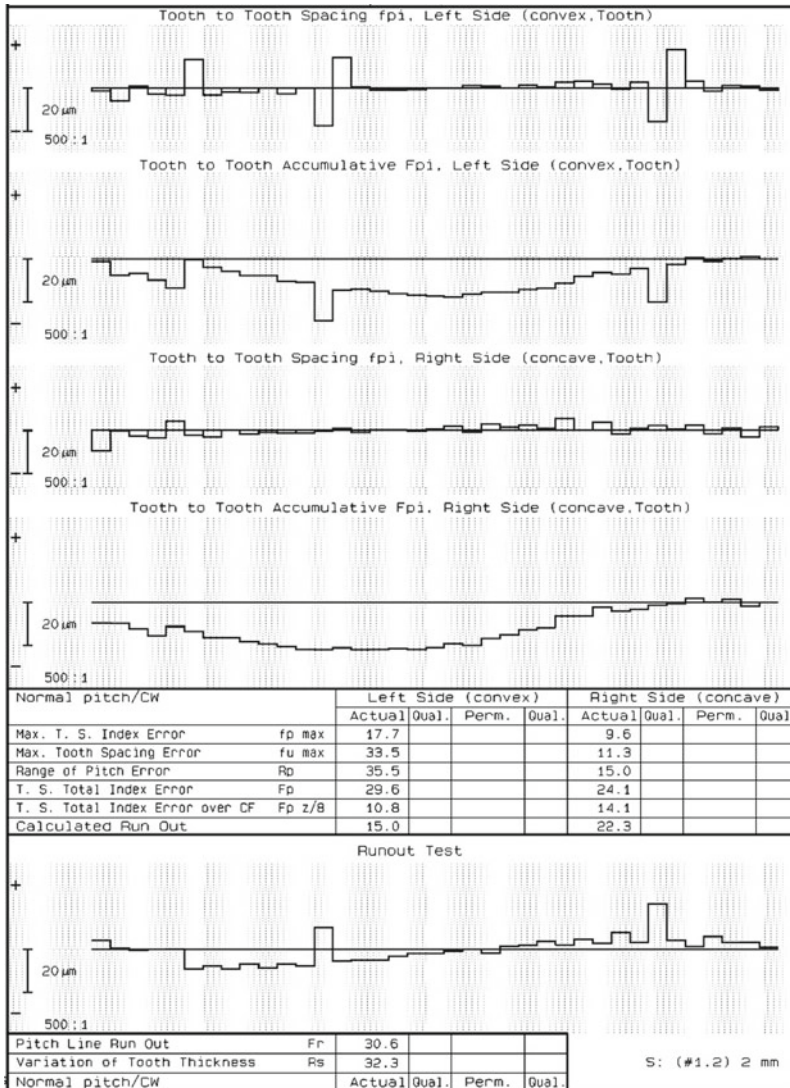


Fig. 15 The typical result of pitch and runout measurement

to improve gear quality in terms of vibration, strength, and mechanical efficiency. Today, scholars worldwide are interested in loaded tooth contact analysis (LTCA)—the new optimization method for improving the power and contact performance of bevel gears.

Artoni et al. [16, 17] developed an approach to automatically optimizing the spiral bevel gear loaded tooth contact pattern. Then, a methodology was presented to

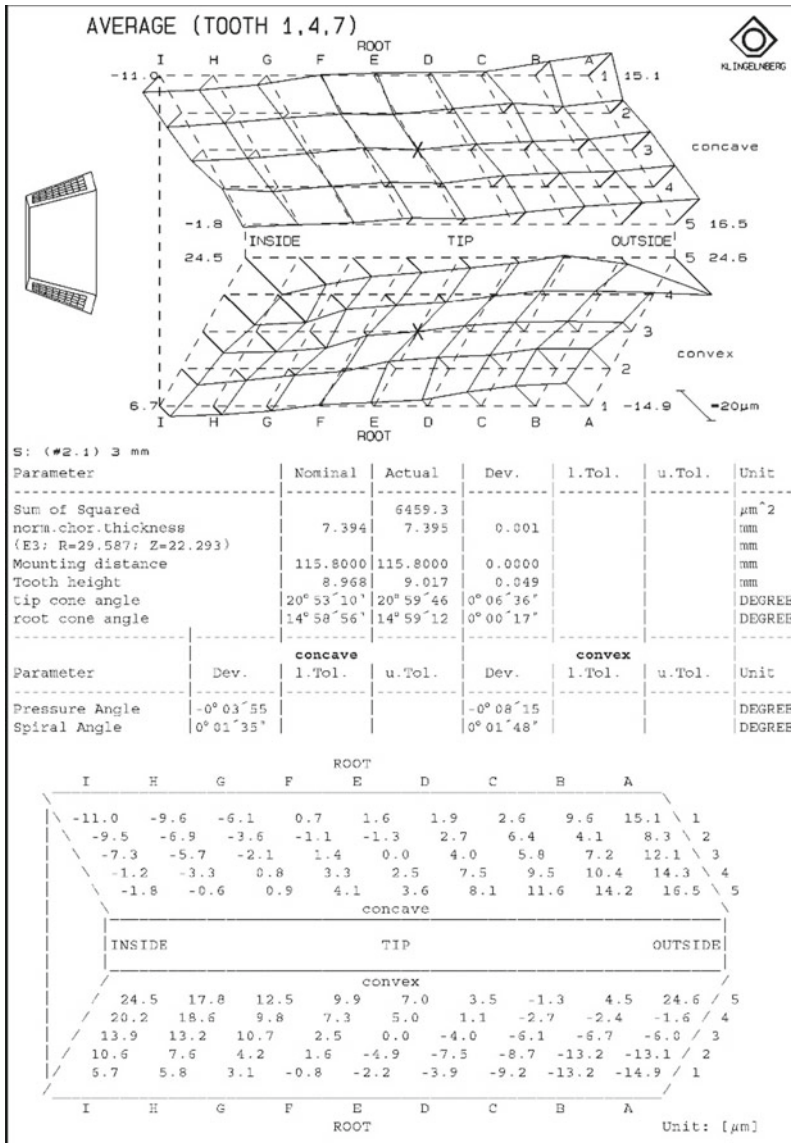


Fig. 16 Typical result of profile error

minimize the hypoid gear loaded transmission error (LTE) by systematically determination of the optimal ease-off topography. Astoul et al. [18] developed a methodology of automatically designing process of the spiral bevel gear flanks to reduce the quasi-static transmission error. Simon [19–21] studied on some of causes of loaded transmission and tooth contact pressure errors included machine settings and

misalignments to propose a method to improve gear meshing performance of hypoid gears by reducing the loaded transmission error and the maximum tooth contact pressure. Zhuo et al. [22] analyzed the spiral bevel gear contact characteristics under quasi-static conditions and presented a method to globally optimize the tooth contact pattern and transmission error.

## 7 Conclusions

Spiral bevel gear manufacturing technology has been developed over the years with advances in cutting machine, cutting tools, measuring machine and software. Today, modern cutting machines without coolant using coated carbide tools allow the spiral bevel gear machining with high precision and productivity.

The measurement method by CMM also decides the gear manufacturing errors become more accessible and accurate. Measurement results evaluate the accuracy level of manufactured gears and adjust the manufacturing process parameters to improve machining accuracy.

The development of simulation tools has provided more modern research methods such as loaded and unloaded tooth analysis. This helps to understand the gearing process better, thereby providing design adjustment solutions to improve the transmission quality of the gears.

## References

1. J. Wang, L. Kong, B. Liu, X. Hu, X. Yu, W. Kong, The mathematical model of spiral bevel gears: a review. *Strojnicki Vestnik* **60**, 93–105 (2014)
2. F. Zheng, X. Han, H. Lin, W. Zhao, Research on the cutting dynamics for face-milling of spiral bevel gears. *Mech. Syst. Sig. Process.* **153**, 107488 (2021)
3. M. Vivet, A. Acinapura, D. Mundo, and T. Tamarozzi, Loaded tooth contact analysis of spiral bevel gears with kinematically correct motion transmission, in *International Gear Conference, Lyon Villeurbanne, France* (2018)
4. C. Gosselin, J. Thomas, N. Meixel, *CNC Face Milling of Straight and Spiral Bevel Gears* (2019), pp. 58–63. [www.geartechnology.com](http://www.geartechnology.com)
5. Á. Álvarez, A. Calleja, N. Ortega, L.N. López De Lacalle, Five-axis milling of large spiral bevel gears: toolpath definition, finishing, and shape errors. *Metals* **8**, 5 (2018)
6. Y. Abe, H. Gumbara, K. Kawasaki, I. Tsuji, Manufacturing method of large spiral bevel gears in a cyclo-paloid system using multi-axis and multi-tasking machine tool. *Gear Technol.* **201**, 56–61 (2011)
7. C. Efstathiou, N. Tapoglou, A novel CAD-based simulation model for manufacturing spiral bevel gears by face milling. *CIRP J. Manufact. Sci. Technol.* **33**, 277–292 (2021)
8. F. Zheng, X. Han, L. Hua, R. Tan, W. Zhang, A semi-analytical model for cutting force prediction in face-milling spiral bevel gears. *Mech. Mach. Theory* **156**, 104165 (2021)
9. Q. Fan, Enhanced algorithms of contact simulation for hypoid gear drives produced by face-milling and face-hobbing processes. *J. Mech. Des.* **129**, 31–37 (2007)
10. V.V. Simon, Optimization of face-hobbed hypoid gears. *Mech. Mach. Theory* **77**, 164–181 (2014)

11. I. Cialis, P. Mamouri, S. Kompogiannis, Design and manufacturing spiral bevel gears using CNC milling machines. *IOP Confer. Ser. Mater. Sci. Eng.* **393**, 012066 (2018)
12. T.J. Maiuri, Spiral bevel and hypoid gear cutting technology update. *Gear Technol.* **24**, 28–39 (2007)
13. H.J. Stadtfeld, *Bevel Gear Cutting Methods* (2016), pp. 54–64. [www.geartechnology.com](http://www.geartechnology.com)
14. F. Zheng, L. Hua, D. Chen, X. Han, Generation of noncircular spiral bevel gears by face-milling method. *J. Manufact. Sci. Eng.* **138**, 1–12 (2016)
15. K. Gupta, N.K. Jain, R.L. Tajmir, *Advanced Gear Manufacturing and Finishing* (Academic Press, 2017)
16. A. Artoni, A. Bracci, M. Gabiccini, M. Guiggiani, Optimization of the loaded contact pattern in hypoid gears by automatic topography. *J. Mech. Des.* **131**, 1–9 (2009)
17. A. Artoni, A. Kahraman, An ease-off based optimization of the loaded transmission error of hypoid gears. *J. Mech. Des.* **132**, 011010–011012 (2010)
18. J. Astoul, E. Mermoz, M. Sartor, J.M. Linares, A. Bernard, New methodology to reduce the transmission error of the spiral bevel gears, in *CIRP Annals: Manufacturing Technology* (2014)
19. V.V. Simon, Influence of tooth errors and misalignments on tooth contact in spiral bevel gears. *Mech. Mach. Theory* **43**(10), 1253–1267 (2008). <https://doi.org/10.1016/j.mechmachtheory.2007.10.012>
20. V.V. Simon, Design and manufacture of spiral bevel gears with reduced transmission errors. *J. Mech. Des.* **131**, 041007–041011 (2009)
21. V.V. Simon, Optimal machine-tool settings for the manufacture of face-hobbed spiral bevel gears. *J. Mech. Des.* **136**, 0811004–1 (2014)
22. Y. Zhuo, X. Xiang, X. Zhou, H.L. Lv, G. Teng, A method for the global optimization of the tooth contact pattern and transmission error of spiral bevel and hypoid gears. *J. Zhejiang Univ. Sci. A* **18**, 377–392 (2017)

# Design of a Face Recognition Technique Based MTCNN and ArcFace



Dang Thai Viet, Phan Van Thien, Nguyen Huu Tu, Hoang Gia Minh,  
and Ngoc-Tam Bui

**Abstract** The current trend of automation and data sharing in manufacturing technologies and daily living is the 4th Industrial Revolution. Computer vision technology has permeated our daily lives as a result of advancements in artificial intelligence and processing capacity. We propose using the ArcFace model, which blends deep neural networks with multi-tasking convolutional neural networks (MTCNN). The coding procedure of the agglomeration neural network facilitates the dimension-appropriate encoding of images. Techniques aimed at enhancing face recognition's most distinctive characteristics. For the face recognition model to operate at peak efficiency, the facial recognition feature must integrate with finger gestures to control smart home activities, communicate with data, and link effortlessly to smart devices via IoT technology. We construct a facial recognition model utilizing an embedded Jetson Nano computer, a fingerprint scanning module, and a Raspberry Pi camera. The IoT smart home utilizes an embedded Raspberry Pi 3B + computer. The results indicate an approximate precision of 96% and a processing speed of 16 FPS. The interface of an Internet of Things (IoT) smart house illustrates the successful execution of real-time functionalities.

**Keywords** Artificial intelligence (AI) · Computer vision · IoT · Smart home · Face recognition · Gesture recognition

---

D. T. Viet (✉) · P. Van Thien · N. H. Tu · H. G. Minh  
Ha Noi University of Science and Technology, Hanoi, Vietnam  
e-mail: [viet.dangthai@hust.edu.vn](mailto:viet.dangthai@hust.edu.vn)

N.-T. Bui  
Shibaura Institute of Technology, Tokyo, Japan  
e-mail: [tambn@shibaura-it.ac.jp](mailto:tambn@shibaura-it.ac.jp)

© The Author(s), under exclusive license to Springer Nature Switzerland AG 2024  
B. T. Long et al. (eds.), *Proceedings of the 3rd Annual International Conference on Material, Machines and Methods for Sustainable Development (MMMS2022)*, Lecture Notes in Mechanical Engineering, [https://doi.org/10.1007/978-3-031-57460-3\\_8](https://doi.org/10.1007/978-3-031-57460-3_8)



## 1 Introduction

In the 4th Industrial Revolution, informatics and data science provided substantial support for automated production [1]. The use of this astonishing innovation resulted in a multitude of accomplishments, such as intelligent monitoring systems, sophisticated transportation infrastructure, automated financial systems and industrial assembly robot manipulators [2–5].

In keeping with this trend, we introduce the MTCNN model of face recognition for intelligent mechatronic systems. By comparing the pre-selected facial features from the image database with the person's face, the system is able to contemplate the correction of the face. Recent research, Local Binary Pattern (LBP), transformed the input image to a binary image, then partitioned the face into blocks and calculated the histogram density per block to produce the histogram feature [6]. However, the extraction of features from the histogram may be influenced by external factors such as input image quality, illumination, etc. In addition, the Dlib method correlated with HOG and SVM [7] was employed. However, there was a possibility that the accuracy would suffer if the face angle was altered. In addition, a well-known research using the FaceNet face recognition system [8] calculated the distance between face vectors using the triplet loss function. However, this technique has the problem that the quantity of math operations the computer must execute grows exponentially as the volume of input data and the overlapping features between the faces rise. To reduce this effect, the researchers employ the ArcFace model, which calculates the distance between face vectors and creates a deviation angle and an additive angular margin  $m$  to separate the characteristics of face vectors. ArcFace has developed and enhanced FaceNet, resulting in a decomposition that prevents misidentification when the original data image resembles a photo taken from a direct angle. The experimental results were reached at a frame rate of 14–16 FPS and an accuracy of approximately 96%. The findings of facial recognition for security are linked with finger gestures for home automation control. All monitoring data in real time is shown via the IoT smart home interface.

## 2 Methodology

The paper proposes to implement a face recognition process summarized as shown in Fig. 1.

MTCNN, an innovative algorithm for detecting faces and facial landmarks with great speed and precision, is utilized in this procedure. The MTCNN method consists of three neural networks (NN) representing three stages. In the first stage, we employ a CNN shallow to create candidate bounding boxes rapidly. The second phase refines the acquired bounding boxes using a more sophisticated CNN network. In the final step, a more advanced CNN network is used to improve the data and generate facial landmarks. Then, Arcface takes each individual's face image as input and generates

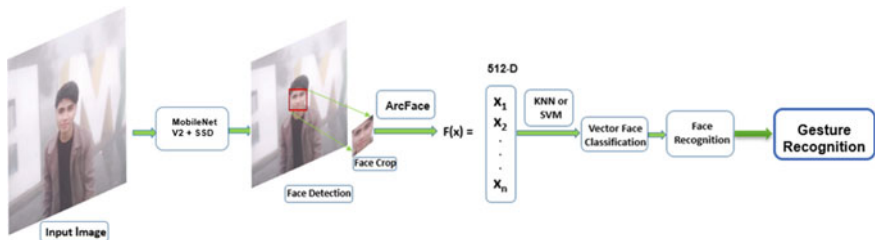


Fig. 1 Face and gesture recognition process

a vector of 512 numbers reflecting the most prominent facial traits. The term for this vector in machine learning is embedding vector. Next, a classifier is utilized to determine the distance between facial traits in order to distinguish between many identities. Due to their effectiveness in multi-class classification, Support Vector Machine (SVM) [9] and K-Nearest Neighbors (KNN) [10] are two of the most popular face recognition methods. Eventually, when the faces have been identified, users continue to run the IoT system via hand gestures.

### 2.1 MTCNN

The image is first rescaled to get an image pyramid that helps the model to detect faces of different sizes (Fig. 2).

### 2.2 ArcFace

Deep Convolutional Neural Network (DCNN) models have become prevalent for the extraction of facial features due to their exceptional benefits. There are two primary techniques to develop a classification model from vectors with facial features in order to improve the accuracy of face recognition: the triplet loss function and the softmax loss function. The softmax loss function is typically applied to situations involving face recognition [11]. The softmax loss function combines the cross entropy loss function with the softmax activation function [12]. Using the softmax function, however, causes the linear transformation matrix to grow according to the number of classes being classified. The softmax loss function  $L_1$  is depicted here:

$$L_1 = -\frac{1}{N} \sum_{i=1}^N \log \frac{e^{W_{y_i x_i} T + b_{y_i}}}{\sum_{j=1}^n e^{W_{y_j x_j} T + b_{y_j}}} \tag{1}$$

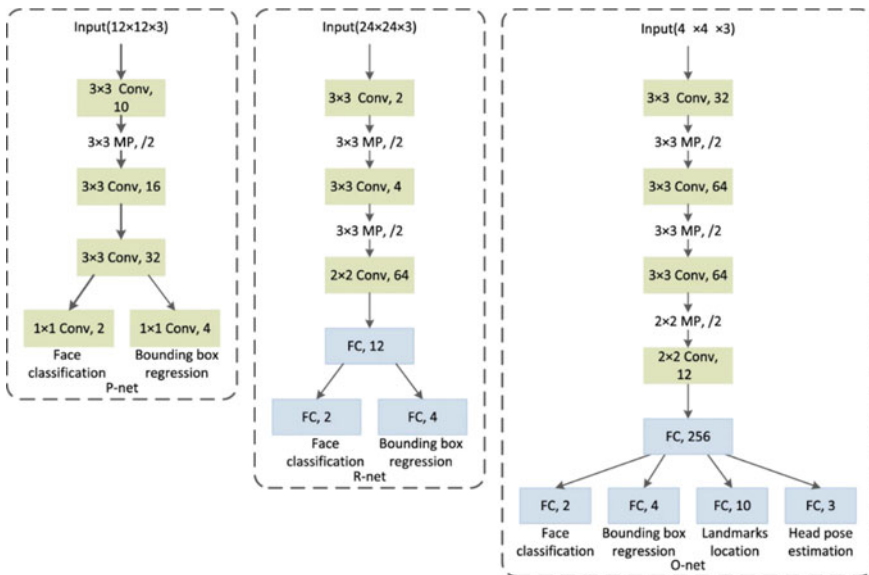


**Fig. 2** MTCNN architecture

where  $x_i \in R^d$  represents the depth feature of sample  $i$ , of class  $y_i$ . Embedded feature size  $d$  is set to 512.  $W_j \in R^d$  represents the  $j$ th column of the weight vector  $W \in R^{d \times n}$  and  $b_j \in R^n$  is the bias. The batch and numeric class sizes are  $N$  and  $n$  respectively.

Since embedded features are dispersed around the center of each feature on the hypersphere, an additive angular margin penalty  $m$  is introduced between  $x_i$  and  $W_{y_i}$ , while intra-class compactness and inter-class differentiation are improved. Due to the fact that the suggested additive angular margin penalty is equivalent to the geodetic distance margin penalty in the normalized hypersphere, the method is referred to as ArcFace Lost  $L_2$  (see Eq. 2).

$$L_2 = -\frac{1}{N} \sum_{i=1}^N \log \frac{e^{s(\cos(\theta_{y_i} + m))}}{e^{s(\cos(\theta_{y_i} + m))} + \sum_{j=1, j \neq i}^n e^{s(\cos(\theta_{y_j} + m))}} \quad (2)$$

Figure 3 shows the process of training a DCNN for face recognition by the ArcFace loss function.

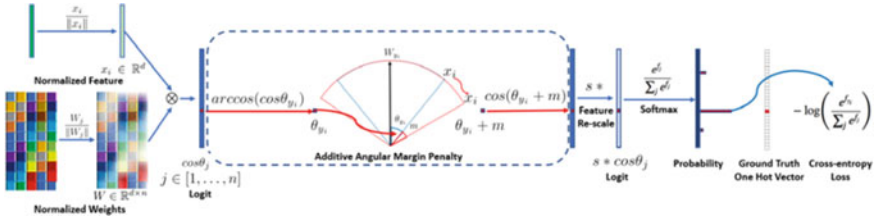


Fig. 3 Procedure for training a DCNN for recognition by ArcFace loss

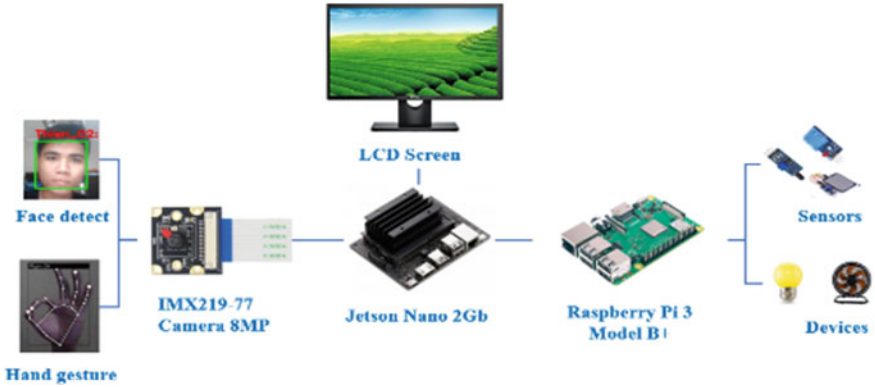


Fig. 4 Block diagram of the proposed hardware system

### 3 System Structure

#### 3.1 Hardware and Software

##### Process and System Design

The face and hand gesture recognition system using Jetson Nano is capable of handling multiple video streams (see Fig. 4).

In this system, based on the input data set, the camera conducts face recognition in real time; if the face matches, the system will continue to allow the operator to manipulate gestures to control the IoT system (see Fig. 5).

### 4 Experimental Results

On training dataset with 5 frames per class. We evaluate the face recognition model using ArcFace with models such as: Dlib, LBP. The ArcFace algorithm achieves predominant performance on the Jetson Nano embedded computer with the accuracy



Fig. 5 The control interface of IoT system

of 95–97 (%) and the frame rate up to 25 (FPS). The results are depicted more clearly in Table 1.

The ArcFace model balances accuracy and speed in facial recognition. With the application of hand gesture recognition after verifying the user’s identity, the user can control the sensor devices, the light in the system is clearly displayed as being shown in Fig. 6.

Table 1 List of facial recognition test results of some models

Model	Accuracy (%)	FPS
LBP	84–88	19–21
DLIB	52–59	9–10
MTCNN + ArcFace	95–97	21–25

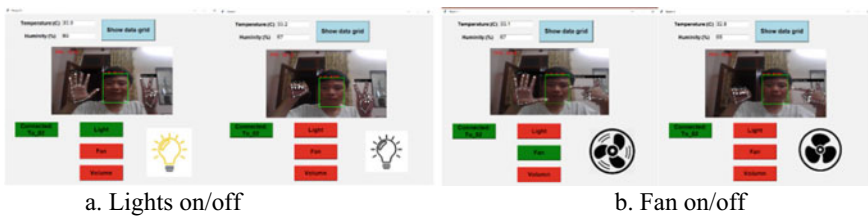


Fig. 6 Control features with display of biological indicators

## 5 Conclusions

Face recognition that improves safety and security has proven to be a formidable obstacle for researchers. We tried the application of the ArcFace model in face recognition and achieved generally favorable results. Real-time testing and evaluation with 30 distinct input faces demonstrate an inference rate of 16 FPS and an accuracy of roughly 96%. In addition, the gesture recognition function that integrates controls with a set of six operations has a 96% accuracy rate. The entire system was developed and implemented on Jetson nano, which yields the best results compared to other embedded computers (Raspberry Pi 3B+, etc.). In addition to facial recognition's security contribution in smart administration system user authentication, gesture combinations are automatically identified by hand figures, enabling automatic control and monitoring of IoT devices.

**Acknowledgements** This research is funded by Hanoi University of Science and Technology (HUST) under project number T2022-PC-029. The authors express grateful thankfulness to Vietnam-Japan International Institute for Science of Technology (VJIIST), School of Mechanical Engineering, HUST, Vietnam and Shibaura Institute of Technology, Japan.

## References

1. R.S. Peres, X. Jia, J. Lee, K. Sun, A.W. Colombo, J. Barata, Industrial artificial intelligence in industry 4.0: systematic review, challenges and outlook. *IEEE Access* **8**, 220121–220139 (2020)
2. T.-V. Dang, N.-T. Bui, Research and design obstacle avoidance strategy for indoor autonomous mobile robot using monocular camera. *J. Adv. Transp.* (2022)
3. T.-V. Dang, N.-T. Bui, Multi-scale fully convolutional network-based semantic segmentation for mobile robot navigation. *Electronics* **12**(3), 1–18 (2023)
4. T.-V. Dang, Smart home management system with face recognition based on ArcFace model in deep convolutional neural network. *J. Robot. Control* **3**(6), 754–761 (2022)
5. T.-V. Dang, D.-S. Nguyen, Optimal navigation based on improved A\* algorithm for mobile robot, in *International Conference on Intelligent Systems and Networks 2023, 18–19 March, Hanoi, Vietnam* (2023)
6. S. Pawar, V. Kithani, S. Ahuja, S. Sahu, Local binary patterns and its application to facial image analysis, in *Proceedings of the 2011 International Conference on Recent Trends in Information Technology (ICRTIT)* (2011), pp. 782–786
7. H.S. Dadi, G.K.M. Pillutla, Improved face recognition rate using HOG features and SVM classifier. *IOSR J. Electr. Commun. Eng.* **11**(4), 33–44 (2016)
8. T.-V. Dang, Smart attendance system based on improved facial recognition. *J. Robot. Control* **4**(1), 46–54 (2023)
9. M.E. Mavroforakis, S. Theodoridis, Tutorial on support vector machine (SVM) through geometry, in *Proceedings of the 2005 13th European Signal Processing Conference* (2015)
10. A. Wirdiani, P. Hridayami, A. Widiari, Face identification based on K-nearest neighbor. *Sci. J. Inform.* **6**(2), 150–159 (2019)

11. J. Wang, C. Zheng, X. Yang, L. Yang, EnhanceFace: adaptive weighted SoftMax loss for deep face recognition. *IEEE Sig. Process. Lett.* **29**, 65–69 (2022)
12. X. Li, D. Chang, T. Tian, J. Cao, Large-margin regularized Softmax cross-entropy loss. *IEEE Access* **7**, 19572–19578 (2019)

# Development of a New Flow-Mode Magneto-Rheological Damper Featuring Tooth-Shaped Duct



Quoc-Duy Bui, Huu-Quan Nguyen, Long-Vuong Hoang,  
and Quoc Hung Nguyen

**Abstract** This article focuses on a novel configuration of flow-mode magneto-rheological fluid (MRF) based damper (MRD). The proposed MRD replaces the conventional annular MRF duct with a tooth-shaped one to lengthen the effective MRF segments, thereby improving the overall damping performance. Following an introductory part, the new MRD configuration is described. A design optimization procedure is then conducted to minimize the off-state force with constraints of desired maximum damping force and damper size. The optimal solutions are presented with discussions and compared with those of conventional MRDs. The advantages of the new MRD are subsequently addressed and its quasi-static behavior is predicted for various input excitations.

**Keywords** Damper · Flow-mode · Magneto-rheological · Optimal design · Tooth-shaped

---

Q.-D. Bui (✉) · H.-Q. Nguyen · L.-V. Hoang  
Faculty of Mechanical Engineering, Industrial University of Ho Chi Minh City, Ho Chi Minh City, Vietnam  
e-mail: [buiquocduy@iuh.edu.vn](mailto:buiquocduy@iuh.edu.vn)

H.-Q. Nguyen  
e-mail: [nguyenhuuquan@iuh.edu.vn](mailto:nguyenhuuquan@iuh.edu.vn)

L.-V. Hoang  
e-mail: [hoanglongvuong@iuh.edu.vn](mailto:hoanglongvuong@iuh.edu.vn)

Q. H. Nguyen (✉)  
Faculty of Engineering, Vietnamese–German University, Thu Dau Mot City, Binh Duong Province, Vietnam  
e-mail: [hung.nq@vgu.edu.vn](mailto:hung.nq@vgu.edu.vn)



## 1 Introduction

It is well-known that vibration control systems usually face the trade-off between conflicting performance indices in the design phase. In conventional vibration control systems, the trade-off is limited because of fixed springs and dampers. To overcome this, smart material-based semi-active vibration control systems have been broadly explored. Among them, MRF-based ones have shown potential in recent applications relying on their reversible, rapid and continuous controllability [1, 2]. One of the most interesting applications is MRD, which has been studied in various industrial fields [3–6]. In the flow-mode MRDs, the MRF is flowing reciprocally between two chambers (one “compression” and one “rebound”) via orifices while the piston is translating. However, the annular duct as well as rectangular exciting coils in the conventional design of the MRDs could not provide best damping efficiency since the MRF was only activated on short paths of the duct. Therefore, in this paper, a novel flow-mode MRD is proposed for semi-active vibration control systems. In the new MRD, a tooth-shaped duct is employed to increase the available length of the MRF. Chamfers are added to the coil geometry to enable each segment of the duct to be magnetized. The major geometry of the MRD is then optimized based on finite element method, in which the objective function is to minimize the off-state force considering the desired maximum damping force and damper size. The optimal solutions of the proposed MRD are then assessed and its quasi-static behavior upon various input excitations is analyzed.

## 2 Modeling of the Flow-Mode MRD Featuring Tooth-Shaped Duct

Figure 1 presents the tooth-shaped duct flow-mode configuration of the proposed MRD. The material of magnetic components (gray) is C45 steel while that of non-magnetic components (blue) is aluminum. The damper piston has a valve-like structure formed from the combination of the piston housing, piston core and tooth-shaped duct. The two chambers are filled with MRF. An accumulator, including a gas chamber and a floating piston, is employed to enable the fluid communication. A magnetic coil is directly wound on the piston housing, leaving thin walls against the MRF duct. By offering two chamfers to the coil geometry, the magnetization is enabled throughout each segment of the tooth-shaped duct as the coil is electrically powered. The MRF in the gap then becomes quasi-solid to resist the fluid flow and produce damping force. It can be realized that this new structure remarkably improves the effective length of the MRF and therefore the overall performance of the MRD.

By disregarding the insignificant friction force at the seals and assuming that the MRF in the duct behaves as a quasi-static fluid, the damping force  $F_d$  of the flow-mode MRD is obtained as follows

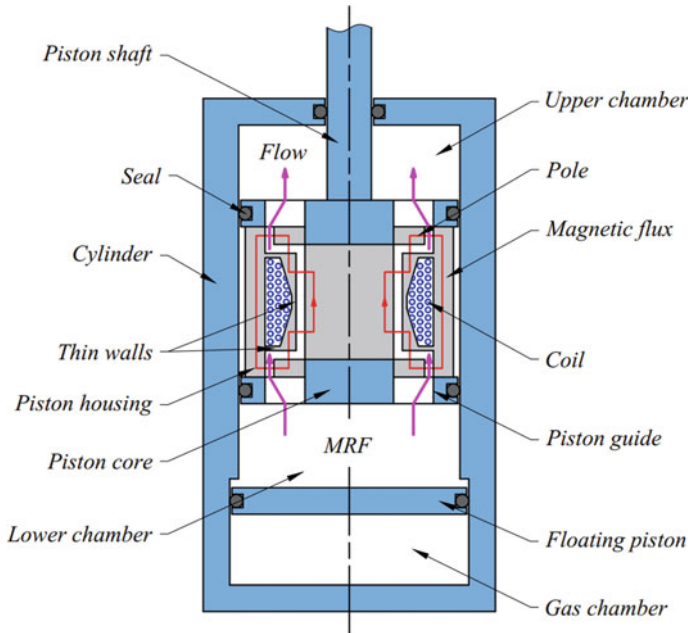


**Fig. 1** Configuration of the flow-mode MRD featuring tooth-shaped duct

$$F_d = P_a A_s + F_\eta + F_\tau \quad (1)$$

In the above,  $A_s$  is the sectional area of the piston shaft and  $P_a$  denotes the pressure in the gas chamber that can be determined by

$$P_a = P_0 \left( \frac{V_0}{V_0 + A_s u} \right)^\alpha \quad (2)$$

where  $u$  is the piston displacement,  $P_0$  and  $V_0$  are respectively the initial pressure and volume of the gas chamber, and  $\alpha$  is the thermal expansion coefficient.  $F_\eta$  and  $F_\tau$  are respectively the viscous and yield stress-induced damping forces which can be calculated as follows

$$F_\eta = 2 \left[ \frac{6\eta l_f}{\pi r_{g.f} t_g^3} + \frac{6\eta}{\pi t_g^3} \ln \left( \frac{r_o}{r_i} \right) + \frac{6\eta l_c}{\pi r_{g.c} t_g^3} \right] (A_p - A_s)^2 \dot{u} \quad (3)$$

$$F_\tau = 2 \left[ \frac{c_p l_f \tau_{y.f}}{t_g} + \frac{c_p (r_o - r_i) \tau_{y.r}}{t_g} + \frac{c_p l_c \tau_{y.c}}{t_g} \right] (A_p - A_s) \quad (4)$$

where  $\dot{u}$  is the piston velocity,  $\tau_y$  and  $\eta$  are respectively the yield stress and post-yield viscosity the MRF,  $r_g$  is the average radius of the MRF gap,  $t_g$  is the MRF gap thickness,  $l$  is the effective MRF length, and  $c_p$  characterizes the flow profile of the

MRF [7]. The three terms in the square brackets in turn express the pressure drops of the MRF flow through the three segments of the tooth-shaped duct, including the flange, radial and core segments. The subscripts  $f$ ,  $r$  and  $c$  are used to denote the corresponding segments, and  $r_o$  and  $r_i$  are the outer and inner radii of the radial segment. By removing the field-dependent third term in Eq. (1), the off-state force  $F_0$  of the MRD is obtained

$$F_0 = P_a A_s + F_\eta \quad (5)$$

In this research, three MRF types manufactured by Lord Corporation, 122-2ED, 132-DG and 140-CG MRFs, are considered for the proposed MRD. The yield stress  $\tau_y$  depending on magnetic field intensity can be given by

$$\tau_y = 2.717 \cdot 10^5 C V_f^{1.5239} \tanh(6.33 \cdot 10^{-6} H) \quad (6)$$

in which  $H$  is the magnetic field intensity,  $V_f$  and  $C$  characterize respectively the iron volume fraction and carrier fluid of the MRF type.

In order to solve the magnetic circuit, the finite element (FE) model of the proposed MRD is built and analyzed on the ANSYS software. An optimization procedure is then conducted to obtain optimal solutions for significant geometrical dimensions of the MRD. The objective function of the problem is to minimize the off-state force  $F_0$ , subjected to the maximum damping force  $F_d$  is greater than an expected value  $F_e$ . Furthermore, the piston radius  $R$  is constrained not to exceed the general value of commercial dampers for compactness and interchangeability. In this study, the first-derivative method associated with the golden-section algorithm of the ANSYS optimization tool is employed for the optimization problem. The detailed process can be found in previous literature [8].

### 3 Results and Discussions

In this section, the optimal solutions for the new flow-mode MRD featuring tooth-shaped duct are described. The 0.511-diameter copper wire is used for winding. Table 1 shows the rheological characteristics of the three MRF types. Assuming that the proposed MRD is designed for a four-wheel car suspension in which: the exciting amplitude of road input is 0.08 m, the damping ratio is 0.7, the sprung mass is 230 kg, and the spring stiffness is 16 kN; the amplitude of the displacement  $u$  and velocity  $\dot{u}$  of the piston are found respectively to be 0.1 m and 0.6 m/s [9], and the expected value of damping force  $F_e$  for the optimization problem is set by 1280 N [10].

The optimal solutions of the proposed damper corresponding to the three MRF types are detailed in Table 2. It is noted that the value of 23 mm is assigned to the upper bound of the piston radius  $R$ , the thin walls thickness is fixed by 0.8 mm considering manufacturing aspects, and the maximum current intensity is set by 2 A for safety and economy. As shown in the table, the piston radius  $R$  tends to reach maximum for

**Table 1** Rheological properties of the three MRF types

Property	122-2ED	132-DG	140-CG
Viscosity $\eta$ (Pa.s)	0.075	0.092	0.28
Carrier fluid coefficient	1	1	1
Volume fraction of iron	0.22	0.32	0.4

**Table 2** Optimal solutions of the proposed MRD

Parameter (mm)	122-2ED	132-DG	140-CG
Coil width $w_c$	33.7	30	28.6
Coil height $h_c$	8.27	7.79	7.38
Width chamfer $w_{ch}$	14.2	12.51	11.94
Height chamfer $h_{ch}$	3.49	2.8	2.15
Flange length $l_f$	6.86	5.61	4.73
Flange thickness $t_f$	2.42	2.34	2.17
Piston core radius $r_c$	8.74	8.82	8.8
MRF gap thickness $t_g$	2.36	2.66	3.06
Piston housing thickness $t_h$	2.81	2.9	2.91
Piston length $L$	53.8	48.1	45.8
Piston radius $R$	23	23	22.9
Off-state force $F_0$ (N)	91	73	125
Max. damping force $F_d$ (N)	1297	1297	1299

all three MRF types. Compared with the 122-2ED MRF, the 132-DG MRF provides most desirable damping performance (lowest off-state force  $F_0$ ). Accordingly, the 132-DG MRF is most reasonable for the proposed MRD in this case study.

Figure 2 shows the FE model, magnetic flux lines and magnetic flux density of the optimal MRD featuring the 132-DG MRF. It is seen from the figure that the magnetic flux covers all segments of the tooth-shaped duct, which activates the MRF throughout the duct length and hence considerably improves the damping efficiency.

For more evaluation of the advantages of the MRD featuring tooth-shaped duct, its performance characteristics are compared to those of a conventional MRD with annular duct. The optimal solution of the conventional MRD in the same case study is as follows:  $F_0 = 106$  N,  $F_d = 1294$  N,  $R = 23$  mm. It is clear that the vibration isolation of the MRD is significantly improved with the new tooth-shaped duct since the off-state force of the proposed MRD is much smaller than that of the conventional MRD.

The responses in time and displacement domain of the optimal MRD featuring the 132-DG MRF are simulated in Fig. 3 under excitations of 1 Hz frequency, 100 mm amplitude and 0–2 A current intensity. The figure shows the essential dependence of the damping characteristic on the exciting magnetic field. It is obvious because the damping force is dominated by the field-dependent yield stress-induced force, according to Eqs. (4) and (6).

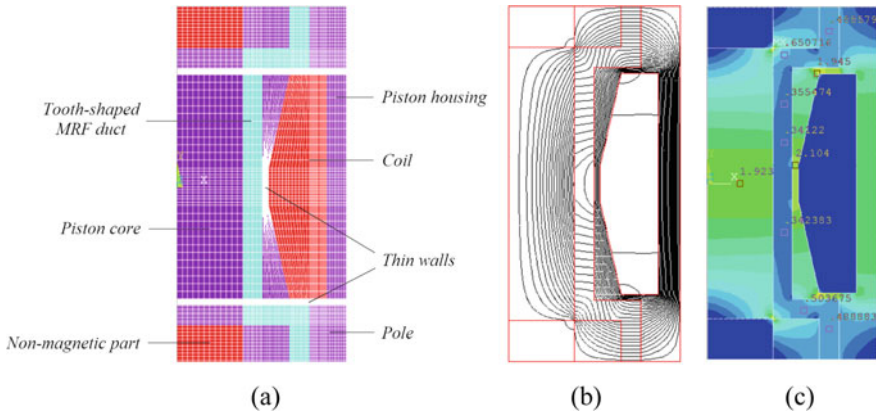


**Fig. 2** Optimal solution of the proposed MRD featuring the 132-DG MRF: **a** FE model, **b** magnetic flux lines, and **c** magnetic flux density

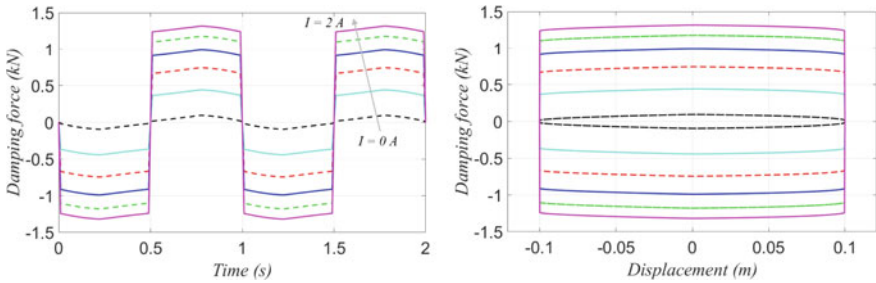


**Fig. 3** Prediction of damping force responses of the optimal MRD under 1 Hz frequency, 100 mm amplitude and 0–2 A current (increment of 0.4 A)

### 4 Conclusions

In this paper, a novel flow-mode MRD with tooth-shaped duct was developed for semi-active vibration control systems. Three MRF types, 122-2ED, 132-DG and 140-CG MRFs, were considered for the MRD modeling. The significant geometry of the damper was then optimized for the case study of four-wheel car suspension using the ANSYS optimization tool. The optimal solutions showed that the 132-DG MRF was most suitable for the proposed MRD in this case study. The quasi-static responses of the optimized damper upon different input excitations were subsequently predicted. It was shown from the simulation results that the MRD energy is dissipated with the exciting magnetic field intensity. In the next study stage, the MRD prototype will be designed, manufactured and assessed via experiments.

**Acknowledgements** This work was supported by research fund from Ministry of Education and Training (MOET) of Vietnam.

## References

1. S. Pisetskiy, M. Kermani, High-performance magneto-rheological clutches for direct-drive actuation: design and development. *J. Intell. Mater. Syst. Struct.* **32**, 2582–2600 (2021)
2. Y. Shiao, M.B. Kantipudi, High torque density magnetorheological brake with multipole dual disc construction. *Smart Mater. Struct.* **31**, 045022 (2022)
3. M. Abdeddaim, S. Djerouni, A. Ounis, B. Athamnia, E.N. Farsangi, Optimal design of magnetorheological damper for seismic response reduction of base-isolated structures considering soil-structure interaction. *Structures* **38**, 733–752 (2022)
4. Q.D. Bui, Q.H. Nguyen, L.V. Hoang, D.D. Mai, A new self-adaptive magneto-rheological damper for washing machines. *Smart Mater. Struct.* **30**, 037001 (2021)
5. Y. Hua, S. Zhu, X. Shi, High-performance semiactive secondary suspension of high-speed trains using negative stiffness and magnetorheological dampers. *Veh. Syst. Dyn.* (2021)
6. M. Jiang, X. Rui, W. Zhu, F. Yang, Y. Zhang, Design and control of helicopter main reducer vibration isolation platform with magnetorheological dampers. *Int. J. Mech. Mater. Des.* **17**, 345–366 (2021)
7. J.D. Carlson, D.M. Catanzarite, K.A.S. Clair, Commercial magneto-rheological fluid devices. *Int. J. Mod. Phys. B* **10**, 2857–2865 (1996)
8. Q.H. Nguyen, Y.M. Han, S.B. Choi, N.M. Wereley, Geometry optimization of MR valves constrained in a specific volume using the finite element method. *Smart Mater. Struct.* **16**, 2242 (2007)
9. Q.D. Bui, Q.H. Nguyen, Development of a novel self-adaptive shear-mode magneto-rheological shock absorber for motorcycles. *Mech. Mach. Sci.* **113**, 744–754 (2021)
10. Q.D. Bui, Q.H. Nguyen, T.T. Nguyen, D.D. Mai, Development of a magnetorheological damper with self-powered ability for washing machines. *Appl. Sci.* **10**, 4099 (2020)

# Design the Abnormal Object Detection System Using Template Matching and Subtract Background Algorithm



Dang Thai Viet and Ngoc-Tam Bui

**Abstract** Computer vision is an artificial intelligence (AI) subfield that enables computers and systems to extract information from digital photos, movies, and other visual inputs. Detection systems are an important use in industrial production lines. In this paper, an automatic small abnormal object system is designed. First, the author obtains an image devoid of anomalous objects, which is then processed using the Candy filter to produce the standard form. Second, define the primary pattern, sub pattern 1, sub pattern 2, and the deviation between the new image and the original image. Then, we use template matching and background subtraction to identify questionable locations. Finally, live picture features will be compared to original image features. With Candy filter, the precision will be enhanced. The findings of image processing will be transmitted to operate the automatic abnormal removal equipment. The result indicates an accuracy of ~ 90%. The processing time is < 5 s, which has no effect on the production line cycle time.

**Keywords** Artificial intelligence · Computer vision · Detection system · Template matching · Subtract background

## 1 Introduction

As a result of the fourth industrial revolution, significant advances have been made in high technology, particularly artificial intelligence. Computer vision is an area of artificial intelligence (AI) that enables computers and systems to extract information from digital images, videos, and other visual inputs [1]. In a range of fields, such

---

D. T. Viet (✉)

Ha Noi University of Science and Technology, Hanoi, Vietnam  
e-mail: [viet.dangthai@hust.edu.vn](mailto:viet.dangthai@hust.edu.vn)

N.-T. Bui

Shibaura Institute of Technology, Tokyo, Japan  
e-mail: [tambn@shibaura-it.ac.jp](mailto:tambn@shibaura-it.ac.jp)

as applications for smart navigation [2, 3], biometric data management [4], transportation [5], quality monitoring system, and smart systems [6], image processing applications have been shown to be highly effective.

Visual inspection refers to the examination of products for quality assurance. Visual inspection has also been used to examine the interior and outside of manufacturing plant storage tanks, tanks, pressure vessels, pipes, and other equipment. The vast bulk of visual checks were performed manually. Consequently, the testing cycle is time-consuming and requires specialized personnel. In manual visual inspection, the naked eye is the major factor; nonetheless, the mistake rate is between 20 and 30% [6]. Human variables such as temperament, health, and boredom, etc. Other environmental variables include light, bonding distance, angle of tilt, etc.

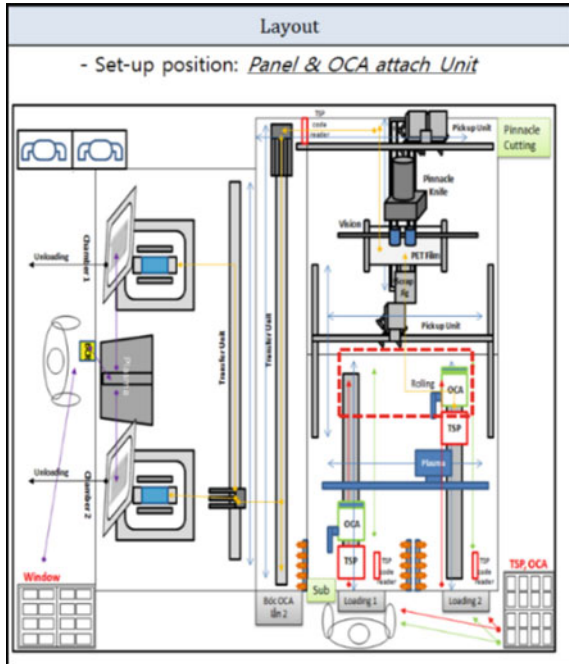
Examining too-small objects visually becomes unrealistic and difficult. In order to overcome the shortcomings, automatic testing systems have included camera vision. Image processing technology helps the creation of an intelligent quality monitoring system. Machine vision contributes to several steps of image processing, including image acquisition, pre-processing, segmentation, classification, and warning. The precision of the technique for automatic quality control will be significantly improved. Image processing is an integral component of computing [7]. The development of an algorithm for image processing to monitor and inspect product quality. Histogram, Canny Edge, RGB color filter, HSV color filter, etc. are often the most essential algorithms [7–10].

Then, a color space is an algebraic representation of a mathematical model used to describe colors in the physical world [7]. Background subtraction method [7, 8] is an image processing and computer vision approach that isolates the foreground (foreground) for further processing (identification object, gesture recognition, motion, etc.). Typically, image areas of interest are in the foreground; consequently, good and precise background separation enables these systems to achieve stability and speed. In the processing steps that follow the pretreatment phase, this background separation technique will be utilized. Separation of background scenes is frequently employed in a variety of fields, including security cameras, object recognition, object gesture recognition, and traffic for counting the number of vehicles [1, 3, 8]. Next, template matching [9, 10] is a digital image processing method that identifies a little image within a large image that is almost identical to the sample image.

The study describes an autonomous quality monitoring system for smartphone panel manufacturing facilities, where manual visual inspection is becoming increasingly burdensome and unproductive. The vision approach combines the concepts of backdrop subtraction and template matching. As following are the panel's technical specifications: The anomalies on the phone's display panel are smaller than 0.2 mm, the testing period is only 5 s, and the error rate is decreased by around 20% from the actual peak production about 40 percent.



**Fig. 1** Set up of camera position



## 2 Mechanical System Design

### 2.1 System Requirements

Firstly, the operation diagram is shown as in Fig. 1. Then, the technical staff will set up suitable positions of Camera. Finally, the vision’s principle diagram of an ordinary panel gluing device in Fig. 2.

### 2.2 Automatic Vision Process

The automatic vision process is introduced in Fig. 3

**Step 1:** Panel loading.

Robot immediately transfers panel from Tray to Panel Stage (Jig).

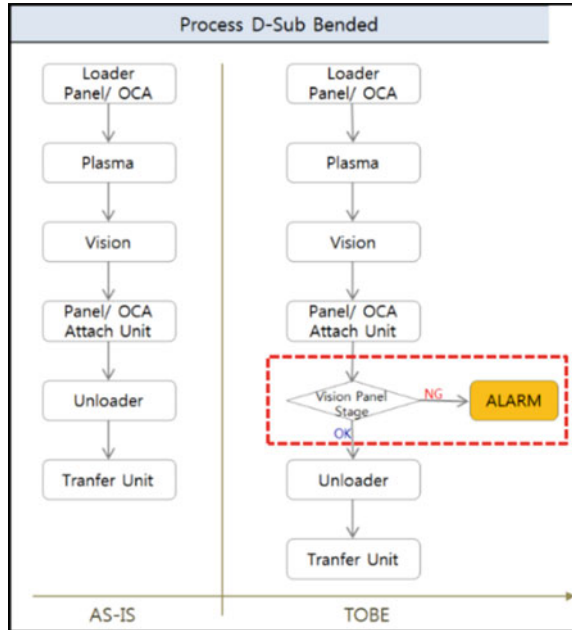
**Step 2:** Plasma surface treatment.

Plasma is utilized to clean the panel surface. Next, a thin coating is adhered to the panel. Robot returns the tray to prepare the subsequent round.

**Step 3:** After the processing of the panel has been completed. Robot introduces a new panel to the state (jig).

**Step 4:** Vision processing is comprised of two case.

**Fig. 2** Principle diagram of vision



- If detecting abnormal, it will be alarm to check the situation of panel. The cleaning processing will be applied in the case of the Reality.
- Otherwise, the case of Virtuality. Software processing will be supported to remove the error.

### 3 Proposed Approach

#### 3.1 Technical Requirements

From the mechanical system (see Fig. 4), the vision program will be designed to detect the abnormal with technical requirements as follows (see Fig. 5):

- Size of abnormal to be detected (requires actual problem):  $> 0.25 \text{ mm}$  ( $\sim 250 \mu\text{m}$ ).
- Maximum processing time per image:  $< 5 \text{ s}$  (product's tact time  $\sim 5 \text{ s/product}$ )

#### 3.2 The Diagram of Control Algorithm

From the original Jig, there are absolutely no disabilities that need to be saved for comparison with subsequent images of Jig in production. The Panels are continuously supplied into the Jig. So, the Jig is possible to get abnormal during the production

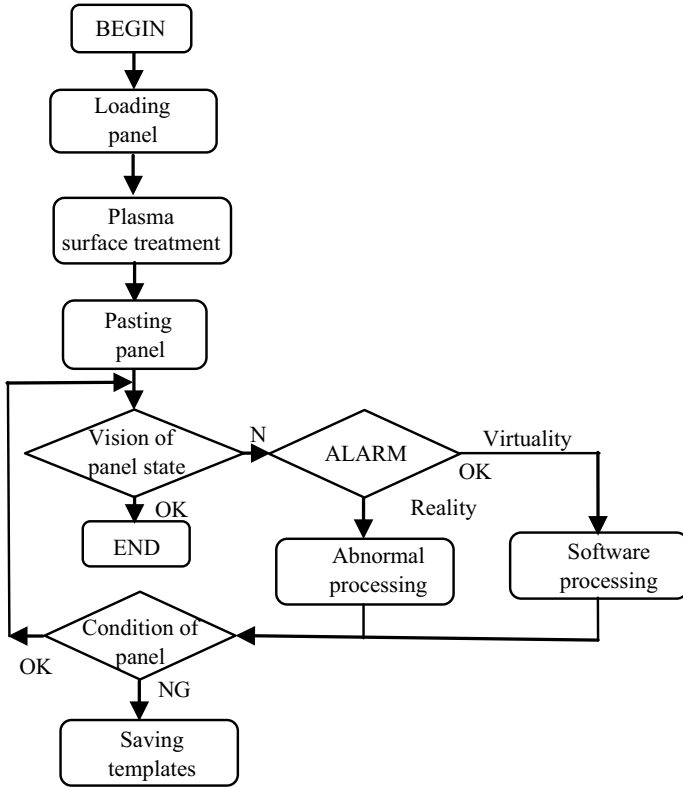


Fig. 3 Automatic vision process

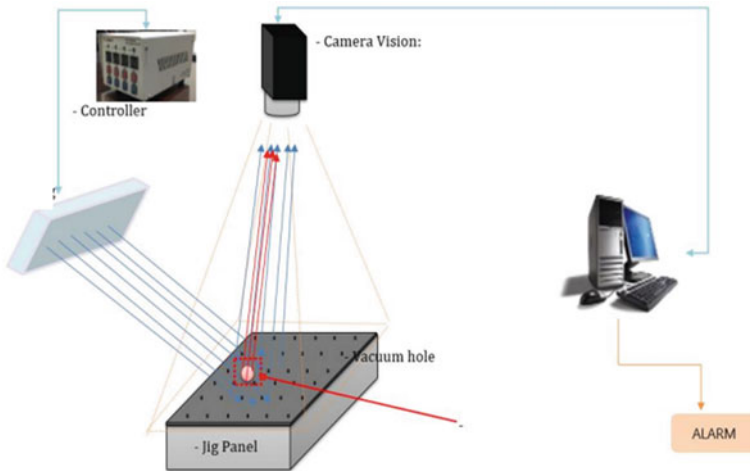
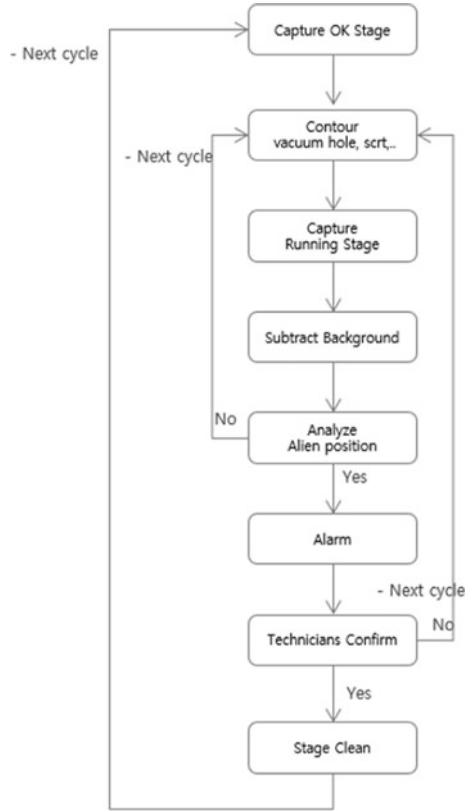


Fig. 4 The system of image processing

**Fig. 5** The vision algorithm diagram



process. The original Jig will be registered exceptions for traits inherent on the Jig as the position of the holes does not have a fixed size and profile  $\varnothing 0.6$  and  $\varnothing 0.8$  mm, scratches are available with fixed size, etc.

There are some suitable methods were used as bellows:

- Party matching (or Template matching): Jig images without any difference become origin image. Compare the new image with the original. If the comparison value is less than threshold, there is an abnormal.
- Check position partical: Save the entire position of the air hole on the Jig. New images will identify all objects including abnormal and air holes. Compare each object with previously trained position. If it is not matched with the positions, it's abnormal.
- Subtract background: Take the Jig image without abnormal as the original. Subtract each new obtained image to gain the original image will be the black background and abnormal. Catch blob to identify abnormal.

**Fig. 6** Detection of 0.2 mm abnormal in automatic vision

Day	Input Qty	NG Qty	Confirm result	Rate
1	1568	15	13	86.7%
2	2314	22	19	86.4%
3	2136	21	18	85.7%
4	1997	13	12	92.3%
5	2712	19	16	84.2%
6	1365	7	7	100.0%
7	2001	29	27	93.1%
8	2452	31	28	90.3%
9	965	12	11	91.7%
10	1544	13	10	76.9%
Ave	19054	182	161	88.5%

To achieve high accuracy and minimize loss time of confirming suspected abnormal, the paper presented the new method of combining the checking position particle and the subtrack background.

## 4 Practical Results

After installing the mechanical system and testing the proposed algorithm, abnormal detection rate is with an accuracy of nearly 90% in a short processing time (< 5 s per cycle). The automatic vision process does not affect the overall takt time of the entire production process. Accuracy average in 10 day with 19,054 products is nearly 90% in Fig. 6 and the real images of experimental results in Fig. 7.

## 5 Conclusions

The paper presents the automatic vision method combining template matching and subtract background. The practical production system improved the quality rate of detection abnormal with the accuracy about 90%. Furthermore, the data of templates will be enhanced because of saving new abnormal samples. The automatic production of panel guarantees the tactile belows 5 s/product and detection of <0.2 mm abnormal. The vision program is optimized and improved the ability in continuous production mode with big data of samples. Mechanical system combining with vision system is designed successfully. PLC program is applied and communicated correctly with all devices.

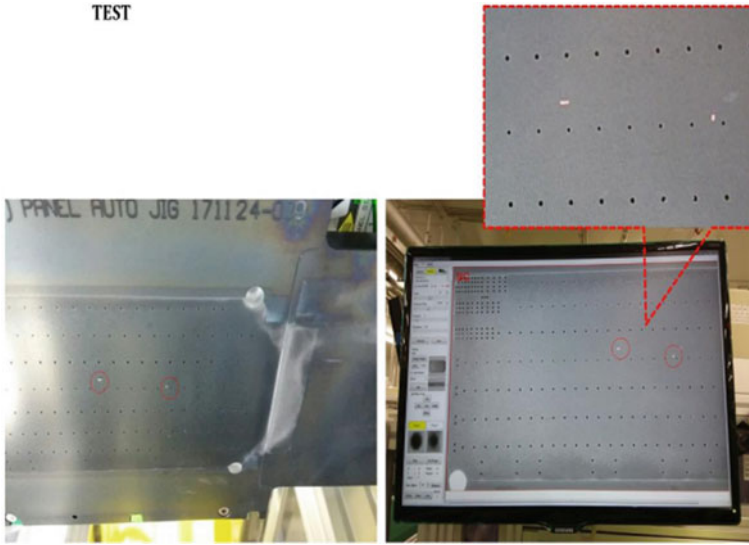


**Fig. 7** The actual images showing experimental results of detecting a 0.2 mm anomaly in automatic vision

**Acknowledgements** This research is funded by Hanoi University of Science and Technology (HUST) under project number T2022-PC-029. The authors express grateful thankfulness to Vietnam-Japan International Institute for Science of Technology (VJIIST), School of Mechanical Engineering, HUST, Vietnam and Shibaura Institute of Technology, Japan.

## References

1. R.S. Peres, X. Jia, J. Lee, K. Sun, A.W. Colombo, J. Barata, Industrial artificial intelligence in industry 4.0: systematic review, challenges and outlook. *IEEE Access* **8**, 220121–220139 (2020)
2. T.-V. Dang, N.-T. Bui, Multi-scale fully convolutional network-based semantic segmentation for mobile robot navigation. *Electronics* **12**(3), 1–18 (2023)
3. T.-V. Dang, N.-T. Bui, Research and design obstacle avoidance strategy for indoor autonomous mobile robot using monocular camera. *J. Adv. Transp.* (2022)
4. T.-V. Dang, Smart home management system with face recognition based on arc face model in deep convolutional neural network. *J. Robot. Control* **3**(6), 754–761 (2022)
5. T.-V. Dang, D.-S. Nguyen, Optimal navigation based on improved A\* algorithm for mobile robot, in *International Conference on Intelligent Systems and Networks 2023, 18–19 March, Hanoi, Vietnam* (2023)
6. T.-V. Dang, Smart attendance system based on improved facial recognition. *J. Robot. Control* **4**(1), 46–54 (2023)
7. I. Delibasoglu, Moving object detection method with motion regions tracking in background subtraction. *Signal, Image and Video Processing* (2023)

8. S.K. Choudhury, P.K. Sa, S. Bakshi, B. Majhi, Combining background subtraction and convolutional neural network for anomaly detection in pumping-unit surveillance. *IEEE Access* **4**, 6133–6150 (2016)
9. I.K.A. Murinto, Detection of object changes in low contrast image using template matching method, in *Proceedings of the 2nd International Conference on Engineering and Applied Sciences (2nd InCEAS)*, *IOP Conferences Series: Materials Science and Engineering*, p. 771 (2020)
10. S. Sharma, Shape-texture debiased training for robust template matching. *Sensors* **22**, 6658 (2022)

# Modeling and Simulation the Drone System Used in the Warehouse



**Thi-Dong-Ngan Nguyen, Minh-Tai Le, Thi-Phuong-Truc Vo,  
and Thanh-Tung Phung**

**Abstract** Currently, Unmanned Aerial Vehicles (UAV) are widely popular and valuable in almost areas such as cinema, rescue, fire fighting. And warehouse management is no exception. From the needs of society, it can be seen that the calculation and design of effective Drone systems are necessary. The Drone is a type of flight device with four engines mounted on the “X” frame that can be flown by the lifting force of the four blades and operated on aerodynamic effects. From the parameters obtained through mechanical calculations to the implementation of 3D simulation with Solidworks software, the authors used Ansys Workbench software to analyze stress and strain in a static state and dynamic state to test the durability and load capacity of Drone. In addition, airflow analysis of the propeller was also performed for thrust calculation and kinematic analysis. On that basis, the model meets the durability condition besides the small displacement value does not affect the frame structure. Thereby, creating a Drone with a small payload will assist in moving goods in the warehouse quickly and flexibly, save time, decrease labor costs and increase competitiveness.

**Keywords** Drone systems · 3D modelling · Static and dynamic simulation · Aerodynamic analysis

---

T.-D.-N. Nguyen · M.-T. Le (✉) · T.-P.-T. Vo · T.-T. Phung  
Department of Industrial Systems Engineering, Faculty of Mechanical Engineering, University of Technology and Education, Ho Chi Minh City, Vietnam  
e-mail: [tailm@hcmute.edu.vn](mailto:tailm@hcmute.edu.vn)

T.-D.-N. Nguyen  
e-mail: [19104028@student.hcmute.edu.vn](mailto:19104028@student.hcmute.edu.vn)

T.-P.-T. Vo  
e-mail: [19104060@student.hcmute.edu.vn](mailto:19104060@student.hcmute.edu.vn)

T.-T. Phung  
e-mail: [19104065@student.hcmute.edu.vn](mailto:19104065@student.hcmute.edu.vn)



# 1 Introduction

As we all know, science and technology are developing very strongly. With the current advances in science and technology, the application of unmanned aerial vehicles (UAV) for smart warehouses can completely be a new trend in the future. Drones are an integration tool in modern society. According to Jackman et al. [1], some statistics show the increasing attention of scholars toward Drone. Therefore, it is necessary to diversify the locations that the Drone can reach. And in order to select Drone components for specific applications, Ajay Vishwath et al. [2] have identified the requirements of each individual application, thereby providing effective combinations that optimize costs.

One of the common problems encountered when building Drones is engine noise. To solve that problem, Malapur et al. [3] did some tests, and the solution used a cased diffuser. Regarding aerodynamic effects, Javir et al. [4] solved from the mechanical part to the electrical part. The research gave accurate results about the weight of the parts and their respective costs. Basit et al. [5] talked about the quadcopter's range and duration, determining the maximum load capacity, flight time, and speed. The result is a design for a quadcopter delivery system that is more cost-effective, faster, and more convenient than a traditional delivery system. Abolorunke et al. [6] studied the improvement of flight time and the maintenance of minimum aircraft weight. Thomas et al. [7] studied the parameters of the quadcopter by defining and analyzing the kinetics of the quadcopter, calculating the parameters, and optimizing the structure affecting its performance. Sapit et al. [8] studied and analyzed the airflow characteristics of unmanned aircraft propellers by Ansys and obtained simulation results and values of the applied forces.

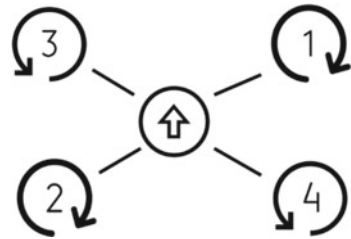
Following the success of those projects, in this paper the authors will design, calculate and simulate the Drone for smart warehouses through the evaluation and analysis of operating principles, 3D simulation to evaluate of static, dynamic and aerodynamic behavior of Drone.

## 2 Method

### 2.1 *Quadcopter Movements*

Drone, also known as quadcopters, crossbody, or multi-engine aircraft, are preferred in uncrewed aerial vehicle (UAV) design. Quadcopter consists of propellers fixed at the end of the frame structure. In this case, a pair of rotors along the wings of the frame rotates clockwise while the pair of rotors rotate counterclockwise (Fig. 1).

**Fig. 1** Diagram of quadcopter



*Motor Rotation Direction*

The Quadcopter can fly into the air thanks to a force greater than or equal to gravity generated. However, a drone has three dimensions of engine rotation in the vertical plane: high, low, or hovering.

*Motor Shafts*

Each propeller has a fixed axis of rotation. Thrust and torque are two fundamental things used for quadcopter movement. The movements are Yaw, Pitch, and Roll.

**2.2 Design Calculation of the Specifications**

**Frame:** An important part of the Drone that holds all other parts of the device. Some of the values that we need to pay attention are the weight, size and material of the frame. These are very important factors, as they directly affect the flight performance of Drones. Here, the authors chose the Kit F450 Quadcopter. The material chosen for the frame in this project was aluminum. The estimated weight of the frame is about 282 g. The selected frame shape is X and the load capacity is from 800 to 1600 g.

**Motor:** is the part used to generate rotational speed for the propellers to help the Drone. In this project, we need four 935 kV brushless motors of 2 clockwise and 2 counterclockwise with the diameter of 27.9 mm, the length of 39.7 mm, and the weight of 55 g.

**Battery:** is the part that provides power for other parts to operate. Drones typically use LiPo batteries of various sizes and configurations. In this project, we used a 2200 Mah 3S 40C LiPo Battery. This battery was chosen because it matches the calculated capacity and provides a durable flight time.

**Propeller:** For 4 motors, we need 4 propellers with the function of generating thrust, and raising the Drone to fly. There are 2 propellers rotating clockwise and 2 propellers rotating in the opposite direction. The authors chose a 1045 propeller with the size of 10 × 4.5 and the weight of 14 g.

From selected input data, 3D simulation of Drone on Solidwork is completed (Fig. 2).

**Fig. 2** Complete Drone

The weight of the entire drone is estimated to be 1500 g. With air pressure at the ground  $1 \text{ atm} = 1.248 \text{ (kg/m}^3\text{)}$ , the parameters of the selected parts are calculated as below.

Diameter: 10 inch = 254 mm = 0.254 m,

$$s = n \times \frac{D^2}{4} = n \times \frac{0.254^2}{4} = 0.05 \text{ m}^2 \quad (1)$$

Total lifting force:

$$\begin{aligned} T_{MT}' &= 4 \times T_{MT} = 4 \times W_P = 4 \times 2 \times p_s \times S \times V_I^2 \\ &= m \times g = 1.5 \times 9.8 = 14.7(N) \end{aligned} \quad (2)$$

Airflow velocity for each propeller:

$$V_I = \sqrt{\frac{W_P}{2 \times p_s \times S}} = \sqrt{\frac{T_{MT}'}{2 \times p_s \times S}} = \sqrt{\frac{14.7}{2 \times 1.249 \times 0.05}} = 10.85 \text{ (m/s)} \quad (3)$$

Thrust force:

$$\begin{aligned} T_{MT} &= 2 \times p_s \times S \times V_I^2 \\ &= 2 \times 1.249 \times 0.05 \times 10.85^2 \\ &= 14.7(N) \end{aligned} \quad (4)$$

Wattage:

$$\begin{aligned} W &= K \times N^3 \times D^4 \times P \times \eta \\ &= 5.3 \times 10^{-15} \times 10,378.5^3 \times 10^4 \times 4.5 \times 0.75 \\ &= 199.94(W) \end{aligned} \quad (5)$$

In which.

$$K = 5.3 \times 10^{-15}$$

$N$  is the speed rotor,  $N = 11.1 \times 935 = 10,378.5$  (round/min).

$\eta$  is efficiency,  $\eta = 0.75$ .

$D$  is the rotor diameter,  $D = 10$  inches.

$P$  is the height of the wing,  $P = 4.5$  inches.

Maximum current:

$$I_{\max} = \frac{W}{V} = \frac{200}{11.1} = 18.018 \text{ (A)} \quad (6)$$

The velocity of downward-accelerated air:

$$V_d = \frac{2W\eta}{T_{MT}} = \frac{2 \times 199.94 \times 0.75}{14.7} = 20.4 \text{ (m/s)} \quad (7)$$

Flight speed:

$$V_a = \frac{1}{2} V_d = \frac{1}{2} \times 20.4 = 10.2 \text{ (m/s)} \quad (8)$$

Propeller head speed:

$$V_{ip} = \frac{nDN}{60} = \frac{n \times 0.254 \times 10,378.5}{60} = 138.03 \text{ (m/s)} \quad (9)$$

Thrust and torque system:

$$C_i = \frac{T_{MT}}{p_s \times A \times V_{ip}} = \frac{14.7}{1.249 \times 0.05 \times 138^2} = 0.01236 \quad (10)$$

$$C_Q = C_r \times \sqrt{\frac{C_r}{2}} = 0.01236 \times \sqrt{\frac{0.01236}{2}} = 9.7166 \times 10^{-4} \quad (11)$$

In which.

$T_{MT}$  is thrust,  $T_{MT} = 14.7\text{N}$ .

$A$  is the propeller area,  $A = n \times R^2 = n \times 0.127^2 = 0.05\text{m}^2$

$R$  is the propeller wheel.

### 2.3 Static, Dynamic and Aerodynamic Analysis

#### Static analysis

The frame's strength is tested under static loads by determining the applied force as the frame's gravity. Then Ansys software is used to simulate the impact force and

**Table 1** Mesh settings

Parameter	Value
Element size	2 mm
Nodes	353,440
Elements	164,007
Minimum element length	4.1839e−002 mm
Maximum element length	1.9572

evaluate the stress and displacement parameters of the structure. From the results obtained, conclusions about the durability of the frame are made.

The acting forces are applied to the frame as shown. The frame weight is estimated at 1.5 kg. Therefore, the force acting on the structure is determined as:

$$1.5 \times 9.8 = 14.7(N)$$

In addition, for accurate analysis, it is necessary to divide the texture into smaller elements. Set the mesh parameters as follows (Table 1).

#### *Dynamic Analysis*

The method of strength testing for the frame is as follows:

- Determine the force acting on the frame including the gravity of the frame, load, and propeller lift.
- Calculate the allowable stress of the frame.
- Examine stress-stable conditions and conclude about the durability of the frame.

#### *Aerodynamic Analysis*

Meshing is important because it affects the simulation and the accuracy of calculation. The finer the mesh quality and the smaller the size, the higher the accuracy of the calculation will be. Therefore, the appropriate mesh should be selected to facilitate the simulation process.

In this study, a 3D propeller model was used with an input speed of 14.7 m/s. Table 2 shows the parameters that need to be set to carry out the calculation process.

## **3 Results and Discussion**

### **3.1 Static Analysis**

The resulting stress obtained when subjected to static load was determined to be the maximum 0.11411 (MPa), and the minimum was  $5.6037e^{-9}$  (MPa).

Based on the durability condition of the material, we have:

**Table 2** Setup for simulation work

Parameter	Values
Time	Transient
Time step	0.5
Number of time step	50
Max iteration per time step	10
The viscous model	Reynolds stress
Flying medium	Air
The density of air, $\rho$	1.225 kg/m <sup>3</sup>
Type of airflow	Turbulent

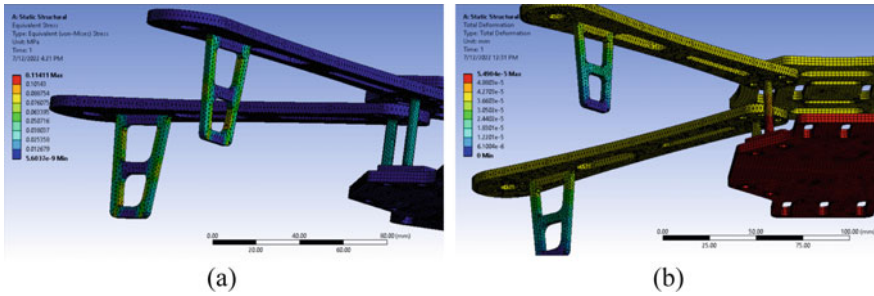


**Fig. 3** Stress behavior and displacement under the static load

$$\begin{aligned} \sigma_{\max} &= 0.11411 \text{ MPa} \leq [\sigma] \\ &= 207 \text{ MPa} (\text{The allowable stress of aluminum}) \end{aligned}$$

Therefore, the structure satisfies the condition of durability.

Figure 3b shows the largest displacement at the frame surface of  $5.4904 \times 10^{-5}$  m and the remaining positions are all extremely small, within a safe level, so the frame still ensures durability.

### 3.2 Dynamic Analysis

Based on the durability condition of the material, we have:

$$\sigma_{\max} = 0.72404 \text{ MPa} \leq [\sigma] = 207 \text{ MPa}.$$

The drone frame structure satisfies the condition of durability.

Figure 4b shows that the maximum displacement is at the frame surface of  $0.25614 \times 10^{-3}$  m and the remaining positions are all extremely small, within the safe level, so the frame is still durable.

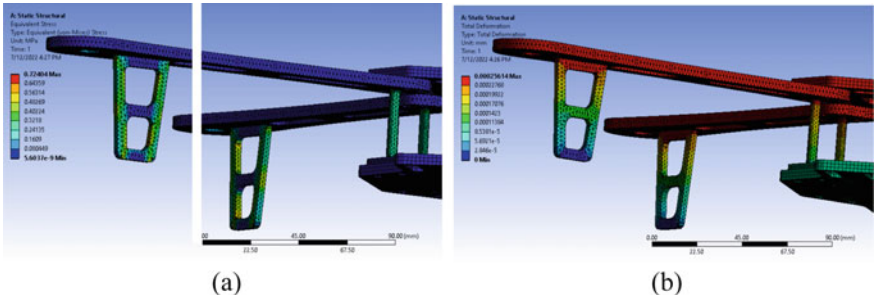


Fig. 4 Stress behavior and displacement under the dynamic load

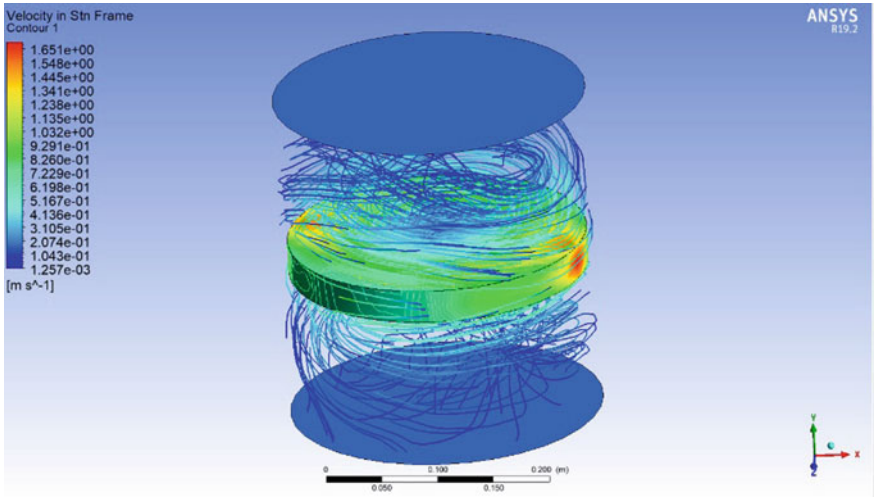


Fig. 5 Contour and Streamline results

### 3.3 Aerodynamic Analysis

With an input velocity of 14.7 m/s to simulate the airflow generated from the propeller, We got the result as shown in Fig. 5. The maximum speed was  $1.65 \text{ m/s}^{-1}$  and the minimum was  $1.257 \times 10^{-3} \text{ m/s}^{-1}$ .

## 4 Conclusion

UAV is an efficient mean of carrying out the transportation of small packages in a smart warehouse. With relatively low costs, less shipping times, and many other benefits, drones will succeed in speeding up the manufacturing process. Drones can

operate normally and transport payloads with a mass of 1.5 kg through theorems, calculations, and simulations. Drones were raised into the air according to Bernoulli's principle and Newton's third law of motion. Its speed increases or decreases according to the direction of rotation and the rotation axis of the motor. The drone was tested to meet an allowable stress condition of 207 MPa. In static and dynamic states, the displacement of the frame is extremely small, 0.00025614 mm. In addition, the impeller kinematics was simulated with the inlet conditions of the airflow and the configuration of the impeller. This is just the beginning of a brief research to drones, but it benefits to the manufacturing automation industry and human needs.

## References

1. A. Jackman, Domestic drone futures. *Polit. Geogr.* **97**, 102653 (2022)
2. N.C. Ajay Vishwath, A.R. Yadav, D. Mehta, J. Belani, R.R. Chauhan, A guide to novice for proper selection of the components of drone for specific applications. *Mater. Today Proceed.* (2022)
3. H. Malapur, Y. Singh, M. Shendkar, A. Barve, M. Bedekar, Diffused casing of drone propeller for reduced operational noise and optimized energy consumption. *Mater. Today Proceed.* (2022)
4. A.V. Javir, K. Pawar, S. Dhudum, N. Patale, S. Patil, Design, analysis and fabrication of quadcopter. *J. Adv. Res. Mech. Civil Eng.* **2**, 2208–2379 (2015)
5. A. Basit, M. Awais, M. Ullah, S.U.A. Shad, Design and fabrication of a quadcopter delivery drone (2021)
6. F. Abolorunke, T. Asem, Design, fabrication and testing of an unmanned aerial vehicle (UAV) (2016)
7. M. Thomas, A.T. Albin, C. Joseph, A.K. Mathew, Design and analysis of a quadcopter using catia. *Int. J. Sci. Eng. Res.* **7**, 2229–5518 (2016)
8. A. Sapit, M.F. Masjan, S.K. Shater, Aerodynamics drone propeller analysis by using computational fluid dynamics. *J. Compl. Flow* **3**(2), 12–16 (2021)



# Research on Capacitive Micromachined Ultrasonic Transducer Array for the Wrist-Type Suspension Control System



Gia-Thinh Bui

**Abstract** This research is to develop a wrist-type suspension control system, which uses a capacitive micromachined ultrasonic transducer (CMUT) to achieve the effect of suspension and non-touch control. The use of polymer-based ultrasonic transducers has the advantages of non-touch, flexibility, transparency, and thinness. It can be made into a wrist device and use an ultrasonic signal to transmit and receive to achieve non-touch control effects. It can be applied to smartwatches. Since the existing touch screen is limited by the size of the finger, the surface cannot be viewed during use, resulting in accidental touch. This suspension control method can be operated without touching the surface. The non-touch method is more convenient. In this study, a  $4 \times 3$  array of numeric keyboards was made by using different frequencies of ultrasonic signals to represent commonly used numbers and symbols, to avoid interference caused by reflective surfaces during operation.

**Keywords** Capacitive micromachined ultrasonic transducer (CMUT) · Wrist (non-contact) control

## 1 Introduction

In 1954, Kuhl et al. [1] proposed the concept of a capacitive transducer combined with an ultrasonic transmitter (Transmitter) and was applied in the air. Until 1994, Haller and Khuri-Yakub [2, 3] used MEMS processing to achieve high performance characteristics, which evolved into today's mainstream technology. In 2007, Chang et al. [4] used sacrificial layer technology to fabricate flexible ultrasonic transducers on polymer substrates, and easily produced acoustic paper with low processing temperature and higher flexibility. In 2006, Chang et al. [5] successfully fabricated a polymer-based capacitive ultrasonic transducer by using MEMS technology, and verified it

---

G.-T. Bui (✉)

Department of Electrical and Mechanical Engineering, Hai Phong University, Haiphong, Vietnam  
e-mail: [thinbgi@dhhp.edu.vn](mailto:thinbgi@dhhp.edu.vn)

by finite element analysis. The analysis was consistent with the experimental results. In 2002, Chou and Najafi [6] used dry etching to fabricate an electrostatic micro-actuator on a curved silicon substrate, which could drive the membrane with a small voltage and generate a large center displacement of the membrane. In 2017, Pang and Chang [7] presents a novel transparent flexible CMUT made by low-temperature roll-lamination fabrication processes.

The purpose of this research is to develop polymer-based ultrasonic transducers has the advantages of non-touch, flexibility, transparency, and thinness. The CMUT can be applied in a non-touching wrist-type suspension control system.

## 2 Research Purpose

### 2.1 Design of Wrist Suspension Control System

This research proposes a wrist-type suspension control system design, as shown in Fig. 1a, in which every single element has buttons with different frequencies and represents multiple functions or the number keys 0 ~ 9 and common symbols such as \* and #.

A  $4 \times 3$  array of high-frequency ultrasonic elements is combined with a wrist-type suspension control system which has 12 different frequencies that are staggered to prevent interference and used for non-contact proximity control, as shown in Fig. 1b.

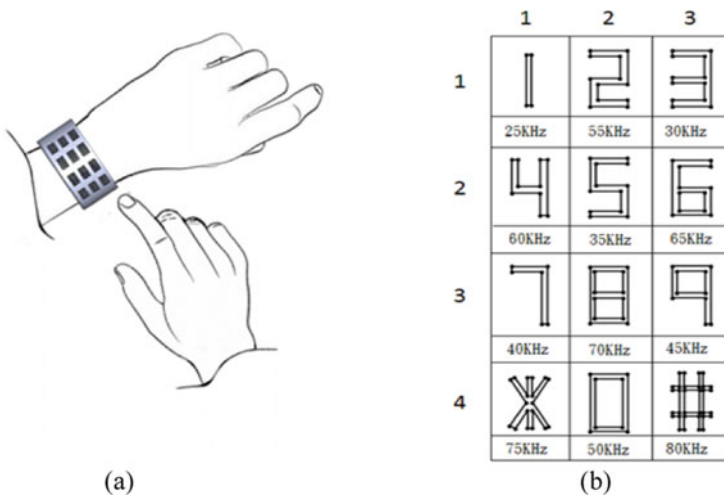


**Fig. 1** Schematic of **a** wrist suspension control system; **b**  $4 \times 3$  elements array

**Table 1** Mechanical dimension of CMUT cell

Parameter	Measurement (μm)
Membrane diameter	92–137
Membrane thickness	5
Sidewall width	50
Cavity height	2
Top electrode diameter	300
Top electrode thickness	0.01
Bottom electrode thickness	0.01

## 2.2 Selection of Frequency

In this study, the Mechanical dimension of the CMUT cell is shown in Table 1, and the single element size is 3 mm × 3 mm. Twelve different frequencies of the CMUT are designed to be used as a 4 × 3 digital panel, which can ensure that the two adjacent components do not interfere with each other (Table 2). Time domain and frequency domain characteristics of components are tested to compare the difference between the experiment and design. According to the natural frequency formula of Blevins [8], the theoretical natural frequency is determined:

$$f = \frac{\lambda^2}{2\pi a^2} \left[ \frac{Eh^3}{12\gamma(1 - \nu^2)} \right]^{1/2} = \frac{\lambda^2 h}{2\pi a^2} \left[ \frac{E}{12\eta(1 - \nu^2)} \right]^{1/2} \tag{1}$$

where  $f$  is the natural resonance frequency (Hz),  $\lambda$  is the shape factor, the hexagonal shape coefficient is 12.81,  $a$  is the radius (cm),  $E$  is the Young’s coefficient of the material (kg/cm<sup>2</sup>),  $h$  is the thickness (cm),  $\nu$  is the Poisson ratio, and  $\gamma$  is the mass per unit area (kg s<sup>2</sup>/cm<sup>3</sup>),  $\eta$  is the density of the material (kg s<sup>2</sup>/cm<sup>4</sup>), and the mass per unit area is calculated by multiplying the density of the material by the thickness.

## 3 Time and Frequency Domain Measurements of Components

### 3.1 Basic Measurements of the CMUT

In this study, a transparent CMUT was used for the experimental measurement of signal amplitude and frequency, and its feasibility was analyzed. Figure 2 is a photo of the experimental measurement setup. JSR Pulse Receiver and DC Power Supply are used to provide AC and DC energy to the two electrodes of the device through the Bias-tee, and the signals are intercepted by the oscilloscope.

**Table 2** Correspondence table of frequency, membrane diameter, and numeric key position

Frequency (kHz)	Membrane diameter ( $\mu\text{m}$ )	Location
25	810	(1, 1)
30	740	(1, 3)
35	690	(2, 2)
40	640	(3, 1)
45	600	(3, 3)
50	570	(4, 2)
55	550	(1, 2)
60	520	(2, 1)
65	500	(2, 3)
70	480	(3, 2)
75	470	(4, 1)
80	450	(4, 3)

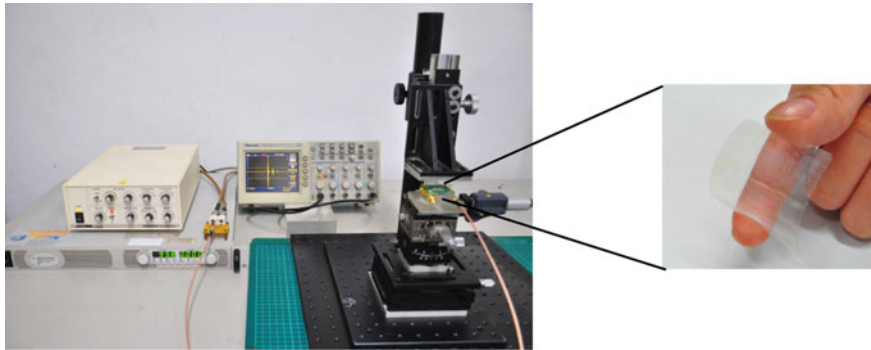
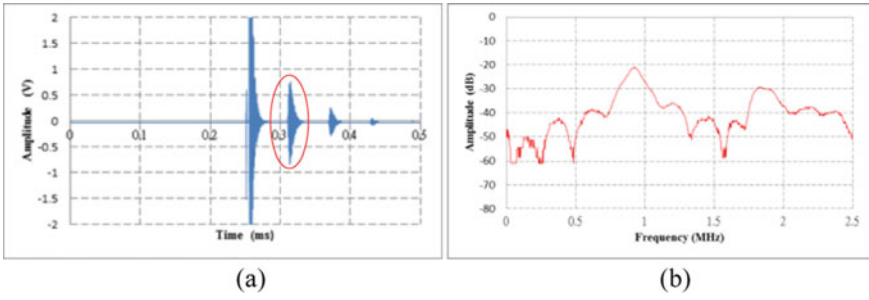


**Fig. 2** Photo of experimental setup

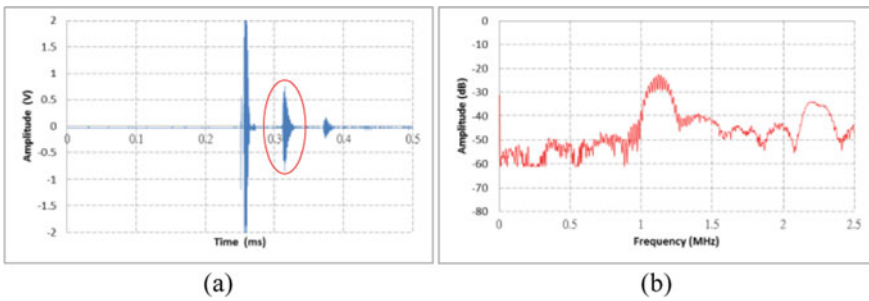
In the measurement conditions of this experiment, an AC voltage of 300 V and a DC voltage of 100 V were applied to the transducer, and the vertical distance between the reflective surface and the transducer was 10 mm. Among 12 different frequency components, four components with different membrane diameters are selected for discussion. The membrane diameters are: 137, 119, 106 and 94  $\mu\text{m}$ . The corresponding, first response signal value of each CMUT is shown in Fig. 3, 4, 5 and 6.

Table 3 below is shown the relationship of the number of cells corresponding to different diameters, the experimental frequency, the time domain, the frequency domain, and the single signal, arranged according to the size of the experiment. The maximum diameter of the membrane is 137  $\mu\text{m}$ , and the single signal is 1.77 mV. The minimum diameter of the membrane is 92  $\mu\text{m}$ , and the single signal is 0.31 mV.

Relationship of the membrane diameter and the theoretical frequencies are shown in Fig. 7. Figure 8a is shown the relationship between the membrane diameter and



**Fig. 3** The first reflected signal of the 137  $\mu\text{m}$  membrane diameter of the CMUT **a** Time domain; **b** Frequency domain



**Fig. 4** The first reflected signal of the 119  $\mu\text{m}$  membrane diameter of the CMUT **a** Time domain; **b** Frequency domain

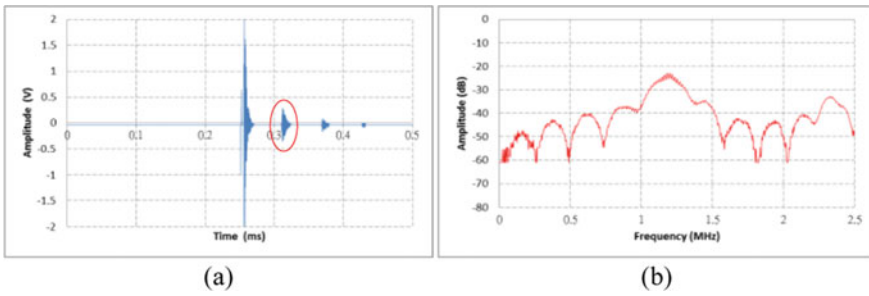


**Fig. 5** The first reflected signal of the 106  $\mu\text{m}$  membrane diameter of the CMUT **a** Time domain; **b** Frequency domain

the frequencies in the theoretical results and the experimental results. The graph of experiment and theory is different, which may be due to poor quality in the manufacturing process. Figure 8b shows the relationship between the frequencies and the amplitudes of signal with different membrane diameters. The result shows

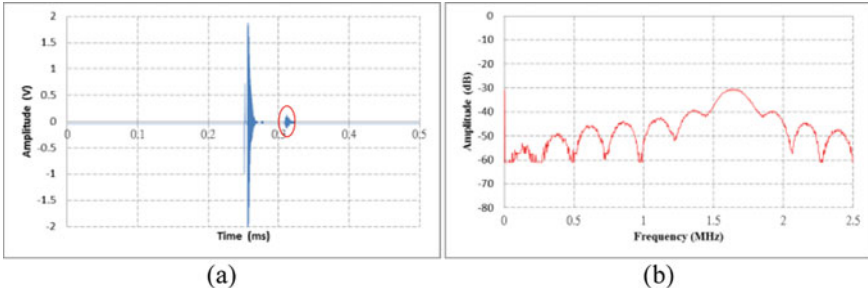


**Fig. 6** The first reflected signal of the 94  $\mu\text{m}$  membrane diameter of the CMUT **a** Time domain; **b** Frequency domain

**Table 3** Relationship between membrane diameter, number of particles, time domain, and frequency domain of components with different sizes

Number of cells	Membrane diameter ( $\mu\text{m}$ )	Frequency (MHz)	Time domain (mV)	Frequency domain signal (dB)	Single signal (mV)
441	137	0.93	780	- 22.97	1.77
484	130	0.86	760	- 19.39	1.57
529	124	0.99	800	- 23.37	1.51
576	119	1.15	720	- 28.57	1.25
600	114	1.07	600	- 26.57	1.00
650	110	1.24	400	- 20.99	0.62
676	106	1.32	320	- 20.99	0.47
729	103	1.35	240	- 34.19	0.33
784	100	1.38	240	- 21.77	0.31
841	94	1.65	240	- 30.57	0.29
841	97	1.52	240	- 29.39	0.29
900	92	1.57	280	- 25.39	0.31

that the experimental frequency of the components at 0.86 and 1.07 MHz are drop, and the rest of the components are consistent with the calculation.

### 3.2 DC and AC Voltage Testing

To obtain the best working conditions of the CMUT, different voltages of the AC pulses and the DC bias are applied. Each changing of the AC voltage is 50 V and the DC voltage is 25 V, and the vertical distance is fixed at 10 mm. The experimental diagram and conditions are shown in Fig. 9 and Table 4.

**Fig. 7** Relationship of the membrane diameter and the theoretical frequencies

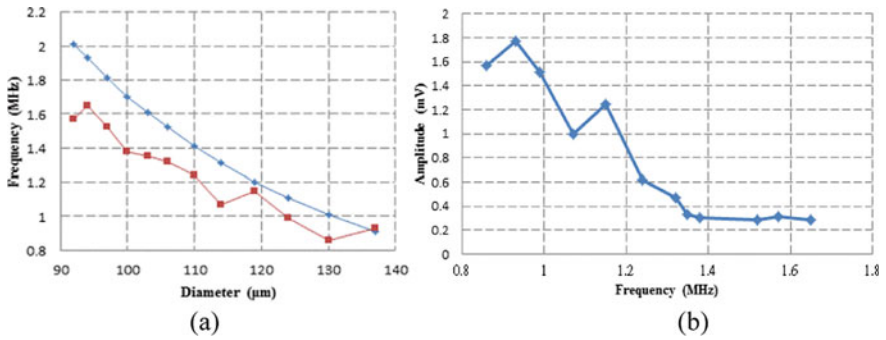
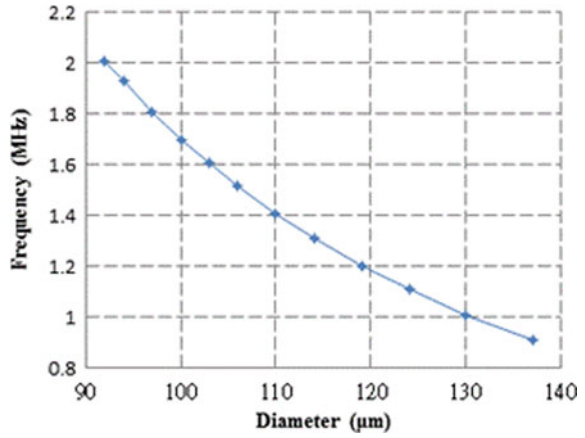


**Fig. 8** The relationship between **a** the membrane diameter and the frequencies in the theoretical results and the experimental results; **b** The frequencies and the amplitudes of signal with different membrane diameters

**Fig. 9** DC and AC working voltage experimental design

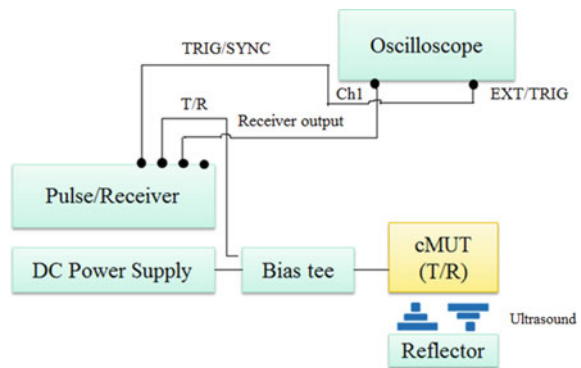


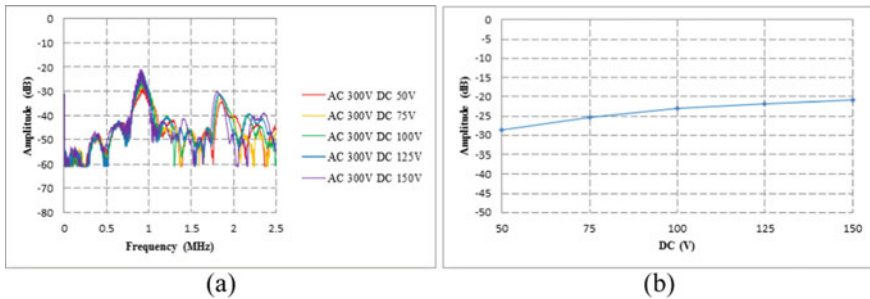
**Table 4** DC and AC voltage testing condition

Element	Value	Changing	Unit
AC pulse	100–300	50/Second-rate	V
DC bias	50–150	25/Second-rate	V
Vertical distance	10	Fixed	mm

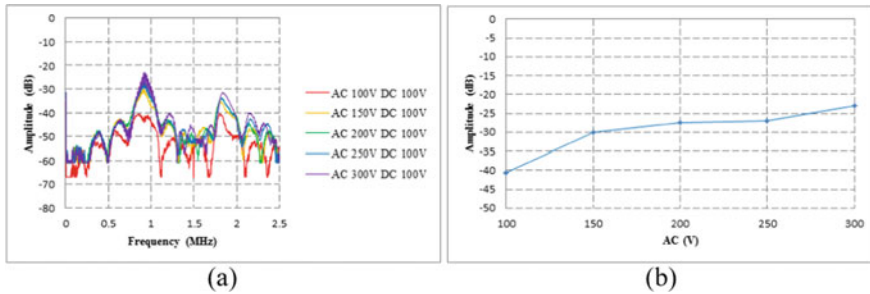
Figure 10a shows the frequency domain and Fig. 10b shows the operating point of components when the AC voltage of 300 V is fixed, and the DC voltage is changed from 50 to 150 V with each change of 25 V.

Figure 11a shows the frequency domain and Fig. 11b shows the operating point of components when the DC voltage of 100 V is fixed, and the DC voltage is changed from 100 to 300 V with each change of 50 V.

The time of flight and reflected signal amplitude of the element was measured with a frequency of 0.93 MHz. The velocity of an ultrasonic signal in air at room temperature was calculated of 350.36 m/s.



**Fig. 10** **a** Frequency domain; **b** the best working point of components with a fixed AC voltage of 300 V, while the DC voltage is varied from 50 to 150 V with each change of 25 V



**Fig. 11** **a** Frequency domain; **b** the best working point of components with a fixed DC voltage of 100 V, while the AC voltage is varied from 100 to 300 V in increments of 50 V.



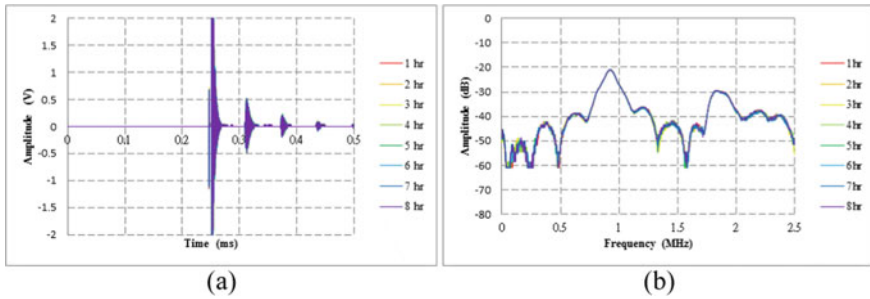


Fig. 12 Diagram of **a** the time domain; **b** the frequency domain

### 3.3 Life Test

This experiment shows that under the continuous testing of different frequencies for 8 h, it will not burn, or the output signal will drop significantly. The CMUT can be worked in a long-term condition (Fig. 12).

## 4 Conclusion

This paper is to develop the CMUT for a non-touching wrist-type suspension control system. This research found that there is a slight error between the theoretical frequency and the experimental measurement result, which may be caused by the slight difference in the thickness of the membrane when fabrication. The numeric keypad is designed so that the ultrasonic frequencies of two adjacent elements will not interfere with each other, but if the frequencies of the components in some diagonals are too close to each other, they may interfere with each other. It is recommended to further improve in the future. The CMUT can be easily integrated with a wrist-type suspension system for non-touching control at short distances and provides more interaction than touch panels.

## References

1. W. Kuhl, G.R. Schodder, F.K. Schodder, Condenser transmitters and microphones with solid dielectric for airborne ultrasonics. *Acustica* **4**, 520–532 (1954)
2. M.I. Haller, B.T. Khuri-Yakub, A surface micromachined electrostatic ultrasonic air transducer. *Proc. IEEE Ultrasonics* **2**, 1241–1244 (1994)
3. M. Haller, B.T. Khuri-Yakub, A surface micromachined electrostatic ultrasonic air transducer. *IEEE Trans. Ultrason. Ferroelect. Freq. Contr.* **43**, 1–6 (1996)
4. M. Chang, H. Deng, D. Pang, M. Chen, A novel method for fabricating sonic paper. *Proc. IEEE Ultrasonics* **12**, 527–530 (2007)

5. M. Chang, M. Deng, J. Gwo, J.D. Mai, E. Hsu, Polymer-based capacitive micromachined ultrasonic transducers (CMUT) for microsurgical imaging applications. *Proc. IEEE Nano/Micro Eng. Mol. Syst.* **53**, 61–65 (2006)
6. T. Chou, K. Najafi, Fabrication of out-of-plane curved surfaces in Si by utilizing RIE lag, in *Proceedings of the Fifteenth IEEE International Conference on Micro Electro Mechanical Systems* (2002), pp. 145–148
7. D.C. Pang, C.M. Chang, Development of a novel transparent flexible capacitive micromachined ultrasonic transducer. *Sensors* **114**, 17 (2017)
8. R.D. Blevins, *Formulas for natural frequency and mode shape*. Van Nostrand Reinhold (1979)

# Optical Recognition of Handwritten by Aiding Computer Vision and Deep Learning



Anh-Son Tran, Duc-An Pham, and Van-Nghia Le

**Abstract** Automatic handwriting detection is becoming a serious difficulty in image processing. In addition, this may be considered a crucial function in the era of technology 4.0. This study describes a technique for detecting handwriting using computer vision and deep learning. During image processing, the original picture is offered to undergo noise reduction and filtering. The input photos will then be divided into two calibrated groups: RGB images and binary images for the model of the enhanced ALEXNET Neuron Network. In addition, a graphical user interface for combining several NN models is created. The test results reveal that the proposed technique is 96.95% effective under varied lighting conditions. In addition, the training model is compared to other NN models to evaluate the effectiveness of the suggested method.

**Keywords** Handwritten recognition · Deep learning · Enhanced ALEXNET · Image processing · Tkinter user interface

## 1 Introduction

Over the last decade, artificial intelligence has made handwritten letter and document identification an everyday practice [1, 2]. Optical character recognition (OCR) [3, 4] translates printed or handwritten files into text. There are two main types: Off-line and online. Off-line character recognition includes handwritten and machine-printed recognition. Due to different writing styles, pen-tip sizes, and distorted handwriting, handwritten character recognition is harder than machine-printed texts. OCR is an interesting and hard pattern recognition topic with many practical applications. Latin

---

A.-S. Tran · V.-N. Le (✉)

Faculty of Mechanical Engineering, Hanoi University of Industry, Hanoi, Vietnam  
e-mail: [levannghia@hau.edu.vn](mailto:levannghia@hau.edu.vn)

D.-A. Pham

School of Mechanical Engineering, Hanoi University of Science and Technology, No. 1, Dai Co Viet, Hanoi, Vietnam

character OCRs have significant technical issues, notably in segmentation. In [5], a recognition of Tamil handwritten character using modified neural network with aid of elephant herding optimization is designed. The four stages that make up the suggested technique. The input handwritten image is preprocessed in the first step using a preprocessing approach. The text is initially divided into lines, words, and characters in the second procedure, which is segmentation. The feature extraction process is the third step. Tamil characters are successfully recognized in the final procedure, which is the recognition process. Kim et al. [6] proposes an adaptive named entity recognition using distant supervision for contemporary written texts. To leverage the poorly supervised data, a transfer-learning technique is developed. The poorly labelled data included unlabeled texts from two domains: Wikipedia and CNN news items. The produced weakly labelled data is trained using a bidirectional (BI) long short-term memory (LSTM) conditional random-field (CRF) natural language understanding (NER) model utilizing static and contextualized embedding approaches. In [7], a Contour Matching and Neural Network technique is applied to detect and classify the isolated Arabic handwritten letters. In order to extract the contour vector of the Arabic handwritten character, several pre-processing methods were used before contour extraction was performed. The resultant vector was then fed into a well-designed and validated neural network for character recognition.

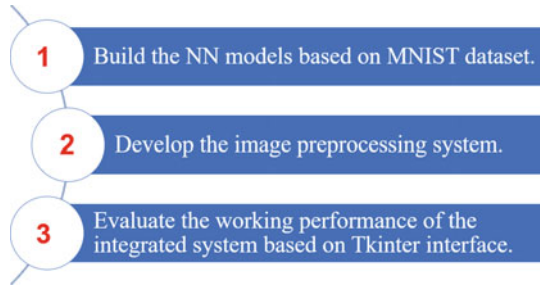
In this paper, a computer vision system integrated with AI to recognize handwritten texts is proposed. The main contributions are indicated as follows:

- (1) Calibrate the quality of the input images based on Sub-Regions Histogram Equalization filters [8] to obtain the clear edges of the handwritten characters.
- (2) Build a deep learning framework based on different neuron network models to inspect the precision of the recognition rate.
- (3) Display continuously the texts extracted from the images by aiding the Tkinter platform [9]. So, the designed system could be friendly user.

## 2 Detail Structure of the Proposed Approach

The proposed method consists of three main stages: Firstly, the MNIST dataset [10] is applied to train several neuron network models. Since then, the defined models have been saved for the third stage. Secondly, we built an image preprocessing system to calibrate and improve the quality of the real-time images (such as static images, drawings, and images captured directly by the cameras). Thirdly, all models and the image preprocessing system are integrated together on the Tkinter platform. The detail structure of the proposed approach is indicated as in Fig. 1.

**Fig. 1** The workflow of the proposed approach



### 2.1 Dataset Processing

The MNIST dataset is a well-known collection of handwritten digits used to train deep learning algorithms for optical recognition. Over 70,000 photographs of handwritten notes were captured (60,000 for training and 10,000 for evaluation). Figure 2 shows all necessary characters for the training process.

In this paper, we designed three different neuron network models including: LeNet [11], Alexnet [12] and enhanced CNN [13]. The summary architecture of LeNet and Alexnet models is illustrated as in Fig. 3.

**Fig. 2** MNIST dataset

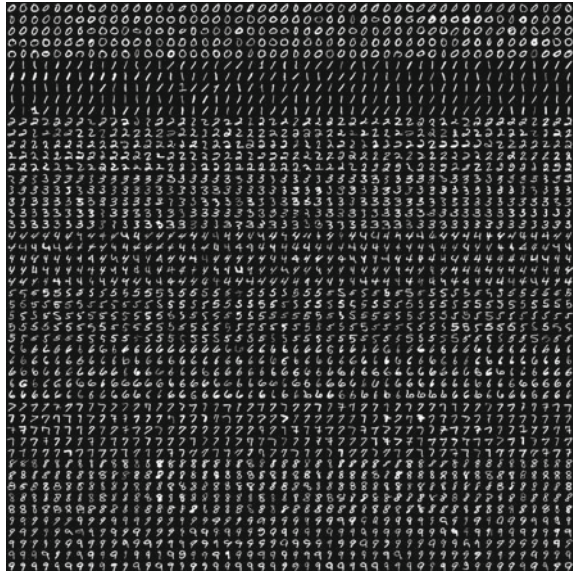
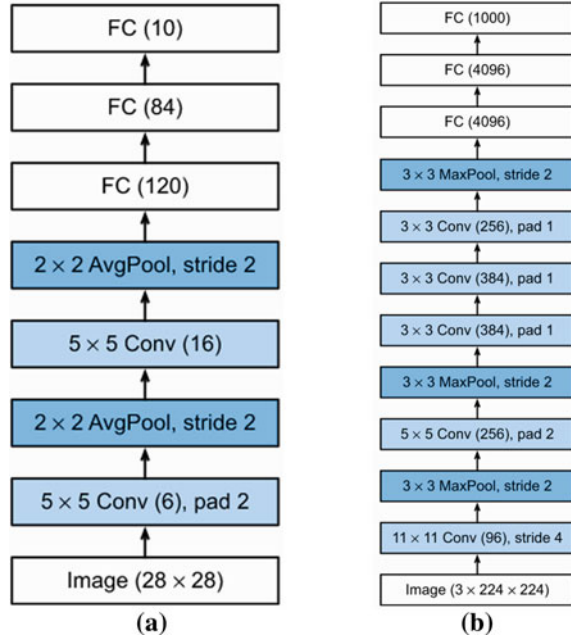


**Fig. 3** The summary architecture of the designed models



## 2.2 Image Preprocessing System

In the second step, a system for image preprocessing is designed to enhance the quality of the input images. The Sub-Regions Histogram Equalization (SRHE) algorithm is applied. This approach might spatially divide the input image into many sub-images. Segmentation is based on the weighted average value of the pixel and its surrounds, which is calculated by convolving the input picture with a Gaussian filter. The coefficients of a 2D Gaussian filter are then determined. After calculating all the coefficients of the Gaussian filter, these values must be normalized such that the total of the coefficients equals one. This phase is essential for maintaining signal strength in certain locations. As a low-pass filter, the Gaussian filter lowers the image's high-frequency components, leaving just the low-frequency components, which are often the basis of the image's objects. Consequently, grouping pixels based on this smoothed value is equivalent to grouping pixels into their respective objects. Consequently, intra-object contrasts might be enhanced. Notably, if the input picture has  $L$  grey levels, the image will be separated into  $L$  sub-images.

### 3 Experimental Results

In order to evaluate the efficiency of designed deep learning model designed for the proposed system, we conducted experiments based on three different cases: static images, images shot on camera, and using live drawing boards. Additionally, a user interface is also developed on Tkinter platform to display the real-time text information which includes the function buttons and results display. Firstly, several sets of static images are inspected. As depicted in Fig. 4, the numerals such as 0, 3, 4, 5, 6, and 9 may be recognized precisely. However, in poor condition light, there is still doubt over the remaining numbers due to their many similarities, notably with number 7.

In the case of the photos taken directly from the camera, convert the colorful images are transformed to the binary images, and then proceed to identify the positions as well as the values of the digits on the pixel area (Fig. 5).

The final case study is conducted directly on the drawing board, as demonstrated in Fig. 6. Because it was drawn directly on a black background, the image is noise-free. Therefore, there is no need to implement the image processing in some minor stages.

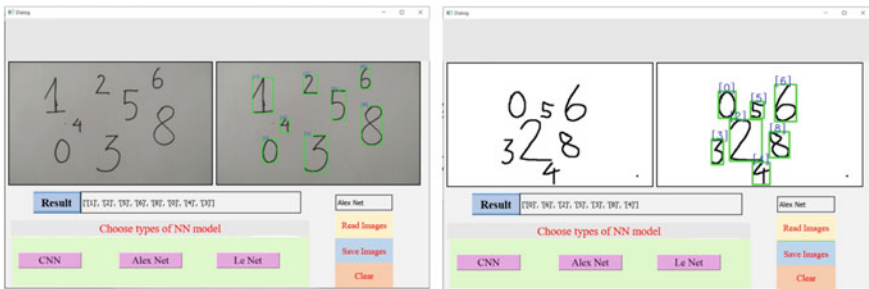


Fig. 4 Static image recognition

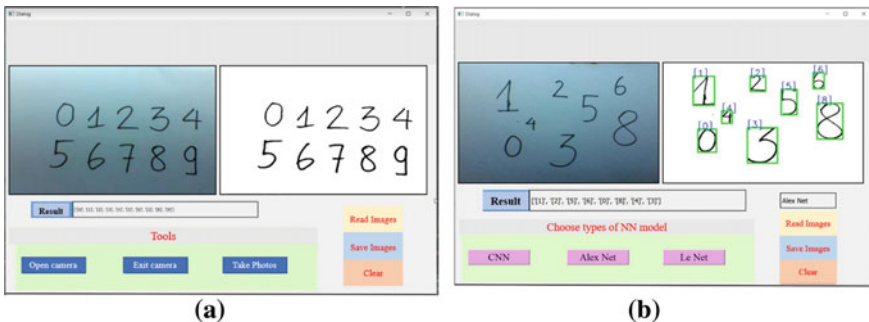


Fig. 5 a Taking a picture from the camera and converting it to the binary form; b the result of recognizing image taken from the camera

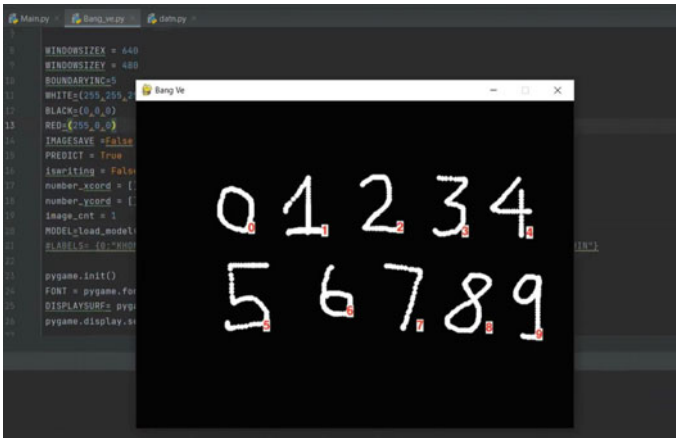


Fig. 6 The recognition result of the drawing board

With the aim of utilizing various artificial networks and contrasting network effectiveness, we keep conducting similar experiments with CNN and LeNet networks to compare the accuracies. The results are displayed as in Fig. 7.

In general, the comparison chart shows that:

- CNN has a lower recognition rate due to the less complex network structure, while LeNet and AlexNet networks have a comparably high and similar recognition rate.
- Only roughly 70,000 samples were used to train the networks in the MNIST library, producing a good accuracy rate.

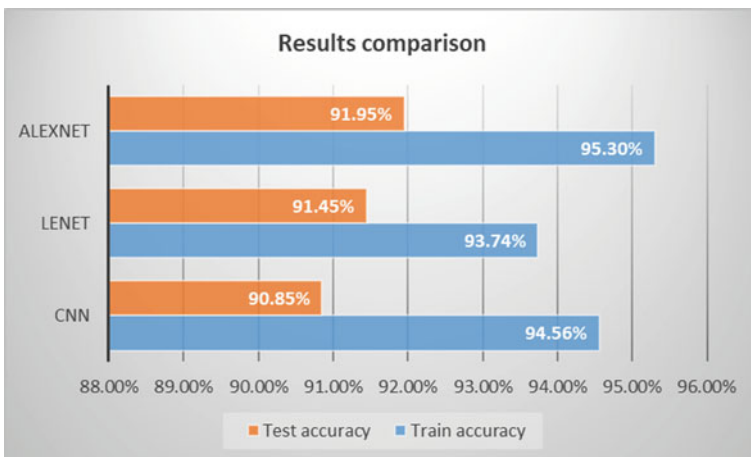


Fig. 7 Compare the recognition precision of three neuron networks: enhanced AlexNet, LeNet and CNN



- Because it is too accustomed to the train data set, the CNN train model network has a greater recognition rate than the other two networks; nevertheless, when the network is switched to operating on the test dataset, it has a lower recognition rate than the other two networks.

## 4 Conclusion

This paper presents a method for handwriting identification that combines deep learning and image processing techniques. Various image processing approaches (such as image blurring and morphological modification) are combined in order to identify which strategy is the most successful. In addition, by incorporating noise reduction on the input photos, the precision of face recognition is significantly enhanced. Consequently, when the picture has been processed by the upgraded AlexNet neural network, the digit characters are automatically identified with a high degree of accuracy. Clearly, the suggested method has been successfully implemented on hardware and field-tested with several measurements. In addition to being based on real-time data, the identification system utilizes camera data. When there are too many illegible handwritten numbers, however, the suggested approach still has trouble recognizing them in certain circumstances. In addition, if the static pictures are sufficiently noisy or ambiguous, the image processing is relatively sluggish, resulting in distortion. In the future, more experiments will build on more intriguing discoveries for enhancing the algorithm using contemporary neuron networks like YOLO, VGG, GoogleNet, etc. We hope that more research will increase and enhance the system's accuracy in real-world applications.

## References

1. N. Sneha, M. Sundaram, N. Preetham, Deep learning based application in identifying originality of the hand written document using convolution neural network, in *Proceedings of the 2022 International Conference on Connected Systems and Intelligence (CSI)*, pp. 1–8 (2022). <https://doi.org/10.1109/CSI54720.2022.9924050>
2. D. Chauhan, D. Verma, A. Aggarwal, Hand-written characters recognition using siamese network design, in *Proceedings of the 2022 1st International Conference on Informatics (ICI)*, pp. 66–70 (2022). <https://doi.org/10.1109/ICI53355.2022.9786908>
3. Y. Yin, W. Zhang, S. Hong, J. Yang, J. Xiong, G. Gui, Deep learning-aided OCR techniques for Chinese uppercase characters in the application of internet of things. *IEEE Access* **7**, 47043–47049 (2019). <https://doi.org/10.1109/ACCESS.2019.2909401>
4. S.M. Darwish, K.O. Elzoghaly, An enhanced offline printed Arabic OCR model based on bio-inspired fuzzy classifier. *IEEE Access* **8**, 117770–117781 (2020). <https://doi.org/10.1109/ACCESS.2020.3004286>
5. S. Kowsalya, P.S. Periasamy, Recognition of Tamil handwritten character using modified neural network with aid of elephant herding optimization. *Multimedia Tools Appl.* **78**(17), 25043–25061 (2019)

6. J. Kim et al., Adaptive named entity recognition using distant supervision for contemporary written texts. *IEEE Access* **9**, 80405–80414 (2021)
7. B.Z. Aljunaeidia, M.S. Alkhasawneh, M.A. BaniYounes, Isolated Arabic hand written letters recognition based on contour matching and neural network. *J. Comput. Sci.* **14**(11), 1565–1576 (2018)
8. H. Ibrahim, N.S. Pik-Kong, Image sharpening using sub-regions histogram equalization. *IEEE Trans. Consum. Electr.* **55**(2), 891–895 (2009)
9. A.D. Moore, *Python GUI Programming with Tkinter: Develop Responsive and Powerful GUI Applications with Tkinter* (Packt Publishing Ltd., 2018)
10. R.F. Alvear-Sandoval, J.L. Sancho-Gómez, A.R. Figueiras-Vidal, On improving CNNs performance: the case of MNIST. *Inform. Fusion* **52**, 106–109 (2019)
11. R.A. Hazarika, A. Abraham, D. Kandar, A.K. Maji, An improved LeNet-deep neural network model for Alzheimer’s disease classification using brain magnetic resonance images. *IEEE Access* **9**, 161194–161207 (2021)
12. J.C. Tan, K.M. Lim, C.P. Lee, Enhanced AlexNet with super-resolution for low-resolution face recognition, in *Proceedings of the 2021 9th International Conference on Information and Communication Technology (ICoICT)*, pp. 302–306 (2021)
13. L. Lu, Y. Yi, F. Huang, K. Wang, Q. Wang, Integrating local CNN and global CNN for script identification in natural scene images. *IEEE Access* **7**, 52669–52679 (2019)

# Proposing Method to Solve Kinematics Problem of a Lower Limb Rehabilitation Robot



Tien Nguyen, Trung Nguyen, and Tam Bui

**Abstract** This study proposed a method to solve the Kinematics of an exoskeleton system based sitting/lying-type lower limb rehabilitation robot. Based on the modularization design, the movable seat can be separated from and grouped into the lower limb rehabilitation robot, which is convenient for patients to sit down. The goal of this research is to help the robot mimic human gait over time accurately, an angular trajectory planning method is proposed based on the polynomial interpolation method of the measured human gait. The parameters measured by sensor of the angular trajectory of the human gait include angle, angular velocity and angular acceleration. The efficiency and accuracy of the proposed method are compared with each other to see if which is the most appropriate to refine the error by angle, angular velocity or angular acceleration.

**Keywords** Kinematics · Lower limb rehabilitation robot · Trajectory planning

## 1 Introduction

Robotic-assisted therapy and rehabilitation is being used more and more frequently, especially robot-assisted active and passive lower limb rehabilitation robots. Diseases of the central nervous system cause gait disturbances. Early rehabilitation for a patient with central nervous system disease has been shown to be beneficial. However, initial gait training is difficult because of muscle weakness and older patients lose leg strength. During the patient's walking training, therapists support the patient's

---

T. Nguyen · T. Nguyen (✉)  
Ha Noi University of Science and Technology, Hanoi, Vietnam  
e-mail: [trung.nguyenthanh@hust.edu.vn](mailto:trung.nguyenthanh@hust.edu.vn)

T. Nguyen  
National Research Institute of Mechanical Engineering, Hanoi, Vietnam

T. Bui  
Shibaura Institute of Technology, Tokyo, Japan

lower extremity movements and control the patient's lower extremity movements. However, supporting movement of the lower extremities is a serious undertaking for therapists. Therefore, research and development of various gait rehabilitation devices are currently underway to identify methods to reduce physical burden for therapists.

The process of restoring function from these impairments with repetitive physiological movements to regain limb strength is known as motor rehabilitation therapy. These types of treatments are offered in platforms such as body weight support (BWS) along with a treadmill, the other type of system is a leg plate based BWS and a stationary exercise machine (without any any body weight support system). For stationary machines, a sitting/lying position is recommended for bedridden patients. One of the popular stationary machines is the Motion Generator which is a commercially available system that offers a wide range of services geared towards lower extremity rehabilitation therapies. Other research-based suggested rehabilitation mechanisms that can treat patients in the sitting/lying position are Physiotherabot, Supine, Lambda, Modified Lambda, ANKUR-LL1 [1], ANKUR-LL2 [2] and LLR-Ro [3] (Table 1).

The design for the rehabilitation robot here is a sitting/lying exoskeleton as shown in Fig. 1 that can help the patient perform exercises that resemble a human gait as much as possible. Section 2 of the paper presents the whole process of researching, calculating and solving problems related to robot kinematics. Unlike the upper extremities, which often include many complex movements, the lower extremities are mainly cyclical, moving with a tendency to repeat [4], so we will calculate to create a cycle of repetitive human gait exercises for the robot. There are many ways to set up motion trajectory such as Firefly Algorithm, Reinforcement Learning [5], Ant Colony. *However, there is no method that can reestablish a motion trajectory similar to human gait in terms of both velocity and acceleration over time, the new trajectory setting method in this paper is designed to solve that problem.* Section 3 is the conclusion and future development direction of the research.

**Table 1** Item function table

No	Item name	Function
1	Sitting-lying chair	Placing patient
2	Hip joint motor	Adjust the angle of the hip joint
3	Thigh frame	Size can be adjusted to suit the patient
4	Thigh strap	Fix the patient's thigh to the thigh frame
5	Knee joint motor	Adjust the angle of the knee joint
6	Leg frame	Size can be adjusted to suit the patient
7	Leg strap	Fix the patient's leg to the leg frame
8	Ankle joint motor	Adjust the angle of the ankle joint
9	Foot frame	Size can be adjusted to suit the patient
10	Foot strap	Fix the patient's foot to the foot frame
11	Chair motor	Adjust the angle of chair

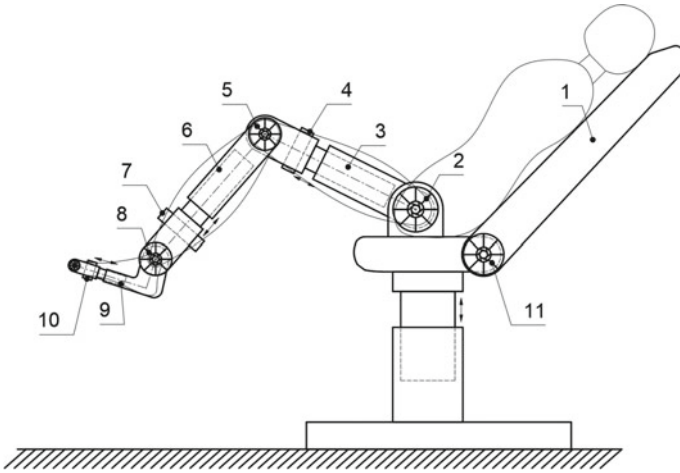


Fig. 1 Principle model of robot

## 2 Kinematic

The robot has 3 rotating joints: hip joint, knee joint and ankle joint. The stitch sizes are shown as Fig. 2, the negative and positive directions of the angle specified counter clockwise are positive.

Robot Kinematics:

- Hip Angle:  $\theta_1$

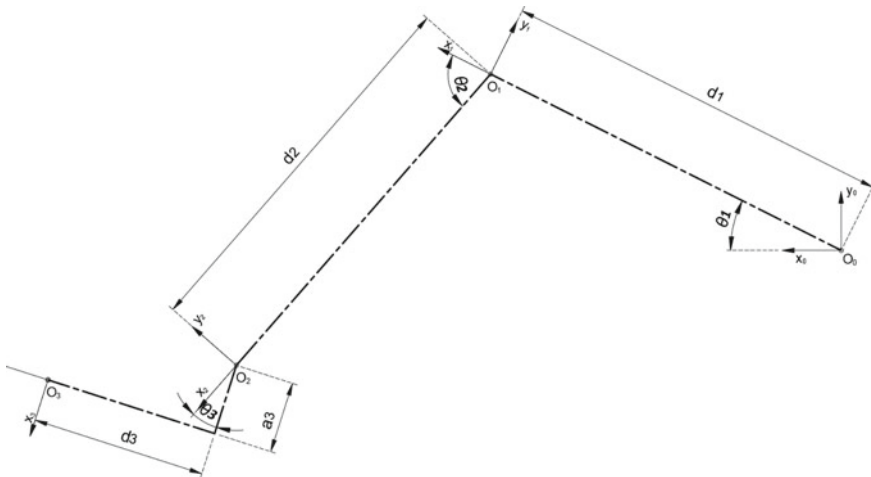


Fig. 2 Computational model

- Knee Angle:  $\theta_2$
- Ankle Angle:  $\theta_3$

The chosen research method is to set up trajectories according to a measured input parameter. To get the input to calculate the motion trajectory, the therapist first needs to sit in the patient's position, place his lower limb on the robot, and perform the desired exercise. The robot's sensor will measure the angle, angular velocity and angular acceleration parameters from the therapist's exercise. In this study, the construction of the robot is not completed yet, so the data will be taken from *BOOK 1. Biomechanics and Motor Control of Human Movement, page 341–349* [6]. The measured parameter is the movement of the human walking in a cycle of 1 s, divided into 70 equal time intervals. After obtaining the parameters of the hip, knee and ankle angles of the person walking while walking. From the book, these data have a different way of correlating the coordinates of the joints than that of the robot model. It is necessary to convert those data to match the coordinate correlation of the joints of the robot and get the graphs of 2 consecutive cycles.

However, the above data is still not accurate, as it is known that the relationship between angle, angular velocity and angular acceleration is expressed through the following equation:

$$\theta_{i+1} = \theta_i + \dot{\theta}_i * t + \frac{\ddot{\theta}_i}{2} * t^2 \quad (1)$$

where:  $\theta_i$  is the angle of the joint at point  $i$ ,  $\theta_{i+1}$  is the angle of the joint after time  $t$ ,  $\dot{\theta}_i$  is the angular velocity of the joint at point  $i$ ,  $\ddot{\theta}_i$  is the angular acceleration of the joint at point  $i$ .

But when replacing the values  $\theta_i$ ,  $\dot{\theta}_i$ ,  $\ddot{\theta}_i$  into the equation, the value  $\theta_{i+1}$  is not the same as the measured data in the book, this happens due to the error of the sensor when measured cannot match the actual parameter. To solve the problem, this paper gives a method to interpolate the measured angular trajectory to find the suitable angular velocity and angular acceleration, interpolate the measured angular velocity to find the angular trajectory and angular acceleration, interpolate the angular acceleration to find the angular trajectory and angular velocity. Then, the most accurate interpolation method among the three options above will be selected. The criterion of the option is consistent with Eq. (1), while ensuring that the motion trajectory must be the most similar to the human gait.

## 2.1 Set Motion Trajectory by Interpolation Method

In this part, although the motion trajectory is established in accordance with Eq. (1), the error caused by the sensor has not been resolved, making the calculated graph shape will have a certain difference from the graph shape from the measured

parameter. Research will focus on solving the problem of error in the following section.

a. Interpolation based on measured angular trajectory:

Taking the angular trajectory as a standard to calculate the angular velocity and acceleration through the following equations:

$$\ddot{\theta}_i = 2 * \frac{\theta_{i+1} - \theta_i + \dot{\theta}_i * t}{t^2} \tag{2}$$

$$\dot{\theta}_{i+1} = \dot{\theta}_i + \ddot{\theta}_i * t \tag{3}$$

As shown in Fig. 3, in the first cycle, there are small sawtooth oscillation, on the second cycle there is a sawtooth oscillation error over the entire period. As for Fig. 4, there was sawtooth oscillation from the beginning, and it got worse in the second period.

It happens because of *Local error* and *Cyclic cumulative error*:

- Local error— $f_i$ : Is the error at point  $i$ , affected by the deviation of the measured trajectory value from the correct trajectory value, this value can be negative or positive
- Cycle cumulative error— $F = f_1 + f_2 + f_3 + \dots f_{70} + D$ , this error exists only when the values at different times of a variable depend on each other.
- Actual cycle deviation— $D$ : In fact, when walking, people can't walk all the same, the value of the starting point of cycle 2 cannot coincide with the value of the starting point of cycle 1 and so on. But in our calculation, the value at points in a cycle is the same for all periods, so this deviation occurs.

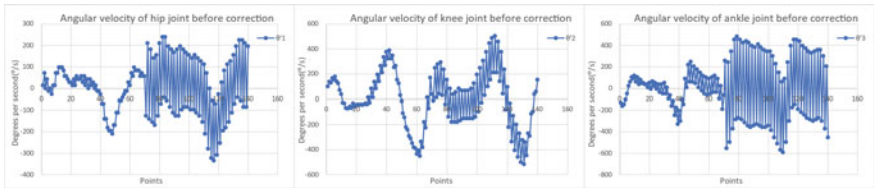


Fig. 3 Graph of angular velocity calculated based on angular trajectory

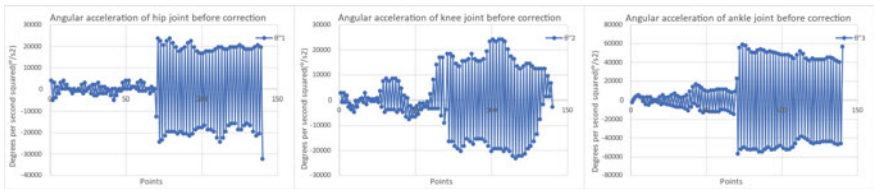
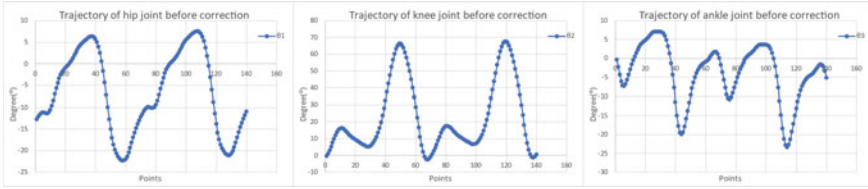
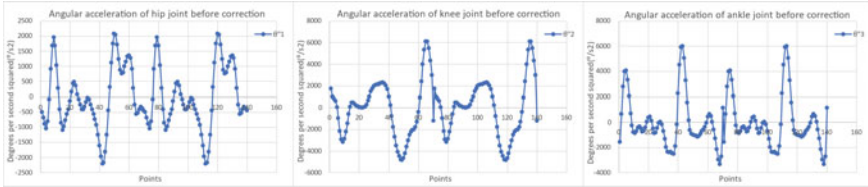


Fig. 4 Graph of angular acceleration calculated based on angular trajectory



**Fig. 5** Graph of angular trajectory calculated based on angular velocity



**Fig. 6** Graph of angular acceleration calculated based on angular velocity

b. Interpolation based on measured angular velocity:

Taking the angular velocity as a standard to calculate the angular trajectory and angular acceleration through the following equations:

$$\ddot{\theta}_i = \frac{\dot{\theta}_{i+1} - \dot{\theta}_i}{t} \tag{4}$$

$$\theta_{i+1} = \theta_i + \frac{\dot{\theta}_i + \dot{\theta}_{i+1}}{2} * t \tag{5}$$

As shown in Fig. 5, during the first and second cycles, the shape of the angular trajectory graph is the same as the data plot in the book in Fig. 3, however, when it comes to the second cycle, all the points are all higher than those in cycle 1 by an amount exactly equal to the cyclic cumulative error. As for Fig. 6, the graph of angular acceleration is similar to the graph of the data in the book with almost all similarities except for two points transitioning from period 1 to period 2, this graph has no cyclic cumulative error.

## 2.2 Error Correction

In this part, the study will find a way to correct the error so that all the cyclic cumulative error are all zero, and at the same time ensure that the effect of the local error is small enough so that the graph resembles the human gait (Fig. 7).



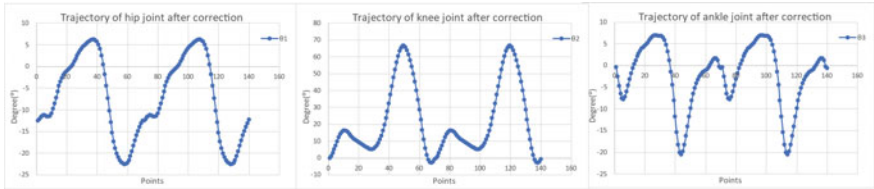


Fig. 7 Corrected angular trajectory graph

The error is corrected by correcting the parameters from the point where the calculated parameters differ the most from the measured parameters. After adjusting this parameter as optimally as possible, continue to move to the point where the difference is currently the largest, and so on until the errors are almost zero.

a. Error correction of the method taking angular trajectory as standard.

As shown in Figs. 8 and 9, although the cyclic cumulative error has been resolved, the oscillation error no longer increases with each cycle. However, the oscillation affected by the local error have not been resolved yet. To completely solve this problem, many complex calculations are needed, the task of solving the local error is still in the process of being studied more thoroughly and perfectly (Fig. 10).

b. Error correction of the method taking angular velocity as standard.

As shown in Figs. 11 and 12, the cyclic cumulative error have been resolved, so that the deviation no longer increases after each cycle, and at the same time the effect of the local error is negligible, enough for us to conclude that this is a precise trajectory.

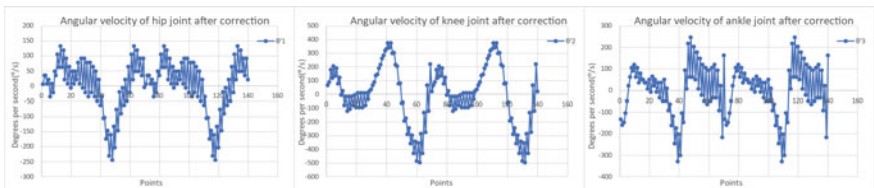


Fig. 8 Corrected angular velocity graph base on angular trajectory

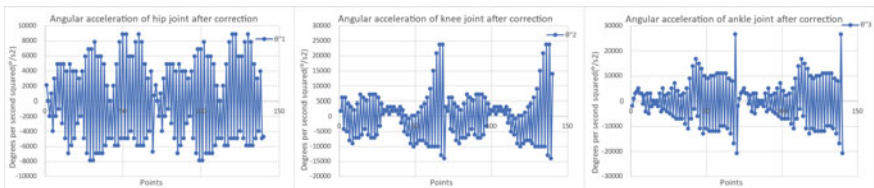


Fig. 9 Corrected angular acceleration graph base on angular trajectory

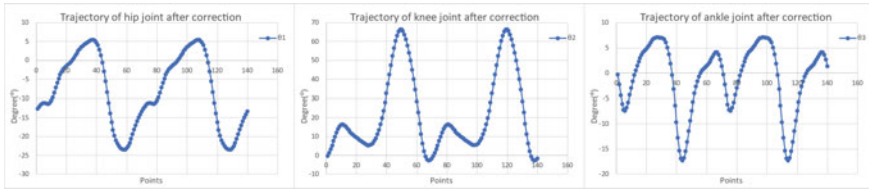


Fig. 10 Corrected angular trajectory graph base on angular velocity

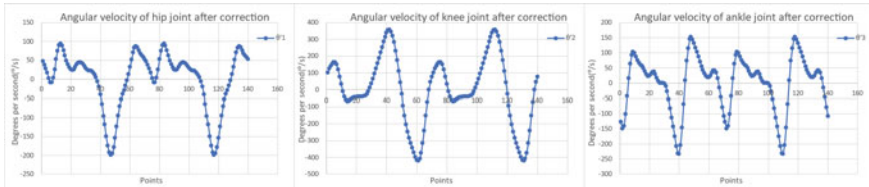


Fig. 11 Corrected angular velocity graph

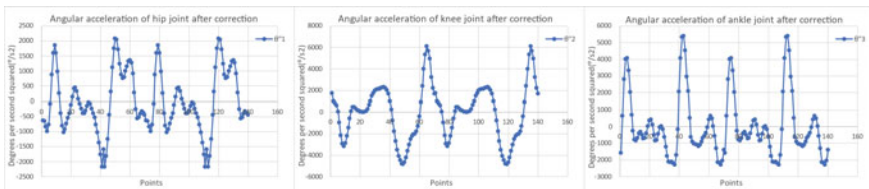


Fig. 12 Corrected angular acceleration graph base on angular velocity

### 2.3 Conclusion of the Kinematic Section

After the whole process of studying kinematic calculations, it can be concluded that calculating and correcting with angular velocity as the standard is the most optimal solution for the following reasons:

- The oscillation error of the method using the angular trajectory as the standard is too complicated to be solved perfectly.
- The cyclic cumulative error in the angular velocity method only appears in the calculated angular trajectory graph, the error has a coefficient of first order with time.
- The cyclic cumulative error in the angular acceleration method occurs in both graphs, with the angular trajectory graph being quadratic with time, angular velocity being linear with time.
- To start the calculation using the angular acceleration method, it is necessary to provide two initial parameters, the angular trajectory and the angular velocity, while the other two options only need to provide one initial parameter.

- After correction, both angular velocity and angular acceleration methods obtain a precise motion trajectory. However, the parameters of the graph taking the angular velocity as the standard are still closer to the parameters of the measured data than the method of taking the angular acceleration as the standard.

### 3 Conclusion and Discussion

The problems of robot kinematics and how to deal with them have been presented in the paper. A new method of setting motion trajectory has been proposed to solve the kinematics problem, along with new concepts such as local error, cyclic cumulative error, etc. This new method of setting motion trajectories requires pre-measured human kinematics, thereby establishing a trajectory for the robot that moves most like a human gait.

We are focusing our research to achieve a method of building a motion trajectory similar to that of a human's gait for the robot, without directly depending on the kinematic parameters measured. To do this, we are currently trying to collect more kinematic parameters of different gaits, and are also looking to upgrade and improve our kinematic calculation method, especially interpolation based on angular trajectories. Although interpolation based on angular trajectories gives the worst results and is the most difficult to deal with, it shows that points in the angular trajectory of the human gait must follow a certain rule or formula. Deviating from that rule or formula results in oscillation errors in angular velocity and angular acceleration. To be able to develop the next step of research, it is essential for us to find that rule or formula.

### References

1. S. Mohan, J.K. Mohanta, S. Kurtenbach, J. Paris, B. Corves, M. Huesing, Design, development and control of a 2PRP-2PPR planar parallel manipulator for lower limb rehabilitation therapies. *Mech. Mach. Theory* **112**, 272–294 (2017)
2. J.K. Mohanta, S. Mohan, P. Deepasundar, R. Kiruba-Shankar, Development and control of a new sitting-type lower limb rehabilitation robot. *Comput. Electr. Eng.* **67**, 330–347 (2017)
3. Y. Feng, H. Wang, Y. Du, F. Chen, H. Yan, H. Yu, *Trajectory Planning of a Novel Lower Limb Rehabilitation Robot for Stroke Patient Passive Training*
4. V. Kukreja, D. Kumar, A. Kaur, *Deep Learning in Human Gait Recognition: An Overview*, *ICACITE* (2021)
5. H. Bae, G. Kim, J. Kim, D. Qian, S. Lee, Multi-robot path planning method using reinforcement learning. *Appl. Sci.* (2019)
6. D.A. Winter, *Biomechanics and Motor Control of Human Movement*

# Applying Dynamic Movement Primitives to Motion Planning and Inverse Kinematics Problems of an Upper Limb Exoskeleton Robot



Huy Nguyen, Trung Nguyen, Hung Dao, Dung Nguyen, and Ha Pham

**Abstract** Motion planning and inverse kinematics (IK) are two important parts of controlling the robot exoskeleton. To make the wearer feel comfortable, the joints variable values need to be similar to the values measured in the actual activities of the human arm. Dynamic movement primitives (DMPs) are a useful solution to this problem. In this study, we proposed to apply DMPs to generate the robot's end-effector position and orientation trajectory as well as the robot's joint variable values trajectory from the actual measured joints values of the robot exoskeleton during Activity of Daily Living exercise such as reaching a cup of water. Then, with the same ADL, when changing position of end-effector, the proposed algorithm could generate the end-effector trajectory and joints' values as well. The results showed that the end-effector position and orientation trajectory and the joints variable had the same form as the sample one. This proved that we can absolutely apply DMP to solve the Inverse Kinematics and Motion planning for robots without solving complicated inverse kinematics problems.

**Keywords** Motion planning · Forward kinematics · Inverse kinematics (IK) · Dynamic movement primitives (DMPs)

## 1 Introduction

The Motion planning and inverse kinematics (IK) problem is important problem in the field of robotics. IK problem is understood as finding the joints variables so that the robot has the desired position and direction of the end-effector [1]. The geometric method and the iterative method (Jacobian) are the classic method commonly used

---

H. Nguyen · T. Nguyen (✉) · H. Dao · D. Nguyen  
Ha Noi University of Science and Technology, Hanoi, Vietnam  
e-mail: [trung.nguyenthanh@hust.edu.vn](mailto:trung.nguyenthanh@hust.edu.vn)

H. Pham  
Hanoi University of Industry, Hanoi, Vietnam

to solve IK problems [2–4]. However, these methods have the limitation that they are only applicable to simple robots. For the exoskeleton rehabilitation robot, finding the joint values solution is extremely necessary because the bad joint variable can cause injury to the patient. The joints values trajectories of the robot need to be stable and continuous. In [5, 6], we have proposed the optimal approaches as improved PSO and DE algorithms to solve the IK problem, we have tested and used these proposed algorithms against the endpoint trajectory of Activities of Daily Living (ADL) as measured by an Exoskeleton type Human Motion Capture (E-HMCS) device [7].

However, in order for the user to be able to move in the most natural way, the trajectories need to be similar to nature human activities, Dynamic Movement Primitives (DMPs) is a commonly used solution to solve this problem. Saveriano et al. [8] provided a systematic and comprehensive review of the existing literature and classified the status of research on the DMPs. In [9] the article’s authors reviewed the motion planning methods to control exoskeleton, especially for the upper extremity, and identified challenges in path planning for the upper extremities. Lauretti et al. [10] the article’s authors presented a demonstration learning approach for planning the upper limb exoskeleton built based on the computation of DMPs and machine learning techniques to generate trajectories for the task and patient based on learned trajectories.

In this study, we experimented with applying DMPs to generate motion trajectories of robots from measured daily activities. At the same time, we also create joint variables by using DMPs instead of using traditional methods to solve IK problem. The results show that the joint values, the position and orientation trajectory of the robot in the 2 cases are similar. The following sections of the rest of the paper: the exoskeleton robot arm model describes in Sect. 2. Section 3 will provide the theory of the DMP algorithm and the application of DMPs in the IK problem. Section 4 shows the expected results after comparing the use of DMP to create angular trajectory matching and the use of DMPs combined with IK to solve motion planning and inverse kinematics. Finally, we will draw conclusions in Sect. 5.

## 2 Human Arm with E-HMCS Model Description

### 2.1 *E-HMCS Model*

The human arm is composed of three anatomical joints (shoulder, elbow, and wrist joints) while ignoring the clavicle and clavicle muscles [11]. We also propose a 3D model to simulate the human arm to ensure the basic anthropometric parameters of Asians in general and especially of Vietnamese people in particular [12]. The length of the joints of the model is selected which basing on the length of the person’s arm who has worn the E-HMCS. To evaluate the efficiency of the proposed algorithm and also determine the endpoint trajectories in the ADL operation, we have also developed the Exoskeleton-type Human Motion Measurement System (E-HMCS)

[13]. It is an exoskeleton measuring device made by 3D printing technology and has a low-cost, simple calculation process. The arm model of the person wearing the device is depicted as shown in Fig. 1 with kinematic parameters, and Denavit–Hartenberg parameters (DH) as shown in Table 1.

**Fig. 1** Human arm model wearing the E-HMCS

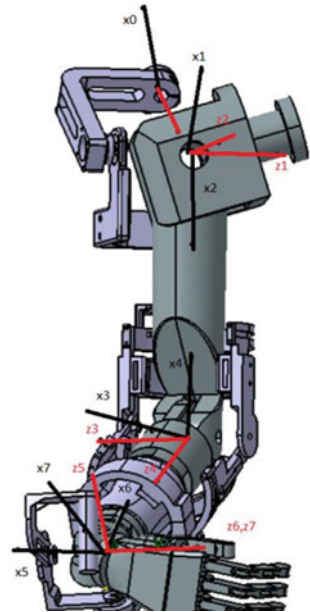


**Table 1** Denavit–Hartenberg parameters of E-HMCS

$\theta$ ( $^{\circ}$ )	$d$ (mm)	$a$ (mm)	$\alpha$ ( $^{\circ}$ )
$q_1$	143	0	90
$90 - q_2$	7	0	- 90
$q_3$	286.9	0	- 90
$q_4$	0	0	90
$90 + q_5$	336	0	90
$90 + q_6$	0	0	- 90
$q_7$	0	0	0

### 3 Dynamic Movement Primitives to Motion Planning and Inverse Kinematics Problems

#### 3.1 Dynamic Movement Primitives Algorithm

The theory behind DMP is well established in [14] where the heart of the model is a point-attractor system modulated with a nonlinear function to enable the generation of complex movements. One point-attractor system is the spring-damper system:

$$\ddot{y} = \alpha_y(\beta_y(g - y) - \dot{y}) + f \quad (1)$$

where  $\alpha_y$  and  $\beta_y$  are positive constants,  $y$  and  $g$  are the initial and final points of the trajectory (system state and goal). The crux of the DMP framework is an additional nonlinear system used to define the forcing function  $f$  over time, giving the problem a well-defined structure that can be solved straightforwardly and easily generalized. The introduced system is called the canonical dynamical system

$$\dot{x} = \alpha_x x \quad (2)$$

The forcing function  $f$  is defined as a function of the canonical system:

$$f(x, g) = \frac{\sum_{i=1}^N \psi_i w_i}{\sum_{i=1}^N \psi_i} x(g - y_0) \quad (3)$$

where  $y_0$  is the initial position of the system:

$$\psi_i = \exp(-h_i(x - c_i)^2) \quad (4)$$

And  $w_i$  is a weighting for a given basis function  $\psi_i$ . The  $\psi_i$  equation above defines a Gaussian centered at  $c_i$ , where  $h_i$  is the variance.  $w_i$  has solution:

$$w_i = \frac{S^T \psi_i \mathbf{f}_d}{S^T \psi_i \mathbf{S}} \quad (5)$$

where:

$$\mathbf{s} = \begin{pmatrix} x_{t_0}(g - y_0) \\ \vdots \\ x_{t_N}(g - y_0) \end{pmatrix}, \quad \psi_i = \begin{pmatrix} \psi_i(t_0) & \cdots & 0 \\ 0 & \ddots & 0 \\ 0 & \cdots & \psi_i(t_n) \end{pmatrix} \quad (6)$$

### 3.2 *Dynamic Movement Primitives for Inverse Kinematic*

In most of the previous studies, the DMP algorithm often used to create a motion trajectory for the robot and be able to control the robot to move along that trajectory, we have to solve the inverse kinematics problem. For non-skeletal robotic arms, joint values solutions need to be naturally obtained to provide comfortable to the user. So why don't we apply DMP to create a most natural trajectories?

One of the challenges when applying DMP to the inverse kinematics problem is that we don't know the value of the joint values at the end of the moving trajectories (the starting point of the trajectory is the current state of the robot). To solve this problem, the research applied the commonly used algorithms DMPs [15] and some IK methods to find the joint variables at the end point of the motion trajectory. After obtaining this value, we applied the DMP algorithm to achieve the desired match trajectory. We tested and compared the results in the following 2 cases:

- To use the DMPs algorithm to create the position trajectory and orientation trajectory of the robot ( $x, y, z$ ) combined with the inverse kinematics problem-solving methods to find the joints values
- Use the algorithm for IK problem to find the joint values at the end point of the new position trajectory, then use DMPs to generate the joint values trajectory ( $q$ ).

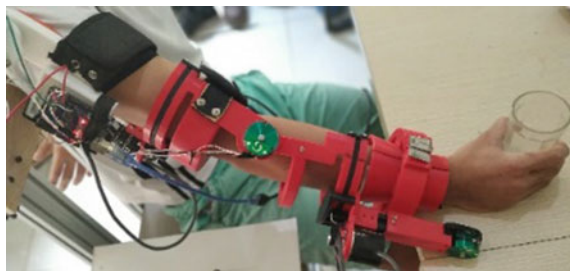
## 4 Experiments and Results

### 4.1 *Experiments Setup*

In this study, to evaluate the efficiency of the algorithms, we used the measuring results of the water cup movement task measured by E-HMCS (Fig. 2). With the matching joint values ( $q$ ) measured by kinematic calculations, we obtain the positional and orientation trajectories of the respective end-effector ( $E$ ). After having these parameters, we performed the following steps:

- Step 1: Run the algorithm to find DMP parameters corresponding to: joint values (DMP with  $q$ ), both position and orientation (DMP with  $P, O$ )

**Fig. 2** Experiment for the water cup movement tasks





- Step 2: Generate new position and orientation trajectories of the end-effector ( $E_{dmp}$ ) with the goal being the point around the measured endpoint of the end-effector ( $e_{goal}$ )
- Step 3: Solve inverse kinematic to find goal joint values ( $q_{goal}$ ) from  $e_{goal}$ .
- Step 4: Generate new joint values trajectory ( $q_{dmp}$ ) with  $q_{goal}$  and DMPs's parameters
- Step 5: Calculate inverse kinematic and forward kinematics with newly created trajectories: use forward kinematics to calculate the end-effector from  $q_{dmp}$  ( $q_{dmp} > FK > E_{q\_DMP}$ ) Calculate inverse kinematics to find to joint values from  $E_{dmp}$  ( $E_{dmp} > IK > q_{ik\_dmp}$ .)
- Compare joint values and end-effectors with each other. ( $E_{dmp}$  and  $E_{q\_DMP}$ ,  $q_{dmp}$  and  $q_{ik\_dmp}$ )

## 4.2 Results

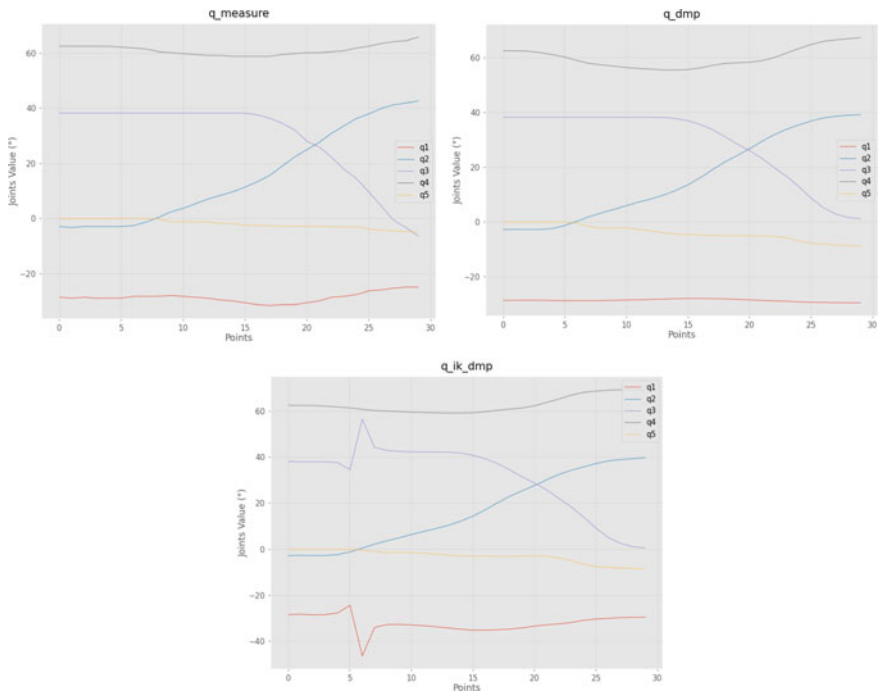
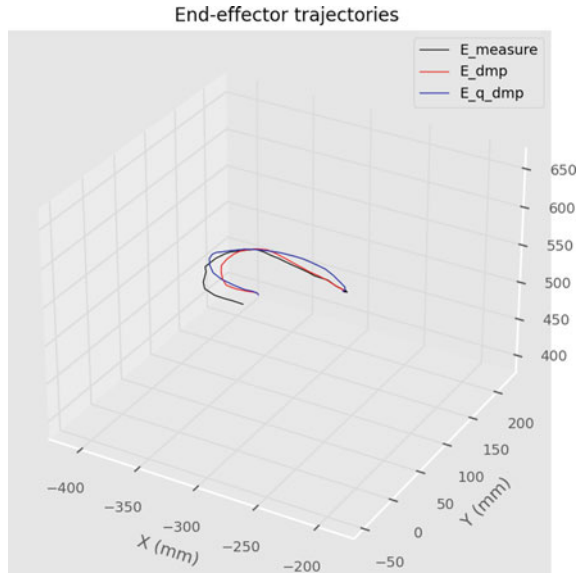
We will compare and evaluate the obtained results based on the position trajectories of the end-effector and the resulting joints values trajectories. From Fig. 3, we can see that the trajectories ( $E_{measure}$ ,  $E_{dmp}$  and  $E_{q\_dmp}$ ) all have similar form, although  $E_{dmp}$  and  $E_{q\_dmp}$  share the same endpoint, but these two trajectories do not coincide. It can be explained causing by the error when generating data by DMP algorithm and the calculation process forward and reverse kinematics. When looking at the cosine similarity table of the end-effector orbital, we can see a specific result when  $E_{q\_dmp}$  has a higher average score than  $E_{dmp}$ , two cosine similarity of trajectories are very high.

Figure 4 shows us the graph of the joint values trajectory in the cases. The  $q_{dmp}$  trajectories are smooth and stable, but the  $q_{ik\_dmp}$  orbital has any unusually abrupt changes. The reason can be the inverse kinematics calculation. When we look at the scores cosine similarity again, we see that  $q_{dmp}$  is significantly higher than  $q_{ik\_dmp}$ , especially at joints  $q_1$  and  $q_3$  exists a significant difference due to their instability in the  $q_{ik\_dmp}$  orbital (Tables 2 and 3).

## 5 Conclusion

In this study, the application of the DMPs algorithm generates the position and orientation trajectory of the end-effector like the joint variables trajectory. Therefore, the research team can conclude that the complete DMP can be applied to solve the invert kinematic problem and generate motion planning of the robot. The results showed that using DMP with joints helps to produce end-effector trajectories and joints, which are more similar to the measured values. It makes it possible for humans to manipulate the robot more naturally and comfortably. In the future, we can use DMP to generate a lot of end-effector position and orientation trajectories as well as

**Fig. 3** Position trajectories of the end-effector



**Fig. 4** Joints values of measure trajectories, DMP trajectories and IK DMP trajectories

**Table 2** Cosine similarity position trajectories end-effector

E_measure	x	y	Z	Avg
E_dmp	0.9991	0.9907	0.9998	0.9965
E_q_dmp	0.9992	0.9972	0.999	0.9987

**Table 3** Cosine similarity of joint's values trajectories

q_measure	q1	q2	q3	q4	q5	Avg
q_dmp	0.997	0.9956	0.9977	0.9994	0.9913	0.9962
q_ik_dmp	0.9938	0.9941	0.9934	0.9993	0.9732	0.9907

joint variable trajectories for control as well as data to train neural networks to help solve complex robot problems.

**Acknowledgements** Research reported in this paper was supported by Ministry of Science and Technology of Vietnam, under award number [ĐTĐLCN.28/20].

## References

1. R. Köker, T. Çakar, A neuro-genetic-simulated annealing approach to the inverse kinematics solution of robots: a simulation based study. *Eng. Comput.* **32**, 553–565 (2016)
2. S.-S. Liaw, H.-M. Huang, G.-D. Chen, Surveying instructor and learner attitudes toward e-learning. *Comput. Educ.* **49**, 1066–1080 (2007)
3. J.J. Rubio, A.G. Bravo, J. Pacheco, C. Aguilar, Passivity analysis and modeling of robotic arms. *IEEE Lat. Am. Trans.* **12**, 1381–1389 (2014)
4. Y.L. Kou, T.P. Lin, C.Y. Wu, Experimental and numerical study on the semi-closed loop control of a planar robot manipulator. *Math. Probl. Eng.* **114**, 1–9 (2014). <https://doi.org/10.1155/2014/769038>
5. T.T. Nguyen, N.L. Tao, V.T. Nguyen, N.T. Bui, V.H. Nguyen, D. Watanabe, Apply PSO algorithm with searching space improvements on a 5 degrees of freedom robot, in *Proceedings of the 2020 3rd International Conference on Intelligent Robotic and Control Engineering (IRCE)* (2020)
6. T.T. Nguyen, V.H. Nguyen, X.H. Nguyen, Comparing the results of applying DE, PSO and proposed Pro DE, Pro PSO algorithms for inverse kinematics problem of a 5-DOF scara robot, in *Proceedings of the 2020 International Conference on Advanced Mechatronic Systems (ICAMechS)* (2020)
7. T. Nguyen, H. Nguyen, K. Dang, P. Nguyen, H. Pham, A. Bui, Simulation and experiment in solving inverse kinematic for human upper limb by using optimization algorithm, in *ACIHDS 2021: Intelligent Information and Database Systems*, pp. 556–568 (2021)
8. M. Saveriano, F.J. Abu-Dakka, A. Kramberger, L. Peternel, Dynamic movement primitives in robotics: a tutorial survey. *Comput. Sci.* (2021)
9. C. Nguiaadem, M. Raison, S. Achiche, Motion planning of upper-limb exoskeleton robots: a review. *Appl. Sci.* **10**, 7626 (2020). <https://doi.org/10.3390/app10217626>
10. C. Lauretti, F. Cordella, A.L. Ciancio, E. Trigili, J.M. Catalan, F.J. Badesa, S. Crea, S.M. Pagliara, S. Sterzi, N. Vitiello, A.N. Garcia, L. Zollo, Learning by demonstration for motion

planning of upper-limb exoskeletons. *Front. Neurobot.* (2018). <https://doi.org/10.3389/fnbot.2018.00005>

11. N. Trung, D. Hiep, D. Thien, B. Tam, W. Dai, Design a human arm model supporting the design process of upper limb rehabilitation robot, in *Proceedings of the 14th South Asian Technical University Consortium Symposium 2020 (SEATUC 2020)*, pp. 2186–7631 (2020)
12. Tổng liên đoàn lao động Việt Nam, Viện nghiên cứu khoa học kỹ thuật bảo hộ lao động (Vietnam), *Atlas nhân trắc học người Việt Nam trong lứa tuổi lao động: dấu hiệu tầm hoạt động khớp và trường thị giác*, Nhà xuất bản Khoa học và kỹ thuật (2002)
13. N. Thanh-Trung, B. Ngoc-Tam, D. Watanabe, Design and manufacture a cheap equipment to measure human arm motion in developing countries, in *The 4th International Conference on Mechatronics Systems and Control Engineering (ICMSCE 2021)*, pp. 48–53 (2021)
14. A.J. Ijspeert, J. Nakanishi, H. Hoffmann, S.P. Schaal, Dynamical movement primitives: learning attractor models for motor behaviors. *Neural Comput.* **25**(2), 328–373 (2013)
15. C. Lopez-Franco, J. Hernandez-Barragan, A.Y. Alanis, N. Arana-Daniel, A soft computing approach for inverse kinematics of robot manipulators. *Eng. Appl. Artif. Intell.* **74**, 104–120 (2018)

# A Study on Building a Motorcycle Finite Element Model for Crashworthiness Base on the Current Transportation in Vietnam



Nguyen Phu Thuong Luu and Ly Hung Anh

**Abstract** This study aimed to construct a finite element model of a small motorcycle with full deformability for simulating frontal crashes, and to provide a comprehensive guide for the entire development process. The Honda Wave 110 cc, a Vietnamese national motorcycle, was selected as the physical motorcycle, and the model was analyzed in the LS-DYNA environment. This paper presents a tutorial on advanced 3D modeling to generate a high-quality 3D geometry and replication model of a motorcycle chassis, and then to set up a model dummy sitting on the motorcycle. This motorcycle FE model can be utilized for crashworthiness analysis and other studies. The motorcycle model was constructed from different materials such as steel and aluminum to make the motorcycle chassis model. The frame of the motorcycle was created by combining the individual parts of the saddle, handlebar, and wheel. The entire model of the motorcycle was then meshed and assigned materials, and its stability was assessed by conducting a crash simulation with a vehicle model. The dummy part was also added to the motorcycle model so that it could be employed to assess the injury of motorcyclists when a collision with other types of traffic occurs.

**Keywords** FEM · Model · Design · Structure · Vietnamese motorcycle

---

N. P. T. Luu (✉)

Faculty of Automotive Engineering, School of Technology, Van Lang University, Ho Chi Minh City, Vietnam

e-mail: [luu.npt@kttk.edu.vn](mailto:luu.npt@kttk.edu.vn); [luu.npt@vlu.edu.vn](mailto:luu.npt@vlu.edu.vn)

Department of Automotive Engineering, Faculty of Engineering and Technology, Binh Duong Economics and Technology University, Binh Duong City, Vietnam

L. H. Anh

Department of Aerospace Engineering, Faculty of Transportation Engineering, Ho Chi Minh City University of Technology (HCMUT), 268 Ly Thuong Kiet Street, District 10, Ho Chi Minh City, Vietnam

Viet Nam National University Ho Chi Minh City, Linh Trung Ward, Thu Duc District, Ho Chi Minh City, Vietnam

# 1 Introduction

Today, the problem of traffic accidents is being warned of worldwide. Especially in developing countries, there are a lot of motorbikes, including in Vietnam. However, there has not been any research on popular motorcycles in Vietnam when they collide. Most studies focus on cars, buses, and trucks [1–5]. For that reason, this paper builds a popular motorcycle model widely used on the market today for research. After building this motorcycle model, it can be used to study the structure and safety when colliding with other vehicles. This paper discussed the use of a dummy to evaluate post-collision head injury and the combination of motorcycle and dummy models to simulate real-world collisions. There are a few studies related to motorcycle structure, as in the article [6]. As mentioned in this article, research on improving crash safety for large motorcycles of this type is not very common in Vietnam. Similarly, there is a study number [7] which focused on the frame structure of a 4-wheel off-road motorcycle only used for off-road areas. This study examined the safety of motorcyclists in collisions with cars, using a popular motorcycle model in Vietnam [8]. The focus was on analyzing the dummy's head injury, with the motorcycle structure assumed to be undistorted.

## 1.1 Motorcycle Model Design

This study used CATIA V6 design software to create a 3D motorcycle frame based on the Honda Wave 110cc (Fig. 1), a popular model in Vietnam. The parts of the frame were refined for increased realism and accuracy, and the model was mapped for size, mass, and precision to simulate a dummy ride.

This study focused on the main frame structure, with the bearing parts being the most impacted in the event of an impact. The plastic truss parts outside the body were omitted to simplify the motorcycle model. The details of the model were designed below.

**Fig. 1** Honda Wave 110cc was selected to design the motorcycle model



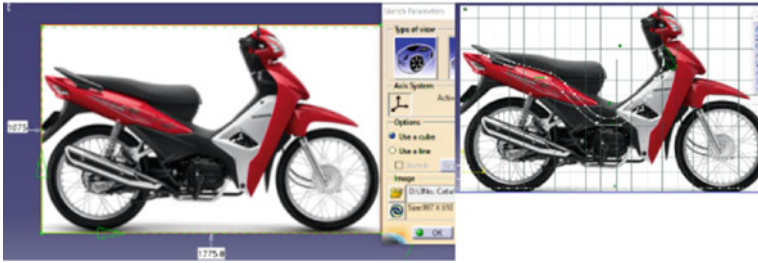


Fig. 2 Size reference from real motorcycle model

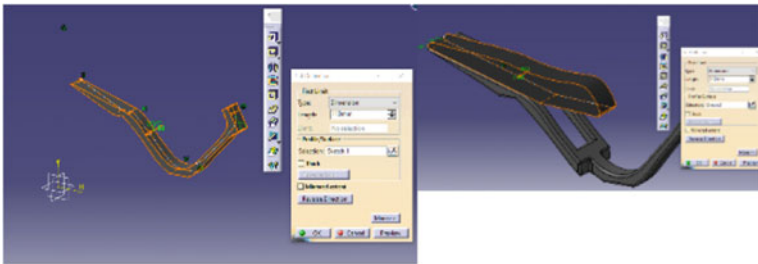


Fig. 3 Motorcycle frame model design process

## 1.2 Motorcycle Chassis

The motorcycle model's frame was redesigned based on the physical size of the Honda Wave motorcycle (Fig. 2) to determine the size of the motorcycle model. The frame part was designed accordingly (Fig. 3).

## 1.3 Motorcycle Wheel and Suspension

The wheel part is designed with wheels and rims. The size is taken according to the actual size in which to simplify the design of the wheel as shown in Fig. 4.

This study focused on the structural part of the motorbike, omitting the kinematic part. To simplify the model, the front and rear suspension systems were simplified with hard-link bars (Fig. 5).

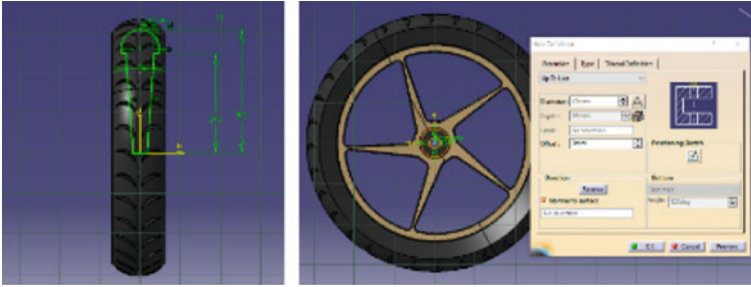


Fig. 4 Wheel design process for motorcycle model

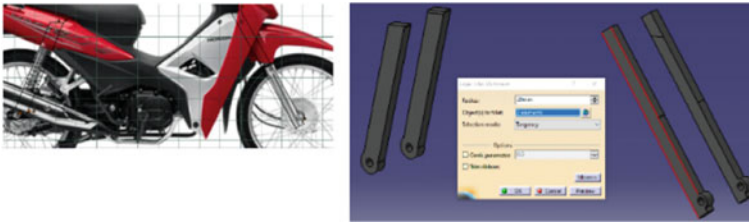


Fig. 5 Motorcycle suspension system design

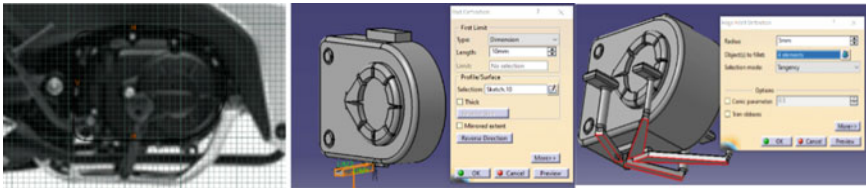


Fig. 6 Motorcycle engine model design

### 1.4 Motorcycle Engine

The engine model was designed with a focus on the exterior shape and size, while internals were simplified to simplify the model. The engine mass was added to match the real engine’s mass. The design process is shown in Fig. 6.

### 1.5 Full Motorcycle 3D Model

The motorcycle handlebar model is simplified, leaving only the control bar, and other parts such as handbrake, cables, taplo meter and control buttons are omitted.



**Fig. 7** Motorcycle handlebar model design

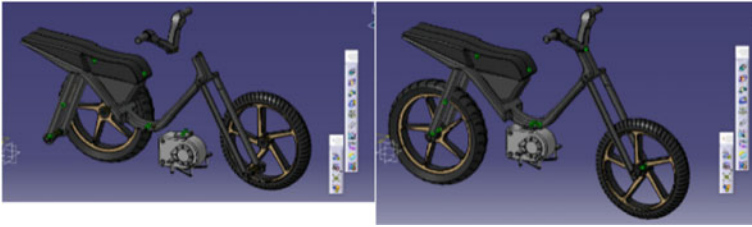
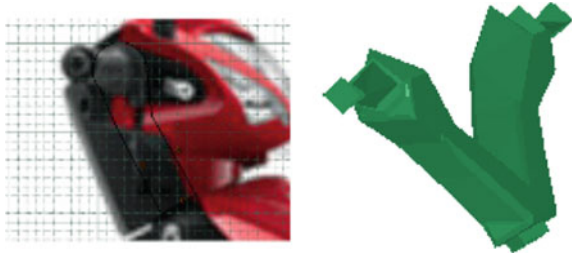


**Fig. 8** Full assembled motorcycle model

The steering wheel model is designed as shown in Fig. 7. In Fig. 8 on the left are all the details of the motorcycle model after being designed in 3D. After assembling the parts together, we have a complete motorcycle model as shown in Fig. 8 on the right.

## 1.6 Simulations Set up

### 1.6.1 Create Mesh Mode and Materials

To simulate, we have to perform the meshing of the motorcycle model designed above and set up boundary conditions as well as collision conditions in reality. In this paper, meshing is done using Hypermesh software. Because the model is the same size as the real car, the details are large. Therefore, the element size of the selected details is 10 mm when meshing. If high precision is not required, we can choose an element size of 50 mm. Depending on the size of the details, we can resize the element accordingly. The model after meshing is shown in Fig. 9. The materials used in the motorcycle model are based on the material description in the LS-DYNA software. Because the details in the motorcycle model are deformable, MAT 24 is mainly used for metal materials, and MAT 07 is used for rubber materials such as tires.

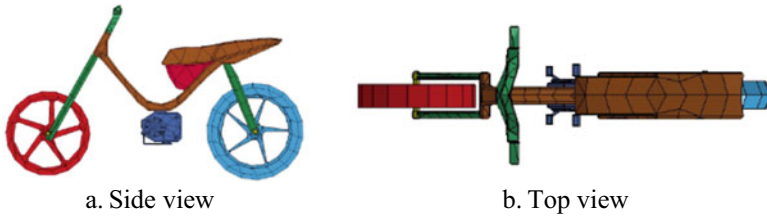


**Fig. 9** The motorcycle model has been meshed and added materials



**Fig. 10** Motorcycle model with dummy

### ***1.7 Set up the Dummy's Posture***

Firstly, import the numerical dummy and car together, which is exact to the first method, then use the “Dummy Positioning tab” in the LS-PrePost to determine the right coordinate position of the simulation posture (right front of the car bumper with 3 orientations:  $0^\circ$ ,  $45^\circ$ ,  $90^\circ$ ). Then, try to remember it and re-open the numerical dummy file. After that, save and replace the old file with the new dummy positioned one, following the process as shown in Fig. 10.

### ***1.8 Motorcycle Model Testing***

To test the operation of the motorcycle model in this paper, we simulate a collision with a passenger car. The crash test model is designed as shown in Fig. 11. In this case, the car is traveling at 20 km/h and the motorcycle is traveling at 10 km/h. The collision occurred on the left side of the car, with a collision percentage of 30%. When running the model analysis, errors about negative solid elements and velocities occur. After fixing the above errors, the model works normally and the simulation results are shown in Figs. 12, 13, 14 and 15.

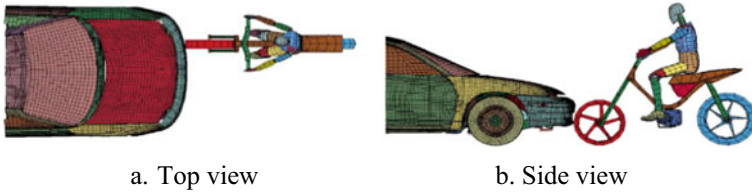


Fig. 11 Frontal impact car to motorcyclist test model

Fig. 12 The motorcycle stress (Pa)

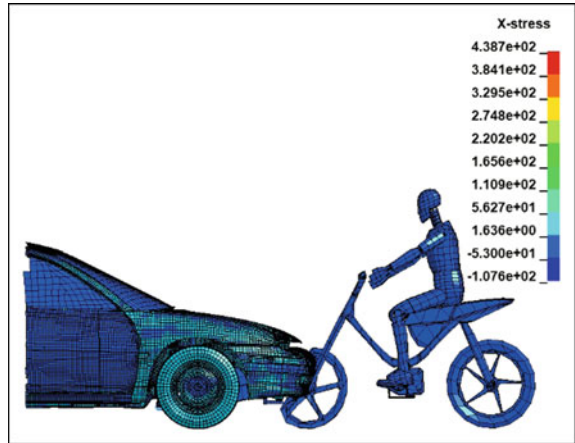
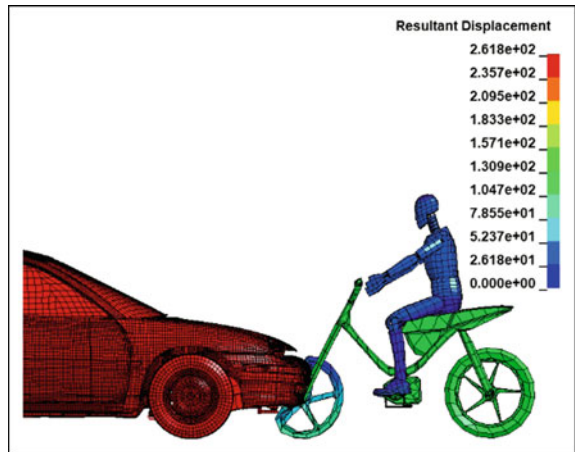
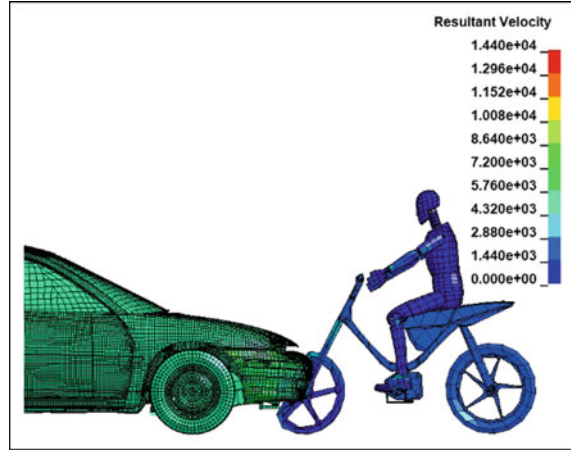


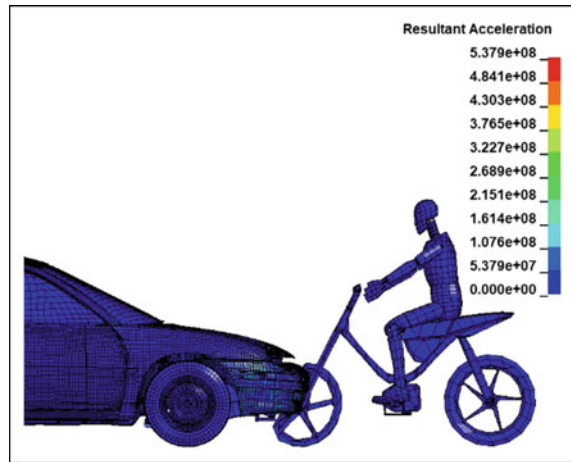
Fig. 13 The resultant displacement of motorcycle model (mm)



**Fig. 14** The resultant velocity of motorcycle model (m/s)



**Fig. 15** The resultant acceleration of motorcycle model ( $m/s^2$ )



Simulation results show that when a collision occurs between a motorcycle and a car, the front part of the motorcycle is deformed, especially the front wheel and steering axle with the front shock absorber system. The stress is concentrated on the motorcycle wheel as shown in Fig. 12. The displacement of the model depends on the traveling speed of the motorcycle and car. Therefore, when the vehicle collides at a high speed, the vehicle will move larger, as shown in Fig. 13. The speed at which the two cars collide also changes. Because the car moves at a higher speed, the simulation results are part of the simulation results shown larger through color, as shown in Fig. 14. Due to the impact energy absorption deformation of the wheel and the front bumper of the car, the acceleration generated at impact is small, as shown in Fig. 15.

## 2 Conclusions

In this paper, a complete motorcycle model has been built that can be used to simulate collisions between motorcyclists and other vehicles such as cars, buses, trucks, pedestrians, and other motorcyclists. The detailed design process of the motorcycle model as well as the construction of the collision model is also given in the section of the article. Based on the simulation results, we can predict the injuries for motorcyclists, or we can improve the motorcycle's frame to improve safety in collisions between motorcycles and other traffic vehicles.

However, due to time and cost constraints, testing the accuracy of the motorcycle model has not been done. Therefore, the accuracy of simulation results has not been tested experimentally. The further research of this paper is to test the actual motorcycle model compared to the experiment to evaluate the accuracy of the model as well as the simulation results.

**Acknowledgements** The authors express their gratitude to Van Lang University in Vietnam for their invaluable contribution in financing this study.

## References

1. N.P.T. Luu, Analysis of bus structural performance during full frontal impact, in *IEEE Proceeding on System Science and Engineering* (2019), pp. 635–638. <https://doi.org/10.1109/ICSSE.2019.8823416>
2. N.P.T. Luu, Vehicle frontal impact to pole barrier simulation using computer finite element model, in *IEEE Proceeding on Green Technology and Sustainable Development* (2018), pp. 273–277. <https://doi.org/10.1109/GTSD.2018.8595702>
3. P.T.L. Nguyen, J.Y. Lee, H.J. Yim, S.B. Lee, S.J. Heo, Analysis of vehicle structural performance during small-overlap frontal impact. *Int. J. Autom. Technol.* **16**(5), 799–805 (2015)
4. P.T.L. Nguyen, J.Y. Lee, H.J. Yim, H.K. Kim, S.B. Lee, S.J. Heo, Optimal design of vehicles structure for improving small overlap rating. *Int. J. Autom. Technol.* **16**(6), 959–965 (2015)
5. N.P.T. Luu, An optimisation approach to choose thickness of three members to improve IIHS small-overlap structural rating. *Int. J. Crashworthiness* **22**(5), 518–526 (2017)
6. M. Inui, N. Umezū, Extraction of vertical cylinder contacting area for motorcycle safety verification. *Comput.-Aided Des. Appl.* **15**(4), 556–564. <https://doi.org/10.1080/16864360.2017.1419643>
7. S.M. Bhale, Design and structural analysis of a quad bike. *Int. Res. J. Eng. Technol. (IRJET)* **4**(1) (2017)
8. P.T. Nguyen, A. Ly Hung, Analysis head injuries of Vietnamese motorcyclist without a helmet in car to motorbike frontal impact using a computer model. *Int. J. Crashworthiness* (2022). <https://doi.org/10.1080/13588265.2022.2075615>

# Simulation and Investigation of the Influence of Pressure on the Stiffness of Air Spring Suspension in Passenger Vehicles Using ABAQUS



Nguyen Thanh Cong and Pham Duy Binh

**Abstract** Air springs have been widely used in commercial vehicles as automobiles owing to many advantages. The stiffness characteristic of the air spring is used to evaluate the quality of the suspension system of the vehicle. Almost research related to the stiffness of air spring in the past were carried out through experiments. For this reason, applying numerical software in the analysis to investigate the stiffness of the air spring in the passenger vehicle is supposed to bring many positive effects. In this study, the stiffness of the air spring in a passenger vehicle subjected to undergoing static load over different pressures was studied. The findings can be used to improve the design and enhance the productivity of suspension systems in the future. The axisymmetric model of an air spring is used to simulate based on the Finite Element Method in the numerical software ABAQUS. The nonlinear material defined by the vulcanization of rubber and cord was used for simulation. The stiffness characteristics of the bellows-type of air spring based on different pressures also were obtained. The findings showed the relationship between the pressure factor and the stiffness of an air spring in a vehicle.

**Keywords** Air spring · ABAQUS · Finite element method · Nonlinear materials

---

N. T. Cong (✉)

Faculty of Mechanical Engineering, University of Transport and Communications, Hanoi City, Vietnam

e-mail: [congnt@utc.edu.vn](mailto:congnt@utc.edu.vn)

P. D. Binh

Faculty of Mechanical Engineering, National Kaohsiung University of Science and Technology, Kaohsiung City, Taiwan, Republic of China

## 1 Introduction

Air springs has been widely used in vehicles, especially in passenger cars thanks to many obvious advantages including reducing vibration, adjustable height, and increasing the load capacity of the vehicle [1–4]. Vertical stiffness is a pivotal design parameter of the air spring and has a direct connection with its performance.

The investigation of the stiffness of air springs is usually obtained through experimental methods [5]. The advantage of this method is high accuracy, but its implementation is costly. Recently, the finite element method has been used widely for the calculation and analysis of air springs owing to the accuracy and significantly reduced cost compared with other methods [6, 7]. In this study, an air spring on a passenger car was modeled and analyzed the influence of the pressure factor on the vertical stiffness using ABAQUS software.

## 2 Finite Element Analysis

### 2.1 Finite Element Model of the Air Spring

The schematic of the analyzed air spring is shown in Fig. 1. The parameters of model are explained as follows:

- O is the origin coordinate.
- $y_1$  is the upper stable point of the air spring.

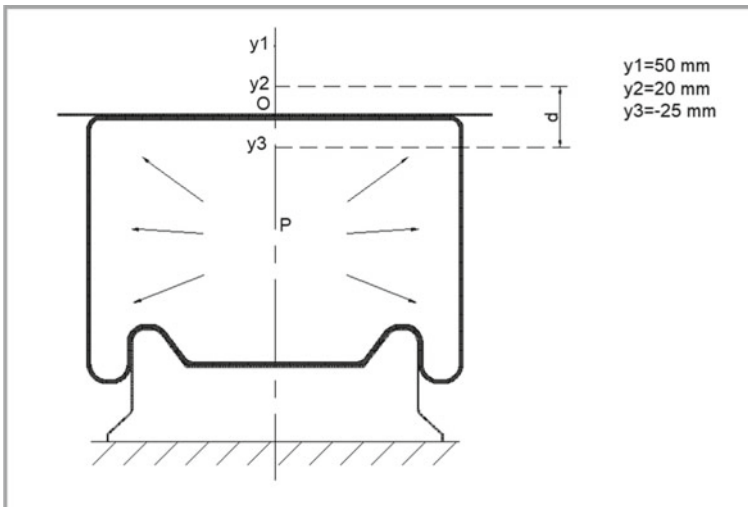


**Fig. 1** The schematic of the air spring

**Table 1** Characteristic of composite material

Layer	Material	Orientation angle	Thickness (mm)
1	Rubber	$-45^\circ$	1
2	Consistent	$45^\circ$	1
3	Consistent	$-45^\circ$	1
4	Rubber	$45^\circ$	1

- $y_2$  is the upper stable point of the air spring.
- $y_3$  is the lower stable point of the air spring.
- P: inner pressure of air spring (P = 4, 5, and 6 bar).
- d: distance between  $y_2$  and  $y_3$  points.

In this study, the axisymmetric model was used to model the air spring. The influence of bolt holes and studs was ignored because they were independent of the performance of the air spring. The simulation of the air spring was divided into two steps. Firstly, the air spring was unloaded, and all the constraints of the upper and lower plate were fixed. Secondly, the pressure then was imposed on its inner surface in terms of different pressure levels: 4 bar, 5 bar, and 6 bar. In addition, the top plate was moved up to reach an axial displacement  $y_1 = 50$  mm from the origin coordinate O before going down to reach an axial compression of  $-75$  mm from  $y_1$ . A composite material defined by the vulcanization of rubber and cord was used to represent the body of the air spring. The characteristic of composite material was defined by four mixed layers as shown in Table 1.

## 2.2 Finite Element Analysis of the Air Spring

The finite element simulations were carried out using ABAQUS based on indicated input. The selected output location was the origin coordination point O that located on the upper plate. The relationship between the displacement and reaction force of the air spring by time in terms of different pressures 4, 5, and 6 bars was shown in Fig. 2.

According to the obtained result, when applying inner pressure, the air spring's reactions have fluctuated during this period, with the highest fluctuation is visible at 6 bar. Then, the reaction force increased gradually before reaching the stability point. The value of reaction force in terms of 4, 5, and 6 bar are 19,604, 17,772.8, and 17,400 N, respectively. During the following three seconds, the air spring moved down an amount of 50 mm, and it was in the compression stage. The reaction force of the air spring increased until reaching the maximum value, with the maximum at 6 bar being approximately 43,300 N.

The relationship between displacement and reaction force in terms of different pressures was presented in Fig. 3. The obtained results show that the air spring at 4 bar was compressed to the position of  $-37.6$  mm and created equilibrium in static



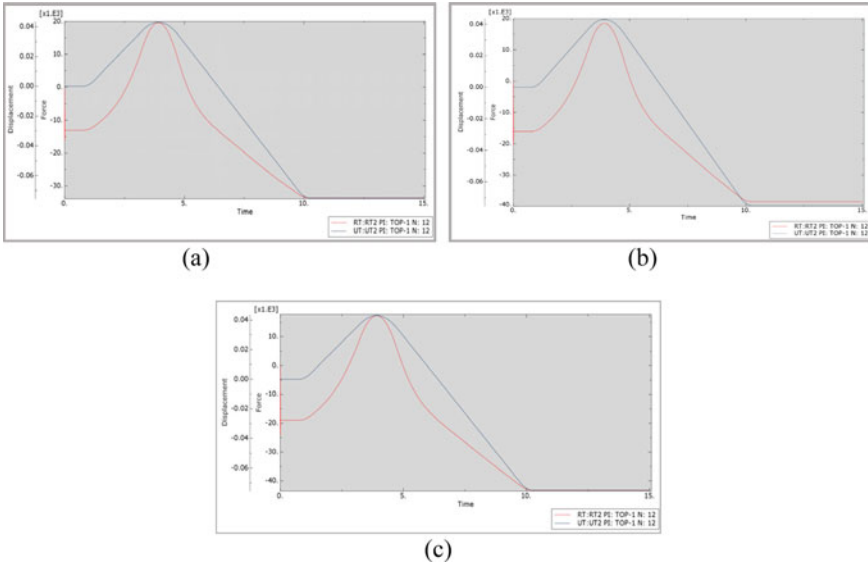


Fig. 2 Relationship between displacement and reaction force by time at: a 4 bar; b 5 bar; c 6 bar

status when the vehicle was full of load (under the maximum load of 24,000 N). With the same amount of load of 24,000 N, the air spring at 5 bar was compressed to the position of  $-25.7$  mm, which is higher than compared with the value of 4 bar. In terms of 6 bar, the air spring was compressed to the highest position among the others, with the figure being approximately  $-14.9$  mm.

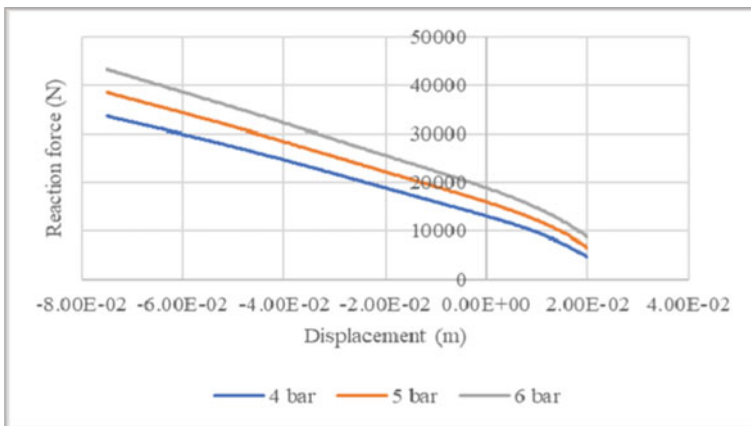
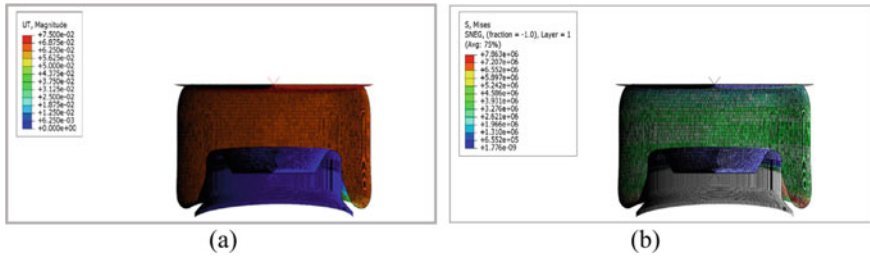
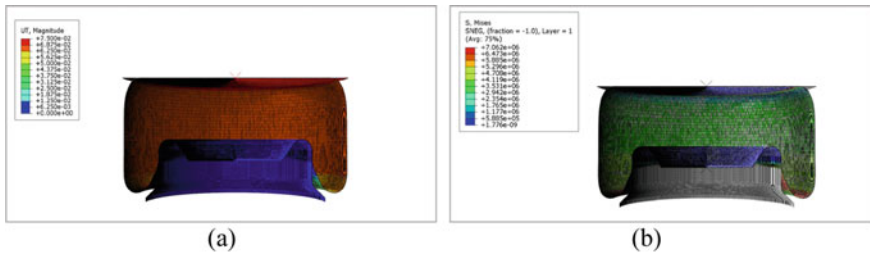


Fig. 3 Relationship between displacement and reaction force (from 20 to  $-75$  mm)



**Fig. 4** a Vertical displacement of air spring; b Von Mises stress distribution of the air spring (P = 4 bar)



**Fig. 5** a Vertical displacement of air spring; b Von Mises stress distribution of the air spring (P = 5 bar)

The simulation results of vertical displacement and von-Mises stress distribution in the air spring at the position of  $-75$  mm was shown in Fig. 4. The highest value of von-Mises stress of the simulated air spring at 4 bar is roughly  $7.863e6$  Pa.

The simulation results of vertical displacement and von-Mises stress distribution in the air spring at the position of  $-75$  mm was illustrated in Fig. 5. The peak value of von-Mises stress of the simulated air spring at 5 bar is approximately  $7.062e6$  Pa, which is slightly lower compared to that of 4 bar.

The simulation results of vertical displacement and von-Mises stress distribution in the air spring at the position of  $-75$  mm was presented in Fig. 6. The maximum von-Mises stress of the simulated air spring at 6 bar is the lowest among the three different pressures, with the figure being near  $6.890e6$  Pa.

The relationship between displacement and reaction force in three different pressures of the air spring was illustrated in Fig. 7. The findings revealed that the elastic property of the air spring depends on its inner pressure. Specifically, the higher inner pressure placed on the air spring, the higher stiffness of the air spring.

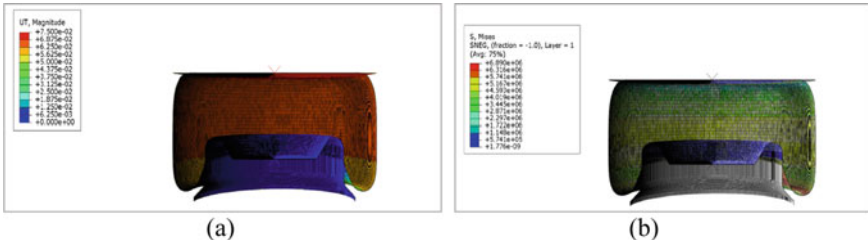


Fig. 6 a Vertical displacement of air spring; b Von Mises stress distribution of the air spring (P = 6 bar)

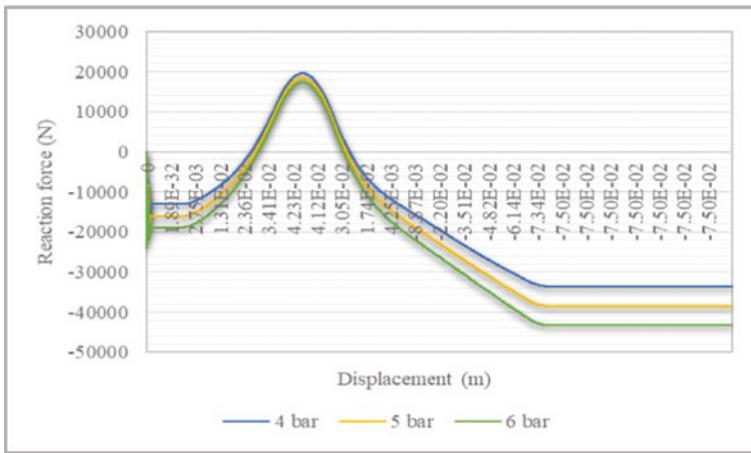


Fig. 7 Relationship between displacement and reaction force (P = 4, 5, 6 bar)

### 3 Conclusion

In this study, the finite element model of the air spring was established and analyzed to investigate the relationship between the inner pressure as well as stiffness of the air spring. The findings showed that the stiffness of the air spring changes and increases significantly when the inner pressure increases. The finite element method not only shortens the inspection and evaluation process but also saves the cost for the manufacturer and avoids the risk in the experiments.

Although reliable and accurate results have been obtained, the error for this method still needs to be verified by experiments in the future. This study only accounted for the static load of a passenger car, future work related to the dynamic load of vehicles will be studied soon.

## References

1. F. Gauterin, K. Sorge, Noise, in *Vibration and Harshness of Air Spring Systems* (2001)
2. J. Rágulík, M. Sivčák, Comparison of approaches to air spring height control. *Eng. Mech.* 325–328 (2022)
3. J. Rágulík, M. Sivčák, Modeling of the controlled air spring. *J. Mech. Eng.*, pp 107–112 (2019)
4. S. Razdan, P.J. Awasare, S.Y. Bhave, Active vibration control using air spring. *J. Inst. Eng.* (2019)
5. T. Zhou, C.F. Zong, S. Chen, Experimental research on the stiffness of air spring. *Adv. Mater. Res.*, pp. 765–767 (2013)
6. J. Ye, H. Huang, C. He, G. Liu, Analysis of vertical stiffness of air spring based on finite element method, in *MATEC Web of Conferences*, vol. 153 (2018)
7. W. Shan-Yue, H. Ying-Yun, Analysis of air-spring's stiffness by finite element method. *J. Nav. Univ. Eng.* **13**, 94–98 (2001)

# A Study on Humanoid Robot Using Ros



Xuan-Thuan Nguyen, Huy-Anh Bui, Van-Quy Hoang, and Duc-An Pham

**Abstract** Nowadays, robots used in industries and laboratories show their usefulness to life, especially the development of humanoid robots. This paper studies the motion simulation of Darwin Op robot by Ros. Here, 3D robot model is built on Gazebo software. A map has been built in Ros to make the environment for the robot to work. The transformation of the robot has been done successfully. In addition, the value coupling is built in the symbol during the movement of the robot.

**Keywords** Humanoid robots · Robotics · ROS

## 1 Introduction

It has been more than a decade ago since the first class of humanoid robot “WABOT-1 (WAseda robot-1) [1]” was born in special summer of 1973 at Japan. Later, the Biped Walking Robot WL-10R [2] was invented by Takanishi and his teammates, and P2 [3] designed by HONDA Co. Ltd. was revealed in 1996. In 2000, the second class of humanoid robot—ASIMO [4] model was released and quickly became famous all around the world. ASIMO was able to identify moving objects, postures, gestures, surroundings, noises, and faces, enabling it to communicate with people. In 1998, the model Cog [5] was born by The Cog Project of MIT Artificial Intelligence Lab. This humanoid robot realized humanlike intelligence by distributed computer systems outside the robot body. Research in humanoid robotics has uncovered a variety of new problems such as smart robotics, artificial intelligence, and control theory. Nowadays,

---

X.-T. Nguyen · D.-A. Pham (✉)

School of Mechanical Engineering, Hanoi University of Science and Technology, Hanoi, Vietnam

e-mail: [an.phamduc@hust.edu.vn](mailto:an.phamduc@hust.edu.vn)

H.-A. Bui

Faculty of Mechanical Engineering, Hanoi University of Industry, Hanoi, Vietnam

V.-Q. Hoang

Faculty Electric-Mechanical Engineering, Hai Phong University, Haiphong, Vietnam

**Table 1** The technical specifications of the DARWIN robot [8]

Category	Description
Dimension	Height (0.455 m); Weight (2.9 kg)
DOF	Head (2 DOF); Arm ( $2 \times 3$ DOF); Leg ( $2 \times 6$ DOF)
Actuator RX—28 M	Holding torque (24 kgf.cm @ 12 VILLS); Speed (45 RPM @ No Load); Position sensor (Magnetic potentiometer)
Sensor	Gyroscope (3—axis); Accelerometer (3—axis); Pressure—meter ( $2 \times 4$ FSR)

along with the development of science and technology, humanoid robots are applied in many fields, especially academic, research and so on. The latest class of humanoid robot is quite different and smarter compared to those in the past. Reem—C [6] is a humanoid robot built by PAL Robotics in 2013. The robot is designed with a weight of 80kg, a height of 165cm and 44 degrees of freedom. NAO [7] is well known as a humanoid robot, first developed in 2006 by Aldebaran. This model is a humanoid robot designed for human interaction. By aiding a modern sensor system and 3D cameras, it is used globally in research, education, and healthcare.

Darwin—Op [8, 9] is a miniature humanoid robot platform which has 20 degrees of freedom, each controlled by a DYNAMIXEL MX-28T servo motor. It is developed and manufactured by Korean robot manufacturer Robotics. In this paper, we developed the mechanism and the sensor systems of Darwin—Op together with its basic specification based on ROS [10]. After that, the motion and performance of this model are evaluated in Gazebo virtual environment. Showing the graph of robot joints on a maze area are also presented at the rest of this paper.

## 2 Robot Simulation

### 2.1 *The Detailed Structure of the Model*

To develop the robot model in the virtual environment, we firstly obtain and classify the specifications of the real DARWIN given by the manufacturer. The information of mechanism as well as the sensor parameters are illustrated as in Table 1.

### 2.2 *Building Robot Model on ROS*

This stage is based on a Robot Operating System (ROS) distributed processing framework. The robot-environment interactive reasoning mechanism is at the core. The structure of the operated process is indicated as follows.

Figure 1 illustrated a workflow that implements a closed-loop controller for DARWIN. The node exchanges data with other nodes through messages forming

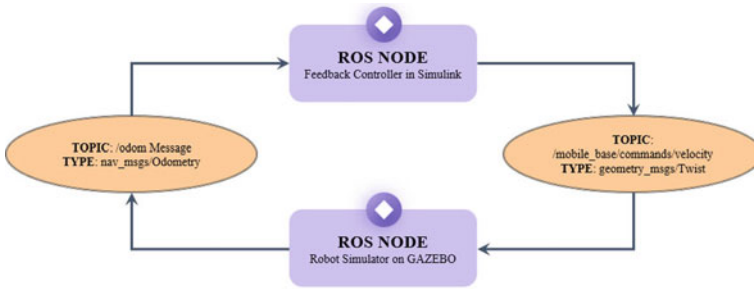


**Fig. 1** The workflow of designed system

a built-in program. Specifically, the controller gets environmental data from a separate ROS-based simulator and provides functional comments to guide the robot to a predetermined destination. At each time step, the algorithm moves the robot ahead and orients it towards the intended destination. The algorithm stops the robot once the required point is reached. While the model is running, adjusting obtained parameters is also integrated to observe the effect on the simulated robot.

### 2.3 *Compile on GAZEBO*

Gazebo [11, 12] is well-known as a powerful open source with several functions for robot simulation. Gazebo provides high quality graphics with convenient graphical and programming interfaces of robotic populations under different scenarios.

In the process of robot operating, scanning the map and then interacting with environment are basic modes. Moreover, how to efficiently and accurately to find the right way from the started point to destination for the robot is an important issue. In this section, we use the complicated modules of the software to create a simple complex—wall scenes for simulation experiments. The generating sensor feedback and providing light sources are also obtained and measured. Since then, we have coupled this data with the maze-solving algorithm in order to address the path-planning problem. As a consequence, the robot is able to reach a particular spot in the designated maze without difficulty.

### 2.4 *Simulation*

Based on the technical parameters provided by the developer, the Darwin Op model is designed in the Gazebo environment as shown in Fig. 4. This simulation model contains 20 actuators modules (12 DOF on two legs, 6 DOF on two arms and 2 DOF of neck part). After that, two complicated motion processes have been established.

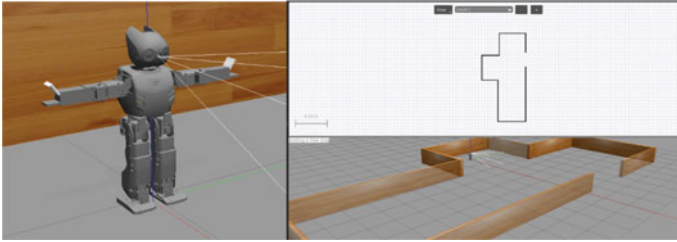


**Fig. 2** Initialize the Gazebo working environment for virtual robot

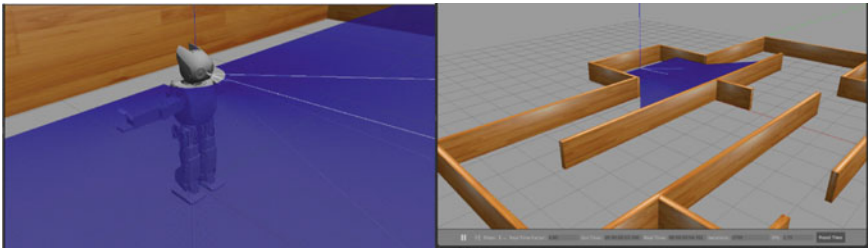


**Fig. 3** Enabling the sensor system on the model

Firstly, to ensure the model stability, different physical behaviors based on body language are applied on the robot model. Secondly, we developed a maze solver and integrated it on the robot. This helps us to observe the interaction between the model and the virtual environment as well as inspect the response time from the user commands to the model. The robot's full motion process is conducted as follows:

- **Step 1:** Initializing Darwin robot model and the maze in Gazebo environment (Fig. 2).
- **Step 2:** Enabling the laser sensor for the Darwin robot model. The blue region displays the limitation of the sensor working space (Fig. 3).
- **Step 3:** Starting the emulator and activating the peripherals. The model continuously scans to discover the maze and obstacles. In the designed program for robot to avoid obstacles, the maze solver algorithm is applied to stick to the right wall and turn left when robot encounters a random obstacle (Fig. 4).

### 3 Result

In this section, we discuss the experimental simulations and in-depth analysis. Figures 5, 6, 7, 8 and 9 shows the specific graphs on different joints of the robot.



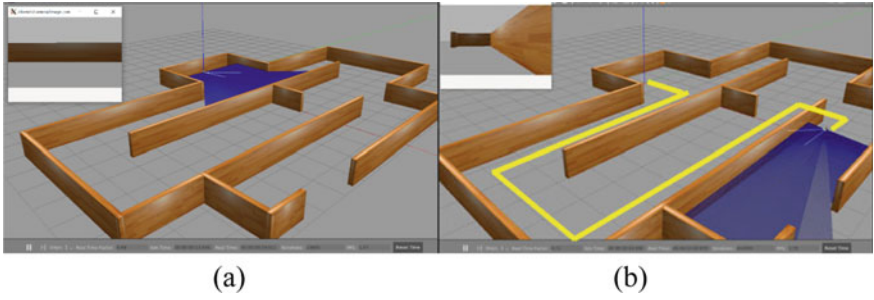


**Fig. 4** The motion process of the robot to solve the maze: **a** Darwin robot is placed at the origin position; **b** Show image from camera on Darwin robot

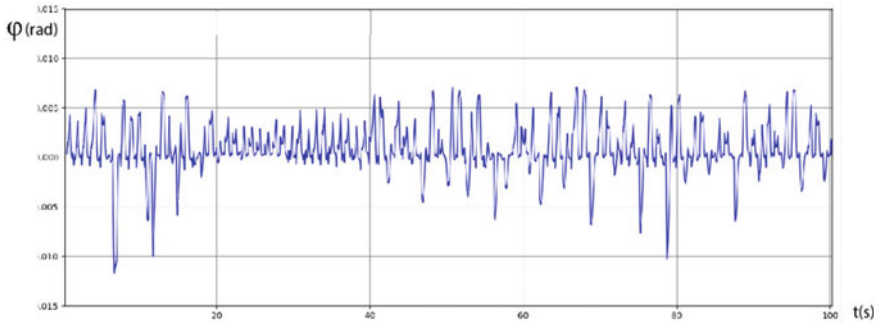


**Fig. 5** Motion graph of left buttock joint

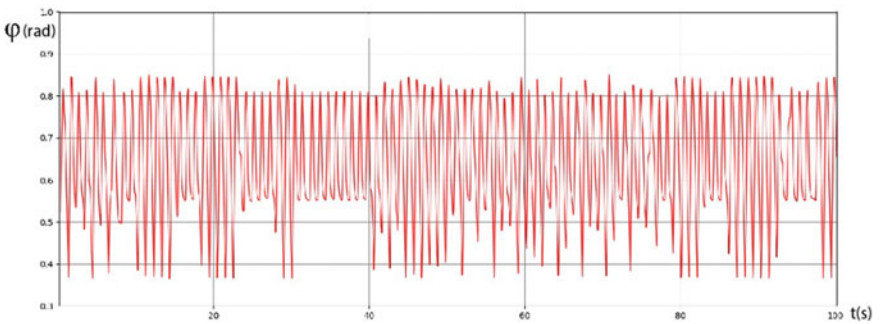


**Fig. 6** Motion graph of the left thigh joint

- (1) During the robot's motion, the left joint rotates about the axis, forming an angle of rotation with an amplitude of 0.11 rad and the motion is almost uniform over time. However, the amplitude would change in case of different states: moving, stopping.

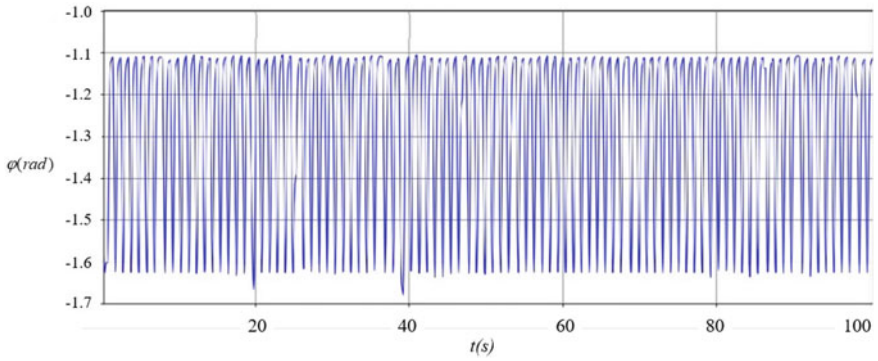


**Fig. 7** Motion graph of joint left leg

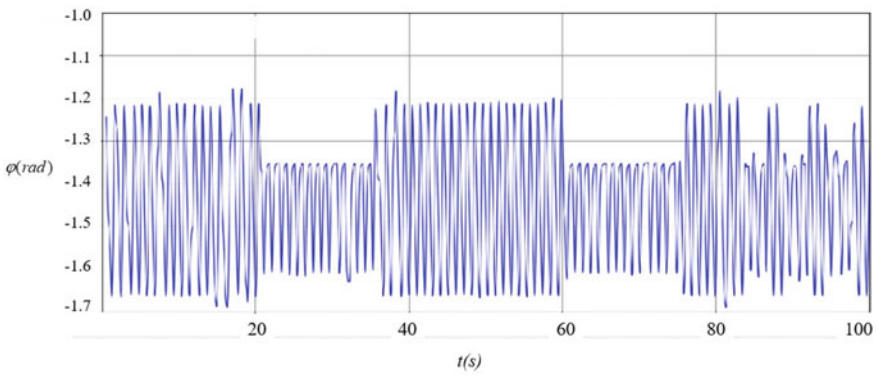


**Fig. 8** Motion graph of left ankle joint

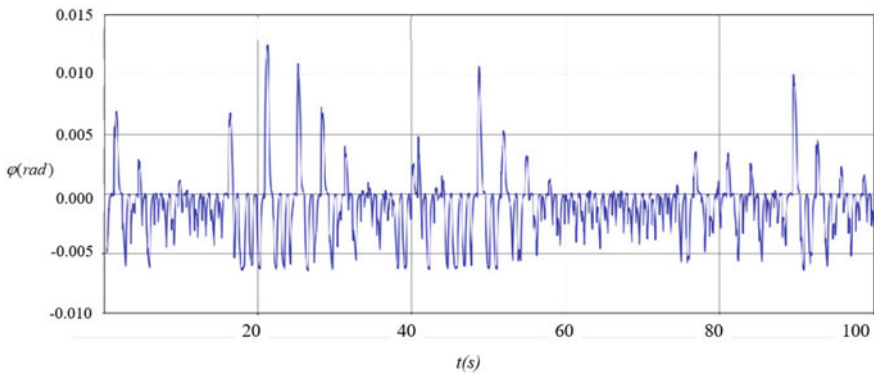


**Fig. 9** Motion graph of left foot joint

- (2) During the moving process, the left buttock joint has an uneven angle of rotation. This phenomenon is caused since the robot leans to ensure its center of gravity. Especially in case of the robot stomps in place, the angular boundary created by the joints could highly increases.
- (3) The angular position of the left thigh joint has a certain change depending on the robot movement. In particular, the angular position amplitude is 0.47 rad in case of reciprocating, while at the moment the robot stomps in place to turn around, the amplitude value of the joint is at about 0.25 rad.
- (4) The joint of the left leg rotates around the axis, forming an angle of rotation with an amplitude of 0.55 rad and the motion is almost uniform over time.
- (5) The angular position of the left ankle joint has a certain change depending on the robot statement. For instance, from beginning to the 20th second, the robot moves straight with an amplitude of rotation of 0.52 rad. From the 20th second to the 36th second, the robot stomps in place, so the rotation amplitude of the ankle joint decreases to 0.27 rad.

## 4 Conclusion

In this paper, the dynamics of Darwin Op Robot based on the real specifications is calculated. Since then, the significance of robot mechanisms has been analyzed through the use of ROS. After that, the detailed motion of the robot is recorded and evaluated on the Gazebo platform. The sensor measurements are taken using some custom-built applications. More precisely, we presented an end-to-end controller that is based on maze solver algorithms only for humanoid robot. Finally, the results revealed that using ROS for DARWIN robots is indeed feasible and that it is possible to achieve promising opportunities in reality. Moreover, the simulation could assist students and instructors get more out of the educational experience and offer a cost-effective complement to classroom learning.

## References

1. I. Kato, S. Ohteru, H. Kobayashi, K. Shirai, A. Uchiyama, *Information-Power Machine With Senses and Limbs*, vol. 201 (International Centre for Mechanical Sciences, 1974).
2. A. Takanishi, G. Naito, M. Ishida, I. Kato, Realization of plane walking by the biped walking robot WL-10R, in *Theory and Practice of Robots and Manipulators*, ed. by A. Morecki, G. Bianchi, K. Kędzior (1985).
3. K. Hirai, M. Hirose, Y. Haikawa and T. Takenaka, The development of Honda humanoid robot, in *IEEE International Conference on Robotics and Automation* (Cat. No.98CH36146), 2 (1998), pp. 1321–1326
4. M.J. Riesenman, Robots stand on own two feet. *IEEE Spectr.* **39**, 24–25 (2002)
5. R.A. Brooks, C. Breazeal, M. Marjanović, B. Scassellati, M.M. Williamson, The cog project: building a humanoid robot, in *Lecture Notes in Computer Science*, vol. 1562 (1999)
6. L. Marchionni, J. Pages, J. Adell, J.R. Capriles, H. Tomé, REEM service robot: how may i help you?, in *Lecture Notes in Computer Science*, vol. 7930 (2013)

7. A.K. Kashyap, D.R. Parhi, M.K. Muni, K.K. Pandey, A hybrid technique for path planning of humanoid robot NAO in static and dynamic terrains. *Appl. Soft Comput.* **96** (2020)
8. I. Ha, Y. Tamura, H. Asama, J. Han, D.W. Hong, Development of open humanoid platform DARwIn-OP, in *SICE Annual Conference* (2011), pp. 2178–2181
9. H. Shin, B.K. Kim, Energy-efficient gait planning and control for biped robots utilizing vertical body motion and allowable ZMP region. *IEEE Trans. Industr. Electron.* **62**, 2277–2286 (2015)
10. P. Estefo, J. Simmonds, R. Robbes, J. Fabry, The robot operating system: package reuse and community dynamics. *J. Syst. Softw.* **151**, 226–242 (2019)
11. A.A. Alajami, G. Moreno, R. Pous, A ROS Gazebo plugin design to simulate RFID systems. *IEEE Access* **10**, 93921–93932 (2022)
12. D.A. Pham, H.A. Bui, X.T. Nguyen, T.T. Mac, H.H. Hoang, A case study on humanoid robot using robotics software in E-learning, in *RCTEMME 2021, Lecture Notes in Mechanical Engineering* (2022)

# Design of a Self-Balancing System of Autonomous Underwater Vehicle



Ton Thien Phuong, Tran Thien Phuc, and Huynh Manh Dien

**Abstract** Mass shifter mechanism (MSM) and internal rolling mass (IRM) are the most essential element in one autonomous underwater vehicle (AUV). Its function is to reorient the centre of mass of the AUV in order to change advancing direction or to produce reverse torque to prevent the hull from rolling which usually caused by the torque of the main thrust motor. In this particular article, we will present the analysis and the design of a mass shifter mechanism for a specific case of a AUV with torpedo profile of 2.5 m length and the hull diameter of 0.25 m. The mass shifter mechanism contains a partial translation mechanism traveling along the hull length which produce a change in the pitch angle of the vehicle. Additionally, two internal rolling mass (IRM) are placed respectively in the front and the rear of the vehicle to generate reverse torque eliminating undesirable torque of the thrust motor and to enhance roll control.

**Keywords** Mass shifter mechanism · Internal rolling mass · AUVs · Autonomous underwater vehicle

## 1 Introduction

Autonomous underwater vehicle (AUV) is currently the most concerned automatic underwater vehicle use for ocean exploration and military defense. Having been developed for a few decades, today AUV is technological saturation in appearance, structure, as well as control method. However, scientists still invest effort to find a way to further optimize efficiency and to enhance AUV capabilities. Simultaneously, the designs are required to keep the AUV in the best stability state in certain circumstances. For AUVs designed for testing, environmental monitoring or seafloor

---

T. T. Phuong (✉) · T. T. Phuc · H. M. Dien  
Faculty of Mechanical Engineering, Ho Chi Minh City University of Technology, Ho Chi Minh City, Viet Nam  
e-mail: [tonphuong@hcmut.edu.vn](mailto:tonphuong@hcmut.edu.vn)

Vietnam National University HCMC, Hồ Chí Minh City, Việt Nam

© The Author(s), under exclusive license to Springer Nature Switzerland AG 2024  
B. T. Long et al. (eds.), *Proceedings of the 3rd Annual International Conference on Material, Machines and Methods for Sustainable Development (MMMS2022)*, Lecture Notes in Mechanical Engineering, [https://doi.org/10.1007/978-3-031-57460-3\\_19](https://doi.org/10.1007/978-3-031-57460-3_19)

mapping, the stabilized equation of the AUV is the most important factor. Therefore, designers have created a separate mechanism to increase the stability of the AUV, some research's problems: designs, control of the AUV, in which use the mass shifter mechanism (MSM) to shift the center of gravity to change the pitch angle of the ship and then obtain the wanted depth [1]; The use of an internal rolling mass (IRM) mechanism is to actively stabilize the roll motion of the AUV. IRM contains a tray that can rotate inside the AUV which shift the AUV's center of gravity by produce the required torque to stabilize the roll motion [2]. The primary design has a torpedo-like hull, it has a propulsion engine inside the ducted propeller rear compartment and use MSM to derive the movement equation and control the depth for the AUV [3].

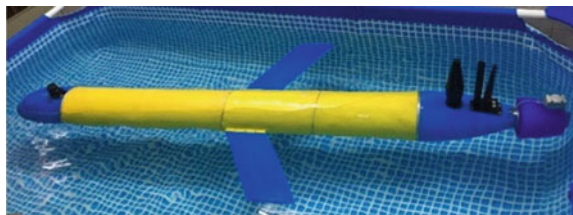
Referring to some scientific reports, we see that most of the research paper either use the MSM to control the depth and stabilize horizontal axis or use IRM to stabilize the roll motion of an AUV. Therefore, we propose an AUV design that combine MSM and IRM for better stabilization so that the AUV can fulfill tasks such as underwater mapping more effectively. This article will present the design of MSM and IRM for a torpedo-like AUV, 2.5 m in length, 0.25 in diameter and  $92 \pm 1$  kg in weight. Furthermore, we compare the important parameters between the prototype model and the CAD design of the AUV for further adjustment.

## 2 Design Concept

### 2.1 AUV ADMP

AUV\_AMDP is design to look like a torpedo with a length of 2.5 m, 0.25 in diameter and weight 96 kgs. It has 3 part: head, body and tail (Fig. 1). The head part will contain a Doppler Velocity log (DVL), sonar,... The body part will contain electric components, MSM and IRM. The tail part (rear compartment, rear chamber) will has a propeller engine inside the ducted propeller, rudder, antennas,... The structure of the AUV will be shown via Fig. 2.

**Fig. 1** AUV\_ADMP's structure



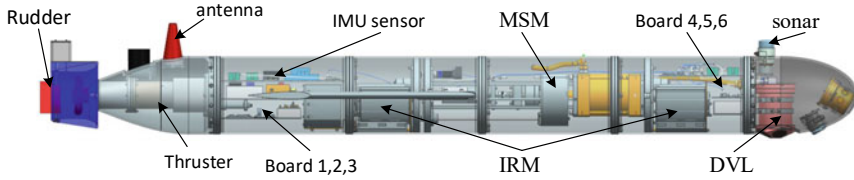


Fig. 2 The internal structure of AUV-ADMP

## 2.2 Design Requirements

AUV\_ADMP is designed with these parameter as:

- Length is 2.5 m long,
- Body diameter is 0.25 m,
- Weight of the AUV is 96 kg.
- Max speed is 1.5 m/s (or 3knot),
- For better horizontal stability and an easier time alter the depth, MSM will be put in the body part of the AUV. With the weight of  $m_s = 7.5$  kg, we will need to find the stroke length  $l_s$  that the MSM move across the body so that the AUV can achieve a pitch angle  $\theta$  between  $[-60^\circ; 60^\circ]$ .
- IRM is design to change the center of gravity G in the sway to achieve a balance for roll equilibrium, an error between  $[-5^\circ; 5^\circ]$  is allowed.
- Furthermore, The structure of the AUV is positioned symmetry across the body for easier calculation and design.

## 2.3 Modeling

G the center of gravity of the AUV with  $\vec{r}_G = [x_G; y_G; z_G]$ . Solve the equation with 6 variables to find the movements of the AUV with Newton's second law, from [4] we have below the equations to describe the movement of the AUV:

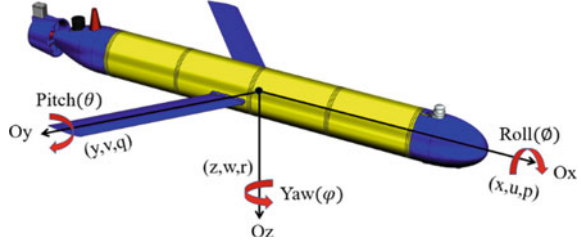
Total force equations impact on the AUV in the direction of OX, OY, OZ are shown below:

$$\begin{aligned}
 m[\dot{u} - vr + wq - x_G(q^2 + r^2) + y_G(pq - \dot{r}) + z_G(pr + \dot{q})] &= X \\
 m[\dot{v} - wp + ur - y_G(r^2 + p^2) + z_G(qr - \dot{p}) + x_G(qp + \dot{r})] &= Y \\
 m[\dot{w} - uq + vp - z_G(p^2 + q^2) + x_G(rp - \dot{q}) + y_G(rq + \dot{p})] &= Z
 \end{aligned} \quad (1)$$

Equation of total momentum on the AUV in the direction of Ox, Oy and Oz are shown below:

$$I_{xx}\dot{p} + (I_{zz} - I_{yy})qr - (\dot{r} + pq)I_{xz} + (r^2 - q^2)I_{yz} + (pr - \dot{q})I_{xy}$$

**Fig. 3** AUV with a coordinate system with 6 degrees of freedom



$$\begin{aligned}
 & + m[y_G(\dot{w} - uq + vp) - z_G(\dot{v} - wp + ur)] = K \\
 I_{yy}\dot{q} + (I_{xx} - I_{zz})rp - (\dot{p} + qr)I_{xy} + (p^2 - r^2)I_{xz} + (qp - \dot{r})I_{yz} \\
 & + m[z_G(\dot{u} - vr + wq) - x_G(\dot{w} - uq + vp)] = M \\
 I_{zz}\dot{r} + (I_{yy} - I_{xx})pq - (\dot{q} + rp)I_{yz} + (q^2 - p^2)I_{xy} + (rq - \dot{p})I_{xz} \\
 & + m[x_G(\dot{v} - wp + ur) - y_G(\dot{u} - vr + wq)] = N
 \end{aligned} \tag{2}$$

Therein:

X, Y, Z are the forces impact on the AUV in direction of OX, OY, OZ respectively.

K, M, N are the momentum on the AUV in direction of OX, OY, OZ respectively.

Lij (i; j ∈ {x,y,z}) are the torque on OX, OY, OZ respectively.

To calculate and design MSM and IRM, we only need to concern about the roll movement and the pitch angle around OY axis of the AUV. Through surveying the changes in the center of gravity cause by the movement of MSM and IRM, the parameter of MSM and IRM will be chose accordingly. For easier modeling, a fixed coordinate system will be put in the body of the vehicle, with the origin point at center of vehicle buoyancy with  $\vec{r}_B = [x_B, y_B, z_B]^T$  as shown in Fig. 3. Then  $x_B = y_B = z_B = 0$  like references.

The movements of MSM and IRM don't affect one another. So that, for easier time calculating and designing, this article will chose the parameter of MSM and IRM by calculating separately, and then build a set of number for each compartment.

## 2.4 MSM Design

When MSM moves across the OX axis, it will cause a shift in the center of gravity in the OX direction and create a pitch angle in OY direction, with the combination of the propulsion in the tail will help the AUV change to the wanted depth. With a weight  $m_s$  of 7.5 kg and required a pitch angle  $\theta$  between  $[-60^\circ; 60^\circ]$ , in this article the equation to find the stroke length  $l_s$  of the MSM with the parameters given in advance. MSM and moving diagram are shown in Fig. 4.

Therein:

$l_{ms}$  is the length of the MSM compartment.



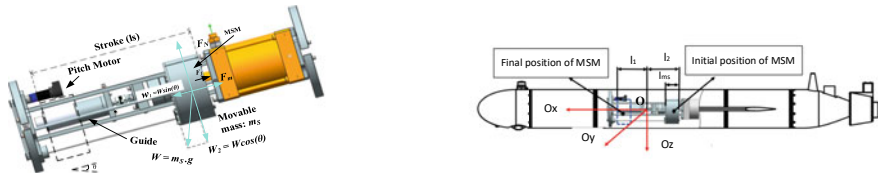


**Fig. 4** MSM and motion diagram

$l_1$  is the distance between the origin point  $O$  to the end point of the MSM when the MSM run to the start of journey and  $l_2$  is the distance between the origin point  $O$  to beginning point when the MSM run to the end of journey.

Call  $H, G$  are the center of gravity of the AUV when doesn't have MSM and has MSM respectively.

Call the centroids of coordinates  $\vec{r}_H = [x_H, y_H, z_H]^T$  and  $\vec{r}_M = [x_M, y_M, z_M]^T$  respectively.

We have:

$$\vec{r}_G = \frac{(M - m_s)\vec{r}_H + m_s\vec{r}_M}{M} \tag{3}$$

In which  $M$  and  $m_s$  are the weight of the AUV and the weight of the MSM.

When the AUV change its pitch angle then from the equilibrium condition of the vehicle:

$$\begin{aligned} x_G - x_B &= (z_G - z_B) \tan \theta \\ \Leftrightarrow x_G &= z_G \tan \theta \end{aligned} \tag{4}$$

From (3) and (4) MSM's coordinates in the direction of  $Ox$  will be shown:

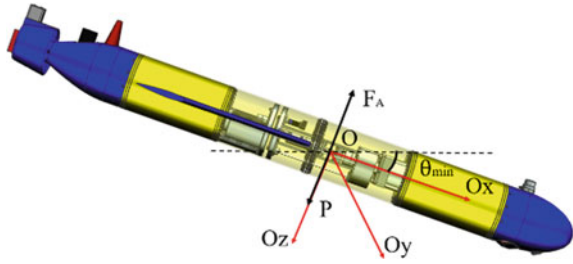
$$x_M = \frac{(M - m_s)(z_H \tan(\theta) - x_H) + z_M \tan(\theta)m_s}{m_s} \tag{5}$$

From the diagram of pic 4, we could deduce:

$$-l_1 + \frac{l_{ms}}{2} \leq x_M \leq l_2 - \frac{l_{ms}}{2} \tag{6}$$

When MSM move to the head of the vehicle which cause a shift in the center of gravity  $G$ , which then change the pitch angle ( $\theta$ ). The max pitch angle ( $\theta$ ) will be achieved at the location where MSM move to the end of the journey, this is shown in Fig. 5. At this moment,  $\theta = \theta_{max}$  and the coordinate position of  $x_{M1}$  of MSM are shown below:

**Fig. 5** Analysis diagram when MSM move to the head of AUV



$$\begin{aligned}
 x_{M1} &= l_2 - \frac{l_{ms}}{2} \\
 \Rightarrow l_2 &= \frac{l_{ms}}{2} + \frac{(M - m_s)(z_H \tan \theta_{\max} - x_H) + z_M \tan \theta_{\max} m_s}{m_s}
 \end{aligned}
 \tag{7}$$

When MSM move the tail of the AUV which cause a shift in center of the vehicle to the back, then create a silly angle ( $\theta$ ). Minimum silly angle ( $\theta$ ) will be achieved at the location where MSM move to the start of the journey as shown in Fig. 6. At this time,  $\theta = \theta_{\min}$  and the coordinate position of  $x_{M2}$  of MSM are shown below:

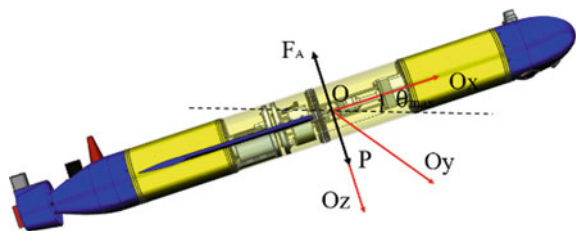
$$\begin{aligned}
 x_{M2} &= -l_1 + \frac{l_{ms}}{2} \\
 \Rightarrow -l_1 &= \frac{-l_{ms}}{2} + \frac{(M - m_s)(z_H \tan \theta_{\min} - x_H) + z_M \tan \theta_{\min} m_s}{m_s}
 \end{aligned}
 \tag{8}$$

From (7) and (8) the stroke length  $l_s$  equation is built with designated parameters as shown below:

$$l_s = l_2 - (-l_1) = l_{ms} + z_H \left( \frac{M}{m_s} - 1 \right) (\tan \theta_{\max} - \tan \theta_{\min}) + z_M (\tan \theta_{\max} - \tan \theta_{\min})
 \tag{9}$$

Here,  $M$  and  $m_s$  are variables with pre-selected, values  $z_H$  and  $z_M$  don't change when MSM moves. Simultaneously, these 2 variable can be calculate and adjust at the start easily with a CAD software (computer-aided design). So, from (9) we can see the  $l_s$  variable only depend on the pitch angle  $\theta$ .

**Fig. 6** Analysis diagram when MSM move to the tail of AUV



### 2.5 IRM Design

To guaranteed a good stabilization cause by torque effect made by the propulsion, AUV is designed with 2 separate IRM with the same weight  $m_r$  and will be put at the body of the vehicle. With the purpose of changing the AUV’s center of gravity  $G$  in the direction of  $Oy$  to create a healing momentum which help balance roll equilibrium for AUV, IRM is designed with the ability to rotate around the body. Call the swivel angle that IRM achieved  $\alpha$ , and  $l_r$  is the distance of the center of IRM to the AUV’s float center  $B$  (note that 2 IRMs arranged symmetrically through the floating center  $B$ ). From here, the design of IRM is decided by 3 parameters  $m_r$ ,  $\alpha_{max}$  and  $l_r$ . IRM and it’s movement diagram are shown in Fig. 7.

For easier time calculating the variables, we will only consider the change of roll angle, the main thing affect the roll torque and the rest like pitch angle, yaw angle are not to be considered. Therefore, according to modeling the motion of the AUV in six degrees of freedom (1). The total torque acting on the  $Ox$  axis causing the roll torque is:

$$K = I_{xx} \dot{p} = I_{xx} \ddot{\phi} \tag{10}$$

When two IRMs arranged in the body cavity perform rotation around the body an  $\alpha$  angle will cause a change in the center of gravity  $G$ . On the other hand, to ensure the stability of the AUV, the center of gravity  $G$  is designed to lie below the floating center  $B$  or in other words,  $z_G$  has a positive value. Then, the coordinates of the new center of gravity are shown as follows:

$$\begin{aligned} y_{G'} &= y_G + \frac{2m_r}{M} l_r \sin \alpha \\ z_{G'} &= z_G + \frac{2m_r}{M} l_r \cos \alpha \end{aligned} \tag{11}$$

According to [5], we have the total momentum impact the AUV causing it to roll around the  $Ox$  axis:

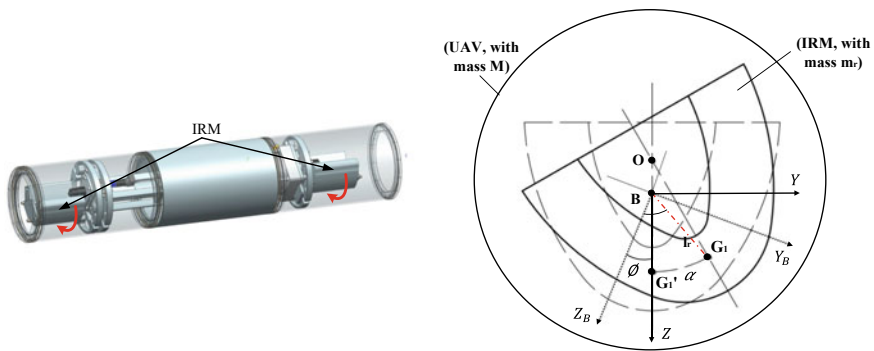


Fig. 7 IRM and motion diagram

$$K = K_{\dot{p}}\dot{p} + K_{\dot{v}}\dot{v} + K_{p|p}|p| - (y_G W - y_B W_B) \cos \theta \cos \phi + (z_G W - z_B W_B) \cos \theta \sin \phi \quad (12)$$

wherein:  $W$  is the weight of the AUV and  $W_B$  is the floating weight of the AUV.

- The moment component  $K_{\dot{p}}\dot{p}$  is the component produced by the added mass which is determined by the water weight movement when the vehicle is accelerating. With a reasonable layout AUV, rolling added mass cause by AUV's body will be small. Therefore, rolling added mass is mainly cause by the wings of the AUV and protruding parts like antennas, motor box,... Here,  $K_{\dot{p}}\dot{p}$  is a factor of rolling added mass and  $\dot{p}$  is the roll angular acceleration. Since we only consider the roll axis here, we have  $\dot{p} = \ddot{\theta}$ .
- Torque component  $K_{p|p}|p|$  is the component produced by the rolling drag. With a torpedo shaped AUV two symmetrical wings with Naca 0010 profile. Therefore, the rolling drag exerted by the body is small, so the main component that creates this torque is due to protrusions such as antennas, motor boxes, sensors,... Here,  $K_{p|p}$  is the number of traction of the rolling drag and  $p$  is the roll angular velocity. We have  $p = \dot{\theta}$ .
- Torque component  $-(y_G W - y_B W_B) \cos \theta \cos \phi + (z_G W - z_B W_B) \cos \theta \sin \phi$  is the hydrostatic momentum that plays an important role in the roll stabilization of the AUV, which cancels out any deflection effects when rolling. Since the origin of inertia is located at the center of buoyancy and only roll motion is considered (ignoring other movements of the AUV), then the hydrostatic momentum component is expressed as follows:

$$M_{hydro} = -y_G W \cos \phi + z_G W \sin \phi \quad (13)$$

From (11) and (13) when the IRM moves by an angle  $\alpha$ , the hydrostatic moment becomes:

$$M_{hydro} = -\left(y_G + \frac{2m_r}{M}l_r \sin \alpha\right)W \cos \phi + \left(z_G + \frac{2m_r}{M}l_r \cos \alpha\right)W \sin \phi \quad (14)$$

- Torque component  $K_{\dot{v}}\dot{v}$  is the torque effect produced by the propulsion. According to Newton's 3rd law "when an object exerts a force on a second object, the second body exerts a force of the same magnitude and opposite direction on the first object". So when the thruster moves clockwise to push the AUV forward, there will be a torque effect counter-clockwise with the thruster acting on the AUV. The magnitude of this torque effect depends on the energy input to the propulsion. We set:

$$M_{te} = K_{\dot{v}}\dot{v} \quad (15)$$

From (10), (12), (14) and (15) we have the following equation:

$$\begin{aligned} (I_{xx} - K_{\dot{p}})\ddot{\phi} = & M_{te} + K_{p|p|}|p|\dot{\phi} - \left( y_G + \frac{2m_r}{M}l_r \sin \alpha \right) W \cos \phi \\ & + \left( z_G + \frac{2m_r}{M}l_r \cos \alpha \right) W \sin \phi \end{aligned} \quad (16)$$

To simplify Eq. (16) we have the following comments:

- The main rolling drag is generated by external protrusions such as antennas, motor boxes, sensors, etc. However, these details are arranged at the top and are located symmetrically along the body of the AUV, so the resulting roll force is negligible so it can be considered as zero.
- Because the AUV is designed to be almost symmetrical along the longitudinal axis of the body, so  $y_G \approx 0$ .
- To design the IRM cluster, we will build the relationship equation between the three quantities to be estimated including the mass  $m_r$ , the distance  $l_r$  and the rotation angle  $\alpha$  of the IRM by linearizing Eq. (16) at  $\phi = 0$ .

From the comments above, the Eq. (16) becomes:

$$M_{te} = \frac{2m_r}{M}l_r W \sin \alpha \quad (17)$$

The IRM is designed so that when rotated to the position in which  $\alpha$  is max will produce the maximum possible recovery torque against the effect torque caused by the propulsion. From Eq. (17) the values of  $m_r$ ,  $l_r$  and  $\alpha_{\max}$  are selected when  $M_{te}$  reaches the maximum value, in other words, the selected parameters must satisfy the following inequality:

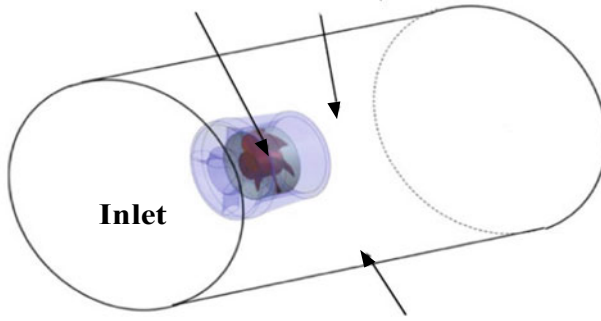
$$M_{te(\max)} \leq \frac{2m_r}{M}l_r W \sin(\alpha_{\max}) \quad (18)$$

Here, the AUV is designed to move at the fastest speed of 1.5 m/s (3knot), i.e. at this speed the thruster reaches the maximum torque value, which is also when the effect torque reaches the extreme ( $M_{te} = M_{te(\max)}$ ). To calculate the maximum value of this effect momentum, we use CFD (Computational Fluid Dynamics) simulation performed on Ansys 2021R1 software. Simulation is performed for the propulsion with the outer conduit, Fig. 8 shows the boundary conditions and simulation results. Thereby, we find the value that the maximum effective torque is  $M_{te(\max)} = 2645$  Nm, at this time the number of revolutions of the propulsion motor is 1885 r/m

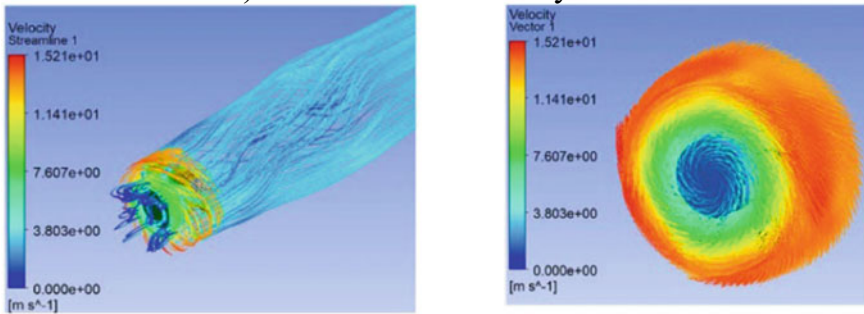
So it is necessary to determine the set of parameters ( $m_r, l_r, \alpha_{\max}$ ) that satisfy the following inequality:

$$\begin{aligned} 2.654 & \leq \frac{2m_r}{M}l_r W \sin(\alpha_{\max}) \\ \Leftrightarrow 1.327 & \leq m_r g l_r \sin(\alpha_{\max}) \end{aligned} \quad (19)$$

where:  $g$  is gravity acceleration with  $g = 9.8 \text{ m/s}^2$



a) Simulated boundary conditions



b) simulation results

**Fig. 8** Boundary conditions and simulation results

From the inequality (19) values can be selected based on the following criteria:

- The internal structure of the AUV body is limited due to the arrangement of many other electrical and mechanical devices, so the rotation angle of the IRM is also limited, so in this article, the maximum rotation angle of the IRM is  $\alpha_{\max} = 300$ .
- The larger the  $l_r$ , the better the roll stability will be, so the position of the 2 IRMs will be arranged as far away from the origin point as possible, however, it should be noted that the 2 IRMs are arranged symmetrically through the floating center so the distance  $l_r$  of both IRMs is also equidistant from the center O.
- Since angles  $\alpha$  and  $l_r$  are limited quantities of choice. Therefore, to be able to satisfy (19) only  $m_r$  can be selected, this is a parameter that can be easily adjusted by machining or material selection.

### 3 Design Finalization and Testing

#### 3.1 Estimating the Parameters

In this section, we calculate and/or select all unknown parameters such as  $l_s$ ,  $m_r$ ,  $l_r$ ,  $\alpha_{max}$ , ... to complete the design of MSM and IRM. The parameters are selected based on criteria and linear equations from the previous sections, other parameters can be determined using computer-aided design (CAD) softwares. Parameters are shown as Tables 1, 2 and 3.

### 4 Fabrication Model Test

After all parameters have been completely determined, 3D model of the AUV is completed using CAD software and then processed and manufactured for actual model. In the next step, both actual and CAD models of MSM are experimented to check the mechanism operation. For details, we check the coordinates of the CG of the AUV on the  $O_x$  axis when the MSM travels to initial and final positions of the stroke using NX12 software, then compare with the CG determined using measurement methods on actual model. After that, we will have a closer look at the mechanism and the results can be used to adjust in the design model.

**Table 1** Default/ predefined parameters

Parameters	M (kg)	Ms (kg)	Lms (mm)	$\theta_{max}$ (°)	$\theta_{min}$ (°)
Values	92	7.5	80	60	-60

**Table 2** Estimated parameters through equations

Parameters	Amax (°)	$l_s$ (mm)	$m_r$ (kg)
Values	30	407	1

**Table 3** Defined parameters using CAD softwares

Parameters	$l_r$ (mm)	$z_H$ (mm)	$z_M$ (mm)
Values	466.284	6.984	15.736



**Fig. 9** Positions of MSM inside the AUV

**Table 4** Centroid G's specified positions along the Ox axis using NX software

Position of MSM	$x_G$ (mm)
Initial position	1217.775
Final position	1192.966

#### 4.1 Determine the CG of the AUV Using Siemens NX12 Software

Setting the coordinate system attached to the body at the bow of the AUV and using “Analysis measure body” feature of the Siemens NX12 software, it is easy to determine the CG of the AUV when the MSM travels to initial and final positions of its stroke. Since the purpose is only to check the operation of the MSM, we only concern the centroid G's coordinates along the Ox axis. Figure 9 show the two positions of MSM and Table 4 show the coordinates of centroid G corresponding to the MSM's positions.

#### 4.2 Determine the CG of the AUV on the Prototype

Instead of using a measurement method [6] that hangs the AUV by two steel wires placed at a known position along the Ox axis to conduct the experiment which need to use steel clamp and can cause measurement (observational) errors, we will place the AUV directly on two digital weighing machines (DWM) to determine the CG. The experimental implementation diagram is shown in Fig. 10. After obtaining all the necessary data, the coordinate of the centroid G can be determined using the formula (20) below:

$$X_G = \frac{X_1 M_1 + X_2 M_2}{M_1 + M_2} \quad (20)$$

where:  $X_G$  is the distance from the bow of the AUV to the centroid.  $X_1$  and  $X_2$  are the calculated value from the AUV's bow to the centroid of DWM1 and DWM2 respectively.  $M_1$  and  $M_2$  are the displayed value corresponding to DWM1 and DWM2.

Since the  $X_1$  and  $X_2$  values have been predefined from the setup of the DWM1 and DWM2 scales, particularly,  $X_1 = 550$  mm and  $X_2 = 1798$  mm, we only have to



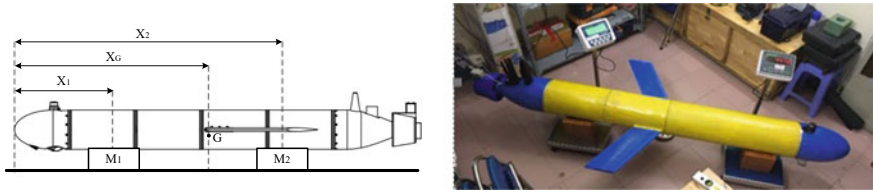


**Fig. 10** The experimental implementation diagram

specify the  $M_1$  and  $M_2$  values corresponding to the DWM1 and DWM2 to determine the value of  $X_G$ . The MSM is moved to the initial and final positions of the stroke, pairs of  $M_1$  and  $M_2$  values displayed on the scales are used to determine the coordinate of  $X_G$  on actual model. Figure 11 shows the measured values of DWM1 and DWM2 when the MSM travel to the initial and final positions of its stroke respectively. Table 5 shows the measured values of each pair of  $M_1$  and  $M_2$ .

From formula (20) and Table 5, we can easily determine the  $X_G$  of the AUV when the MSM is at its stroke’s initial and final positions. Table 6 shows the values of  $X_G$ :

By testing with Siemens NX12 software and actual measurement method, it is visible that the theoretical and actual AUV’s centroid values are different, but the deviation is not significant. This error is caused by the fact that the theoretical model has not taken into account the wires and electrical connection devices. This shows that the MSM of the actual AUV model has almost reached the values according to the theoretical calculation.

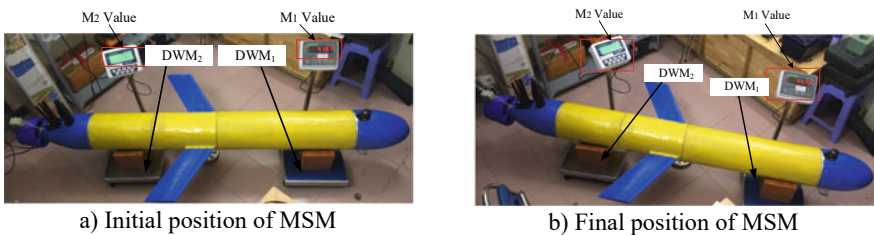


**Fig. 11** Displayed value of DWM corresponding to the MSM’s movements

**Table 5** Values of each pair of  $M_1$  and  $M_2$

Positon of MSM	DWM1	DWM2
Initial positon	$M1 = 41.57 \text{ kg}$	$M1 = 44.79 \text{ kg}$
Final positon	$M2 = 50.96 \text{ kg}$	$M2 = 47.79 \text{ kg}$

**Table 6**  $X_G$ ’s values along the  $Ox$  axis on actual model

Position of MSM	$X_G$ (mm)
Initial position	1237.32
Final position	1189.57

## 5 Conclusion

This paper presents the calculation of preliminary parameters for the design of MSM and IRM mechanisms. A nonlinear equation is used to calculate the required stroke length that the MSM can travel to produce the AUV's desired pitch angle. Simultaneously, we have also proved that the theoretical calculations of the MSM mechanism's parameters are completely reliable through the comparison between using CAD software and measurement method on the actual model. Moreover, a nonlinear model was built to describe the dynamics of the AUV's roll. From the evaluation criteria, a model was built to represent the relationship between the essential parameters in the design of IRM mechanism from which it is easy to calculate and estimate these parameters.

**Acknowledgements** We acknowledge Ho Chi Minh City University of Technology (HCMUT), VNU-HCM for supporting this study.

## References

1. N.H. Tran, H.S. Choi, J.H. Bae, J.Y. Oh, J.R. Cho, Design, control, and implementation of a new AUV platform with a mass shifter mechanism. *Int. J. Precis. Eng. Manuf.* **16**, 1599–1608 (2015)
2. Y.H. Eng, M. Chitre, Roll control of an autonomous underwater vehicle using an internal rolling mass. *Field Serv. Rob.* **105**, 229–242 (2015)
3. M.B. Loc, H.-S. Choi, J.-Y. Kim, J. Yoon. Design and control of an AUV with weight balance, in *2012 Oceans – Yeosu* (2012), pp. 1–8
4. T.I. Fossen, *Handbook of Marine Craft Hydrodynamics and Motion Control* (Wiley, New York, 2011)
5. R. McEwen, K. Streitlien, Modeling and control of a variable-length AUV, in *Proceedings of 12th UUST* (2001)
6. Y. Singh, CFD approach to modelling hydrodynamic analysis and motion characteristics of a laboratory underwater glider with experimental results. *J. Ocean Eng. Sci.* **2**(2), 90–119 (2017)

# Design of Educational Robot for Multilevel Steam Education



Dinh-Ba Bui and Duc An Pham

**Abstract** SMART JOYBOT is a programmable smart robot that helps children stimulate their creative curiosity and become interested in learning programming, AI and Robots. AI and Robot are the trend of the world and receive a lot of attention from scientists. Sharing this interest, the we have conducted research and manufacturing SMART JOYBOT. Make a Smart Robot for STEAM Education and Home Entertainment. The product was born to help solve social problems such as: Busy life makes family members have less time to interact with each other, young children spend too much time on smartphones, affecting on children's psychosocial development. And moreover, students lack modern equipment to study, research, stimulate thinking. SMART JOYBOT includes intelligent features: recognizing people, avoiding obstacles, packing things, arranging small objects and learning with your baby. We have studied practically the models of robots available in the world, referenced, applied control theory and programed robots. From there, it is applied to calculate, design, simulate, evaluate system quality and overcome limitations. The process of researching and manufacturing intelligent robot products to meet the learning needs of students, students and family entertainment. The obtained results show the potential as well as the necessary demand in building intelligent robots with AI features and low cost.

**Keywords** Smart Joybot · AI robot · Steam robot · Home entertainment robot

## 1 Introduction

With the development of science and technology, recreational assistive robots are also a very fast growing field today. Some types of robots can move, arm robots can pick up objects, some types of robots can talk, or a combination of the above. The

---

D.-B. Bui (✉) · D. A. Pham

Mechatronics Department, School of Mechanical Engineering, Ha Noi University of Science and Technology, Ha Noi, Vietnam

e-mail: [ba.buidinh@hust.edu.vn](mailto:ba.buidinh@hust.edu.vn)

robot moves based on wheels to move faster. The arm robot is designed to hold, lift and move objects. Combining them makes robots more functional.

Krofitsch et al. [1] introduces intelligent robots for education and research. By using a smartphone approach, it makes controlling the robot more flexible than traditional ways. However, there is no live video and audio playback feature yet.

López-Rodríguez et al. [2] low-cost robot module design based on Android and Arduino, with Internet and Local Area Network (LAN) connectivity. This design has the disadvantage of lagging and limited functionality.

Vanitha et al. [3] designed a surveillance robot that could be controlled over the Internet using a Raspberry Pi board. This robot uses a PIR sensor to detect when a person or object enters the monitoring area and a smoke sensor detects a fire. Successfully designed a website to monitor and control robots over the internet.

Sun et al. [4] designed a surveillance robot capable of recording real-time images, video and audio footage for a specific area or person. This approach uses the ZigBee network to control the robot. In addition, the system includes a face recognition feature, which can recognize faces with maximum accuracy matching 70% of faces.

Pahuja and Kumar [5] designed an Android smartphone-controlled robot. Using Bluetooth HC-06 and microcontroller 89c2051 on Android smartphone device. The data received by the Bluetooth module from the Android Smartphone is provided as input to the controller. The system was able to live stream ambient video.

Bokade and Ratnaparkhe [6] have designed an Android-based application to control the robot wirelessly. The Android app will open a web page with a video screen for monitoring and buttons for controlling the robot and camera. Test results show that good quality video is very fast and clear, up to 15 frames per second.

Alli et al. [7] designed an obstacle detection and avoidance system for unmanned lawn mowers. Using ultrasonic and infrared sensor modules placed in front of the robot, the signal is transmitted to the Arduino microcontroller which calculates the distance and programs the robot to avoid obstacles. The performance of the system shows 85% accuracy and 0.18% failure probability respectively.

Pedre et al. [8] proposal on the design of a versatile low-cost mobile robot for research and education. However, the robot is complicated for pre-teens and teenagers, and its design focuses on vision-based automatic navigation, excluding audio capabilities.

This study aims to design, and control a mobile robot have a robotic arm with 3 degrees of freedom, which can be controlled via smartphone, hand gestures and voice.

## 2 System Overview

Figure 1 is the robot model. The robot consists of a movable robot body and a robotic arm with clamps, camera and micro. The robot is controlled by voice, hand gestures and smartphone. The Smartphone can connect to the robot via the HC-05 Bluetooth module to send and receive signals. These signals are used to control the Robot. The

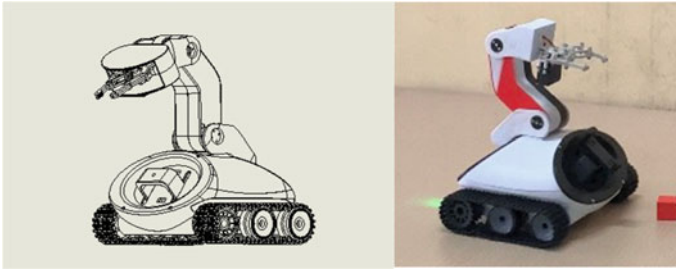


Fig. 1 Smart Joybot

camera is used to capture images, recognize and mark points on the hand to control the robot according to hand gestures. Voice control commands will be received through the mic. These parameters are used by the robot to recognize and fulfill requests.

### 3 Control the Robot

In this robot, Arduino Mega is selected to control servo motor, send and receive signals from module bluetooth HC-05 and Raspberry Pi. Module bluetooth is used to connect to the Smartphone and Raspberry Pi. Camera and micro are used for hand gesture and voice recognition. The system for controlling the robot is shown in Fig. 2. The power supply includes three 3.7 V batteries responsible for supplying power to the system through the L298 driver circuit to provide 12 V power for the DC motor and 5 V for the Raspberry Pi, DC control board, super sensor audio, servo motor, camera module and USB microphone (each with operating voltage between 3 and 7 V).

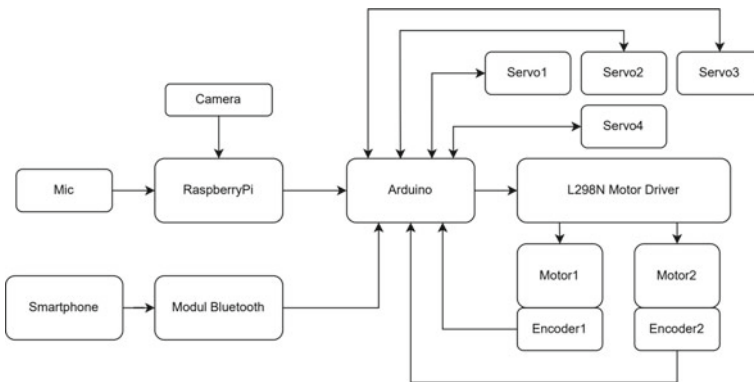


Fig. 2 Hardware connection diagram of the system

The robot servos are controlled via Arduino. Arm servomotors are controlled position precisely. The 2 wheel motors are speed controlled by pulse width modulation and encoder feedback for precise control of the robot's speed.

### 3.1 Control by Smartphone

To control the robot to move and pick up objects at the desired positions, the robot is connected to the phone via the bluetooth module HC 05. Using the control app programmed on the MIT App Inventor. We design a GUI like scratch for elementary and middle school students as in Figs. 3 and 4. Student can drag block to control the wheel on mobile robot, camera angle, servo of mobile robot arm.



Fig. 3 Smart phone control with drag and drop GUI

Fig. 4 Object picking task



### **3.2 Voice Recognition**

The voice recognition system supports humans in interacting with robots more flexibly. In this study, Speech Recognition library [9] was used to simplify speech recognition and give commands to the robot to perform. A simple system: The received sound will be heard by the smartphone and recognize the words and phrases use google voice recognition. Voices in predefined cases are recognized to give tasks to the robot to perform.

### **3.3 Hand Gesture Recognition**

The ability to perceive hand shapes and movements can be a key component in improving user experience. Robust real-time hand perception is a decidedly challenging computer vision task. In this robot, MediaPipe Hands library [10] is used for easy hand gesture recognition.

MediaPipe Hands is a high-fidelity hand and finger tracking solution. It employs machine learning (ML) to infer 21 3D landmarks of a hand from just a single frame.

MediaPipe Hands utilizes an ML pipeline consisting of multiple models working together: A palm detection model that operates on the full image and returns an oriented hand bounding box. A hand landmark model that operates on the cropped image region defined by the palm detector and returns high-fidelity 3D hand keypoints.

### **3.4 Palm Detection Model**

To detect initial hand locations, we designed a single-shot detector model optimized for mobile robot in real-time. Detecting hands is a decidedly complex task: our lite model and full model have to work across a variety of hand sizes with a large scale span ( $\sim 20\times$ ) relative to the image frame and be able to detect occluded and self-occluded hands. The lack of such features in hands makes it comparatively difficult to detect them reliably from their visual features alone. Instead, providing additional context, like arm, body, or person features, aids accurate hand localization.

### **3.5 Hand Landmark Model**

After the palm detection over the whole image, our subsequent hand landmark model performs precise keypoint localization of 21 3D hand-knuckle coordinates inside the detected hand regions via regression, that is direct coordinate prediction. The model

learns a consistent internal hand pose representation and is robust even to partially visible hands and self-occlusions.

To obtain ground truth data, we have manually annotated ~30 K real-world images with 21 3D coordinates, as shown below (we take Z-value from image depth map, if it exists per corresponding coordinate). To better cover the possible hand poses and provide additional supervision on the nature of hand geometry, we also render a high-quality synthetic hand model over various backgrounds and map it to the corresponding 3D coordinates (Figs. 5 and 6).

**Fig. 5** Marked points of the hand

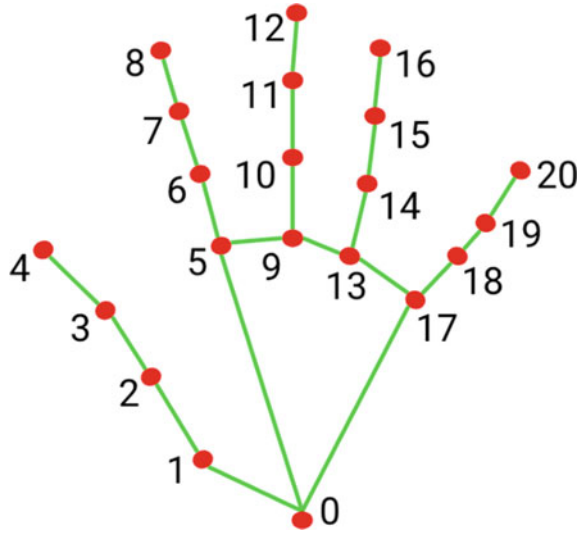


**Fig. 6** Hand follow task





## 4 Results

After conducting programming and control on the actual model we have the following results:

The robot can be precisely controlled by smartphone such as moving, picking and dropping objects, saving and re-executing saved actions in turn.

The robot can recognize hand gestures with high accuracy, performing simple operations according to hand gestures such as go straight, turn left, turn right, stop.

Robot identifies and successfully fulfills voice request. In some case due to the influence of the environment and pronunciation, the robot may not be able to recognize the voice command.

## 5 Conclusions

Successfully designed Smart JOYBOT capable of manual control and automatic movement, capable of picking and releasing small objects. By using the front-mounted smartphone as Camera and receiving voice, Smart JOYBOT can display images and receive control commands while being remotely controlled manually or automatically via an app. installed in Android smartphone via internet.

In addition, the robot can also be controlled by hand gestures or voice, and can be programmed to move simply by the drag-and-drop Scratch interface. Therefore, it can be applied in teaching STEAM at all levels from primary school to university level.

**Acknowledgements** This research is funded by Hanoi University of Science and Technology (HUST) under project number T2021-TT-008.

I would like to acknowledge and give my warmest thanks to my students Dang Van Quy, Pham Van Truong, Tran Van Phuc and Nguyen Quoc Viet who made this work possible.

## References

1. C. Krofitch, H. Christian, M. Munir, K. Gottfried, Smartphone driven control of robots for education and research, in *Proceedings of the 2013 International Conference on Robotics, Biomimetics, Intelligent Computational Systems* (IEEE, Jogjakarta, Indonesia, November 2013), pp. 148–154
2. F.M. López-Rodríguez, F. Cuesta, C. Federico, Andruino-a1: low-cost educational mobile robot based on android and arduino. *J. Intell. Rob. Syst.Intell. Rob. Syst.* **81**(1), 63–76 (2016)
3. M. Vanitha, M. Selvalakshmi, R. Selvarasu, Monitoring and controlling of mobile robot via internet through raspberry Pi board, in *Proceedings of the 2016 Second International Conference on Science Technology Engineering and Management (ICONSTEM)*, March 2016, pp. 462–466
4. W. Sun, S. Tang, H. Gao, J. Zhao, Two time-scale tracking control of nonholonomic wheeled mobile robots. *IEEE Trans. Control Syst. Technol.* **24**(6), 2059–2069 (2016)

5. R. Pahuja, N. Kumar, Android mobile phone controlled bluetooth robot using 8051 microcontroller. *Int. J. Sci. Eng. Res.* **2**(7), 14–17 (2014)
6. A.U. Bokade, V.R. Ratnaparkhe, Video surveillance robot control using smartphone and raspberry pi, in *Proceedings of the IEEE International Conference on Communication and Signal Processing (ICCSP)*, Melmaruvathur, India, April 2016, , pp. 2094–2097
7. K.S. Alli, M.O. Onibonjo, A.S. Oluwole et al., Development of an Arduino-based obstacle avoidance robotic system for an unmanned vehicle. *ARPN J. Eng. Appl. Sci.* **13**, 886–892 (2018)
8. S. Pedre, N. Matias, P. Facundo, C. Javier, P. De Cristoforis, Design of a multi-purpose low-cost mobile robot for research and education, in *Proceedings of the Conference Towards Autonomous Robotic Systems* (Springer, Cham, Switzerland, 2014), pp. 185–196
9. Speech Recognition library, [Online] Available: [https://github.com/Uberi/speech\\_recognition](https://github.com/Uberi/speech_recognition)
10. Mediapipe Hands library, [Online] Available: <https://google.github.io/mediapipe/solutions/hands.html>

# A Study on Effects of Design Parameters on Extrusion Product Quality Using Comsol LiveLink for Inventor



Van-The Than, Jin H. Huang, Chi-Chang Wang, Tat-Tai Truong,  
and Thi-Thao Ngo

**Abstract** An investigation of some design parameters in hollow extrusion die by Comsol LiveLink Inventor is presented in this paper. Three-dimensional extrusion die of a rectangle profile is designed by Autodesk Inventor. This model is then linked to Comsol for simulating extrusion process to obtain temperature, velocity, stress etc. Some design parameters will be automatically changed to consider their effects on the extrusion process. Results provide useful information for designer during the constructing extrusion die which can improve product quality.

**Keywords** Aluminum extrusion · Design parameters · Comsol software · Autodesk inventor

## 1 Introduction

Aluminum alloys with advantages of corrosion resistance, recyclable, low density etc. have been used in the aerospace and automotive industries. Aluminum extrusion method is being applied to produce high-yield profiled aluminum alloy products. During the extrusion process, hot aluminum is pressed through the die with the same shape as the product. However, during the extrusion process may occur some defects such as unbalanced flow, too high mold temperature which are ultimately affect the product quality and mold life. In particular, the defects are common appeared with aluminum products having complex profiles. In the past, designers had to use many tests to correct die designs to improve product quality. However, this process often takes a lot of time and costs for manufacturing and testing. Fortunately, numerical simulation with high accuracy is a useful solution. Many researchers have simulated to predict the product quality for the extrusion process. Lee et al. [1] used a 3D FEM

---

V.-T. Than · T.-T. Truong · T.-T. Ngo (✉)

Hung Yen University of Technology and Education, Hung Yen, Khoai Chau, Vietnam  
e-mail: [ngothaohnt@gmail.com](mailto:ngothaohnt@gmail.com)

J. H. Huang · C.-C. Wang

Feng Chia University, Taichung, Taiwan 40724, Republic of China

© The Author(s), under exclusive license to Springer Nature Switzerland AG 2024  
B. T. Long et al. (eds.), *Proceedings of the 3rd Annual International Conference on Material, Machines and Methods for Sustainable Development (MMMS2022)*, Lecture Notes in Mechanical Engineering, [https://doi.org/10.1007/978-3-031-57460-3\\_21](https://doi.org/10.1007/978-3-031-57460-3_21)

to simulate and consider extrusion process of cooling tubes in automobiles. Variation of chamber shape on porthole die was performed to find its effects on material flow, welding pressure, extrusion load, and. An optimal structure of the die used for extrusion of a rectangular hollow pipe was obtained based on numerical analysis software Msc/SuperForge by Wu et al. [2]. A more uniform velocity distribution has been acquired by modifying porthole and bearing lengths. Numerical method was also utilized to investigate the correlation between die design and process parameters after multiple-cycles to extrusion welds prediction and die deformation [3]. HyperXtrude software was applied in their simulation. Chen et al. [4] considered effects of pyramid angle on evaluation parameters of extrusion by using finite element simulation. Three modifications for the porthole die were proposed by Liu et al. [5] to achieve a uniform flow velocity and enough die strength. The optimal porthole die was then validated by experiment. From above analysis, it is clear that the numerical simulation method is widely applied and effective in optimizing the design of aluminum extrusion molds.

In this study, a synchronous solution from extrusion mold design to extrusion analysis is performed through Inventor link software with Comsol software. In this way, the design parameters will be easily changed to consider their effect on the temperature as well as the balance of the flow during extrusion.

## 2 Modeling Extrusion Die

### 2.1 Die Design

In this study, a rectangle hollow product is considered and its geometry is displayed in Fig. 1. It is clear that thickness of the product is constant and equals 2 mm. Based on theory and experiences, a porthole die type is chosen and designed as shown in Fig. 2.

From Fig. 2, it can be seen that there are many dimensions which need to be set during design. In this study, effect of bridge angle and bearing length (see Fig. 3) on extrusion process will be analyzed.

### 2.2 Modeling Extrusion Process

Aluminum Alloy 6063 (AA6063) common used varying application will be chosen for simulation. Properties of AA6063 and die materials (H-13 tool steel) are listed in Table 1.

The extrusion is a complex process combining heat transfer, fluid flow and structure analyses. Therefore, Comsol Multiphysics has been chosen for modeling and analyzed the extrusion process. Figure 4 presents the model extrusion process; each

**Fig. 1** Geometry of rectangle hollow product

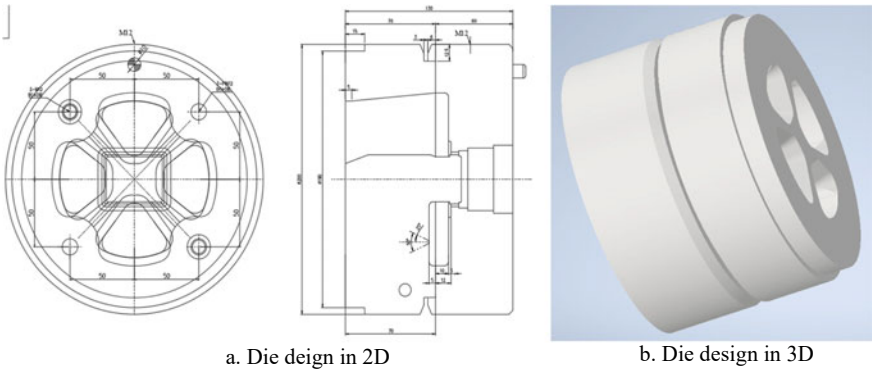
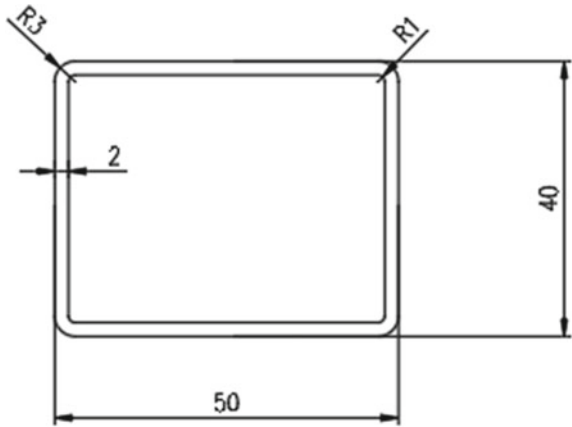


**Fig. 2** Porthole die

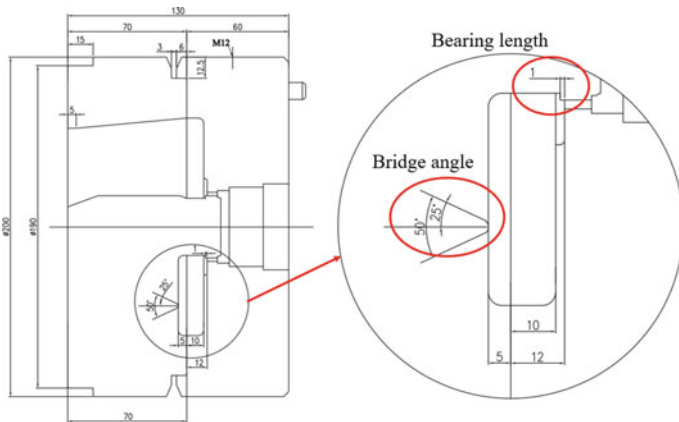


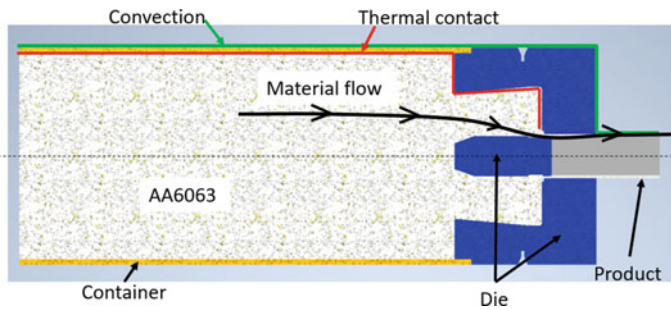
**Fig. 3** Some investigate dimensions

**Table 1** Materials properties

Name	AA6063	H-13 tool steel
Density (kg/m <sup>3</sup> )	2700	7760
Young Module (MPa)	68,950	210,000
Poisson ratio	0.293	0.3
Thermal expansion coefficient (1/°C)	$1 \times 10^{-5}$	$1.2 \times 10^{-5}$
Specific heat [J/(kg K)]	900	460
Thermal conductivity (W/m K)	198	24.3
Emissivity	0.05	0.15
Yield strength (MPa)	260	1200

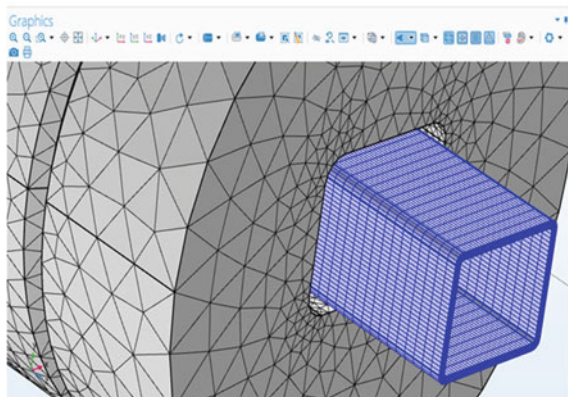
phenomenon will be set for corresponding to surfaces or regions. Meshing of the model is given in Fig. 5.

After solving, results of temperature, flow velocity, stress etc. will be obtained as displayed in Fig. 6.



**Fig. 4** Modeling extrusion process

**Fig. 5** Meshing



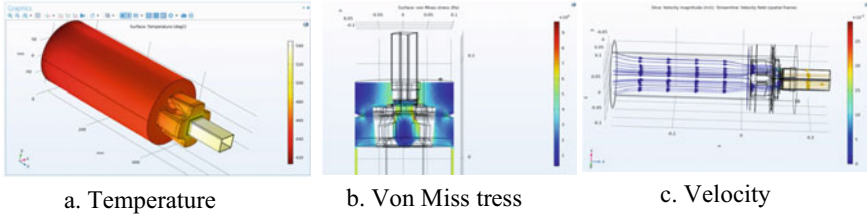


Fig. 6 Simulation results

### 3 Results and Discussions

In the previous section, the extrusion analysis model was established and solved to obtain the results. In this section, some geometrical parameters of the mold will be changed to consider their effect on the extrusion process. The LiveLink tool between Inventor and Comsol will be applied to support the parametric design process on Inventor synchronize with Comsol. Figure 7 shows the synchronize tool in Inventor which allows user can select parameters for simulation process.

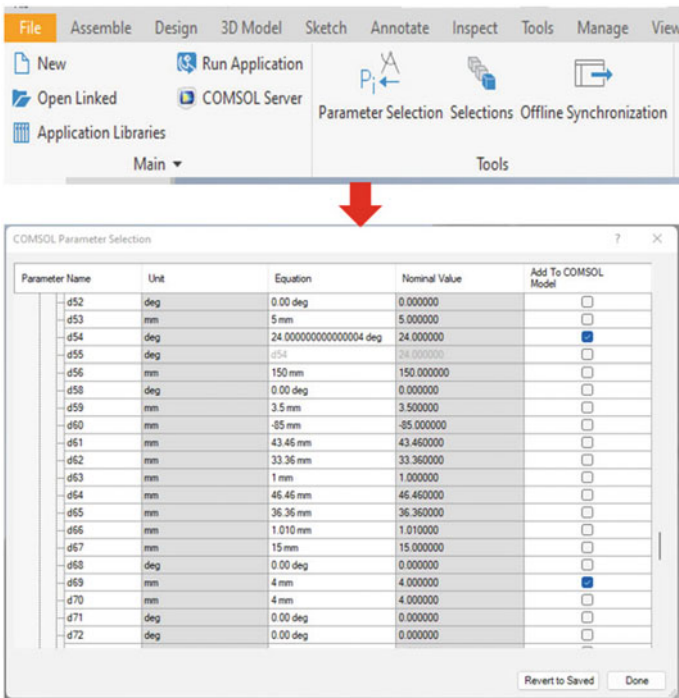
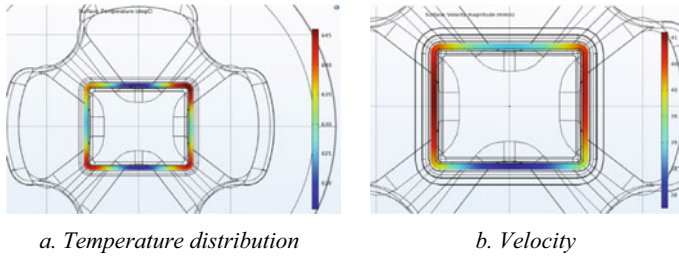


Fig. 7 Synchronize tool in inventor



**Fig. 8** Case of 22° bridge angle

**Table 2** Results for different bridge angles

	$T_{\max}$ (°C)	$\Delta T$ (%)	$V_{\max}$ (mm/s)	$V_{\min}$ (mm/s)	$\Delta V$ (%)
22°	647	4,5	41.5	36.5	12.05
<b>23°</b>	<b>604</b>	<b>3</b>	<b>40.4</b>	<b>39</b>	<b>3.46</b>
25°	645	4,3	41.2	37.8	8.25
27°	647	4,5	41.8	36.1	13.6

## 4 Effects of Bridge Angle

In this case, other parameters are selected as  $V_{\text{ram}} = 0.5$  mm/s,  $T_{\text{billet}} = 460$  °C; difference between feeder and bearing equaled 1 mm;  $P_{\text{press}} = 180$  bar. The temperature and velocity results at out gate are presented in Fig. 8 for case of 22°. Similarly, simulate results of temperature and velocity for other angles are carried out and collected in Table 2.

From Table 2, results indicate that under bridge angle in range of 22° to 27°, the maximum temperature is 647 °C. At 23°, the maximum temperature is only 604 °C. Results also show that different velocity ( $\Delta V$ ) get minimum (3.46%) and maximum (13.6%) at 23° and 27°, respectively. Through analysis, it is clear that the appropriate bridge angle is 23°.

## 5 Effects of Difference Between Feeder and Bearing

Similarly, effect of difference in feeder and bearing will be analyzed with fixed some other parameters as  $V_{\text{ram}} = 0.5$  mm/s,  $T_{\text{billet}} = 460$  °C, bridge angle = 23 °C  $P_{\text{press}} = 180$  bar. The simulation for three levels of difference between feeder and bearing is performed and results are given in Fig. 9 and Table 3. As seen, varying the difference between feeder and bearing, the maximum temperature of all cases has a slight difference. Moreover, the difference in extrusion velocity is in range of 3.46% and



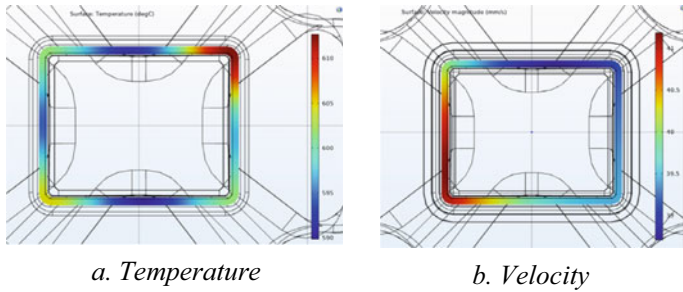


**Fig. 9** Difference between feeder and bearing equaled 1 mm

**Table 3** Results for variation of feeder and bearing

No	T <sub>max</sub> (°C)	T <sub>min</sub> (°C)	Δ <sub>T</sub> (%)	V <sub>max</sub> (mm/s)	V <sub>min</sub> (mm/s)	Δ <sub>V</sub> (%)
0.5	612	590	3.6	41.2	38.7	6.07
<b>1</b>	<b>604</b>	<b>586</b>	<b>3</b>	<b>40.4</b>	<b>39</b>	<b>3.46</b>
1.5	615	589	4.23	40.9	37.9	7.33
2	618	593	4.45	41.2	38.3	7.04

7.33%. Based on the obtained results, using the difference of 1 mm between feeder and bearing will have the lowest temperature and velocity variation.

## 6 Conclusions

Comsol LiveLink to Inventor has been applied to model and analyze extrusion of the rectangle hollow profile in this paper. With dimension of the product, a three-dimensional die was designed by Inventor software which can parametric dimension. Choosing parametric dimension will be synchronized to Comsol. Extrusion process including heat transfer, fluid flow and static structure phenomenon is then constructed and solved by Comsol software. Results indicate that bridge angles and variation of feeder and bearing have affected on temperature and velocity of the extrusion process. Based on considering some values of these dimension design, the appropriation of bridge angles and difference between feeder and bearing are sequently 23° and 1 mm. Herein results provide useful method and information for optimal design for the extrusion die.

## References

1. J.M. Lee, B.M. Kim, C.G. Kang, Effects of chamber shapes of porthole die on elastic deformation and extrusion process in condenser tube extrusion. *Mater. Des.* **26**, 327–336 (2006)
2. X. Wu, W. Zhao, Y. Luan, X. Ma, Numerical simulation and die structure optimization of an aluminum rectangular hollow pipe extrusion process. *Mater. Sci. Eng. A* **435**, 266–274 (2006)
3. T. Pinter, B. Reggiani, L. Donati, L. Tomesani, Numerical assessment of the influence of process and geometric parameters on extrusion welds and die deformation after multiple-cycles. *Mater. Today Proc.* **2**, 4856–4865 (2015)
4. L. Chen, G. Zhao, J. Yu, W. Zhang, Evaluation of a pyramid die extrusion for a hollow aluminum profile using FE simulation. *J. Mech. Sci. Technol.* **29**, 2195–2203 (2015)
5. Z. Liu, L. Li, S. Li, J. Yi, G. Wang, Simulation analysis of porthole die extrusion process and die structure modifications for an aluminum profile with high length-width ratio and small cavity. *Materials* **11**, 1517 (2018)

# The Application of the Reinforcement Learning Method for Mobile Robot Navigation in an Unknown Environment



Anh-Tu Nguyen and Hong-Son Nguyen

**Abstract** Mobile robots have attracted the attention of researchers because of their potential use in industry and daily life. Traditional navigation methods based on the predefined path or known map have been successfully applied to robots working in various scenes. When a robot is operating in an unknown environment, it must learn how to navigate through obstacles, identify risks, and design new trajectories in order to achieve its target. This paper presents the application of the reinforcement learning (RL) method in which the RL algorithm is based on the Q-table for robot navigation. A simulation model is designed on the Gazebo platform for the initial training of RL policies. The simulation and experimental results have proven the proposed method is efficient and the robot works well in an unknown environment involving different obstacles.

**Keywords** Navigation method · Reinforcement learning · Unknown environment

## 1 Introduction

Nowadays mobile robots can be found in numerous applications in logistic systems in factories, surveillance systems, disaster fighting, medical assistance, transportation systems, etc. The navigation term is always concerned with getting to a destination, conserving energy, avoiding collisions, and keeping on schedule. Traditional methods generate paths that are of a purely geometric nature and employ a controller to determine velocities for following such paths [1–3]. However, it is very difficult to create a precise robot dynamics model for practical applications. Vachhani et al. [4] present a control law based on a Lyapunov function to construct the 2D—generalized Voronoi diagram (GVD) for the mobile robot. However, this controller sometimes

---

A.-T. Nguyen (✉) · H.-S. Nguyen  
Faculty of Mechanical Engineering, Hanoi University of Industry, 298 Cau Dien Str., Bac Tu  
Liem District, Hanoi, Vietnam  
e-mail: [tuna@hau.edu.vn](mailto:tuna@hau.edu.vn)

could make undesirable decisions since they mainly utilize part of the known information from ultrasonic sensors. Numerous control methods, such as PID control, fuzzy logic control, and adaptive control, have also been introduced to deal with complex scenarios during mobile robot operations. Rengifo et al. [5] designed an affordable set of controllers for multi-agent system. This solution focused on PID and fuzzy algorithms to ensure safety and optimize predictable navigations. The Z-number based Fuzzy Logic control is proposed in [6] to track the trajectories for differential wheeled mobile. This research aims to the ability of encoding constraints and the reliability in multi-input and multi-output rules. Hence, the complexity of encoding error gradients is normally eliminated. However, these methods still have several disadvantages since the robot might not automatically adapt to the continuous complexity of the environment or completely maintain the smooth transition between trajectory segments in all cases. In [7], a vision-based mapping algorithm based on edge computing is designed to reconstruct 3D grid-map for mobile robots in the farm environment. The edge data is managed by a cloud server and synchronized with the robot model. However, this process requires high computation tracking algorithm and appropriate hardware to adapt the map maintenance task.

Generally speaking, there is always a significant disparity between what the global map shows and what the robot really perceives in the real world. Comparing the current local sensory data, such as range image and dead reckoning, with the global map is used to identify the robot's location while it is in motion. This method is not usually strong enough for situations that have a large number of continuous disturbances. Recently, Reinforcement Learning (RL) has been emerging as a powerful solution to deal with these mentioned problems. RL could help the robot to identify optimum behaviors in its surroundings via trial-and-error encounters. In RL, the designer of a control task delivers feedback in the form of a scalar objective function that assesses the robot's performance over a single step. This method has been successfully applied in solving speed control and path planning problems of the mobile robot [8, 9].

This paper addresses an application of RL for solving the mobile robot in an unknown environment. The Q-learning algorithm is calculated to update the states and action values. After the training process, the model is examined in different simulation scenarios and in the context of real-world use cases. The empirical results indicate that the robot can avoid different obstacles to reach the desired targets.

## 2 Reinforcement Learning Model

Reinforcement learning is a class of learning by interacting with the environment. Hence, it is suitable for solving the robotics field. The problem is formally defined based on the framework of Markov decision process (MDP) [10], in which the learner and decision maker is called the agent (robot) and everything outside the agent has comprised the environment. At state  $S_t$ , the agent applies action  $A_t$  to the environment and the consequence of this action is a numerical reward  $R_{t+1}$ , then the agent moves to a new state  $S_{t+1}$ . The random variables  $R$  and  $S$  depend only on the current state  $s$  and the applied action  $a$ , so for all next states  $s_0 \in S$ ,  $r \in R$ , and  $a \in A(s)$  (Fig. 1).

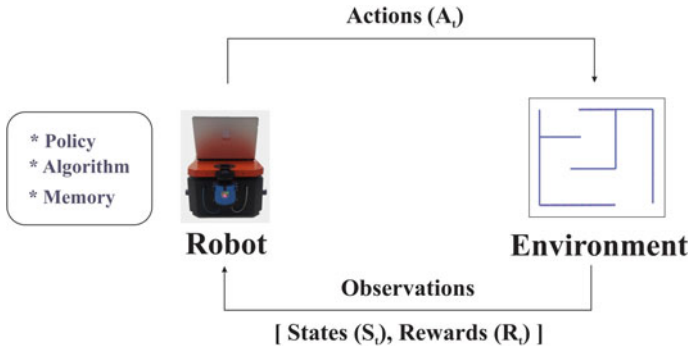


Fig. 1 The robot-environment interaction process

Reinforcement algorithms are upon maximizing policy value, which is a direct indicator of the long-term desirability of states considering the rewards available in those states. Q-learning is probably the most practical and effective algorithm that belongs to temporal difference learning, a model-independent, and fully incremental algorithm. The state value function gives information about the desirability of that state for an agent under a policy. The environment model of the robot takes into account the information about the surrounding obstacles and the location of the target point (Fig. 2).

The state space of the robot is based on the measurement from a laser scanner which can measure the maximum distance up to 50 m and scan the view field of 270°. The state space consists of four variable states ( $s_1, s_2, s_3, s_4$ ) in which  $s_1$  and  $s_2$  are binary variables for the distance between the robot and the obstacle,  $s_3$  and  $s_4$  are binary variables for the position of the obstacle relative to the robot, where  $s_3$  and  $s_4$  correspond to the left side the right side, respectively.

$$[S] = [s_1, s_2, s_3, s_4] \tag{1}$$

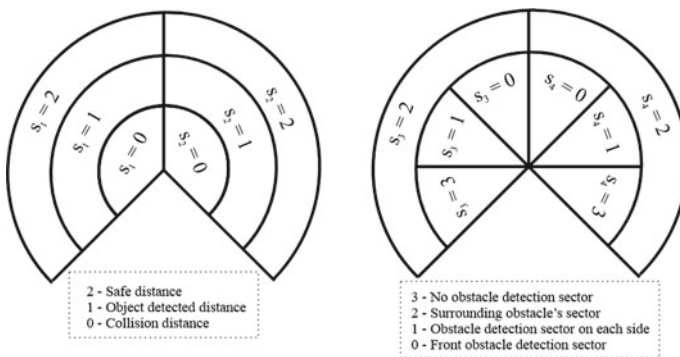


Fig. 2 State space definition from lidar sensor range

The robot action space is defined into three main actions, namely:

$$[A] = [go\_forward, turn\_left, turn\_right] \quad (2)$$

The  $\epsilon$ -greedy strategy is used to select the appropriate actions in which each possible action of the robot is represented by a pair of linear and angular velocities. These parameters are then fed into a controller to navigate the robot move to the desired position.

Since reinforcement has always revolved around the rewards which are generated by the interaction between the robot and the environment. The design of reward parameters directly affects the convergence speed of the algorithm. In the present study, the reward function is defined as three distinct values:

$$R = \begin{cases} r_1 : go\_forward \\ r_2 : turn\_left/right \\ r_3 : obstacle\_collision \end{cases} \quad (3)$$

The reward values are all constant, when the robot can move forward or turn left or right, it will be given reasonable positive rewards ( $r_1 > r_2$ ). When the robot encounters an obstacle, it will be given a negative reward ( $r_3 < 0$ ). The total reward  $R_t$  in each episode is the accumulative reward over the motion steps. The algorithm for updating the Q-table is presented as follows [11]:

**Initialize:**

State Dataset:  $S = \{1, \dots, s_n\}$   
 Action Dataset:  $A = \{1, \dots, a_n\}$   
 Q-table is filled with zeros:  $[S \times A]$   
 Hyper-parameters:  $\alpha, \gamma, \epsilon, T$

**Learning process:** where  $episode := 1$

if  $episode$  is not  $final\_episode$ :

Perform collection set of states based on observations:

$s = [s_1, s_2, s_3, s_4]$

if  $state$  is not  $terminal\_state$ :

Choose the best action from the optimal function:

$a = Epsilon\_Greedy\_Exploration\_Function$

Receive a new set of states:

$s' = new[s_1, s_2, s_3, s_4]$

Accumulating rewards calculation:

$R = r_1 + r_2 + r_3$

Update Q-table by Q-learning Algorithm:

$Q_{st,at} = Q_{st,at} + \alpha * [r_t + \gamma * \max Q(st+1, a) - Q_{st,at}]$

else:

$step := step + 1$

$a_{previous} := a$

$s := s'$

else:

$episode := episode + 1$

$\epsilon = \sigma_\epsilon \epsilon$

$s := s'$

**End.**

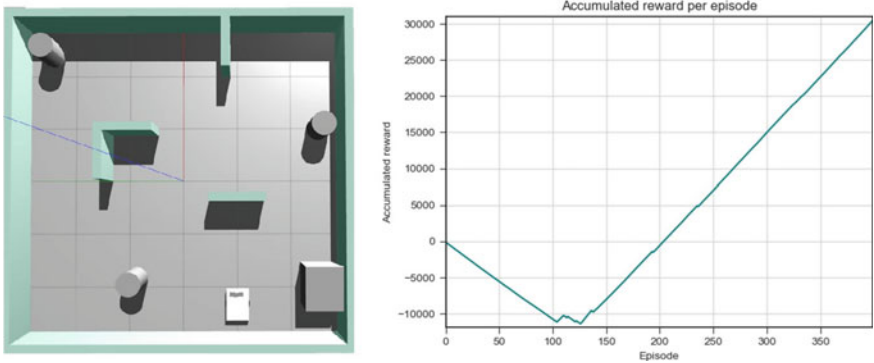


**Fig. 3** The virtual environment on Gazebo platform and the accumulative rewards of the model during the training process

### 3 Experiment and Analysis

#### 3.1 Training in the Virtual Environment

The simulated robot is trained in a virtual environment, given by the Gazebo platform. First, the environment area is divided into a grid mesh of  $6 \times 6 \text{ m}^2$  bounded by green walls. Secondly, we set up various types of obstacles inside the area (Fig. 3). To ensure general objectivity, the obstacles with different sizes and shapes (circle, rectangle) are designed and arranged randomly at several positions in the area. The mission of the mobile robot is to generate highly curvy paths based on the predefined start point and destination point. During the training process, the robot was initialized randomly in the whole area in each episode.

In Fig. 3, it can be seen that the convergence is obtained after about 500 steps in each episode. The accumulative reward increases as the number of episodes increases.

#### 3.2 Results and Discussion

To ensure the applicability as well as the stability of the proposed method, we built and deployed it on a real mobile robot. The model of the robot consists of two driving wheels and two castor freewheels. DC motors are used to power the active wheels. The robot’s control system was embedded into a laptop. In particular, a microcontroller—STM32F407VET6 transfers control signals from the laptop to the drive motor, while the NAV245 collects real-time ambient characteristics necessary for localization and obstacle avoidance. In addition, two encoder sensors are directly linked to the driving wheels. It helps the system easier to provide feedback on the motor speed. To precisely evaluate the performance of the proposed method, the experimental space

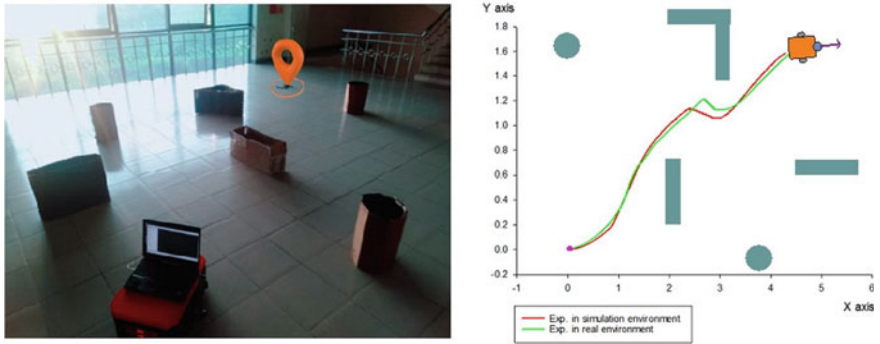


**Fig. 4** The motion path of the robot in simulation and real environment

for robot motion mimicked the training environment. The robot is also initiated at a random point and required to generate trajectories for the target destination (Fig. 4). The experimental metrics indicated that the robot successfully overcame the topographic without any collisions with the obstacles after 45 independent trials. Figure 4 illustrates the specific comparisons between the experimental result and the simulation result.

## 4 Conclusion

Traditional approaches normally applied predefined paths or scanner maps for robot navigation. Unlike previous works, this paper proposes an application of the RL to deal with avoiding obstacles and navigation missions in unknown environments for mobile robots. The training process is conducted in the Gazebo virtual platform to obtain and collect the parameters. Since that, the main data is deployed on the real model for further testing. The simulation and experimental results have revealed that the proposed method maintains high stability as well as superior efficiency when working in a sophisticated environment containing various obstacles.

**Acknowledgements** The authors would like to acknowledge the financial support provided by the Hanoi University of Industry under Grant No. 04-2022-RD/HĐ-ĐHCN.



## References

1. C. Chou, F. Lian, C. Wang, Characterizing indoor environment for robot navigation using velocity space approach with region analysis and look-ahead verification. *IEEE Trans. Instrum. Meas.* **60**, 442–451 (2011)
2. A. Stephen, Y. Sun, A.L. Taher, Implementation of autonomous navigation algorithms on two-wheeled ground mobile robot. *Am. J. Eng. Appl. Sci.* **7**, 149–164 (2014)
3. S. Lu, C. Xu, R. Y. Zhong, An active RFID tag-enabled locating approach with multipath effect elimination in AGV. *IEEE Trans. Autom. Sci. Eng.* **13**, 1333–1342 (2016)
4. L. Vachhani, A.D. Mahindrakar, K. Sridharan, Mobile Robot navigation through a hardware-efficient implementation for control-law-based construction of generalized Voronoi diagram. *IEEE/ASME Trans. Mechatron.* **16**, 1083–1095 (2011)
5. A. Rengifo, F.E. Segura-Quijano, N. Quijano, An affordable set of control system laboratories using a low-cost robotic platform. *IEEE/ASME Trans. Mechatron.* **23**, 1705–1715 (2018)
6. M. Abdelwahab, V. Parque, A.M.R. Fath Elbab, A. A. Abouelsoud, S. Sugano, Trajectory tracking of wheeled mobile robots using Z-number based fuzzy logic. *IEEE Access* **8**:18426–18441
7. W. Zhao, X. Wang, B. Qi, T. Runge, Ground-level mapping and navigating for agriculture based on IoT and computer vision. *IEEE Access* **8**, 221975–221985 (2020)
8. W. Kaifang, L. Bo, G. Xiaoguang, H. Zijian, Y. Zhipeng, A learning-based flexible autonomous motion control method for UAV in dynamic unknown environments. *J. Syst. Eng. Electron.* **32**, 1490–1508 (2021)
9. L. Yehezkel, S. Berman, D. Zarrouk, Overcoming obstacles with a reconfigurable robot using reinforcement learning. *IEEE Access* **8**, 217541–217553 (2020)
10. R.S. Sutton, A.G. Barto, *Reinforcement Learning: An Introduction*, vol. 1 (MIT press Cambridge, 2018)
11. L. Aleksa, J. Kosta, in *Application of Artificial Intelligence in Mobile Robotics and Autonomous Driving*. Master rad. The University of Belgrade, Faculty of Electrical Engineering, 2020

# Optimisation of Parameters When Polishing Aluminium Cookware Using Wool Felt Wheel



Truong Dinh Luan, Nguyen Trong Doanh, and Bui Qui Luc

**Abstract** Aluminium is used a used material in houseware (e.g. cookwares, kettles, sinks, etc.). Often rusted, tarnished after a period of use; especially in hot, humid environments. It will lose the beauty and clean of the product. For that reasons, polishing aluminium to a required roughness surface is necessary before using. An experimental study showed that roughness surface is correlated with factors: Velocity, friction force, time, polishing material, workpiece material. Experimental also shows that to decrease the surface roughness quickly if the velocity and friction force are increased but will happen oscillator, lots of power loss; If the friction force and time are increased, it will generate heat, burn marks in the polishing material, the surface will turn orange, not productive. So, to achieve the optimal surface roughness, it is necessary to optimize the above coefficients. This paper presents optimization of coefficient of friction force and time, (F, t) pair with fixed velocity  $v = 22$  m/s for minimization of surface roughness.

**Keywords** Polishing · Aluminium · Wool felt · Optimization · Regression

## 1 Introduction

Metal polishing is a finishing method that uses abrasive materials to smooth a surface. When polished, the surface of metal is removed from defects and becomes more reflective and shiny. In addition to beauty value, metal polishing also serves a practical purpose. Such as, it eliminates oxidation and prevents further corrosion of the metal, greatly extending its working life.

The aluminium cookware is normally produced by shaping under the mold. Although the required shape of the finished product is obtained, its surface is still rough, dull and waviness mark so called an orange peel is appeared. Thus, the

---

T. D. Luan (✉) · N. T. Doanh · B. Q. Luc  
School of Mechanical Engineering, Hanoi University of Science and Technology, Hanoi, Vietnam  
e-mail: [luanck30121979@gmail.com](mailto:luanck30121979@gmail.com)

polishing process to diminish such marks is necessary in order to obtain better surface appearance and make it attractive.

However, there has been little discussion on the polishing of aluminium cookware. P. Tevinpibanphan et al. conducted an experiment to investigation into the polishing of stainless steel using sisal wheels [1]. Cheng and Chang experimentally investigated the electro-polishing of 304 stainless steel in order to formulate a surface roughness model [2]. Tongqing et al., optimized the chemical–mechanical polishing of a 12-inch wafer [3]. Dickman and Millman attempted to optimize polishing and buffing [4]. Gianpaolo et al., optimized a surface roughness predictive model in deterministic polishing of ground glass moulds [5].

In this paper, research the influence of some factors on surface roughness such as velocity, friction force, process time and propose a fitted model Rz. Experiments were conducted on a CNC polishing machine.

## 2 Experimental Procedure

### 2.1 Experimental Condition

Polishing experiments were conducted on a reconfigurable CNC polishing machine based on a lathe. Polishing velocity is  $v = 22$  m/s. The workpiece used is cookwares aluminium size  $\phi 160 \times 80$ , whose chemical composition includes Fe 0.26%, Mg 0.04%, Zn 0.216%, Cu 0.052%, Pb 0.698%, Mn 0.029% and Si 0.88% in addition to Al, medium hardness 171.5HB, original surface roughness are shown in Table 1. The polishing material used is wool felt wheel with Properties are shown in Table 2.

### 2.2 Surface Roughness Measurement

Surface roughness was measured by Mitutoyo SJ-301 which is portable surface roughness tester, by probe measurement method, the probe is placed in contact with the surface (Fig. 1). The arithmetic mean values (Ra, Rz) is the most popular method to describe surface roughness in engineering practice. In this paper, the Rz is selected to describe the surface roughness. Figure 2 shows measurement result when polishing using wool felt wheel ( $v = 22$  m/s;  $F = 40$ N;  $t = 55$  s).

### 2.3 Design of Experiments and Results.

In this paper, a proposed method is to determine the equation of the fitted model Rz(F, t) and then optimisation of polishing parameters for minimize (Rz). The dependent

**Table 1** Original surface roughness

Surface roughness	No												Average
	1	2	3	4	5	6	7	8	9	10	11	12	
Ra	1.67	1.42	1.24	1.94	1.37	1.51	2.08	1.91	2.03	1.31	2.21	2.09	1.73
Rz	9.68	7.10	6.92	9.88	7.95	7.63	10.74	10.25	10.31	7.66	10.72	10.9	9.15

**Table 2** Properties of wool felt wheel

Diameter (mm)	Thickness (mm) (Accuracy 0.1)	Hardness
150	20	Soft

**Fig. 1** Surface roughness measurement method

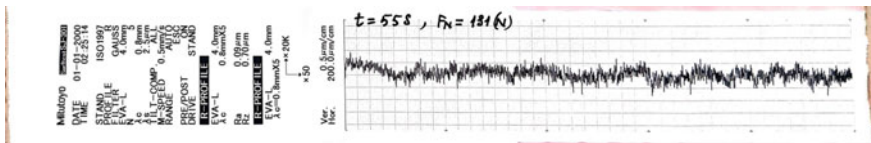


**Fig. 2** Measurement result

variable is surface roughness  $R_z$ , the independent variable is Force Friction ( $F$ ), process time ( $t$ ) and velocity ( $v$ ). In this experimental design, choose a fixed value of  $v = 22$  m/s (corresponds to the polishing wheel speed is 2500 rpm và cookware speed 300 rpm), the selected polishing wheel speed is the maximum speed of the motor because mechanism polishing of metal without abrasives is surface flow [6], if the speed increases, the surface roughness decreases quickly. Therefore, determine the equation of the fitted model of the dependence  $R_z$  on 2 parameters is  $F$  and  $t$ . First, investigate the dependence  $R_z$  ( $\mu\text{m}$ ) on force  $F$ (N), experimental results are shown in Table 3 and Fig. 3.

In Fig. 3, when increasing the force to 24N, the surface roughness decreases quickly ( $R_z = 2.36 \mu\text{m}$ ), then continuing to increase the force, the surface roughness also decreases but slowly ( $R_z = 2.12 \mu\text{m}$ ), up to the value of 40N, the surface roughness tends to increase (due to the pressure of the polishing wheel on the workpiece reduces the polishing speed, about 10%). Therefore, estimate the polishing force parameter domain to  $24 \div 40\text{N}$ .

Second, continue to investigate the dependence  $R_z$  ( $\mu\text{m}$ ) on process time  $t$ (s), experimental results are shown in Table 4 and Fig. 4.

**Table 3** Experimental results of relation Rz and F

t = 15 s		t = 25 s		t = 35 s	
F [N]	Rz [ $\mu\text{m}$ ]	F [N]	Rz [ $\mu\text{m}$ ]	F [N]	Rz [ $\mu\text{m}$ ]
0	9.15	0	9.15	0	9.15
7.8	6.18	7.8	5.70	8.1	4.18
12.6	5.05	13.5	5.42	19.5	3.03
17.1	4.93	24	2.36	30	1.59
25.5	4.51	39	2.05	34.2	1.44
36.9	3.92	45	2.12	45	1.60

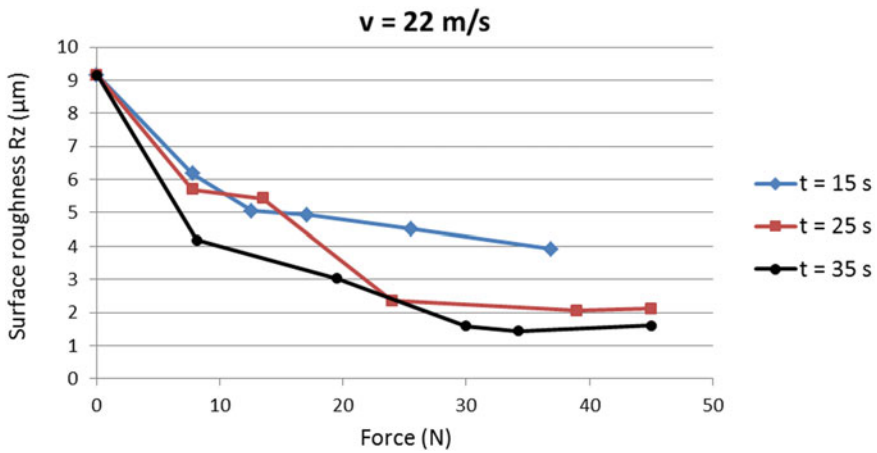


**Fig. 3** Relation surface roughness Rz and force F

**Table 4** Experimental results of relation Rz and time t

F = 24[N]		F = 31[N]		F = 38[N]	
t [s]	Rz [ $\mu\text{m}$ ]	t [s]	Rz [ $\mu\text{m}$ ]	t [s]	Rz [ $\mu\text{m}$ ]
0	9,15	0	9,15	0	9,15
25	3,01	25	1,33	25	1,57
35	1,43	35	1,50	35	1,54
45	1,50	45	1,09	45	1,51
55	1,39	55	1,25	55	1,00

In Fig. 4, during 25 s the surface roughness decreases quickly ( $Rz = 1.33 \mu\text{m}$ ), from 25 s ÷ 45 s the surface roughness decreases but slowly ( $Rz = 1.09 \mu\text{m}$ ), from 45 s ÷ 55 s the surface roughness remained almost the same, sometimes increased. The Fig. 4 shows that plots Rz due to the force  $F = 31\text{N}$  and the force  $F = 38\text{N}$  is almost the same, so in order to minimize the negative effects of the large F force,

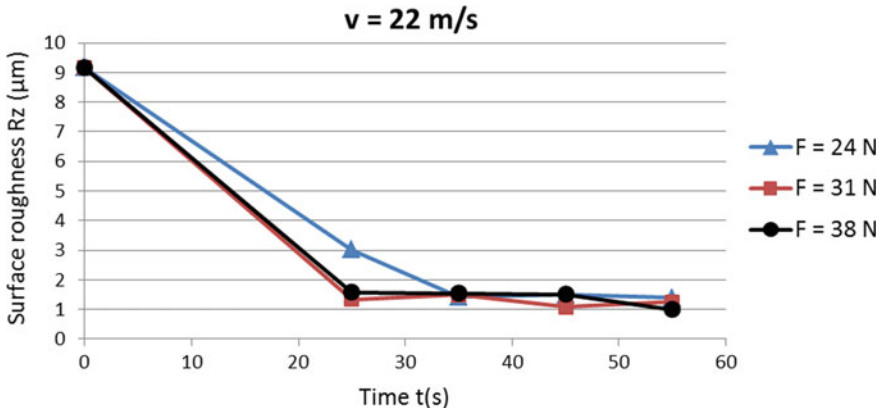


Fig. 4 Relation surface roughness Rz and time t

such as: high temperature, lots of power loss, burn marks in the polishing material, system oscillator. So choose the maximum force to be 32N.

The domain is defined as follows:

Friction force varies in the range:

$$F = 24 \div 32N$$

Time process varies in the range:

$$t = 25 \div 45s$$

Using Stat graphics Centurion XV software, designing with 2 factors (F and t), 3<sup>2</sup> experiments with 3 experiments at the center, so total of 12 experiments were conducted randomly (to reduce noise factors may be affect the experiments). The experimental results are shown in Table 5.

After analyzing the variance, shows a result, Table 6.

Variables A; B; A.B; BB corresponds to the parameters F; t; F.t; t<sup>2</sup> have P values < 0.05, there is a significant on surface roughness Rz. But with the variable AA, corresponding parameter F<sup>2</sup> has a value of P = 0.4455 (>0.05, 95% confidence), there is not much influence on surface roughness Rz, so removing in the regression equation. After removing, re-estimate the regression coefficients are shown in Table 7.

With R<sup>2</sup> = 87.8%, statistic indicates that the model as fitted explains 87.8% of the variability in Rz. The equation of the fitted model in polishing process of aluminium cookware is:

$$Rz = 19.1108 - 0.384167.F - 0.577833.t + 0.00825.F.t + 0.00426667.t^2$$

**Table 5** Experimental results randomly

No	F [N]	t [s]	Rz [ $\mu\text{m}$ ]
1	28	25	2,55
2	24	35	1,55
3	32	35	1,42
4	28	45	1,62
5	28	35	1,46
6	24	45	1,48
7	32	25	1,38
8	28	35	1,39
9	24	25	3,12
10	28	35	1,42
11	32	45	1,06
12	28	35	1,41

**Table 6** ANOVA analysis

Source	Sum of squares	Df	Mean square	F-ratio	P-value
A:F	0,874,017	1	0,874,017	12,93	0,0114
B:t	1,39,202	1	1,39,202	20,59	0,0039
AA	0,0,450,667	1	0,0,450,667	0,67	0,4455
AB	0,4356	1	0,4356	6,44	0,0442
BB	0,589,067	1	0,589,067	8,71	0,0256

**Table 7** Regression coefficients

Coefficient	Estimate
Constant	19.1108
A:F	-0.384167
B:t	-0.577833
AB	0.00825
BB	0.00426667

In Fig. 5, the optimal condition was found using Statgraphics Centurion XV software, the values are shown in Table 8.

The optimal value (with the slowest surface roughness) is:  $Rz = 1.05$  with  $F = 32\text{N}$  and  $t = 37\text{ s}$ .



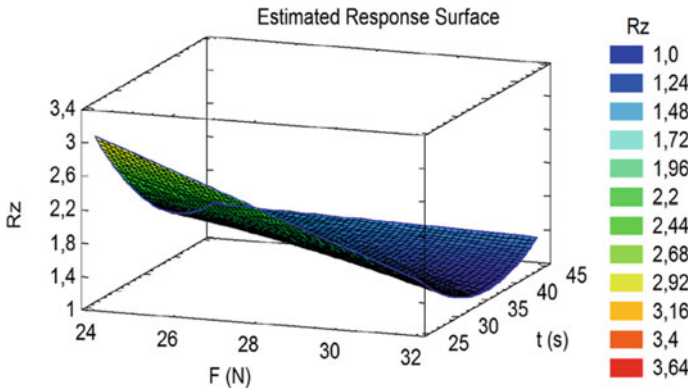


**Fig. 5** Influence of force F và time t to surface roughness Rz

**Table 8** Surface roughness optimization

Factor	Low	High	Optimum
F	24.0	32.0	32.0
t	25.0	45.0	36.777

### 3 Conclusion

This paper determined the optimisation of parameters of polishing aluminium cookware using wool felt wheel. There are three factors have significant to the surface roughness of aluminum, but in this study only two factors, friction force (F) and process time (t). The optimal conditions were found to be 32 N and 37 s.

The optimal surface roughness value is  $Rz = 1.05 \mu\text{m}$ .

The surface roughness can be predicted by using the fitted model was reported. In this study, surface roughness is inverse to force and time, but proportional to force and time interaction. This means that determining the optimal (F, t) pair is necessary when polishing aluminium.

In addition, It is the basis for calculating the optimal algorithms in the polishing control process aluminium cookwares.

### References

1. P. Tevinpibanphana, S. Prombanpong, V. Tangwarodomnukun, Investigation into the polishing of stainless steel using sisal wheels. *Appl. Mech. Mater.* **548–549**, 491–495 (2014)
2. C.-C. Linb, C.-C. Hu, Electropolishing of 304 stainless steel: Surface roughness control using experimental design strategies and a summarized electropolishing model. *Electrochimica Acta* **53**, 3356–3363 (2008)
3. T. Wang, X. Lu, D. Zhao, Y. He, J Luo, Optimization of design of experiment for chemical mechanical polishing of a12-inch wafer. *Microelectron. Eng.* **112**, 5–9 (2013)

4. A. Dickman, B. Millman, Polishing and buffing, in *Metal Finishing* (1999), pp. 32–49
5. G. Savio, R. Meneghello, G. Concher, A surface roughness predictive model in deterministic polishing of ground glass moulds. *Int. J. Mach. Tools Manuf.* 1–7 (2009)
6. L.E. Samuel, in *ASM Metals Handbook*, vol. 18 (2017), pp. 352–366

# Analysis of Pedestrian Head Kinematics During Impact to Car Process Using a Full Deformable Pedestrian Model



Van-Luc Ngo, Ngoc-An Tran, and Van-Hai Nguyen

**Abstract** Pedestrian head safety test is one of requirements in the safety inspection of new models of car. Therefore, pedestrian head protection is considered for all new model of car in process of research and development. There are two solutions to analyze the protection of car for pedestrian head in collisions that are using full pedestrian model or pedestrian headform impactor. Previous research has analyzed and shown that the two solutions give different evaluation results, but there is no analysis of the cause of the difference or indicating which method is more reliable. Pedestrian head injuries were assessed by the HIC value which is determined through the resultant acceleration of the pedestrian head center of gravity during collisions. Thus, the kinematic characteristics of the pedestrian head will affect the HIC value or the results of assessing the pedestrian safety. This study will analyze the pedestrian head kinematics during impacting process using a full deformable pedestrian model. The obtained results will be compared with the kinematic characteristics of the head impactor to find out the cause of the difference in the evaluation results. This research is very useful to develop the more reliable method of pedestrian head safety tests.

**Keywords** Full deformable pedestrian model · Pedestrian head kinematics · HIC value · Pedestrian head safety test method

## 1 Introduction

More and more new models of car appear on the market to meet all the demand of consumers. Pedestrian head safety test is one of the mandatory tests for new model of car to sold in many markets [1]. Therefore, in the process of research and

---

V.-L. Ngo (✉) · N.-A. Tran · V.-H. Nguyen  
Faculty of Mechanical Engineering and Mechatronics, Phenikaa University, Hanoi 12116,  
Vietnam  
e-mail: [luc.ngovan@phenikaa-uni.edu.vn](mailto:luc.ngovan@phenikaa-uni.edu.vn)

Phenikaa Research and Technology Institute (PRATI), A&A Green Phoenix Group JSC, No.167  
Hoang Ngan, Trung Hoa, Cau Giay, Hanoi 11313, Vietnam

© The Author(s), under exclusive license to Springer Nature Switzerland AG 2024  
B. T. Long et al. (eds.), *Proceedings of the 3rd Annual International Conference on Material, Machines and Methods for Sustainable Development (MMMS2022)*, Lecture Notes in Mechanical Engineering, [https://doi.org/10.1007/978-3-031-57460-3\\_24](https://doi.org/10.1007/978-3-031-57460-3_24)

219

development, all new car models are analyzed for pedestrian head safety in collisions. Whether analyzed by simulation or experience, there are two kind of pedestrian models used for impacting tests with cars that are the full pedestrian model and the headform impactor [2, 3]. Figures 1 and 2 show experimental and finite element models using to analyze pedestrian head safety, respectively. Previous research has performed experimental tests to analyzed and shown that the two solutions give different evaluation results [4], but there is no analysis of the cause of the difference or indicating which solution is more reliable.

The level of pedestrian head injury in car to pedestrian impacting tests is calculated base on the HIC (Head Injury Criterion) value, which depend on the variation characteristic of the resultant acceleration of pedestrian head center of gravity (A) in process of collision as following equation [2]:

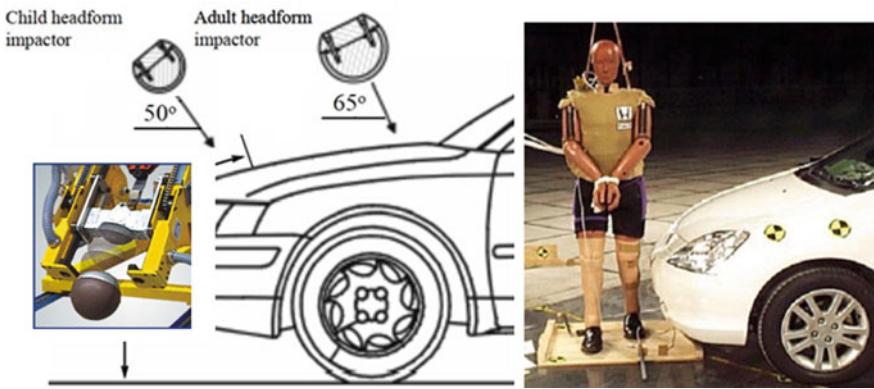


Fig. 1 Pedestrian head models for experimental tests of pedestrian safety [2, 3]

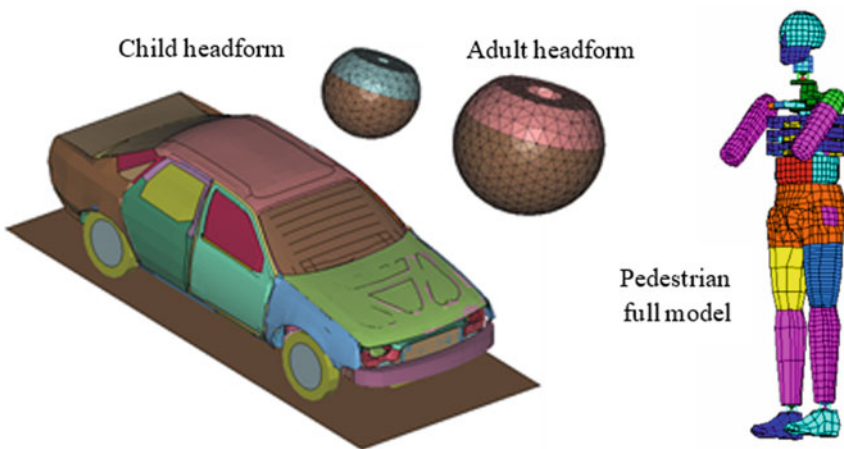


Fig. 2 Finite element models of pedestrian for simulation tests of pedestrian head safety [5, 6]

$$\text{HIC} = \text{Max} \left[ \frac{1}{T_2 - T_1} \int_{T_1}^{T_2} \text{AdT} \right]^{2.5} (T_2 - T_1) \quad (1)$$

$$\text{With condition } \Delta T = T_2 - T_1 \leq 15 \text{ ms (mini - second)} \quad (2)$$

The resultant acceleration of pedestrian head center of gravity (A) can be divided into some kinematics components to analyze the variation and the influence of each component on A, including tangential acceleration ( $A_t$ ), normal acceleration ( $A_n$ ), resultant velocity (V), curvature of pedestrian head model center of gravity trajectory (K).

$$A = \sqrt{A_t^2 + A_n^2} \text{ with } A_n = K.V^2 \quad (3)$$

Above equations show that the HIC value will depend on the variable characteristics of K, V and  $A_t$ . Previous research has analyzed the variation characteristics of pedestrian headform impactor in tests at different locations [7, 8]. That study has shown that testing at different locations the variation characteristics of V and  $A_t$  are not much different, but the variation of K is very complex and has a decisive significance to the A variation characteristic. In this study, the simulation of car impact to the full deformable pedestrian model (Fig. 1) will be performed to analyze the variation characteristic of K. The obtained results will be compared with the result of tests with pedestrian headform impactor to find out the cause of different in results evaluation with two kind of model. The results of this study will be of great significance in the development of an increasingly more accurate test of pedestrian safety.

## 2 Impacting Simulation to Analyze the Pedestrian Head Kinematics

The full deformable pedestrian model used in this study was developed from the passenger model [6]. This is a finite element model whose deformation is similar to that of real people. This full deformable pedestrian model has been validated to be qualified for use in car-pedestrian collision simulation. The purpose of this study is to analyze the kinematics so the finite model of the car is simplified to reduce the time of simulation. The car model only includes the outside part and assigning a block with a weight equal to the weight of the full car model at the center of gravity of the vehicle. The deformation characteristics of the car shape remain the same as the full car model. The full deformable pedestrian model is setup at rest and the car is impacting at 32 km/h to the leg of pedestrian model at the center of the car bumper. The curvature of pedestrian head center of gravity trajectory (K) is determined by the following formula [9] (Fig. 3):

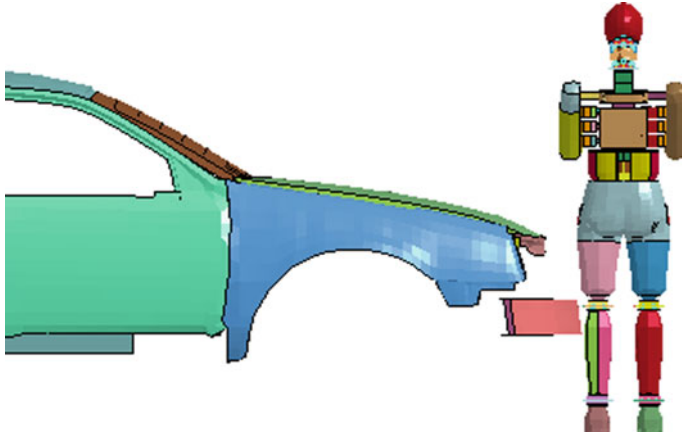


**Fig. 3** Setup of car to full deformable pedestrian model impacting simulation

$$K = \frac{\sqrt{(\ddot{z}\dot{y} - \dot{y}\ddot{z})^2 + (\ddot{x}\dot{z} - \dot{z}\ddot{x})^2 + (\dot{y}\ddot{x} - \ddot{x}\dot{y})^2}}{(\dot{x}^2 + \dot{y}^2 + \dot{z}^2)^{\frac{3}{2}}} \tag{4}$$

where:

$$\dot{x} = V_x; \dot{y} = V_y; \dot{z} = V_z; \ddot{x} = A_x; \ddot{y} = A_y; \ddot{z} = A_z \tag{5}$$

These parameters are determined from the simulation results through the NODE which locates at pedestrian head center of gravity.

### 3 Results and Discussion

Figure 4 describes the variation of V and K in the simulation of collision between a car and full deformable pedestrian model. The process of collision between car and full deformable pedestrian model can be divided into two stages. The first stage from the moment the leg of full deformable pedestrian model touches the bumper of car until the shoulder of full deformable pedestrian model touches the bonnet surface. The second stage follows the first stage to the end of the pedestrian head to bonnet surface collision.

The results show that V increases slightly in the first stage. The V accelerate slowly in the initial time due to inertia of head part and this part can rotates flexibly relative to the body part. Meanwhile, K increases sharply at the moment of the leg touch the bumper, and then decreases rapidly to the stable value until the head touches the bonnet surface. The sharp increase of K in the initial moment is due to the head jerking and the trajectory of head center of gravity changed direction suddenly, then

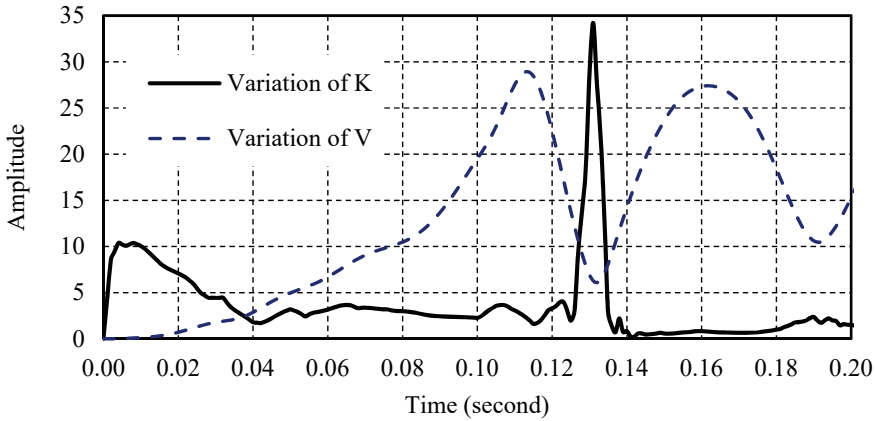


**Fig. 4** The variation of K and V when test with the full deformable pedestrian model

the head model center of gravity is almost moving in a circular curve, so K keeps stable. The center of circular curve is the contact point between the leg, hip, shoulder and the car, respectively.

In the second stage, V increases very rapidly at the initial moment because of the collision between the pedestrian shoulder and bonnet surface until the pedestrian head part touches the bonnet surface. From the time of the head part of full deformable pedestrian model touches bonnet surface to the time bonnet surface reaches maximum deflection V decrease suddenly due to the resistance of the bonnet surface. Then the bonnet surface tends to be elastic and V increases significantly due to receiving part of the elastic energy. At this moment, pedestrian head bounces back cause K increases suddenly to a very large value. After that, the trajectory of pedestrian head part has little change in the direction of motion because of moving with the body thrown out, so K decreases sharply to a low stable value. Figure 5 shows more closely about the variation of K corresponding to duration of the head part of full deformable pedestrian model impact to the bonnet surface to compare with the variation of K in pedestrian head safety test using headform impactor.

Figure 5 shows the variation of K in simulation of pedestrian head safety tests with adult headform impactor [8]. The full deformable pedestrian model is an adult human model and the position of impact with the bonnet also corresponds to the impacting test area with the adult headform impactor. The K of full deformable pedestrian model forms a very clear and symmetrical peak. Meanwhile, the K of adult headform impactor forms an asymmetrical peak, after time of headform impact to bonnet surface, K remains quite large value. At many positions, K forms a very skewed peak, at the end of the collision K decreases a little and then continues to increase to a larger value. The variable characteristics of K show that the trajectory of head center of gravity direction only drastic changes at the moment of bonnet reaches maximum deflection in tests with the full deformable pedestrian model. In contrast, in tests using headform impactor, the direction of head center of gravity

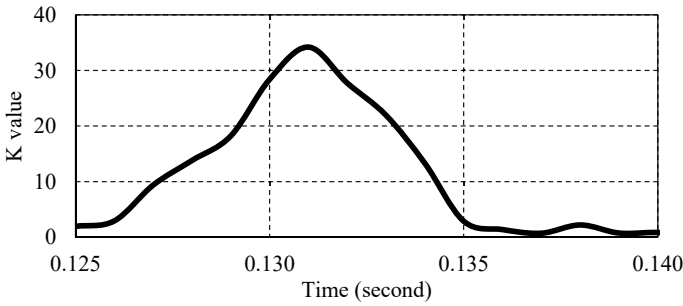


Fig. 5 The variation of K of full deformable pedestrian model in the moment of impact

trajectory change continuously from time of bonnet reaches maximum deflection to the end of impact process.

The simulation shows that in process of testing, the full deformable pedestrian model the head is connected to the body so the head bounces back and squeezes close to the body and moves together. In contrast, the headform impactor is a separate part with a spherical structure that moves freely in impact process. In tests using headform impactor, because of the friction force between the head and the bonnet surface, the headform impactor rotates hard, this rotation continues after the end of the collision, so direction of head center of gravity trajectory change continuously or K keep the high value. Moreover, at some positions due to the great resistance, the headform impactor rotates very strongly, causing the direction of head center of gravity trajectory change to be very large. Equation (3) shows the dependence of  $A_n$  on K and V. After the collision, although V decreases but K increases and keep in very high value, it will make  $A_n$  still large. Therefore, A is still large and will affect to the HIC value. This result shows that there is a difference in the variability characteristics of K, this cause the difference in the variability characteristics of A as well as HIC value or testing results (Fig. 6).

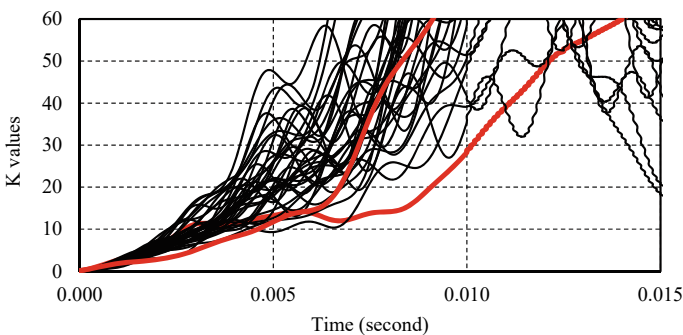


Fig. 6 The variation of K of headform impactor in the moment of impact [8]



## 4 Conclusions and Recommendations

This study has simulated the collision between car and a full deformable pedestrian model to analyze the variation of head kinematics as well as  $K$  which is curvature of pedestrian head model center of gravity trajectory. The results show that in the duration of collision between the head and the bonnet surface  $K$  forms a very symmetrical peak in variation diagram. This result is different from the variable characteristics of  $K$  when tested with the headform impactor. Thus, it can be seen that the results of pedestrian head safety tests with full deformable pedestrian model and headform impactor models will have different results due to the different variation characteristic of  $K$ . Further research should analysis more detailed to answer the question which model gives more accurate results in pedestrian head safety testing and solutions for improving the tests.

**Acknowledgements** This research is funded by Phenikaa University under grant number: 2-06.2021.01

## References

1. Directive 2003/102/EC of the European Parliament and of the Council of 17 November 2003
2. EEVC/WG 17 Report, *Improved Test Methods to Evaluate Pedestrian Protection Afforded by Passenger Cars*, European Enhanced Vehicle-safety Committee (1998, updated 2002).
3. C. Masson, T. Serre, *Pedestrian-Vehicle accident-Analysis of 4 Full Scale Tests with PMHS* (Project French National Institute for Transport and Safety Research, 2007)
4. Y. Matsui, A. Wittek, A. Konosu, *Comparison of Pedestrian Subsystem Safety Tests Using Impactors and Full-Scale Dummy Tests*. SAE Technical Paper Series (2015)
5. T.-L. Teng, T.-H. Nguyen, Development and validation of FE models of impactor for pedestrian testing. *J. Mech. Sci. Technol.* **22**(9), 1660–1667 (2008)
6. T.-L. Teng, T.-K. Le, Development and validation of a pedestrian deformable finite element model. *J. Mech. Sci. Technol.* **23**, 2268–2276 (2009)
7. T.-L. Teng, V.-L. Ngo, Analyzing pedestrian head injury to design pedestrian-friendly hoods. *Int. J. Autom. Technol.* **12**(2), 213–224 (2011)
8. V.-L. Ngo, Analysis of headform impactor kinematics during the collision process, in *International Conference on Advanced Mechanical Engineering, Automation and Sustainable Development* (2021), pp. 389–395
9. Information on <https://en.wikipedia.org/wiki/Curvature>

# Development of Point to Point Algorithm AMR Navigation



Minh Khong, Van-Luc Ngo, Minh-Hiep Le, Van-Tung Nham,  
and Quoc-Dat Do

**Abstract** AMR (Autonomous Mobile Robots) are used popular increasingly, especially in industry to solve logistical problems in factories. The navigation algorithm affects not only the motion characteristics, but also the specifications of AMR. The simpler the algorithm, the smaller the computational volume, the less demanding the hardware, and the lower the cost of AMR. The smoother the movement, the less energy is consumed and the larger the cargo capacity. By simulation, this study will analyze the characteristics of some algorithms currently being used for AMR such as Pure pursuit or Follow the Carrot Algorithms. The advantages and disadvantages of each algorithm will be analyzed to proposing a new algorithm that can overcome the disadvantages of the algorithms being used for AMR navigation. The algorithm was developed in this research has been tested on Phenikaa-X AMR, sensory evaluation gives better results.

**Keywords** AMR · Autonomous mobile robots · Point to point · Navigation algorithm · Logistics in factories · Pure pursuit · Follow the carrot

## 1 Introduction

The problem of control a AMR moving from point to point is one of the most common problems in industry such as moving from a station to a work place or performing logistical tasks between two specified location in factories. There are

---

M. Khong · V.-L. Ngo (✉)

Faculty of Mechanical Engineering and Mechatronics, Phenikaa University, Hanoi 12116, Vietnam

e-mail: [luc.ngovan@phenikaa-uni.edu.vn](mailto:luc.ngovan@phenikaa-uni.edu.vn)

V.-T. Nham · Q.-D. Do

Faculty of Vehicle and Energy Engineering, Phenikaa University, Hanoi 12116, Vietnam

M. Khong · V.-L. Ngo · M.-H. Le · V.-T. Nham · Q.-D. Do

Phenikaa Research and Technology Institute (PRATI), A&A Green Phoenix Group JSC, No. 167 Hoang Ngan, Trung Hoa, Cau Giay, Hanoi 11313, Vietnam

many algorithms that can be applied to control AMR move point to point, such as Pure Pursuit [1], Follow the Carrot [2], Stanley, MPC, etc. Each algorithm has its own advantages and disadvantages and is suitable for a type of AMR structure. The model of AMR in this research is a robot that uses two independent control wheels on both sides to navigate and adjust speed based on changing the speed of each wheel. The Pure Pursuit and Follow the Carrot algorithm which is described in Fig. 1 are more suitable to navigate this type of AMR. By simulation, this research will analyze motion characteristics of this type of AMR using Follow the Carrot algorithm to develop a better navigation algorithm.

Pure Pursuit is a navigation algorithm for AMR in particular and mobile devices moving in general, first introduced in 1992 [1]. Until now, this algorithm is still an effective tracking algorithm used in navigation and control for autonomous vehicles [3–6].

Figure 1a shows the geometry of Pure Pursuit algorithm (a). With this algorithm, the robot will move on a circular path with radius (r) and depends on the look ahead distance (l), from the geometry on Fig. 1 the relationship between r and l can be determined as follows:

$$x^2 + y^2 = l^2 \text{ and } x + d = r \Rightarrow r = \frac{l^2}{2x}$$

If the lookahead distance (l) is small, the moving robot has a small deviation from the target path but fluctuates more than the large value (l) and vice versa. If the look ahead distance (l) is reduced to allow the robot to close the target path, the robot will fluctuate a lot as shown in Fig. 2, which may affect the wares it carries. Conversely, if look ahead distance (l) is increase to reduce oscillation, the robot will not move closed to the target path and may deviate from the space that allows the robot to operate. Thus, this algorithm is not really suitable for robots operating in factories to do logistical tasks in some case.

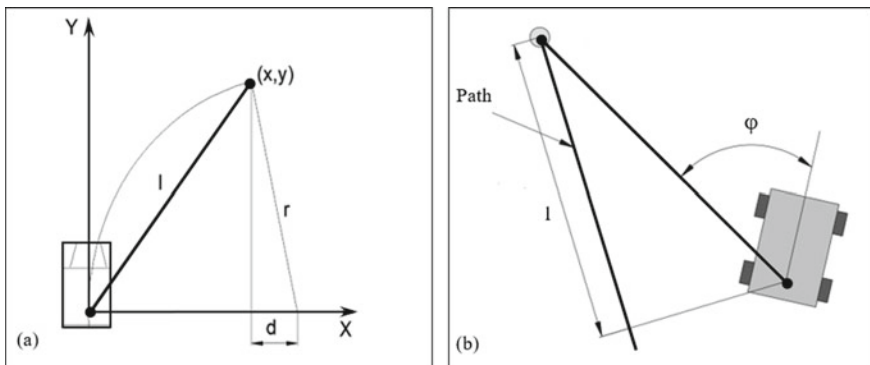


**Fig.1** Algorithm geometry of Pure Pursuit (a) and Follow the Carrot (b) [1, 2]

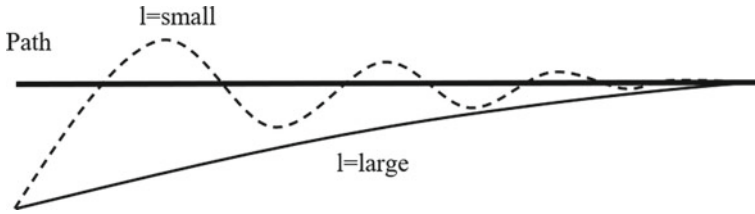


**Fig. 2** The response of the Pure Pursuit algorithm tracker [1]

Compared with the Pure Pursuit algorithm, the Follow the Carrot algorithm has a smaller computational volume because it does not have to perform the coordinate system conversion operations, but it requires a device to determine the direction of the robot at the current location [1]. With the algorithm of Follow the Carrot, the robot always tends to turn towards the goal point by calculating the angle deviation of direction ( $\varphi$ ) between the robot direction and the direction to the goal point before moving towards to the goal point as described in Fig. 1b. Theoretically, the Follow the Carrot algorithm can give more accurate results. However, experiments have shown that due to inertia, accuracy of the system, etc., the robot tends to rotate over the direction to the goal point and the motion is wobbly when traveling at the high of velocity [2].

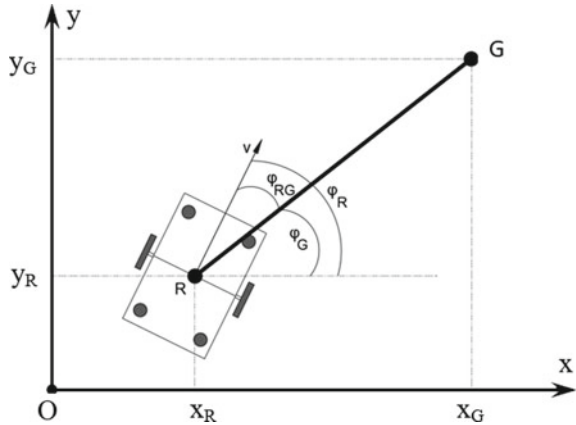
The above analysis shows that with the Pure Pursuit algorithm the computation volume is high and the fluctuations are large or larger deviated to the target path. For the Follow the Carrot algorithm, although the calculation volume is smaller, but it requires equipment to determine the direction of the robot at the current position and still vibrates when moving at high velocity. This study will propose an algorithm developed on the idea of taking advantage and limiting the disadvantages of Pure Pursuit an Follow the Carrot algorithm.

## 2 Development of Point to Point Navigation Algorithm

The proposed algorithm in this study comes from the idea of developing the advantages and limiting the disadvantages of the Pure Pursuit an Follow the Carrot algorithm to achieve the goal of better control and reduce the cost of AMR. Accordingly, this algorithm will control the robot to move with large of look ahead distance to get smoother movement. In order to reduce the error of the robot trajectory and the target path, both linear and angular velocity of robot are controlled for the robot to move gradually to close to the target path. With the this algorithm the robot also does not need equipment to determine the direction of the robot at the current position, Fig. 3 show geometry of proposal algorithm.

Base on the geometry of proposal algorithm, some parameter can be calculated:

**Fig. 3** Geometry of proposal algorithm



- The distance from the robot to the goal point G:  $l_{RG} = \sqrt{(x_G - x_R)^2 + (y_G - y_R)^2}$ .
- Deviation angle between the vehicle direction and the line connecting the vehicle to the goal point:  $\varphi_{RG} = \varphi_R - \varphi_G = \varphi_R - a \tan\left(\frac{y_G - y_R}{x_G - x_R}\right)$ .

The linear and angular velocity ( $v, w$ ) should be limited to not exceed the allowable value ( $v_{max}, w_{max}$ ) and the magnitude is proportional to the distance from the robot position (R) to the goal point (G).

Choose the motion control law for ( $v$ ) and ( $w$ ) of the robot is:

$$\begin{cases} v = v_{max} \sin\left(\frac{l_{RG} \pi}{l_{max} 2}\right) \\ w = w_{max} \sin\left(\frac{\varphi_{RG} \pi}{\varphi_{max} 2}\right) \end{cases}$$

The meaning of the above parameters is explained as follows:

- $l_{RG}$  is the distance from the current point of robot (R) to the goal point (G).
- $l_{max}$  is the maximum of  $l_{RG}$  or  $l_{max}$  is the distance from the start point of robot to goal point (G).
- $\varphi_R, \varphi_G$  and  $\varphi_{RG}$  are explained and illustrated in Fig. 3 and  $\varphi_{max}$  is maximum of  $\varphi_{RG}$ .

The linear and angular velocity of robot will gradually decrease as the robot reaches the goal point (G) and does not exceed the allowed value ( $v_{max}, w_{max}$ ). The more moving, the more  $w$  decreases and the robot direction closes to the target path. At the time robot reaches the goal point (G) then  $l_{RG} = 0$  and  $\varphi_{RG} = 0$  so  $v = 0$  and  $w = 0$ , in other words the robot will stop at the goal point (G) in the direction of the target path.

To evaluate the purpose response of the proposed algorithm, this study will perform simulations with the following example parameters:

- The coordinates of the starting point of the robot:  $\begin{cases} x_R = 0(m) \\ y_R = 0(m) \\ \varphi_R = 90^\circ \end{cases}$
- The coordinates of the goal point of the robot:  $\begin{cases} x_G = 2(m) \\ y_G = 3(m) \end{cases}$

### 3 Results and Discussion

Figure 4 shows the movement of the robot with the proposal and Pure Pursuit algorithm. This result shows that the robot controlled by the proposed algorithm follows the target path more closely and stops when it reaches the goal point. In contrast, the robot controlled by the Pure Pursuit algorithm is more deviated from the target path and it did not stop at the goal point. The variation of  $I_{RG}$  with robot used the proposal and Pure Pursuit algorithm as shown in Fig. 5 indicate that that the robot controlled by the Pure Pursuit algorithm reached the goal point earlier at the time of 4.2 s, and then went over it again because it can stopped. The robot controlled by the proposal algorithm arrives at the goal point later, but the robot is getting more and more closer to the goal point. The proposal with the control law of the robot as proposed above, both the angular velocity ( $w$ ) and the linear velocity ( $v$ ) decrease with time, making the robot reach the goal point later.

Figures 6 and 7 show the comparison of the linear and angular velocity variation when robot is controlled by proposal and Pure Pursuit algorithm. The angular velocity of the proposal algorithm change faster in the first period, resulting in the robot quickly tracking to the path direction. This explains why the robot controlled by

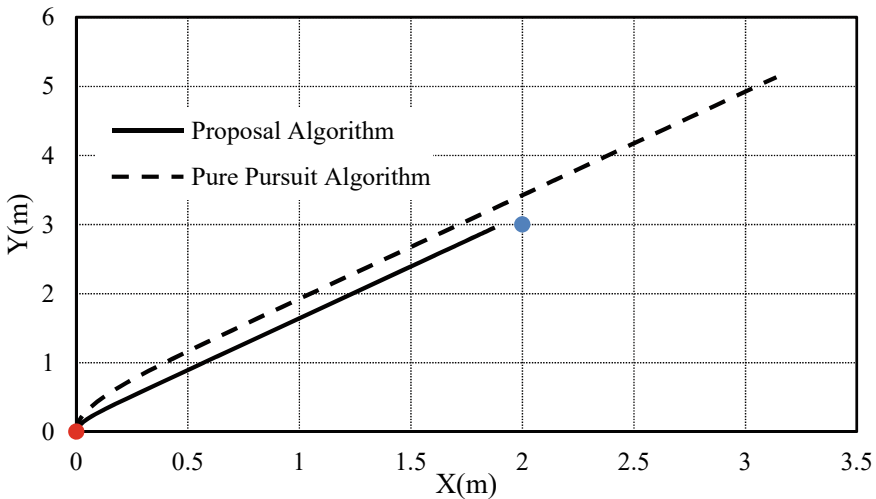


Fig.4 The movement of the robot with the proposal and Pure Pursuit algorithm

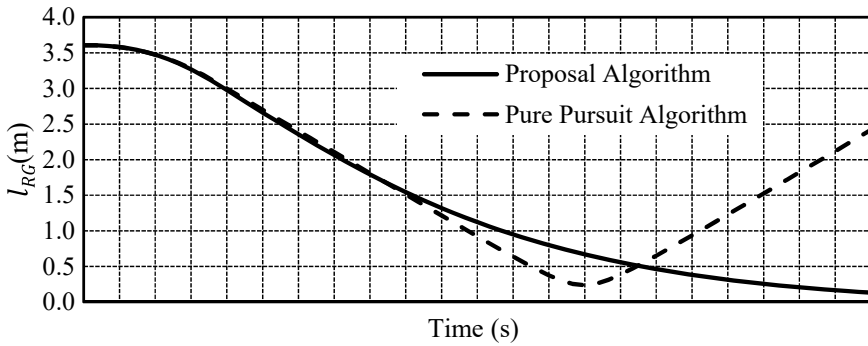


Fig.5 The variation of  $l_{RG}$  of the proposal and Pure Pursuit algorithm

the proposal algorithm closed to the target path compared to that controlled by pure pursuit algorithm. When robot is controlled by both algorithms then angular velocity is fast to zero but proposal algorithm driven angular velocity goes faster. This result shows that the proposal algorithm is better the Pure Pursuit algorithm in driven robot direction. Figure 7 shows that the linear velocity controlled by the proposal algorithm varies smoother than that controlled by the Pure Pursuit algorithm and steadily decreases towards zero as the robot approaches the goal point. The curve of linear velocity variation controlled by pursuit algorithm has a folding position. This feature indicates that the robot will be jerked at this position.

The proposal algorithm was tested to navigate the AMR which developed by Phenikaa-X company as shown in Fig. 8. Sensory evaluation gives better results such as moother speed change, AMR stops at target position. This is result of the velocity in the proposal algorithm varies with the sine function while the velocity in the PP and FTC algorithm is constant. The AMR stops at target position also consistent with the analysis above.

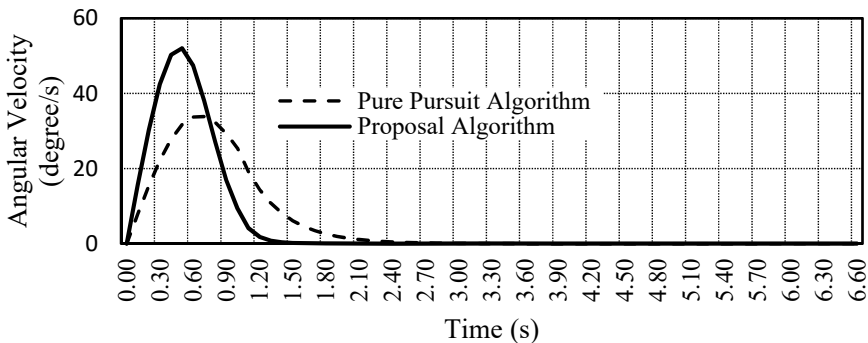


Fig. 6 The variation of angular velocity of the proposal and Pure Pursuit algorithm

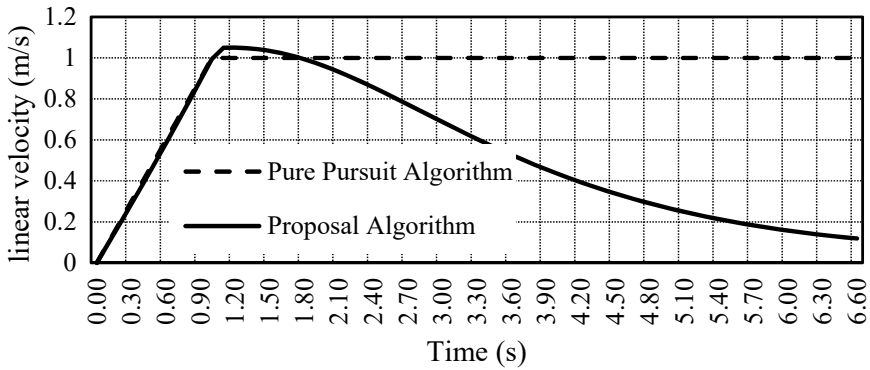


Fig. 7 The variation of linear velocity of the proposal and Pure Pursuit algorithm



Fig. 8 The AMR was developed by Phenikaa-X Company

### 4 Conclusions and Recommendations

This study has proposed a new algorithm to control AMR to move in point to point in straight path. The proposal algorithm is developed from those commonly used in AMR control. Simulation results have shown that the proposed algorithm controls the AMR better in tracking the path, navigation, and the robot can stop when it reaches the goal point. With this algorithm, the robot does not need a device to determine the direction of the robot at the current position as the Follow the Carrot algorithm. However, this study only consider base on theoretical analysis and simulation. The proposal algorithm was tested to navigate the real AMR and gives better results such as moother speed change, AMR stops at target position, these are the goals of this



research. Further research should analyzed by experiment and compare with simulation results to have more accurate conclusions about the advantages of the proposed algorithm. The analysis and evaluation of the results also need to be analyzed more detailed such as the parameters of oscillation, jerking, productivity.

## References

1. R. Craig Conlter, *Implementation of the Pure Pursuit Path Tracking Algorithm* (Robotics Institute Carnegie Mellon University, 1992)
2. M. Lundgren, *Path Tracking for a Miniature Robot*. Excerpt from Master's thesis 2003 Supervisor: Thomas Hellström (2003)
3. S. Dominguez-Quijada, A. Ali, G. Garcia, P. Martinet, Comparison of lateral controllers for autonomous vehicle: experimental results, in *IEEE 19th International Conference on Intelligent Transportation Systems (ITSC 2016)* (2016)
4. W. Naeem, R. Sutton, S.M. Ahmad, *Pure Pursuit Guidance and Model Predictive Control of an Autonomous Underwater Vehicle for Cable/Pipeline Tracking* (Marine and Industrial Dynamic Analysis Research Group Department of Mechanical and Marine Engineering, 2003)
5. T. Hellström, O. Ringdahl, Follow the past: a path-tracking algorithm for autonomous vehicles. *Int. J. Veh. Auton. Syst* **4** (2006)
6. G. Klancar, A. Zdesar, S. Blazic, I. Skrjanc, *Wheeled Mobile Robotics* (Butterworth-Heinemann is an imprint of Elsevier, 2017)

# Systematic Design of a Sitting-Type Lower Limb Rehabilitation Robot for Stroke Patient



Duc Luu, Trung Nguyen, and Tam Bui

**Abstract** This study presented the design of a sitting type robot to support the lower limb rehabilitation for patients after stroke during the early stages. The robot was designed based on the exoskeleton structure, with hip, knee, and ankle joints, and at the calf and thigh wraps. The segments' length can be adjusted to fit each patient object. The article presented the structure and operating principle of the joints. Kinetics and dynamics analysis were used to calculate and choose the power source for the device. Numerical and computational tests were used to check the safety of the structure. In addition, this paper uses a numerical simulation method to derive the motion trajectory of an ordinary person, which is the input data used in the device control process.

**Keywords** Lower limb rehabilitation · Exoskeletons robot · Sitting type · Gait cycle · Design engineering

## 1 Introduction

A stroke is a serious brain injury that occurs when blood flow to the brain is interrupted or a blood vessel in the brain bursts. Within minutes, brain cells begin to slowly die and cause many dangerous complications for the patient. In Vietnam, stroke is the leading cause of death with 200,000 new cases per year [1]. In which 50% of cases are fatal and 90% of survivors experience post-stroke sequelae such as cognitive disturbances, impaired mobility, and problems with communication and eating.

Rehabilitation for patients is to minimize sequelae, create equal opportunities, and soon bring patients back to integrate into family and social life. Rehabilitation for patients begins as soon as possible after a stroke. Especially in the early stages

---

D. Luu · T. Nguyen (✉)

HaNoi University of Science and Technology, Ha Noi, Vietnam  
e-mail: [trung.nguyenthanh@hust.edu.vn](mailto:trung.nguyenthanh@hust.edu.vn)

T. Bui

Shibaura Institute of Technology, Tokyo, Japan

© The Author(s), under exclusive license to Springer Nature Switzerland AG 2024  
B. T. Long et al. (eds.), *Proceedings of the 3rd Annual International Conference on Material, Machines and Methods for Sustainable Development (MMMS2022)*, Lecture Notes in Mechanical Engineering, [https://doi.org/10.1007/978-3-031-57460-3\\_26](https://doi.org/10.1007/978-3-031-57460-3_26)

235

after severe stroke sequelae, patients must undergo passive exercises. This creates pressure and difficulties for doctors and family members in the treatment process.

With the importance of rehabilitation treatment, treatment support devices for patients are increasingly interested, especially in this study focusing on rehabilitation after stroke for the patient's lower extremities. In the world, there have been researches and publications about rehabilitation devices for lower extremities. However, each type of rehabilitation robot has its own characteristics and is suitable for each patient in each stage of the rehabilitation process. Some typical devices can be followed such as: robot MotionMaker, Lambda-robot, robot Lokomat [2–4]. These types of researched devices are expensive, cumbersome in structure and not really suitable for patient recovery at the early stages of therapy. Through researching and studying published documents, it shows that the rehabilitation process of patients in severe form in the early stages has not been interested and develop in accordance with social needs.

The objective of this study is to present the design of a device that supports rehabilitation for lower limbs in the form of sitting easily for patients, restoring movement for hip joints, knee joints, and ankle joints for patients with severe sequelae in the early stages of treatment. The device can be individually tailored for each patient with the ability to change links lengths and have exercises for each type of exercise. The mobility at the joints of the device corresponds to the joint range of motion in the lower limbs of normal people, helping the patient to feel the most comfortable when using.

## **2 Calculation and Structural Design of Rehabilitation System**

### **2.1 Anthropometry**

In the process of researching and designing, it is necessary to collect parameters of body size and joint range of normal people. Dimensional parameters are used as the basis for calculating and designing device. The size of the links in the robot is calculated to match the patient's lower limb size, they need to satisfy the correctness in rehabilitation and safety for the patient when used.

The mobility of each joint is characterized by the musculoskeletal and ligamentous structure of each joint. It is defined by the number of degrees of freedom (DOF) of the joint when moving separately in a 3-dimensional coordinate system. However, in fact regular daily activities are mainly: walking, climbing stairs, walking. During such operations, the lower limb moves only on a plane parallel to the sagittal plane. Meanwhile, to set up all the degrees of freedom of the lower extremities on the robot structure makes the robot structure more complicated but setting the entire degrees of freedom of the lower limbs is not really necessary for the process patient recovery in the early stages. Therefore, in this study for order to optimize the design and

**Table 1** Range of angular in the lower limbs

No.	Joint	Movement	Min[°]	Max[°]
1	Hip	Extension—Flexion	−32	128
2	Knee	Extension—Flexion	0	142
3	Ankle	Dorsiflexion—Plantarflexion	−60	20

manufacturing costs, the focus will be on developing the device structure to meet the exercises for the lower limb operating on a plane. Therefore, the data in Table 1 have been obtained for solving the operation of 3 joints only on the sagittal plane.

Based on statistics from the group of survey subjects, the group of patients suitable for the studied device has a height of 1350 mm to 1850 mm and a maximum weight of 80 kg [5]. From the height of the group of patients determined above, based on the ratio coefficient obtained from the book [6], a table can be calculated to solve the size value of the sutures in the lower extremities.

## 2.2 Proposed Rehabilitation Robotic

The device to support lower limb rehabilitation for patients with sequelae after stroke has had a few published studies and design models. However, each design model can only meet a few specific rehabilitation exercises for each patient. In general, rehabilitation devices are designed based on basic principles. In this study, the focus is on rehabilitation for the lower extremities, so we synthesize and classify the structures into basic groups as diagrams (Fig. 1).

With the goal of the robot sitting and restoring movement for the joints in the lower extremities, and the ability to follow the exercises. With each different exercise, the trajectory of joint movement will be different, so the design principle according to the exoskeleton structure is the most reasonable. The exoskeleton is a frame-like structure that covers the lower extremities, including the structure of the suture and the joint. Because the patient will be in a sitting state, the hip joint will have a reduced range of motion compared to the standard position, so the structure of the recliner to help the patient recline is the best solution. It helps to increase the trajectory of the joint, reduce the body load on the robot skeleton and at the same time help the patient have a more comfortable posture.

## 2.3 Design Robot Structural

The sitting limb rehabilitation device for stroke patients has been designed based on anthropometric data. The device model structure is described as follows (Fig. 2).

The model structure includes:

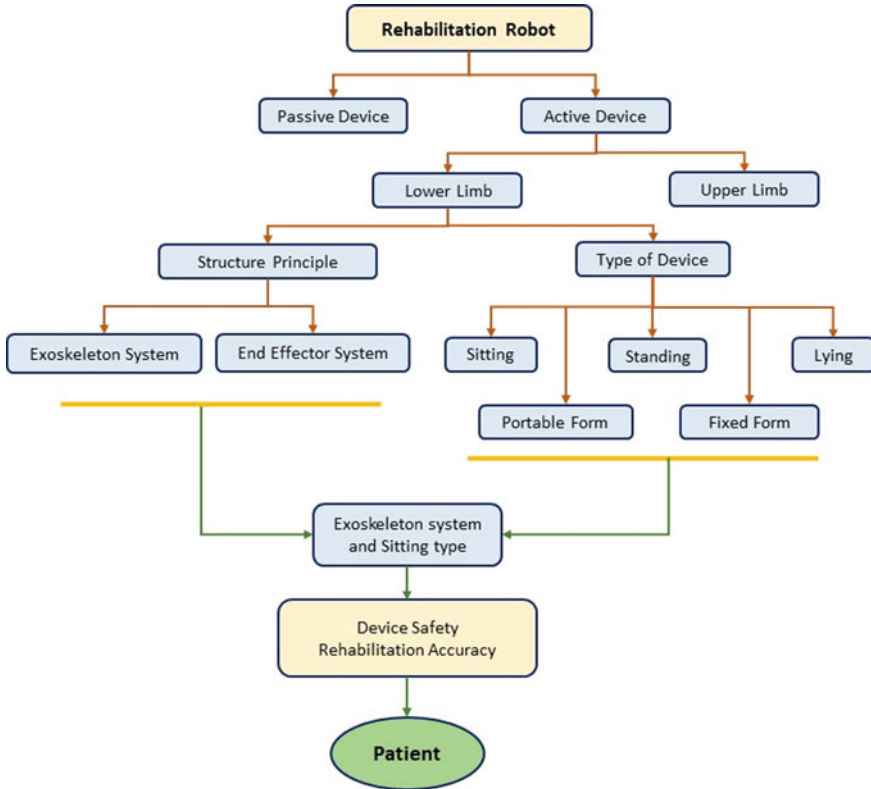
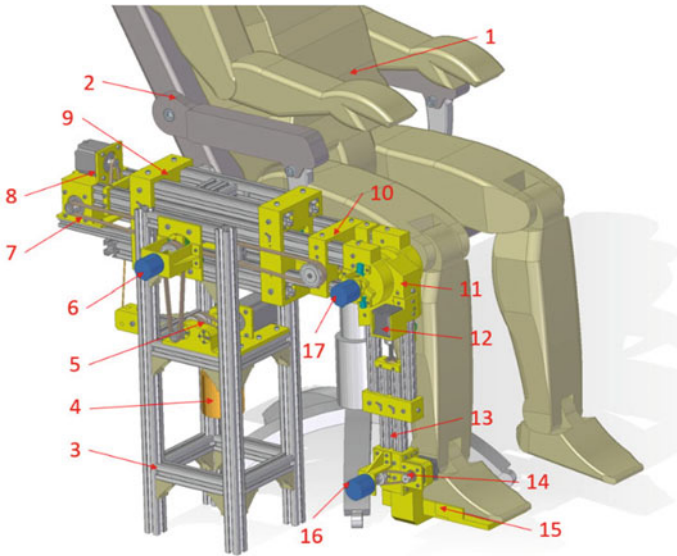


Fig. 1 Classification of rehabilitation equipment and proposed model principle

1. Patients
2. Recliner
3. Base links
4. Counterweight system
5. Hip joint motor block
6. Hip joint encoder
7. Knee joint motor block
8. Thigh adjustment motor
9. Fixed thigh links
10. Movable thigh links
11. Fixed calf links
12. Calf adjustment motor
13. Movable calf links
14. Ankle joint motor block
15. Base of foot
16. Ankle joint encoder



**Fig. 2** Proposed rehabilitation robotic

17. Knee joint encoder.

The structure of the rehabilitation device is made in the form of an exoskeleton including 4 links and 3 joints. The separate seat section offers flexible patient mobility, including the ability to recline at an angle to reduce the load on the robot frame. In which there are 2 main parts, which are thigh links and calf links, which can adjust the length and size according to the patient's height. The device model has 3 rotary joints: hip joint, knee joint, ankle joint. The transmission used for rotary joint motion is a toothed belt transmission combined with a tooth pulley, although the structure of the transmission is compact, the transmission ratio is not high. Therefore, the ability to increase engine torque will decrease, so a large torque motor is required. The motor used is a stepper motor, capable of moving in the form of micro step, so the accuracy of the rotation angle output at the joint can meet the treatment exercise. The transmission used for the length adjustment of the thigh and leg links uses a lead screw type transmission, which converts the rotation of the motor into a reciprocating motion so that the movable part of the suture slides over the fixed part determined. At each output angle on the 3 joints, 3 additional rotary encoders are installed to feedback the current position of each joint, helping to determine the accuracy when controlling the robot.

### 3 Analysis of the Robot's Working Trajectory

#### 3.1 Workspace of Robot

After the robot design and calculation process, once the robot structure and motion transmitter have been obtained, it is necessary to define the robot workspace.

Analyzing the robot's workspace helps determine the limits of movement, the trajectory of the exercises will be in the workspace of the machine. Here consider on the descartes coordinate system with X, Y axes being the axes of the point coordinates in space. The robot's workspace is all the point coordinates that the robot can generate when operating within the established angle limits. The stroke of the stitches will be determined based on the change of angle at each inner joint as shown in Table 2.

From the long size and angular limit of each joint, the simulation of the number of trajectories on Matlab software obtains all the points in the robot's workspace. The end point of the previous links will be the position of the next joint, so the end point of the link is determined by the point coordinates of the next joint on the robot workspace. Figures 3 and 4 show the workspace of each joint and the main workspace of the robot. Since the hip joint is determined to be stationary with the patient's sitting or lying position, the position of the hip joint is considered as the origin in the orbital space of the robot. The red line shown in Fig. 3 is the working trajectory of the thigh's link when the hip joint rotates within the angular range (from  $-20^\circ$  to  $40^\circ$ ), which is the orbital curve of the knee joint. The blue angular cloud is the set of all the trajectories of the calf link produced when the hip joint ( $-2^\circ$  to  $40^\circ$ ) and knee joint motion (from  $0^\circ$  to  $110^\circ$ ) are combined works at the same time. The end point of the calf link is the ankle joint, so the blue point cloud is the working space of the ankle joint. Figure 4 shows the purple point cloud, which is the collection of all the trajectories of the foot suture created when all 3 joints move simultaneously: hip joint (from  $-20^\circ$  to  $40^\circ$ ), knee joint (from  $0^\circ$  to  $110^\circ$ ) and toe joints (from  $-60^\circ$  to  $20^\circ$ ). Considering the foot length is calculated as the toe joint, so the end point of the foot stitch is the toe joint, and the robot's end point. So, the purple point cloud set in Fig. 4 is the robot workspace in 2-D space. The motion trajectories of all exercises will be within the working space of the given joints. See that there are no singularities in the robot workspace.

**Table 2** Limiting movement of joints in robots

Joint	Range of motion
Hip	$-20^\circ$ to $40^\circ$
Knee	$0^\circ$ to $110^\circ$
Ankle	$-60^\circ$ to $20^\circ$

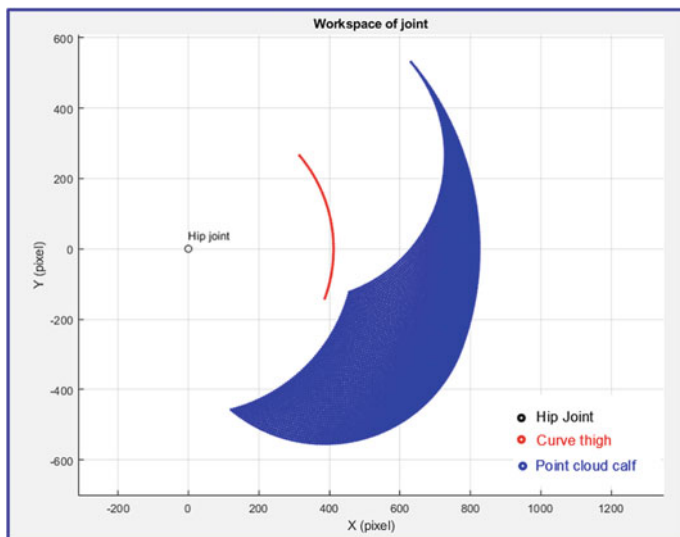


Fig. 3 Workspace of knee, ankle joint

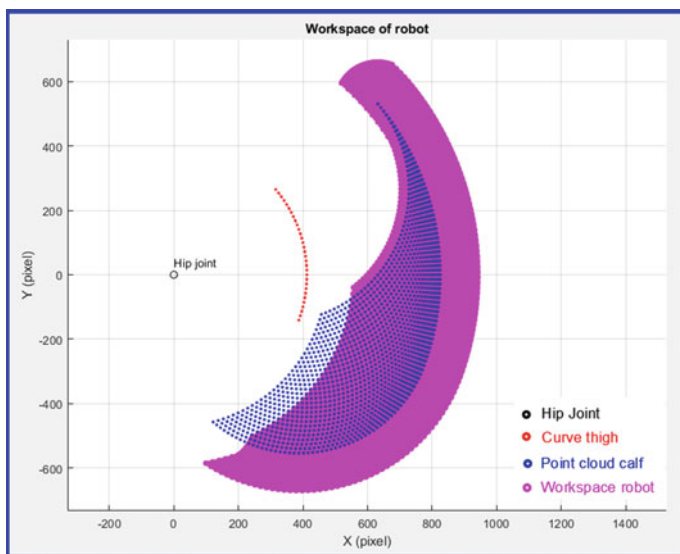


Fig. 4 Workspace of robot



### 3.2 Data Analysis of Robot Exercises

After analyzing the robot’s workspace, it is very important to build exercises for the robot to work. Rehabilitation exercises will directly affect the patient, affecting the recovery process during the period. In this study, set up two basic exercises for the robot to work. The exercises are referenced in [7, 8], including single-joint exercises and exercises that combine joints to work at the same time. The trajectory of the exercises will always be in the workspace of the robot. As a result of the operation simulation, the angle values of the joints are obtained according to the progress of the exercise. With a single exercise for each hip joint (Fig. 5), knee joint (Fig. 6), and ankle joint (Fig. 7). Proceed to rotate the link according to the rotation angle of the joint, obtain the total motion trajectory of the robot and solve the angle value over time. At the exercise combining the joints at the same time, we choose the cycling exercise in a circle (Fig. 8). The trajectory of the exercise is in the robot’s workspace, approximated to 24 points on the trajectory. The angle values of the 3 joints are distributed according to 24 points as shown in the graph (Fig. 8). The angle value convention is followed by the anthropometric convention mentioned above. We get the following results from the analysis:

The simulation results show that in the separate exercise of each joint, only the joint is regulated to move, the other joints are stationary, satisfying the correctness of the individual recovery for each joint.

The exercise combining joints in a circular orbit gives the results that the values of all joints are within the given limit. The matching value varies evenly, the distribution curve is smooth, and the start and end points in the value cycle coincide.

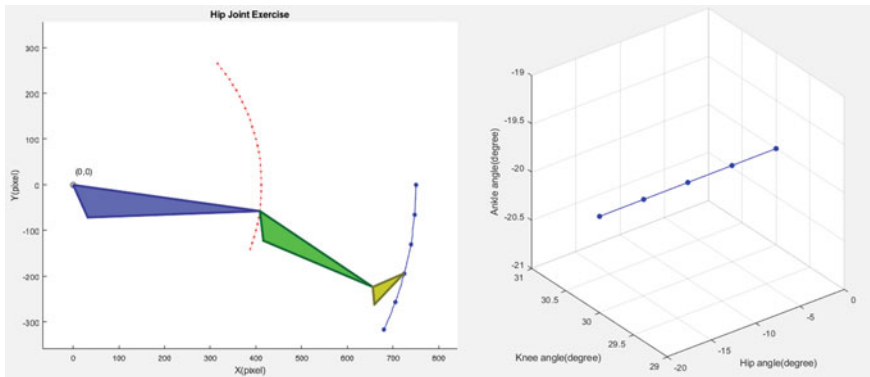


Fig. 5 Analysis of the exercise trajectory for the hip joint

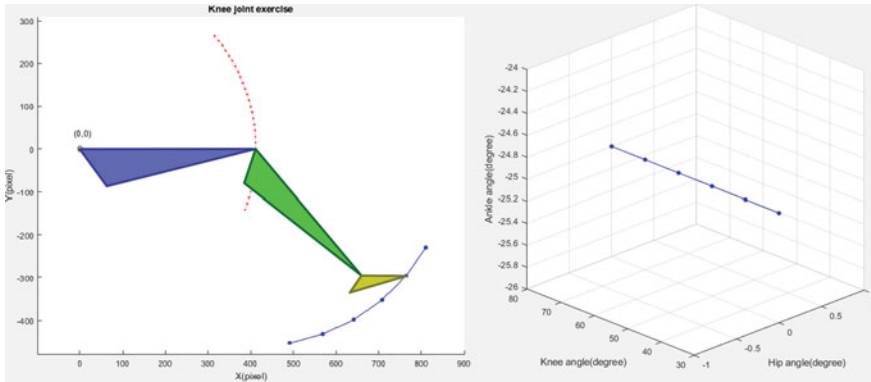


Fig. 6 Analysis of the exercise trajectory for the knee joint

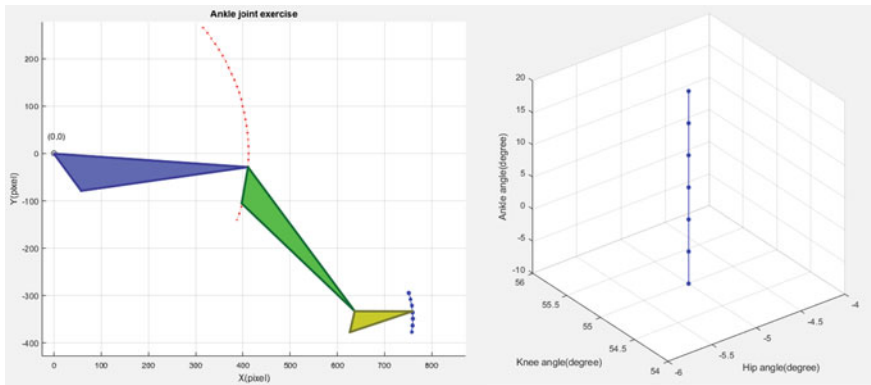


Fig. 7 Analysis of the exercise trajectory for the ankle joint

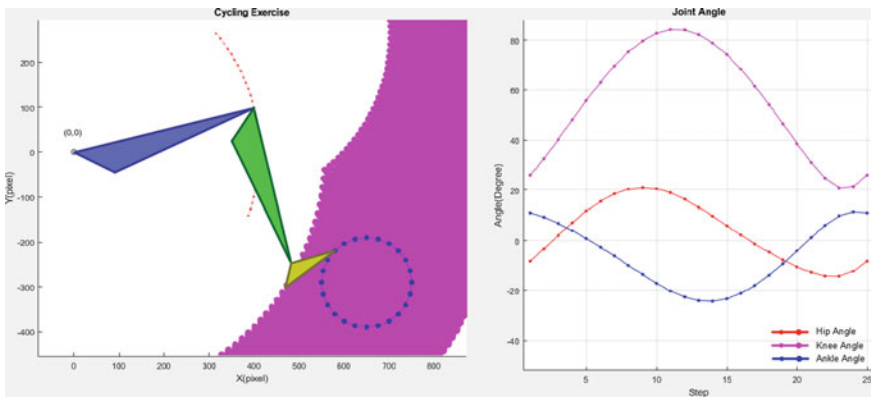


Fig. 8 Trajectory analysis of joint exercises

## 4 Result and Discussion

After the process of researching and designing a sitting rehabilitation device for patients after a stroke at an early stage. The initial prototype model has been successfully built and put into trial operation. The initial operation process is too simple exercises such as rotating each joint, combined with slow walking, showing that the device runs stably and safely for the patient. Besides, the compact weight is easy to transport and disassemble, making the robot more flexible. Regarding the correctness in rehabilitation therapy, the robot can respond to basic exercises such as movement of each joint, stable operation with exercises such as walking steadily. The device can be used in both sitting and reclining positions. The ability to safely recover at an early stage after a stroke, and the low cost give the device a prominent advantage over conventional devices. However, at present the prototype model only stops rehabilitation for one side of the lower limb and does not have high aesthetics. The next direction of future research is to improve the design to help restore the disease for both lower limbs, and at the same time commercialize the product in the future. Through the above research paper, it will be the basis for further development of research and design of assistive devices for humans.

## 5 Conclusion

In the above study, a systematic design sitting type of a lower limb rehabilitation robot for post-stroke patients was presented in the early stages of treatment. The study also goes into the analysis of human anthropometry, which is the basis for calculation and device design. The design calculations of the study are based on meeting the goal of a compact, easy-to-use, low-cost device. Endurance testing for the device shows that the device is safe for patient use. At the same time, the ability to exercise exercises for each joint separately or exercises to combine joints together helps the patient's recovery training process become better. The angular position feedback sensor system provides feedback on the exercise trajectories, ensuring the accuracy of the exercises performed. Next, the research will develop a rehabilitation system for the other leg that is similar in structure and kinematics, and will research and develop rehabilitation exercises for the patient that are suitable for the structure and workspace of robot.

## References

1. K. Le, *Increasing Number of Stroke Centers, Advances in Treatment Save More Patients in Vietnam* (VN Express International, 2022)
2. C. Schmitt, P. Métrailler, The motion Maker<sup>TM</sup>: a rehabilitation system combining an orthosis with closed-loop electrical muscle stimulation, in *8th Vienna International Workshop on Functional Electrical Stimulation* (2004), pp. 117–20. No. LSRO2-CONF-2006-011
3. M. Bouri, B. Le Gall, R. Clavel, A new concept of parallel robot for rehabilitation and fitness: the Lambda, in *Robotics and Biomimetics (ROBIO)* (2009)
4. R. Riener, L. Lunenburger, S. Jezernik, M. Anderschitz, G. Colombo, V. Dietz, Patient cooperative strategies for robot-aided treadmill training: first experimental results. *IEEE Trans. Neural Syst. Rehabil. Eng.* **13**(3), 380–394 (2005)
5. Viện nghiên cứu khoa học kỹ thuật bảo hộ lao động, Atlas nhân trắc học người Việt nam trong lứa tuổi lao động: Dấu hiệu tầm hoạt động khớp và trường thị giác, Nhà xuất bản khoa học và kỹ thuật (1997)
6. D.A. Winter, D.A. Winter, in *Biomechanics and Motor Control of Human Movement* (New York: Wiley, 1990)
7. T. Eiammanussakul, V. Sangveraphunsiri, A lower limb rehabilitation robot in sitting position with a review of training activities. *J. Healthc. Eng.* **2018**, 1–18 (2018). <https://doi.org/10.1155/2018/1927807>
8. J.K. Mohanta, S. Mohan, P. Deepasundar, R. Kiruba-Shankar, Development and control of a new sitting-type lower limb rehabilitation robot. *Comput. Electr. Eng.* **67**, 330–347 (2018). <https://doi.org/10.1016/j.compeleceng.2017.09>

# Kinematics Analysis of 7-DOF Collaborative Robotic Manipulators with Offsets at Shoulder and Wrist



Nguyen Quang Hoang, Do Tran Thang, Dinh Van Phong,  
and Thai Phuong Thao

**Abstract** In this paper, the inverse kinematics of a 7-DOF redundant manipulator with offsets at shoulder and wrist is presented based on the Jacobian matrix. Three Euler angles of roll-pitch-yaw are used for parameterization of the orientation of the end-effector. Then the linear relationship between joint velocities and Cartesian velocity is given for the inverse kinematic problem at velocity level. The null space of the Jacobian matrix is also used to exploit the advantages of the redundancy of the manipulator. The effectiveness of the proposed approach is verified by some numerical simulations.

**Keywords** Redundant manipulator · Forward kinematics · Inverse kinematics · Jacobian based method

## 1 Introduction

In recent years, with the development of actuator technology such as hollow shaft motors with high torque, collaborative robots have made rapid developments. Compared with traditional industrial robots, this type of collaborative robot has advantages such as: as lightweight, flexible, safe, easy to install and relocate.

To increase dexterity when operating, some cobot arms are designed with 7 degrees of freedom (DOF) with a structure like a human arm. Without offsets at shoulder and wrist, this structure allows us to find analytical solutions of the inverse kinematic problem by the method of position and orientation decoupling (Pieper's method, [1]). However, this structure challenges the mechanical design because it is difficult to allocate three axes intersect at one point. Contrariwise, it is more easier

---

N. Q. Hoang (✉) · D. Van Phong · T. P. Thao  
School of Mechanical Engineering, Hanoi University of Science and Technology, Hanoi, Vietnam  
e-mail: [hoang.nguyenquang@hust.edu.vn](mailto:hoang.nguyenquang@hust.edu.vn)

D. T. Thang  
Institute of Mechanics, Vietnam Academy of Science and Technology, Hanoi, Vietnam

© The Author(s), under exclusive license to Springer Nature Switzerland AG 2024  
B. T. Long et al. (eds.), *Proceedings of the 3rd Annual International Conference on Material, Machines and Methods for Sustainable Development (MMMS2022)*, Lecture Notes in Mechanical Engineering, [https://doi.org/10.1007/978-3-031-57460-3\\_27](https://doi.org/10.1007/978-3-031-57460-3_27)

to design and manufacture a manipulator with offsets at shoulder and wrist. Though, the structure with offsets makes the difficulties in inverse kinematics problem.

The inverse kinematics problem of a redundant manipulator, such as a cobot 7-DOF, has attracted several researchers [1–4]. Several methods are introduced to solve inverse kinematics problem such as: analytical method, position and orientation decoupling, and numerical method based iterative Newton–Raphson, Jacobian Transpose [2, 3], Pseudoinverse, Damped Least Squares, or convert to optimal problem with constraints. The analytical method can be applied only in some special structures, in which if the position and orientation can be decoupled [1, 5, 6].

For inverse kinematics of a redundant robotic manipulator, the Jacobian-based method has some advantages. Because the relationship between joint velocity and Cartesian velocity is linear, it is easy to solve for joint velocity using Jacobian transposed or pseudo-inverse. The avoidance of obstacles, of joint mechanical limits, and of singularity can be handled easily with damped least squares inverse and null space of Jacobian matrix.

## 2 Kinematic Analysis

### 2.1 Direct Kinematics

The direct kinematics of serial manipulators is easy to solve by the Denavit-Hartenberg (DH) method. For the considered 7-DOF manipulator (Fig. 1), the DH parameters is shown in Table 1. Based on this table, the position and orientation of the  $k$ th link-fixed frame are given by:

$$\mathbf{T}_k^0(\mathbf{q}) = \mathbf{A}_1^0(q_1)\mathbf{A}_2^1(q_2) \dots \mathbf{A}_k^{k-1}(q_k) = \begin{bmatrix} \mathbf{R}_k^0(\mathbf{q}) & \mathbf{r}_{O_k^0}^{(0)}(\mathbf{q}) \\ \mathbf{0} & 1 \end{bmatrix}, \quad k = 1, 2, \dots, 7 \quad (1)$$

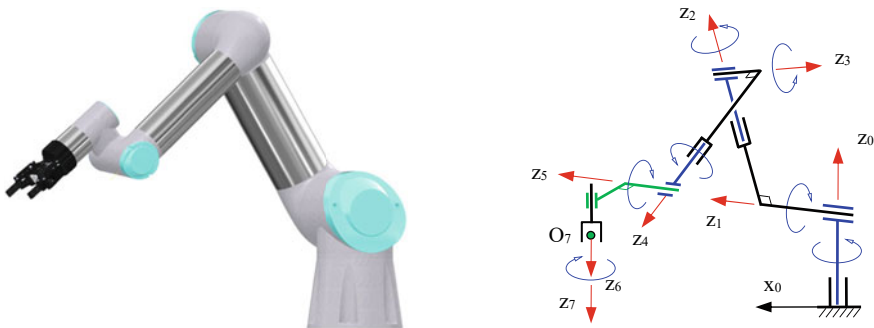


Fig. 1 7-DOF manipulator and link-frames based on DH convention

**Table 1** DH parameters

Link $i$	$\theta$ (rad)	$d$ (m)	$a$ (m)	$\alpha$ (rad)
1	$q_1$	$d_1$	0	$\pi/2$
2	$q_2$	$d_2$	0	$\pi/2$
3	$q_3$	$d_3$	0	$\pi/2$
4	$q_4$	$d_4$	0	$\pi/2$
5	$q_5$	$d_5$	0	$\pi/2$
6	$q_6$	$d_6$	$a_6$	$\pi/2$
7	$q_7$	$d_7$	0	0

where  $\mathbf{A}_i^{i-1}(q_i)$  is the relative homogeneous transformation matrix from link  $i$  to link  $i - 1$  defined by:

$$\mathbf{A}_i^{i-1}(\theta_i) = \begin{bmatrix} \cos \theta_i & -\sin \theta_i \cos \alpha_i & \sin \theta_i \sin \alpha_i & a_i \cos \theta_i \\ \sin \theta_i & \cos \theta_i \cos \alpha_i & -\cos \theta_i \sin \alpha_i & a_i \sin \theta_i \\ 0 & \sin \alpha_i & \cos \alpha_i & d_i \\ 0 & 0 & 0 & 1 \end{bmatrix} \quad (2)$$

Linear velocity and angular velocity of the end-effector are given by

$$\mathbf{v}_E^{(0)} = \mathbf{J}_T(\mathbf{q})\dot{\mathbf{q}} \quad (3)$$

and

$$\boldsymbol{\omega}^{(0)} = \mathbf{J}_R(\mathbf{q})\dot{\mathbf{q}} \quad (4)$$

where  $\mathbf{J}_T(\mathbf{q})$  and  $\mathbf{J}_R(\mathbf{q})$  are translational and rotational Jacobian matrices.

## 2.2 Kinematic Analysis

Let  $\boldsymbol{\eta}_1 = [x_E \ y_E \ z_E]^T$  and  $\boldsymbol{\eta}_2 = [\psi \ \theta \ \phi]^T$  be the vector containing position and orientation of the end-effector. The rotation matrix of the end-effector as function of  $\boldsymbol{\eta}_2$  as follow:

$$\mathbf{R} = \mathbf{R}_z(\psi)\mathbf{R}_y(\theta)\mathbf{R}_x(\phi)$$

The angular velocity of the end-effector is calculated from Z-Y-X euler angles as:

$$\boldsymbol{\omega}^{(0)} = \mathbf{Q}(\boldsymbol{\eta}_2)\dot{\boldsymbol{\eta}}_2 \quad (5)$$

and

$$\dot{\eta}_2 = \mathbf{Q}^{-1}(\eta_2)\omega^{(0)} \quad (6)$$

Combination of (3), (4) and (6), we obtain

$$\begin{aligned} \dot{\eta}_1 &= \mathbf{J}_T(\mathbf{q})\dot{\mathbf{q}}, \\ \dot{\eta}_2 &= \mathbf{Q}^{-1}(\eta_2)\mathbf{J}_R(\mathbf{q})\dot{\mathbf{q}} \quad \text{or} \quad \dot{\eta} = \begin{bmatrix} \dot{\eta}_1 \\ \dot{\eta}_2 \end{bmatrix} = \begin{bmatrix} \mathbf{J}_T(\mathbf{q}) \\ \mathbf{Q}^{-1}(\eta_2)\mathbf{J}_R(\mathbf{q}) \end{bmatrix} \dot{\mathbf{q}} = \mathbf{J}(\eta_2, \mathbf{q})\dot{\mathbf{q}} \end{aligned} \quad (7)$$

### 2.3 Inverse Kinematics

In the inverse kinematics problem, the position and orientation of the end-effector  $\mathbf{r}_7^{(0)}$  &  $\mathbf{R}_7^0$  defined by six parameters  $\eta_1$  &  $\eta_2$  are given, we need to solve for the joint variables  $q_k$ ,  $k = 1, \dots, 7$ . Assuming that the Jacobian  $6 \times 7$  matrix  $\mathbf{J} = \mathbf{J}(\eta_2, \mathbf{q})$  has a rank of 6. If  $\eta$  and  $\mathbf{q}$  are known, Eq. (7) is a set of 6 linear equations with 7 unknown, which is a vector of joint velocity  $\dot{\mathbf{q}}$ . By using generalized pseudo inverse we get an optimal solution for  $\dot{\mathbf{q}}$  as

$$\dot{\mathbf{q}} = \mathbf{J}_W^+ \dot{\eta} + [\mathbf{I} - \mathbf{J}_W^+ \mathbf{J}] \mathbf{z}_0 \quad (8)$$

where

$$\mathbf{J}_W^+ = \mathbf{W}^{-1} \mathbf{J}^T [\mathbf{J} \mathbf{W}^{-1} \mathbf{J}^T]^{-1} \quad (9)$$

is called as the weighting pseudo-inverse of  $\mathbf{J}$  [7];  $\mathbf{z}_0 \in \mathbb{R}^n$  is an arbitrary vector,  $\mathbf{I} \in \mathbb{R}^{n \times n}$  is a unit matrix and  $\mathbf{W} \in \mathbb{R}^{n \times n}$  is a positive definite matrix—the so called weighting matrix. In particular cases, if the weighting matrix  $\mathbf{W}$  is chosen to be the identity matrix, one obtains  $\mathbf{J}^+ = \mathbf{J}^T [\mathbf{J} \mathbf{J}^T]^{-1}$ . Matrix  $\mathbf{J}^+$  is pseudo-inverse of  $\mathbf{J}$  and (8) becomes:

$$\dot{\mathbf{q}} = \mathbf{J}^+ \dot{\eta} + [\mathbf{I} - \mathbf{J}^+ \mathbf{J}] \mathbf{z}_0 \quad (10)$$

By choosing vector  $\mathbf{z}_0$ , advantages of the redundancy are exploited (avoiding singularities in configuration, impact with joint limitations and obstacles in workspace).

The joint variables  $\mathbf{q}(t)$  are obtained by following integration

$$\mathbf{q}(t) = \mathbf{q}(t_0) + \int_{t_0}^t \dot{\mathbf{q}} dt \quad (11)$$

To restrict the cumulative error when integrating, we use the kinematic error feedback technique. Instead of (10), we calculate:



$$\dot{\mathbf{q}} = \mathbf{J}^+(\dot{\boldsymbol{\eta}} + \mathbf{K}(\boldsymbol{\eta} - \boldsymbol{\eta}(\mathbf{q})) + [\mathbf{I} - \mathbf{J}^+\mathbf{J}]\mathbf{z}_0) \quad (12)$$

## 2.4 Determination of Initial Configuration by Genetic Algorithm

To determine the initial configuration  $\mathbf{q}(t_0)$  from  $\boldsymbol{\eta}(t_0)$ , an optimal problem with constraints is formulated. Minimize the objective function

$$S(\mathbf{q}) = \frac{1}{2} \sum_{k=1}^7 c_k \left( \frac{q_k - \bar{q}_k}{q_{kM} - q_{kM}} \right)^2 \rightarrow \min, \quad c_k > 0 \quad (13)$$

with the constraints

$$\mathbf{f}(\mathbf{q}) - \boldsymbol{\eta} = 0 \text{ and } q_k - q_{kM} < 0 \ \& \ q_{kM} - q_k < 0, \quad k = 1, \dots, 7.$$

This optimal problem will be solved by Genetic Algorithm GA, [8–10].

## 3 Numerical Experiments

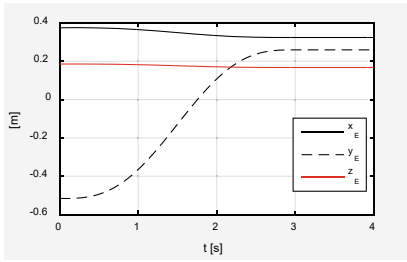
In this section, two numerical simulations are carried out on the model of the 7 DOF manipulator shown in Fig. 1 to confirm the effectiveness of the proposed algorithms. In these simulations, the motion of the endpoint along a given trajectory is defined as:

$$s(t) = s_i + \frac{s_f - s_i}{\pi} \left( \frac{\pi t}{t_f} - \frac{1}{2} \sin \frac{2\pi t}{t_f} \right), \quad 0 \leq t \leq t_f \quad (14)$$

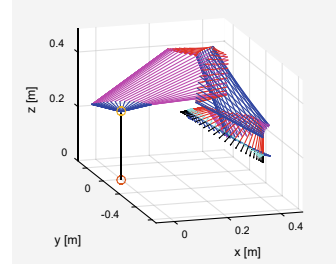
while the orientation of the end-effector along its trajectory is defined by three Euler angles ZYX:

$$\boldsymbol{\eta}_2(t) = \boldsymbol{\eta}_2(0) + \frac{\boldsymbol{\eta}_2(t_f) - \boldsymbol{\eta}_2(0)}{\pi} \left( \frac{\pi t}{t_f} - \frac{1}{2} \sin \frac{2\pi t}{t_f} \right), \quad 0 \leq t \leq t_f \quad (15)$$

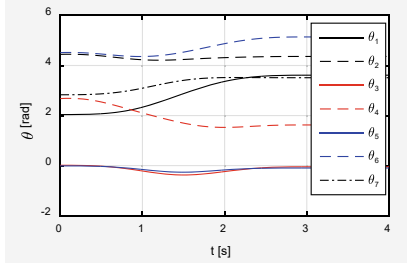
The results of the two simulations corresponding to rectilinear trajectory and curvilinear trajectory are shown in Figs. 2 and 3, respectively. These simulation results show that the position and orientation of the end-effector track the desired trajectory with small position errors about  $1.5 \times 10^{-4}$  m. With these results, it can say that the proposed approach can be exploited for kinematic control of the 7-DOF manipulator.



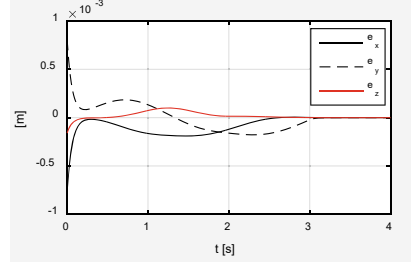
a) Position of the end-effector vs. time;



b) Robot configurations

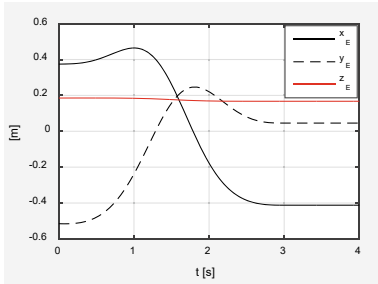


c) Joint variables vs. time;

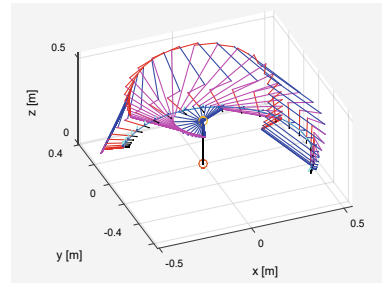


d) Position error of end-effector vs. time

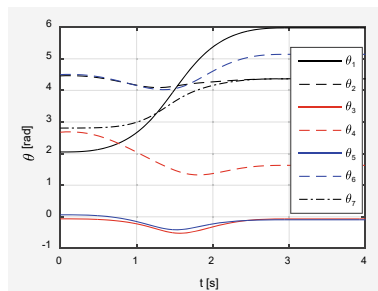
**Fig. 2** Tracking of the end-effector along a rectilinear trajectory



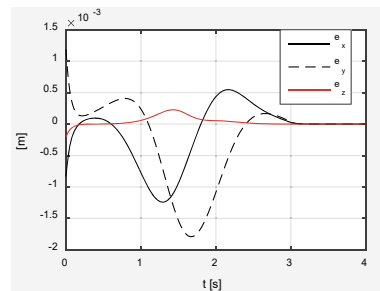
a) Position of the end-effector vs. time;



b) Robot configurations



c) Joint variables vs. time;



d) Position error of end-effector vs. time

**Fig. 3** Tracking of the end-effector along a curvilinear trajectory

## 4 Conclusion

In this paper, the inverse kinematics problem of a redundant robotic manipulator with offsets at shoulder and wrist is solved successfully based on Jacobian matrix. The joint velocities are first found by pseudoinverse of the Jacobian matrix. Then, the joint variables are obtained by integration. The initial values of the joint variables are determined by genetic algorithm. The accumulated error due to integration is suspended thank to error feedback. The numerical experiments verified the effectiveness of the proposed method. The use of quaternion for orientation of the end-effector will be considered in the future instead of three Euler angles.

**Acknowledgements** This work was supported in part by the National Program: Support for research, development, and technology application of industry 4.0 (KC-4.0/19-25), under the grant for the project: Research, design and manufacture of Cobot applied in industry and some other fields with human-robot interaction (code: KC-4.0-35/19-35).

## References

1. J.J. Craig, *Introduction to Robotics: Mechanics and Control* (Pearson/Prentice Hall, 2005)
2. J. Wang, Y. Li, X. Zhao, Inverse kinematics and control of a 7-DOF redundant manipulator based on the closed-loop algorithm. *Int. J. Adv. Robot. Syst.* **7**(4) (2010)
3. B. Siciliano, L. Sciavicco, L. Villani, G. Oriolo, *Robotics: Modelling, Planning and Control* (Springer Science & Business Media, 2010)
4. M.W. Spong, S. Hutchinson, M. Vidyasagar, *Robot Modeling and Control* (John Wiley & Sons, New York, 2006)
5. X. Tian, Q. Xu, Q. Zhan, An analytical inverse kinematics solution with joint limits avoidance of 7-DOF anthropomorphic manipulators without offset. *J. Franklin Inst.* (2020). <https://doi.org/10.1016/j.jfranklin.2020.11.020>
6. Y. Wang, P. Artemiadis, Closed-form inverse kinematic solution for anthropomorphic motion in redundant robot arms. *Adv Robot Autom* **2**, 110 (2013). <https://doi.org/10.4172/2168-9695.1000110>
7. Y. Nakamura, *Advanced Robotics/Redundancy and Optimization* (Addison-Wesley Publishing Company, Reading, 1991)
8. J. Holland, *Adaptation in Natural and Artificial Systems* (MIT Press, Cambridge, MA, 1992)
9. David A Coley (1997): *An Introduction to Genetic Algorithms for Scientists and Engineers*, World Scientific Publishing Co. Pte. Ltd.
10. R.L. Haupt, S.E. Haupt, *Practical Genetic Algorithms*, 2nd edn. (Wiley & Sons, Inc., 2004)

# Accumulation of Permanent Deflection of Steel Plates Subjected to Repeated Slamming Impact Loadings



Dac Dung Truong, Van Vu Huynh, Sang-Rai Cho, Xuan-Phuong Dang, and Hao Dinh Duong

**Abstract** Slamming phenomenon unavoidably occurs on marine structures while in service. The extreme slamming events induced repeated impact pressures can cause damage to the structures and possible crew and compartment casualties. This paper presents investigations of accumulated damages of steel plates subjected to such repeated loadings. The numerical analysis model was developed, in which the load input was as the impulse-triangular profile simplified from the test slamming pressure time history data. The developed analysis model was validated by a comparison with test data. Subsequently, a parametric study on steel plates with actual scantlings used in marine applications was performed. Key parameters in estimating the permanent set of marine plates due to repeated impact pressures were then identified. Accumulation of the plate's permanent deflection under repeated slamming loads was evaluated accordingly.

**Keywords** Slamming · Repeated impact pressures · Steel plate · Permanent deflection · Numerical simulation

## 1 Introduction

During their service, marine structures are frequently subjected to repeated impact pressures induced by slamming. Such loads can damage the structures which was reported in Cho et al. [1].

Several studies on the structural response to slamming loads were reported in the literature. However, these studies considered only single pulse which is different from

---

D. D. Truong (✉) · V. V. Huynh · X.-P. Dang · H. D. Duong  
Nha Trang University, 02 Nguyen Dinh Chieu Str., Nha Trang City, Vietnam  
e-mail: [truongdacdung@ntu.edu.vn](mailto:truongdacdung@ntu.edu.vn)

S.-R. Cho  
University of Ulsan, 93 Daehak-Ro, Nam-Gu, Ulsan, South Korea  
UlsanLab Inc., Ulsan 44610, South Korea

the loads come from slamming events. Besides, simple structure models were only used to study damage extents under such loads through various approaches (experimental, theoretical, numerical). For example, Weinig [2] investigated the effects of the elasticity of the impacted structure on the impulsive pressure due to slamming. Khedmati and Pedram [3] numerically investigated large deformations of stiffened aluminum plates due to single slamming pressure, and some design recommendations regarding loads and geometry were provided. Recently, the large deformation of aluminum plates due to water impact has also been studied by Abrahamsen et al. [4] by wet drop tests. It is apparent that less structural responses could be certainly observed when only considering single impulsive loading.

Regarding the repeated slamming loads, there are some experimental and numerical studies on the effect of such loads [5–11]. Mori [5] carried out several wet drop tests to investigate the response of aluminum-alloy plates of high-speed crafts to slamming loads. Caridis and Stefanou [6] numerically studied the response of steel plates under several impacts. The accumulation of plastic deflection after repeated impacts was reported. Shin et al. [7] and Seo et al. [8] investigated the accumulation of the deformation of plates by several repeated wet drop tests on steel plates with zero and  $10^\circ$  dead-rise angles. The results showed the accumulation of deflections was unnegotiable when the plate was subjected to repeated impact pressures. Besides, the simplified method is also preferable in the early design stage because of its simplicity. Recently, Truong et al. [9–11] developed the empirical formulae to predict the permanent set evolution of aluminum and steel plates subjected to repeated slamming pressures.

This study aims at developing a numerical analysis model for predicting the permanent deflection of steel plates due to repeated impact slamming pressures. The numerical model is validated by comparing with the test data. A parametric study for actual plates used for marine structures is performed, and effect of key parameters on the structural response is investigated.

## 2 Brief Description of Wet Drop Tests

To investigate the damage extents of structures due to repeated impact pressures, a series repeated wet drop tests was conducted using the drop testing machine; the machine consists of a guide rail system, an electromagnetic system and a water tank, as shown in Fig. 2a; drop height ( $h$ ) can be varied from 1.0 to 2.0 m. Different nominal thicknesses were used to fabricate six plate models in which the thickness's each two plate models is identical, while the size of the plate was fixed as  $L \times B = 2000 \text{ mm} \times 1200 \text{ mm}$ ; all the plate models were also supported by the 5-mm thick surrounding-plate walls with  $H = 277 \text{ mm}$ . The plate body model is shown in Fig. 2b. To measure the water pressure and strain, several pressure sensors and strain gauges were used.

Several impacts with the same drop height  $h$  were performed for each model. A deflection measuring device was used to record the permanent deflection after each

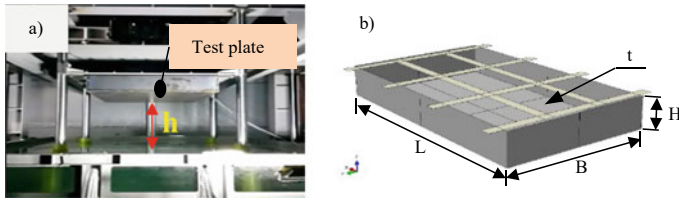


Fig. 2 a Set up for wet drop test, b geometry of the test plate model

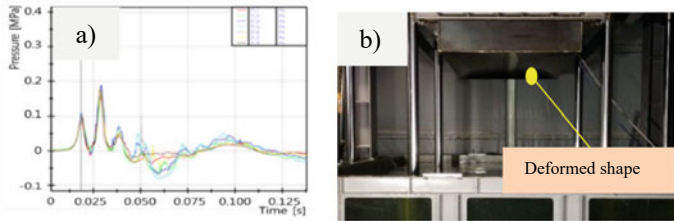


Fig. 3 a Pressure recorded, b deformed shape of plate after several pressure impacts

impact. Detailed experimental work can be found in Shin et al. [7]. Figure 3 shows the water impact pressure time history recorded during the tests and the deformed shape of the 8-mm thick plate model after several impacts. From the pressure time histories obtained, the peak pressure, and its duration were determined to be applied for the numerical as a load input. The permanent deflection test results of the 8-mm thick plate model for four impacts are utilized for the validation, as in the following sections.

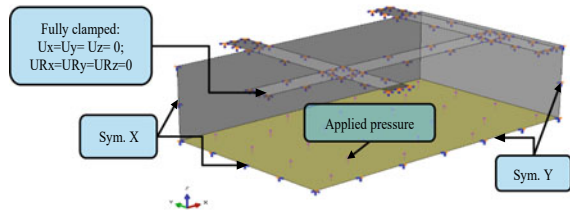
### 3 Numerical Modeling and Validation

#### 3.1 Finite Element (FE) Model

The numerical computations are established using the FE software package ABAQUS/Explicit. A quarter FE model consisting of the plate model and the supporting part, was considered to reduce the required computation time, as shown in Fig. 4.

The plate model and the supporting part are meshed with the four-node shell element S4R. Five integration points through the plate’s thickness are used and the hourglass controls were used as default. After performing mesh convergence tests, the optimum mesh size of the model was determined as roughly twice times the plate’s thickness.

**Fig. 4** Quarter FE model of test model



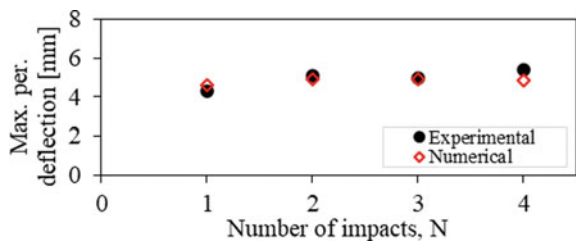
In order to represent the material of the test plate models, the relevant material properties which are available in Seo et al. [8], were used herein. The true stresses and strains are determined to be used in the numerical simulation. The hardening expression for a true stress–strain relation which was proposed by Cho et al. [12], are employed. To consider the strain rate effect, the Cowper-Symonds equation [13] is used. Details of the material constitutive equations and its confirmation can be found in Refs. [14–16].

In the numerical model, a damping model value is also applied to cause the impacted plate quickly approaches a static equilibrium state where the next impact load can be simulated. The simulation duration for each impact is set as 0.4 s.

### 3.2 Verification of FE Model

Figure 5 shows a comparison between the obtained numerically permanent deflection and test results. A good agreement between the predictions and the test results is achieved. The percentage difference between the test and numerical results is less than 5%. It is evident that the deflection of the plates numerically obtained increased with the number of impacts, and its increment was generally reduced. Besides, as seen that the numerical model gives an underestimation except for the first impact.

**Fig. 5** Comparison of prediction and test results for permanent deflection



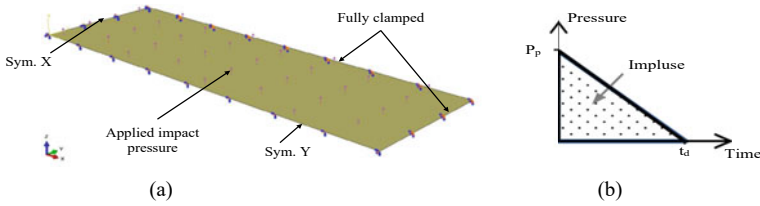


Fig. 6 a 1/4 FE model of a plate model and b impulsive load profile

## 4 Parametric Study

### 4.1 FE Plate Models and Material Properties

Based on typical stiffener spacings of marine-steel structures, the plate model is selected as 800 mm in breadth ( $b$ ), and its lengths ( $a$ ) are of 2400, 3200, 4000, and 4800 mm. The thicknesses of the plate ( $t$ ) are 10, 15, and 20 mm. The typical values of the aspect ratios,  $\alpha$  ( $a/b$ ) and plate slenderness ratios,  $\beta$  ( $b\sqrt{\sigma_Y/E}/t$ ), are then generated.

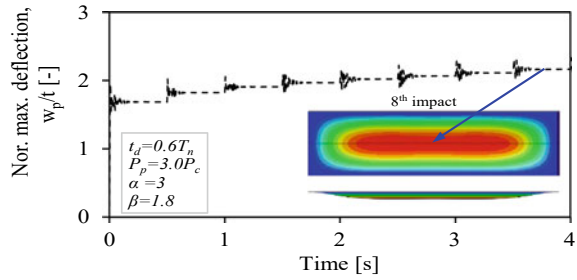
The mild steel ( $\sigma_Y = 235$  MPa) is adopted. A similar simulation methodology described in Sect. 2 is used herein. The plate is fully clamped at its edges. The 1/4 FE model is shown in Fig. 6a. The simulation duration is set as 0.5 s.

### 4.2 Definition of Impact Pressure Loads

The impulse characterized by a peak pressure ( $P_p$ ) and a duration ( $t_d$ ), as shown in Fig. 6b, is adopted. The peak pressure ratio ( $P_p/P_c$ ) is 3.0 as a typical value;  $P_c$  is the static collapse pressure [13]. Note that the  $P_p$  value is selected to sufficiently cause the plate deforms in plastic ( $w_p/t$  within a range of 1 to 4, without any fractures). It is assumed that the plate is uniformly loaded by the impulse, and 8 identical impacts are analyzed. The  $t_d/T_n$  is selected as 0.6, where  $T_n$  ( $1/f$ ) is the fundamental period of a clamped plate. Note that  $f$  is the fundamental frequency of a clamped plate considering submersion effects, and it can be determined by using the modified formulations taken from [17].



**Fig. 7** Typical deflection time history and deformed shape of the plate after 8<sup>th</sup> impact



## 5 Results and Discussion

### 5.1 Effect of Load Repetition

Figure 7 shows the deflection time history at the plate’s center for eight impacts. A deformed shape at the last impact is presented to show the typical profile of plate under impulsive loadings.

As seen that the permanent deflection get an increase with the impact numbers  $N$ . After 1st impact, the plate deforms significantly, while with consecutive impacts, the deformation increases gradually. In the following sections, the plot of  $w_p/t$  for 8 impacts is presented for evaluating the response of the various plates subjected to repeated impacts.

### 5.2 Effect of Plate Slenderness Ratio and Aspect Ratio

The effect of  $\beta$  on the permanent deflection accumulation of the plates is presented in Fig. 8a. As seen that  $w_p/t$  increases gradually when  $\beta$  is increased regardless of  $N$ . However, the increment of the deflection is identical for various  $\beta$ , which is line with the observation of Truong et al. [9–11]. In addition, for the large  $\beta$  the permanent deflection evolution is somewhat greater for the eight impacts.

Figure 8b indicates accumulation of  $w_p/t$  for various  $\alpha$  with  $N$ . It is evident that the deflection gradually decreased when increasing  $\alpha$ , regardless  $N$ ; however, the deflection is negligibly decreased and approaches a certain value when  $\alpha$  is greater than 5.

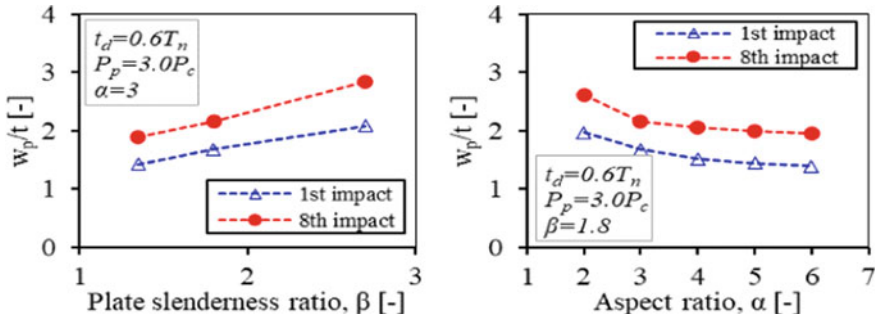


Fig. 8 Variation in normalized residual deflection of plate for different **a**  $\beta$  and **b**  $\alpha$

## 6 Conclusions

This study developed the numerical analysis model for estimating the permanent deflection accumulation of steel plates under repeated impact pressures induced by slamming. A parametric study was performed for various actual scantlings of marine plates to assess the structural response to repeated impact loadings. It was found that the steel plates undergo a significant deflection after the first impact, and subsequently it experiences the accumulation of deflection following by several consecutive impacts regardless of  $\alpha$  and  $\beta$ . In addition, the permanent deflection of the plates was gradually increased and decreased when increasing  $\beta$  and  $\alpha$ , respectively regardless of  $N$ . It was also found that when plate is subjected to repeated impact pressures, its deflection was almost unchanged for the case of  $\alpha$  greater than 5.

**Acknowledgements** Dac Dung Truong was funded by the Postdoctoral Scholarship Programme of Vingroup Innovation Foundation (VINIF), code VINIF.2022.STS.03.

## References

1. S.-R. Cho, M. Elangovan, A. Engle, T. Ha, J.J. Jensen, G. Kapsenberg, S. Malenica, J. Matagne, H. Ren, A. Rosen, S. Saevik, P. Temarel, S. Uhlenbrock, T. Yoshikawa, Report of committee V.7: impulse pressure loading and response assessment, in *Proceedings of 18th international ship and offshore structures congress (ISSC2012)*, Rostock, Germany (2012), pp. 275–329
2. Weinig, F., *Impact of a Vee-Type Seaplane on Water with Reference to Elasticity*. National Advisory Committee for Aeronautics Technical Memorandums, No. 810 (1936)
3. M.R. Khedmati, M. Pedram, A numerical investigation into the effects of slamming impulsive loads on the elasticplastic response of imperfect stiffened aluminium plates. *Thin-Walled Struct.* **76**, 118–144 (2014)
4. B.C. Abrahamsen, H.S. Alsos, V. Aune, E. Fagerholt, O.M. Faltinsen, Ø. Hellan, Hydroplastic response of a square plate due to impact on calm water. *Phys. Fluids* **32**, 082103 (2020)
5. K. Mori, Response of the bottom plate of high-speed crafts under impulsive water pressure. *J. Soc. Naval Archit. Jpn.* **142**, 297–305 (1977)

6. P. Caridis, M. Stefanou, Dynamic elastic/viscoplastic response of hull plating subjected to hydrodynamic wave impact. *J. Ship Res.* **41**(2), 130–146 (1997)
7. H.K. Shin, B.C. Seo, S.-R. Cho, Experimental investigation of slamming impact acted on flat bottom bodies and cumulative damage. *Int. J. Nav. Archit. Ocean Eng.* **10**, 294–306 (2018)
8. B.C. Seo, D.D. Truong, S.-R. Cho, D.J. Kim, S.K. Park, H.K. Shin, A study on accumulated damage of steel wedge with  $10^\circ$  due to slamming loads. *Int. J. Nav. Archit. Ocean Eng.* **10**, 520–528 (2018)
9. D.D. Truong, V.V. Huynh, H.N. Quach, X.-P. Dang, H.T. Tran, H.D. Duong, N.A.V. Le, Numerical investigation on the damage extents of plates due to repeated slamming loads, in *Computational Intelligence Methods for Green Technology and Sustainable Development GTSD 2022. Lecture Notes in Networks and Systems*, vol 567, ed. by Y.P. Huang, W.J. Wang, H.A. Quoc, H.G. Le, H.N. Quach (Springer, Cham, 2022)
10. D.D. Truong, H.K. Shin, S.-R. Cho, Permanent set evolution of aluminium-alloy plates due to repeated impulsive pressure loadings induced by slamming. *J. Mar. Sci. Technol.* **23**, 580–595 (2018)
11. D.D. Truong, V.V. Huynh, B.S. Jang, H.N. Quach, X.-P. Dang, H.D. Duong, S.-R. Cho, Empirical formulations for prediction of permanent set evolution of steel plates due to repeated impulsive pressure loadings induced by slamming. *Ocean Eng.* **268**, 113430 (2023)
12. S.-R. Cho, S.I. Choi, S.K. Son, Dynamic material properties of marine steels under impact loadings, in *Proceedings of the 2015 World Congress on Advances in Structural Engineering and Mechanics, ASEM15* (Incheon, Korea, 2015).
13. N. Jones, *Structural Impact*, 2nd edn. (Cambridge University Press, Cambridge, UK, 2012)
14. D.D. Truong, B.S. Jang, H.B. Ju, Development of simplified method for prediction of structural response of stiffened plates under explosion loads. *Mar. Struct.* **79**, 103039 (2021)
15. D.D. Truong, H.K. Shin, S.-R. Cho, Response of low temperature steel beams subjected to single and repeated lateral impacts. *Int. J. Nav. Archit. Ocean Eng.* **10**(6), 670–682 (2018)
16. D.D. Truong, B.S. Jang, H.B. Ju, S.W. Han, Prediction of slamming pressure considering fluid-structure interaction. Part I: numerical simulations. *Ships Offshore Struct.* **17**(1), 7–28 (2022)
17. Lloy's Register, *Rule and Regulations for the Classification of Naval Ships*, vol. 1, p. 6, Ch. 2, Sec. 4 (2022)

# Influence of Blank Holder Force and Limiting Drawing Ratio on Fracture Height During Cup—Drawing Process of SECC Sheet Metal



Thi-Bich Mac, Ngoc-Quyét Ly, and The-Thanh Luyen

**Abstract** This paper analyzes the influence of blank holder force ( $F_{BH}$ ) and limiting drawing ratio ( $M_t$ ) when drawing cylindrical parts from electrolytic zinc-coated steel blank (SECC) with a thickness of 0.6 mm. Firstly, initial survey experiments were performed to determine the study limits of the input parameters. Then the influence of the  $F_{BH}$  and the  $M_t$  on the fracture height ( $H$ ) is evaluated. When the  $M_t$  is fixed and  $F_{BH}$  increases from 8 to 12 kN, the  $H$  decreases. Meanwhile, if the  $M_t$  is fixed and the  $F_{BH}$  is increased from 1.94 to 2.09, the  $H$  increases, but when continuing to increase the  $M_t$  to 2.24, the  $H$  decreases. Finally, study the simultaneous influence of the  $F_{BH}$  and  $M_t$  on the  $H$ , and the optimal set of technological parameters to achieve the maximum forming height are  $F_{BH} = 8$  kN and  $M_t = 2.09$ .

**Keywords** Electrolytic zinc-coated steel (SECC) · Blank holder force · Limiting drawing ratio · Fracture height · Drawing

## 1 Introduction

In the sheet metal drawing, flat sheet is forced into a drawing mold's cavity by a punch to create a product of the desired shape. This process is applied in a diversity of industries because it means to produce product with geometric shapes that are not only simple but also complex by using a thin sheet metal [1]. This process is widely used in many fields like home appliances sectors, aerospace, automotive, and various areas. There are some parameters, which have an effect on product quality of drawing process as lubricant, blank holder force, drawing speed, and sample material [2]. Drawing products need to ensure that they are without fracture, wrinkle and reach the required height.

---

T.-B. Mac (✉) · N.-Q. Ly · T.-T. Luyen  
Faculty of Mechanical Engineering, Hung Yen University of Technology and Education, Hung Yen, Vietnam  
e-mail: [bich.utehy@gmail.com](mailto:bich.utehy@gmail.com)

© The Author(s), under exclusive license to Springer Nature Switzerland AG 2024  
B. T. Long et al. (eds.), *Proceedings of the 3rd Annual International Conference on Material, Machines and Methods for Sustainable Development (MMMS2022)*, Lecture Notes in Mechanical Engineering, [https://doi.org/10.1007/978-3-031-57460-3\\_29](https://doi.org/10.1007/978-3-031-57460-3_29)

**Table 1** The chemical composition of SECC steel sheet [4]

Element code	C	Si	Mn	P	S
Content (%)	<0.12	<0.05	<0.50	<0.025	<0.025

SECC steel is electro-galvanized commercial quality cold rolled steel that is cold rolled and then coated with zinc in an electro-galvanizing line [3]. SECC is a material grade and designation defined in the JIS G3313 standard. It is commonly used in cars, household appliances, office machines, construction, production machinery, and clean industry such as body panels, air filters, washing machines, air conditioners, electronic computer cases, agricultural machinery, wall decoration in the operating room, etc.

In this study, the limiting domain of  $F_{BH}$  and  $M_t$  was established through tests to exclude wrinkle and fracture phenomena while forming height was not reached. Experiments were built to evaluate the effect of  $F_{BH}$  and  $M_t$  on cylindrical cup's fracture height, respectively. In addition, the design of experiment Taguchi and analysis of variance ANOVA method were used to evaluate the simultaneous influence of  $F_{BH}$  and  $M_t$ , as well as determine the optimal set of control parameters to achieve the maximum forming height.

## 2 Material and Experimental Design

### 2.1 Material

The sample with a thickness of 0.6 mm is made from an electrolytic zinc-coated steel sheet (SECC) according to the JIS-G-3313 standard used for experimental performance. The chemical composition of SECC steel material is presented in Table 1.

Requirements of meeting the content of other residual elements:

Cu < 0.15%, Ni < 0.15%, Cr < 0.15%, As < 0.05%, Sn < 0.05%.

### 2.2 Experimental Design

Experiments were carried out on a four-post double hydraulic press, code Y28-200. The drawing mold set consists of the main parts: die, punch, and blank holder as shown in Fig. 1. These parts are made of SKD11 material and heat treated to ensure required hardness. During the drawing process, the punch and the blank holder are fixed, while the die moves in the vertical direction to shape the product.

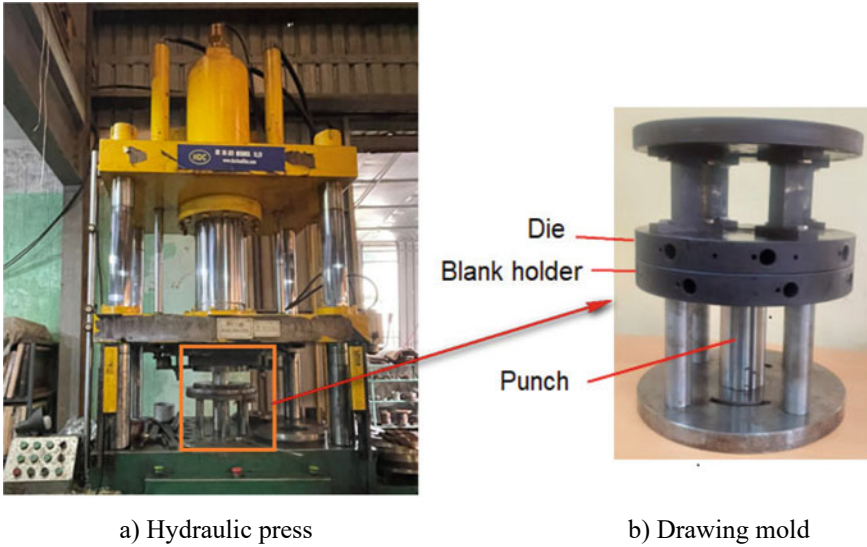


Fig. 1 Experimental design of drawing process

### 2.3 Height Measuring Device

The height of the cylindrical cup is measured by a height gage of Mitutoyo – Japan. Equipment’s measuring range of 200 mm, division 0.02 mm. The measurement method is presented in Fig. 2. Each experiment is performed 3 times and the product height is the average value of 3 measurements.

## 3 Result and Discussion

### 3.1 Setting Limited Input Parameters

The paper studies the influence of the blank holder force ( $F_{BH}$ ) and limiting drawing ratio ( $M_t$ ) on the fracture height of the cylindrical cup product. In which the  $M_t$  is determined according to the formula (1) [5]:

$$M_t = \frac{D_w}{D_p} \tag{1}$$

where  $D_w$  and  $D_p$  are workpiece’s diameter and punch’s diameter respectively. In this research, the punch has diameter of 67 mm.

**Fig. 2** Product height measurement method



Firstly, the limits of the input parameters were studied. Initial stamping tests with workpiece diameters of 130, 140, 150, and 160 mm as Fig. 3 were corresponding to the  $M_t$  of 1.94, 2.09, 2.24, and 2.39. The survey with a fixed  $F_{BH} = 8$  kN showed that the workpiece with a large  $M_t$  of 2.39, the product had fracture prematurely when the forming height was not reached as shown in Fig. 4a. Therefore, the study selected the workpiece with the  $M_t$  in the range from 1.94 to 2.24.

The surveys with  $F_{BH}$  of 6, 8, 10, 12, and 14 kN were corresponding established. In these experiments, the  $M_t$  was constant at 2.09 ( $D = 140$  mm). The results showed that when the  $F_{BH}$  of 6 kN was low value, the workpiece was wrinkled on the cylindrical cup rim. Meanwhile, when the  $F_{BH}$  of 14 kN was high value, the fracture appeared prematurely before reaching the forming height. Therefore, the research has chosen the range of  $F_{BH}$  to be studied as from 8 to 12 kN.

### 3.2 Studying the Effect of $F_{BH}$ on the Fracture Height ( $H$ )

In order to investigate the effect of FBH on the forming height of cylindrical parts, experimental studies with  $F_{BH}$  varying from 8 to 12 kN respectively were carried out when stamping the samples with  $M_t$  of 1.94, 2.09, and 2.24. The results of forming height in different experiments were presented as Table 2. The graph depicted the effect of  $F_{BH}$  on forming height when stamping various samples with various  $M_t$  as shown in Fig. 5.

The results showed that, in the studied range of  $F_{BH}$ , the forming height graphs corresponding to the cases of different  $M_t$  tended to decrease when the  $F_{BH}$  increased

**Fig. 3** Experimental workpiece



**Fig. 4** The fracture (a) and wrinkling (b) on the cylindrical cup

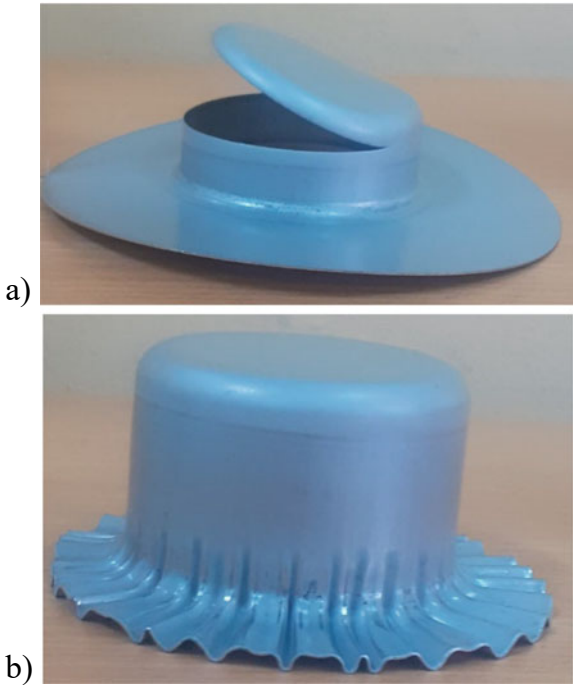
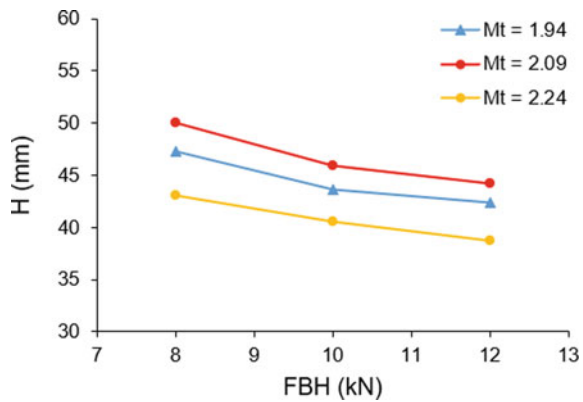




**Table 2.** Experimental data to evaluate the effect of  $F_{BH}$  on  $H$

Ex. No	$M_t$	$F_{BH}$ (kN)	$H$ (mm)
1	1.94	8	47.24
2	1.94	10	43.64
3	1.94	12	42.39
4	2.09	8	50.03
5	2.09	10	45.86
6	2.09	12	44.15
7	2.24	8	43.10
8	2.24	10	40.52
9	2.24	12	38.70

**Fig. 5** Effect of  $F_{BH}$  on forming height of cylindrical parts with different  $M_t$



from 8 to 12 kN. Specifically, with  $M_t = 1.94$ , the forming height decreased from 47.24 to 42.39 (mm); when  $M_t = 2.09$ , the forming height decreased from 50.03 to 44.15 (mm); when  $M_t = 2.24$ , the forming height decreased from 43.10 to 38.70 (mm). The highest forming height was 50.03 when  $M_t = 2.09$  and  $F_{BH} = 8$  kN. The lowest one was 38.70 when  $M_t = 2.24$  and  $F_{BH} = 12$  kN.

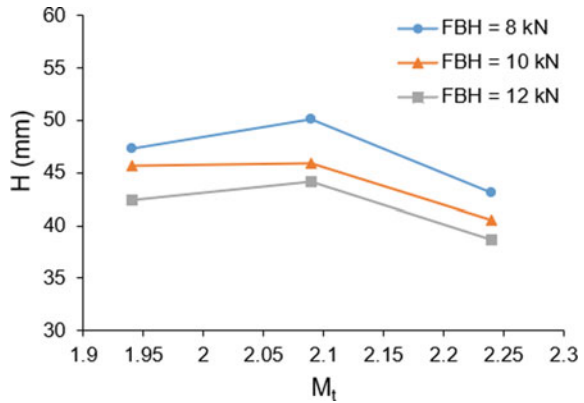
### 3.3 Studying the Effect of $M_t$ on the Fracture Height ( $H$ )

In order to investigate the influence of the  $M_t$  on the forming height of the cylindrical part, an experimental study was carried out with the  $M_t$  varying from 1.94 to 2.24. Experiments were performed when stamping with the cases of the  $F_{BH}$  was 8, 10, 12 kN, respectively. The results of forming height at different experiments were presented as Table 3. The graph depicting the influence of the  $M_t$  on the forming height was shown as Fig. 6.

**Table 3.** Experimental data to evaluate the effect of  $M_t$  on  $H$

Ex. No	$F_{BH}$ (kN)	$M_t$	$H$ (mm)
1	8	1.94	47.24
2	8	2.09	50.03
3	8	2.24	43.10
4	10	1.94	45.64
5	10	2.09	45.86
6	10	2.24	40.52
7	12	1.94	42.39
8	12	2.09	44.15
9	12	2.24	38.70

**Fig. 6** Effect of  $M_t$  on forming height of cylindrical parts with different  $F_{BH}$



The results showed that, in the range of the  $M_t$  was studied, the forming height when stamping in the different cases of  $F_{BH} = 8; 10; 12$  kN, the forming height tended to increase when  $M_t$  increased from 1.94 to 2.09. Meanwhile, the forming height tended to decrease when the  $M_t$  increased from 2.09 to 2.24. Besides, the forming height graph was at the highest position in the case of  $F_{BH} = 8$  kN and the forming height graph is at the lowest position when the  $F_{BH} = 12$  kN. The results also showed that the forming height was highest when  $F_{BH} = 8$  kN and  $M_t = 2.09$ ; the lowest forming height when  $F_{BH} = 12$  kN and  $M_t = 2.24$ .

### 4 Conclusion

In this paper, the influence of input parameters including the  $F_{BH}$  and  $M_t$  when stamping a cylindrical part of SECC material has been studied. The results obtained were as follows:

- The limits of input parameters were studied to achieve the efficiency of the SECC cylindrical part drawing process, including the  $F_{BH}$  was from 8 to 12 kN and the  $M_t$  was from 1.94 to 2.24 (equivalent to the workpiece's diameter was from 140 to 160 mm);
- The forming height was inverse proportion to the  $F_{BH}$ , which was in the range from 8 to 12 kN when studying with different  $M_t$ ;
- The forming height was in direct proportion to  $M_t$  when  $M_t$  was in the range from 1.94 to 2.09, but it was inverse proportion to  $M_t$  when  $M_t$  continued to increase to 2.24 in all three experimental cases with various  $F_{BH}$ .

## References

1. T. Ogawa, N. Ma, M. Ueyama, Y. Harada, Analysis of square cup deep-drawing test of pure titanium. J. Phys. Conf. Ser. **734**, 1–4 (2016)
2. A.R. Joshi, K.D. Kothari, R.L. Jhala, Effects of different parameters on deep drawing process: review. Int. J. Eng. Res. Technol. (IJERT) **2**, 1–5 (2016)
3. A. Abdul Ghafa, A.B. Abdulla, J.I. Mahmood, Experimental and numerical prediction on square cup punch–die misalignment during the deep drawing process. Int. J. Adv. Manuf. Technol. **113**, 379–388 (2021)
4. <https://www.cosasteel.com/secc-steel/>
5. G. Behrens, F.O. Trier, H. Tetzl, F. Vollertsen, Influence of tool geometry variations on the limiting drawing ratio in micro deep drawing. Int. J. Mater. Form. **9**, 253–258 (2016)

# Automatically Abnormal Detection for Radiator Fans Through Sound Signals Using a Deep Learning Technique



Minh-Tuan Nguyen, Tien-Phong Nguyen, and The-Van Tran

**Abstract** In this study, an abnormal detection model of a fan through sound is developed using a deep learning technique. The fan sound datasets include two classes, OK and NG. First, the sound signals are framed to a consistent duration; then, the log-mel spectrogram features are extracted. A deep learning model is proposed to classify fan sound signals based on the extracted features. The results show the high performance and accuracy of the proposed model and can be used to develop a computer application for the abnormal detection of radiator fans through sound signals.

**Keywords** Abnormal detection · Log-mel spectrogram · Data augmentation · Deep learning · Convolution neural network

## 1 Introduction

During the maintenance of industrial systems, abnormal detection plays an important role. Abnormal detection helps reduce maintenance costs, increase machine life, and prevent problems from escalating and becoming severe. Most machine abnormal detection research was directed toward analyzing vibrations [1], and only a few studies used sound signals [2]. The sound signals contain information about the operating status of the machine. When the components in the machine fail, the sound signal changes; different bugs make different sounds.

Furthermore, based on the difference between the abnormal modes, the faults can be detected according to their respective sound signals [3]. The disadvantage of abnormal detection through sound signals is that it is difficult to recover the machine's signature because the signal is often drowned in noise [4]. Noise reduction techniques and source separation algorithms are used to reduce the noise effect [5]. However, these techniques must be improved to get better results. A promising research line

---

M.-T. Nguyen (✉) · T.-P. Nguyen · T.-V. Tran  
Hung Yen University of Technology and Education, Hung Yen 160000, Vietnam  
e-mail: [tuanctm7@gmail.com](mailto:tuanctm7@gmail.com)

**Table 1** Detail of the datasets

Dataset	Number of samples		
	OK	NG	Total
DT-1	48	104	152
DT-2	48	104	152

in abnormal sound detection is developing better algorithms for sound signal classification, including improving deep learning algorithms. The widespread adoption of abnormal sound detection techniques will significantly improve the testing of industrial environments. For this reason, sound-based error detection techniques need further research effort.

The proposed approach consists of signal processing methods: preprocessing, feature extraction, data augmentation, and classification. A deep learning model is designed to classify fan sound signals based on log-mel spectrogram. The trained model was used to develop a computer application that detects fan anomalies via sound signals.

## 2 Material and Method

Abnormal detection in fans through sound signals comprises three steps. The first step is the preprocessing technique that transforms each sound signal into a consistent duration. The second step is extracting the appropriate feature of the sound signals for use as the prediction model's input. The last step is to design a prediction model to implement prediction tasks.

### 2.1 Data Collection

The sound signals were collected from 152 computer radiator fans, at a speed of 6,700 rpm with a voltage of 3.5 V and a speed of 10,000 rpm with a voltage of 5.0 V. The datasets include two sets, DT-1 and DT-2. Each dataset consists of 152 sound samples in .mp3 format with a sampling frequency of 48 kHz, divided into normal (OK) and abnormal (NG) classes. DT-1 is a sound dataset that contains much ambient noise, and DT-2 includes only fan sound without noise and are listed in Table 1.

### 2.2 Feature Extraction

Based on the Discrete Fourier transform (DFT) [6], the fan sound signals were converted into a log-mel spectrogram. The DFT  $\mathbf{y}(k)$  of signal  $\mathbf{x}$  is determined as

Eq. (1).

$$\mathbf{y}(k) = \sum_{n=1}^N 5\mathbf{x}(n)e^{\frac{-j2\pi(k-1)(n-1)}{N}}, \quad k = 1 \dots N \quad (1)$$

where  $N$  is the length of vector  $\mathbf{x}$ .

The logarithm of the log-mel spectrogram was obtained using the small deviation  $\varepsilon$ , and the log-mel spectrogram was defined as Eq. (2) to get data with a smoother distribution. When the input is normalized and distributed reasonably and smoothly, training the network becomes more accessible.

$$s(k) = \log_{10}(y(k) + \varepsilon) \quad (2)$$

where,  $\varepsilon = 10^{-9}$  is a small offset.

### 2.3 Data Augmentation

To increase the efficiency of the training data and help prevent overfitting, an augmented image datastore was created to enhance and resize the spectrograms automatically. The log-mel spectrograms were randomly shifted in the horizontal direction up to 10 frames (100 ms) forward or backward in time and scaled the time axis up or down by 10%. The augmented data store generates augmented images in real-time during training and imports them into the model. No enhanced spectrograms are stored in memory. Figure 1 depicts the waveforms and log-mel spectrogram of some fan sound samples.

### 2.4 Proposed Deep Learning Model

Deep learning is a type of machine learning that works based on the structure and function of the human brain. It uses artificial neural networks to perform sophisticated computations on large amounts of data. Previous studies have focused on using deep learning models, including artificial neural networks (ANNs) [7], recurrent neural networks (RNNs) [8], and convolution neural networks (CNNs) [9, 10], and have achieved specific results in image and sound classification. In [11], Nguyen et al. used simple CNN models in fault detection for water pumps, and the results achieved high accuracy, up to 99.9%. Reference [12] showed that the CNN model gave better results in audio signal classification than the RNN. Therefore, this study proposed the CNN model for the automatically abnormal detection task.

A CNN model is designed model for the automatically abnormal detection task. It includes three convolutional layers and two fully connected layers. As shown in

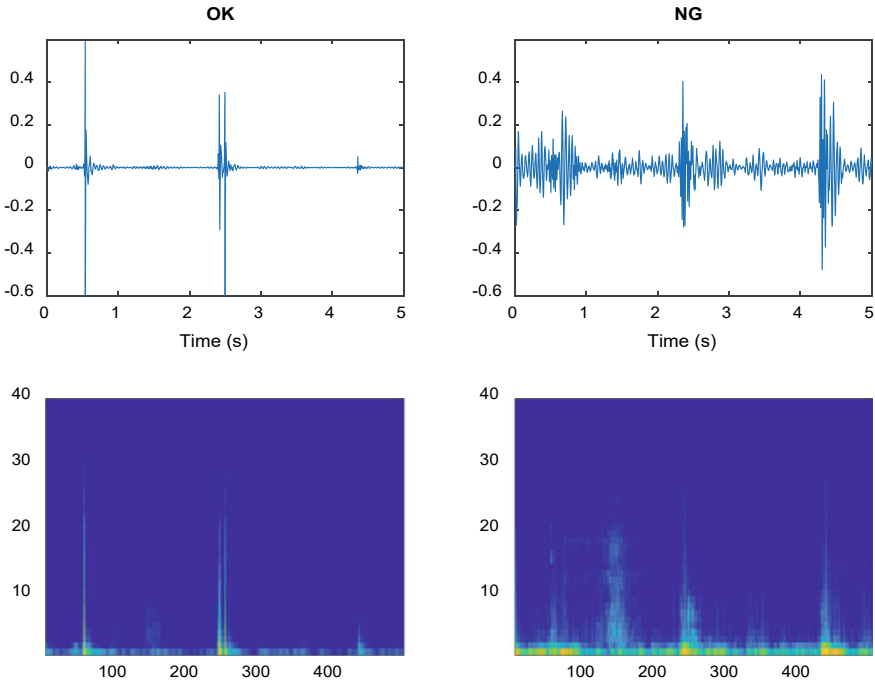


**Fig. 1** Waveform and log-mel spectrogram of audio signal samples

Fig. 2, the first two convolutional layers are followed by overlapping max-pooling layers. The third convolutional layer is connected directly to the first fully connected. The second fully connected layer feeds into a soft-max classifier with two classes.

### 2.5 Evaluation Metrics

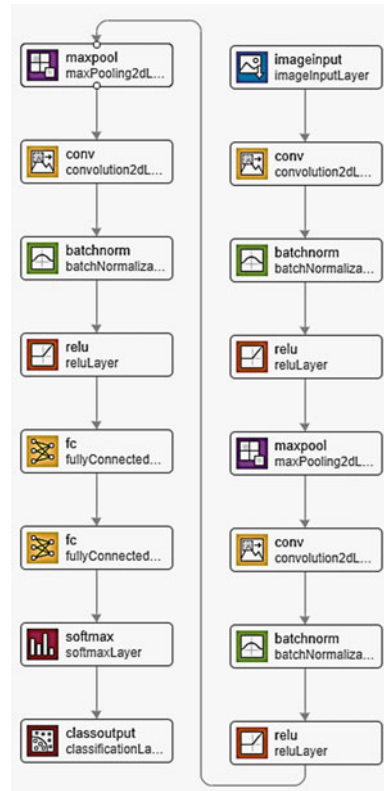
The evaluation criteria used in this study are Precision, Sensitivity, and Overall accuracy (Acc) based on Eqs. (3–5). To measure these metrics, we need the numbers of true-positive (TP), false-positive (FP), and false-negative (FN) for each class.

Where: TP is the true-positive of a class is the total number of correct predictions in the data labelled this class; FP is the false-positive of a class is the total number of false predictions that predicted is this class, and FN is the false-negative of a class is the total number of false predictions in the data labelled this class.

$$\text{Precision} = \frac{\text{TP}}{\text{TP} + \text{FP}} \tag{3}$$

$$\text{Sensitivity} = \frac{\text{TP}}{\text{TP} + \text{FN}} \tag{4}$$

**Fig. 2** Architecture of the proposed deep learning model



$$Acc = \frac{\text{Total number of correct predictions}}{\text{Total number of testing entries}} \tag{5}$$

### 3 Experiment Results

#### 3.1 Training the Datasets

Each dataset was split into two subsets: the training set and the validation set in experiment. The training set contained 80% of the whole dataset, while the validation set contained the rest. Some training tests were performed to find appropriate hyperparameters that ensure high accuracy and stable training processes. Figure 3 presents the validation precision, sensitivity, and overall accuracy. For the DT-1, the



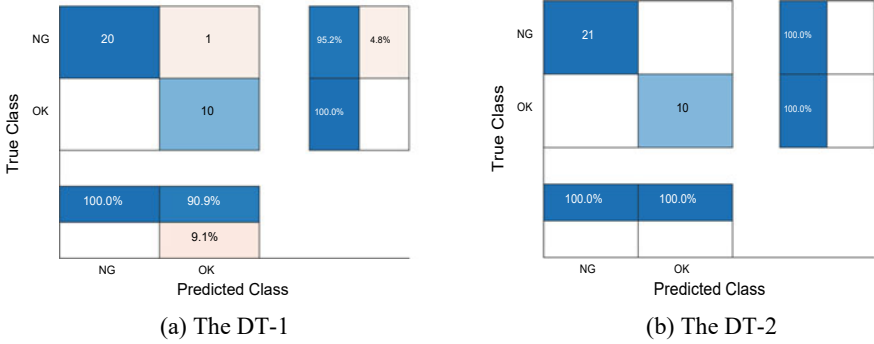


Fig. 3 The confusion matrix of the validation datasets

precisions are 100% and 90.9%, corresponding to OK and NG classes; the sensitivities are 100% and 90.9%, while the overall accuracy is 96.8%. The precisions, sensitivities, and overall accuracy of the DT-2 were 100% in both OK and NG classes.

### 3.2 Testing Results

The testing result with the prediction model trained by the DT-1 showed that 15 samples were OK and 15 samples were NG. This result is due to the data collection heterogeneity between the training and testing datasets. The training dataset has noise, while the testing dataset has no noise, leading to inaccurate testing results. The testing result with the prediction model trained from the DT-2 set showed that 29 samples were OK and only one sample is NG; the accuracy reached 96.67%. The high accuracy is because the training and test datasets were collected under the same condition without noise. Thus, the training and testing datasets must be collected under the same conditions for the fan abnormality detection process to be accurate.

### 3.3 Automatically Abnormal Detection Computer Apps for Fans

The trained models can be used to develop a system for automatic abnormality detection of a fan. The system consists of a unit directly receiving sound from a fan (microphone) and a data processing unit, a PC with an installed anomaly detection application, as shown in Fig. 4.

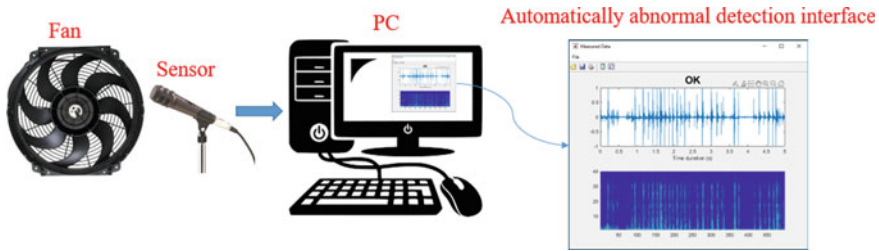


Fig. 4 Describing the system for automatic abnormality detection of a fan

## 4 Conclusions

In this study, a deep learning model was proposed to automatically detect anomalies in a fan through the sound signals. Some conclusions are obtained as follows:

- Fan abnormality detection can be implemented by analyzing the fan sounds.
- CNN model gives high classification accuracy when used for fan sounds.
- An automatic fan abnormality detection system can be developed through sound using deep learning techniques.

## References

1. A. Aherwar, An investigation on gearbox fault detection using vibration analysis techniques: a review. *Aust. J. Mech. Eng.* **10**(2), 169–183 (2012)
2. A. Suman, C. Kumar, P. Suman, Early detection of mechanical malfunctions in vehicles using sound signal processing. *Appl. Acoust.* **188**, 108578 (2022)
3. Y.E. Karabacak, N.G. Özmen, Common spatial pattern-based feature extraction and worm gear fault detection through vibration and acoustic measurements. *Measurement* **187**, 110366 (2022)
4. P. Henriquez, J.B. Alonso, M.A. Ferrer, C.M. Travieso, Review of automatic fault diagnosis systems using audio and vibration signals. *IEEE Trans. Syst. Man Cybern. Syst.* **44**(5), 642–652 (2013)
5. H. Hammam et al., Blind signal separation with noise reduction for efficient speaker identification. *Int. J. Speech Technol.* **24**(1), 235–250 (2021)
6. J.O.S. Iii, *Mathematics of the Discrete Fourier Transform (DFT)* (Julius Smith, 2002)
7. K.M. Silva, B.A. Souza, N.S.D. Brito, Fault detection and classification in transmission lines based on wavelet transform and ANN. *IEEE Trans. power Deliv.* **21**(4), 2058–2063 (2006)
8. Y. Huang, C.-H. Chen, C.-J. Huang, Motor fault detection and feature extraction using RNN-based variational autoencoder. *IEEE access* **7**, 139086–139096 (2019)
9. M.-T. Nguyen, J.-H. Huang, Location estimation of receivers in an audio room using deep learning with a convolution neural network. *J. Inf. Sci. Eng.* **38**(2) (2022)
10. M.-T. Nguyen, J.-H. Huang, Snore detection using convolution neural networks and data augmentation, in *International Conference on Advanced Mechanical Engineering, Automation and Sustainable Development* (2022), pp. 99–104

11. M.T. Nguyen, J.H. Huang, Fault detection in water pumps based on sound analysis using a deep learning technique. *Proc. Inst. Mech. Eng. Part E J. Process Mech. Eng.* **236**(2), 298–307 (2022)
12. W.-W.L. Minh-Tuan Nguyen, J.-H. Huang, Heart sound classification using deep learning techniques based on log-mel spectrogram. *Circ. Syst. Signal Process.*, p. 10 (2022). <https://doi.org/10.1007/s00034-022-02124-1>

# Interference Fit Calculation with Numerical and Simulation Methods



Vi Phong Lam and Huu Loc Nguyen

**Abstract** This study presents the steps of calculation and selection of interference fits. According to Lamé's formula, we can determine the stress and strain values generated when assembling the joint. We also show the modeling and simulation of interference fit for evaluating these same values. Then, we compare the calculated values with Lamé's formula and simulation results, which is the basis of further interference assembly experiments to find the load capacity for different pairs of assembly materials.

**Keywords** Interference fit · Simulation method · Finite element method (FEM) · Tolerance · Stress · Strain

## 1 Introduction

Researchers worldwide have conducted many studies on interference fits, focusing mainly on joint strength, selection of reasonable fit tolerance, simulation of concentrated stresses at the interface, and technological solutions to improve the workability and longevity of interference fits.

Traditionally, researchers have utilized Lamé's formula to develop analytical techniques to design the interference fits based on the analysis of plane stresses in the elastic region of the material. Following that, there are analyses of interference fit between shafts and spur gears, which apply analytical and numerical methods and conclude that, for highly complex geometry, Lamé's formula becomes up to 78% inaccurate in evaluating the actual contact pressure [1].

---

V. P. Lam · H. L. Nguyen (✉)

Department of Machine Design, Faculty of Mechanical Engineering, Ho Chi Minh University of Technology (HCMUT), Ho Chi Minh City 700000, Vietnam

e-mail: [nhloc@hcmut.edu.vn](mailto:nhloc@hcmut.edu.vn)

Vietnam National University Ho Chi Minh City, Ho Chi Minh City 700000, Vietnam

Moreover, analysts also apply analytical models to mathematical tools in studying the interface pressure, the distribution of stresses, and the influence of surface conditions or thermal processes. Some studies emphasized the importance of the surface roughness value in fixed joints and reported that the load transmission wasting could be up to 300% with surface roughness values ranging from 0.24 to 6.82  $\mu\text{m}$  [2]. In addition to determining the interference fit stresses with mathematical formulas, many studies applied the finite element method (FEM) with many different coupling 3D models. The experimental results are similar to Lamé’s formula results [3].

This study introduces the calculation and selection steps of the regular interference fits. Then, by using mathematical calculation with Lamé’s formula and simulating the interference joints with the finite element method on ANSYS Workbench 2019 R2 software, we determine the displacement in the radial direction, the stress values, and the residual interface stresses. Finally, we analyze the obtained results.

## 2 Basis of the Interference Fit Calculation

### 2.1 Selection of Interference Fit Tolerance

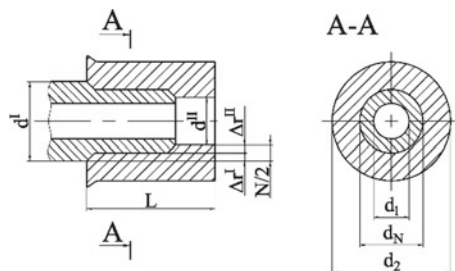
The selection and calculation of interference fit usually follow a typical material strength problem called the Thick-wall cylinder theory, also known as Lamé’s problem or Lamé’s equations.

Usually, we carry out the calculation process according to the calculation model (see Fig. 1) and go along with the following steps [4–6]:

- Step 1: Calculation of the specific pressure  $[p_{min}]$ : The minimum interface pressure depends on the case of the applied load. This value depends on its loading condition: Torque transmission  $T$ ; axial force transmission  $F_a$ ; and sometimes both of them. In turn, we have:

$$[p_{min}] \geq \frac{2 \cdot K \cdot T \cdot 10^3}{\pi \cdot d_N^2 \cdot l \cdot f}; [p_{min}] \geq \frac{K \cdot F_a}{\pi \cdot d_N \cdot l \cdot f}; [p_{min}] \geq K \cdot \frac{\sqrt{F_t^2 + F_a^2}}{\pi \cdot d_N \cdot l \cdot f}$$

**Fig. 1** Basic calculation model of interference fit



whereas:  $p$  is the interface pressure mean value (MPa);  $K$  is the coefficient of contact safety ( $K = 3 \div 4, 5$ );  $f$  is the coefficient of friction;  $l$  and  $d_N$ , respectively, the fit length and nominal assembly diameter (mm).

- Step 2: Determination of Lamé's coefficients— $C_1$  and  $C_2$ , for the inner and outer parts.
- Step 3: Determination of the minimum theoretical interference value that is sufficient to power transmission:

$$N_{mintt} = [p_{min}] \cdot d_N \cdot \left( \frac{C_1}{E_1} + \frac{C_2}{E_2} \right) \quad (1)$$

where:  $E_1$  and  $E_2$  are Young's modulus of the inner and outer part material (MPa);  $d_1$  and  $d_2$  are the inner diameters of the inner and outer part (with a solid shaft,  $d_1 = 0$ ) (mm);  $\mu_1$  and  $\mu_2$  are The Poisson's ratios of the inner and outer part material.

- Step 4: Range of the damaged asperities value  $H$ .
- Step 5: Determination of the minimum allowable interference value taking into account the effect of surface roughness:

$$N_{pmin} = N_{mintt} + H = N_{mintt} + 1.2 \cdot (R_{zd} + R_{zD}) \quad (2)$$

where:  $H$  is the damaged asperities value ( $\mu\text{m}$ ),  $R_{zd}$  and  $R_{zD}$  are the ten-point mean roughness values of the inner and outer parts ( $\mu\text{m}$ ).

- Step 6: Determination of the maximum allowable specific pressure [ $p_{max}$ ]:

$$[p_{max}] = \max[p_1; p_2] \quad (3)$$

$$\text{with } p_1 = 0.58 \cdot \sigma_{y1} \cdot \left[ 1 - \left( \frac{d_1}{d_N} \right)^2 \right]; p_2 = 0.58 \cdot \sigma_{y2} \cdot \left[ 1 - \left( \frac{d_N}{d_2} \right)^2 \right] \quad (4)$$

where:  $\sigma_{y1}$  and  $\sigma_{y2}$  are the material yield strengths of the inner and outer parts (MPa).

- Step 7: Determination of the maximum theoretical interference value:

$$N_{maxtt} = [p_{max}] \cdot d_N \cdot \left( \frac{C_1}{E_1} + \frac{C_2}{E_2} \right) \quad (5)$$

- Step 8: Determination of the maximum allowable interference value taking into account the effect of surface roughness:

$$N_{pmax} = N_{maxtt} + 1.2 \cdot (R_{zD} + R_{zd}) \quad (6)$$

- Step 9: Selection of standard interference fits: According to Ref. [7], select the suitable assembly tolerance which can fulfill these conditions:

$$\begin{cases} N_{pmin} \leq [N_{min}] \\ N_{pmax} \geq [N_{max}] \end{cases} \tag{7}$$

### 2.2 Calculation of Interference Fit Stress and Strain

We can evaluate the radial stress  $\sigma_r$ , the tangential stress  $\sigma_t$ , or the interface pressure  $p$  with Lamé’s equations, as follows:

$$\sigma_{r,t}(r) = A \pm \frac{B}{r^2}; p = \frac{[N_{maxit}]}{d_N \cdot \left(\frac{C_1}{E_1} + \frac{C_2}{E_2}\right)} \text{ (MPa)} \tag{8}$$

where:  $A$  and  $B$  are the integral constants determined by the boundary conditions that depend on the under-consideration radius value  $r$ ;  $[N_{maxit}]$  is the maximum actual interference value, with  $[N_{max}]$  is the maximum interference value obtained according to the selected joint tolerance ( $\mu\text{m}$ ). Considering the boundary conditions of the solid shaft, the hollow shaft and the outer part, we can get the equations in Table 1.

From Fig. 1, we can consider the interference value  $N$  as the difference between the actual outer diameter of the inner part  $d^I$  and the actual inner diameter of the outer part  $d^{II}$ . After assembling,  $d^I$  will decrease by an amount of  $\Delta r^I$ , and  $d^{II}$  will increase by an amount of  $\Delta r^{II}$ . Alternatively, we can present this as:

$$\frac{N}{2} = |\Delta r^I| + \Delta r^{II} = \left| \frac{p \cdot d^I}{2 \cdot E_1} \cdot (1 - \mu_1) \right| + \frac{p \cdot d^{II}}{2 \cdot E_2} \cdot \left( \frac{d^{II^2} + d_2^2}{d_2^2 - d^{II^2}} + \mu_2 \right) \text{ (mm)} \tag{9}$$

**Table 1** Boundary conditions and tangential stresses of the hollow shaft and the outer part

	Boundary conditions	Tangential stresses
Solid shaft	$\begin{cases} \sigma_r^I(r = r_1 = 0) = -p \\ \sigma_r^I(r = r_N) = -p \end{cases}$	$\begin{cases} \sigma_t^I(r = r_1 = 0) = -p \\ \sigma_t^I(r = r_N) = -p \end{cases}$
Hollow shaft	$\begin{cases} \sigma_r^I(r = r_1) = 0 \\ \sigma_r^I(r = r_N) = -p \end{cases}$	$\begin{cases} \sigma_t^I(r = r_1) = -\frac{2 \cdot p \cdot r_N^2}{r_N^2 - r_1^2} \\ \sigma_t^I(r = r_N) = -\frac{p \cdot (r_N^2 + r_1^2)}{r_N^2 - r_1^2} \end{cases}$
Outer part	$\begin{cases} \sigma_r^{II}(r = r_N) = -p \\ \sigma_r^{II}(r = r_2) = 0 \end{cases}$	$\begin{cases} \sigma_t^{II}(r = r_N) = \frac{p \cdot (r_N^2 + r_2^2)}{r_2^2 - r_N^2} \\ \sigma_t^{II}(r = r_2) = -\frac{2 \cdot p \cdot r_N^2}{r_2^2 - r_N^2} \end{cases}$

### 3 Calculation Results and Simulation of Interference Fit

We select the input parameters as follows: the nominal joint diameter  $d_N = 30$  mm, the inner part's inner diameter  $d_I = 0$  mm, the outer part's outer diameter  $d_2 = 50$  mm, the coupling length  $l_2 = 55$  mm, the inner part's length  $l_I = 70$  mm; and the material properties: assembly parts elastic modulus  $E = 2.06 \cdot 10^{11}$  Pa, Poisson's ratio  $\mu = 0.3$ , material yield strength  $\sigma_y = 350$  MPa, coefficient of friction  $f = 0.14$ , coefficient of contact safety  $K = 3$ , inner part contact surface roughness value  $R_{zd} = 0.8 \mu\text{m}$  and outer part contact surface roughness value  $R_{zD} = 1.6 \mu\text{m}$ . We specifically investigate the loading condition for only torque transmission  $T = 20$  Nm.

From the results between theoretical and simulating results, there is a good agreement. So from here, we can use simulation to determine the coefficients considering the influence of roughness on the calculated interference fit with different diameter sizes and material pairs (Fig. 2; Table 2).

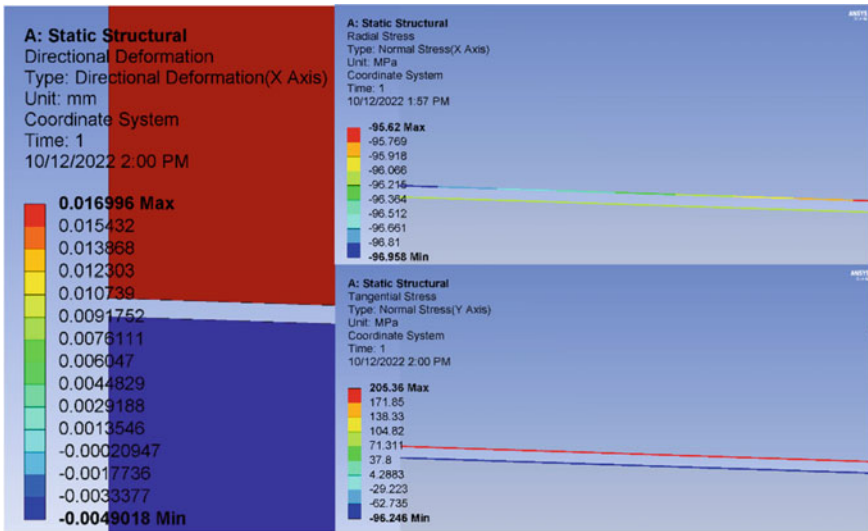


Fig. 2 Stress and strain simulation results at the interface



**Table 2** Comparison of stress and strain

	Section	Results		Deviation (%)
		Simulation	Theoretical calculation	
Radial stress		(MPa)	(MPa)	
Shaft— $\sigma_r^I$ (MPa)	$r_I = 0$	-96.180	-98.5285	+ 2.38
	$r = r_N$	-96.207	-98.5285	+ 2.36
Hub— $\sigma_r^{II}$ (MPa)	$r = r_N$	-96.958	-98.5285	+ 1.59
	$r = r_2$	-0.0128	0	
Tangential stress		(MPa)	(MPa)	
Shaft— $\sigma_t^I$ (MPa)	$r_I = 0$	-96.180	-98.5285	+ 2.38
	$r = r_N$	-96.246	-98.5285	+ 2.32
Hub— $\sigma_t^{II}$ (MPa)	$r = r_N$	205.360	209.373	+ 1.92
	$r = r_2$	108.280	110.845	+ 2.31
Strain		(mm)	(mm)	
Shaft— $\Delta r^I$ (mm)		0.0049018	0.00502210	+ 2.39
Hub— $\Delta r^{II}$ (mm)		0.0169960	0.01739792	+ 2.31

## 4 Conclusion

The above comparison tables show that the calculated results according to Lamé's formula and the values inferred from the simulation by the finite element method have certain similarities (deviation less than 5%). Because of this similarity, we can test the fit strength by transferring the existing 3D-designed model to the finite element environment, which could reduce the calculation steps or shorten the design time.

In addition, when simulating interference fits using finite element software, we can consider more variables, including temperature effects, contact pressure, thermal conductivity, and even values that traditional calculations cannot achieve.

This study has succeeded in the strength analysis of the interference fits by applying modern methods of simulation based on the conditions to ensure the functional ability of the transmission system. We could conduct more experiments to check the calculation and simulation results for further research. From there, we could discover technical solutions to improve the strength of the interference fits, which might be about new assembly techniques or enhancing the contact surface properties by coating and plating technologies [8, 9].

**Acknowledgements** We acknowledge Ho Chi Minh City University of Technology (HCMUT), VNU-HCM for supporting this study.

## References

1. Y. Zhang, B. McClain, X.D. Fang, Design of interference fits via finite element method. *Int. J. Mech. Sci.* **42**(9), 1835–1850 (2000). [https://doi.org/10.1016/s0020-7403\(99\)00072-7](https://doi.org/10.1016/s0020-7403(99)00072-7)
2. G.M. Yang, J.C. Coquille, J.F. Fontaine, M. Lambertin, Influence of roughness on characteristics of tight interference fit of a shaft and a hub. *Int. J. Solids Struct.* **38**(4243), 7691–7701 (2001). [https://doi.org/10.1016/s0020-7683\(01\)00035-x](https://doi.org/10.1016/s0020-7683(01)00035-x)
3. N.S. Prasad, P. Sashikanth, V. Ramamurti, Stress distribution in interference joints. *Comput. Struct.* **51**(5), 535–540 (1994). [https://doi.org/10.1016/0045-7949\(94\)90060-4](https://doi.org/10.1016/0045-7949(94)90060-4)
4. H.L. Nguyen, V.P. Lam, Probabilistics design and analysis of metal interference fits. *Adv. Eng. Forum* **47**, 11–18 (2022). <https://doi.org/10.4028/p-904z3i>
5. H.L. Nguyen, *Machine Design and Machine Elements* (Vietnam National University Ho Chi Minh City Publishing House (VNUHCM Press), 2020)
6. M.P. Groover, *Fundamentals of Modern Manufacturing: Materials, Processes, and Systems* (John Wiley & Sons Singapore Pte Ltd., 2021)
7. International Organization for Standardization, Geometrical product specifications (GPS)—ISO code system for tolerances on linear sizes—Part 2: Tables of standard tolerance classes and limit deviations for holes and shafts (ISO Standard No. 286–2:2010) (2010)
8. H.L. Nguyen, V.P. Lam, Study of interference fit between steel and brass parts. *EUREKA Phys. Eng.* **5**, 140–149 (2022). <https://doi.org/10.21303/2461-4262.2022.002524>
9. H.L. Nguyen, V.P. Lam, Effects of nickel plating on interference fit between medium carbon steel and copper-zinc alloy parts. *Metals* **13**(2), 247. <https://doi.org/10.3390/met13020247>

# Analysis and Optimisation of Magnetorheological Dampers Using Ansys Workbench



Kim-Thach Tran, Nguyen Van Bien, Quoc Hung Nguyen, and Weihua Li

**Abstract** This paper presents the analysis and optimisation of damper featuring magnetorheological fluid (MRF), shortly called MR dampers, numerically using finite element method. In other words, this work documents the analysis and optimisation of MR dampers using finite element method and design optimisation function provided by ANSYS Workbench software package. Firstly, the performance of a MR damper is analysed using ANSYS Parameter Design Language (APDL). The APDL program used to analyse the behaviour of the MRF damper is then implemented into the ANSYS Workbench Design Optimisation Tool to perform design optimisation. Different single objective optimisation methods were implemented to minimise the objective function derived for the MR damper at different configurations. The optimisation analysis will be extended to prototype MR dampers and evaluate their performances.

**Keywords** Magnetorheological fluid · MR damper · Optimisation · ANSYS workbench

---

K.-T. Tran · W. Li (✉)

School of Mechanical, Materials, Mechatronic and Biomedical Engineering, University of Wollongong, Wollongong, NSW 2522, Australia  
e-mail: [weihuali@uow.edu.au](mailto:weihuali@uow.edu.au)

N. Van Bien

Faculty of Mechanical Engineering, Industrial University of Ho Chi Minh City, Ho Chi Minh City, Vietnam

Q. H. Nguyen (✉)

Faculty of Engineering, Vietnamese–German University, Thu Dau Mot City, Binh Duong Province, Vietnam  
e-mail: [hung.nq@vgu.edu.vn](mailto:hung.nq@vgu.edu.vn)

## 1 Introduction

Magnetorheological fluid (MRF) is a class of smart materials that consists of non-colloidal suspension of magnetisable particles in a non-magnetisable fluid [1]. When exposed to magnetic fields, the particles in the MRF align themselves along the line of the magnetic flux, which changes the state of the fluid from a viscous liquid to a semi-solid state [2]. This property makes MRF suitable for semiactive damper applications because the magnetic field can be applied to the MRF flow using an electromagnetic coil and controlled by controlling current through the coil supplied by an external power source [3]. Semiactive magnetorheological damper, shortly called MR damper, features electromagnetic coils that are designed to apply magnetic field to the flow of MRF within the damper. Controlling the current supplied to the built-in coil controls the flow behaviour of MRF in the damper, thus controls the damping force of the device [4]. Different MR damper configurations proposed by literature employs either single flow mode, shear mode, mixed mode, and multi-mode operation [5].

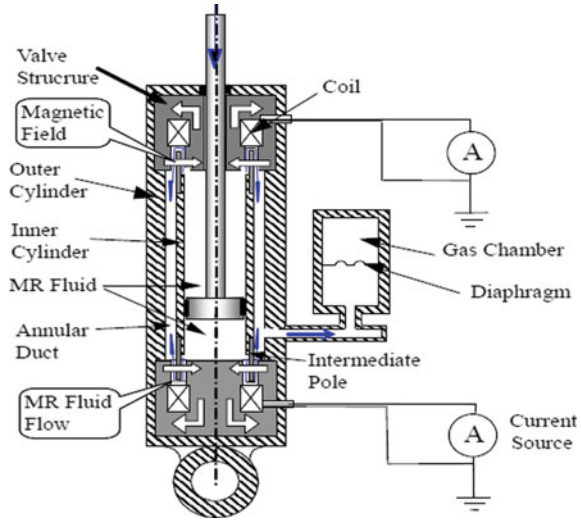
MR dampers are electromagnetic devices therefore analysing the performance of such devices requires the solution of the magnetic field distribution of the device's magnetic circuit. From this distribution, one can determine the magnetic field applied to the flow of MRF and from there determine the performance (such as damping force) of the damper [6]. The magnetic field distribution in a body can be determined analytically, or numerically using Finite Element Analysis FEA method. Since the magnetic circuits in MR dampers are complicated, FEA method is more preferred. This work involves the use of FEA method to analyse the performance of MR dampers via ANSYS software package and utilises the design optimisation function in ANSYS Workbench to find the optimal design parameters for the MR damper. Here, both local and global optimisation methods are used in an endeavour to determine the global optimum damper design within the specified domain of design variables.

## 2 Analysis of the MR Monotube Damper

### 2.1 Overview

This work considers the MR damper used for vehicle suspension studied in reference [6], which uses the valve mode of MRF. Figure 1 presents the schematic of the MR damper configuration. This MR damper features two concentric cylinders. The inner cylinder features a single rod piston that can move linearly within its barrel. The piston separates the working fluid volumes into two chambers, and the working volume of the damper is filled with MRF. The outer cylinder is purposed to duct the flow of fluid from one chamber to another, and there is MRF valve mechanism is located at each end of the cylinder to control the flow of MRF between the inner and outer cylinder. The MRF valve consists of excitation coils connected to an external

**Fig. 1** Schematic of the MR damper



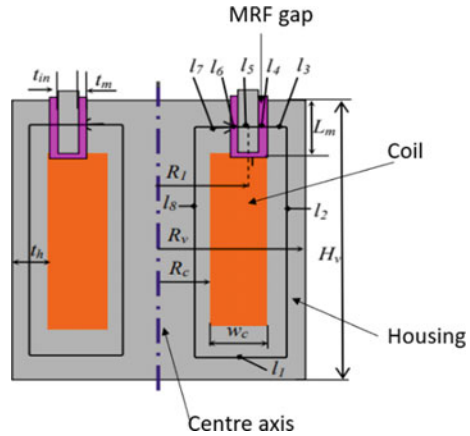
current source supplying magnetic field to a small MRF gap. The magnetic field at the MRF gap can be controlled by controlling the current supplied to the coil. Therefore, the damping effect of this damper is controllable by controlling the current supplied to the coil. To ensure that the working volume is filled with MRF, an external fluid compensator is used.

## 2.2 Magnetic Circuit of the Damper

The distribution of magnetic field intensity in the magnetic circuit of the damper is important for the analysis of the MR damper performance. Figure 2 presents the schematic of the section view of the approximated magnetic circuit of the MR damper. In this magnetic circuit, the housing and intermediate pole of the damper are shown in grey; the coils are shown in orange and the MRF gaps are indicated in dark pink. The variables used in Figure 2 presents dimension parameters in the magnetic circuit of the damper. They are annotated as follows:  $t_h$  is the housing thickness of the damper;  $H_v$  is the height of the valve element,  $L_m$  is the length of the magnetic pole;  $R_1$  is the average radii of the intermediate pole;  $R_v$  is the radii of the valve element;  $R_c$  is the valve core radius;  $t_m$  is the gap of the orifice of the MR valve structure;  $w_c$  is the width of the coil and  $t_{in}$  is the intermediate pole thickness.

This magnetic circuit will be modelled into ANSYS APDL to solve for the magnetic field intensity distribution within the MRF damper. PLANE13 Axisymmetric element are used in the FEA model. The required inputs include the geometry of the magnetic circuit, properties of materials (BH relationships of the materials), meshing information (type of element and mesh size), excitation current intensity and

**Fig. 2** Approximated magnetic circuit



boundary conditions. The average magnetic field intensity at the MRF gap obtained from the solution of the FEA of the circuit will be used for calculating the MRF yield stress, while the magnetic flux density at the coil will be used for calculation of the inductive time constant of the coil.

### 2.3 Materials

#### 2.3.1 MR Fluid

In this work, a B-H curve is used to represent magnetic property of MRF. The relationship between yield stress of a MRF  $\tau_y$  and average steady state magnetic field intensity at the MRF gap  $H_{mr}$  (kA/m) can be mapped using the following polynomial [6].

$$\tau_y = c_0 + c_1 H_{mr} + c_2 H_{mr}^2 + C_3 H_{mr}^3 \text{ (kPa)} \tag{1}$$

whereas  $c_0$ ,  $c_1$ ,  $c_2$  and  $c_3$  are experimentally determined coefficients for specific designation of MR fluid. Lord corporation MRF132DG magnetorheological fluid is used in this work. Its values of  $c_0$ ,  $c_1$ ,  $c_2$  and  $c_3$  are presented respectively as 0.30, 0.42,  $-0.00116$  and  $1.5 \times 10^{-6}$ . The post-yield viscosity of MRF  $\eta$  is assumed to be constant. For MRF132DG, the post-yield viscosity is  $\eta = 0.092$  Pa s.

#### 2.3.2 Housing and Coil Material

The coil was assumed to be made of copper, which has the relative permeability of  $\mu = 1$ . The resistivity of copper used in the coil is  $\rho_{wire} = 1.68 \times 10^{-8} \Omega\text{m}^{-1}$ . The

housing of the MR valve in the damper is made of silicon steel, and similarly to the MRF, the B-H relationship of silicon steel is provided to the ANSYS APDL as tabulated data.

### 3 Optimisation

#### 3.1 Overview

This section documents the optimisation of the MR damper. The damper with optimised performance is the damper that has the minimum value of the objective function *OBJ*. The objective function *OBJ* is derived from the performance parameters of the damper [6], which can be represented as:

$$OBJ = \alpha_F \frac{F_{MR}}{F_{mr,r}} + \alpha_D \frac{\lambda_d}{\lambda_{d,r}} + \alpha_T \frac{T_{in,r}}{T_{in}} \quad (2)$$

where  $F_{MR}$  is the damping force caused by MR effect at current iteration;  $\lambda_d$  is the dynamic range at current iteration;  $T$  is the inductive time constant at the current iteration;  $F_{MR,r}$  is the reference damping force  $\lambda_{d,r}$  is the reference dynamic range;  $T_{inr}$  is the reference inductive time constant;  $\alpha_F$  is the damping force weight factor;  $\alpha_d$  is the dynamic range weight factor and  $\alpha_T$  is the inductive time constant weight factor. The reference values of  $F_{mr}$ ,  $\lambda_d$  and  $T_{in}$  are the values of the performance parameter at the initial iteration of the optimisation. It must be noted that  $\alpha_F + \alpha_D + \alpha_T = 1$  and the determination of such weighing factors depends on the design objective of the damper. In this work, the damping force, the dynamic range, and the response speed of the damper is of equal important. Thus,  $\alpha_F = \alpha_T = \alpha_D = 1/3$ .

#### 3.2 ANSYS Optimisation Methods

ANSYS Workbench design optimisation function is used to perform the design optimisation. This design optimisation function uses an algorithm to change the design variables then use them to run the ANSYS APDL program at each iteration. The group of design variables at each evaluation is called a “design point”. The constant dimensions variables as well as other constant physical quantities are kept constant. The performance parameters returned by ANSYS APDL after each calculation is recorded, and the aim of the algorithm is to evaluate and determine a design point of design variable such that the value of OBJ is minimum. In this work, ANSYS Workbench Multiple Objective by Generic Algorithm (MOGA), Adaptive Multiple Objective (AMO), Nonlinear Programming by Quadratic Lagrangian (NLPQL) and Mixed Integer Sequential Quadratic Programming (MISQP) are used to perform the

optimisation. The MOGA and AMO methods determines the global optimum design point whereas the NLPQL and MISQP methods determines the local optimum point. These methods permit multiple constraints to be imposed to the optimisation problem in ANSYS. The global optimisation methods used here are adopted from the Non-dominated Sorted Generic Algorithm II (NSGA-II) whereas the local methods are based on nonlinear programming.

### 4 Results and Discussion of Results

Table 1 presents the design (input) parameters comparison between the initial and optimal design point determined by different methods; while Table 2 presents the performance (output) parameter comparison between the initial and optimal design point.

The results shown that the value of *OBJ* for optimised damper determined by different ANSYS optimisation methods ranges from 0.750 to 0.808. The lowest value of *OBJ* is 0.750, which was determined by the NLPQL local optimisation method. This is a 25–19.2% decrease of the value of *OBJ* compared to the initial design point. Interestingly, the optimal values of *OBJ* determined by global methods such as AMO and MOGA are within close proximity to 0.750 however they are slightly larger than the minimum value of 0.750. Since global optimisation methods examines all the possible design parameter sets within the specified domain, there is a high possibility that the monotube damper with the optimal performance within the specified design variables domain, using the constant dimensions and variables specified previously has a value of *OBJ* being 0.750. While the optimisation program was running, it was observed that some of the design point has failed to generate and returned error messages instead of the values of the performance parameters. This can be

**Table 1** Design parameters comparison between initial and optimised design point

Design parameter	Initial design point	Domain		Optimised design point			
		Minimum (m)	Maximum (m)	MOGA method	AMO method	NLPQL method	MISQP method
Pole length $L_m$	0.01	0.003	0.015	0.009547	0.014201	0.011165	0.010984
MRF orifice gap $t_m$	0.00075	0.0005	0.002	0.000755	0.000827	0.000629	0.000626
Width of coil $w_c$	0.0035	0.0035	0.01	0.009353	0.004563	0.003500	0.003907
Housing thickness $t_h$	0.003	0.001	0.005	0.003975	0.004786	0.004220	0.003671
Intermediate pole thickness $t_{in}$	0.002	0.001	0.005	0.001088	0.002857	0.002143	0.002641



**Table 2** Performance parameters comparison between initial and optimised design point

Performance parameter (unit)	Initial design point	Optimised design point value			
		MOGA method	AMO method	NLPQL method	MISQP method
Magnetorheological force $F_{MR}$ (N)	3195.7954	7598.253	8985.167	9384.900	6881.573
Damping force $F_d$ (N)	3536.7956	8200.0	9647.629	9625.100	7440.778
Inductive time constant $T_{in}$ (ms)	2.204	2.608	2.820	2.761	2.597
Dynamic range $\lambda_d$	10.372	13.511	14.559	15.256	13.289
Objective function $OBJ$	1	0.790	0.783	0.750	0.808

attributed to minor errors happened while the program was modelling the geometry of the magnetic circuit in ANSYS PDL. Nevertheless, the optimisation calculations for finding the optimal design point of the damper using different methods still converges and provided optimal design points.

With the aforementioned results, it can be a good practice for one adopt the following procedure for optimisation using ANSYS Workbench. Firstly, a global optimisation method is chosen to find an approximated global optimum design point within the initially specified domain of design variables. Secondly, a local optimisation program (using NLPQL method, etc.) can be run with the approximated design point determined by the global optimisation method.

## 5 Conclusions

This work presented the analysis and optimisation of a MR damper configuration using ANSYS Workbench. The optimal design point provided by local and global methods are similar to each other, while the local NLPQL method has resulted in the design point lowest value of the objective function  $OBJ$  (0.750). This brings to the suggestion that one shall begin the optimisation procedure by using a global optimisation method then use the approximated global optimum design point as a starting point to initiate a local optimisation program to find the refined global optimum. From the findings of this work, a prototype of a MR damper can be constructed to experimentally verify the calculated performance parameters. Experimental verification with a functional prototype is the most common approach to verify the results obtained from theoretical calculations and simulations.

## References

1. J. Vincente, D. Klingenberg, R. Hidalgo-Alvarez, Magnetorheological fluids: a review (2010)
2. A. Hajalilou, S. Mazlan, S. Shila, Magnetic carbonyl iron suspension with Ni-Zn ferrite additive and its magnetorheological properties. *Mater. Lett.* **181**, 196–199 (2016)
3. K. Choi, H. Jung, S. Cho, I. Lee, Application of smart passive damping system using MR damper to highway bridge structure. *J. Mech. Sci. Technol.* **21**(6), 870–874 (2007)
4. Z. Xu, L. Sha, X. Zhang, H. Ye, Design, performance test and analysis on magnetorheological damper for earthquake mitigation. *Struct. Control. Health Monit.* **20**(6), 956–970 (2012)
5. M. Abdul Aziz, S. Mohtasim, R. Ahammed, State-of-the-art recent developments of large magnetorheological (MR) dampers: a review. *Korea-Australia Rheol. J.* **34**(2), 105–136 (2022)
6. H. Nguyen Quoc, S. Choi, Optimal design methodology of magnetorheological fluid based mechanisms (2012)

# Development of the Control Method for AGV to Navigate in the Warehouse



Van Hieu Phan

**Abstract** Logistics activities with automatic guided vehicles (AGV) are essential in the warehouse in Industry 4.0. With the help of AGV, transporting goods in the warehouse will become more accessible and convenient. AGV navigation operating in friendly environments is currently being researched and developed because the AGV must maneuver in an area with moving obstacles. An RGB-D camera is used for automatic navigation to scan the working environment and recognize barriers in front of the AGV. A cylinder is mounted on AGV to perform lifting tasks. The mapping method used in this paper is Rao-Blackwellized. This method is implemented with the support of ROS. The motion navigation is performed by the A\* algorithm. In the process of moving, if the AGV detects a person in front of it, it will re-plan the trajectory with its current position by the AMCL method. These proposed methods were tested and applied successfully in a narrow environment.

**Keywords** AGV · Navigation · ROS · Robotics

## 1 Introduction

One of the essential functions of the AGV is the ability to automatically plan and navigate the trajectory so that the robot can move to its destination on its own. The first generation of AGVs used a magnetic stripe for navigation. Later methods similar to laser scanning on various colors were also developed to reduce costs. In this case, the AGV only acts as a self-propelled trolley with low travel speed.

There are different types of industrial AGVs on the market today. When AGV is used in any known or unknown context, it is primarily considered in terms of localization, mapping, and navigation.

---

V. H. Phan (✉)

School of Mechanical Engineering, Hanoi University of Science and Technology (HUST), No.1 Dai Co Viet Street, Ha Noi 100000, Vietnam

e-mail: [hieu.phanvan@hust.edu.vn](mailto:hieu.phanvan@hust.edu.vn)

Most AGVs use laser rangefinders for mapping [1] and zoning, and with the route planning algorithm's global path planning approach [2], all paths are simulated once. The scoring formula selects the way with the highest score to reach the destination [3]. This study proposes a low-cost method of developing automated unmanned trolleys with artificial intelligence that can efficiently and accurately map, navigate, and be used in production lines. Industrial output with a depth camera [4–10].

## 2 AGV Design and Implementation

### 2.1 Hardware Structure

The AGV in this study is made of aluminum. The ROS system is controlled by a laptop embedded in the AGV. The RGB-D Kinect camera collects point cloud data for system image recognition and deep learning. The Kinect camera both scans the map through depth imaging and recognizes people. All collected data will be processed by the laptop using the UART protocol. The smartphone is connected to the microcontroller via the Bluetooth module to control the AGV to scan the map manually. The MPU module allows the user to define the current rotation of the AGV, which in turn serves as an input data source for the algorithm to determine the vehicle's position in a dynamic environment (Fig. 1).

AGV has a four-wheel structure, with one pair of self-selecting wheels at each end and two drive wheels in the center (controlled by 2 DC encoder motors). The structure allows the vehicle to move with flexibility thanks to the 2-wheel drive speed control while also allowing it to rotate at an arbitrary angle at the center (2 wheels rotate at the same speed, opposite each other). The design accommodates large loads suitable for container handling implementations, and the lifting mechanism allows the goods to be lifted to higher positions. The camera position must be in the direction of the robot's approach to create a map and navigate it. As a result, the camera will be mounted on the front of the robot (Fig. 2).

### 2.2 Software Structure

ROS and the STM32 Cube IDE were among the software architectures used. ROS is used mainly for AGV navigation and control. The UART protocol is used to communicate between the AGV and the computer. To send control commands from ROS to the microcontroller and receive encoder data, we must write a program that communicates via UART between the microcontroller and the computer. Two USB UARTs are required to perform the task, one for sending control signals from ROS to the microcontroller and the other for sending the encoder to ROS. Because both of

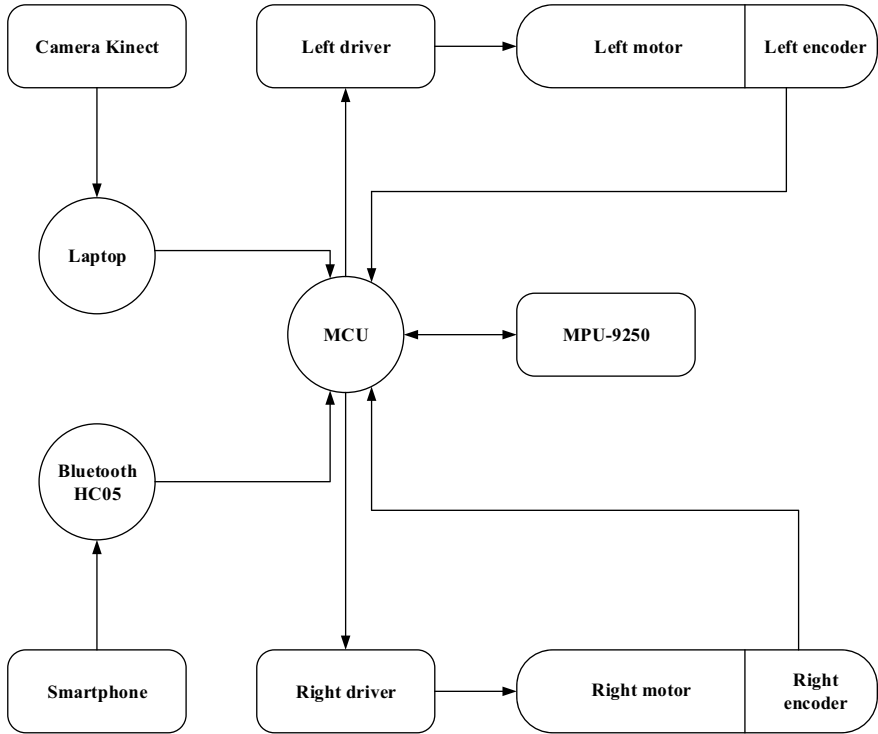
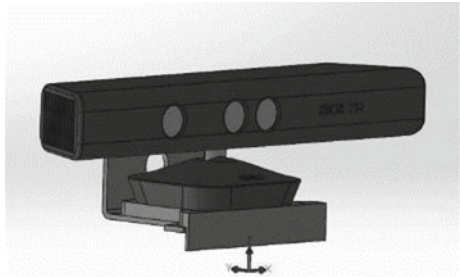


Fig. 1 Electrical system

Fig. 2 Camera fixture



the other signals are constantly sending high frequencies, using only one USB will cause congestion; two USBs are required.

### 3 Method and Implementation

This paper will use the ROS environment to develop self-propelled AGVs indoors. The robot model with mapping and positioning capabilities, as shown in Fig. 3 divided into different Nodes. Each Node will perform a separate function and have an IP address similar to TCP/IP. When a node wants to send data to another node, it will connect to the Master. The Master performs a handshake for two nodes exchanging data through a topic.

#### 3.1 Keyteleop Node

The Keyteleop Node receives control information from the user to convert to the robot’s angular and linear velocity. Input is user-control information from the keyboard. Output is linear velocity  $v(m/s)$  and angular velocity  $w(rad/s)$  (Table 1).

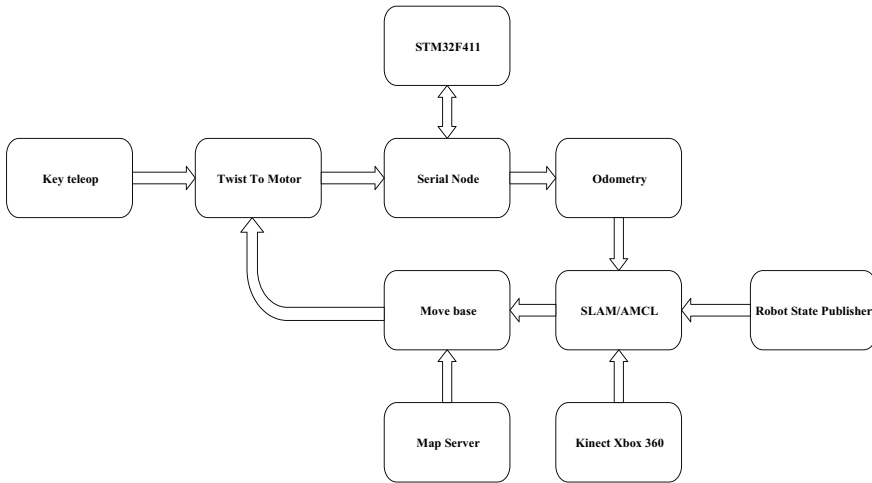
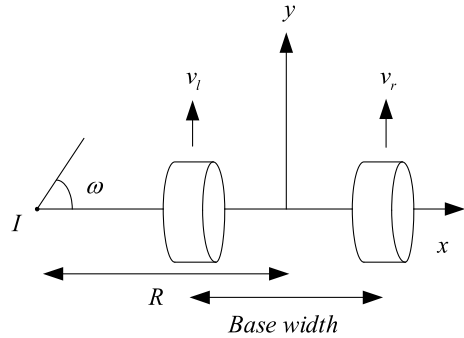


Fig. 3 ROS platform

Table 1 Velocity corresponding to control command

Command	Linear velocity (m/s)	Angular velocity (rad/s)
Forward	$v$	0
Backward	$-v$	0
Rotate left	0	$w$
Rotate right	0	$-w$
Stop	0	0

**Fig. 4** Velocity values of the robot



### 3.2 Twist to Motor Node

The Node Twist to Motor converts linear and angular velocity to velocity values for each Motor. The relationship between linear velocity  $v$ , angular velocity  $w$ , and velocity of the left  $v_l$  and the right Motor  $v_r$  is shown in Fig. 4.

With:

- + Base width: distance between two wheels (m).
- + I: virtual center of the circle when the robot is run in sub-orbits.
- + R: distance from virtual center to center of gravity of the robot.

### 3.3 Serial Node

Serial Node implements communication between MCU and ROS through serial communication. The two main functions of a Serial node are:

1. Read the left and right encoder values. These values are sent as <encoderLeft > < encoder right > . The serial Node will perform string processing to separate the corresponding value. These values will be exported to the Odometry node to estimate the robot's position.
2. They are getting the speed value driving the two motors and sending it down to the MCU. These two velocity values are shipped from the Twist to the Motor Node.

### 3.4 Odometry Node

The Odometry Node estimates the robot's position (x,y, theta) from the information of the encoder and the MPU. The robot's position is represented by a triple of the parameter where is the coordinate of AGV in the Descartes coordinate system, and theta is the robot's distance relative to the x-axis. The trajectory of the robot after

time  $t$  is:

$$\begin{bmatrix} x' \\ y' \\ \theta' \end{bmatrix} = \begin{bmatrix} \cos \theta_0 & -\sin \theta_0 & 0 \\ \sin \theta_0 & \cos \theta_0 & 0 \\ 0 & 0 & 1 \end{bmatrix} \begin{bmatrix} x \\ y \\ \theta \end{bmatrix} + \begin{bmatrix} x_0 \\ y_0 \\ \theta_0 \end{bmatrix} \quad (1)$$

whereas:

- +  $x_0, y_0, \theta_0$ : Initial position of AGV.
- +  $x', y', \theta'$ : Present position of AGV.
- +  $x, y, \theta$ : Position of AGV after  $\Delta t$ . It can be calculated by:

$$\begin{cases} x = d \cos \theta \\ y = d \sin \theta \\ \theta = w \cdot \Delta t \end{cases} \quad (2)$$

The angular speed  $w$  can be calculated from the encoder and then converted to the robot's rotation angle. However, during the test, the angular speed calculation from the encoder has a significant error, affecting the positioning problem. Therefore, the MPU reads the robot's rotation value directly. The moving distance  $d$  of the robot is calculated from the independent travel distances of two of the left and right wheels through the encoder's reading value according to the formula:

$$\begin{cases} d = d_{left} + d_{right} \\ d_{right} = \frac{\Delta_{encoder\_right}}{tick\_meter} \\ d_{left} = \frac{\Delta_{encoder\_left}}{tick\_meter} \end{cases} \quad (3)$$

With:

- +  $\Delta_{encoder\_right}, \Delta_{encoder\_left}$ : number of encoder pulses after  $\Delta t$  (pulse).
- +  $d_{left}, d_{right}$ : the distance between the left and right wheels traveled (m).
- +  $tick\_meter$ : number of pulses for the wheels to travel one meter.

### 3.5 *Kinect and Depthimage\_to\_Laserscan Node*

The Kinect node performs data reading from the Kinect camera. The OpenNI driver is used to retrieve RGB and depth images from Kinect. A depth image is used to map and identify obstacles around AGV (Figs. 5 and 6).



**Fig. 5** The process of converting depth data to point cloud data

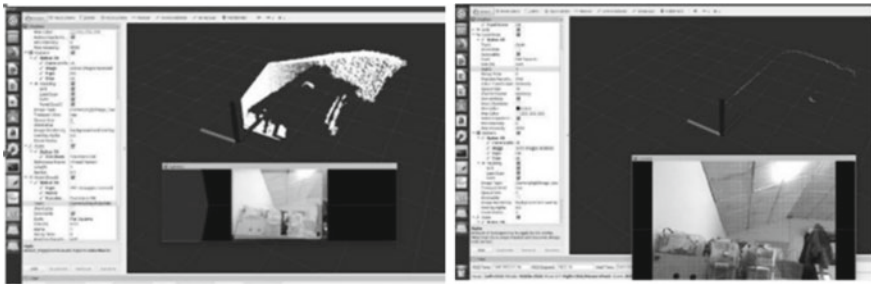
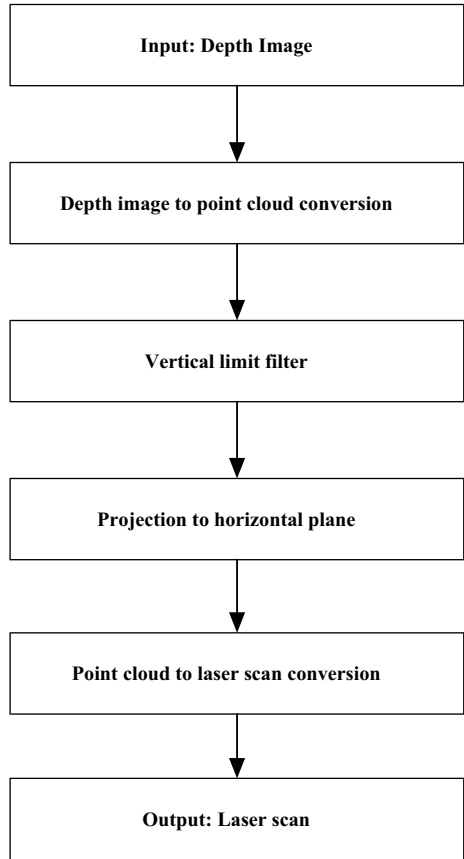


**Fig. 6** Depth map (left) and laser scan map (right)

### 3.6 SLAM/AMCL Node

The SLAM node maps the environment when the robot receives the location estimate and data from the Kinect sensor. To locate and avoid obstacles, the robot needs to know the map of the environment. For the first time, the user will control the robot to move manually to draw a domain map. The map is drawn using the mapping method. The AMCL node performs the task of determining the position of the robot on the map. Therefore the AMCL button works when the robot locates itself and moves on the map. Two SLAM and nodes AMCL do not work at the same time.

### 3.7 Map Server Node and Move Base Node

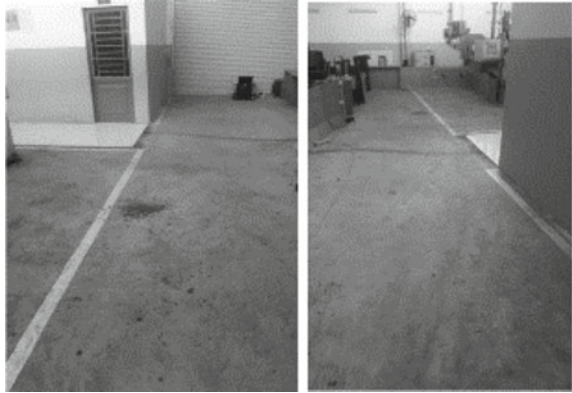
The node map server is used to manage the map used by the robot. The map server provides tools to save maps drawn from SLAM and load maps for use by AMCL nodes. The map is held in two different files. A YAML file stores map parameters like map name, resolution, original origin (usually (0, 0, 0)), and obstacle level threshold. The other file is an image file of the map, usually a grayscale image. A pixel with black color is an obstacle, white means no impediment, and gray indicates a map area with no information because it has not been detected yet (Fig. 7).

Node move base uses robot position from AMCL and Map Server map to control the robot's movement to the destination. The predefined path will be found using the A\* algorithm. In moving, the robot will find a new route to the destination if an obstacle appears. Control information, including linear and angular velocity, is transmitted by the Node Twist to the Motor to control the robot.

**Fig. 7** Map of the environment managed by map server



**Fig. 8** The robot's operation space



## 4 Results and Discussion

### 4.1 Results of Building Map with ROS Package

The AGV is manually controlled and moves around the environment to conduct data scans. Users using the phone connect to the Bluetooth module and move the AGV at a speed of 0.2 m/s for the best data retrieval (Fig. 8).

The map correctly represents the boundaries that the environment has set. Due to a lot of shaking during the robot movement, the sensor value returned from the Kinect is overlapped.

### 4.2 Results of Experimental Navigation of AGV Based on a Pre-built Map

The controller constructs a path for the robot from start to finish. This path is built based on the A\* algorithm, and the robot's position is continuously updated to the computer via AMCL Nodes.

After assigning the destination as the point with the arrow, the robot proceeds to find the way using the A\* algorithm. Figure 9 shows the estimated path of the robot. Finally, the robot moves to the destination, as shown in Fig. 10, with the particle more focused than the original, thanks to the map observation process. Map and actual destination locations are measured to determine offset distances (in meters) (Table 2).

The average position error of the robot is: 0.0126 m.

**Fig. 9** Mapping result

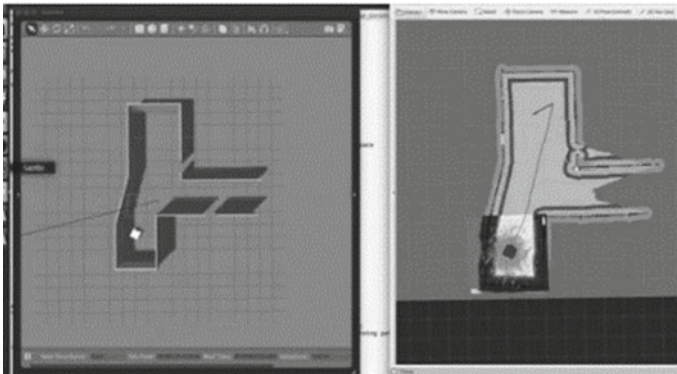
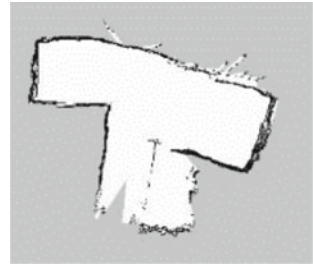


**Fig. 10** Creating a path for AGV

**Table 2** Actual measurement data table of robot position

Times	Map position		Real position		Error	
	$x$	$y$	$x$	$y$	$\Delta x$	$\Delta y$
1	3.4001	-0.8817	3.29	-0.74	0.1101	0.1417
2	2.7794	-1.1419	2.80	-1.09	0.0206	0.0519
3	3.5318	-1.1089	3.43	-1.15	0.1018	0.0411
4	3.3475	-0.8695	3.23	-0.85	0.1175	0.0195
5	2.8559	-0.9629	2.71	-0.95	0.1459	0.0129
Average					0.09918	0.05342

### 4.3 Discussion of Results

AGV navigation is based on pre-recorded maps to highlight key application areas. The output is a powerful demonstration for exploring AGV's Navigation based on the built-in map system. Further research needs further investment using smart diagrams.

## 5 Conclusion

This paper presented a method for building a map base on a single-depth camera. The quality of the map is only affected by the unevenness of the road surface. The map envelope dimensions are guaranteed, allowing the AGV to perform precise trajectory planning. The limitation of the paper lies in the integration of obstacle avoidance during the movement. When the AGV encounters an obstacle, it takes a long to re-plan the trajectory, leading to interrupted movement. However, the A\* algorithm is successfully applied to help AGV move to the destination with the error within an acceptable range.

## References

1. C.C. Peng, Y.T. Wang, C.L. Chen, LIDAR based scan matching for indoor localization, in *2017 IEEE/SICE International Symposium on System Integration (SII)* (2017)
2. A. Babineca, M. Kajana et al., Path planning with modified a star algorithm for a mobile robot. *Procedia Eng.* **96**, 59–69 (2014)
3. S. Satake, T. Kanda, D.F. Glas, M. Imai, H. Ishiguro, N. Hagita, A robot that approaches pedestrians. *IEEE Trans. Rob.* **29**(2), 508–524 (2013)
4. P. Estefo, J. Simmonds, R. Robbes, J. Fabry, The robot operating system: package reuse and community dynamics. *J. Syst. Softw.* **151**, 226–242 (2019)
5. Y.C. Huang, *Development of Automated Guided Vehicle under ROS Architecture* (National Taipei University of Technology, Taipei, Taiwan, 2018)
6. J.P. Machado dos Santos, in *SmokeNav—Simultaneous Localization and Mapping in Reduced Visibility Scenarios* (2013)
7. M. Ben-Ari, F. Mondada, Robotic motion and odometry, in *Elements of Robotics* (Springer International Publishing, Cham, 2018), pp. 63–93.
8. T.P. Nguyen, H. Nguyen, V.H.ieu Phan, H.Q.T. Ngo, Modeling and practical implementation of the motion controller for stable movement in a robotic solar panel dust-removal system. *Energy Sources, Part A: Recov. Utilizat. Environ. Effects* (2021). <https://doi.org/10.1080/15567036.2021.1934194>
9. V.H. Phan, Research on motion control by filtering performance for aerial robotic system, in *Lecture Notes in Mechanical Engineering (Indexed in Scopus)* (2022), pp. 942–947. ISBN: 978-3-030-99666-6
10. V.H. Phan, Research of vision-based approach for assisted-robot, in *Lecture Notes in Mechanical Engineering (Indexed in Scopus)* (2022), pp. 924–929. ISBN: 978-3-030-99666-6

# Structural Topology Optimization of a Large-Sized Link Mechanism in a Radar Antenna Lifting System



Van Doan Cao, Duc Dung Le, and Duc Son Hoang

**Abstract** Topology optimization is performed to reduce material and get the optimum shape of a component that sustains the load transmitted to it. This paper presents the generation and analysis of the optimized design of a bar in the large-sized link mechanism that is used in the radar antenna lifting system. First, the load acting on the bar during antenna lifting is investigated. Next, the most crucial load is applied to the bar under the topology optimization procedure using the SW Ansys Workbench 2021. Based on the finite element analysis using ANSYS, the optimized link mechanism shape is finally modified to achieve the stiffness and strength of the origin requirement. The reduction in initial shape weight achieved is 18.3%. The final link shape is possible to produce using conventional technologies. The article gives the recommendations for further large-sized planer linkages.

**Keywords** Finite element analysis · Lightweight design · Link mechanism · Structure · Topology optimization

## 1 Introduction

Topology optimization (TO) is an optimization technique where the material distribution of a structure is spatially optimized by minimizing or maximizing one or more objective functions, such as stiffness and cost, with respect to given constraints, for example, a specific weight reduction [1]. Structural optimization, in general, has been well described over the past decades in the literature [2, 3].

---

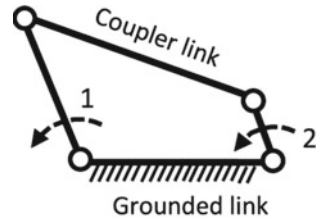
V. D. Cao (✉)

Radar Centre, Viettel High Technology Industries Corporation, Viettel Building, Hoa Lac Hi-Tech Park, Thach That, Ha Noi, Vietnam  
e-mail: [doancv@viettel.com.vn](mailto:doancv@viettel.com.vn)

D. D. Le · D. S. Hoang

Centre for Mechanical Technology and Automation, Viettel High Technology Industries Corporation, Viettel Building, Hoa Lac Hi-Tech Park, Thach That, Ha Noi, Vietnam

**Fig. 1** Typical four-bar mechanism



Linkage mechanisms are very important in mechanical systems because they enable the optimisation of forces and motions [4, 5]. One of the earliest recorded designs of linkage mechanisms was in 1784 when James Watt published his parallel four-bar linkage for converting rotary into linear motion in steam engines [6]. Since this time, four-bar linkages have been extensively used in a wide range of applications, including: vehicle steering units, windscreen wiper drives, vehicle window lifting mechanisms, crane level luffing systems, angle poise lamps, riser recliner chairs, up-and-over doors, and double-glazing window hinges.

The ability of linkage mechanisms to fine-tune mechanical performance is due to the very large range of possible layouts. As is common practice, one link is shown as grounded, whilst the opposite link is referred to as the coupler link. There is normally one input link and one output link. In general, the input and output links can be any of the three links that are not the grounded link.

Figure 1 shows a typical four-bar mechanism used in the antenna lifting system: link 1 input (amplify force), amplify movement (link 2 input). By adjusting the length of the bars, a vast range of motions of the coupler link is possible. The lifting mechanism should be light enough to minimize operating costs and the amount of steel used while keeping stress values under designated stress limits against fatigue failure.

This article takes a certain type of input link mechanism in the antenna lifting system as the research object and uses the variable density method based on the variable density theory to carry out lightweight research on it. Due to the overall weight limitation of a certain type of large-size linkage, all structural parts need to be considered for lightweight design. Although the link mechanism is only one of the structural parts, it is particularly important to carry out a lightweight design due to the large number of components used in the large radar system that is integrated into specialized vehicles.

## 2 Material and Method

Optimizing topology distributes the limited quantity of materials in the field of design, which improves structural efficiency in relation to a set of design and performance constraints [1]. This study used a common technique of Solid Isotropic Material with Penalization (SIMP) [7]. In the SIMP, each structural element in the discretized

design area can have a material density value between 0 (void) and 1, and its stiffness is calculated as follows:

$$K = (\rho_e)^p K_0; p > 1 \tag{1}$$

where:  $K$ —element stiffness,  $\rho_e$ —element density,  $p$ —penalization factor which usually is three or larger,  $K_0$ —stiffness of the material. The higher the penalty factor ( $p$ ), the more aggressive elemental density values are driven to 0 or 1. The sensitivity analysis becomes simpler for traditional compliance minimization since the objective function shown below becomes differentiable.

$$\min_{\rho_e} C = U^T K U = \sum_{e=1}^n U_e (\rho_e) U_e = \sum_{e=1}^n (\rho_e)^p U_e K_0 U_e \tag{2}$$

$$\text{Subject to : } V = f(V_0) = \sum_{e=1}^n \rho_e V_e \leq V^* \tag{3}$$

$$F = K U \tag{4}$$

$$0 < \rho_{min} \leq \rho_e \leq 1 \tag{5}$$

where:  $C$ —structural compliance,  $U$ —displacement,  $U_e$ —elemental displacement,  $V$ —volume,  $V^*$ —volumetric constraint,  $F$ —applied forces.  $\rho_{min}$ —small value to avoid any singularities.

The mechanism in the antenna lifting system is actuated by an electric cylinder. The input link applies a launching force to take the intermediate link from a horizontal position to a vertical position and vice versa. According to kinetic analysis of the antenna lifting process, the input link is applied the greatest load at the horizontal position (state of folding). Therefore, topology-optimized geometry of the input link in this research was carried out at this position.

When the input link is placed horizontally, the axis of the three holes is parallel to the horizontal plane. The three holes are non-designed areas, and the remaining areas are designed areas. Set the grid size to 5 mm in ANSYS, add a fixed constraint to two holes at the lower end and middle of the link, and the last hole at the upper end to bear the tensile force. In addition, the input link has to bear its own gravity. In the process of topology optimization, the design goal is to retain 25–30% of the mass of the full solid geometry. The original structure and topology optimization of the link are shown in Fig. 2.



Fig. 2 Original structure and its shape after topology optimization of the input link



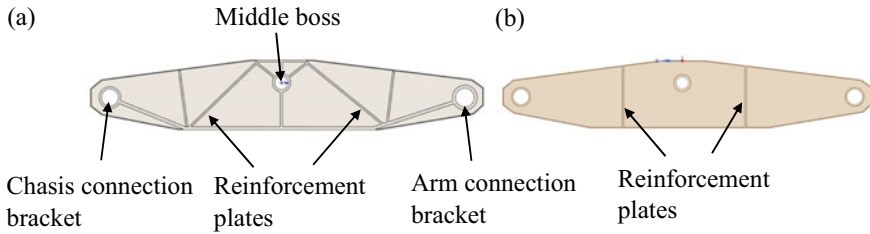


**Fig. 3** **a** Reconstructed model of the link based on TO. **b** Initial model of the link based on excavator booms

The input link will be manufactured mainly from high-strength structural steel that has an allowable stress of 600 MPa. Permissible limited stress after adding safety factor 3 for design is 200 MPa. The allowable mass is under 400 kg. The outer dimensions (length  $\times$  width  $\times$  height) are not greater than 3320  $\times$  590  $\times$  210 mm. According to the topological structure of the link, combined with the cost of the structure in actual manufacturing, the mechanism link structure is modeled and reconstructed as shown in Fig. 3a.

The large-size link mechanism has a normal initial design, almost like the booms of excavators (Fig. 3b). The general excavator boom body is constructed with upper, lower, and vertical side plates welded to each other at right angles to form a rectangular cross section. Reinforcement plates connect to form a closed box section in pursuance of the design criteria. Based on topology optimization, the link of the antenna lifting mechanism has different structural reinforcement plates. Inside the closed box, several reinforcement plates are added to create a link between shaft holes with upper and lower plates. Additionally, vertical side plates are also reduced in thickness from 20 to 5 mm, with the aim of reducing the overall weight. Meanwhile, the upper and lower side plates keep the same 5 mm of thickness. The thickness of reinforcement plates is 15 mm in both designs.

Simultaneously, the mass of the link should be kept as low as possible in order to reduce the operating costs of the antenna lifting system, such as fuel consumption and lifting-lowering cycle time. Hence, the aim is to minimize the weight of a mechanism link while limiting stress values to a predetermined range (Fig. 4).

### 3 Results and Discussion

In recent years, the finite element method (FEM) has become popular for increasing the precision of a stress evaluation. The FEM is a powerful tool to solve complex structural systems. The results obtained from simulation are very realistic solutions for the structure [8].

The external forces were applied to geometries using ANSYS Static Structural to conduct the equivalent static analysis (Fig. 4). These force values are enacted on

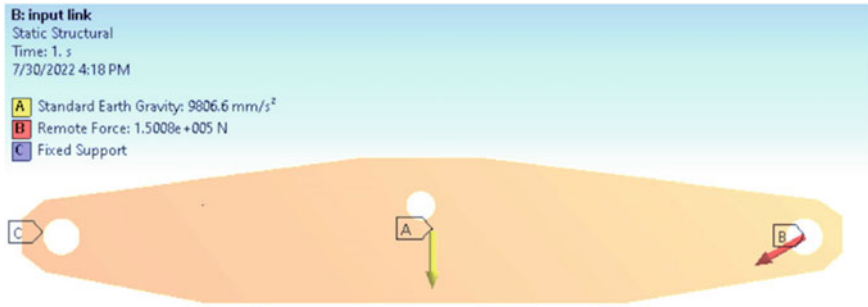


**Fig. 4** Force and constraints are applied in ANSYS Static structural

the weight of components that are lifted. The equivalent static structural method was carried out using the forces obtained from the rigid dynamic analysis. These forces imitated the dynamic loads as the static loads on the model. Loads and boundary conditions were applied to the model. Fixed supports are used on the lower and middle shaft hold regions. The forces are applied to the upper shaft hole region. The stresses and deformations obtained from the static response of three link structures are shown in Table 1. Stress cloud diagrams are shown in Fig. 5.

It can be seen from the figure that the maximum stress before and after optimization is concentrated at the middle hole of the input link, and the stress value is increased from the original 16.1–196.0 Mpa. The actual stress value of the structure is smaller than the permissible limit stress of the material. Therefore, the optimized performance of the link fully meets the requirements of use. When compared to the normal design

**Table 1** Results from ANSYS static structural analysis

Type of design	Weight (kg)	Maximum stress (MPa)	Maximum deformation (mm)
Original shape	2490	16.1	0.48
Initial design	398	199.2	1.88
TO design	325	196.0	1.98

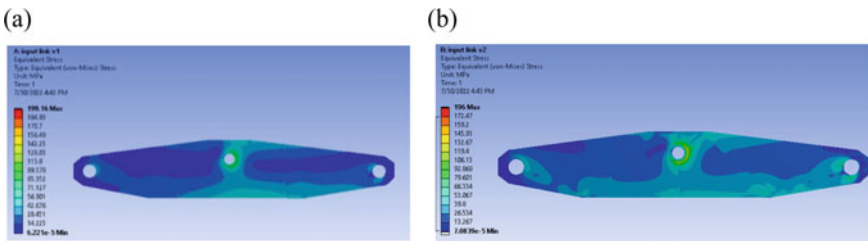


**Fig. 5** Equivalent stress results: **a** Initial design based on excavator booms. **b** TO design

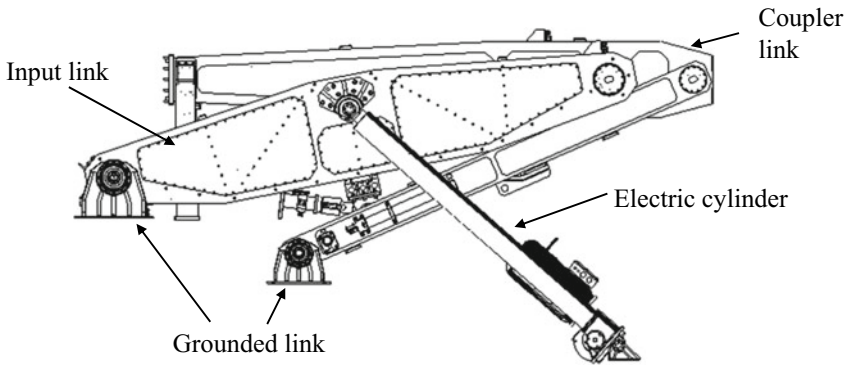


**Fig. 6** Radar antenna lifting system in the folded state

based on excavator booms, the TO design decreases 18.3% of weight. The maximum deformation is increased from 0.48 to 1.98 mm in the TO design. This value is higher than the excavator boom design by 0.1 mm, but is not a critical value.

The result obtained in the article is not optimal for this link mechanism. However, it shows one of the good results that meet main technical criteria. Hence, the results can be a reference for another designer in order to continue optimization or finish optimization earlier.

Based on the optimization and stress analysis, a detailed design of the input link was considered before proceeding to the product manufacturing process. The input link in this paper is the main link in the antenna lifting system as shown in Fig. 6.

## 4 Conclusions

In this paper, the input link structure of the antenna lifting system is used as the research object. The TO design and strength analysis were carried out using ANSYS Workbench. The weight of the optimized input link is reduced by 18.3% of its original weight when compared to the initial structure. Meanwhile, the equivalent stress is changed from 199.2 to 196.0 Mpa, which is less than the material's allowable stress. The structure's strength meets the requirements of use. Based on the analysis results, the optimized input link design completes the lightweight design of the input link while meeting the strength requirements. This study provides a quick and efficient design methodology not only for the linkage mechanism but also for other mechanical parts.

## References

1. M.P. Bendsøe, O. Sigmund, *Topology Optimization: Theory, Methods, and Applications* (Springer Science & Business Media, Berlin/Heidelberg, Germany, 2013), p. 370
2. M.P. Bendsøe, Optimal shape design as a material distribution problem. *Struct. Optim.* **1**, 193–202 (1989)
3. M.P. Bendsøe, O. Sigmund, Material interpolation schemes in topology optimization. *Arch. Appl. Mech.* **69**, 635–654 (1999)
4. M. Zhou, G.I.N. Rozvany, The COC algorithm, Part II: topological, geometrical and generalized shape optimization. *Comput. Meth. Appl. Mech. Eng.* **89**, 309–336 (1991)
5. E. Andreassen, A. Clausen, M. Schevenels, B.S. Lazarov, O. Sigmund, Efficient topology optimization in MATLAB using 88 lines of code. *Struct. Multidiscip. Optim.* **43**, 1–16 (2011)
6. O. Querin, V. Young, G. Steven, Y. Xie, Computational efficiency and validation of bi-directional evolutionary structural optimisation. *Comput. Meth. Appl. Mech. Eng.* **189**, 559–573 (2000)
7. (NHTSA), N.H.T.S.A, *Crash Simulation Vehicle Models* (2021)
8. J. Wang, Design optimization of rigid metal containers. *Finite Elements Anal. Des.* **37**, 273–286 (2001)

# Optimization of Machining Factors Affects Chip Shrinkage Coefficient, Surface Roughness When High-Speed Milling of Aluminum Alloy A7075



Thi-Hoa Pham, Duc-Toan Nguyen, Viet-Hoi Tran, and Dang-Thuc Phan

**Abstract** This study uses the Taguchi method to estimate the influence of cutting factors: cutting speed, depth of cut and feed rate ( $V$ ,  $t$ ,  $S$ ) on chip shrinkage coefficient ( $K$ ) and surface roughness ( $Ra$ ) when high-speed milling (HSM) of A7075 aluminum alloy. The results show that the  $t$  greatly influences the  $Ra$  is 51.16%, the second level of influence on the feed rate is 29.77%, then the cutting speed is 19.06%. With the chip shrinkage coefficient, the  $t$ ,  $S$ , and  $V$  affecting  $K$  are 64.9%, 21.8%, and 13.4%, respectively. Research using Gray multi-objective optimization to invent the applicable set of cutting factors for  $K$  and  $Ra$  with the corresponding minimum criteria as follows:  $V = 1695$  (m/min),  $t = 1.0$  (mm), and  $S = 600$  (mm/min) respectively.

**Keywords** A70751 aluminum alloy · Chip shrinkage coefficient · Surface roughness

## 1 Introduction

Chip shrinkage coefficient and surface roughness are factors that reflect phenomena occurring during chip formation such as material deformation and cutting heat [1]. Joshi et al. [2] analyzed  $Ra$  and chip parts during the machining of circular milling cutters. The results presented that the  $Ra$  is affected by the inclination angle.

---

T.-H. Pham (✉)

Hung Yen University of Technology and Education, Hung Yen, Vietnam

e-mail: [hoapt2108@gmail.com](mailto:hoapt2108@gmail.com)

V.-H. Tran

Hanoi University of Industry, Ha Noi, Vietnam

D.-T. Nguyen

School of Mechanical Engineering, Hanoi University of Science and Technology, Ha Noi, Vietnam

D.-T. Phan

Bac Ninh Industrial College, Bac Ninh, Vietnam

Increased tilt angle reduces surface roughness. As the irritated sectional part of the chip increases, the angle of inclination decreases. The  $S$  and  $t$  increase the chip irritated-sectional width and height and significantly affect the chip cross-sectional area. Ribeiro et al. [3] studied on optimization of cutting factors to minimize  $Ra$  during finishing by the Taguchi method. The result showed that the parameter of cutting depth has the most effect on the  $Ra$ . Joshua et al. [4] investigated the parameters affecting the  $Ra$  during the milling of A6061 aluminum alloy using MQL (Minimum Quantity Lubrication). Their result showed that the surface roughness in milling by MQL is better than in rough milling.  $Ra$  is mostly predisposed by cutting speed and cutting depth. Besides, several surface roughness optimization methods are based on response surface methodology and genetic algorithms [5]. In the study [6], the author experimented and showed the effect of cutting factors on the  $Ra$  in the finishing milling of 6061 aluminum alloy. Madariaga et al. [7] studied the effect of  $V$  on  $Ra$  responsiveness in the milling of A7050 aluminum. Pham et al. [8] experimented with evaluated the effect of cutting factors on the  $Ra$ , vibration, and tool–chip contact length. It can be observed that previous studies mainly investigate the cutting factors affecting the  $Ra$  of machine parts. There are very few studies on the chip shrinkage that occurs during the machining of A7075 aluminum alloy. This study evaluates the percentage influence of cutting factors, including  $V$  (cutting speed),  $S$  (feed rate), and  $t$  (cutting depth), on  $Ra$  and  $K$  during high-speed milling (HSM) of the A7075 aluminum alloy. The multi-objective optimization by Taguchi Gray method for cutting factors is applied to minimize the  $Ra$  and  $K$  values. As a result, a common set of cutting factors satisfying the requirements for  $Ra$  and  $K$  is revealed.

## 2 Experimental Conditions

### 2.1 Cutting Workpiece

An experimental study using A7075 aluminum alloy (Fig. 1). This is a line of durable deformed alloys and is the highest-strength aluminum alloy. It is commonly used mainly in the aerospace industry and blow molding and precision mechanics... The physical and motorized properties of A7075 are exposed in Table 1.

**Fig. 1** A7075 aluminum alloy workpiece

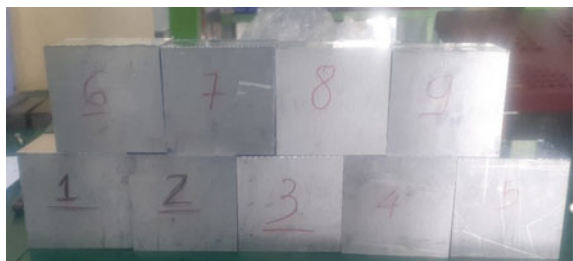


**Table 1** Chemical compositions of aluminum alloy A7075 (%)

Si	Fe	Cu	Mn	Mg	Cr	Zn	Ti	Al
0.4	0.5	1.2–2.0	0.3	2.1–2.9	0.18–0.28	5.1–6.1	0.2	87.1–91.4

## 2.2 Machining Machine and Cutting Tools

The study used end mills with size  $\Phi 63$  (mm), carbide alloy pieces and hardness. The dimensions of the tool cutting as shown in Fig. 2 are respectively  $l = d = 12$  (mm),  $m = 3$  (mm),  $d_1 = 6$  (mm). Investigational study on high-speed milling of A7075 aluminum alloy on CNC 700HS (Fig. 3). The machine is a trademark of Knuth of Bac Ninh Industrial College, the table size is  $750 \times 450$  mm, the X, Y, Z axis travel is  $700 \times 500 \times 500$  mm. The machine uses the control system of Siemens828D. The speed of the X, Y, and Z axes advances as fast as 60,000 mm/min. A-axis rotation ranges from 30 to 1200, and C-axis rotates at 3600.

**Fig. 2** Cutting tool geometry

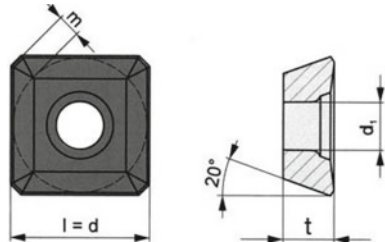


**Fig. 3** CNC 700HS milling machine





**Fig. 4** Roughness measuring device SJ410

### 2.3 *Measuring Devices*

Research using the roughness measuring device SJ410, metrology laboratory—Department of mechanical engineering—Hung Yen University of Technology and Education (Fig. 4). The SJ410 can measure micro-steps and strength using the non-slip measurement function. The roughness parameter conforms to the latest ISO, DIN, ANSI, and JIS standards. Figure 3 shows the surface roughness measurement diagram after high-speed machining of A7075 aluminum alloy. We are measuring range: 800  $\mu\text{m}$ , resolution 0.000125  $\mu\text{m}$ .

### 2.4 *Experimental Conditions*

The Taguchi method prepared experimental parameters for HSM of aluminum alloy A7075. The levels of cutting factors are selected based on the machining equipment, tool material, and rigidity of the machine-tool-jigsaw system, given according to the following levels:  $942 \text{ (m/min)} \leq V \leq 1695 \text{ (m/min)}$ ;  $600 \text{ (mm/min)} \leq S \leq 1000 \text{ (mm/min)}$ ;  $1.0 \text{ (mm)} \leq t \leq 2.0 \text{ (mm)}$ .

The experimental matrix and measurement results of  $Ra$  and  $K$ , respectively, are given in Table 2.



**Table 2** L9 orthogonal array and measurement results

No	Cutting parameters			Ra (μm)	K
	V (m/min)	t (mm)	S (mm/min)		
1	1(942)	1(1.0)	1(600)	0.1580	1.597
2	1(942)	2(1.5)	2(800)	0.1620	1.585
3	1(942)	3(2.0)	3(1000)	0.1803	1.675
4	2(1318)	1(1.0)	2(800)	0.1190	1.633
5	2(1318)	2(1.5)	3(1000)	0.1766	1.596
6	2(1318)	3(2.0)	1(600)	0.1790	1.644
7	3(1695)	1(1.0)	3(1000)	0.1583	1.512
8	3(1695)	2(1.5)	1(600)	0.1143	1.599
9	3(1695)	3(2.0)	2(800)	0.1703	1.646

**Table 3** Analysis of the effect of cutting factors on Ra

Parameters	S/N			Sum of squares	Distribution percentage
	1	2	3		
V (m/min)	15.57	16.16	16.74*	2.05	0.1906
t (mm)	16.84*	16.57	15.06	5.49	0.5116
S (mm/min)	16.60*	16.56	15.32	3.19	0.2977

\*optimum values

### 3 Results and Discussion

#### 3.1 Effect of Cutting Factors on Ra

ANOVA analysis for surface roughness affected by cutting factors is assumed in Table 3. The table shows that the *t* greatly influences the *Ra* is 51.16%, then the feed amount is 29.77%, and finally, the cutting speed is 19.06%. From Table 3, a set of cutting parameters can be selected so that the *Ra* is the minimum consistent with the cutting factors: *V* = 1695 (m/min); *t* = 1.0 (mm); *S* = 600 (mm/min). The influence of these parameters is also shown visually in Fig. 5, corresponding to the highest peak of the parameters compared to the average value curve.

#### 3.2 The Influence of Cutting Factors on K

Measure the chip shrinkage coefficient when high-speed milling of aluminum alloy A7075 according to the chip weight method. The measurement results agree to the experiments shown in Table 4.

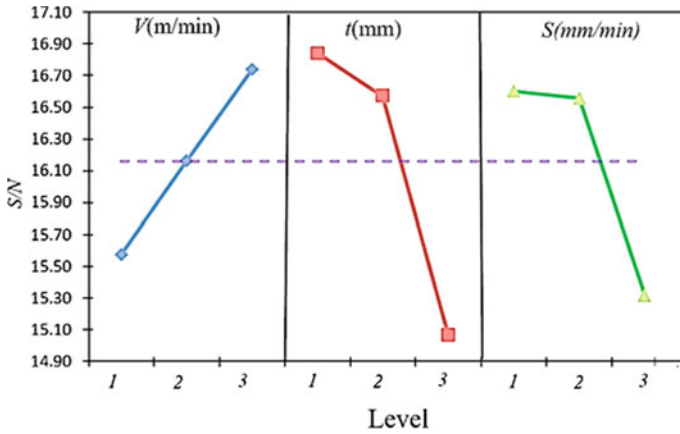


Fig. 5 S/N ratio of Ra

Table 4 Analyze the influence of cutting factors on K

Parameter	Meaning of S/N of each level			Sum of squares	Distribution percentage
	1	2	3		
V (m/min)	-3.794	-3.948	-3.617*	0.165	0.094
t (mm)	-3.440*	-3.610	-4.309	1.272	0.722
S (mm/min)	-3.578*	-4.037	-3.744	0.323	0.184

\*optimum values

ANOVA analysis of the influence of cutting factors on the K when HSM of aluminum alloy A7075 is given in Table 4. On the table, the effect of the cutting factors is as follows:  $t = 72.2\%$ ,  $S = 18.4\%$ , and  $V = 9.4\%$ . Thus, the optimal set of cutting factors for the smallest K is respectively  $V = 1695$  (m/min);  $t = 1$  (mm);  $S = 600$  (mm/min). This set of cutting factors is also shown in Fig. 6 as the highest point of the S/N relation for each factor.

### 3.3 Multi-objective Optimization of the Influence of Cutting Factors on K and Ra

Gray correlation analysis is used to simultaneously assess the effect of the cutting factor on the outputs Ra and K. With the slightest characteristic being the best, and the initial sequence is normalized as follows:

$$S_{kj} = \frac{\max X_{kj} - X_{kj}}{\max X_{kj} - \min X_{kj}} \tag{1}$$

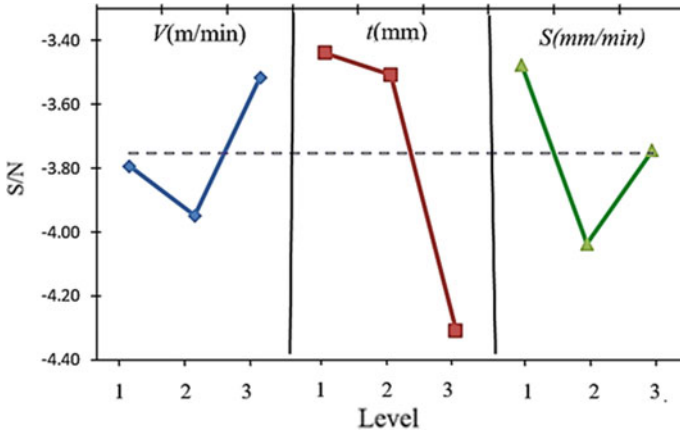


Fig. 6 S/N ratio of K

where:  $j = 1, 2, 3, \dots, m$ ,  $m$  is the amount of experiments in the Taguchi orthogonal array;  $k = 1, 2, \dots, n$ ,  $n$  is the amount of experiments;  $\max X_{kj}$  is the maximum significance of  $X_{kj}$ ;  $\min X_{kj}$  is the minimum significance;  $S_{kj}$  is the value after Gray correlation analysis; GRG is the weight of the real Gray relationship.

The properties are evaluated based on the relationships between each Gray relation given by formula (2)

$$GZ_{kj} = \frac{S_{k \min} + \mu S_{k \max}}{S_{kj} + \mu S_{k \max}} \tag{2}$$

where  $\mu$  is the discriminant coefficient in the range  $(0 \div 1)$  and choose  $\mu = 0.5$

The output parameter is better when the Gray correlation coefficient has the most significant value, and in 9 experiments, there are three experiments with good results, which is experiment 8, 1, and 7, as shown in Table 5. The most considerable Gray relation classification value in experiment 8 is 0.893. The highest level of GRG is said to be optimized for the parameters.

From the table of features of the Gray relationship classification, Table. 6 shows the rank order of the cutting factors to the output parameters  $K$  and  $Ra$  with a depth of cut of 60.89%, a feed rate of 21.80%, and a cutting speed of 17.31%. The cutting speed is 14.133%. The common set of cutting factors for the smallest  $K$  and  $Ra$  are  $V = 1695$  (m/min),  $t = 1.0$  (mm), and  $S = 600$  (mm/min) respectively.

**Table 5** Grey relationship rating

No	S ( <i>K</i> )	S ( <i>F</i> )	GZ-( <i>K</i> )	GZ-( <i>F</i> )	G
1	0.136	0.710	1.000	0.413	0.707
2	0.655	0.765	0.454	0.395	0.425
3	1.000	1.000	0.333	0.333	0.333
4	0.684	0.088	0.441	0.850	0.645
5	0.496	0.955	0.545	0.344	0.444
6	0.949	0.984	0.347	0.337	0.342
7	0.180	0.714	0.907	0.412	0.659
8	0.000	0.000	0.830	1.000	0.915
9	0.988	0.875	0.336	0.364	0.350

**Table 6** Grey relationship grade

Parameter	Grey relationship grade			Max–min	Rank	Sum of squares	Distribution percentage
	1	2	3				
<i>V</i>	0.488	0.477	0.641*	0.164	1	0.0168	17.307
<i>t</i>	0.670*	0.595	0.342	0.329	2	0.059	60.891
<i>S</i>	0.654*	0.473	0.479	0.181	3	0.021	21.802

\*optimum values

## 4 Conclusions

The study evaluates the effect of cutting factors on *Ra* and *K* in HSM of A7075 aluminum alloy. The results show that cutting depth has the greatest influence on *Ra* with 51.16%, followed by the effect of *S* at 29.77%, and the effect of *V* at 19.006% is the smallest. With the *K*, the cutting depth, feed rate, and cutting speed affecting *K* value are 64.9%, 21.8%, and 13.4%, respectively. The set of cutting factors for *K* and *Ra* matching the minimum criteria using Gray multi-objective optimization is found as follows: cutting depth of 60.89%, feed rate of 21.08%, and cutting speed of 17.31%.

## References

1. T.S. Tuy, B.T. Long, T.T. Luc, N.L.G.C.V. Lieu, N.K.H.K. Thuat (2013)
2. U.A. Dabade, S.S. Joshi, N. Ramakrishnan, Analysis of surface roughness and chip cross-sectional area while machining with self-propelled round inserts milling cutter. *J. Mater. Process. Technol.* **132**(1–3), 305–312 (2003). [https://doi.org/10.1016/S0924-0136\(02\)00949-4](https://doi.org/10.1016/S0924-0136(02)00949-4)
3. J. Ribeiro, H. Lopes, L. Queijo, D. Figueiredo, Optimization of cutting parameters to minimize the surface roughness in the end milling process using the Taguchi method. *Period. Polytech. Mech. Eng.* **61**(1), 30–35 (2017). <https://doi.org/10.3311/PPme.9114>

4. I.O.S. Ojolo Sunday Joshua, M.O. David, Experimental investigation of cutting parameters on surface roughness prediction during end milling of aluminium 6061 under MQL (minimum quantity lubrication). *J. Mech. Eng. Autom.* **5**, 1–13 (2015)
5. B. Sidda Reddy, J. Suresh Kumar, K. Vijaya Kumar Reddy, Optimization of surface roughness in CNC end milling using response surface methodology and genetic algorithm. *Int. J. Eng. Sci. Technol.* **3**(8), 102–109 (2012). <https://doi.org/10.4314/ijest.v3i8.8>
6. O.S. Joshua, M.O. David, I.O. Sikiru, Experimental investigation of cutting parameters on surface roughness prediction during end milling of aluminium 6061 under MQL (minimum quantity lubrication). *J. Mech. Eng. Autom.* **5**(1), 1–13 (2015). <https://doi.org/10.5923/j.jmea.20150501.01>
7. A. Madariaga et al., ScienceDirect effect speed on the surface of face milled effect of cutting on surface integrity face milled 7050–T7451 aluminium workpieces a new methodology to analyze the functional and physi. *Procedia CIRP* **71**, 460–465 (2018). <https://doi.org/10.1016/j.procir.2018.05.034>
8. T.H. Pham, D.T. Nguyen, T.L. Banh, V.C. Tong, Experimental study on the chip morphology, tool–chip contact length, workpiece vibration, and surface roughness during high-speed face milling of A6061 aluminum alloy. *Proc. Inst. Mech. Eng. Part B J. Eng. Manuf.* **234**(3), 610–620 (2020). <https://doi.org/10.1177/0954405419863221>.

# Design an Intelligent Braking System Using Ultrasonic Sensors and IR Sensors



Vu Hai Quan, Nguyen Anh Ngoc, Le Hong Quan, Nguyen Xuan Khoa, Nguyen Quoc Khanh, and Ngo Quang Tao

**Abstract** The increasing rate of accidents is alarming and any vehicle without an effective braking system is prone to accidents with human and property consequences. This is due to human error when driving, which involves delays in reaction time and distraction. Intelligent Braking System (IBS) is an active safety system equipped on modern cars to minimize the possibility of collisions while participating in traffic. The IBS system helps alert the driver to an impending collision while helping the driver brake with a maximum force or automatically brake the car in an emergency. This study analyzed the working principles of IBS braking systems, 3D model design, and the fabrication of a practical model of an intelligent braking system (IBS).

**Keywords** Intelligent braking system · Automatic emergency braking system · IBS · AEB · Ultrasonic sensor · IR sensor

## 1 Introduction

The braking mechanism is the active safety structure of the car, used to slow down or stop and park the car in case of need. The automobile industry is growing strongly, the number of cars is increasing rapidly, and the density of traffic on the road is increasing. The cars are increasingly designed with higher power, and faster movement speed, the requirements set with the brake mechanism are also higher and stricter. To avoid accidents or minimize the number of casualties caused by collisions between vehicles, the braking system plays a very important role. There are many braking systems developed to create smooth and compatible braking systems. ABS is one of the examples of brakes. But the braking system desperately needs to be set up to be able

---

V. H. Quan · N. A. Ngoc (✉) · L. H. Quan · N. X. Khoa · N. Q. Khanh · N. Q. Tao  
Automobile Technology Department, Hanoi University of Industry, Hanoi, Vietnam  
e-mail: [ngocnguyencnoto@hau.edu.vn](mailto:ngocnguyencnoto@hau.edu.vn)

V. H. Quan  
e-mail: [quanvh@hau.edu.vn](mailto:quanvh@hau.edu.vn)

© The Author(s), under exclusive license to Springer Nature Switzerland AG 2024  
B. T. Long et al. (eds.), *Proceedings of the 3rd Annual International Conference on Material, Machines and Methods for Sustainable Development (MMMS2022)*, Lecture Notes in Mechanical Engineering, [https://doi.org/10.1007/978-3-031-57460-3\\_36](https://doi.org/10.1007/978-3-031-57460-3_36)

to brake for the most appropriate period. If the system is not activated on time, it will be difficult to prevent or minimize the possibility of collisions between vehicles. But the sudden appearance of vehicles in front of other vehicles can cause panic in the driver. So, to face those problems smart braking system was born. If the driver does not pay attention to the obstacles in front of the vehicle, the automatic braking system can send an alert to the driver and directly impact to avoid potential collisions [1–6].

## 2 The Basis Theoretical of Intelligent Braking System

### 2.1 Principles of the General Operation of the System

The IBS intelligent braking system uses sensors or radar mounted in front of the car, some above the windshield to monitor the road ahead. Based on factors including speed and distance from the vehicle in front, a control unit will detect potential hazards. Based on the above principle, the driver is informed of the risk of an accident and is required to impact the brake pedal while the IBS system controls the brakes at the same time, thus allowing the vehicle to react promptly and reasonably. If the driver is unable to react in time, IBS technology can impact the brakes with just enough force, causing the car to stop to avoid an accident, or at least reduce the damage.

### 2.2 Basic Theories

The real-time distance is the distance between the moving car and the pedestrian and also the distance between the two moving vehicles. The time required for the back-and-forth movement of ultrasonic waves after hitting an obstacle is the receiving time (the time required  $\times 2$ ). The real-time distance obtained from the ultrasonic sensor is:

$$d_{c2} = V_A t_r + \frac{(V_A - V_B)t_i}{2} + \frac{V_A^2 - V_B^2}{2\mu g} + d_{\min} \quad (1)$$

Pedestrian's velocity is ignored compared to car A and is thought to be zero [7]. The critical braking distance between car A and pedestrians is then said to be:

$$d_{c1} = V_A \left( t_r + \frac{t_i}{2} \right) + \frac{V_A^2}{2\mu g} + d_{\min} \quad (2)$$

This equation is used for obstacles that do not move or pedestrians whose velocity is assumed to be zero. The microcontroller used the speed of the car ( $V_A$ ) to determine

the critical braking distance ( $d_{c1}$ ) that was compared to the real-time distance ( $d$ ) between the vehicle and the obstacle that did not move. If the relative real-time distance ( $d$ ) is greater than the  $d_{c1}$  critical braking distance, the vehicle can hold the original speed and the pedestrian can safely cross the road. If the distance is relatively lower than or equal to the critical braking distance and the driver still does not slow down or take other safety measures, this state is considered dangerous and the deceleration thanks to automatic braking on the car will be carried out using the anti-lock braking system. After receiving a command from the controller to slow down or stop the car.

The critical braking distance between two moving vehicles (Vehicle A and Vehicle B) can be calculated according to the safe distance model during braking as follows [7].

$$d_{c2} = V_A t_r + \frac{(V_A - V_B)t_i}{2} + \frac{V_A^2 - V_B^2}{2\mu g} + d_{\min} \quad (3)$$

where  $d_{c1}$ ,  $d_{c2}$  = braking distance due to deceleration,  $V_A$  = speed of car A,  $V_B$  = speed of car B,  $\mu$  = friction coefficient of the road,  $t_r$  = total reaction time of the driver, and braking coordination time ranges from 0.8 to 1.2 s,  $t_i$  = the increased time of braking deceleration varies from 0.1 to 0.2 s,  $g$  = gravity acceleration ( $9.81 \text{ m/s}^2$ ) and  $d_{\min}$  = minimum distance between the vehicle and obstacles when stopping the vehicle from 1 to 4 m.

If the real-time distance  $d$  between vehicle A and vehicle B is greater than the braking distance due to  $d_{c2}$ , it is a safe state and the vehicle can run at the current speed. Conversely, if the driver does not decelerate or take other safety measures when the current distance is lower than or equal to the critical braking distance, this state is assessed as dangerous and the reduction of automatic braking speed on car A needs to be done immediately by the driver to avoid a collision with car B.

### 3 Building a Model of Smart Braking System

#### 3.1 3D Model Designing

Our model consists of three main components: the mechanic structure, the sensors, and the central controller. The main traction motor is used for rolling the wheel by a belt transmitter. A stepper motor is used to control the brakes.



**Fig. 1** Ultrasonic sensor and IR sensor



a) Ultrasonic sensors

b) IR sensor

## 3.2 *Electronic Components Are Equipped on the Model*

### 3.2.1 Ultrasonic Sensor and IR Sensor

Ultrasonic sensor with the principle of operating based on ultrasonic wave transmission and reception. When powered, the device will broadcast ultrasound with a certain cycle to space. When encountering an obstruction, the ultrasonic wave will reflect toward the device. The sensor will record the reflected waves and calculate how long by the time of broadcasting and receiving it back. From there, calculate how far the barrier is. Best working range 0.2–4 m (Fig. 1a).

IR sensors are electronic devices that emit light to sense certain objects in the surrounding environment. The sensor is used to measure the speed at which the brake disc rotates by sensing the photocopying radiation changes when scanning through the dictionary marked on the disc (Fig. 1b).

### 3.2.2 Central Processor and LCD Screen

Arduino UNO R3 with the central processor is Atmega328 has 14 pins I/O digital signal, of which 6 pins can be used as PWM pulse wide mode modulator, 6 analog signal inputs, using 16 MHz oscillating quartz, USB connection, with ICSP Header ... Arduino UNO can use 38 bit AVR family controllers: ATmega8, ATmega168, ATmega328. This brain can handle simple tasks such as controlling flashing LEDs, processing signals for remote-controlled vehicles, making a temperature-humidity measuring station, and displaying them on an LCD screen, or other applications (Figs. 2 and 3).

The green 1602 LCD screen uses the HD44780 driver, capable of displaying 2 lines with each line of 16 characters, a high-strength display, very popular, has more sample code, and is easier to use if accompanied by an I2C transition circuit.

### 3.2.3 Warning Devices

- SFM27 Chip Whistle: Used in civil alert systems as well as in industry. Having a sound intensity  $\geq 85$  dB good sound quality should be widely used in the market today.

Fig. 2 Arduino processor

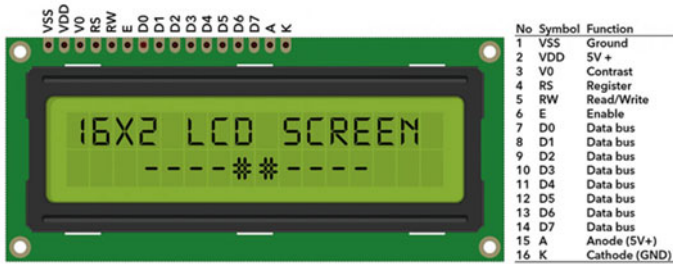
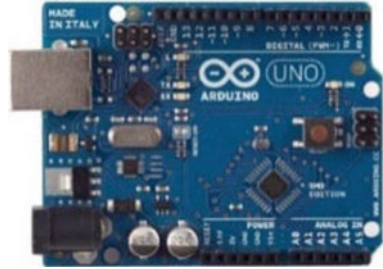


Fig. 3 LCD 1602 pin diagram



Fig. 4 Warning devices

- Belt recoil mechanism: The RC Servo MG90S motor is small in size with gears made of metal for strong traction and greater accuracy than those made of plastic. Metal gears for strong force and high durability, the engine has a compact size, the same control as the RC Servo engines popular on the market today: MG996, MG995, 9G,..
- Sprinkler structure: mini submersible pump with long lead head, large flow, low noise... (Fig. 4).

### 3.2.4 Drive Structure and Brake Mechanism

Drive motor: DC engine with a maximum speed of 5600 V/p; PWM Motor Speed Control Module; The mechanical disc brakes of the bike for simulation replace the brakes and wheels. The diameter of the brake disc is 160 mm; Brake motor:

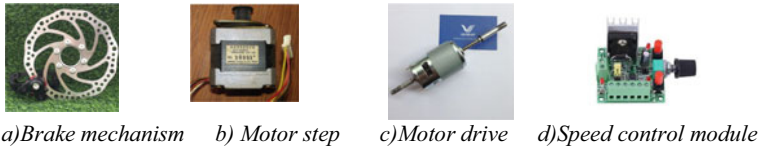


Fig. 5 Motor drive and braking mechanism

42HS33MF stepper motor is a widely used engine in many application models with high accuracy, and sufficient impact force (Fig. 5).

### 3.3 Build a Smart Braking System Model

The system uses ultrasonic sensors, if there are any obstacles along the way, then the sound waves will reflect. This reflected sound wave receiver is called “IR RECEIVER.” The IR receiver receives the reflected IR waves and delivers the control signal to the control circuit. The control circuit is used to activate some warning devices such as bells and vibrating seat belts. If the driver has not yet shown signs of interference with the steering system that changes direction or brake pedals to slow down, the electromagnetic valve is activated to affect the brakes of the vehicle (Fig. 6).

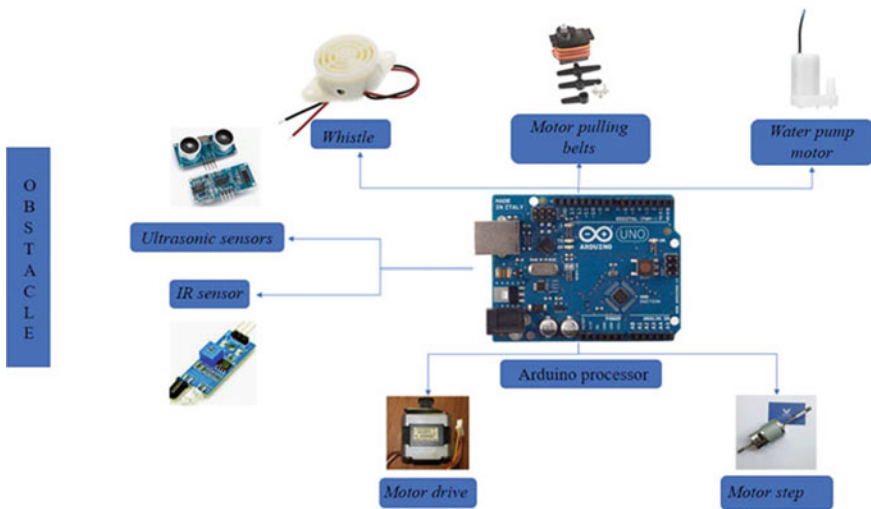
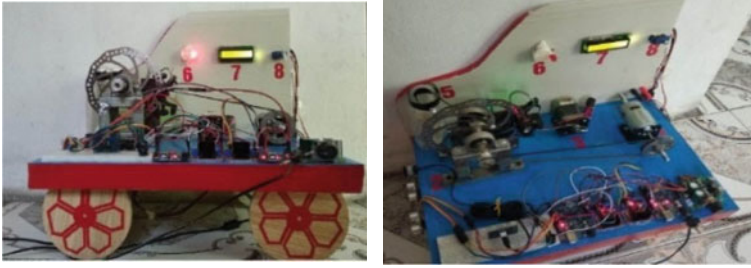


Fig. 6 The principal diagram of the smart braking system model



**Fig. 7** The actual model of the intelligent braking system finishing model

Signals from distance sensors and speed sensors are collected and processed by microcontrollers. After calculating the distance from the obstacle and the current speed, the microcontroller decides to activate the warning levels by the situation.

- Warning No. 1: The lights and whistles will be flashed continuously to alert the driver.
- Warning No. 2: The belt pull motor is activated in combination with the siren light signaling to the driver.
- Warning No. 3: The water pump motor is activated to spray light water on the driver to wake the driver in case the driver falls asleep or loses focus.

At the end of the above 3 warnings, the driver has not yet activated the brake system will automatically activate the brakes on the car to minimize the possibility of a collision. The actual model of the intelligent braking system is shown in Fig. 7.

## 4 Results and Analysis

Based on theoretical calculations of the model and the principle of operation built we experimented. Experimental results show that the model works in a variety of speed ranges, operates stably, operational alert levels, and gives warning levels in line with the model’s operating theory when building. Table 1 shows the results of the experiment.

**Table 1** Table of experimental results of the model

Velocity (m/s)	Velocity (rpm)	Level 1 warning time (m)	Level 2 warning time (m)	Level 3 warning time (m)
1.96	235	1.96	0.9	0.5
2.51	300	2.51	1.255	0.8
3.18	380	3.18	1.54	1.29

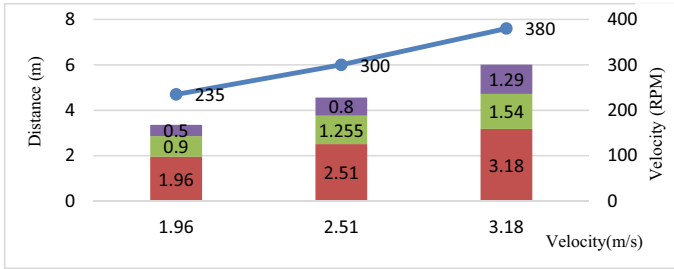


**Fig. 8** Experimental results of the model

In the process of building the model, we also encountered many difficulties from the stages of technology selection, and equipment preparation, to the stage of manufacturing and running model experiments but finally, the team has perfected the model with many results beyond the original idea. Below is a chart describing the experimental results of the model (Fig. 8).

At a speed of 1.96 m/s, if the system detects any obstacles ahead, it will emit a level 1 warning signal at a distance of 1.96 m, warning level 2 at a distance of 0.9 m, warning level 3 at a distance of 0.5 m. We simulate in the absence of any reaction from the driver, that after the 3rd warning level the system will automatically brake. Similarly, in different velocity ranges, the level of warning will be given in proportion to the distances measured from the sensor.

## 5 Conclusions

Through the process of theoretical research, we have built a model, that simulates the working principle of intelligent braking systems in cars with stages from 3D models to actual models. The model is designed with 03 different levels of warning from low to high to help warn the driver about the risks that may occur during the operation of the vehicle including Warning level 1 is the horn warning, warning level 2 is the warning of straps, Warning level 3 is a sprinkler warning. After 3 warning levels that the driver is still not aware of the danger, the brake system will be automatically activated. Experimental research has confirmed that our original approach and design direction is correct.

## References

1. M. Abramov, *Autonomous Emergency Braking System Simulation Using SIMULINK*
2. C. Grover, I. Knight, F. Okoro, I. Simmons, G. Couper, P. Masse, B. Smih, *Automated Emergency Braking Systems: Technical requirements, costs, and benefits* (TRL Limited, 2008)

3. EURO NCAP'S first step is to assess autonomous emergency braking (aeb) for vulnerable road users
4. Euro NCAP Rating Assessment. <http://www.euroncap.com/Content-Web-Page/c6f9d381-1889-4c66-bfcdc5c0a69a364d/technical-papers.aspx>
5. Autonomous Emergency Braking (AEB) Test Definition Group, Thatcham. [http://www.thatcham.org/safety/pdfs/AEB\\_group\\_paper\\_Jun2010.pdf](http://www.thatcham.org/safety/pdfs/AEB_group_paper_Jun2010.pdf)
6. Comparative test of advanced emergency braking systems, ADAC. [http://www.activetest.eu/pdf/adac\\_aebs\\_report\\_en.pdf](http://www.activetest.eu/pdf/adac_aebs_report_en.pdf)
7. Development of a test target for AEB systems, Volker Sandner, ADAC, in *Proceedings of the 23rd International Technical Conference on the Enhanced Safety of Vehicles* (Paper 0406) (Seoul, 2013)

# An Investigation of Transverse Shrinkage in Single V and Bevel-Groove Butt Joints Using GMAW Process



Thi-Thao Ngo, Jin H. Huang, Chi-Chang Wang, and Van-The Than

**Abstract** This paper presents an investigation of transverse shrinkage in single V and bevel-groove butt joints using Gas Metal Arc Welding (GMAW) process. Comsol software is applied to set up a thermal model and simulate welding temperature as well as transverse shrinkage of two welded joint types with changing the groove angle and root opening. Results indicate that the transverse shrinkage increases with increasing the groove angle and root opening for both single V and bevel-groove butt joints. In addition, simulated transverse shrinkages are compared to experimental finding of previous publication. A good agreement of simulated and experimental transverse shrinkages is observed for both welded joints. It can be seen that the simulated model, initial conditions, boundary conditions, and setting heat sources on the simulation software is similar to the actual experimental conditions. The simulation method can be used to quickly predict not only the shrinkage of the butt weld, but also stress and distortion of other welds types using other welding processes.

**Keywords** Transverse shrinkage · Single V-groove · Bevel-groove · Root opening

## 1 Introduction

Welding distortion is an unavoidable factor that affects the workability and aesthetics of a structure. The welding distortion which caused by uneven heating and cooling of the weld and base metal can appear in a butt joint as longitudinal and transverse shrinkage [1]. The distribution of transverse shrinkage in the weld joint is uneven and depends on factors weld length, root opening, weld joint, weld process, groove angle, weld condition, etc. [2]. B. N. Sathyanarayana Reddy and N. Lakshmana

---

T.-T. Ngo · V.-T. Than (✉)

Faculty of Mechanical Engineering, Hung Yen University of Technology and Education, Hung Yen, Vietnam

e-mail: [thanthe.ck@gmail.com](mailto:thanthe.ck@gmail.com)

J. H. Huang · C.-C. Wang

Feng Chia University, Taichung, Taiwan, Republic of China

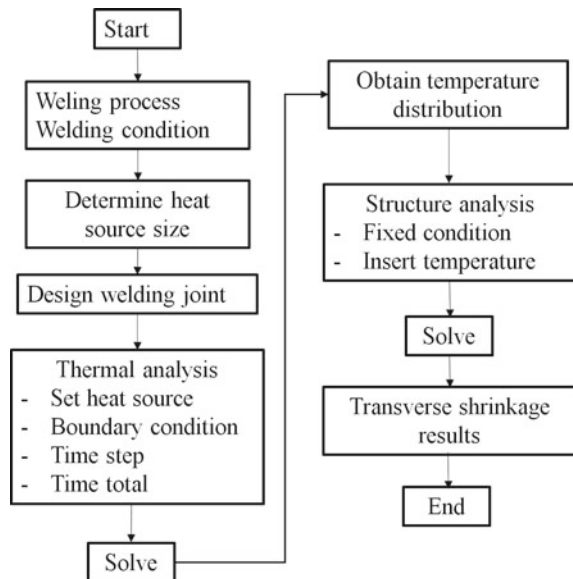
Swamy [3] studied on effect of groove angle in single V and double V-groove butt joints on transverse shrinkage in gas arc welding process. Besides, influence of bevel angle in bevel groove butt joints on shrinkages in CO<sub>2</sub> arc welding process was also researched and discussed [4]. In above literatures, many experiments were obtained to evaluate the impact of the parameters on the transverse shrinkage of the welded joint. This gave reliable results, but it was costly and time consuming. In this study, the transverse shrinkages of single V and bevel-groove joint are quickly determined by applying Comsol software based on the finite element method. To evaluate the reliability of the proposed method, simulation results are compared with experimental results in previous researches [3, 4].

## 2 Simulation of GMAW

In this work, Comsol software is utilized to simulate the GMAW process based on finite element method. The Comsol software can quickly simulate and achieve high accuracy in the engineering field. In particular, material properties, process data, and boundary conditions can be arbitrary functions based on variables. A GMAW welding simulation sequence is briefly described in the following diagram as seen Fig. 1.

In order to obtain the result of the transverse shrinkage, a thermal problem must first be solved. A heat transfer problem is used to model the GMAW process with governing and boundary equations as below [5].

**Fig. 1** A process to simulate welding transverse shrinkage





$$\frac{\partial}{\partial x} \left( k(T) \frac{\partial T}{\partial x} \right) + \frac{\partial}{\partial y} \left( k(T) \frac{\partial T}{\partial y} \right) + \frac{\partial}{\partial z} \left( k(T) \frac{\partial T}{\partial z} \right) + q = \rho(T) C_p(T) \frac{\partial T}{\partial t} \quad (1)$$

where  $\rho$ ,  $k$  and  $C_p$  are the density, thermal conductivity and heat capacity of the workpiece;  $t$  and  $T$  stand for time and temperature, respectively. In Eq. (1),  $q$  records an input arc heat according to the volumetric heat source. The general boundary condition can be expressed as:

$$k_n(T) \frac{\partial T}{\partial x} + h(T - T_0) + \sigma \varepsilon (T^4 - T_0^4) = 0 \quad (2)$$

A double semi-ellipsoid heat source is considered in this study with a smaller and a larger semi-ellipsoid at the back to calculate the arc heat energy in welding pool. The generated heat can be given as:

$$q = \frac{6\sqrt{3}f_i P \eta}{\pi \sqrt{\pi} a_i b c} \exp\left(-\frac{3x^2}{a_i^2} - \frac{3y^2}{b^2} - \frac{3z^2}{c^2}\right) \quad (3)$$

The semi-major, minor axes and depths of the front and rear ellipsoid are described as  $(a_1, b, c)$  and  $(a_2, b, c)$  which can be calculated as  $a_1 = f_1 a$ ;  $a_2 = f_2 a$ ;  $c = \sqrt{(a^2 - (a - a_1)^2)}$ ;  $b = (2a^3)/[(a_1 + a_2)/c]$ .

In addition,  $P = \alpha U_h I_h$  is the arc power,  $\alpha$ ,  $\alpha$ ,  $I_h$  and  $U_h$  are efficiency coefficient, current and voltage.  $\alpha$  and  $\eta$  are set at 0.75 and 0.8, respectively [6]. The heat source is inserted in Comsol software as a function to determine temperature distribution in the workpiece.

In this work, mild steel (AISI 1018) is used as the base material. Single V and bevel-groove butt joint with different angle for various root openings are prepared in a single pass using the GMAW process for both of simulation and experiment. Workpieces with  $250 \times 250 \times 8$  in mm (length  $\times$  width  $\times$  thickness) are welded under welding conditions of 100 Amp current, 22 V voltage, 6 m/min wire feed rate using for all cases.

### 3 Results and Discussion

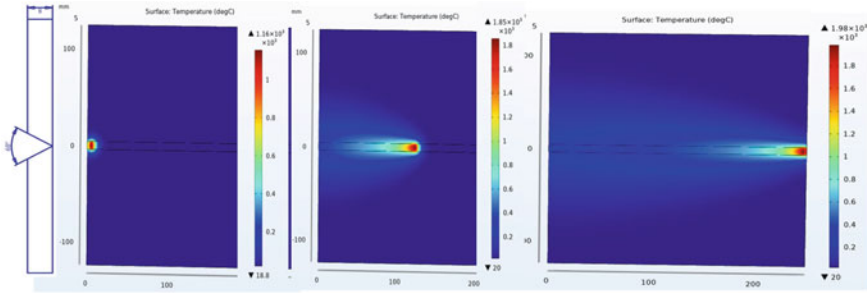
#### 3.1 The Transverse Shrinkage in V Groove Butt Joint

In order to investigate the transverse shrinkage in single V and bevel-groove butt joints, 12 cases are used to simulate for receiving the temperature distribution and shrinkage for each joint type. Table 1 shows 12 cases under groove angle of 0, 30, 45, 60 degree and root opening of 0, 1, 2 mm, respectively, for single V butt joint. Based on the welding conditions including current, voltage, velocity and joint type, the heat source dimensions are determined for each case. The heat source as given

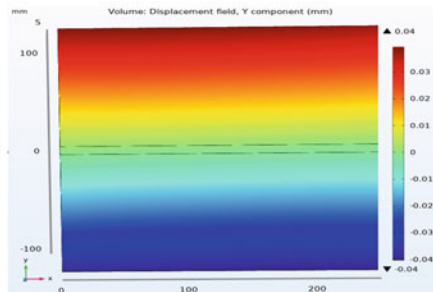
in Eq. (2) is inserted to Comsol software with related boundary condition, initial condition, etc. Figure 2 illustrates simulated results using the second case in Table 1. Obtained temperature distributions in the workpiece at various times are found in Fig. 1a. As seen, at beginning, the temperature is still low at about 1160 °C because of the unstable arc. This can be explained by the large amount of heat transferred to the initial workpiece, thus, the temperature is lower. Stable welding temperature is about 1850 °C. It is clear that the highest temperature reaches 1980 °C at the end of the weld line because there is overheating and heat transfer area is narrowed. Figure 2b represents the transverse shrinkage distribution of single V-groove butt joint. Results show that the symmetrical transverse shrinkage through the welding axis is 0.04 mm each side. Simulation transverse shrinkage of the other 11 cases is also summarized in Table 1. Table 1 shows that changing the groove angle, the transverse shrinkage tends to increase. At a groove of 0° and 60° the transverse shrinkages are the smallest and the largest, respectively. Thus, it shows that the transverse shrinkage increasing with increasing in the groove angle. According to Table 1, the root opening changes relative to the transverse shrinkage, it shows that increasing the root opening, the transverse shrinkage increases about 2.6 times compared to the absence of root opening (refer to case 1 and case 4). Thus, it can be seen that the shrinkage increases with increasing the groove angle and root opening. Therefore, in order to reduce the transverse shrinkage of the workpiece, the groove angle and root opening need be decreased.

**Table 1** Heat source size and simulated transverse shrinkages for single V-groove butt joints

No.	Groove angle	Root opening	Heat source size				Transverse shrinkage (mm)
	$\beta$ (deg)	$\alpha$ (mm)	b (mm)	C (mm)	$a_1$ (mm)	$a_2$ (mm)	
1	0	0	8.9	7.5	4.9	11.5	0.07
2	30	0	8.9	7.48	4.9	11.4	0.08
3	45	0	8.99	7.55	4.94	11.5	0.13
4	60	0	9.01	7.65	5	11.6	0.18
5	0	1	8.88	7.46	4.88	11.3	0.18
6	30	1	8.92	7.49	4.9	11.4	0.23
7	45	1	8.99	7.55	4.92	11.5	0.24
8	60	1	9.08	7.65	4.99	11.6	0.3
9	0	2	8.88	7.46	4.88	11.3	0.28
10	30	2	8.92	7.49	4.91	11.4	0.34
11	45	2	8.98	7.54	4.93	11.5	0.38
12	60	2	9.06	7.61	4.98	11.6	0.46



a. Temperature distribution at different times



b. Transverse shrinkages

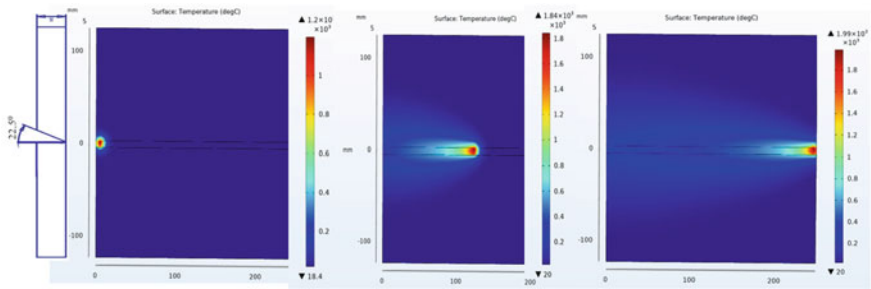
Fig. 2 Results of single V-groove butt joint for case 2

### 3.2 The Transverse Shrinkage in Bevel Groove Butt Joint

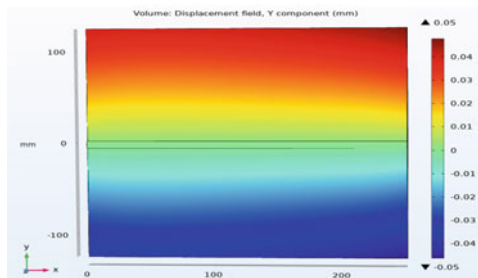
Similarly, 12 cases with different groove angles and root opening are performed for bevel-groove butt joint given in Table 2. Figure 3 depicts the temperature distribution in the workpiece and the transverse shrinkage of the weld using case 3 in Table 2. A stable welding temperature is obtained in the middle of the weld about 1840 °C, while the maximum transverse shrinkage is achieved at 0.05 mm on each side. The simulated transverse shrinkage of other weld joints with different root opening and groove angle is also summarized in Table 2. Results show that the transverse shrinkage increases with increasing chamfer angle and root opening. These transverse shrinkages are slightly smaller comparing to the results of the single V-groove joint. It may be due to the smaller volume of the molten metal of bevel-groove joint leading to the smaller shrinkage results in a smaller transverse shrinkage. Thus the type of joint also affects the transverse shrinkage of the weld.

**Table 2** Heat source size and simulated transverse shrinkages for bevel-groove butt joints

No.	Groove angle	Root opening	Heat source size				Transverse shrinkage (mm)
	$\beta$ (deg)	$\alpha$ (mm)	b (mm)	C (mm)	$a_1$ (mm)	$a_2$ (mm)	
1	0	0	8.9	7.5	4.9	11.5	0.07
2	15	0	8.88	7.46	4.88	11.4	0.07
3	22.5	0	8.99	7.53	4.94	11.5	0.1
4	30	0	9.03	7.58	4.96	11.6	0.2
5	0	1	8.88	7.46	4.88	11.3	0.19
6	15	1	8.93	7.5	4.91	11.5	0.2
7	22.5	1	9.02	7.58	4.96	11.6	0.24
8	30	1	8.93	7.51	4.99	11.7	0.26
9	0	2	8.88	7.46	4.88	11.3	0.28
10	15	2	9.01	7.56	4.95	11.5	0.31
11	22.5	2	9.06	7.62	4.95	11.6	0.36
12	30	2	9.14	7.68	5.02	11.7	0.47



a. Temperature distribution at different times



b. Transverse shrinkages

**Fig. 3** Results of bevel-groove butt joint for case 2

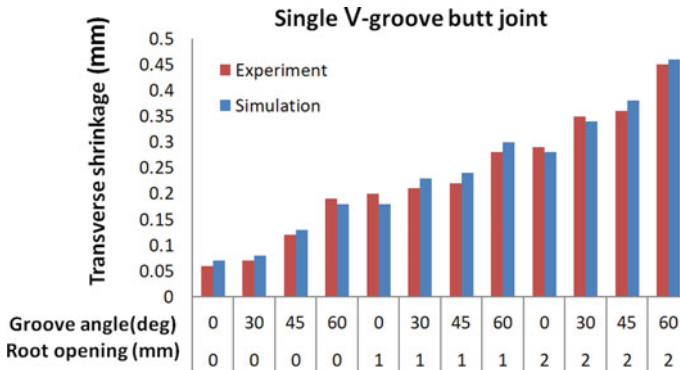


Fig. 4 Simulation and experiment transverse shrinkage of single V-groove butt joint

### 3.3 Comparison of Simulated and Experimental Results

To evaluate the reliability of the simulation results as well as simulation method, the simulated transverse shrinkage of both welded joints is compared to the experimental transverse shrinkage under the same conditions which has been published in references [3, 4]. Figures 4 and 5 show a comparison of simulation and experiment transverse shrinkage of single V and bevel-groove butt joints, respectively. A good agreement of simulation and experimental results is found in both Figures. As observed, the simulation shrinkages agree well with the experimental shrinkages in tend and value. A clear comparison with percentage error of simulated and experimental transverse shrinkage for each case is also shown in Table 3. Results show that although the error between simulation and experimental results still exists, the error value is within the allowable range except for cases 1 and 2 for both welding joint. From all results, the simulation method used in this study has high reliability. It can be applied to simulate not only shrinkage of butt joints, but also to other welding processes, other welding joints for determining welding stress and deformation as well.

## 4 Conclusions

Comsol software has been successfully used to determine the transverse shrinkage of single V and bevel-groove butt joints under various angle and root opening. Simulation results display that the transverse shrinkage increases with an increase in the groove angle and root opening for both welded joints. Simulated transverse shrinkage is compared to experimental transverse shrinkage in references [3, 4]. The simulated

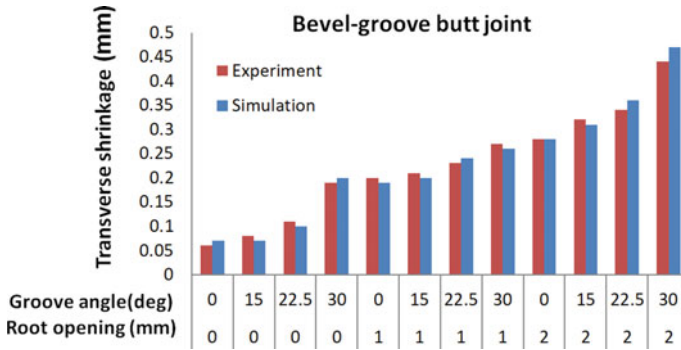


Fig. 5 Simulation and experiment transverse shrinkage of bevel-groove butt joint

results agree well with the experimental results. It can be said that presented simulation method is a reliable tool to quickly determine the shrinkage of the welded joint, thereby reducing the cost and time of experiments.

**Table 3** Comparison of simulation and experiment transverse shrinkage

Transverse shrinkages/No.		1	2	3	4	5	6	7	8	9	10	11	12
Single V-groove joint	Simulation (mm)	0.07	0.08	0.13	0.18	0.18	0.23	0.24	0.3	0.28	0.34	0.38	0.46
	Experiment (mm)	0.06	0.07	0.12	0.19	0.2	0.21	0.22	0.28	0.29	0.35	0.36	0.45
	Error (%)	16.7	14.3	8.3	5.3	10.0	9.5	9.1	7.1	3.4	2.9	5.6	2.2
Bevel-groove joint	Simulation (mm)	0.07	0.07	0.1	0.2	0.19	0.2	0.24	0.26	0.28	0.31	0.36	0.47
	Experiment (mm)	0.06	0.08	0.11	0.19	0.2	0.21	0.23	0.27	0.28	0.32	0.34	0.44
	Error (%)	16.7	12.5	9.1	5.3	5.0	4.8	4.3	3.7	0.0	3.1	5.9	6.8

## References

1. K. Masubuchi, in *Residual Stresses and Distortion* (Welding Handbook), pp. 218–264
2. V.I. Pavlovsky, K. Masubuchi, Research in the U. S. S. R. on residual stresses and distortion in welded structures. WRC Bull. **388**, 1–62
3. B.N. Sathyanarayana Reddy, N. Lakshmana Swamy, Influence of Groove angle in V-groove butt joints on transverse shrinkage in CO<sub>2</sub> arc welding process. *Int. J. Eng. Sci. Technol.* **J(2)**, 410–412 (2013)
4. B.N. Sathyanarayana Reddy, N. Lakshmana Swamy, Effect of bevel Angle in bevel groove butt joints on shrinkages in CO<sub>2</sub> Arc welding process. *Int. J. Sci. Adv. Technol.* **3**, 38–41 (2013)
5. A.A. Syed, A. Pittner, M. Rethmeier, D.E. Amitava, Modeling of gas metal arc welding process using an analytically determined volumetric heat source. *ISIJ Int.* **53(4)**, 698–703 (2013)
6. J.F. Lancaster, *The Physics of Welding* (Pergamon Press, New York, 1984), p.204



# Robotic Bin-Picking System Based on Voice Recognition, Deep Learning, and Point Cloud Processing



Van-Dung Tran, Thanh-Hung Nguyen, Dinh-Ba Bui, and Minh-Ha Le

**Abstract** This paper presents an automatic object localization system, which is used to pick the random and on-demand objects in the workspace. The system includes a robotic arm system integrated with a RealSense camera. Firstly, the target object is estimated from the speech recognition algorithm. Secondly, the Yolo-V3 algorithm is applied to detect and classify the target from the color image. Then, individual feature point clusters were extracted using segmented 2-D features and depth maps. To determine the position and orientation of the target, each cluster is matched to the CAD model using the ICP algorithm. Finally, collision avoidance techniques are applied to select objects for the picking task. The feasibility and effectiveness of the developed system have been verified experimentally. The test ended again showing that the system was able to successfully locate and pick up 3-D target objects via voice commands.

**Keywords** Deep learning · 3-D object detection · 3-D object localization · Voice recognition · Robot bin picking · Yolo V3 detection

## 1 Introduction

Along with the strong development of the industrial revolution 4.0, the field of robotics develops rapidly and continuously, being applied in all fields and different uses such as: underwater robots, robots on the ground, robots in the sky, robots in space, ... Some specific types of robots can reduce human work such as: Mobile robots, Robot Manipulators, Bio Inspired Robots, Personal Robot. In automated factories, smart factories, robotic arms are widely used to assist people in holding, lifting, moving objects, increasing work productivity or supporting people in a toxic and dangerous environments.

---

V.-D. Tran · T.-H. Nguyen (✉) · D.-B. Bui · M.-H. Le  
Hanoi University of Science and Technology, Hanoi 10999, Vietnam  
e-mail: [hung.nguyenthanh@hust.edu.vn](mailto:hung.nguyenthanh@hust.edu.vn)

Robotic systems can be controlled manually by buttons, handles, ..., or controlled by software using microcontrollers. A research study in [1] focuses on the design of a mobile robot equipped with a robotic arm utilizing a microcontroller and wireless communication. Another study in [2] outlines the design and control of a two-armed robot with seven degrees of freedom (DOF). In [3], a study explores the design of a robotic arm with 4 DOF, capable of performing individual tasks such as grasping, lifting, placing, and releasing objects. Another study in [4] presented on a 3D object recognition and pose estimation for random garbage selection using partition view-point feature histogram. More recently, a study in [5] presented a 3-D objects pose an estimation method for bin-picking using a combination of the semantic point pair feature method and the Mask-RCNN algorithm.

Building upon previous studies, the objective of this study is to design and control a robotic arm with six degrees of freedom, capable of picking up 3D objects through the integration of 3D image processing, voice recognition and deep learning technology.

## 2 System Overview

Figure 1 shows the object picking robot system. The system includes a robotic arm with gripper, RealSense camera, windows forms control interface. The RealSense camera is used to acquire the RGB-D images. The resulting images are used for object detection through deep learning technology. The RealSense camera also captures 3-D point clouds representing various objects. The evolved 3-D object recognition and localization algorithm is utilized to accurately determine the position and orientation of the target object. Voice control commands are integrated through the laptop's audio acquisition system. The robot uses these parameters to recognize and pick up randomly requested objects.

**Fig. 1** The developed robotic bin-picking system



### 3 3-D Object Recognition and Segmentation

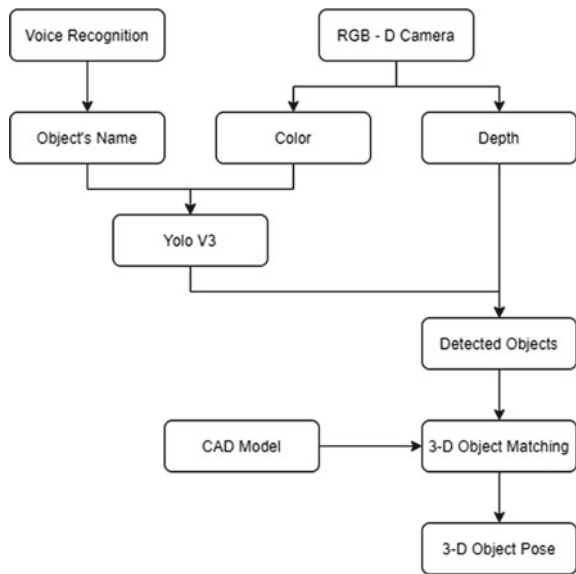
We have random objects with different properties on the table. The goal of this study is to identify individual objects through the prediction of object features and input point cloud segmentation. Each object will be represented by a name label and point cloud. The position of the name label and the point cloud are compared, thereby representing the final object in the orientation bounding box. Finally, the object's name label, location coordinates and orientation are determined for the robot to pick up the object as required. The flowchart of the proposed method is shown in the Fig. 2.

#### 3.1 Voice Recognition

The voice recognition system supports humans in interacting with robots more flexibly. In this study, Microsoft's speech API [6] was used to simplify speech recognition and give commands to the robot to perform.

A simple system is consisting of 2 components: speech synthesis and speech recognition system. Speech synthesis is the process of creating sound or speech through a computer. The received sound will be heard by the computer and recognize the words and phrases, called speech recognition. Voices in predefined cases are recognized to give tasks to the robot to perform.

Fig. 2 Flowchart of the proposed method



### 3.2 2-D Object Detection

Object detection is one of the fundamental and important tasks of machine learning. Currently, there are many different algorithms that effectively support the detection and classification of interested objects. Such as deep learning algorithms based on convolutional neural networks (Fast R-CNN, Faster R-CNN, Mask R-CNN, etc.). Regression-based algorithms for fast detection of layers and bounding boxes objects such as Yolo, which can be used to recognize objects in real time. Deep learning algorithms based on convolutional neural networks are prioritized for using in many machine learning models. For example, the multi-layered fruit classification model using robot vision and Faster R-CNN network by Wan and Goudos [7], the segmentation model and damage detection in cars using Mask R-CNN by Zhang et al. [8]. The advantages of these algorithms are very good recognition performance and high accuracy. However, in the model we built, the chosen algorithm is Yolo-V3 due to its advantages of fast detection speed, which can be run in real time. The effectiveness of this algorithm is demonstrated through recent publications such as the tomatoes recognition model of Liu et al. [9], the real-time face recognition machine learning model of Chen et al. [10].

The Yolo-V3 model leverages the network architecture of Darknet-53, comprising of 53 convolutional layers and 5 maximum pooling layers. To mitigate overfitting, batch normalization and dropout operations are incorporated after each convolutional layer. The Darknet-53 architecture features five residual blocks, incorporating the concept of residual neural networks. The network diagram of Darknet-53 is depicted in Fig. 3, and the overall structure of the Yolo-V3 network can be seen in Fig. 4.

	Type	Filters	Size	Output
	Convolutional	32	3 × 3	256 × 256
	Convolutional	64	3 × 3 / 2	128 × 128
1x	Convolutional	32	1 × 1	
	Convolutional	64	3 × 3	
	Residual			128 × 128
	Convolutional	128	3 × 3 / 2	64 × 64
2x	Convolutional	64	1 × 1	
	Convolutional	128	3 × 3	
	Residual			64 × 64
	Convolutional	256	3 × 3 / 2	32 × 32
8x	Convolutional	128	1 × 1	
	Convolutional	256	3 × 3	
	Residual			32 × 32
8x	Convolutional	512	3 × 3 / 2	16 × 16
	Convolutional	256	1 × 1	
	Convolutional	512	3 × 3	
	Residual			16 × 16
4x	Convolutional	1024	3 × 3 / 2	8 × 8
	Convolutional	512	1 × 1	
	Convolutional	1024	3 × 3	
	Residual			8 × 8
	Avgpool		Global	
	Connected		1000	
	Softmax			

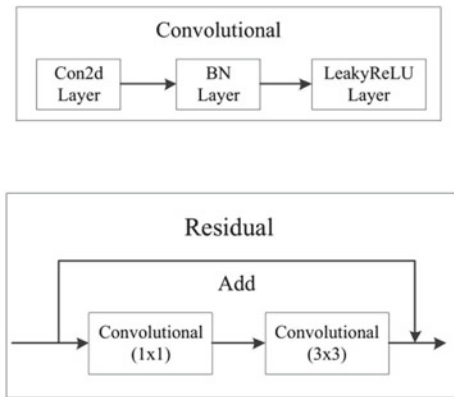


Fig. 3 Darknet-53 structure

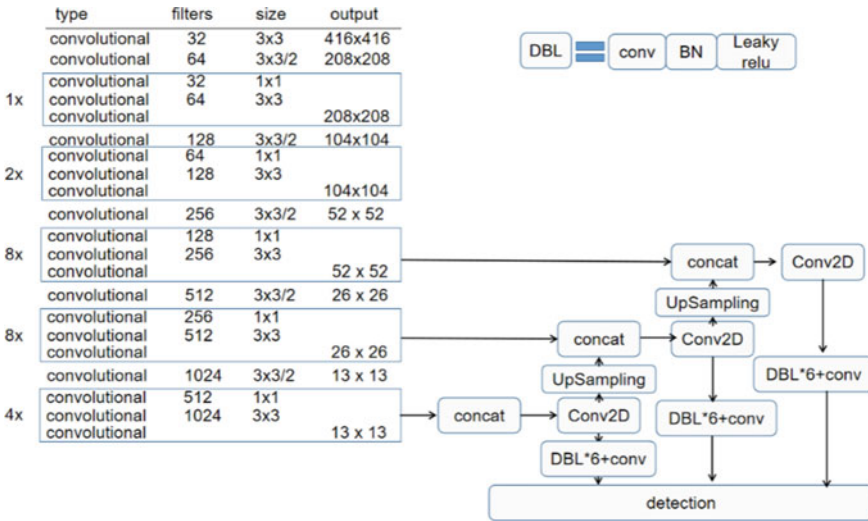


Fig. 4 Yolo-V3 network structure

### 3.3 Point Cloud Segmentation

The 3-D point cloud obtained from the camera contains information about the various objects in the scene. Splitting the input point cloud into smaller point clouds containing information that distinguishes each individual object, for later use. Several other studies have been published using Voxel Net, a LiDAR-based on the 3-D object detection network [11] or the 3-stage point cloud segmentation as introduced in [12]. The idea proposed in this study is to combine the detected objects in 2-D color image and the depth map to extract the target objects. After that, the extracted point clouds are filtered to remove noise and unnecessary data. The result of the point cloud segmentation is shown in Fig. 5.

Fig. 5 Point cloud segmentation



**Fig. 6** The target is picked by the robot arm



### ***3.4 Object Localization and Pose Estimation***

To estimate 3-D position and orientation of the target object in the scene point cloud, the extracted target point cloud is aligned with the CAD model by employing the Iterative Closest Point (ICP) algorithm [13]. The ICP algorithm is used to obtain the transformation to refine the original estimated 3-D pose. The ICP algorithm is a matching process being employed to minimize the fitting deviation between two matching point clouds. The ICP algorithm iteratively revises the transformation needed to minimize the distance between the points of two raw scans. After the object recognition and localization, the target object will be picked by a parallel jaw clamp as depicted in Fig. 6.

## **4 Experimental Results**

The experiment was tested with many kinds of objects with randomly positions and orientations. Minimum size of the objects is  $0.01 \times 0.01 \times 0.01$  m. Calibration results are highly accurate, so robot control can be applied to pick up the right objects as required. The data was processed on a computer with a core I7 processor (2.8 GHz and 8 GB RAM). The average processing time of 20 experiments is about 1.5 s for object localization. If using GPU, the result will be processed much faster (about 10 times faster than using CPU). Through voice control commands, the robot successfully determines the task of finding the location of the 3D objects that coincides with the required mask to carry out the object picking. In some cases, due to the influence of the environment and pronunciation, the robot may not be able to recognize the voice commands.

## 5 Conclusion

This research has achieved the following purposes:

1. Designing a robot arm model, which can detect, grab, and move objects to the required area.
2. Robot successfully identifies and locates objects through camera and 3-D image processing algorithm. Successfully controlling objects through voice commands and recognizing objects through using deep learning technology.

**Acknowledgements** This research is funded by Hanoi University of Science and Technology (HUST) [grant number T2021-SAHEP-008].

## References

1. I.B. Alit Swamardika, I.N. Budiastara, I.N. Setiawan, N. Indra Er, Design of mobile robot with robotic arm utilising microcontroller and wireless communication. *Int. J. Eng. Technol.* **9**, 838–846 (2017)
2. J. Tarek, C. Zaoui, M. Aref, Design and control of a dual-arm robot. *Int. J. Latest Res. Sci. Technol.* **4**, 110–116 (2015)
3. R. Mourya, S. Amit, S. Sourabh, K. Sushant, B. Manoj, Design and implementation of pick and place robotic arm. *Int. J. Recent Res. Civ. Mech. Eng. (IJRRCE)* **2**, 232–240 (2015)
4. D. Li, N. Liu, Y. Guo, X. Wang, J. Xu, 3D object recognition and pose estimation for random bin-picking using partition view-point feature histograms. *Pattern Recogn. Lett.* **128**, 148–154 (2019)
5. C. Zhuang, Z. Wang, H. Zhao, H. Ding, Semantic part segmentation method based 3D object pose estimation with RGB-D images for bin-picking. *Robot. Comput.-Integr. Manuf.* **68**, 102086 (2021)
6. Microsoft's Speech API. <https://docs.microsoft.com/en-us/dotnet/api/microsoft.cognitiveservices.speech>. Accessed 20 May 2021
7. S. Wan, S. Goudos, Faster R-CNN for multi-class fruit detection using a robotic vision system. *Comput. Netw.* **168**, 107036 (2020)
8. Q. Zhang, X. Chang, S.B. Bian, Vehicle-damage-detection segmentation algorithm based on improved mask RCNN. *IEEE Access* **8**, 6997–7004 (2020)
9. G. Liu, J.C. Nouaze, P.L. Touko Mbouembe, J.H. Kim, YOLO-tomato: a robust algorithm for tomato detection based on YOLOv3. *Sensors* **20**, 2145 (2020)
10. W. Chen, H. Huang, S. Peng et al., YOLO-face: a real-time face detector. *Vis. Comput.* **37**, 805–813 (2021)
11. S.S. Shi, X.G. Wang, H.S. Li, PointRCNN: 3D object proposal generation and detection from point cloud. [arXiv:1812.04244](https://arxiv.org/abs/1812.04244)
12. G. Pang, R. Qiu, J. Huang, S. You, U. Neumann, Automatic 3D industrial point cloud modeling and recognition, in *14th IAPR International Conference on Machine Vision Applications (MVA)* (2015), pp. 22–25
13. P.J. Besl, N.D. McKay, A method for registration of 3-D shapes. *IEEE Trans. Pattern Anal. Mach. Intell.* **14**, 239–256 (1992)

# A Lightweight Design of End Effector for Industrial Robot



Giang-Nam Le and Thanh-Xuan Nguyen

**Abstract** Reducing end-effector weight is significant for industrial robots, especially for transport robots. This article will present an approach to solving the above problem through the finite element method and topology optimization. The result is a general process for the lightweight design of the robot's end-effector. This process applied to the grip structure of the auxiliary robot, which plays the role of material transport in the automatic machining system of the car rim. Although this method requires more time and cost than the conventional design process, it effectively solves the problem of overloading for low-load robots, while still ensuring manufacturability by traditional machining methods to be suitable for industrial applications.

**Keywords** Lightweight design · Industrial robots · End-effector · Topology optimization

## 1 Introduction

### 1.1 Urgency of the Study

Robot with many advantages is increasingly applied in various fields in the industry [1]. In principle, some disadvantages of commonly used industrial robots include large power consumption, low load-to-weight ratio, bulky construction, and complex ancillary systems [2]. Replacing hardware with lighter structures is one of the effective, proposed solutions to reduce the weight and inertia that the robot has to bear during work [3]. Motor control torque can be reduced, robots need less power and are easier control [3], thus improving their working accuracy as well as their lifespan.

The end-effector is significant part of all industrial robots, helping them to interact with their surroundings. For transport robots, the weight and bulky construction of

---

G.-N. Le (✉) · T.-X. Nguyen

School of Mechanical Engineering, Hanoi University of Science and Technology, Hanoi, Vietnam

e-mail: [nam.legiang@hust.edu.vn](mailto:nam.legiang@hust.edu.vn)



this component directly limit their payload and workspace. Therefore, the study of solutions to reduce the volume of these stages is necessary to improve the operational efficiency of using the robot, which is also the goal that the authors conducting this study are aiming for.

## 1.2 Lightweight Design Methods

Among the methods, topology optimization is still an important method to reduce the volume of parts and increase the performance of the systems [4]. Therefore, this paper will present the topology optimization using the finite element analysis method in the original design space domain, provided that the loads are significant working positions. The free material distributions can be difficult for conventional forms of production, so this study will consider additional constraints to increase manufacturability, as well as apply some experience to design the design in accordance with the actual manufacturing conditions.

## 2 Research Method

### 2.1 General Mathematical Model

Solid Isotropic Material with Penalization method (*SIMP*) is one of the most popular mathematical methods for topology optimization. It helps to predict the optimal material distribution based on constraints such as mass, compliance, or manufacturing conditions [5]. The general mathematical model is shown below [2]:

$$\left\{ \begin{array}{l} x = (x_1, x_2, \dots, x_n)^T \\ \text{Min}C(x) = F^T U = U^T K U \\ \text{Subject to} \left\{ \begin{array}{l} V \leq V^* \\ F = K U \\ 0 < x_{\min} \leq x_i \leq 1 (x = 1, 2, \dots, n) \end{array} \right. \end{array} \right. \quad (1)$$

where:

- $x_i$  is design variables, characterizing the existence or non-existence of the material, corresponding to the value 0 or 1.
- $n$  is the number of design variables, depending on the finite element analysis in the original design domain.
- $K$  is the stiffness matrix.
- $F$  is the applied force vector.
- $U$  is the displacement vector.

- $V$  and  $V^*$  are the part volumes after and before optimization, volume constraint is equivalent to the mass constraint.
- In addition, the design variables must meet other constraints: local stress, maximum displacement, geometric shape, etc.

To avoid the binary feature of the design variable, *SIMP* uses a continuous function that characterizes the density distribution in each element. Then the density of the elements can change in the range of values ( $x_{min}; 1$ ). Elements with intermediate density are called gray elements.

A penalty factor  $p$  is introduced to reduce the contribution of gray elements to the total stiffness. The factor  $p$  directs the density of the elements to the value  $x_{min}$  or 1 to decide to remove or keep this element. Then, the elastic modulus is calculated in terms of:

$$E(x_e) = (x_e)^p E_0 \quad (2)$$

where:  $E_0$  is the material elastic modulus.

Overall hardness is calculated in:

$$K_{SIMP(x)} = \sum_{e=1}^n [x_{min} + (1 - x_{min})x_e^p] K_e \quad (3)$$

Experiments show that the penalty coefficient  $p = 3$  is appropriate [5].

## 2.2 Sensitivity Analysis

*SIMP* performs sensitivity analysis of the design variable to the objective function through loops. Mathematically, the sensitivity analysis is expressed as the derivative of the objective function for the matter density [5].

$$\frac{dC}{dx_e} = -p(x_e)^{p-1} [u_e]^T [K_e] [u_e] \quad (4)$$

The weight elements with the lowest material density value that do not have a significant role in the overall stiffness will be removed in subsequent iterations. This will continue until the objective function, or its variants converge.

However, if only calculating sensitivity for the independent elements without considering the surrounding elements, causes a “checkerboard” effect, it means the discontinuity of the material. To overcome this, *SIMP* applied a sensitivity filter, which is calculated as the difference between the pre-selected mean radius  $R$  and the distance from the center of an element to the centers of its neighbors (Fig. 1). Filters and some of the enhancements presented in [6] have proven effective in increasing fineness along the material-space boundary. The effect of using sensitivity filter on

**Fig. 1** Neighboring elements participate in filtering for element  $i$  [6]

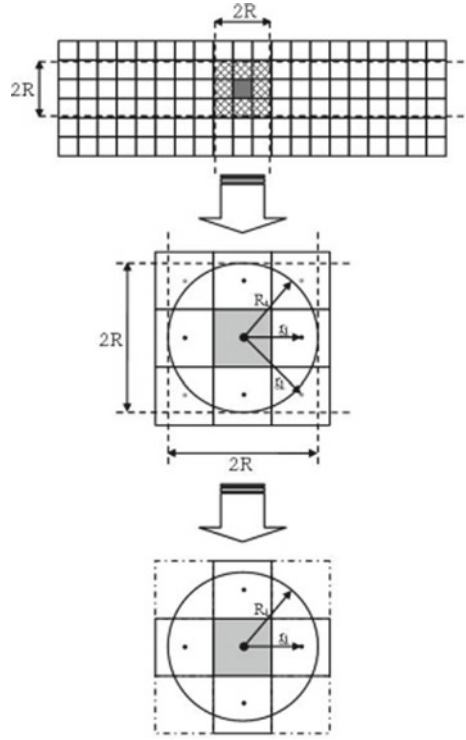


**Fig. 2** Material distribution without filter (left) and use (right) [7]



the material distribution is illustrated in Fig. 2. The robotic gripper in the automatic car rim production system is depicted in Fig. 3.

### 2.3 Optimization Process

In this study, the analysis and optimization software used is Ansys Workbench. The general process is presented as follows (Fig. 4).

**Fig. 3** Robotic gripper in automatic car rim production system

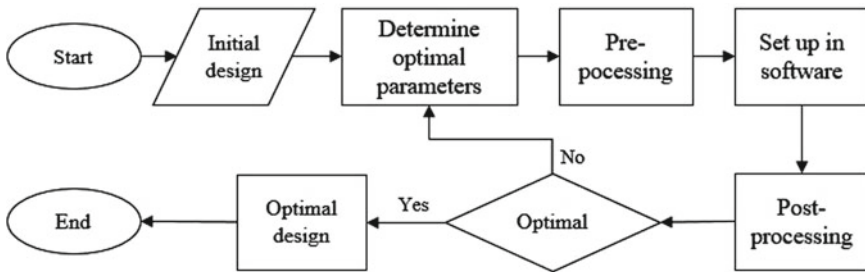


**Fig. 4** Optimization process

### 3 Results

#### 3.1 System Analysis

The object of processing is an aluminum alloy car rim, size 16 inches, weight 7 kg. The robot has a maximum acceleration of 0.5 g (where g is the acceleration due to gravity).

In automatic car rim processing systems (Fig. 3), usually robots play the role of transporting workpieces between machining stations or input–output of production cells. The grip structure not only ensures the grip function but also requires the precise positioning of the rim on the robot. Therefore, in this study, load boundary conditions investigated in the following two load cases:

- The position of placing the rim: The recommended error is  $\leq 0.2$  mm (Fig. 5).
- Accelerated state: The maximum acceleration considered is 0.5 g. The maximum stress is compared with the Yield strength of the structural material.

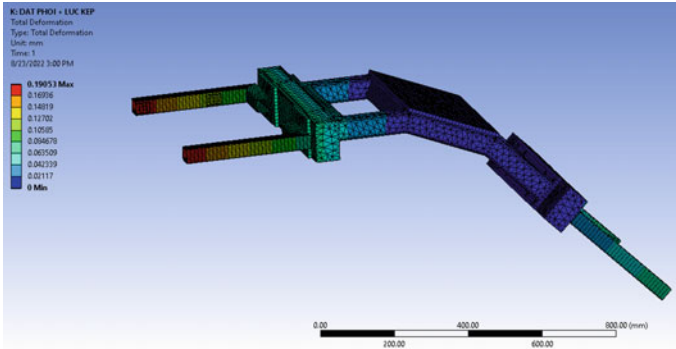


Fig. 5 Deformation at placing position

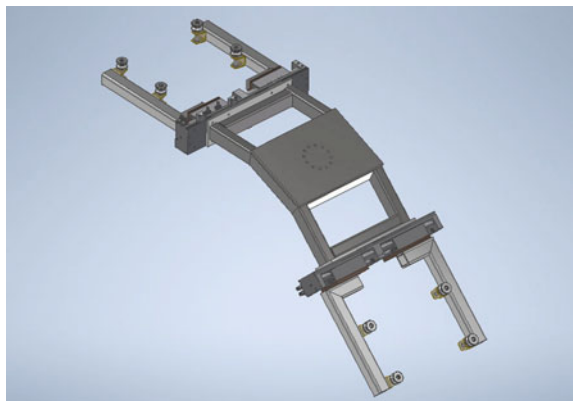
In addition, the grip mechanism always maintains a gripping force to keep the rim. In this case, the force value in this case is 147 N.

### 3.2 Optimization

The initial grip structure design included steel structures and standard components. Initial mass is 51.46 kg (Fig. 6). However, to facilitate modeling in finite element analysis, the standard components will be replaced by simplified models. At the same time, these components will be removed from the optimized materials because they are not suitable for the weight optimization in this case (Fig. 7). Material specifications of the grip structure are given in Table 1.

Constraints declared in the software (Fig. 8) including Maximum displacement of the grip structure 0.2 mm; Volume of material retained at 35%; Geometric symmetry constraints.

Fig. 6 The initial design



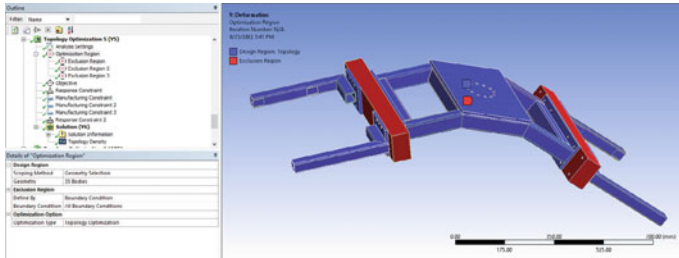


Fig. 7 Optimized material zoning

Table 1 Material used in study

Material	Density (kg/m <sup>3</sup> )	Yield strength (Mpa)	Ultimate strength (Mpa)	Poisson's ratio
Steel	7850	250	460	0.3
Custom*	1820	250	460	0.3

\* Applied to the pneumatic grippers to keep their actual mass and mechanical properties

**TABLE 08**  
Model (8 Systems) > Topology Optimization 5 (YS) > Response Constraint

Object Name	Response Constraint	Manufacturing Constraint 2	Manufacturing Constraint 3	Response Constraint 2
State	Fully Defined			
<b>Scope</b>				
Scoping Method	Geometry Selection			Optimization Region
Geometry	4 Bodies			
Optimization Region Selection				Optimization Region
<b>Definition</b>				
Type	Response Constraint	Manufacturing Constraint		Response Constraint
Response	Displacement			Mass
Coordinate System	Nodal Coordinate System			
X Component (Max)	0.2 mm			
Y Component (Max)	0.2 mm			
Z Component (Max)	0.2 mm			
Environment Selection	All Static Structural			
Suppressed		No		
Subtype		Symmetry		
Define By				Constant
Percent to Retain				35 %
<b>Location and Orientation</b>				
Coordinate System		Origin2		
Axis		X Axis	Y Axis	Z Axis

Fig. 8 Constraints

The simulation results are shown in Fig. 9. The material distribution domain has no major discontinues and obeys the defined constraints. The results of the redesigned model are shown in Fig. 10, in which some material positions have been adjusted to better match the actual fabrication. Two tests with the initial load conditions were performed to evaluate the effectiveness of the new end effector (Figs. 11 and 12).

## 4 Conclusion and Discussion

The weight of the new end-effector is reduced by 29.3% compared to the original. Structural analysis results show that the new end-effector meets the requirements of two load conditions.

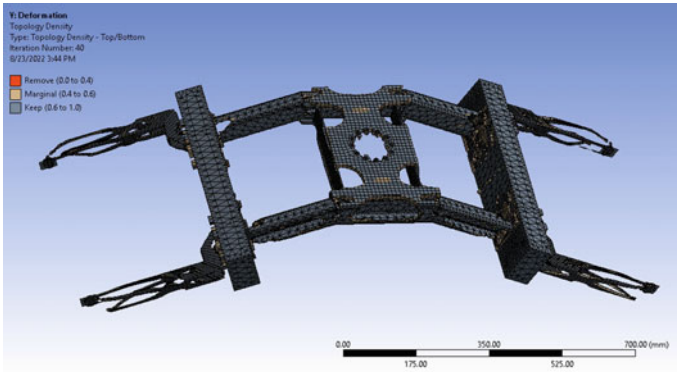


Fig. 9 Optimal material distribution result

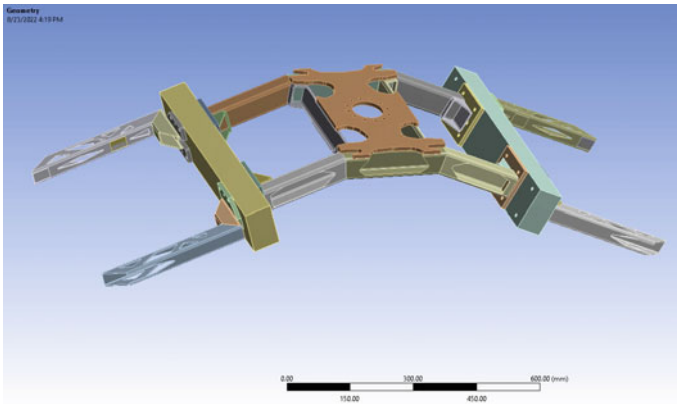


Fig. 10 The grip structure after redesign

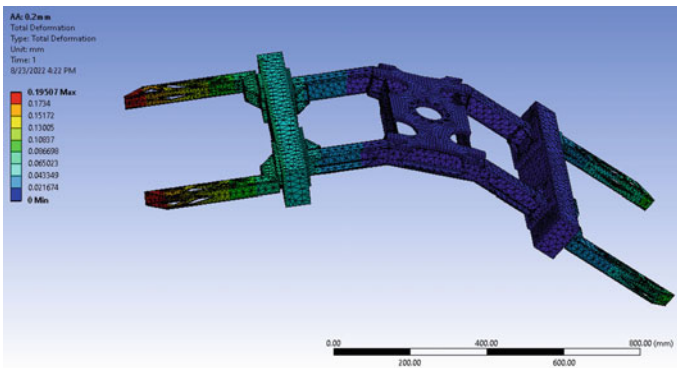
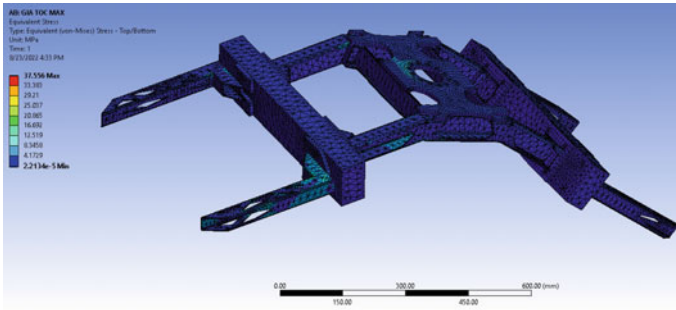


Fig. 11 Deformation at placing position after redesign (0.195 mm)



**Fig. 12** Stress at maximum acceleration (37.56 MPa)

In practice, sometimes the weight of the end-effector does not overload the robot, but minimizing the load on them is still preferable due to issues related to energy consumption and stability of the robot during movement, which helps to reduce overshoot and vibration when running at high speed.

The complex geometry of the components can increase fabrication costs. Computational simulation and redesign also extend the total time in the product development process. However, the results obtained have great implications for transport robots and other types of machines in many areas of life. That general optimized design process can be applied to other components.

## References

1. M. Wilson, in *Implementation of Robot Systems* (Butterworth-Heinemann, 2015), pp. 75–102
2. P. Yao, K. Zhao, Y. Lin, Y. Tang, Light-weight topological optimization for upper arm of an industrial welding robot. *Metals* **9**(9) (2019)
3. G. Carabin, E. Wehrle, R. Vidoni, A review on energy-saving optimization methods for robotic and automatic systems. *Robotics* **6**(4) (2017)
4. G. Lakshmi Srinivas, A. Javed, Multi-body dynamic optimization for upper arm of industrial manipulation, in *AIP Conference Proceedings* (2020)
5. D. Systemes, *SIMP Method for Topology Optimization*. [Online]. Available: [https://help.solidworks.com/2019/English/SolidWorks/cworks/c\\_simp\\_method\\_topology.htm](https://help.solidworks.com/2019/English/SolidWorks/cworks/c_simp_method_topology.htm). Accessed 20 Aug 2022
6. C.G. Pedersen, J.J. Lund, L. Damkilde, A. Kristensen, Anders, Topology optimization—improved checker-board filtering with sharp contours, in *Proceedings of the 19th Nordic Seminar on Computational Mechanics* (Esbjerg, 2006)
7. R. Larsson, Methodology for topology and shape optimization: application to a rear lower control arm (Department of Applied Mechanics, Göteborg, 2016)



# An Integrated Design of Industrial Robots and Machine Vision for Product Sorting System



Giang-Nam Le, Ngoc-Sang Vu, and Ngoc-Phu Doan

**Abstract** Utilizing automated sorting system with industrial robots in industrial production lines has numerous economic and productivity advantages. In the case of sensory-based product classification, industrial robots managed by machine vision proven to be clever and superior. This paper describes the procedure for calculating, designing, and testing a product sorting system utilizing a basic ABB IRB 120 industrial robot and machine vision. Deep learning techniques are combined with a pure image processing engine to extract information from the image. Specifically, the communication between system components is addressed, with the employed protocol and tools explained in detail.

**Keywords** Product classification · Industrial robot control · Machine vision

## 1 Introduction

Throughout history, sorting systems for goods have existed. This industrial solution replaces human labor in the classification of products with human-specified criteria. Robots are the equipment that can respond to the rapidly changing and adaptable characteristics of modern manufacturing, vastly expanding the usefulness of equipment and enhancing the efficiency of production processes. In addition, machine vision is a research field that has been cultivated for a long time. This technology has been implemented in everyday life and industrial automation environments due to its speed, precision, efficiency, and cost-effectiveness.

---

G.-N. Le (✉) · N.-S. Vu · N.-P. Doan

School of Mechanical Engineering, Hanoi University of Science and Technology, Hanoi, Vietnam

e-mail: [nam.legiang@hust.edu.vn](mailto:nam.legiang@hust.edu.vn)

N.-S. Vu

e-mail: [sang.vn184599@sis.hust.edu.vn](mailto:sang.vn184599@sis.hust.edu.vn)

N.-P. Doan

e-mail: [phu.dn183605@sis.hust.edu.vn](mailto:phu.dn183605@sis.hust.edu.vn)

Historically, robotics and machine vision were two separate areas of research and development. However, when the two areas merge, they will serve as a stepping stone for the robust growth of automation technology. Robots using machine vision have fueled the development of every industry [1]. J. Arentsa et al. recently proposed a controlled object-picking robot based on the ROS operating system and the results of deep learning and image processing [2]. The system includes a Kinect V2 RGB + depth camera and a Universal Robots UR5 robot that can distinguish between two types of objects (tubes and cans). Noteworthy at the model level, a robotic gripper controlled by an Arduino Nano and image processing [3]. The system includes a six-degree-of-freedom (DOF) robotic arm that can lift and position things based on their color and height using the Haar Cascade algorithm. In [4], the issue of operating ABB's industrial robot to pick up objects depending on the findings of image analysis is raised. However, the preceding publications simply offer suggestions or concentrate on control techniques. In the meantime, the problem of communication between system components, comprising numerous aspects such as protocols, settings, and employed tools, has not been clarified.

This paper actualizes the concept of an automatic product sorting system with industrial robots controlled by machine vision at its core. In it, the research team emphasized how the components function and interact. The utilized robot is the ABB IRB120, a standardized general-purpose robot that will pick up objects from the conveyor depending on the position and direction provided by the machine vision module, and then place them in the position corresponding to their type. Using the OpenCV library, the technique to extract information from the image is implemented. A convolutional neural network is the foundation of the object classifier (CNN). All system information and control commands are centralized on a personal computer-based integrated interface.

## 2 Related Works

### 2.1 VDI 2206 Methodology and Design Process

Mechatronics is a system where mechanical engineering, electronic engineering, and information technology engineering are synergistically linked. VDI 2206 is derived from the V design model, a mechatronic system design strategy [5]. It is the result of research, work, and development by the A127 committee of the German Society of Engineers (VDI). VDI 2206 outlines the basic framework of a mechatronic system with flows of matter, energy, and information.

At the system level, the mechatronics design process is managed using the V model. Key design techniques include design requirements definition, system design, module-specific design, modeling and model analysis, system integration, and properties verification. This study will establish a system based on VDI 2206 to create a design process consisting of steps: analyzing design requirements and

providing system structure designing a single module, integrating multiple modules, and evaluating the system.

## 2.2 *RobotStudio*

RobotStudio is an application software for offline training, creation, programming, simulation, and optimization of ABB robot systems without impacting the actual system; it can also be used in online mode on the controller [6]. The ABB virtual controller guarantees a highly realistic simulation. This software converts CAD data for precise robot programming, hence enhancing product quality. In this study, NX software was used for modeling, and then RobotStudio was implemented.

## 2.3 *Projection of a Point from the Real World onto the Image Plane*

On the basis of the projection described in [7], it can be concluded that a point belonging to a three-dimensional real-world object will be projected as a corresponding point on the picture plane of the pinhole camera model roughly corresponding to our actual camera.

The expression of the projection is  $m = \frac{1}{s}K(RM + t)$ . Where  $K$  represents the camera matrix, often known as the internal parameters of the camera. The components  $R$ ,  $t$  are a rotation matrix and a translation vector, respectively, for transforming the three-dimensional real-world coordinate system into a fixed camera coordinate system. Vector  $M = [X_{3D} Y_{3D} Z_{3D}]^T$  represents the picture's coordinates in a true three-dimensional coordinate system (meter dimension),  $m = [x_{2D} y_{2D} 1]^T$  with  $(x_{2D}, y_{2D})$  is the pixel coordinate of the corresponding spot on the digital image and  $s$  is the scaling factor.

## 2.4 *Convolutional Neural Networks (CNN)*

CNN is a subfield of Deep Learning that addresses vision-related issues including object recognition, tracking, and detection. A typical CNN consists of two components: Firstly, a feature extractor with convolutional layers at its core, used to recognize characteristics in an image, such as edges and groups of features. Secondly, classifiers utilize neural networks or other machine learning models based on picture characteristics.

### 3 System Design

#### 3.1 System Architecture and Design Requirements

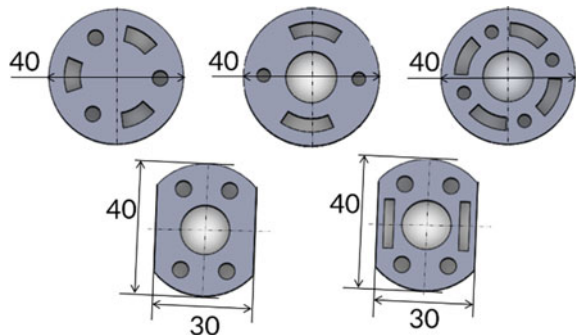
The system must be able to classify products based on their physical appearance, placing them in specified positions that correspond to their type. The selected items have the same color, but the shape, size, and position of the slots and holes varied, as shown in Fig. 1. The weight of each product is  $m = 6$  g, and its thickness is 10 mm. The system layout must facilitate the arrangement of the control system and the disassembly of the modules, while simultaneously ensuring synchronous coordination between the modules during system operation. The system's structure must assure its stability, security, and rigidity.

The main structure of the system, as depicted in Fig. 2, is formed from the system's requirements and the product's input characteristics, and includes the following elements:

- Mechanical—electrical—pneumatic module: With simple construction, installation, and cheap cost, the belt conveyor system is suited for feeding the system's input items. To pick and store the product in the correct location requires a mechanism with at least four degrees of freedom (three for translational motion and one for rotation); a robot mechanism with a clamping cylinder is optimal.
- Machine vision module: using a camera as its primary device, it acquires photographs of the workpiece's properties for computer processing.
- Power and control module: proposed in parallel based on mechanical structures. For robots, use the built-in controller of the selected industrial robot. For the belt conveyor, the commonly used microcontroller for IOT projects is the Arduino Uno.

From there, we can give the operating diagram of the system which is the combination of Machine Vision and Robot as shown in Figs. 3 and 4.

**Fig. 1** Types of products to be classified



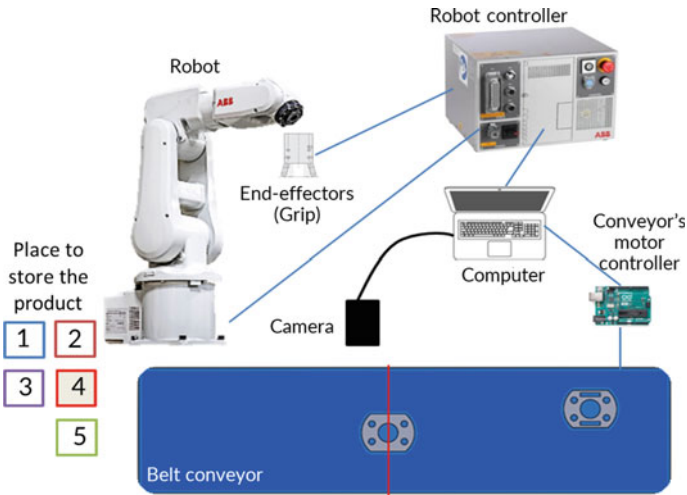


Fig. 2 Proposed system structure

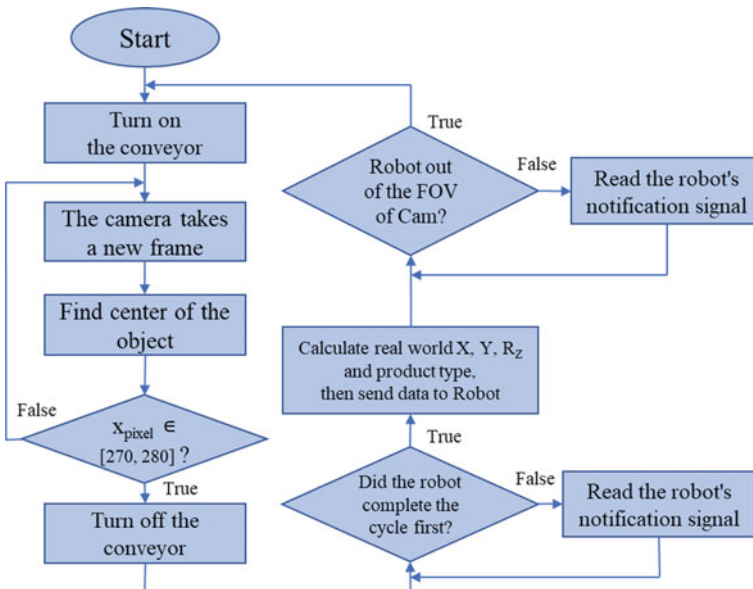


Fig. 3 Block diagram of machine vision module's operating cycle

### 3.2 Single Module Design

Components of mechanical–electrical–pneumatic module are selected and structured on a 3D CAD software. The control module is based on the system's operations and I/

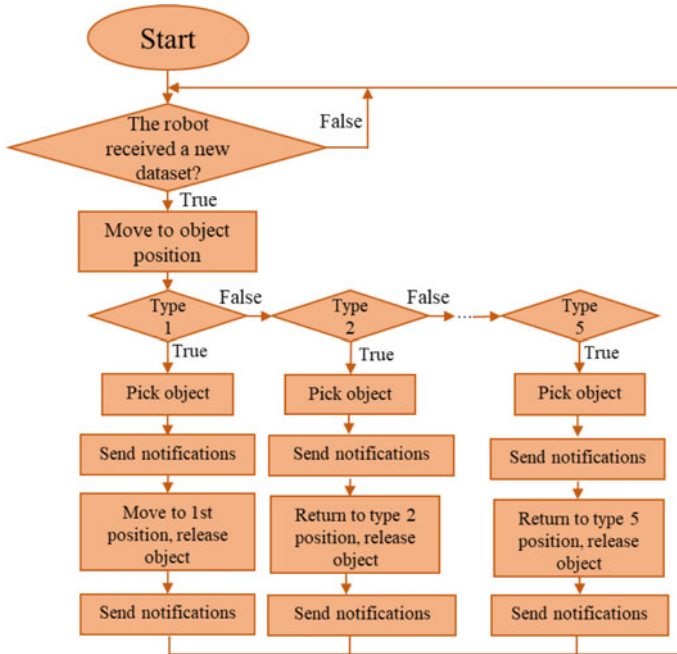


Fig. 4 Block diagram of robot’s operating cycle

O signals, which were constructed simultaneously in RobotStudio and Arduino IDE. The machine vision module is constructed according to the problem’s specifications and experimental conditions.

The mechanical structure’s equipment can be chosen in accordance with Table 1 based on input parameters and system requirements.

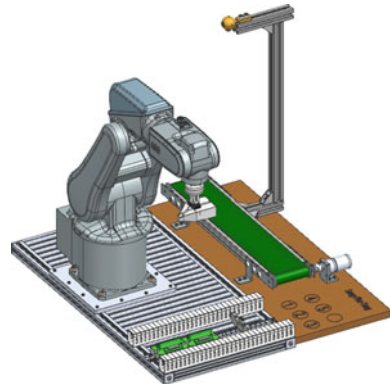
After developing each component for the system, the 3D drawings of each individual assembly are combined to form the system’s entire structure as shown in Fig. 5.

Then, import the system’s 3D model into the Robot Studio software. Next, configure the system’s I/O signals, the working environment, and the clamp’s center.

Table 1 Proposed components

Structure	Parameter
Belt conveyor	Width $w = 100$ mm, length $L = 600$ mm Drive speed $v = 100$ mm/s
Robot ABB IRB 120	6 DOF, maximum speed 6200 mm/s
Clamping hand cylinder MHZJ2-16D	Clamping force $F = 40$ N
Solenoid valve	5/3
Throttle valve	Self-regulating type

**Fig. 5** Mechanical structure of the system



In RobotStudio, the robot control algorithm is implemented using the RAPID programming language. Then, synchronize the robot control program in RobotStudio with the robot's actual IRC5 Compact controller. Due to the fact that the conveyor system is not the focus of this work, the Arduino controller was chosen due to its simplicity and universality in the research models.

Images captured by the camera are transformed to grayscale in order to reduce computational volume and noise is removed by Gaussian filter. The object-containing region of the image is highlighted using the binary thresholding method, and is defined by the encompassing contour. The rectangle with the smallest area enclosing the contour provides information about the position and orientation of an object as shown in Fig. 6.

The employed CNN network contains convolutional layers with  $3 \times 3$  kernels and ReLU activation function for each output. The convolution stage has 32 channel outputs. The model's full connection layer block consists of two fully connected stages with corresponding outputs of 128 and 5. The output layer contains five units, which correspond to the number of product kinds to be categorized.

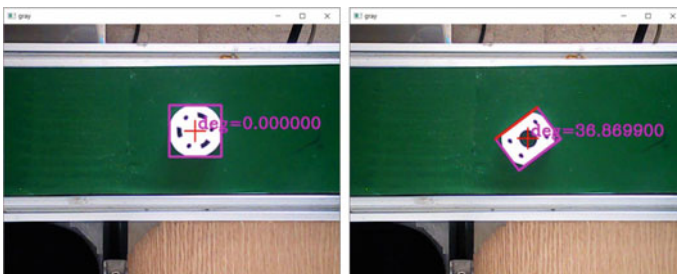


**Fig. 6** Result of determining the position and direction of the object

### 3.3 System Integration Design

Information between the Robot's IRC5 controller and the Machine Vision module is shared via OPC DA industrial communication. Originally, ABB IRC5 OPC Configuration was utilized for the robot controller. Then, the open-source "OPC-DAClientSync.h" library is used in programming to make the connect available. To exchange data between the Machine Vision system and the motor controller for the conveyor, the Serial protocol for USB port on Arduino controller is used.

It can be seen that information is dispersed across the system. We proposed that there should be an understandable interface for the operator to engage with the system, where the information of the system's components converge.

## 4 Experimental Results

The system was subjected to 500 classification cycles to collect data. The number of right classifications is 500 times, achieving 100% for all cases, guaranteeing that the classification process is error-free.

In terms of picking precision, the system is generally uniform across all product types as show in Table 2. We discovered that all instances of improper handling had one thing in common: the conveyor stopped when the object got close to the image's left edge. The problem may be the internal camera, as the left side of the image is deformed and the camera calibration process is not 100% precise. This can be resolved by selecting a higher-quality camera as opposed to the standard webcam chosen by the team. Resolution of the image, chain effect on the accuracy of the algorithm to find the position and direction of the object, the accuracy of the algorithm to convert from coordinate pixels (2D) to robot manipulation coordinates (3D), and the accuracy of the camera calibration all affect the robot's grasping accuracy.

The mean communication time between modules is computed as shown in Table 3. It has been determined that communication time has no impact on system operation time.

A product sorting cycle lasts 9.8 s on average. The robot's operating speed has a direct influence on the productivity of the system. This speed can be increased

**Table 2** Accuracy of picking

Product type	Total number of picks	Wrong number of picks	Exact ratio (%)
Type 1	100	14	86
Type 2	100	13	87
Type 3	100	13	87
Type 4	100	16	84
Type 5	100	9	91



**Table 3** Time of communication

Case	OPC protocol (s)	Serial protocol (s)
Computer sends data	0.018	0.010
Computer receives data	0.020	0.010

through programming, but the robot fixture's lack of rigidity prevents it. The motor's (conveyor's) speed and the camera's FPS rate. It is possible to choose a faster motor, but the image captured by the camera will be blurry due to the low FPS, which will prevent it from keeping up with the moving object's frame.

## 5 Conclusion

The stated design objective at the beginning of the article can be assumed to have been met. The machine vision system aids in detecting and classifying workpieces, as well as establishing a connection between the machine vision system and the industrial standard robot were presented. The mechatronic system design method VDI 2206 has been applied to the design of a product sorting system using robots and machine vision. The problem can be expanded by enhancing the limitations and optimizing the current system to increase productivity, in addition to changing the classification object to actual products.

## References

1. K. Okarma, Applications of computer vision in automation. *Appl. Sci.* **10**, 6783 (2020)
2. J. Arent, R. Cacurs, M. Greitans, Integration of computer vision and artificial intelligence subsystems with robot operating system based motion planning for industrial robots. *Autom. Control. Comput. Sci.* **52**, 392–401 (2018)
3. A.S. Shaikat, S. Akter, U. Salma, Computer vision based industrial robotic arm for sorting objects by color and height. *J. Eng. Adv.* **1**(04), 116–122 (2020)
4. P. Andhare, S. Rawat, Pick and place industrial robot controller with computer vision, in *2016 International Conference on Computing Communication Control and Automation (ICCUBEA)* (2016), pp. 1–4
5. VDI 2206: Design methodology for mechatronic systems (Beuth Verlag GmbH, 10772-Berlin, Düsseldorf, Germany, 2004)
6. N.W. Gosim, T. Faisala, Al-Assadi, M. Iwan, Pick and place ABB working with a liner follower robot. *Procedia Eng.* **41**, 1336–1342 (2012)
7. Robert Collins (CSE Department, Penn State University), Lecture 12: Camera Projection, CSE/EE486 Computer Vision I: Introduction to Computer Vision (2007)

# Computational Fluid Analysis and Experiment Verification of a Liquid Cooling System for an Array Radar's Transmit-Receive Module



Van Doan Cao, Duc Dung Le, Anh Quang Dang, and Anh Duc Hoang

**Abstract** The present research aims to analyze the performance of a liquid cooling plate for an array radar's transmit-receive module by using computational fluid dynamics (CFD) and measurement experiments. Firstly, a model of the purchased cold plate was built in SolidWorks. Simulation parameters of the heat dissipation of the liquid cooling system were considered, which provide the basis for high-accuracy numerical simulation. In particular, the temperature measurement experiment was carried out in order to verify the results of the simulation. The comparison results have proved that a thickness of 0.7 mm of thermally conductive glue between high-power electronic equipment and the cold plate's surface in the model is usable. The results in this article can be used as a reference for designing heat dissipation systems in high-power electronic equipment.

**Keywords** CFD · Cold plate · Heat dissipation · Temperature · T/R module

## 1 Introduction

A cold plate performs heat sinking by making indirect contact between the heat source and the cooling fluid. It is a feasible scheme for high heat flux electronic modules, and it has been extensively used in military and commercial electronic devices. In the case of press-pack and high-power operations, the cooling performance of a cold plate is the key factor in an electronic system's performance [1, 2].

The radio frequency of a high-performance millimeter wave transmit/receive (T/R) antenna module transfers high-power pulse signals to the antenna by converting

---

V. D. Cao (✉)

Radar Centre, Viettel High Technology Industries Corporation, Viettel Building, Hoa Lac Hi-Tech Park, Thach That, Ha Noi, Vietnam  
e-mail: [caodoan2006@gmail.com](mailto:caodoan2006@gmail.com)

D. D. Le · A. Q. Dang · A. D. Hoang

Centre for Mechanical Technology and Automation, Viettel High Technology Industries Corporation, Viettel Building, Hoa Lac Hi-Tech Park, Thach That, Ha Noi, Vietnam

electricity into high-power electromagnetic wave signals. When the energy of the power amplifier of the power equipment increases continuously, the electronic equipment needs to be cooled down and maintained by a high heat transfer liquid cooling system at a safe temperature so as to maximize the efficiency and stability of the equipment [3].

In this study, an integrated heat dissipation with a fluid circulation-type cold plate structure was used for a T/R module in order to be suitable for high-power electronic equipment, where the size and weight of the system are limited. A CFD analysis was carried out for different thicknesses of thermally conductive glue between high-power electronic equipment and the cold plate's surface to find out a value that is similar to the measurement experiment. Based on a proper thickness of the adhesive layer, the optimized integrated heat dissipation system was found in different positions of electronic equipment on a cold plate. According to the simulation and experiment validation results, the performance and practicality of the heat dissipation mechanism proposed in this paper can be verified, and a reference can be provided for the optimized design heat dissipation systems in high-power electronic equipment.

## 2 Material and Method

In this research, a closed-loop liquid cooling system was used for the electronic equipment. The closed-loop liquid cooling system requires a liquid-to-air heat exchanger. Therefore, several calculations are needed to fully understand the performance and for a preliminary selection of suitable equipment for the cooling system.

The liquid cooling system in this article has three major components: a cold plate, a heat exchanger, and a pump. The cold plate is usually made of aluminum alloy and is attached to the device being cooled via an intermediate layer of thermal paste. The plate has a copper alloy pipe that has a coolant flowing through it in order to transfer heat. A cooling cycle is shown in Fig. 1. The pump drives the fluid through the loop. Therefore, the liquid moves from the cold plate to the heat exchanger. In this component, the heat is transferred to the ambient air via forced convection [5].

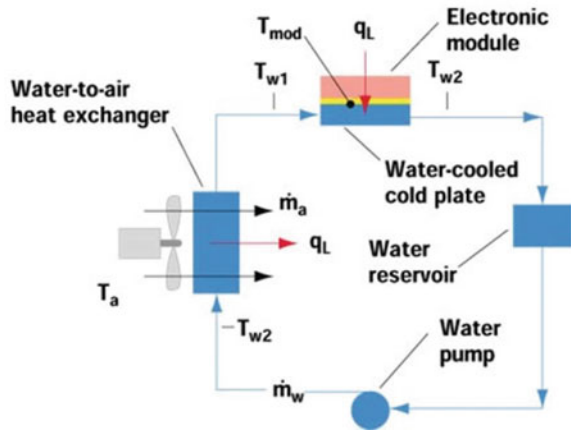
The temperature rise of the water on the plate following heat absorption is calculated as follows:

$$\Delta T = T_{w1} - T_{w2} = \frac{q_L}{G \cdot C_0} \quad (1)$$

where:  $\Delta T$ —water's temperature rises;  $T_{w1}$ —water's temperature entering the cold plate;  $T_{w2}$ —water's temperature as it exits the cold plate and enters the heat exchanger;  $G$ —mass flow rate of the water;  $q_L$ —heat dissipated by the device;  $C_0$ —water's specific heat.

Altair AcuSolve was used for CFD analysis in order to evaluate the performance of a liquid cooling plate that was prepared in SolidWorks. Simultaneously, the real cooling plate was purchased, and its structure and material properties are similar to

**Fig. 1** Closed loop liquid cooling system [4]



the CAD model. The Altair AcuSolve software is used as a tool for the numerical solution. The basic equations governing the motion of fluids are the Navier–Stokes equations. The flow is assumed to be turbulent, incompressible, steady-state, with no radiation. Three governing equations are shown:

- Continuity Equation:

$$\frac{\partial \rho}{\partial t} + \nabla \cdot (\rho \vec{u}) = 0 \tag{2}$$

- Momentum Equation:

$$\rho \frac{\partial \vec{u}}{\partial t} + (\rho \vec{u} \cdot \nabla) \vec{u} = -\nabla p + \rho b + \nabla \cdot \tau \tag{3}$$

- Energy Equation:

$$\rho \frac{\partial h}{\partial t} + (\rho \vec{u} \cdot \nabla) h = \nabla \cdot (k \nabla T) + \nabla \vec{u} \cdot \tau + \frac{Dp}{Dt} + S \tag{4}$$

where:  $u$ —velocity;  $\rho$ —density;  $p$ —pressure;  $\tau$ —shearing stress;  $b$ —body force;  $S$ —energy sources [6].

In addition to the dimensions of the model and the characteristics of the material, the thickness of the thermal paste on the interface between each part should be defined in order to make the high-accuracy numerical simulation. Therefore, the first step is to find out the corresponding thickness of thermally conductive glue between high-power electronic equipment and the cold plate’s surface in the model based on measuring its implementation (Fig. 2).

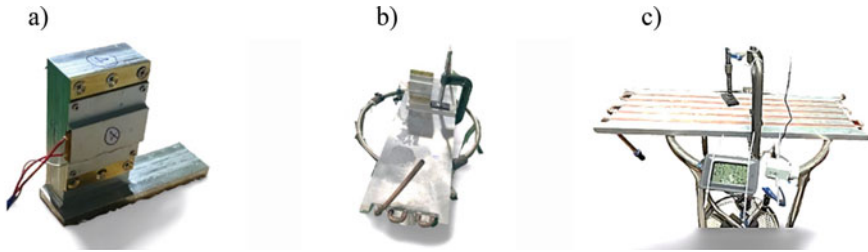


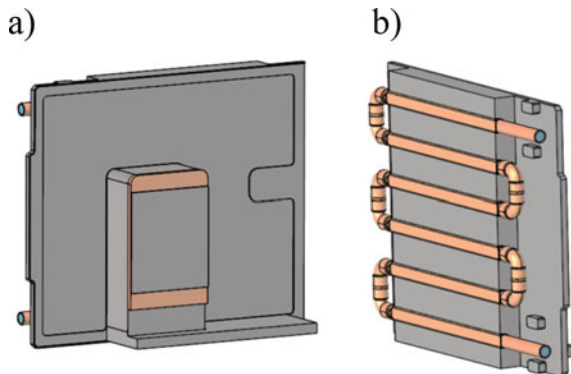
**Fig. 2** Temperature measurement experiment of the T/R module on a purchased cold plate. **a** T/R module. **b** T/R module on the cold plate. **c** Measurement experiment

In this experiment, a cold plate is a purchased part and a T/R module is a simplified design and fabrication. A heat-generating device was mounted on the T/R module in order to supply 120 W of heat capacity. Copper pipe was used for the flow channel with a diameter of 9.52 mm and a thickness of 0.81 mm. The adhesive glue for the bonding process of the base plate and copper pipe is Kafuter 5202, which has a thermal conductivity of  $2 \text{ W m}^{-1} \text{ K}^{-1}$ .

The cold plate model has been designed by SolidWorks software to be the same size as in reality. Then, it was analyzed in AcuSolve with three different thermal shell thicknesses, 0.5, 0.7, and 1 mm, respectively. The simulation results were compared to the measurement experiment to find out the proper shell thickness. In this stage, the T/R module is placed perpendicular to the surface of the cold plate. The temperature of the cold plate and chip were measured by a handheld infrared thermometer gun.

The second phase is the evaluation of the new fabricated cold plate design by simulation that is able to be used for the T/R module. This cold plate model is similar in design to the purchased device in terms of the materials it's made of. However, this model is sized to match the size of the T/R module and the space it contains. The simplified T/R module was mounted horizontally on the cold plate as shown in Fig. 3.

**Fig. 3** A new cold plate design. **a** Side of the T/R module. **b** Side of a pipeline



The Reynolds numbers of the cooling system models had been calculated in order to define the flow in the simulation. The results show that the Reynolds number ( $Re = 4021$ ) is bigger than 2300 in this article, hence turbulent flow conditions are selected.

The inlet boundary type was mass flow inlet. The outlet boundary type was outflow. The mass flow rate was set to 1.5 lpm. The initial temperature of the coolant was 35 °C. The Heat Transfer Coefficient were set to  $10 \text{ W m}^{-1} \text{ K}^{-1}$  and 35 °C ambient temperature. Cells and cold plate to air contact surfaces were set to Convection Thermal Condition.

### 3 Results and Discussion

In the first phase of this paper, a heat capacity of 120 W was supplied in simulation and experiment. Based on the simulation results, the temperature of the water inside the cold plate and the temperature distribution of the cold plate were analyzed for three different thermal shell thicknesses. In the experimental model, the thermal glue thickness was in a range from 0.5 to 1 mm. This value has no significant influence on the measurement results. However, simulation results were significantly changed when changing the adhesive layer thickness. The measurement and simulation results are summarized in Table 1.

The results show that the value of 0.7 mm of thermal glue thickness provides a result close to the measurement results. The acceptable difference between measurement and simulation is in the range of 2–4.8%. This value of thickness is useful for further simulation of detailed design. However, the temperature of the chip processor is higher than its allowable value (70 °C). The dimension of the purchased cold plate is too big for T/R size. Therefore, the cold plate is required to be designed on T/R module dimensions and will be.

In the second phase, a new design of cold plate was designed and evaluated by simulation with the main purpose of bringing the chip temperature to the permitted temperature. From the simulation and experimental results in the previous phase, a value of 0.7 mm was built and defined in the model as an adhesive layer. All other boundary conditions are the same as for purchased cold plates. Figure 4 shows temperature-contour diagrams of the cold plate and T/R module.

**Table 1** Measurement and simulation results of T/R module on purchased cold plate

Temperature (°C)	Experiment	Thickness in simulations		
		1 mm	0.5 mm	0.7 mm
On the chip processor	82.4	92.2	72.1	80.7
On the top of the copper plate	56.5	63.5	54.3	58.0
On the bottom of the copper plate	50.1	55.6	45.8	49.1
On the back surface of the T/R block	50.6	54.1	50.1	51.2
On the front surface of the T/R block	49.8	56	50	52.0

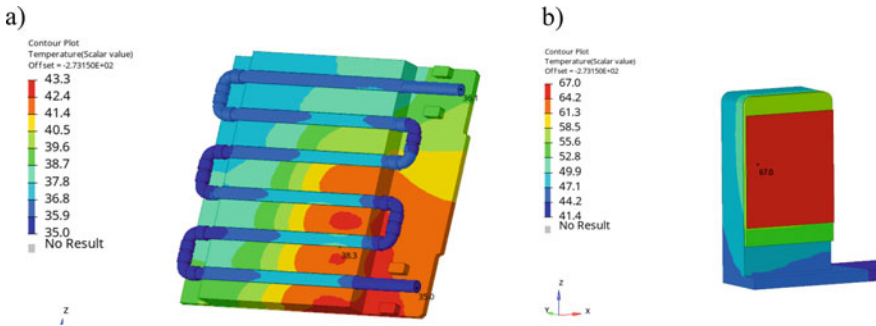


**Fig. 4** Temperature-contour diagram of new design cold plate. **a** Heat distribution on the pipeline side. **b** Heat distribution on the T/R module

The liquid flow temperature and heat distribution on the cold plate are shown in Fig. 4a. The temperature of the chip processor and T/R module is shown in Fig. 4b. The inlet water temperature of the cold plate and the working environment temperature are both 35 °C. This liquid flow absorbs heat generated by the chip processor to keep the chip temperature at 67 °C, which is lower than the temperature requirements (70 °C). The flow rate of water is 1.5 lpm, and the outlet temperature of the water is 36.1 °C which is an increase of 1.1 °C. In the calculation, the cold plate's material properties and flow parameters are the same as in simulation. The temperature difference in water flow between the inlet and outlet is 1.16 °C. Thus, the simulation results are acceptable. The new cold plate fabrication can be carried out to be used for T/R modules.

## 4 Conclusions

Radar performance is directly affected by the temperature equalization and heat dissipation performances. Based on the fact that the T/R module of the array radar is limited by its size and weight, this study integrated a fluid circulation-type cold plate and a T/R module to develop an integrated heat dissipation system. In addition to ensuring the similarity in size and materials of the model, the thickness of the glue layer is also a factor that is required to be accurately determined in the simulation in order to ensure the reliability of the simulation results. According to the simulation and experimental results for the purchased cold plate, the thickness of the adhesive layer in the simulation was 0.7 mm. When this thickness was defined in AcuSolve, the difference between measurement and simulation was in the 2–4.8% range, which is acceptable and useful for the second stage of simulation. The new design of the cold plate was also analyzed by simulation. In this stage, the T/R module is placed horizontally on the cold plate. This design provides noticeably better heat dissipation than the vertical position in the initial experiment. The chip processor temperature

was at 67 °C which was less than the temperature requirement (70 °C). Therefore, the fabrication of the new cold plate can be carried out to be used for the array radar T/R module. This paper's findings can be applied to other heat dissipation systems in high-power electronic equipment.

## References

1. S. Wiriyasart, P. Naphon, Liquid impingement cooling of cold plate heat sink with different fin configurations: high heat flux applications. *Int. J. Heat Mass Trans.* **140**, 281–292 (2019)
2. S. Wiriyasart, P. Naphon, Heat spreading of liquid jet impingement cooling of cold plate heat sink with different fin shapes. *Case Stud. Therm. Eng.* (2020). <https://doi.org/10.1016/j.csite.2020.100638>
3. Y.J. Liang et al., Design of an integrated heat dissipation mechanism for a quad transmit receive module of array radar. *Appl. Sci.* **11** (2021). <https://doi.org/10.3390/app11157054>
4. R. Simons, Estimating temperatures in a water-to-air hybrid cooling system. *Electron. Cool.* (2002)
5. M. Iyengar, S. Garimella, Thermal optimization and design for manufacturability of liquid-air hybrid cooling systems. *Electron. Cool.* (2008)
6. A. Muhammad et al., Design and analysis of liquid cooling plates for different flow channel configurations. *Therm. Sci.* (2021). <https://doi.org/10.2298/TSCI201111196F>



# Evaluate the 3D Measurement System Accuracy Through 3D Point Cloud Processing Algorithm



Nguyen Thi Kim Cuc, Cao Xuan Binh, and Tien Dung Vu

**Abstract** Measuring 3D shapes by structured light is currently being widely studied and applied. The accuracy of this measurement method is highly dependent on calibration and point cloud processing. Currently determining the accuracy of a non-contact 3D measuring system also needs to be evaluated. In this paper, a method to evaluate the accuracy of the measurement system by using phase shift combined with Graycode method (PSGC) is proposed. With the construction of algorithms to evaluate accuracy through the criteria of size and spatial accuracy, a measurement system was evaluated. The test results on the experimental measurement system by the phase shift combined Graycode compared with the measurement results by the Graycode method showed that the measurement system has higher accuracy. In addition, the method of determining the spatial accuracy according to the position and orientation of the reference plane is also evaluated.

**Keywords** Point cloud processing · 3D measurement · Fitting algorithm · Calibrate system

## 1 Introduction

A measurement system requires several corresponding standards to evaluate its accuracy. At present, structural light measuring devices do not have any standardized scale or system of measurement. With the tremendous rising of technology and manufacturing industry, requirements for more intricate non-contact measure systems and tools are increasing, yet there is no international standard for the method. The accuracy of measuring PSGC depends on the accuracy of the optical system itself and the reflective characteristics of workpieces. Furthermore, during measurement, the sine wave shape of the resulting image has deviated from the ideal sine wave shape and noises due to interference, ambient light, projector Gamma nonlinearity [1]; or

---

N. T. K. Cuc · C. X. Binh · T. D. Vu (✉)

Hanoi University of Science and Technology, No. 1, Dai Co Viet, Hai Ba Trung, Hanoi, Vietnam  
e-mail: [Dung.vutien@hust.edu.vn](mailto:Dung.vutien@hust.edu.vn)

due to incorrect system calibration [2, 3]; interference caused by surface reflection or uneven reflectivity on the surface of the object to be measured, the intensity of ambient light, the deviation of the focus of the optical system [4]; causing errors in the phase analysis process and the results lead to absolute phase map deviations, causing errors to reconstruct the 3D profile of the measurement detail. The accuracy of 3D shape measurement using digital ridge projection depends on the quality of the reconstruction phase if a projector and a camera are used. This system reconstructs the image directly from the phase, and the depth value in the z direction is a function of the phase [5]. In addition, the accuracy of the PSGC measurement system also depends on the 3D measuring point cloud processing algorithm and the image compositing algorithms, finishing the surface of the measured detail. After obtaining the 3D point cloud, the surface needs to be processed by an appropriate method so that the size of the measured part can be measured from the coordinates of the point cloud. Some methods for matching basic surfaces such as planes and spheres are being studied such as: least squares, SVD, RANSAC [6–8]... However, each method has its own advantages and disadvantages for each specific surface type.

In this paper, the algorithm for evaluating the accuracy of measurement systems is built based on international standards of measurement for surface profile analysis. The standards for accuracy evaluation include standards for measuring depth (or order) and standards for measuring contour coordinates. The experiments performed to evaluate the accuracy of the system within the scope of the study are the system calibration accuracy and the point cloud pairing accuracy. In addition, standards for measuring area accuracy according to the reference plane are also suggested in this paper.

## 2 Method

### 2.1 *Evaluation of the Accuracy of the Measuring System in Term of Standard Plans*

The accuracy of the 3D measuring system depends on the method of processing the reconstructed 3D point clouds. Point cloud processing with the detection of planes, to measure the size and relative position of the surfaces is a process that requires high precision. With the use of the height step standard for the measurement system using the PSGC method, the measurement standards are the distances between planes that need to be determined. Therefore, it is necessary to build algorithms and software to evaluate and compare the measurement results of this system. To determine the distances between the planes, built planes and fitting plane algorithms are proposed. The algorithm and software are implemented by applying the RANSAC algorithm presented in the study [9]. After the planes are fitted, those cross-sections are taken to determine the distance of the planes. On the cross-sections, straight lines will be defined. The dimensions of  $h_i$  can be calculated from here. These intervals will then

be compared with the actual size  $h_t$ . The relative error of the size measured by the measurement method is determined as follows:

$$Relative\ error = \frac{|h_t - h_i|}{h_t} \cdot 100\% = \frac{\Delta h}{h_t} \cdot 100\%$$

Where:  $\Delta h$  means deviation of the measurements.

The accuracy of measured volume is estimated using a 2D standard plane with  $A \times B$  (mm) dimension that is placed in the measured volume at various positions and inclination with respect to the reference plane. The measured volume of the system is defined as  $w \times h \times d$ . The displacement of the plane at positions within the measurement area affects the ability of the camera to obtain clear images. Therefore, it is necessary to determine the accuracy of the positions in the measuring area by measuring a reference plane in distinct positions and orientations. The coordinates position of the measure standard plane are arranged on the Z-axis, and those angles are organized to rotate around the Y-axis of the sample plane as shown in Fig. 1. The angle of the measuring standard plane relative to the reference plane is determined by an encoder that measures the rotation angle of the turntable.

The positions and orientations of the standard plane in Fig. 1 are described as follows.

Position 1: the standard plane is centered in the measured area, parallel to the rereference plane, and a distance L on the aperture. Position 2 and 3: From position 1, incline the standard plane angles of  $10^\circ$  and  $20^\circ$  respectively. Position 4 and 6: The standard plane is at position 1, then being translated distances of  $+\Delta z$  and  $+2\Delta z$  respectively on the positive z-axis. Position 8 and 10: The standard plane is at position 1, then being translated distances of  $-\Delta z$  and  $-2\Delta z$  respectively on the negative z-axis. The orientations of planes at positions 4, 6, 8, and 10 are parallel to the direction of the plane when the plane is at position 1. Positions 2 and 3 of the standard planes coincide with position 1 but are inclined at a corresponding angle to the plane. Position 5 and 7: the standard plane is at position 2, The standard plane is

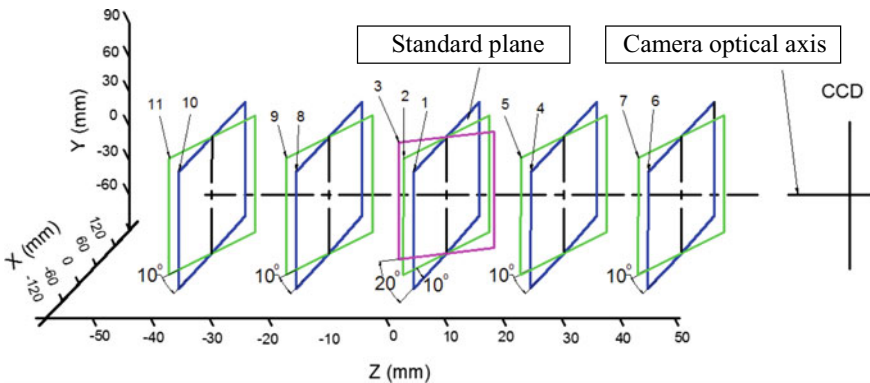


Fig. 1 Diagram of positions and orientations of the standard plane

at position 1, then being translated distances of  $+\Delta z$  and  $+2\Delta z$  respectively on the positive z-axis. Position 9 and 11: the standard plane is at position 2, The standard plane is at position 1, then being translated distances of  $-\Delta z$  and  $-2\Delta z$  respectively on the positive z-axis.

The measurement results and construction of point clouds in the standard plane are then applied to the plane matching software (in this paper, the appropriate number of matching planes is set to 1). For each measured measurement, the average distance between points in the point cloud of the sample plane and the fit plane calculated and analyzed, and the standard deviation of each measurement is obtained.

The purpose of measuring the standard plane in the measured region is to determine its accuracy over the entire region. The point cloud of the standard plane with distinct positions and angles, is reconstructed. After that, the planes that fit the reconstructed standard plane's point clouds are calculated to determine the difference between these two planes.

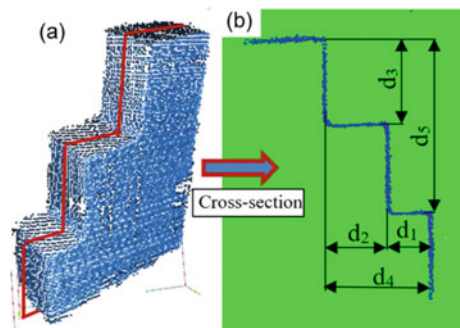
## 2.2 Experiment Result and Discussion

The measurement results using Gray and PSGC methods are compared with the actual size of the measuring piece measured with a caliper. The measurement results of the CNC (Computer Numerical Control) milling height step part and fitting standard plane in the measured volume have shown as follows.

The height step part measurement is the result of two methods with 30 cross-sections that are separated by 0.4 mm. On the cross-section, the fitting lines are detected and the distances between them are measured. After fitting the planes on the point cloud of the height step part, the dimensions between the planes were shown in Fig. 2. The measurement results using Gray and PSGC methods are compared with the actual size of the measuring piece measured with a caliper.

According to Fig. 3, the maximum deviation measured by the PSGC method is 0.239 mm compared to the measurement method using the Gray code of 0.611 mm. The maximum standard deviation of the PSGC method is 0.187 mm, and that of the

**Fig. 2** The point cloud of height step part (a) and cross-section (b)



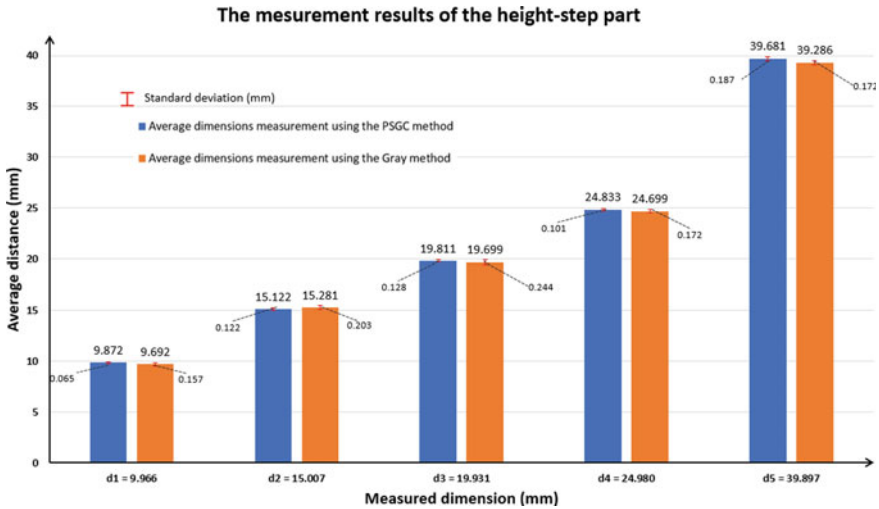


Fig. 3 The measurement results of the height step part

Gray code method is 0.202 mm. The relative error of the PSGC method is 0.59%, and that of the Gray-code method is 1.53%. This shows that the PSGC method has higher accuracy and reliability than the Gray-code method.

Experiment results with plane position and orientation using experimental equipment and area measurement. Experimental estimated with positions and orientations of plane with experimental equipment with measuring area  $245 \times 180 \times 130$  (mm), measuring plane with size  $150 \times 80$  (mm); distance  $L = 500$  (mm) and value  $\Delta z = 10$  (mm).

Table 1 of fitting plane results in different orientations and positions shows the correlation between the error and the angle and position of the reference plane. As shown in the table, the error is insensitive to the position of the reference plane, but the error changes as the plane's rotation about the x-axis changes.

**Table 1.** Fitting plane measurement data in distinct positions and orientations

Numerical order	Angle	Position	n (points)	d (mm)	Standard deviation (mm)
1	0	0	17,602	0.54	0.2415
2	10	0	17,787	0.583	0.327
3	20	0	17,470	0.642	0.363
4	0	20	17,293	0.557	0.244
5	10	20	17,047	0.751	0.368
6	0	40	18,652	0.525	0.255
7	10	40	18,486	0.551	0.2765
8	0	-20	16,472	0.473	0.228
9	10	-20	16,512	0.503	0.273
10	0	-40	16,515	0.531	0.299
11	10	-40	16,624	0.562	0.399

### 3 Conclusion

The article has built algorithms and software programs suitable for many planes to determine the sizes and positions in the measuring area using the standard of step and plane form in the measuring area. Experiments have determined that on the aluminum part, the most deviation was measured by the GCSP method, which is more accurate than the gray-coded measurement method. It demonstrates that the GCSP method has greater precision and consistency than the Gray Code method. The system can be calibrated with the reference plane precision standard, with locations and angles to determine the accuracy across the whole measurement area. In this study, the experiment did not consider the impact of shiny surfaces on measured results from structured light. There are some losing-information regions in point clouds achieved in shiny areas. So, the effects of the specular surface of the measurement part are to be further studied.

**Acknowledgements** This research is funded by the Hanoi University of Science and Technology (HUST) under project number T2021-TT-006.

### References

1. P. Cong, Z. Xiong, Y. Zhang, S. Zhao, F. Wu, Accurate dynamic 3D sensing with fourier-assisted phase shifting. *IEEE J. Sel. Top. Sig. Proc.* **9**(3), 396–408 (2015). <https://doi.org/10.1109/JSTSP.2014.2378217>
2. G. Wu, Y. Wu, L. Li, F. Liu, High-resolution few-pattern method for 3D optical measurement. *Opt. Lett.* **44**(14), 3602–3605 (2019)

3. B. Li, N. Karpinsky, S. Zhang, Novel calibration method for structured-light system with an out-of-focus projector. *Appl. Opt.* **53**(16), 3415–3426 (2014). <https://doi.org/10.1364/AO.53.003415>
4. L. Alvarez, L. Gomez, R. Sendra, Algebraic lens distortion model estimation a new energy function to measure the distortion error. *Image Process. Line* **1**, 1–10 (2010). <https://doi.org/10.5201/ipol.2010.ags-alde>
5. S. Zhang, Recent progresses on real-time 3D shape measurement using digital fringe projection techniques. *Opt. Lasers Eng.* **48**(2), 149–158 (2010). <https://doi.org/10.1016/j.optlaseng.2009.03.008>
6. S.J. Ahn, W. Rauh, H.J. Warnecke, Least-squares orthogonal distances fitting of circle, sphere, ellipse, hyperbola, and parabola. *Patt. Recognit.* **34**(12), 2283–2303 (2001). [https://doi.org/10.1016/S0031-3203\(00\)00152-7](https://doi.org/10.1016/S0031-3203(00)00152-7)
7. C. Xiaobo, X. Jun tong, J. Tao, J. Ye, Research and development of an accurate 3D shape measurement system based on fringe projection: model analysis and performance evaluation. *Precis. Eng.* **32**(3), 215–221 (2008). <https://doi.org/10.1016/j.precisioneng.2007.08.008>
8. J. Beraldin, M. Rioux, L. Cournoyer, F. Blais, M. Picard, J. Pekelsky, Traceable 3D imaging metrology. *Measurement* **6491**(January), 1–11 (2007). <https://doi.org/10.1117/12.698381>
9. N.T.K. Cuc, N.V. Vinh, C.X. Binh, Multiple plane fitting algorithm to evaluated the accuracy of 3D point cloud using structured light measurement. *J. Sci. Technol.* 12–17, 2354–1083 (2020)

# Study on the Impact of Structural Parameters on the Vibration of Automobiles



Van Hoang Tran

**Abstract** As people's needs in life increase more and more, automobile has become the means of transport that is being popularly used in their daily activities. In addition to cost and form, ride and handling is among the important criteria for modern automobiles; and the vibration level of a vehicle directly affects its smoothness level. Nowadays, digital simulation is being widely used in studying the mechanical system of an automobile, more than that, the simulation process has proven its preeminence as it can depict the nonlinear system when simulating the vibration level of an automobile. Basing on mentioned requirements, the research team has simulated the oscillation system of an automobile while taking nonlinear factors into consideration by setting reasonable structural parameters with a view to ensure smooth ride and handling for coaches. In this article, they will clarify the impact of structure on the smoothness of coaches and how to select a suitable structure for each type of coach.

**Keywords** Coach · Nonlinear · Oscillation · Simulation

## 1 Introduction

Vietnam's auto industry is on its way to become the country's leading industry. However, in order to attain that goal, there was a lot of work needed to be done, one of which was to do deeper study on oscillation, ride and handling, as well as the quality of the vehicle's kinematics and dynamics to optimize its properties.

Based on the mentioned facts, there have been a few researches in the automotive industry that refer to the vibration of automobile. In this study, the research team builds an oscillation model for a 16-seat Mercedes sprinter. The sprinter's body and frame are a solid block on which they install suspension systems, the front suspension

---

V. H. Tran (✉)

Faculty of Mechanical Engineering, University of Economics and Technical Industries, Hanoi, Vietnam

e-mail: [tvhoang@uneti.edu.vn](mailto:tvhoang@uneti.edu.vn)



follows McPherson type, the rear suspension is a dependent suspension system [1, 2]. The space model consists of masses bound together by the constraining force.

On the basis of the oscillation model, they apply D’Alambe principle so as to set up a system of differential equations representing the oscillation. The system consists of 7 differential equations which represent the oscillations [3–5].

## 2 Build the Model and Establish a Set of Differential Equations Representing the Oscillation

The oscillation model of the coach is depicted in Fig. 1. Set up differential equations.

In accordance with D’Alambe’s principle:  $\vec{F} + \vec{F}_{qt} = 0$ .

$\vec{F}$  \_ is the total external pressure acting on an object.

$\vec{F}_{qt}$  \_ is the total fictitious pressure acting on an object.

$$\left\{ \begin{array}{l} -m_{1T} \cdot g - m_{1T} \cdot \ddot{\xi}_{1T} + F_{1T} + F_{L1T} = 0 \\ -m_{1P} \cdot g - m_{1P} \cdot \ddot{\xi}_{1P} + F_{1P} + F_{L1P} = 0 \\ -m_2 \cdot g - m_2 \cdot \ddot{\xi}_2 + F_{2T} + F_{L2T} + F_{2P} + F_{L2P} = 0 \\ -J_{2x} \cdot \ddot{\theta}_2 + \frac{B_{2g}}{2}(F_{2T} - F_{2P}) + \frac{B_2}{2}(F_{L2T} - F_{L2P}) = 0 \\ -M \cdot g - M \cdot \ddot{Z} - F_{1T} - F_{1P} - F_{2T} - F_{2P} = 0 \\ -J_y \cdot \ddot{\varphi} - a(F_{1T} + F_{1P}) + b(F_{2T} + F_{2P}) = 0 \\ -J_X \cdot \ddot{\varphi} - \frac{B_1}{2}(F_{1T} - F_{1P}) + \frac{B_{2g}}{2}(F_{2T} - F_{2P}) = 0 \end{array} \right.$$

The set of equations consists of 7 differential equations, with 7 unknowns as:  $\xi_{1T}$ ;  $\xi_{1P}$ ;  $\xi_2$ ;  $\theta$ ;  $\theta_2$ ;  $\varphi$ ;  $Z$ . using Matlab—Simulink to solve the set of differential equations with a view of simulating the vibration of vehicle body [3].

## 3 Simulation of Oscillation

From the Simulink library, we get the block-diagram simulator (Fig. 2).

Therefore, the general diagram has met the requirements of accurate and scientific vehicle vibration simulation.

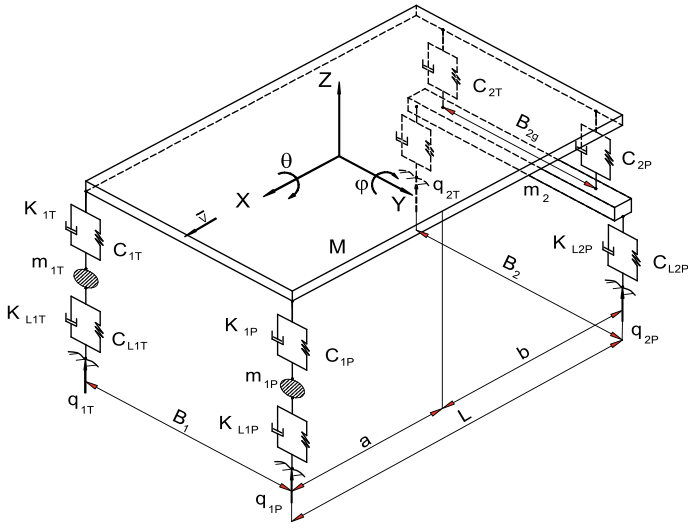


Fig. 1 Oscillation model of coach

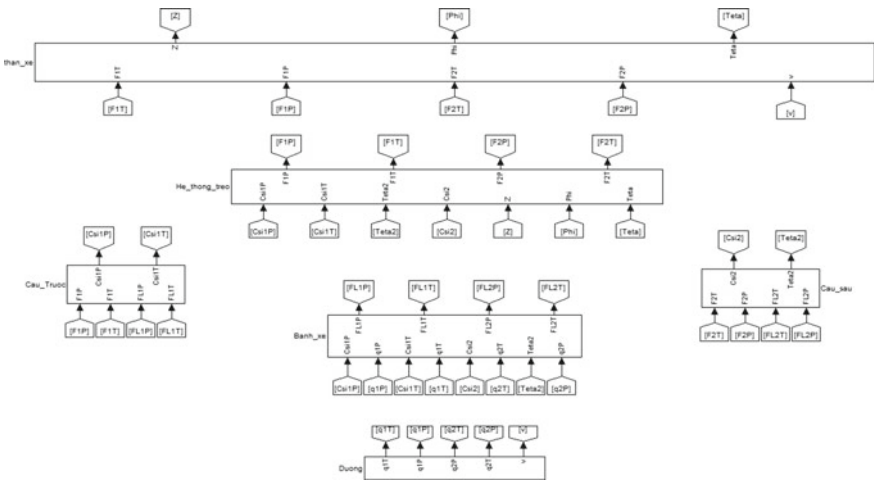


Fig. 2 Oscillation general diagram [4]

## 4 Simulation Report

### 4.1 Parameters Included in the Calculation

The specifications of suspension system are based on the 16-seat Mercedes sprinter. The set of parameters listed below includes parameters both measured and calculated in accordance with the documents [1, 2].

### 4.2 Simulation Report

#### 4.2.1 Oscillation Simulating Results

When the vehicle runs at the speed of 60 km/h for a test distance of 01 km, the total time is 60 s.

- Oscillation coordinate Z and oscillating acceleration of the vehicle body center of gravity.

Based on the diagrams in Fig. 3, we can see that the vehicle body steadily oscillates around the equilibrium position  $Z_{cb} = -0.14$  m and stabilizes after about 2 s.

- Longitudinal pitch angle (Theta) and horizontal roll angle (Phi) around the axes of the vehicle body and passing through the vehicle body center of gravity.

The pitch angle along the longitudinal axis of the vehicle (Theta angle) in Fig. 4 oscillates around point 0, and is smaller in amplitude than the roll angle along the longitudinal axis of the vehicle (Phi angle).

- Coordinates of the car axle center of gravity.

The coordinates Csi1T and Csi1P do not have much difference since the surface profiles on both sides are similar, the tire hardness on both sides is equal (Fig. 5).

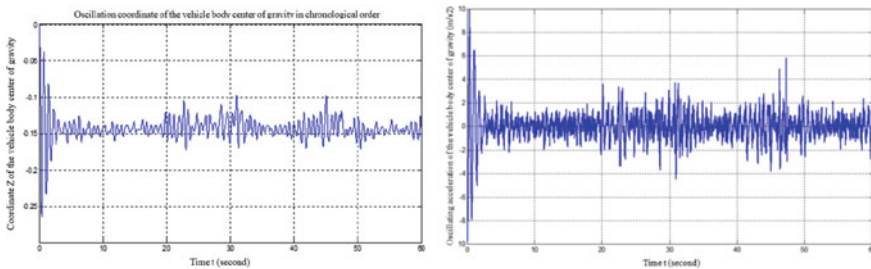
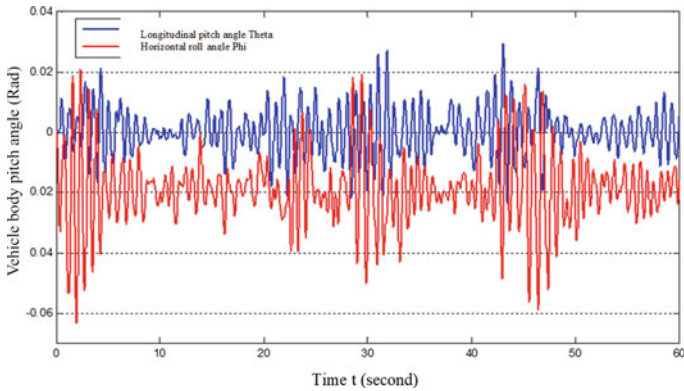
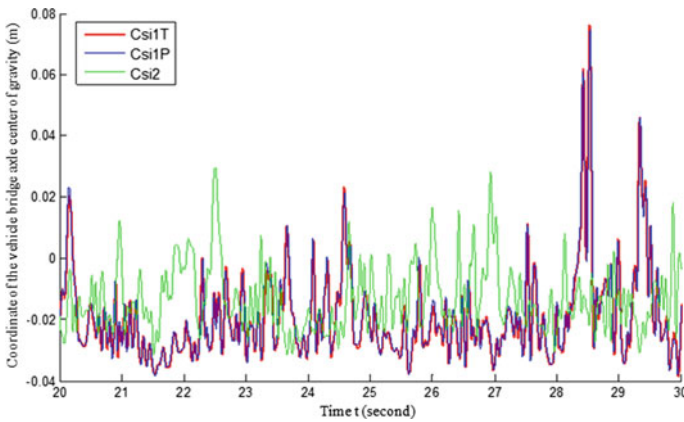


Fig. 3 Oscillation coordinates of the vehicle body center of gravity in chronological order



**Fig. 4** Longitudinal pitch angle and horizontal roll angle of vehicle body



**Fig. 5** Coordinates of the car axle center of gravity in chronological order

**4.2.2 The Impact of Parameters on Vehicle Vibration**

**The Impact of Vehicle Velocity**

The vehicle speed is modified from 10 to 100 km/h on the actual road 1 km long from Hanoi to Lang Son under uniform speed motion.

The root-mean square deviation on the coordinate  $D_Z$  of the vehicle body center of gravity gradually rises as engine speed is increased.

- The effect of vehicle speed on root-mean square deviation on the vehicle body center of gravity.
- The impact of vehicle speed on the root-mean square deviation on vehicle body pitch angles  $D_{Phi}$ ,  $D_{Theta}$  (Rad) (Fig. 6), the vehicle’s bridge axle center of gravity  $D_{Csi1T}$ ,  $D_{Csi1P}$ ,  $D_{Csi2}$  (Fig. 7).

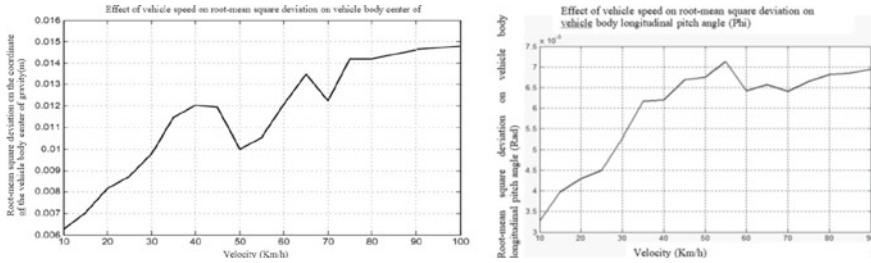


Fig. 6 Root-mean square deviation on vehicle body pitch angle  $D_\phi$  based on velocity

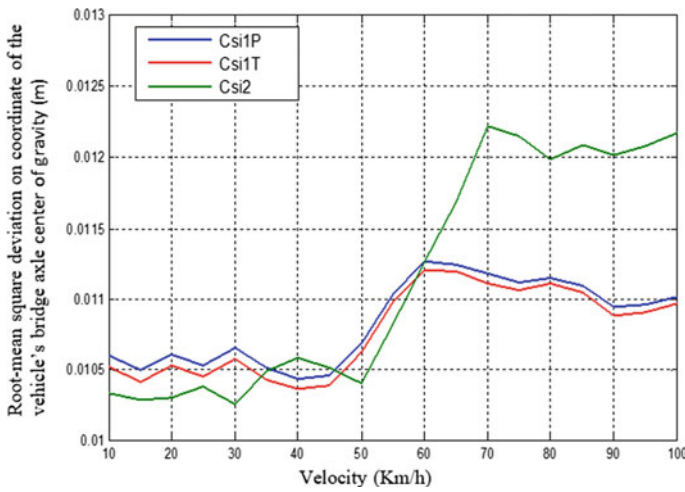


Fig. 7 Root-mean square deviation on coordinate of the vehicle's bridge axle based on velocity

### Effect of Damping Damping Coefficient

Based on two mentioned diagrams, we can clearly see that both  $D_z$  and  $D_{\dot{z}}$  decrease when the damper coefficient is increased; thus, when we increase the damping level, the smoothness of ride and handling increases (Fig. 8).

### The Impact of Tire Hardness

As we can see, the deviation  $D_z$  and  $D_{\dot{z}}$  increase as tire hardness is increased. However, the values of  $D_z$  and  $D_{\dot{z}}$  do not increase too much, not exceeding the tolerance (Fig. 9).

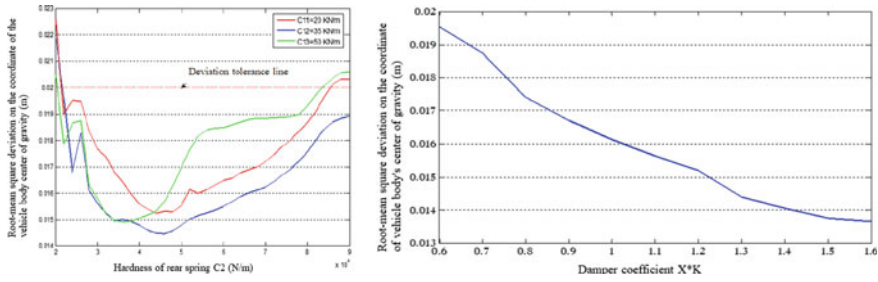


**Fig. 8** The impact of damper coefficient on root-mean square deviation on the coordinate  $D_z$  of the vehicle body center of gravity

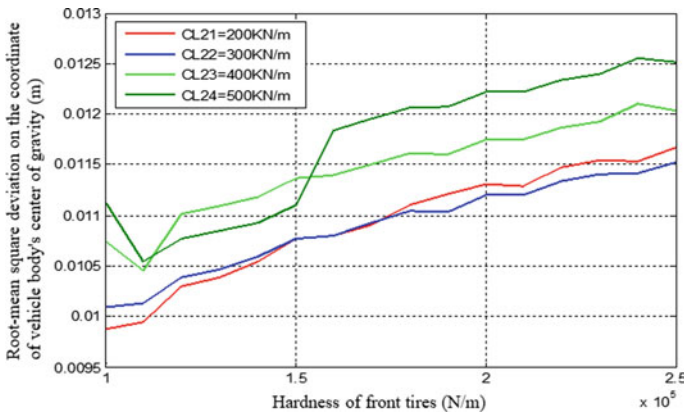


**Fig. 9** The impact of tire hardness on root-mean square deviation on the coordinate of the vehicle body center of gravity  $D_z$

The Impact of Vehicle Body Mass and Hardness of Horizontal Stabilizer bar

We can see that  $D_z$  decreases when we increase the number of passengers and reaches the minimum value when  $n = 8$  people, then it increases again. However,  $D_z$  is still within the tolerance level (Fig. 10).

Again, we see that  $D_z$  decreases as the number of passengers is increased and reaches the minimum value at  $n = 16$  people,  $D_z_{min} = 1 \text{ m/s}^2$ . However, even when  $D_z$  reaches the maximum value,  $D_z_{max}$  does not exceed the tolerance.

The Root-mean square deviation on vehicle body horizontal roll angle slightly changes and tends to decrease when we change the anti-torsion hardness  $C_{od}$ .

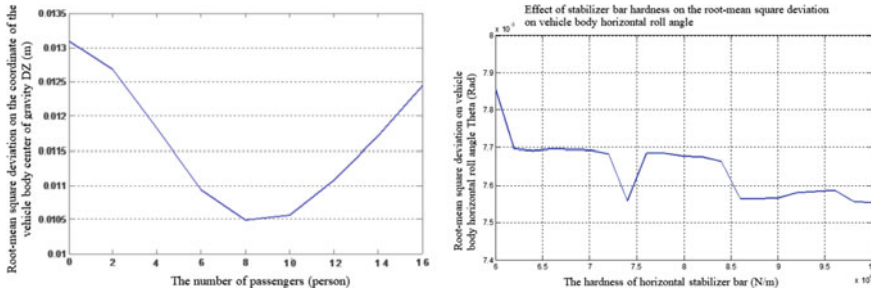


**Fig. 10** The impact of suspension mass on root-mean square deviation on the coordinate of the vehicle body center of gravity  $D_z$

## 5 Conclusion

In this study, we have built a space oscillation model for a 16-seat coach, obtained results include.

The car body oscillates around the equilibrium position  $Z_{cb} = -0.14$  m and stabilizes after around 0.2 s; the longitudinal pitch angle and horizontal roll angle of the vehicle body are around point 0; vehicle body center of gravity  $C_{si} = -0.2-0.2$  during the process; the vehicle body oscillation changes from 0.01 to 0.125 when the tire hardness changes from 200 to 500  $KN/m$ ; vehicle body center of gravity ranges from 0.0105 to 0.013 when changing the number of passengers on the vehicle; the horizontal roll angle ranges from 7.5 to 7.9 Rad when changing the anti-torsion hardness of the stabilizer bar; acceleration of body oscillation from 1.1 to 1.8  $m/s^2$  when changing the number of passengers on the vehicle; the vehicle body center of gravity ranges from 0.015 to 0.022 when changing the spring hardness; and it fluctuates from 0.014 to 0.019 when changing the damper coefficient from 0.6 to 1.6; the vehicle’s center of gravity ranges from 0.006 to 0.015 when the speed changes from 10 to 100  $km/h$ ; the rear horizontal roll angle ranges from 0.0095–0,–0.135 when the vehicle speed changes from 10 to 100  $km/h$ ; oscillation of the body horizontal roll angle is from 3 to 6 Rad when vehicle speed changes from 10 to 100  $km/h$ .

## References

1. Đ.M. Hung, Determination of driving pressure between truck tires and road surface in Vietnam transport conditions, Technics PhD Thesis, 2004
2. L. Van Tuan, D.Q. Thinh, Đ.X. Hai, *A Study on Ride and Handling of Cars Assembled in Vietnam* (Research T.16/90 of Hanoi University of Science and Technology, 1991)
3. T. Van Nghia, *Applied Informatics in Mechanical Design* (Vietnam Education Publishing House Limited Company, 2004)

4. V. Van Huong, Study on the completion of survey model of vibration on multi-axle trucks. Technics PhD Thesis, 2003
5. N.H. Can, D.Q. Thinh, P.M. Thai, N. Van Tai, L.T. Vang, *Theory on Tractors* (Science and Technics Publishing House, 2003)



# A Case Study on Impact of Ethanol-Mixed Gasoline on Exhaust Emissions of Automobile Engines



Van Hoang Tran, Thanh Huan Nguyen, Trong The Tran, Van Phuong Dinh, and Thanh Binh Nguyen

**Abstract** In this study, AVL-Boost software is used to simulate the impacts of using RON 92 gasoline in combination with E5, E10, E20, E85 biofuel. Specifically, the article studies the engine emissions when mixing biofuel with RON 92 gasoline at certain ratios. When testing on Toyota engine—5A, all structural parameters of the engine are kept original. Research results show that when using biofuel in combination with RON 92 gasoline, the engine's emissions tend to be as follows: the emissions of CO and HC decrease, the concentration of NO<sub>x</sub> increases. From the above simulation study, recommendations for manufacturers as well as users can be made to change the ratio of biofuel in RON 92 gasoline when used.

**Keywords** Engine · Emissions · Ethanol · Simulation

## 1 Introduction

Today, the demand for fuel and petroleum products has risen considerably, leading to many problems that need solving such as: increasing fuel depletion, environmental pollution due to engine exhaust, industrial furnaces [1], oil production plants and oil product storage facilities, power loss, engine life. On the other hand, as we all know, national security and economic security are always associated with energy security. Therefore, energy security is always placed on top of each country's development strategy. Based on the current level of oil use, this amount of mineral oil will only be enough for another 50–60 years if no new oil fields are discovered. Therefore, in order to reduce environmental pollution, to ensure long-term energy security and sustainable development, many countries have focused on studying the use of biofuels [2] to replace part of the oil use in the past few decades. As a result, it is essential to have studies on how the ratio of ethanol-mixed gasoline affects the emissions of

---

V. H. Tran (✉) · T. H. Nguyen · T. T. Tran · V. P. Dinh · T. B. Nguyen  
Faculty of Mechanical Engineering, University of Economics and Technical Industries, Hanoi,  
Vietnam  
e-mail: [tvhoang@uneti.edu.vn](mailto:tvhoang@uneti.edu.vn)

automobile engines, thereby encouraging users to use biofuel products to reduce environmental pollution.

## 2 Bio Fuel Used for Petrol Engines

Ethanol, also known as ethyl alcohol or grain alcohol or alcohol is an organic compound in the homologous series of ethyl alcohol which is flammable, colorless and is one of the ingredients of alcoholic beverages. In real life, it is often referred to as alcohol for short. The chemical formula is  $C_2H_5OH$ , abbreviated as  $C_2H_6O$ . The most suitable raw material is sugar (from beets, sugarcane, palm oil,...), which is produced a lot in countries like Brazil,... Denatured ethanol parameters are determined according to the methods ASTM 1613, ASTM D5510, ASTM E1064, or a series of Vietnam Standards.

## 3 Theoretical Basis and Model Building

With the AVL BOOST version 2020, the simulation of the fuel mixture in general, and the mixture of gasoline and an alternative fuel in particular, can be easily performed, can be modified using the General Species Transport option [3]. The initial parameters of the engine, fuel, running cycles... are set in this step. Basing on the features of AVL BOOST, we can set up models to calculate thereby determining the appropriate gasoline-air ratio, gasoline-ethanol ratio for the results of engine emissions.

### 3.1 *The Process of CO Emission Formation*

In fact, the CO content increases rapidly in the flame film area, mainly generated by the pyrolysis of incompletely oxidized hydrocarbons, and continues to be completely oxidized to produce  $CO_2$  through the dynamic control mechanism [4]. Simulation mode: engine speed at 3000 rpm, full load (Fig. 1).

The CO molar fraction is predicted by this model in the same test engine which is depicted in Fig. 2 as a function of the spark advance and the residual air coefficient. CO emissions are driven mainly by the A/F ratio. In fact, the amount of CO decreases with increasing A/F ratio, as more  $O_2$  participates in the oxidation reaction.

**Fig. 1** Predicted CO molar fraction: equilibrium CO and kinetic CO content

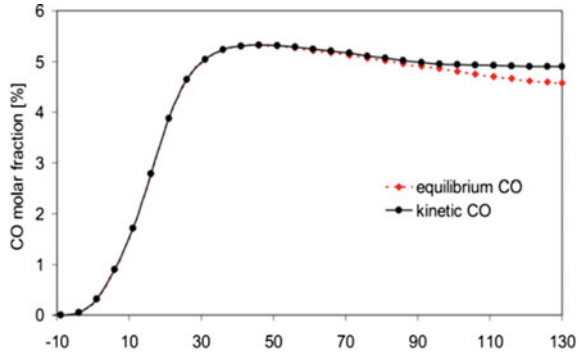
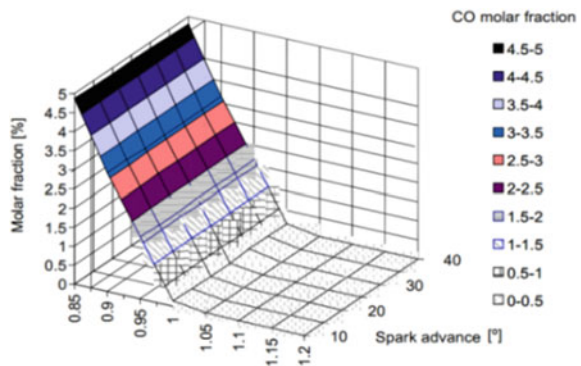


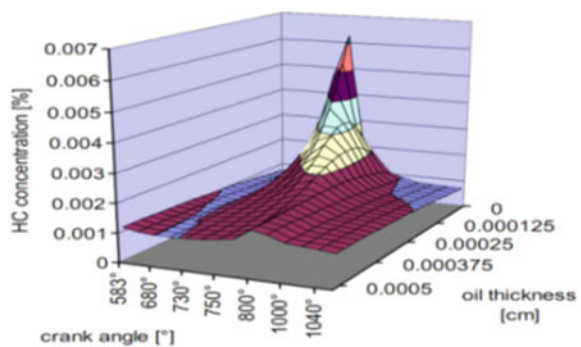
**Fig. 2** Predicted CO molar fraction as a function of spark advance and residual air coefficient



### 3.2 The Process of HC Emission Formation

The methodological model that explains the main formation mechanism can be applied to study functional HC formation with engine operating parameters [4]. Especially the formation from the gap is considered important, the wall effect and incomplete combustion (Fig. 3).

**Fig. 3** Predicted HC fraction ratio as a function of spark advance and residual air coefficient



### 3.3 The Process of NO<sub>x</sub> Emission Formation

NO<sub>x</sub> formation is calculated according to input parameters such as the engine speed, fuel, pressure, temperature, residual air coefficient  $\lambda$ , volume and mass, time, as well as the number of combustion zones. The calculation process starts as soon as the combustion starts. In NO<sub>x</sub> emissions of petrol engines, NO holds the majority (90–98%) but the N<sub>2</sub>O produced in the exhaust [5] is still taken into account.

## 4 Simulation Process and Results

### 4.1 Process of Simulating an Engine Using Ethanol-Mixed Gasoline

#### 4.1.1 Process of Simulating

Based on the actual engine, the elements available in AVL Boost [3] and the engine specifications, we can build the Toyota—5A engine model as follows (Fig. 4).

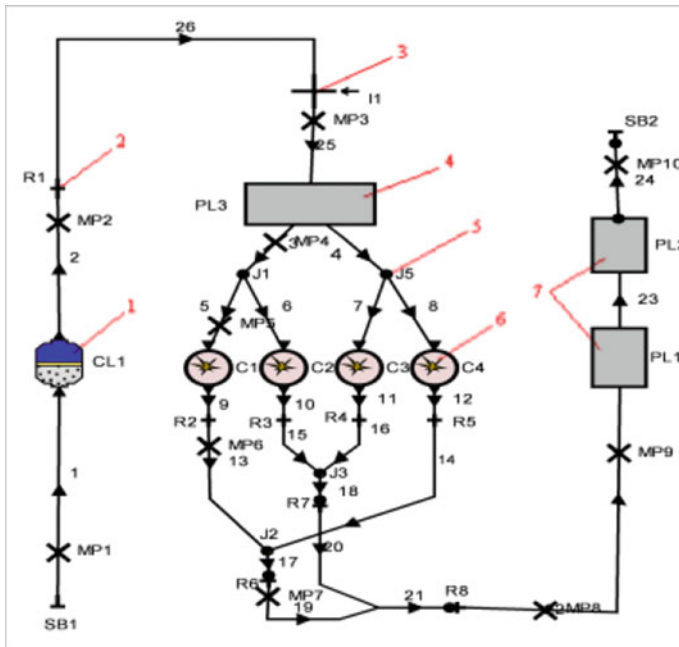


**Fig. 4** Simulation model (1) air filter; (2) current blocking element (3) carburetor; (4) pressure stabilizer; (5) joining element; (6) cylinder; (7) absorption silencer

### 4.1.2 Model Running

The amount of fuel and spark advance of the engine are kept unchanged. The simulation of the model is run to get comparison results of engine emissions when changing the ratio of ethanol in the fuel; thereby we get E0, E5, E10, E20, E85.

## 4.2 Simulation Results

### 4.2.1 CO Emissions

There is a sharp reduction in CO thanks to the improved combustion. Therefore, when raising the ratio of ethanol in the fuel, the concentration of CO decreases as illustrated in Table 1 and Fig. 5.

**Table 1** CO concentration in accordance with engine speed when using several fuel types

Speed (rpm)fuel	E0	E5	E10	E20	E85
1500	194.89	147.7	133.37	117.59	55.51
2000	243.88	185.97	168.19	157.16	65.12
2500	276.04	212.98	192.09	180.03	68.7
3000	1032.64	257.9	244.57	217.62	75.07
3500	1426.87	303.67	309.68	241.28	76.6
4000	2250.67	346.35	321.26	267.59	77.53
4500	2355.82	387.27	343.55	296.4	78.78
4800	2464.51	409.38	364.97	315.64	80.82

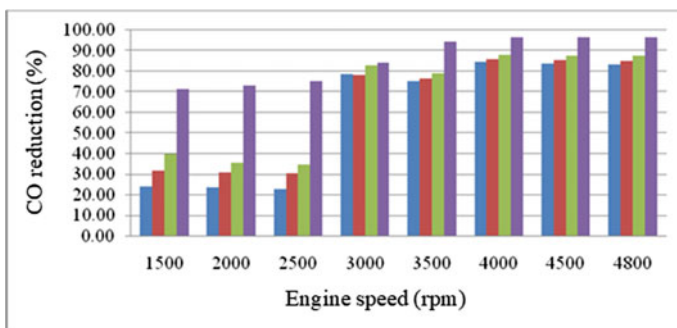


**Fig. 5** Change of CO concentration at 100% load using ethanol-mixed gasoline in comparison with RON92 gasoline

### 4.2.2 HC Emissions

For E5, E10, E20, the oxygen component in the fuel mixture helps it burn in the condition that is not too deficient in oxygen. Besides, thanks to the good volatility of the ethanol-mixed gasoline, E5, E10, and E20 fuel mixtures burn more exhaustingly, thereby reducing the concentration of HC emissions.

According to [6], when using E85 fuel mixture, the mixture becomes too dilute, outside the range of  $\lambda$  to reach the smallest HC concentration from 1.1 to 1.25 (high ethanol mixing ratio), so the concentration of HC must increase. From reality and from the simulation results (in Fig. 6), the molecular ratio between carbon and hydrogen is lower, the quantity of local areas with low  $\lambda$  is reduced, and at the same time, the combustion process of E85 fuel mixture produces 20 times the amount of Aldehyde compared to when using gasoline [6] (Table 2).

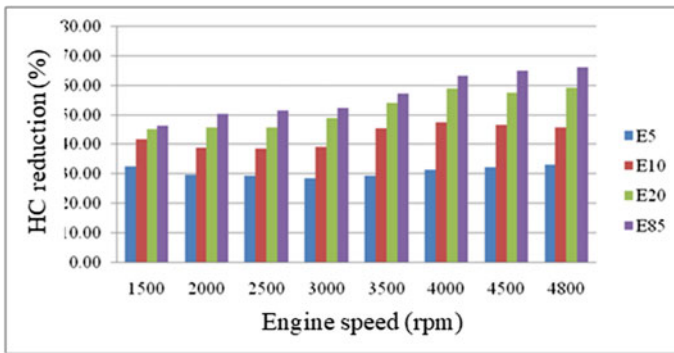


**Fig. 6** Change of HC concentration at 100% load using ethanol-mixed gasoline in comparison with RON92 gasoline

**Table 2** HC concentration in accordance with engine speed when using several fuel types (ppm)

Speed (rpm)fuel	E0	E5	E10	E20	E85
1500	237.01	159.95	137.83	121.82	127.05
2000	238.83	168.25	146.28	129.54	114.18
2500	234.16	165.26	144	127	113.4
3000	237.23	169.36	144.68	121.44	112.92
3500	213.91	151.28	116.83	94.15	101.58
4000	213.72	146.7	112.31	87.94	97.57
4500	208.31	141.16	111.02	88.31	95.23
4800	189.92	126.79	103.1	85.76	94.9

### 4.2.3 NOx Emissions

When using E5, E10, E20, the temperature of combustion process is still too high to form oxygen and atomic nitrogen with high activation performance, the quantity of oxygen atoms is increased, thereby creating favorable conditions for the oxidation of nitrogen, thus the amount of NOx is increased [5] (Table 3).

However, when using E85 fuel, due to the lower molecular ratio of carbon and hydrogen, and much higher heat of evaporation than other fuels, the combustion temperature is drastically reduced. Therefore, the NOx concentration of engines using E85 fuel decreases sharply (Fig. 7).

**Table 3** NOx concentration in accordance with engine speed when using several fuel types (ppm)

Speed (rpm)\fuel	E0	E5	E10	E20	E85
1500	3282.07	4482.88	5321.01	5758.19	75.8
2000	3482.13	4631.45	5383.76	5409.38	55.02
2500	3613.54	4823.5	5672.1	5835.92	59.21
3000	3686.41	4893.03	5606.34	5527.43	54.77
3500	3823.01	4899.56	5478.74	4926.26	47.23
4000	3847.40	4906.15	5491.45	4958.73	55.09
4500	3907.08	5065.56	5683.13	5068.29	53.31
4800	4114.57	5083.86	5569.12	4658.71	47.89

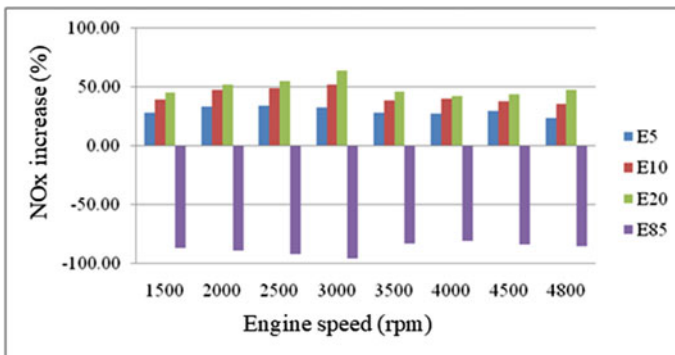


**Fig. 7** Change of NOx concentration at 100% load using ethanol-mixed gasoline in comparison with RON92 gasoline

## 5 Conclusion

The study on the simulation of gasoline mixture of RON 92 and biofuel was carried out, giving the following main results:

The average reduction of CO when using ethanol-mixed gasoline E5, E10, E20, E85 was 59.48%, 62.99%, 66.89% and 86.08%, respectively, in comparison with when using gasoline E0.

The average HC reduction when using ethanol-mixed gasoline fuel compared to pure gasoline over the operating speed range can be calculated. When using E5, E10, E20, E85, the average reduction of HC concentration is 30.78%; 42.92%; 51.90% and 56.59%, respectively.

The concentration of NO<sub>x</sub> in the exhaust emissions when using ethanol-mixed gasoline E5, E10, E20, E85 compared to E0 is increased by 29.65%; 42.38%; 49.68% and 87.56%, respectively.

## References

1. D.G. Kesse, Global warming-facts, assessment, counter-measures. J. Pet. Sci. Eng. **26**, 157–168 (2000)
2. The Royal Society, *Sustainable Biofuels: Prospects and Challenges* (UK, 2008)
3. AVL–List GmbH, *BOOST v.2009 Theory*. Hans–List–Platz 1, A–8020 Graz, Austria, 2020
4. P.M. Tuan, *Engine Emissions and Environmental Pollution* (Science and Technics Publishing House, 2008)
5. G. Lavoie, P.N. Blumberg, A fundamental model for predicting consumption, NO<sub>x</sub>, and HC emissions of the conventional spark-ignition engines. Combust. Sci. Technol. **21**, 225–258 (1980)
6. L.A. Tuan, et al., Investigation of motorcycle engine's characteristics fueled with ethanol-gasoline blends, in *4th AUN/SEED-Net Regional Conference on New/Renewable Energy* (HCM city, Vietnam, 2011)



# Face Recognition and Hand Gesture Control for Tello Drone Navigation



Huy-Anh Bui, Anh-Tu Nguyen, Thanh-Hung Nguyen,  
and Xuan-Thuan Nguyen

**Abstract** These days, low-cost commercial drones are rapidly used in variety of fields, ranging from manufacturing and logistics to STEM education. This paper addresses a fully-actuated Tello Drone's control under random positions and in an indoor environment. For this purpose, we designed a closed-loop controller based on computer vision techniques for face recognition and a gesticulation rule for navigable motion. To be more detailed, Local Binary Pattern Histogram combined with SQLite 3 is initially applied to detect the right target. After that, the built-in controller determines the hand gesture on the human target to transmit the commands to Tello Drone. Additionally, the user interface is also developed to summary and display the drone info during operation process. The experimental results revealed the effectiveness of the suggested strategy and the reliability of the drone under different scenarios.

**Keywords** Face recognition · Local binary pattern histogram · Hand gesture tracking · Machine learning · Drone navigation

## 1 Introduction

With the booming developments of technology in recent years, drones or unmanned aerial vehicles (UAVs) [1, 2] are finding their ways to crept into the modern civilian life almost in every aspect such as searching objects, delivering goods and medical supplies, surveying, mapping lands, rescue supporting, farming, and much more. It is no exaggeration to say that drones provide innovative solutions in various applications for daily activities. However, benefits like small size, low cost, and autonomous deployments can result in restricted control and operation of drones in certain regions

---

H.-A. Bui · A.-T. Nguyen

Faculty of Mechanical Engineering, Hanoi University of Industry, Hanoi, Vietnam

T.-H. Nguyen · X.-T. Nguyen (✉)

School of Mechanical Engineering, Hanoi University of Science and Technology, No. 1, Dai Co Viet, Hanoi, Vietnam

e-mail: [thuan.nguyenxuan@hust.edu.vn](mailto:thuan.nguyenxuan@hust.edu.vn)

to some extent. For the past few years, optimizing drone navigation and target tracking [3, 4] has received much attention from many researchers all around the world. In Ref. [5], a real-time video streaming system based on histogram of oriented gradients and linear support vector machine is proposed for autonomous drone. By combing the GPS information and the real-time landmark detection with the acquired images, the proposed method is able to reconstruct 3D environment and find the safe landing areas for the drone. In another examples, the study in Ref. [6] using a single image sensor with a blinking LED ring marker on drone to investigate the temporal-difference image processing. By applying enhanced Volterra series, the method can accurately localize a target over a wide range on a novel 3-D spatial map. Kaplan et al. [7] designed a frequency hopping spread spectrum signals system with uniform linear antenna array to keep track of drones. The experiments revealed that the proposed approach could be implemented stably on hardware and estimate precisely the angle of arrival for the drone operation.

In light of the remarkable importance and advantages previously mentioned, a real-time control system for Tello Drone navigation is proposed. The key contributions of this paper can be summarized as follows:

- (1) Utilize the Local Binary Pattern Histogram algorithm [8] to build and investigate the possibility of human tracking and face recognition on different human targets for the low-cost commercial drone series.
- (2) Structure and update the images continuously by aiding the SQLite 3 platform. Thus, the designed system generates a small amount of data to be processed.
- (3) Develop a machine learning framework based on Media Pipe [9, 10] that allows the drone to be automated and programmed to determine human behaviors via hand gestures.

## 2 Brief Overview of the Proposed System

### 2.1 Data Preprocessing

To standardize the data training, the input dataset is established based on images collaborated with a specific user. We set up a camera with a 16-megapixel resolution to capture 200 photos at different side view for each human target as shown in Fig. 1.

After taking photos process, the input dataset is converted to grayscale images and then calibrated with the use of adaptive fuzzy median filtering [11]. Hence, the salt and pepper noise phenomenon is eliminated completely. The result images are stored automatically in the SQLite3 database. Since then, each user who has been confirmed will be provided with a unique ID and password to log into the system. Table 1 summarize the number of pre-training photos with each ID.

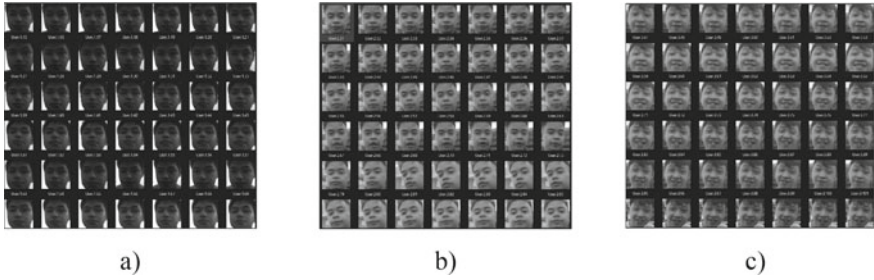


**Fig. 1** The gray images of confirmed user: **a** User ID 1; **b** User ID 2; **c** User ID 3

**Table 1** The training dataset

Target user	ID	Username	Side—view photos of user face				
			Front view	Upside view	Downside view	Left skewed	Right skewed
Human 1	01	luu	40	48	42	35	37
Human 2	02	kien	43	45	40	33	41
Human 3	03	toan	46	40	36	44	36

### 2.2 Local Binary Pattern Histogram Algorithm

Local Binary Pattern Histogram (LBPH) is a Face-Recognition method used to identify a human face. The Local Binary Pattern (LBP) operates based on a block size of  $3 \times 3$ , in which the centre pixel serves as a threshold parameter for the pixels that is adjacent to it, and the LBP code of a centre pixel is formed by encoding the calculated threshold value into a decimal value. The core formulations of the LBP encoding are indicated as follows:

$$LBP = \sum_{i=0}^{M-1} s(G_{n_i} - G_{center}) \cdot 2^i; \quad s(G_{n_i} - G_{center}) = \begin{cases} 1 & \text{if } (G_{n_i} - G_{center}) > 0 \\ 0 & \text{if otherwise} \end{cases} \quad (1)$$

whereas:  $M$  is the neighborhood pixels;  $n_i$  represents the  $i$ th neighboring pixel;  $G_{n_i}$  is the grayscale value of the  $i$ th neighboring pixel;  $G_{center}$  is the grayscale value of the centre pixel.

From the acquired LBP code, the histogram features of size  $2^M$  are retrieved. Therefore, for eight adjacent pixels, the length of the histogram feature vector is determined to be 256. The output images and the LBP pixel bucket sample are shown in Fig. 2.



**Fig. 2** a The pre-training image; b The LBP training image; c The LBP pixel bucket of the sample image

### 2.3 Hand Gesture Detection Based on Media Pipe

After applying LBPH to recognize the correct target, the proposed system will detect the right-hand motions on the target by utilizing the Media Pipe Hand Tracking. To be more specific, a machine learning pipeline that is composed of various stages is designed with two models. The first model is a palm detection model that functions on the entire image and provides an orientated hand bounding box. After the palm detection over the whole image, the second one—a hand landmark model then works on the cropped image region and performs precise key point localization of 21 3D hand-knuckle coordinates via regression. Thus, the high-fidelity 3D key points are returned along the fingers. Figure 3 shows the different landmarks on the hand skeleton.

Based on the different types of the hand gestures, the navigation commands are transmitted from the system controller to the Tello Drone. The base rule of hand gestures is proposed as follows:

- *Rule base 1:* The landmark shape is only drawn on the right hand of the target.
- *Rule base 2:* The coordinates of the peak points on the fingertips (8, 12, 16, 20) are taken to compare with the second points (6, 10, 14, 18) of the corresponding



**Fig. 3** 21 landmarks on the hand area [12]

**Table 2** The definition of the control command

No.	Finger status	Drone command
0	Hand clasped	Keep position
1	One raised finger	Move forward
2	Two raised fingers	Move backward
3	Three raised fingers	Move to the right
4	Four raised fingers	Move to the left

finger. If the peak point is higher than the second point on the same finger, the finger is determined to be raised.

- *Rule base 3:* The thumb finger is defined as a special case. Since the `thump_tip` is always higher than the other points, we will evaluate whether the `thump_tip` is to the right or the left of the `thump_mcp`. If the `thump_tip` is on the right of the `thump_mcp`, the thumb finger is defined as raising.
- *Rule base 5:* The raising status of the finger is then encoded with binary 1. In contrast, the statement is encoded with binary 0. Hence, the encoding range of all fingers is from “0 0 0 0 0” to “1 1 1 1 1”.

After that, this binary encoded string is converted to the drone controller’s command as shown in Table 2.

### 3 Experimental Results

In order to inspect the efficiency of each machine learning model designed for the proposed system, several experiments were carried out. Besides, a user interface is also developed on Tkinter platform to display the real-time images. To begin with, we conducted tests on the face recognition feature in normal and complex light environments. As shown in Fig. 4, if the camera on the Tello Drone detects and recognizes the correct target, a notification will display on the controller interface that allows the target to grant permission. On the other hand, if the captured target does not belong to the confirmed USERID library, a face mesh will be established on the target face.

At the following phase, we concentrate more on drone navigation experiments to evaluate the stability as well as the time response of the hand gesture tracking and control for the Tello Drone. Figures 5 and 6 indicate the drone operation process with different types of commands. In all cases, the drone’s speed always maintains balancing and manages the camera direction to the centre of the target arm. The response time from the moment the hand transmits the command to the moment it affects the drone’s movement is calculated at about 2–3 s. The distance for target tracking is estimated between 100 and 300 cm.

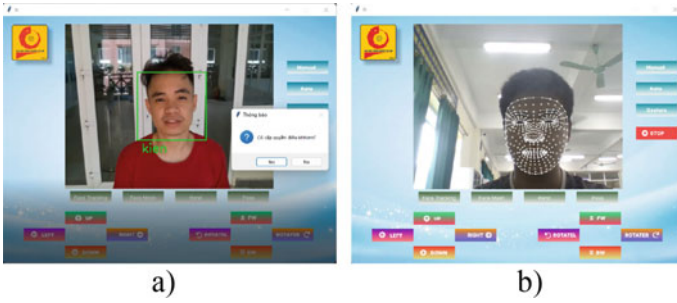


**Fig. 4** **a** The recognition result of the machine learning pipeline; **b** The grid mesh displays on the wrong target face

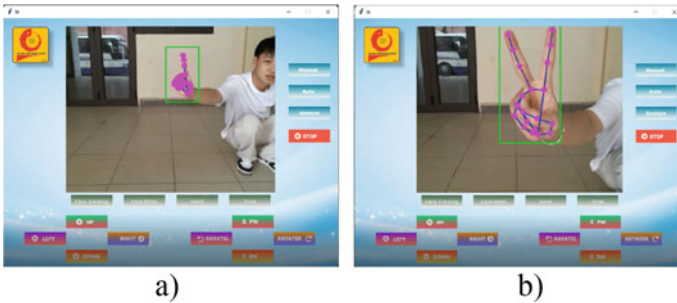


**Fig. 5** **a** The drone is moving forward to the commander; **b** The drone is moving backward to the commander



**Fig. 6** **a** The drone is moving to the right of the commander; **b** The drone is moving to the left of the commander

## 4 Conclusion

In this paper, a real-time drone navigation system based on LBPH and hand gesture control with Medipipe is proposed. We proved that simple artificial intelligence mechanisms combined with suitable control strategies are a viable solution to broaden the spectrum of applications of low-cost drones. It is evident that the proposed approach has been successfully implemented on hardware and tested with several field measurements. To be more detailed, by coupling the noise reduction on the input images with LBPH, the accuracy of face recognition is improved significantly. Moreover, the next stage of control process with finger gestures is ensured validity based on the clear base rule definition. Finally, this research has given rise to many potential areas in need of future investigation. We hope that our further tests will expand more interesting findings for drone navigation.

## References

1. M. Alwateer, S.W. Loke, N. Fernando, Enabling drone services: drone crowdsourcing and drone scripting. *IEEE Access* **7**, 110035–110049 (2019)
2. M. Balasingam, Drones in medicine—the rise of the machines. *Int. J. Clin. Pract.* **71**, e12989 (2017). <https://doi.org/10.1111/ijcp.12989>
3. T.-V. Dang, Smart home management system with face recognition based on ArcFace model in deep convolutional neural network. *J. Robot. Control* **3**(6), 754–761 (2022)
4. B. Patle, S.-L. Chen, B. Patel, S.K. Kashyap, S. Sanap, Topological drone navigation in uncertain environment. *Ind. Robot.* **48**(3), 423–441 (2021)
5. Y.-P. Huang, L. Sithole, T.-T. Lee, Structure from motion technique for scene detection using autonomous drone navigation. *IEEE Trans. Syst. Man, Cyber. Syst.* **49**(12), 2559–2570 (2019)
6. I. White, D. K. Borah, W. Tang, Robust optical spatial localization using a single image sensor. *IEEE Sens. Lett.* **3**(6), 1–4 (2019), Art no. 7000904
7. B. Kaplan et al., Detection, identification, and direction of arrival estimation of drone FHSS signals with uniform linear antenna array. *IEEE Access* **9**, 152057–152069 (2021)
8. N.J. Sairamya et al., Hybrid approach for classification of electroencephalographic signals using time–frequency images with wavelets and texture features, in *Intelligent Data Analysis for Biomedical Applications* (Academic Press, 2019), pp. 253–273
9. C. Lugaresi et al., Mediapipe: a framework for perceiving and processing reality, in *Third Workshop on Computer Vision for AR/VR at IEEE Computer Vision and Pattern Recognition (CVPR)*, vol. 2019 (2019)
10. F. Zhang et al., Mediapipe hands: on-device real-time hand tracking. arXiv preprint [arXiv:2006.10214](https://arxiv.org/abs/2006.10214) (2020)
11. P. Luo, X. Zhang, Z. Chang, W. Liu, Research on salt and pepper noise removal method based on adaptive fuzzy median filter, in *2021 IEEE 5th Advanced Information Technology, Electronic and Automation Control Conference (IAEAC)* (2021), pp. 387–392
12. V. Bazarevsky, F. Zhang, On-device, real-time hand tracking with mediapipe. Google AI Blog (2019)

# Optimization Toolpath Generation for Drill Hole on Three Axes CNC Machine Using Genetic Algorithms



Van Quy Hoang, Ngoc Tuyen Bui, Xuan Dung Pham, and Gia Hai Vuong

**Abstract** Flat metal sheets with many holes are widely used in industries for example, box shells, plates, or PCB boards. The selection of the tool path becomes extremely difficult as the number of holes increases. Longer paths reduce machining productivity. Among those routes, each route is a different total length. If the route is chosen for the tool path too long, the total machining time will increase, and productivity will be reduced. This paper presents a simple method for optimizing tool paths when drilling multiple holes in large steel plates. The tool path includes two styles of cutting and un-cutting tool paths and other parameters. We investigated the un-cutting tool path for the proposed method. The presented method was applied to a drilling problem to find an optimal tool path with the shortest total length. The proposed method can be applied to three-axis CNC machines with interpolated movements to predict the shortest total distance of tool paths.

**Keywords** 3 axes CNC · CAM · Genetic algorithm · Tool path · Optimization toolpath

## 1 Introduction

During the machining process, the tool must perform complex movements, including rotation, step-over, feed rate... But tool path cares about two elements, includes are cutting, and un-cutting movements. The goal of machining, in addition to improving accuracy as required by technology, shortening the machining time is essential, and there are many studies to improve this problem. In practice, it is expanding to have holes in large metal sheets by laser cutting methods on numerical control machines. The G-codes used in these processes are usually programmed by humans or using

---

V. Q. Hoang (✉) · G. H. Vuong  
Haiphong University, Haiphong, Vietnam  
e-mail: [quyhv@dhhp.edu.vn](mailto:quyhv@dhhp.edu.vn)

N. T. Bui · X. D. Pham  
Hanoi University of Science and Technology, Hanoi, Vietnam

© The Author(s), under exclusive license to Springer Nature Switzerland AG 2024  
B. T. Long et al. (eds.), *Proceedings of the 3rd Annual International Conference on Material, Machines and Methods for Sustainable Development (MMMS2022)*, Lecture Notes in Mechanical Engineering, [https://doi.org/10.1007/978-3-031-57460-3\\_46](https://doi.org/10.1007/978-3-031-57460-3_46)



available CAM software. However, with large metal sheets and a lot of many holes to be machined, this process of self-programming is highly complex CAM software to output G-command code. The G-codes will control the tool to move with two processes, the rapid and the machined feed. To optimize machining time, it is necessary to optimize these two parameters (machining time and unmachining tool time). With large parts with many machining holes, the un-machining process can take up a great deal of time, thus making the machining efficiency not high. In this study, we use an evolutionary algorithm, one of the effective tools in practical intelligence, to optimize the uncut toolpath, thereby optimizing the machine's time. The optimization of rapid tool paths when drilling is an essential requirement because it solves the problem of optimizing tool travel distances, thus shortening machining times. This is especially effective for parts that are very large and have a large number of holes and complex layouts. Currently, there are many research studies on the application of optimal search algorithms applied in toolpath optimization. Widely applied fields from cutting, spark machining, and laser machining.

## 2 Related Works

Lee et al. [1], studied the optimization of the toolpath in the CNC machining process in both directions. The authors proposed a GA solution in two steps. It is a combination of local and global searches to define the optimal point and then connect all of the optimal points to create an optimal tool path. This algorithm can be easily applied to other CNC machining processes such as laser, plasma, water-jet, etc. Abu Qudeiri et al. [2], Meanwhile, Jaber Abu et al. have taken an alternative approach which is to determine the optimal sequence of tool operations according to asymmetric positions, and then define the optimal toolpath. Naturally, the authors also use GA in this case. After determining the optimal toolpath, the G-codes are used to generate the corresponding machining program. In this study, the authors applied the GA algorithm to the TSP issue, and the outcomes were evaluated by creating G-codes using commercial CAD/CAM programs. Du et al. [3], introduced a new algorithm to optimize the toolpath during CNC grinding. The algorithm is a combination by adding a hill climbing algorithm to the genetic algorithm. In this study, the authors re-designed the crossover and mutation operators to enhance the local search capability and accelerate convergence. The results of this algorithm show that non-cutting tool movements are significantly reduced. Thereby improving the efficiency of the machining process. In order to process multi-contoured pieces in the cutting of tanning products for the apparel sector, Yang et al. [4], have developed a method for improved genetic simulated annealing algorithm is applied to optimize the cutting path selected arbitrarily firstly, and an optimal contour sequence is founded, then problem is changed into multi segment map problem solved with dynamic programming algorithm. The results show that the algorithm is more effective. Gupta et al. [5], in their research on 2.5D milling have developed a new method to optimize the tool path. The authors claim that about 13% of production costs can be reduced

by choosing the optimal tool diameter and cutting width. In addition, there is also a 50% reduction in cost per unit volume and an approximately 61% increase in material rejection compared to manual optimization methods using the handbook to selecting optimal cutting parameter. Mohamad et al. [6], presented to optimization of the tool path through removal using Finite Element Analysis and control via Genetic Algorithm. Pezer [7] proposed modifying the genetic algorithm using some of the known metaheuristic methods (ACO, PSO, etc.), and combining it with one of the methods for searching for local optimum. As a result, the convergence of the algorithm occurs faster. This is a very potential global search solution.

Raja and Saravanan [8], presented tool path optimization to improve the energy efficiency of the machine. The authors built a genetic algorithm with a modified hybridization method. The results show that the new toolpath is more energy efficient than the previously optimized toolpath. This method can be adapted to multi-axis CNC machines with the interpolated motion to predict the optimal tool path.

### 3 Methodology

In the process of drilling holes (Fig. 1), tool must perform a three-step movement with a total length describe in Eq. (1). The tool is a distance of  $L_1$  from the part surface, the machining process of the tool will move in the part with a length of  $L_2$ , and the cutting tool must move exit the hole with a length of  $L_3$ . When the distance between  $L_1$  and  $L_3$  is reduced, the machining time is reduced as well. However, this distance has a limit, which is also visible during the machining process.

$$L = L_1 + L_2 + L_3 \tag{1}$$

In Fig. 2, after drilling one hole, the tool must move on to another. Euclid distance between two center points is a part of tool path length. The procedure is repeated

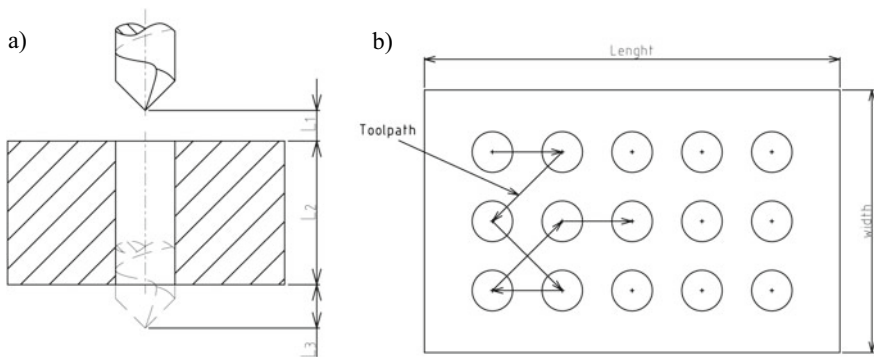
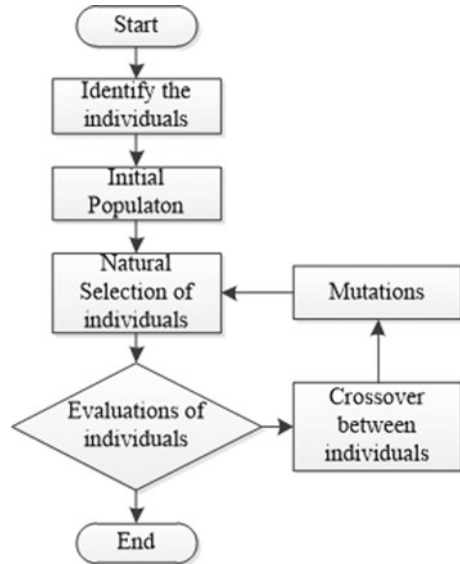


**Fig. 1** a Cutting length for one hole. b Example a route across all holes

**Fig. 2** The algorithm diagram



until the tool reaches the end hole and returns to the first hole. We get a route by connecting all the moving tools.

When the number of holes to be machined increases, so does the number of routes, making it difficult to choose the optimal route for tool path generation. Because determining the optimal route necessitates a significant amount of computation. The total number of routes is calculated in Eq. (2), where n is amount of holes.

$$Sum\ of\ routes = n! \tag{2}$$

To use the genetic algorithm, a general equation to calculate the total length of the routes must be created. This total length is the sum of the Euclidean distances between two consecutive hole centers that do not repeat until the first hole is reached.

### 3.1 Genetic Algorithm Model

Genetic algorithms are algorithms that mimic animal evolution in the wild. Therefore, to apply to the technical’s problem, we construct the following steps: Step 1: Identify the individual; Step 2: Initial population; Step 3: Natural selection of individuals in the population; Step 4: Crossover between individuals; Step 5: Mutations in the process of evolution; Step 6: Evolution and Results. The summary of the steps in the algorithms is as Fig. 3.

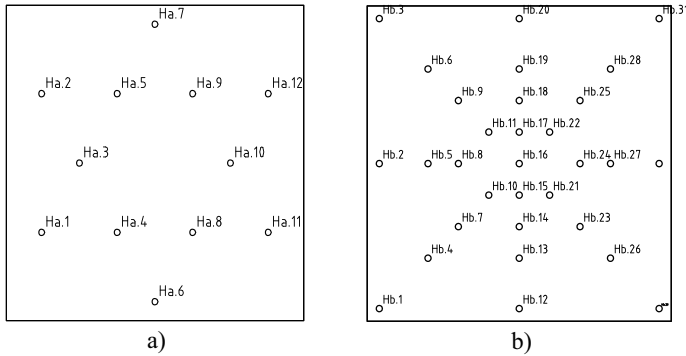


**Fig. 3** Coordinates of experimental models

**Step 1.** To encode an individual for the genetic algorithm, we select random a hole for starting to create the route. From the center of that hole, randomly connect to the center of another hole, keep repeating until all the points are gone, then return to the starting point. In this method, each starting point can create multiple different routes. However, in this study, it was not necessary to create all routes. Which number of routes to create is determined by the number of individuals in the population size. Each individual was described as a 1-row, n-column array Eq. (3).

$$\begin{aligned}
 I_1 &= \{P_1 P_2 P_3 P_4 \dots P_i \dots P_j \dots P_{n-1} P_n\} \\
 I_2 &= \{P_3 P_2 P_1 P_i \dots P_j \dots P_{n-1} P_n \dots P_5\} \\
 &\dots\dots\dots \\
 I_i &= \text{random}(\{P_i\}), i = 1, n
 \end{aligned}
 \tag{3}$$

**Step 2.** In the first generation, collecting individuals  $I_i$  will produce a population. Permuting the elements in the original  $I_1$  with the number of times appropriate to the population size will yield the number of individuals in each population. Assuming that the population size ( $P_s$ ) is m and that each individual has n elements (node), the population formed by the procedure mentioned above can be represented as a two-dimensional array with m rows and n columns Eq. (4).

$$\{pop\} = \begin{pmatrix} P_1 & P_2 & \dots & P_{n-1} & P_n \\ P_2 & P_3 & \dots & P_1 & P_5 \\ P_n & P_i & \dots & P_{i+2} & P_{i+\dots} \\ \dots & \dots & \dots & \dots & \dots \\ P_{n-i} & P_7 & \dots & P_i & P_5 \end{pmatrix}
 \tag{4}$$

At this stage, it is necessary to determine the Fitness function to assess the fitness of individuals in the population. In stage 1, each instance is formed as a route which

is the sum of segments. Therefore, the fitness function is the sum of the lengths of the segments, the fitness function is described in Eq. (5).

$$f(x_i, y_i) = \sum_{i=1}^{n-1} d(P_i, P_{i+1}) = \sum_{i=1}^{n-1} \sqrt{(x_{i+1} - x_i)^2 + (y_{i+1} - y_i)^2} \quad (5)$$

The goal is to find the minimum length value of the routes, it means that the value of the fitness function small is better. Each individual will be assessed through Eq. (5); individuals in good condition (small distance value) will be kept and added to the population in the next generation, and individuals can poor condition (large distance value) will be discarded. This process is repeated until the required individual is found for the target. However, if all the tests are tried, the number of tests is too large. Therefore, stage 3 will perform crossover operations and mutation to reduce the amount of computation.

**Step 4, 5:** Nature's evolution is described by the process of crossover and mutation. This procedure will result in the next generation. Crossover can be created by combining parents to produce generations of offspring. Individuals with special properties can be created as a result of the mutation process. The process of hybridization frequently has a much higher probability than the process of mutation. As a result, future generations will have better health. Selecting a pair of parents and then combining a portion of the father's genes with a portion of the mother's genes to create a new individual is the process of crossbreeding. As a result, each set of parents can have two children. We reverse engineer from an instance to create a new instance during the mutation process.

**Step 6:** Individuals will be evaluated using the fitness function after each generation. When the fitness function value for each person does not converge, the process continues and new generations arise. When too many people are physically similar, there is no change, and the process convergence takes place. The calculation's outcome has been determined. The algorithm is terminated. The result is saved and exported optimal route. The evaluation of convergence error  $e$  is represented in Eq. (6). The algorithm loop will stop when  $e$  reaches the given value. The algorithm is shown in Fig. 3.

$$e = |f_i - f_j|, \{i, j = (1, n)\} \quad (6)$$

## 4 A Case Study

Two models with dimensions of  $500 \times 500 \times 20$  mm are designed with 12 and 31 holes respectively (Fig. 3). We utilized Matlab 2010a to create a script with an algorithm suggestion and test it with two models to evaluate the proposed method. The two workpieces will be built with an increasing number of holes and a greater

degree of placement complexity. The holes correspond to the letters Ha, Hb, and Pa, Pb will be the hole center points for each hole corresponding. The two models' coordinates are provided below:

$$\begin{aligned} \mathbf{H}_a &= \{\mathbf{P}_{ai}\} = [\mathbf{P}_{a1}; \mathbf{P}_{a2}; \dots; \mathbf{P}_{a12}] = [x_{a1}y_{a1}; x_{a2}y_{a2}; \dots; x_{a12}y_{a12}] \\ &= [59.47\ 140; 59.47\ 360; 122.98\ 250; 186.49\ 140; 186.49\ 360; \\ &\quad 250\ 30; 250\ 470; 313.51\ 140; 313.51\ 360; \\ &\quad 377.02\ 250; 440.53\ 140; 440.53\ 360] \end{aligned}$$

$$\begin{aligned} \mathbf{H}_b &= \{\mathbf{P}_{bi}\} = [\mathbf{P}_{b1}; \mathbf{P}_{b2}; \dots; \mathbf{P}_{b31}] = [x_{b1}y_{b1}; x_{b2}y_{b2}; \dots; x_{b31}y_{b31}] \\ &= [20\ 20; 20\ 250; 20480; 100\ 100; 100\ 250; 100\ 400; 150\ 150; \\ &\quad 150\ 250; 150\ 350; 200\ 200; 200\ 300; 250\ 20; 250\ 100; 250\ 150; \\ &\quad 250\ 200; 50\ 250; 250\ 300; 250\ 350; 250\ 400; 250\ 480; \\ &\quad 300\ 200; 300\ 300; 350\ 150; 350\ 250; 350\ 350; 400\ 100; \\ &\quad 400\ 250; 400\ 400; 480\ 20; 480\ 250; 480\ 480] \end{aligned}$$

Figure 4 shows a graph that assesses the level of converging across generations of the two samples.

Sample 1: Results converge at the 23th generation number. The total length of the tool path is 1.5242 mm.

Sample 2: Results converge at the 286th generation number. The total length of the tool path is 2.870,3658 mm.

Table 1 statistics the parameters after applying the algorithm to the experimental respectively. The most important is the points connected to generate optimal path and optimal length path.

where:

*Num\_of\_gen* is the preset number of generations.

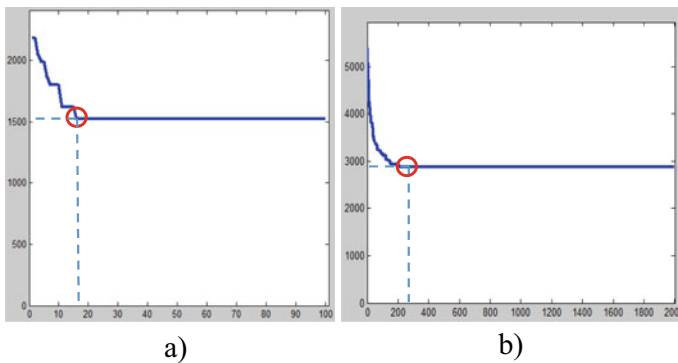


Fig. 4 Optimal number of generations of exp 1 and exp 2

**Table 1** Simulation results for three models using a genetic algorithm

No	Num_ of_gen	P_ size	Optimal_path	Min_length_ path (mm)	Gen
Exp 1	100	200	[8-11-10-12-9-7-5-2-3-1-4-6]	1,524,2000	23
Exp 2	100	200	[10-7-4-1-2-5-8-11-9-6-3-20-19-18-17-22-25-28-31-30-27-24-21-23-26-29-12-13-14-15-16]	2,870,3658	286

$P\_size$  is the number of individuals in the population and is an integer and constant for all generations.

$Optimal\_paths$  is the optimal route to guide the tool in machining.

$Min\_length\_paths$  is the total minimal toolpath length.

$gen$  is the number of generations in which the optimal value of total tool paths length converges.

The tool path is shown in Fig. 5, with a and b being the optimal paths generated by the algorithm for the two parts, and c and d being the paths generated in CAM soft.

Table 2 shows a comparison of path lengths between the proposed method and the traditional method. The results show that the proposed solution has the optimal path;

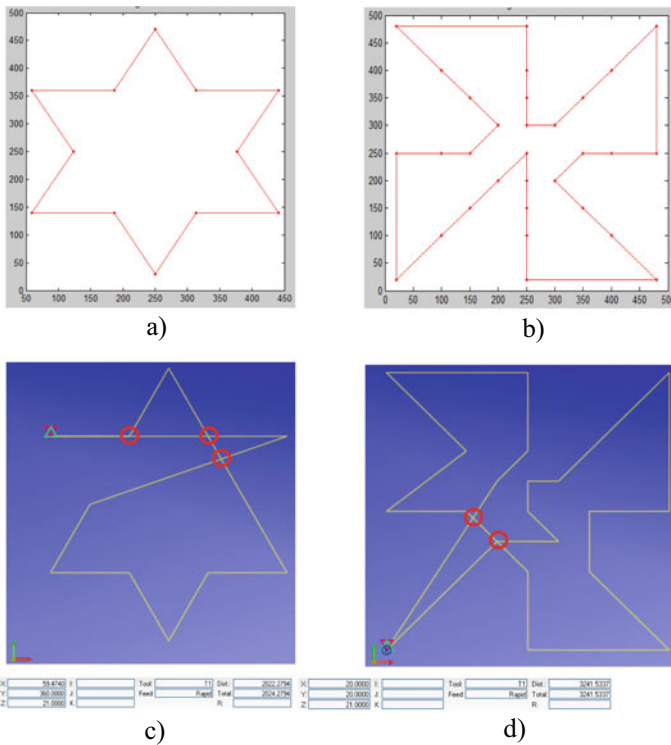


**Fig. 5** Toolpath generated from proposed method (a and b) and generated from CAM Software (c and d)

**Table 2** Path length comparison between the method proposal and traditional

Models	Method proposal	Traditional	Rate of reduction %
Exp 1	1524.2 mm	2022.2794 mm	24.63
Exp 2	2870.3658	3241.5337 mm	11.45



the total path length is significantly reduced compared to the tool path generated in Catia software's CAM module.

## 5 Conclusion

The results show that the algorithm we propose with simple hybridization and mutation solutions through matrix operations has high efficiency. The algorithm is especially suitable for multi-hole machining problems on flat metal sheets. To demonstrate the efficiency of the algorithm, we compare the same sample, which outputs G-code using Catia V5 and the proposed algorithm. Simulation execution was performed on Cimco Edit V7 software. The results show that. To demonstrate the efficiency of the algorithm, we compare the same sample, which outputs G-code using Catia V5 and the proposed algorithm. Simulation execution was performed on Cimco Edit V7 software. We built 2 templates with a variable number of holes, one simple with 12 holes and one with a large number of holes and complicated placement with 31 holes. Through simulation, we find that when the number of holes is large, the optimal time will be longer. However, this is negligible for large series production models. The results obtained when comparing the tool path by the proposed algorithm with the commercial Cad/cAm software described in Fig. 6 shows that. For the proposed algorithm, the path segments are not intersected, while for commercial cad/cam software this happens a lot, with multiple tool paths intersecting each other which is time consuming. machining time, thereby reducing productivity. This solution is applicable not only to large sheet metal drilling, but also to other machining problems such as laser, plasma, and waterjet machining. It demonstrates that the proposed algorithm has a broad range of applications and is suitable for industrial production.

## References

1. M.K. Lee, K.B. Kwon, Cutting path optimization in CNC cutting processes using a two-step genetic algorithm. *Int. J. Prod. Res.* **44**(24), 5307–5326 (2006). <https://doi.org/10.1080/00207540600579615>
2. J. Abu Qudeiri, H. Yamamoto, R. Ramli, Optimization of operation sequence in CNC machine tools using genetic algorithm. *J. Adv. Mech. Des., Syst., Manuf.* **1**(2), 272–282 (2007). <https://doi.org/10.1299/jamdsm.1.272>
3. H. Du, J. Qi, Application of a hybrid algorithm based on genetic algorithm and hill-climbing algorithm to tool path optimization in CNC machining. *Adv. Mater. Res.* **102–104**, 681–685 (2010). <https://doi.org/10.4028/www.scientific.net/AMR.102-104.681>
4. W. Yang, Y. Zhao, J. Jie, W. Wang, An effective algorithm for tool-path airtime optimization during leather cutting. *Adv. Mater. Res.* **102–104**, 373–377 (2010). <https://doi.org/10.4028/www.scientific.net/AMR.102-104.373>
5. A.K. Gupta, P. Chandna, P. Tandon, Optimization of machining parameters and tool selection in 2.5D milling using genetic algorithm. *Optimization.* 21–27 (2011)

6. N. Mohamad, M.K.A. Ariffin, Development of genetic algorithm toolbox using MATLAB in cutting tool path optimization. *Sci. Res.* **8**(38), 1848–1857 (2013). <https://doi.org/10.5897/SRE10.550>
7. D. Pezer, Efficiency of tool path optimization using genetic algorithm in relation to the optimization achieved with the CAM software. *Procedia Eng.* **149**(June), 374–379 (2016). <https://doi.org/10.1016/j.proeng.2016.06.681>
8. B. Raja, M. Saravanan, Tool path optimization by genetic algorithm for energy efficient machining, **14**, 1670–1679 (2018)

# Kinetic Analysis of a Spatial Structure by Orthographic Projection



Pham Van Son and Van Hieu Phan

**Abstract** There are many methods to solve the kinetic analysis problem in the world, and each method has its advantages. This paper proposes a new method to solve the kinetic analysis problem for aspatial structure. By setting up some linking equations and simulating the spatial structure's motion, the kinetic analysis could be solved simply and easily. Besides that, this study used orthographic projection to analyze the movement of a specific spatial structure. The calculation was also validated by using CATIA software.

**Keywords** Spatial structure · kinetic analysis · Orthographic projection · linking equation

## 1 Introduction

The kinetic problem is the first problem that needs to be solved for any structure, which is a base for studying some further problems such as machine dynamics and durability, machine balance, optimization, etc. In the world, there are many methods to solve the problem of kinematic analysis. However, these methods are often quite complex, especially since they would become more complicated when the research object is spatial structures [1–8]. This paper proposes the perpendicular projection method to analyze spatial structure kinematics, intending to help to solve the kinematic analysis problem more simply and easily.

---

P. Van Son · V. H. Phan (✉)

School of Mechanical Engineering, Hanoi University of Science and Technology, No. 1 Dai Co Viet Road, Hanoi, Vietnam

e-mail: [hieu.phanvan@hust.edu.vn](mailto:hieu.phanvan@hust.edu.vn)

## 2 Kinetic Analysis of Spatial Structures by Using the Orthographic Projection Method

Each spatial mechanism is a mechanical system subject to a hold-and-stop holonomy link and its binding conditions of the form:

$$\sum l_i = 0 \quad (1)$$

We use independent generalized coordinates  $q_1, q_2, q_3, \dots, q_f$ . To determine the position of the mechanism  $f$  degrees of freedom. In addition, we add additional extrapolation coordinates to easily set up analytic expressions to determine the position of the mechanism. Let  $z_1, z_2, z_3, \dots, z_r$  be the dependent extension coordinates. The linking equations have the form:

$$f_i(q_1, q_2, \dots, q_f, z_1, z_2, \dots, z_r) = 0 \quad (i = 1 \div r) \quad (2)$$

where  $z_k = z_k(q_1, q_2, \dots, q_f)$  ( $k = 1 \div r$ )

Solving the system of nonlinear algebraic Eq. (1) to determine the  $z_i$  functions and their first and second derivatives by the iterative method is the central task of the spatial structure kinematic analysis problem. This study aims to apply the orthographic projection method and introduce generalized residual coordinates to build the linking equations of the spatial structures. Figure 1 describes the steps of the orthogonal projection method for kinetic analysis.

Some assumptions could be noted:

When choosing the fixed coordinate system Oxyz, it is necessary to follow the principle: If the link connecting the rack rotates around the fixed axis, choose the rotation plane parallel to the axis of rotation. If the link is a translation, choose one of the x or y axes parallel to the translation. For each link, it is necessary to determine the angle between the projection of the two coordinate axes attached to the link and the ox (or oy) and oz axis. If there is a translational joint, it is necessary to select additional interpolation coordinates for the long displacement. Projecting the spatial linkage equation onto the coordinate axes is a very difficult. To be able to solve that task, we first project the system onto the coordinate planes to turn the spatial problem into a flat problem. CAD/CAM software can be used to support or use projection matrices (if using automatic programming) [1].

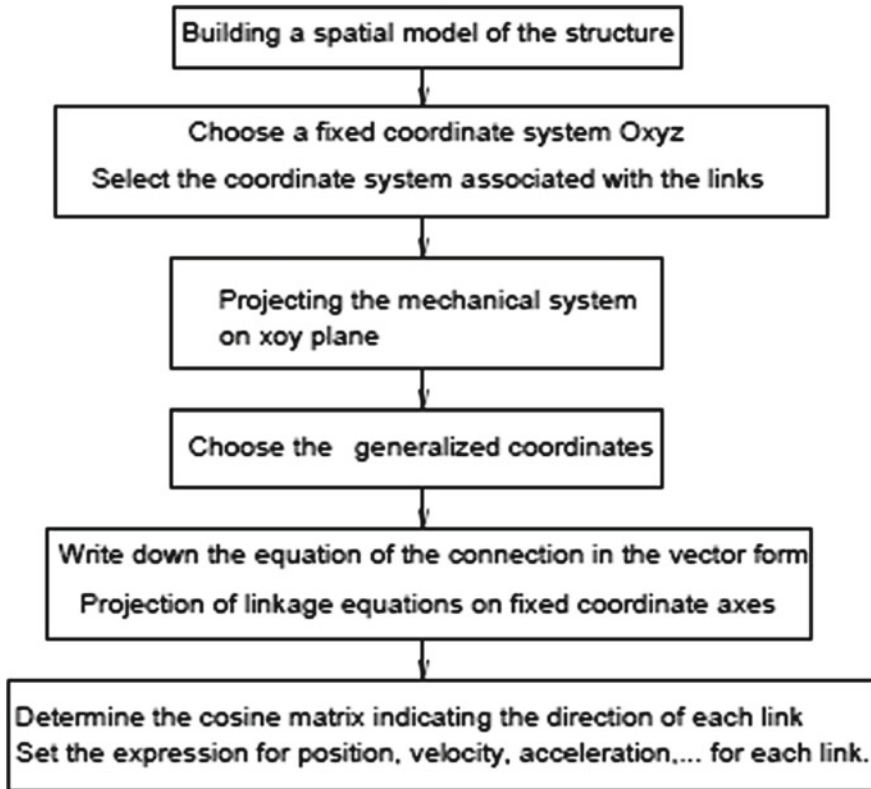


Fig. 1 Steps of kinetic analysis by using orthographic projection

### 3 Kinematic Analysis of Space Structures with Two Rotary Joints (R) and Two Spherical Joints (S)

#### 3.1 Establishing the Link Equation

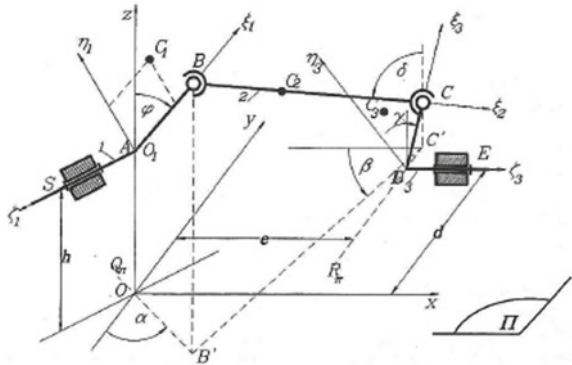
Figure 2 depicts a 4-stage RSSR spatial structure in which AB is perpendicular to SA; CD is perpendicular to DE. The lengths  $AB = l_1$ ,  $BC = l_2$ ,  $CD = l_3$ . The SAB stitch rotates around the fixed axis SA. The CDE stitch rotates around the fixed axis DE. Select the fixed axis system and the axes attached to the links, as shown in Fig. 2.

By choosing the independent generalized coordinate  $\varphi$ , the residual generalization coordinates are  $\beta$ ,  $\gamma$  and  $\delta$ .

From Fig. 2, we have the following vector linkage equation:

$$\vec{OA} + \vec{AB} + \vec{BC} + \vec{CD} + \vec{DO} = 0 \tag{3}$$

**Fig. 2** Structure of 4 spatial links RSSR



Projecting on the  $x, y,$  and  $z$  coordinate axes, we have the equations:

$$\begin{cases} f_1 = l_1 \sin \varphi \sin \alpha + l_2 \sin \delta \cos \beta - e = 0 \\ f_2 = -l_1 \sin \varphi \cos \alpha + l_2 \sin \delta \sin \beta - l_3 \sin \gamma - d = 0 \\ f_3 = h + l_1 \cos \varphi - l_2 \cos \delta - l_3 \cos \gamma = 0 \end{cases} \quad (4)$$

### 3.2 Determination of the Generalized Coordinates, Their Velocities, and Accelerations

Derivative (4) concerning  $\varphi$  we get:

$$\begin{cases} l_1 \cos \varphi \sin \alpha - l_2 \beta' \sin \delta \sin \beta + l_2 \delta' \cos \delta \cos \beta = 0 \\ -l_1 \cos \varphi \cos \alpha + l_2 \beta' \sin \delta \cos \beta + l_2 \delta' \cos \delta \sin \beta - l_3 \gamma' \cos \gamma - d = 0 \\ -l_1 \sin \varphi + l_2 \delta' \sin \delta + l_3 \gamma' \sin \gamma = 0 \end{cases} \quad (5)$$

In the other form:

$$\begin{bmatrix} 0 & l_2 \sin \beta \sin \delta & l_2 \cos \beta \cos \delta \\ -l_3 \cos \gamma & l_2 \cos \beta \sin \delta & l_2 \sin \beta \cos \delta \\ l_3 \sin \gamma & 0 & l_2 \sin \delta \end{bmatrix} \begin{bmatrix} \gamma' \\ \beta' \\ \delta' \end{bmatrix} = \begin{bmatrix} -l_1 \cos \varphi \sin \alpha \\ l_1 \cos \varphi \cos \alpha \\ l_1 \sin \varphi \end{bmatrix} \quad (6)$$

If we enter the symbols:

$$J_z = \begin{bmatrix} 0 & l_2 \sin \beta \sin \delta & l_2 \cos \beta \cos \delta \\ -l_3 \cos \gamma & l_2 \cos \beta \sin \delta & l_2 \sin \beta \cos \delta \\ l_3 \sin \gamma & 0 & l_2 \sin \delta \end{bmatrix}, z' = \begin{bmatrix} \gamma' \\ \beta' \\ \delta' \end{bmatrix},$$

$$d_1 = \begin{bmatrix} -l_1 \cos \varphi \sin \alpha \\ l_1 \cos \varphi \cos \alpha \\ l_1 \sin \varphi \end{bmatrix}$$

Then (6) can be written:

$$J_z z' = d_1 \quad (7)$$

Solving Eq. (7), we get  $z'$ , then we can determine  $\dot{z}$  according to the equation  $\dot{z} = z' \cdot \dot{\varphi}$ . Derivative (5) concerning  $\varphi$  we get:

$$J_z z'' = d_2 \quad (8)$$

With:

$$z'' = \begin{bmatrix} \gamma'' \\ \beta'' \\ \delta'' \end{bmatrix},$$

$$d_2 = \begin{bmatrix} l_1 \sin \varphi \sin \alpha + l_2 \beta'^2 \sin \delta \cos \beta + 2l_2 \beta' \delta' \cos \delta \sin \beta \\ + l_2 \delta'^2 \sin \delta \cos \beta \\ -l_1 \sin \varphi \cos \alpha + l_2 \beta'^2 \sin \delta \sin \beta - 2l_2 \beta' \delta' \cos \delta \cos \beta \\ + l_2 \delta'^2 \sin \delta \sin \beta - l_3 \gamma'^2 \sin \gamma \\ l_1 \cos \varphi - l_2 \delta'^2 \cos \delta - l_3 \gamma'^2 \cos \gamma \end{bmatrix}$$

By solving Eq. (8), we get  $z''$ , then we can determine  $\ddot{z}$  according to the equation:  $\ddot{z} = z'' \dot{\varphi}^2 + z' \ddot{\varphi}$ .

The functions  $\gamma(\varphi)$ ,  $\beta(\varphi)$ ,  $\delta(\varphi)$  are approximated according to Taylor's criterion as follows:

$$\gamma(\varphi_0 + \Delta\varphi) = \gamma(\varphi_0) + \gamma'(\varphi_0)\Delta\varphi + \frac{1}{2}\gamma''(\varphi_0)\Delta\varphi^2 + \dots$$

$$\beta(\varphi_0 + \Delta\varphi) = \beta(\varphi_0) + \beta'(\varphi_0)\Delta\varphi + \frac{1}{2}\beta''(\varphi_0)\Delta\varphi^2 + \dots$$

$$\delta(\varphi_0 + \Delta\varphi) = \delta(\varphi_0) + \delta'(\varphi_0)\Delta\varphi + \frac{1}{2}\delta''(\varphi_0)\Delta\varphi^2 + \dots$$

Then determined more precisely by the Newton iterative method.

### 3.3 Determination of the Position, Velocity, Acceleration of the Center of Mass, Angular Velocity, and Angular Acceleration of the Links of the Mechanism

Let  $C_1$  be the center of mass of the link SAB and suppose, in the coordinate system  $O_1\xi_1\eta_1\zeta_1$  the coordinates of  $C_1$  are  $(\xi_{11}, \eta_{11}, 0)$ . The equation for determining  $C_1$  in a fixed coordinate system is as follows:

$$\begin{cases} x_{C1} = \xi_{11} \sin \varphi \sin \alpha - \eta_{11} \cos \varphi \sin \alpha \\ y_{C1} = -\xi_{11} \sin \varphi \cos \alpha + \eta_{11} \cos \varphi \cos \alpha \\ z_{C1} = h + \xi_{11} \cos \varphi + \eta_{11} \sin \varphi \end{cases} \quad (9)$$

Let  $C_2$  be the center of mass of the link BC and suppose, in the coordinate system  $O_2\xi_2\eta_2\zeta_2$  the coordinates of  $C_2$  are  $(\xi_{22}, 0, 0)$ . The equation for determining  $C_2$  in a fixed coordinate system is as follows:

$$\begin{cases} x_{C2} = l_1 \sin \varphi \sin \alpha + \xi_{22} \sin \delta \cos \beta \\ y_{C2} = -l_1 \sin \varphi \cos \alpha + \xi_{22} \sin \delta \sin \beta \\ z_{C2} = h + l_1 \cos \varphi - \xi_{22} \cos \delta \end{cases} \quad (10)$$

Let  $C_3$  be the center of mass of the link CDE and suppose, in the coordinate system  $O_3\xi_3\eta_3\zeta_3$  the coordinates of  $C_3$  are  $(\xi_{33}, \eta_{33}, 0)$ . The equation for determining  $C_3$  in a fixed coordinate system is as follows:

$$\begin{cases} x_{C3} = l_1 \sin \varphi \sin \alpha + l_2 \sin \delta \cos \beta \\ y_{C3} = -l_1 \sin \varphi \cos \alpha + l_2 \sin \delta \sin \beta - l_3 \sin \gamma + \xi_{33} \sin \gamma - \eta_{33} \cos \gamma \\ z_{C3} = h + l_1 \cos \varphi - l_2 \cos \delta - l_3 \cos \gamma + \xi_{33} \cos \gamma + \eta_{33} \sin \gamma \end{cases} \quad (11)$$

Deriving expressions (9), (10), and (11) concerning time, we have equations to determine the velocity of points  $C_1$ ,  $C_2$ , and  $C_3$ . Then the derivative of the equations determining the velocity of the points  $C_1$ ,  $C_2$ , and  $C_3$ , over time, we will get the equations determining the acceleration of those points.

Suppose lead 1 rotates with angular velocity  $\omega_1 = \dot{\varphi}$  and acceleration  $\varepsilon_1 = \ddot{\varphi}$ . According to Fig. 2, the direction cosine matrix of the SAB link is determined by three consecutive rotations:

- Rotation around the  $oz$  axis with an angle  $(90^\circ - \alpha)$ , in the negative direction.
- Rotation around the  $oy$  axis with an angle  $(90^\circ - \varphi)$ , in the negative direction.
- Rotate around the  $ox$  axis with an angle of  $90^\circ$  in the positive direction.

As a result, we can calculate the direction cosine matrix of the segment SAB as follows:



$$A = \begin{bmatrix} \sin \alpha \sin \varphi & -\sin \alpha \cos \varphi & -\cos \alpha \\ -\cos \alpha \sin \varphi & \cos \alpha \cos \varphi & -\sin \alpha \\ \cos \varphi & \sin \varphi & 0 \end{bmatrix} \tag{12}$$

We can determine the angular velocity according to the following equation:

$$\tilde{\omega}_1 = \begin{bmatrix} 0 & -\omega_{1x} & \omega_{1y} \\ \omega_{1z} & 0 & -\omega_{1x} \\ -\omega_{1y} & \omega_{1x} & 0 \end{bmatrix} = \dot{A}A^T = \begin{bmatrix} 0 & 0 & \dot{\varphi} \sin \alpha \\ 0 & 0 & -\dot{\varphi} \cos \alpha \\ -\dot{\varphi} \sin \alpha & \dot{\varphi} \cos \alpha & 0 \end{bmatrix} \tag{13}$$

Then, we have:

$$\omega_1 = \begin{bmatrix} \omega_{1x} \\ \omega_{1y} \\ \omega_{1z} \end{bmatrix} = \begin{bmatrix} \cos \alpha \\ \sin \alpha \\ 0 \end{bmatrix} \dot{\varphi}, \varepsilon_1 = \begin{bmatrix} \cos \alpha \\ \sin \alpha \\ 0 \end{bmatrix} \ddot{\varphi}, \tag{14}$$

By analogy for the CDE link, we have:

$$\omega_3 = \begin{bmatrix} \omega_{3x} \\ \omega_{3y} \\ \omega_{3z} \end{bmatrix} = \begin{bmatrix} 1 \\ 0 \\ 0 \end{bmatrix} \dot{\gamma}, \varepsilon_3 = \begin{bmatrix} 1 \\ 0 \\ 0 \end{bmatrix} \ddot{\gamma}, \tag{15}$$

### 3.4 Numerical Simulation of the Mechanism's Movements

To conduct numerical simulation, we give the values of the parameters of the structure as follows:  $h = 15$  cm,  $l_1 = 18$  cm,  $l_2 = 40$  cm,  $l_3 = 22$  cm,  $d = 20$  cm,  $e = 15$  cm,  $\alpha = 45^\circ$ . The coordinates of the centers of mass in the coordinate system associated with the links (Fig. 2) are taken as follows:  $C_1 (5, 2, 0)$ ,  $C_2 (20, 0, 0)$ ,  $C_3 (6, 3, 0)$ . The simulation is programmed and run on the MAPPLE application. Some results are presented in the following graphs (Figs. 3, 4, 5, 6, 7, 8, 9 and 10).

The author built the structure's stages using CATIA software, then assembled it into the structure (Fig. 11). Comparing the results of running dynamic simulations on

Fig. 3 Location graph C1

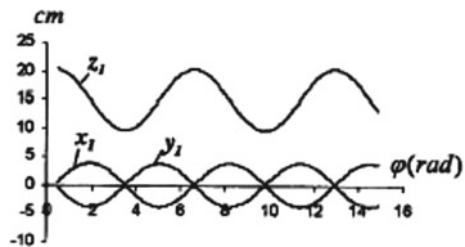


Fig. 4 Location graph C2



Fig. 5 C1 velocity graph

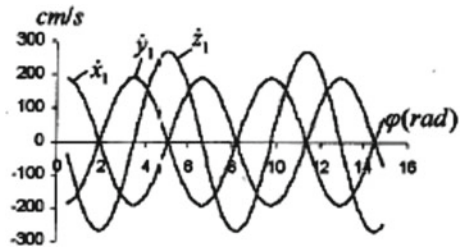


Fig. 6 C2 velocity graph

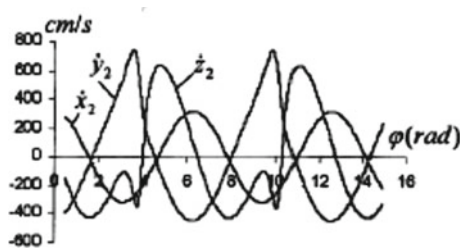


Fig. 7 Acceleration graph C1

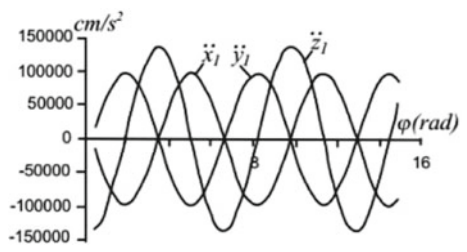
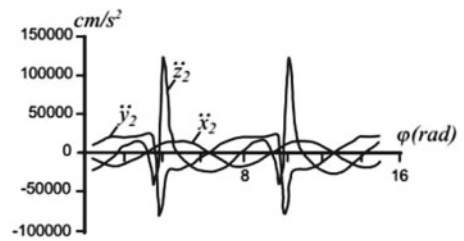
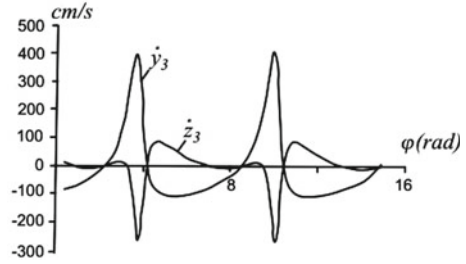
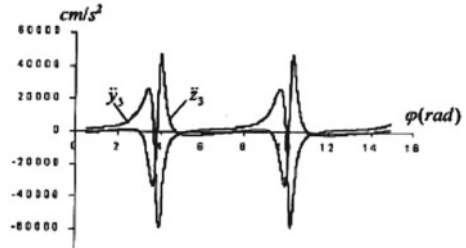
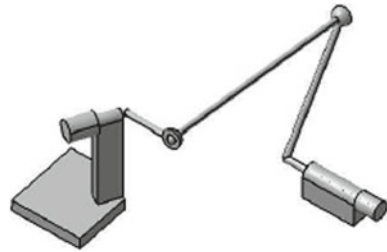


Fig. 8 Acceleration graph C2



**Fig. 9** Velocity graph C3**Fig. 10** Acceleration graph C3**Fig. 11** RCCR. Structure

CATIA and comparing them with the above results, the author found that the largest deviation was 0.5%. This partly demonstrates the reliability of the perpendicular projection method.

## 4 Conclusion

This paper has utilized the orthographic projection method to analyze the kinetic problem of a spatial structure. This method is simple and can be easily applied in the manufacturing process. Besides proposing steps to analyze the kinetic problem of a spatial structure using the orthographic projection method, this study also applied to two specific structures, such as two rotating joints and two spherical joints. The simulation results were compared with those of the most advanced software CATIA, proving the effectiveness of the proposed method.

## References

1. J.B. Foley, A. van Dam, S.K. Feiner, J.F. Hughes, *Computer Graphics: Principles and Practice*. (Reading, MA, Addison, Wesley, 1992)
2. N. Van Khang, *Basic Technical Mechanics* (National University Publishing House, Hanoi, 2005)
3. N. Van Khang, *Multi-body System Dynamics* (Science and Technology Publishing House, Hanoi, 2006)
4. D. Van Phong, *Numerical Methods in Mechanics* (Science and Technology Publishing House, Hanoi, 1999)
5. D.G. Tuong, T.K. Lam, *Principles of Machines* (Science and Technology Publishing House, Hanoi, 1999)
6. E.J. Haug, *Computer Aided Kinematic and Dynamics of a Mechanical System* (Allyn and Bancon, Boston, 1989)
7. J.E. Shigley, J.J. Vicker, *Theory of Machines and Mechanisms* (McGraw-Hill, New York, 1995)
8. J. Wang, C.M. Gosselin, Static balancing of spatial four-degree-of-freedom mechanism. *Mechan Mach Theory* **35** (2000)

# Use Perpendicular Projection to Prove Some Properties of Disphenoid and Some of Its Applications in Engineering



Manh Hong Do

**Abstract** An isosceles of the tetrahedron, also called disphenoid, is a tetrahedron where all four faces are congruent acute-angled triangles and every two edges that are opposite each other have the same length (Disphenoid—Wikipedia, the Free Encyclopedia, p. 1, <https://en.wikipedia.org/wiki/Disphenoid>, 1). If the four faces of the disphenoid are equilateral triangles, it is a regular tetrahedron. So, the regular tetrahedron is a special case of the disphenoid. A disphenoid has some characterizations and properties. They are widely used in the design of steel structures. This paper aims to solve some spatial geometry problems of a disphenoid to apply to the process of calculating, designing, and making technical drawings of it quickly and accurately.

**Keywords** Tetrahedron: Thd · Disphenoid: Dpd · Projection: Prj

## 1 Introduction

A Th is a basic geometrical block. It is widely used in engineering. Its properties will help design calculations and make drawings quickly and accurately [1–7]. This paper not only proves some new properties but also gives some practical applications of it. Here are its 3 new properties that will be demonstrated in this paper.

A Thd is a disphenoid if and only if it has one of the following properties:

- All faces have the same area.
- The center of the circumscribed sphere and the inscribed sphere coincide.
- The centroid of the Dpd and the circumscribed sphere coincide.

---

M. H. Do (✉)

Hanoi University of Science and Technology, Hanoi, Vietnam

e-mail: [hong.domanh@hust.edu.vn](mailto:hong.domanh@hust.edu.vn)

## 2 Prove the Above Properties

### 2.1 Problem 1

A Thd is a disphenoid that all faces of it have the same area. (See Fig. 1).

ABCD is a Dpd.

The plane of prj  $\Pi$  not only passes through AB but is also parallel to CD.

The orthogonal projection of CD onto the prj plane  $\Pi$  is  $C'D'$ .

$CC_1$  is the altitude of triangle CAB.

$DD_1$  is the altitude of triangle DAB.

The area of triangle CAB is equal to the area of triangle DAB.

So, we infer those two altitudes must be equal. Therefore, we have:

$$CC_1 = DD_1 \tag{1}$$

$$CD // (P) \Rightarrow CC' = DD' \tag{2}$$

From results (1) and (2)  $\Rightarrow \Delta CC'C_1 = \Delta DD'D_1$ .

Therefore, we have:

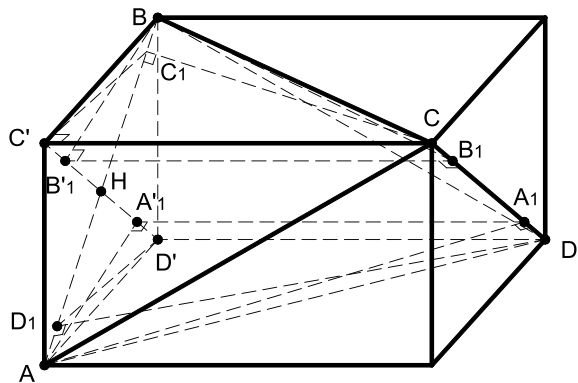
$$C'C_1 = D'D_1$$

We have:

$$CC' \perp \Pi \tag{3}$$

$$AB \perp CC_1 \tag{4}$$

Fig. 1 A Dpd ABCD



$$\text{From results (3) and (4)} \Rightarrow AB \perp C'C_1 \tag{5}$$

Similarly, we have:

$$DD' \perp \Pi \tag{6}$$

$$AB \perp DD_1 \tag{7}$$

$$\text{From results (6) and (7)} \Rightarrow AB \perp D'D_1 \tag{8}$$

These are the results of the trigonometric theorem.

From results (5) and (8) we have:  $C'C_1 // D'D_1$ .

So, AB goes through the midpoint H of  $C'D'$ .

Similarly, the area of triangle CDA is equal to the area of triangle CDB.

We have:

$$AA_1 = BB_1 \tag{9}$$

$AA_1$  and  $BB_1$  are the altitudes of triangles ACD and BCD, respectively.

Points  $A'_1$  and  $B'_1$  are perpendicular prj of points  $A_1$  and  $B_1$  onto the plane  $\Pi$ , respectively.

We have:

$$A_1A'_1 = B_1B'_1 \tag{10}$$

From results (9) and (10)  $\Rightarrow \Delta AA'A_1 = \Delta BB'B_1$ .

Therefore, we have:

$$AA'_1 = BB'_1$$

$$CD // (\Pi) \Rightarrow C'D' // CD$$

$$AA_1 \perp CD \Rightarrow AA_1 \perp C'D' \Rightarrow C'D' \perp AA'_1 \tag{11}$$

This is the result of the trigonometric theorem.

Similarly, we have:

$$BB'_1 \perp CD \text{ and } C'D' // CD \Rightarrow C'D' \perp BB'_1 \tag{12}$$

From results (11) and (12) we have  $C'D'$  also goes through the midpoint H of AB. So  $AC'BD'$  is a parallelogram.

We have:

$$CC' = DD' \tag{13}$$

$$AC' = BD' \tag{14}$$

From results (13) and (14)  $\Rightarrow \Delta CC'A = \Delta DD'B$ .

$$\Rightarrow AC = BD$$

Similarly, we have:

$$BC' = AD' \tag{15}$$

$$CC' = DD' \tag{16}$$

From results (15) and (16)  $\Rightarrow \Delta CC'B = \Delta DD'A \Rightarrow AD = BC$ .

We have:

$$AB = C'D', C'D' = CD \Rightarrow AB = CD$$

**Conclusion:**

Based on the above proof, we see that the edges of the Dpd are diagonals of a rectangular box.

Thus, if the planes of this rectangular box are taken as the basic prj planes, the basic prj of the Dpd are the rectangles of this rectangular box.

If the  $AB = BC = AD$ , it is a regular Thd. The rectangular box becomes a cube. Six faces of it are squares.

**2.2 Problems 2 and 3**

The center of the circumscribed sphere and the inscribed sphere coincide.

The centroid of the Dpd and the circumscribed sphere coincide.

To prove these problems, we will first prove some properties for any Thd.

Assuming a Thd ABCD, we in turn prove its following properties.

The bisector of the dihedral angle AB divides the opposite side CD according to the ratio of the areas of the two triangles ABC and ABD. (See Fig. 2).

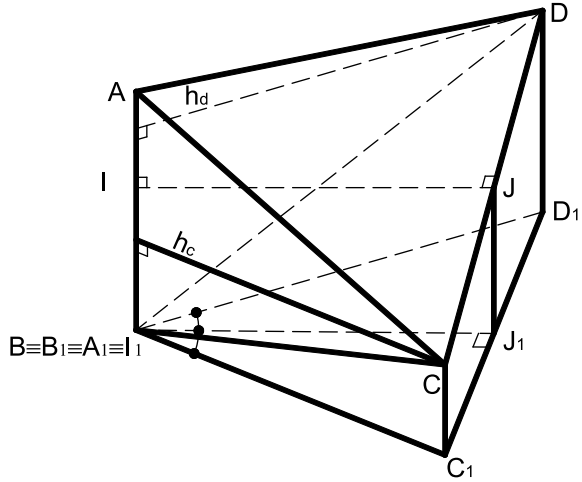
We project the Thd ABCD on the plane that passes through point B and is perpendicular to side AB. The Prj of two points A and B are points  $A_1$  and  $B_1$ . They coincide with point B. The prj of two points C and D are points  $C_1$  and  $D_1$ .

The bisector of the dihedral angle of side AB intersects CD at point J. The prj of point J is point  $J_1$ . Obviously,  $BJ_1$  is the bisector of angle  $C_1BD_1$ .

The altitude of triangle ABC is hc and the altitude of triangle ABD is hd.



Fig. 2 Thd ABCD



We have:

$$\frac{JC}{JD} = \frac{J_1C_1}{J_1D_1} = \frac{BC_1}{BD_1} = \frac{h_c}{h_d} = \frac{S_{ABC}}{S_{ABD}}$$

$S_{ABC}$  is the area of triangle ABC.

$S_{ABD}$  is the area of triangle ABD.

If the area of triangle ABC is equal to the area of triangle ABD, then J is the midpoint of CD. Therefore,  $BJ_1$  is both the median and the bisector at the vertex B of the triangle  $C_1BD_1$ . So, triangle  $C_1BD_1$  is isosceles triangle at the vertex B.

Hence, we have:

$$BJ_1 \perp C_1D_1$$

Construct a straight line IJ perpendicular to AB. Point I belongs to AB.

Right angle  $C_1J_1B$  is the projection of angle  $CJI$ .

$$IJ // (BC_1D_1) \Rightarrow CJ \perp IJ.$$

So, IJ is the common perpendicular line of AB and CD. Point I is also the midpoint of AB. IJ is the symmetry axis of the tetrahedron.

$\Rightarrow AD = BC, AC = BD$ . Because they are symmetric about IJ. (See Fig. 3).

Therefore if 4 faces of a tetrahedron have the same area, the Thd will have 3 symmetry axes. Those are the lines connecting the midpoints of the opposite sides. We have:

$$AB = CD; AD = BC; BD = AC.$$

**Fig. 3** AB and CD are symmetrical about IJ

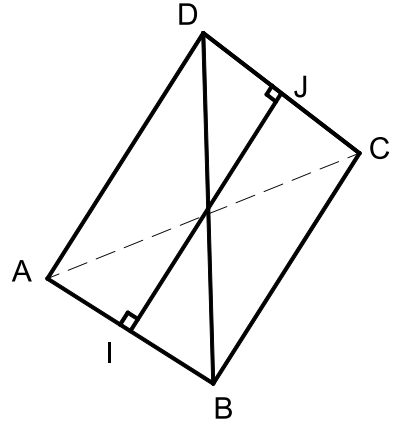
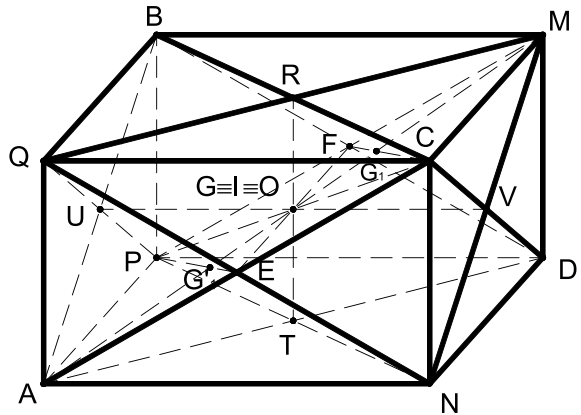


**Fig. 4**  $G \equiv I \equiv O$



Thus, the Thd is a disphenoid.

Note: Point O is the centroid of Dpd ABCD. The vertices M, N, P, and Q are symmetrical to the points A, B, C, and D through the centroid O. So, the tetrahedron MNPQ is symmetrical to the Dpd ABCD through point O.

Let I and G be the center of the sphere inscribed and circumscribed of Dpd ABCD, then the three points O, G, and I coincide.

**Conclude:** The centers in the circumscribed and inscribed spheres coincide with the centroid of the Dpd (See Fig. 4).

### 3 Some Applications of Dpd

The Thd is widely used in Engineering. For example:

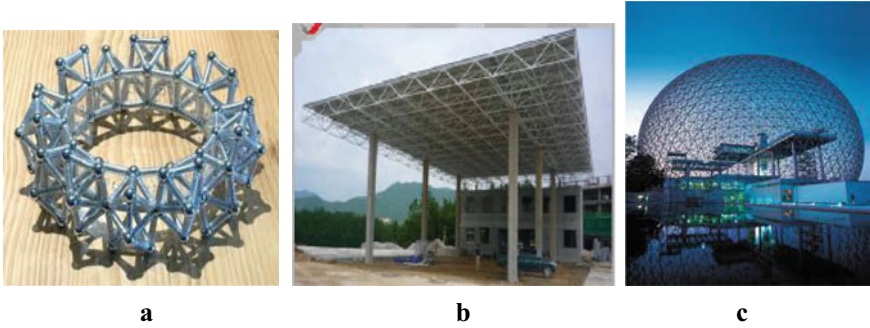


**Fig. 8** The snub Dpd in engineering

Applications in Mechanics (Fig. 8a) [2], applications in steel structure (Fig. 8b) [3], application in architecture (Fig. 8c) [4].

## 4 Conclusion

The Th is the most basic polyhedron for creating complex polyhedra. It is widely used in engineering. The study of its properties helps to calculate the design and make drawings quickly and accurately. This study aims to show and further demonstrate some new properties of it.

## References

1. Desphenoid—Wikipedia, the Free Encyclopedia, p. 1. lines 2 and 3 <https://en.wikipedia.org/wiki/Disphenoid>
2. <http://rm.geomagmasters.com/bj84.html>. Copyright © Rafael Millán, 2006–2008, The ring, found by Karl Horton
3. Jaingsu Andy steel structure
4. *The Montreal Biosphere* (Quebec, Canada, 1967)
5. H. Long, T.L. Banh, Graphics 1 (Publishing house of Hanoi University of Science and Technology, 2016)
6. H. Long, T.L. Banh, Graphics 2 (Publishing house of Hanoi University of Science and Technology, 2016)
7. V.T. Hoang, D.N. Kim, D.T. Tho, *Descriptive Geometry* (Science and Technology Publishing House, 2005)

# Motion and Condition Monitoring of an Industrial Robot Based on Digital Twins



**Nguyen Nguyen, Chu Anh My, Chi Hieu Le, Nikolay Zlatov, Georgi Hristov, James Gao, Ho Quang Nguyen, Jamaluddin Mahmud, Trung Thanh Bui, and Michael S. Packianather**

**Abstract** This paper presents a study and experimental evaluations of monitoring industrial robots based on a digital twin system, with the focus on motion monitoring and condition monitoring. Motion monitoring aims to detect, monitor, and control motion and speed, especially evaluation of the working area and determination of the motion trajectory of a robot. Condition monitoring aims to evaluate the health state during operation, to determine the condition of in-service equipment or systems, in order to predict the health and safety for predictive maintenance, and to estimate the remaining useful life of in-service equipment or systems. The conceptual digital twin system is deployed on the Game Engine Unity3D which has an intuitive user interface, with the emerging 3D graphics technologies, and the capability of providing the bidirectional connection between the virtual robot and the real robot. The proof-of-concept prototype for the proposed conceptual digital twin system was successfully developed for the basic tests and investigations, as the foundation for

---

N. Nguyen · C. A. My (✉)

Institute of Simulation Technology, Le Quy Don Technical University, Hanoi, Vietnam  
e-mail: [myca@lqdtu.edu.vn](mailto:myca@lqdtu.edu.vn)

C. H. Le · J. Gao

Faculty of Science and Engineering, University of Greenwich, Kent ME4 4TB, UK

N. Zlatov

Institute of Mechanics, Bulgarian Academy of Sciences, 1113 Sofia, Bulgaria

G. Hristov

University of Ruse “Angel Kanchev”, 8 Studentska Street, 7004 Ruse, Bulgaria

H. Q. Nguyen

Institute of Engineering and Technology, Thu Dau Mot University, Binh Duong, Vietnam

J. Mahmud

College of Engineering, Universiti Teknologi MARA, Shah Alam, Selangor, Malaysia

T. T. Bui

Hung Yen University of Technology and Education, Hung Yen, Vietnam

M. S. Packianather

School of Engineering, Cardiff University, Cardiff CF24 3AA, UK

further development of the cost-effective digital twin models and systems which can be used for higher educations or research, with potentials for industrial applications.

**Keywords** Digital twin · Condition monitoring · Motion monitoring · Industrial robot · Unity3D · Smart manufacturing · Industry 4.0

## 1 Introduction

The applications of industrial robots (IRs) have been well-documented, and today IRs plays an important role in automation of manufacturing processes and enhancement of productivity and efficiency, with a consistent quality of manufactured. Especially, IRs have capabilities of operating in harsh environments, with the high working intensity and long working hours. Under the impacts of Smart Manufacturing and Industry 4.0, the importance of IRs and collaborative robots is more and more increased, and they are one of the key functional elements of smart manufacturing systems. However, the risks of failure always exist in products, machines, equipment and engineering systems, including the robots. There have been efforts to develop solutions for evaluating, preventing and correcting the failures, including the failure mode and effect analysis (FMEA), risk management strategies, and maintenance plans such as preventive maintenance, corrective maintenance, condition-based maintenance and predictive maintenance. In this way, with the well-recognized importance and roles of IRs in the modern manufacturing systems, there is an emerging need of developing effective monitoring solutions, especially motion monitoring and condition monitoring of IRs. Motion monitoring aims to detect, monitor, and control motion and speed, especially evaluation of the working area and determination of the motion trajectory of a robot. Condition monitoring aims to evaluate the health state during operation, to determine the condition of in-service equipment or systems, in order to predicts the health and safety for predictive maintenance, and to estimate the remaining useful life of in-service equipment or systems.

There were studies about applications of the Internet of things (IoT) and smart sensor technologies for remotely monitoring and controlling industrial robots [1–6]. In terms of virtual or digital simulations, the monitoring of industrial robots can be performed on the Robot Operating System (ROS) environment and Unity3D [7, 8]. In recent years, Digital Twin (DT) has emerged as a potential technology for controlling and monitoring industrial robots, based on the capability of integrating the real and virtual environments, the ability to pre-build simulation scenarios [9–11]. The DT technologies have been successfully developed and applied with a wide range of applications, with participations from the hi-tech companies and corporations, including General Electric, Siemens, Microsoft, Ansys, IBM and Bosch.

In the areas of IR monitoring, researchers developed the DT systems for the real-time monitoring of the energy consumption, manipulations of complex tasks, and collision detections [5, 12, 13]. Choi et al. [13] described development of the DT model for an integrated surveillance system, with the use of edge devices, data

analysis, and realistic 3D visualization [13]. Stan et al. [14] developed the DT-based platform for remotely monitoring the robotic workcell, especially to trigger alerts for unexpected events and to allow the control to authorized personnel [14].

The DT technologies allow to construct the exact replica in digital format of a physical object or system which can be a process, a product, or a service, or an engineering system; and the real-world data is used as the input for “real-time” simulations, to predict how a product, a system or process will perform. With the combination of real-time simulations and big data analytics, as well as Artificial Intelligence (AI) and Machine Learning (ML), we can obtain real-time monitoring and predictions of the behavior of a physical object, system or process. This leads to the useful applications of DT in applications of remotely monitoring and controlling industrial robots, especially motion monitoring and condition monitoring. In the area of predictive maintenance, DT technologies provide solutions for overcoming the challenges and limitations of corrective maintenance and preventive maintenance solutions. It is noted that, condition monitoring is an important component of predictive maintenance. Today, predictive maintenance plays an important role in maintenance, management and operation of equipment or engineering systems as well as manufacturing processes, especially to evaluate performance, anomaly detection, health monitoring, and the remaining useful life (RUL) prediction [15]. However, the integration of condition monitoring into the DT system has not been well-studied and applied in industrial practices [16].

This study proposes an investigation and demonstrations about the application of DT, with the focus on CM and motion monitoring of IRs, taking into account the emerging 3D graphics, data processing and simulation technologies.

The rest of the paper is organized as follows. Section 2 presents the development of a DT system for monitoring IRs, with the proposed framework for monitoring the performance and motions of IRs. Section 3 presents the experimental demonstrations and results, for the typical case of monitoring the RV12SD robot, based on the developed DT system presented in Sect. 2. Finally, Sect. 4 presents the summaries and conclusions.

## 2 Development of a Digital Twin System for Monitoring IRs

The framework for development of a DT system for monitoring IRs is basically presented in Fig. 1. The proposed DT system has the following fundamental elements: (i) a physical element which is the Mitsubishi RV-12SD robot with 6 degrees of freedom (DOF), (ii) a digital or virtual element which monitors, simulates and analyses the real-time data collected from the physical element, and (iii) a connection element which allows bidirectional exchanges and transfer of information and data between the physical and virtual elements of the DT system.

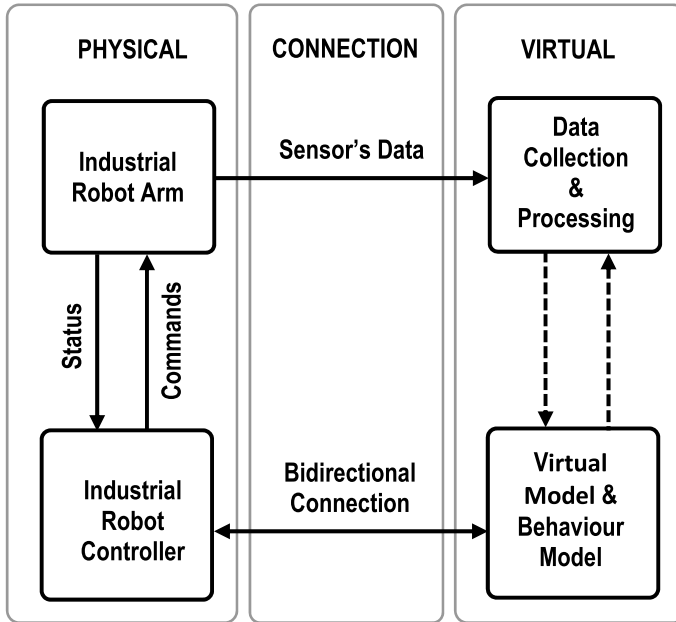


**Fig. 1** A framework for development of a DT system for monitoring IRs

### ***2.1 A Physical Element of the DT System***

The physical element is the industrial robot which is the Mitsubishi RV-12SD robot with 6 DOF. The industrial robot includes the following functional units: the robot arm or manipulator RV-12SD with 6 DOF, the teaching pedant and the controller CR3D-700, as shown in Fig. 2. The robot arm consists of 6 joints, with a maximum load of 12 kg and a maximum reach of 1086 mm.

### ***2.2 A Digital or Virtual Element of the DT System***

The digital element or virtual element of the DT system is used to monitor, simulate and analyze the data and information which are collected from the physical element. The digital element includes the following functional units: (i) the virtual model of the industrial robot, (ii) the behaviour model which is used to simulate the behaviour of the industrial robot during the task performance, and (iii) the data collection and processing unit which is used for bidirectional connections between the digital element and the physical element, as well as implementing the key data processing tasks.

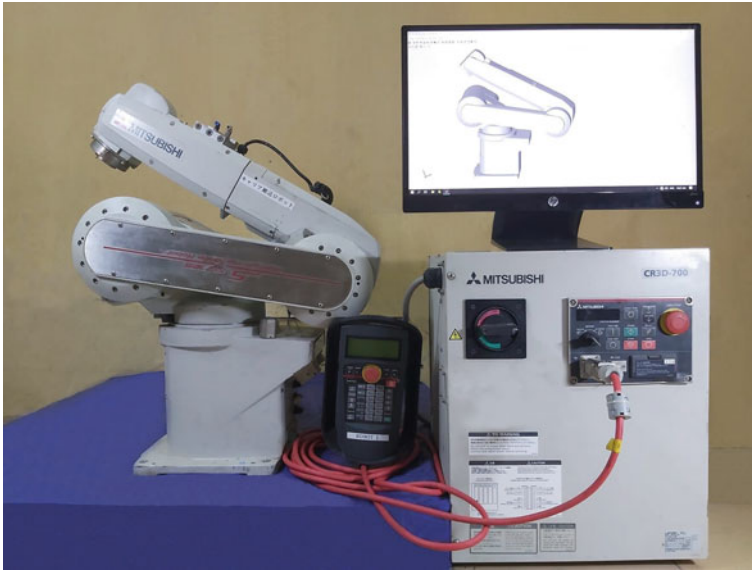


**Fig. 2** The functional units of the Mitsubishi RV-12SD robot with 6 DOF

The virtual model is a mirror that reflects the physical element in the virtual world, with the details of 3D CAD models of the IR, and information about the physics and dynamics of the IR. In this study, a virtual model of the IR was constructed, based on Reverse Engineering of the Mitsubishi RV-12SD robot.

The behaviour model in the virtual element of the DT system is used to simulate the robot's behaviour during the task performance, and to perform the kinematic and dynamic analysis tasks, especially to calculate the changes of the parts, the joints, and the end effector of the IR.

The data collection and processing unit is used to perform the tasks of data collection, data mining and features extractions, and finally to calculate and results in the necessary indicators and information about the behaviors of the whole DT system during the operations.

### ***2.3 The Connection Element of the DT System***

The bidirectional connection between the physical and virtual elements of a TD system plays a very important role. The controller of the Mitsubishi RV-12SD robot provides two methods for the communication: Ethernet (TCP/IP) and RS232. In this study, the communication via the use of the RS232 standard was used.



### 3 The Experimental Evaluation of the DT System

#### 3.1 The Experiment Set-Up

The Mitsubishi RV-12SD robot with 6 DOF was used as the key units of the physical element of the DT system (Fig. 2). The Mitsubishi RV-12SD robot consists of 6 joints with 6 AC servo motors. Figure 3 presents the experiment set-up for demonstration of the DT system. Figure 4 presents the DT system with the interfaces for control and monitoring the industrial robot.

As the electronic-mechanical system, there are two types of errors that may occur for the IR, including the electrical failure and the mechanical failure. The electrical failure is normally related to the AC servo motors, and the current signal is used to assess the issues related to the electrical failure. The failures related to mechanical parts are normally detected based on analysis of the temperature, vibration and acoustic signals. In this study, the current signal is collected from the AC servo motors, then to calculate the necessary indicators and information about the behaviors of the RI during the operations. The robot's motion trajectory is monitored based on the execution of control commands to perform the specific tasks.

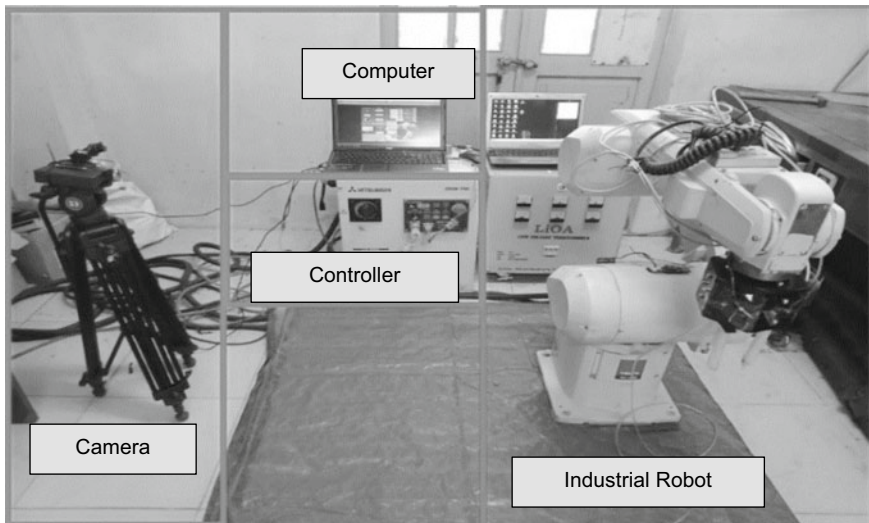


**Fig. 3** The experiment set-up for demonstration of the DT system

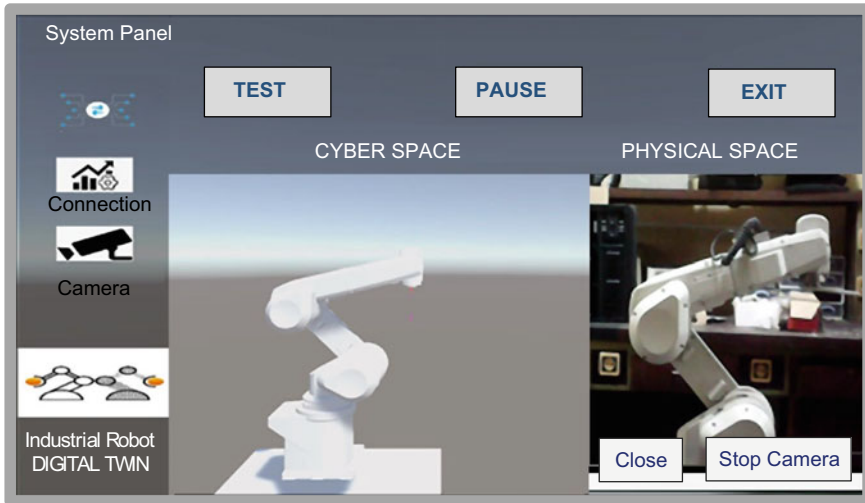


Fig. 4 The Digital Twin system with the interfaces for control and monitoring the IR

### 3.2 Data Collection and Processing

The first experimental evaluation of the DT system is to test and evaluate the capability of data collection and processing. The AC current sensor SCT013 (100 A/1 V) was used to measure the current of the AC Servo motors. The sensor SCT013 provides the non-contact measurement, in which the input signal is the alternating current, and the output signal is the current mA or the voltage V. The following are the specific steps of collecting and processing the sensor data, including 3 main steps: data collection, feature extraction, and evaluation of the system health with the health indicators.

- **STEP 1: Data collection from the physical element—the industrial robot**

The sensor SCT013 is used to measure the current of 06 AC servo motors of the RV-12SD robot. The output of the sensor is an analog signal that is put into the analog pin of the microcontroller for reading. The microcontroller is an Arduino Mega2560 which has 6 analog-read pins A0-A5. Arduino Mega2560 is connected to the computer via USB port. The data is saved and stored as the \*.csv or \*.txt file for processing and creating the robot operating data set. Figure 5 presents a functional diagram of the sensor data acquisition module.

- **STEP 2: Feature Extraction from the collected data**

Figure 6 represents the data collection & analysis interface of the DT system for monitoring the IR. After the data is collected, there are many data processing techniques that can be used for the feature extraction. It is noted that, selection of the most suitable method for each specific task is a major challenge in the condition

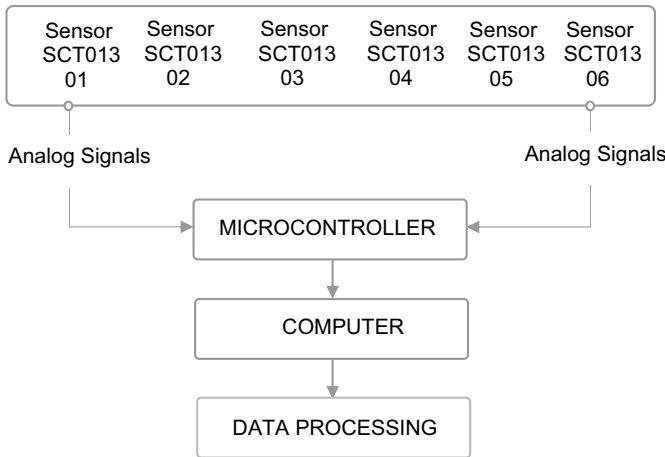


Fig. 5 A functional diagram of the sensor data acquisition module

monitoring of the IR. The signal processing techniques are classified, based on the use of the time domain, the frequency domain and the time–frequency domain methods.

The time-domain method directly processes the raw data without being transformed into another domain. Statistical features from the time domain include RMS (Root Mean Square), Mean, STD (Standard Deviation), Skewness, and Kurtosis. These features are suitable for error detections; however, they are not capable of diagnosing the errors.

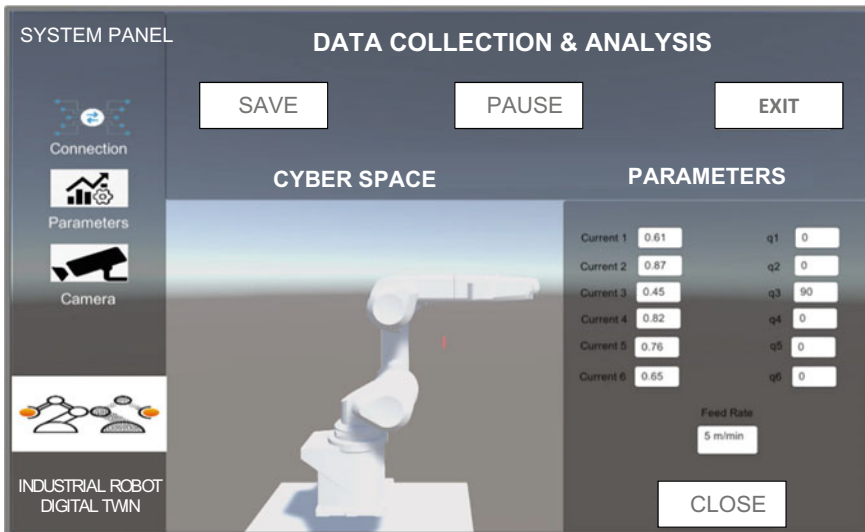


Fig. 6 The data collection & analysis interface of the DT system for monitoring the IR

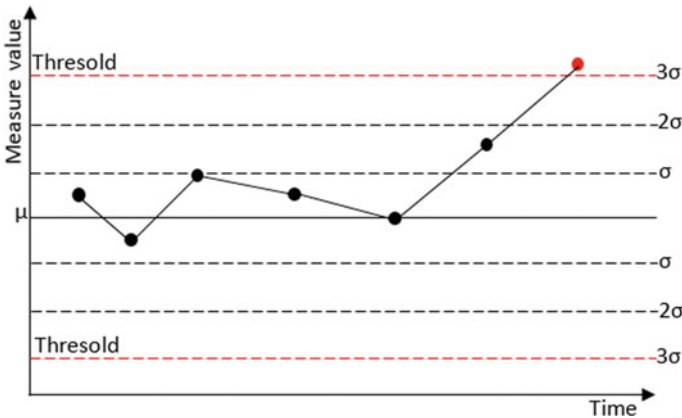


Fig. 7 The anomaly detection rule for evaluation of the system health

• **STEP 3: Evaluation of the system health with the health indicators**

The Nelson method [17] uses the mean value and standard deviation to determine if a measured variable is out of control or presents a trend. The real-time data collection and analysis module is used to monitor the system health, detect the anomalies, diagnose and predict the faults, and optimize the system operations.

The condition monitoring rule detects the current abnormality when the current value is greater than the threshold (the mean + 3 standard deviations). This rule performs two tasks, including (i) to compare with the thresholds which are established from the previous operations to generate the relevant alarms, and (ii) to perform the data processing to determine the service thresholds for subsequent operations. The main objective is to obtain the real-time monitoring of the system health of the IR. However, it is necessary to create a standard operating data set when the IR performs the specific tasks, and this data set will be used to calculate the mean, standard deviation, and to determine the threshold before getting the real-time monitoring. The data is saved as a training dataset for the next operation of the IR. Collecting and processing data in such a sequential manner forms the full operational log of a robot, or an entire production line. This database can be used as a training dataset for the artificial intelligence algorithms, to calculate the remaining useful life (RUL). Figure 7 presents the diagrams of the anomaly detection rule.

**3.3 Monitoring the Robot Motions**

Welding is the typical application of the IR. In the welding tasks, the exact determination of the welding trajectory is very important; and this depends on the accuracy

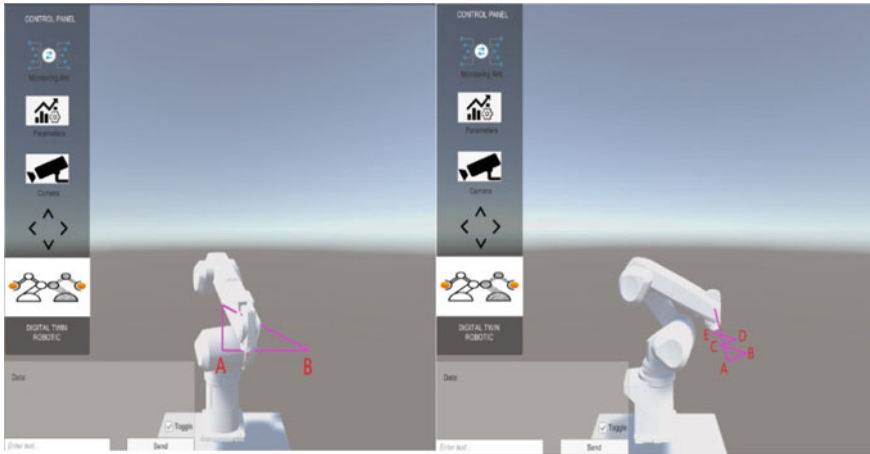


**Fig. 8** Simulations of the robot motions, with the trajectory from A to B & E

of the welding workpiece and the experience of the programmer. The use of simulation for evaluation of the welding trajectory is therefore necessary and important to obtain the expected quality of the welding operation.

Figure 8 presents the tests and simulations of the robot motions, with the trajectories from A to B and from A to E, with the detailed positions as follows:

- TEST 01 with the start point at (370.0, 0.00, 690.0):
  - Point A: (370.0, 0.00, 500.0)
  - Point B: (370.0, 500.0, 500.0)
- TEST 02 with the start point at (370.0, 0.00, 690.0):
  - Point A: (370.0, 0.00, 500.0)
  - Point B: (400.0, 100.0, 500.0)
  - Point C: (370.0, 200.0, 500.0)
  - Point D: (400.0, 300.0, 500.0)
  - Point E: (370.0, 400.0, 500.0)

The experimental evaluation of the robot motions aims to evaluate the motion performance when moving to the predetermined points. The developed DT system can be used to simulate and program the robot to move with the different trajectories, including the complex curves such as Bezier, Spline and NURBS (Non-uniform rational basis spline), and the simulated results can be used for programming on real robots. Finally, the analysis of the motion trajectory via the use of simulations in the developed DT system can be used for evaluation of robot safety and collision detections.

## 4 Summary and Conclusions

In this paper, a study and experimental evaluations of monitoring industrial robots based on a digital twin system were presented and discussed, with the focus on motion monitoring and condition monitoring which play an important role in operations, control and management of production systems in general and manufacturing processes in particular, especially under the impacts of Smart Manufacturing and Industry 4.0 [18, 19, 20]. The conceptual DT system is deployed on the Game Engine Unity3D which has an intuitive user interface, with the emerging 3D graphics technologies, and the capability of providing the bidirectional connection between the virtual robot and the real robot. The proof-of-concept prototype for the proposed conceptual digital twin system was successfully developed for the basic tests and investigations. The monitoring process was demonstrated, including data collection and visualization of the data from the sensors, feature extraction, and evaluation of the system health with the health indicators of the IR, as well as to build a database of robot activities. The sensors SCT013 are used to measure the current of 6 AC servo motors of the RV-12SD robot with 6 DOF, in which in which the input signal is the alternating current, and the output signal is the current mA or the voltage V. The motion monitoring is done via monitoring the motion trajectories of the IR, to determine the IR's workspace, and to support programming of the complex trajectories. The proposed conceptual DT system has potentials for applications of evaluating the remaining useful life of the RI, robot safety and collision detections; and it can be used as the foundation for further development of the cost-effective DT models and systems which can be used for higher educations or research, with potentials for industrial applications.

**Funding Information** This work was supported by the Vingroup Innovation Foundation (VINIF) annual research support program under Grand VINIF.2019.DA08.

## References

1. P. Brizzi, et al.: Bringing the internet of things along the manufacturing line: a case study in controlling industrial robot and monitoring energy consumption remotely. In: *IEEE 18th Conference on Emerging Technologies and Factory Automation (ETFA)*, (2013). <https://doi.org/10.1109/ETFA.2013.6647947>
2. R.A. Atmoko, D. Yang.: Online monitoring and controlling industrial arm robot using MQTT protocol. In: *2018 International Conference on Robotics, Biomimetics, and Intelligent Computational Systems*. (Bandung, Indonesia, 2018). <https://doi.org/10.1109/ROBIONETICS.2018.8674672>
3. J. Kim, et al.: Real-time monitoring and control system of an industrial robot with 6 degrees of freedom for grinding and polishing of aspherical mirror. In: *International conference on electronics, information, and communication (ICEIC)*, (2018). <https://doi.org/10.23919/ELINFOCOM.2018.8330691>
4. M. Vanitha, et al.: Monitoring and controlling of mobile robot via internet through raspberry PI Board. In: *Second International Conference on Science Technology Engineering and Management (ICONSTEM)*, (2016). <https://doi.org/10.1109/ICONSTEM.2016.7560864>

5. K. Yan et al., Digital Twin-based energy modeling of industrial robots. *CCIS* **946**, 333–348 (2018)
6. M.M. Lutovac, Remote monitoring and control of industrial robot based on android device and wi-fi communication. *Automatika* **56**(3), 281–291 (2015)
7. J. Pan, et al.: Research on simulation system of welding robot in Unity3D. In: *Proceeding of the 15th ACM SIGGRAP Conference on Virtual-Reality Continuum and its Applications in Industry—Volume 1*, (2016), pp. 107–110. <https://doi.org/10.1145/3013971.3013982>
8. E. Sita, et al.: ROS-Unity3D based system for monitoring of an industrial robotic process. In: *IEEE/SICE International Symposium on System Intergration (SII)*, 2017. <https://doi.org/10.1109/SII.2017.8279361>
9. M.D. Vu, et al.: A conceptual digital twin for cost-effective development of a welding robotic system for smart manufacturing. In: *Proceedings of the 2nd Annual International Conference on Material, Machines and Methods for Sustainable Development (MMMS2020)*, pp. 1018–1025
10. M.D. Vu, et al.: Design and implementation of a digital twin to control the industrial robot Mitsubishi RV-12SD. In: *Advances in Asian Mechanism and Machine Science*, pp.422–432
11. F. Tao, M. Zhang, A.Y.C Nee.: *Digital Twin Driven Smart Manufacturing*, 1st edn. (Elsevier, 2019). ISBN: 9780128176306
12. X. Zong et al., A multi-robot monitoring system based on digital twin. *Procedia Comput. Sci.* **183**, 94–99 (2021)
13. S. Choi et al., Digital Twin-based integrated monitoring system: Korean application cases. *Sensors* **22**(14), 5450 (2022). <https://doi.org/10.3390/s22145450>
14. L. Stan, et al.: Digital Twin and web services for robotic deburring in intelligent manufacturing. *J. Intell. Manuf.* (2022). <https://doi.org/10.1007/s10845-022-01928-x>
15. R. van Dinter et al., Predictive maintenance using digital twins: a systematic literature review. *Inf. Softw. Technol. Softw. Technol.* **151**, 107008 (2022). <https://doi.org/10.1016/j.infsof.2022.107008>
16. H. Liu, et al.: Digital Twin-driven machine condition monitoring: a literature review. *J. Sens.* (2022)
17. L.S. Nelson, The Shewhart control chart-tests for special causes. *J. Qual. Technol.* **16**(4), 237–239 (1984). <https://doi.org/10.1080/00224065.1984.11978921>
18. D. Arey, C.H. Le, X. Gao, Lean industry 4.0: a digital value stream approach to process improvement. *Procedia Manuf.* **54**, 19–24 (2021). <https://doi.org/10.1016/j.promfg.2021.07.004>
19. C.H. Le, et al.: Challenges and conceptual framework to develop heavy-load manipulators for smart factories. *Int. J. Mechatron. Appl. Mech.* (8), 209–216 (2020)
20. F. Pires, et al.: Digital Twin experiments focusing virtualisation, connectivity and real-time monitoring. In: *2020 IEEE Conference on Industrial Cyberphysical System (ICPS)*, (2020). <https://doi.org/10.1109/ICPS48405.2020.9274739>

# Novel Exoskeleton Design of Lower Limb Rehabilitation Robot Using Pneumatic Cylinder



Van-Thuc Tran and Tuan-Anh Bui

**Abstract** Many people nowadays suffer physical limits because of spinal cord injury, stroke, or an accident. Lower limb difficulties are a major source of disruption in these people's everyday lives. Many assistance devices for lower limb movement have been developed to help people with their daily duties. This study introduced a novel exoskeleton design based on a pneumatic cylinder for a lower limb rehabilitation robot. The pneumatic cylinder system was used as the actuators to implement the robot movement and to ensure operational safety, rapid point-to-point movement, and cleanliness for rehabilitation. The results showed that the lower limb gait training robot was developed with parallelogram mechanism and a suggested control system can be utilized to satisfy the gait training robot requirements.

**Keywords** Gait training system · Health-care system · Pneumatic cylinder · Modeling

## 1 Introduction

Physical Rehabilitation aim's maximizing the opportunity of a person who has suffered some type of illness that happen to muscles due to an accident. Working in rehabilitation procedures affects the independence and quality of life of people living with brain and/or muscular injuries [1].

Recent research has demonstrated that extensive, repetitive, task-specific training can help to improve the mobility constraints of robotic exoskeletons, resulting in considerable gains in quality of life [2]. Many types of equipment are being developed to aid in the rehabilitation process. Most systems have direct contact with the patient and hence rely heavily on a comfortable design that is decided by its form and functionality. It is critical to consider safety when interacting with a rehabilitation

---

V.-T. Tran · T.-A. Bui (✉)

School of Mechanical Engineering, Hanoi University of Science and Technology, No. 1, Dai Co Viet Rd., Hanoi, Vietnam

e-mail: [anh.buituan@hust.edu.vn](mailto:anh.buituan@hust.edu.vn)



robot and a patient, which is especially significant when the individual has a neurological disorder. It is feasible to maintain a safe interaction by controlling the actuators or by utilizing safe actuators to avoid unwanted forces created by the robot's activity. This means that the natural compliance of the actuators should provide intrinsic safety and allow for a gentler and more comfortable human–robot connection.

Pneumatic actuators are a viable solution for adding safety to a robot's functioning. The most common pneumatic actuator is McKibben artificial muscle which is made up of two main components sealed at both ends: an outer shell made of nylon mesh, and rubber tubes as inner [3]. The artificial muscle actuator has some advantages such as very high power/mass ratio, a flexible mechanism, and therefore easily applied in biomedical and rehabilitation equipment. However, the rehabilitation system using artificial muscle actuators would have some major disadvantages such as: poor reliability, strong nonlinearity of the actuators then controllable difficulty.

Pneumatic cylinder actuator has outstanding advantages in stability and reliability in comparison with the artificial muscle. Rapid point-to-point positioning [4], ease of maintenance, safety, cleanliness, and simple operating mechanisms [5, 6] are all advantages of this actuator. It could also absorb unwanted forces because its primary energy source is air. In this study, authors presented a novel of exoskeleton design for lower limb rehabilitation robot using cylinder. The suggested architecture was mathematically modeled using energy model. The open loop and simple close loop control system was simulated and compared.

## 2 Mechanical System Design

Basically, the gadget was founded on fundamental geometrical mathematics and the Vietnamese human anthropometric approach, Economy, which was based on the correlation of gait movement and angular kinematics of the human leg [7, 8]. According to research on human anthropometry in Vietnam (in 2022) [9], the average leg length and weight of Vietnamese individuals is 84 cm and 56 kg. Winter et al. indicated that the human leg segments could be calculated based on the human height or leg length [10]. In this study, the basic dimensions of the lower limb rehabilitation robot were selected as showed in Fig. 1, but adjustable:

The dimension of the hip joint and knee are visible in the Fig. 1:

- A Femur is a bone that extends from the hip to the knee joint and has a flexion operating angle of  $\alpha = (\alpha_3; \alpha_1) = (20^\circ; 30^\circ)$ .
- The stitch from the knee joint to the ankle is 38.05cm long, and the flexion operating angle is  $\beta = (\beta_1; \beta_2) = (0^\circ; -50^\circ)$ , which is called the 'Shin bone'.
- For design, quadrangular parallelism in the form of a pneumatic cylinder mechanism is used.

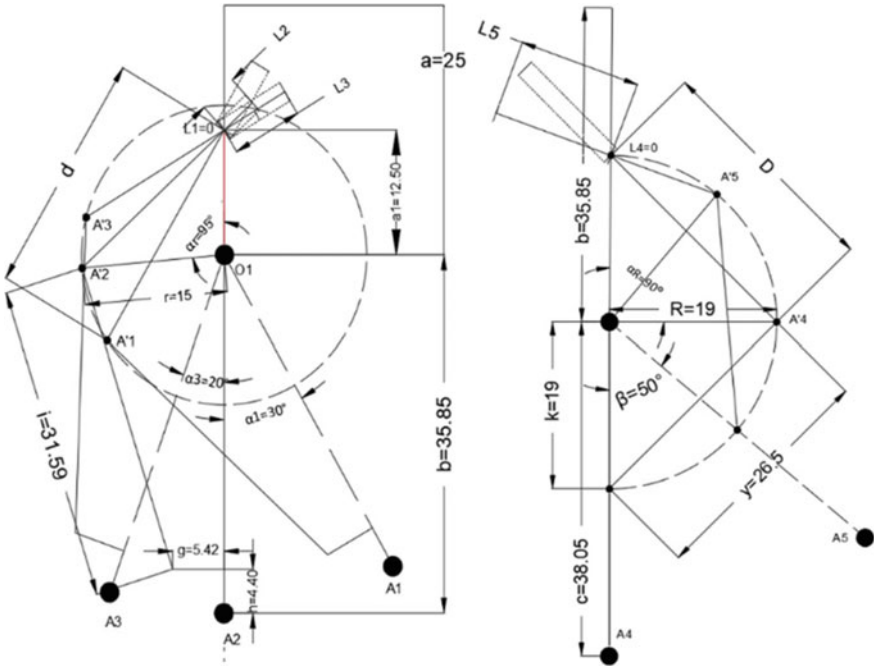


**Fig. 1** The model calculated the approximate length and dimensions of the hip and knee joints of the lower limb rehabilitation robot

### 3 Mathematical Modeling

In this study, rather than traditional force analysis, energy analysis is used to construct the actuator model. To put it another way, the kinetic and potential energy is extracted, to combine them to get the actuator’s Lagrange, and then utilize the Euler–Lagrange equation to obtain the proper equation of motion.

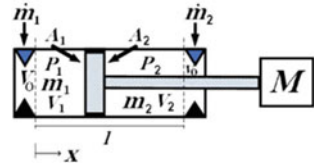
The Euler–Lagrange equation of motion (sometimes known as the Lagrange equation) is defined which based on the working principle of a pneumatic cylinder in Fig. 2 as,

$$\frac{d}{dt} \frac{\partial L}{\partial \dot{x}} - \frac{\partial L}{\partial x} = 0 \tag{1}$$

where  $x$  is the system’s state,  $t$  is the time,  $L$  is Lagrangian which is determined by the kinetic energy and potential energy. In the case of the actuator,  $x$  and  $\dot{x} = \frac{dx}{dt}$  denote the piston’s displacement and velocity, respectively.

The Lagrangian equation of motion of an ideal actuator, which is a frictionless actuator acting under zero external force, is derived, and is obtained by equation:

**Fig. 2** A piston separates a closed volume container into two chambers and connects it to mass M



$$L(x, \dot{x}) = \frac{1}{2}M\dot{x} + RT \left[ m_1 \ln \left( \frac{A_1 x}{V_0} \right) + m_2 \ln \left( \frac{A_2 (l-x)}{V_0} \right) \right] \tag{2}$$

The result of carrying out the derivatives in the Euler–Lagrange Eq. (1) is.

$$M\ddot{x} - RT \left( \frac{m_1}{x} - \frac{m_2}{l-x} \right) = 0 \tag{3}$$

After denoting  $\zeta$  as the Potential energy, and the mass flow rate as a linear model with the control signal  $\dot{m} = \alpha_i u_v + \beta_i$  [11]. The state space form is defined as follows:

$$f(x) = \begin{bmatrix} \dot{x}_1 \\ \dot{x}_2 \\ \dot{\zeta} \end{bmatrix} = \begin{bmatrix} x_2 \\ \frac{1}{M}\zeta \\ \left( \frac{\beta_1}{x_1} - \frac{\alpha_2}{l-x_1} - x_2 \left( \frac{m_1}{x_1^2} - \frac{m_2}{(l-x_1)^2} \right) \right) RT \end{bmatrix} + \begin{bmatrix} 0 \\ 0 \\ -RT \left( \frac{\alpha_1}{x_1} - \frac{\alpha_2}{l-x_1} \right) \end{bmatrix} \tag{4}$$

where,  $\dot{x}$  is the velocity and  $\ddot{x}$  is the acceleration of the load M.

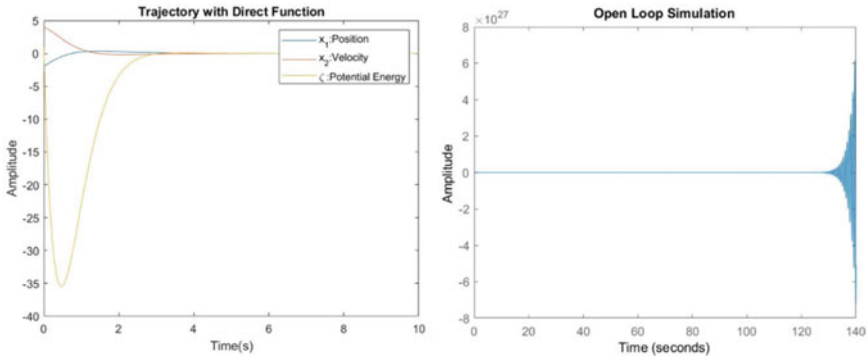
In Table 1, some parameter values are used to determine the values of the dynamic system.

**Table 1** The table of parameter values of the real system

Parameter	Value
R	8.314 J mol <sup>-1</sup> K <sup>-1</sup>
$\beta_1$	5 * 10 <sup>-4</sup>
$\beta_2$	5 * 10 <sup>-4</sup>
T	298 K
$m_1$	5.68 * 10 <sup>-4</sup> kg
$m_2$	5.13 * 10 <sup>-4</sup> kg
M	10 kg
l	0.115 m
$\alpha_1$	- 0.004736
$\alpha_2$	0.004736

### 4 Results and Discussions

The simulation results were shown in Fig. 3. State variables  $x_1$  and  $x_2$  reach the equilibrium point in about 1.2 s, whereas  $\zeta$ , which was known as the cylinder's potential energy, reaches the equilibrium point in around 3 s. Following that, the open loop system represented the system model was unstable. The simulation of the stable close loop system with the pole placement strategy was shown in Fig. 4.



(a) The trajectory with Direct Function. (b) Open-Loop Simulation Result

**Fig. 3** The simulation results with Dirac function of each state variable with given initial values and the open-loop simulation result

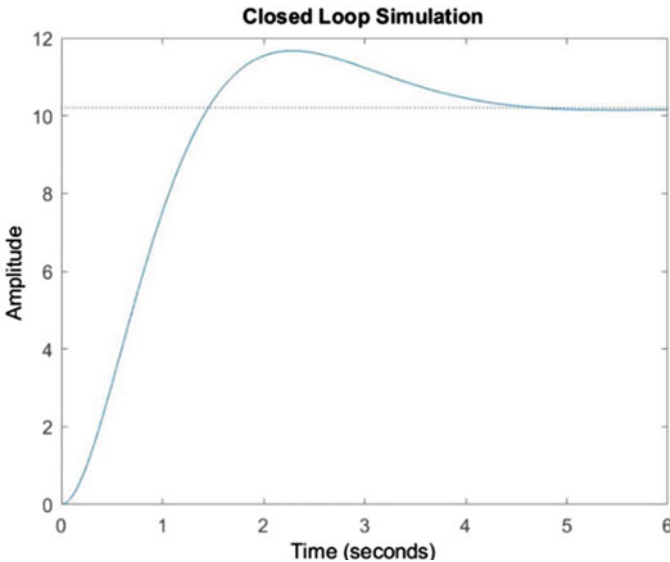


**Fig. 4** The simulated of the close loop with the pole placement strategy

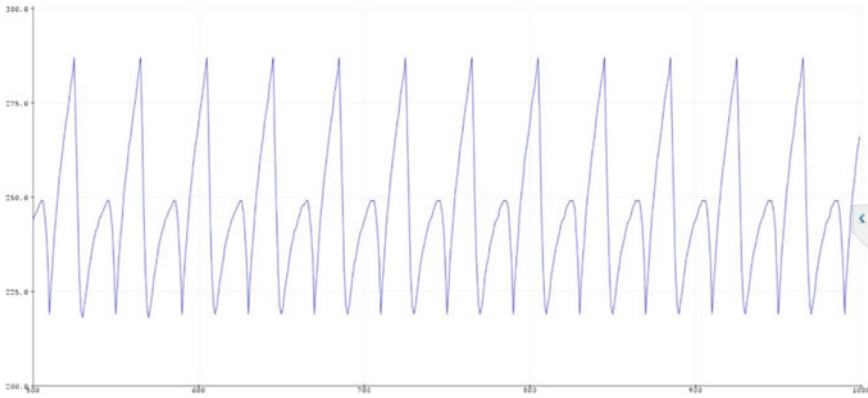


**Fig. 5** The actual raw data of the knee joint

The experiment was set up using Arduino Uno based on the Microchip ATmega328P, a micro-controller. The proportional directional control valve (MPYE-5-1/8-hf-010-b) was used to generate the desired air flow rate with the voltage range of 0–10 V. On Fig. 5, the actual raw data of the knee joint was shown. We can see the control strategy was successfully generated the requirement joint trajectory of knee joint. The result showed the potential application of the mechanical design and the control system design in lower limb rehabilitation robot.

The Pole Placement method is one of the most important and widely used control strategies for solving a wide range of control issues in many different engineering domains. Because of its intuitive appeal and clear algorithmic structure, synthesis of the pole placement controllers, in which the closed-loop eigenvalues are put in some given position in a complex plane to match a set of performance parameters, has proven particularly popular for linear systems.

## 5 Conclusion

This paper described the mechanical design, mathematical modeling, and control system design concept for a Novel Exoskeleton Design Using Pneumatic Cylinder for Lower Limb Rehabilitation Robot. A proposed design was made to assist a patient's lower limb. The Euler–Lagrange equation was used for mathematical modeling, which was combined with energy modeling. Following the calculation of the fixed point in Matlab, the suggested control system architecture was simulated. Then, another simulation was run to determine if the open-loop or closed-loop architecture is preferable. Following that, the pole placement technique could be chosen as the controlling method. The experiment results showed the potential application of the mechanical design and the control system design in the lower limb rehabilitation robot. In future work, after completing the design of the control system in Matlab,

a comparison of the outcomes of the simulated model and the actual whole system will be performed.

**Acknowledgements** This research is funded by Hanoi University of Science and Technology (HUST) under project number T2022-PC-021.

## References

1. M. Cardol, et al., On autonomy and participation in rehabilitation. **24**(18), 970–974 (2002)
2. S. Mazzoleni, et al., An integrated gait rehabilitation training based on functional electrical stimulation cycling and overground robotic exoskeleton in complete spinal cord injury patients: preliminary results. In: *2017 International Conference on Rehabilitation Robotics (ICORR)*. (IEEE, 2017)
3. T. Van Thuc, S. Yamamoto, Development of a body weight support system using pneumatic muscle actuators: controlling and validation. *Adv. Mech. Eng.* **8**(12) (2016)
4. J. Wang, et al., Identification of pneumatic cylinder friction parameters using genetic algorithms. **9**(1), 100–107 (2004)
5. F. Soleymani, et al., Position control of a servo-pneumatic actuator with mis-matched uncertainty using multiple-surface sliding mode controller and high-gain observer. **39**(10), 1497–1508 (2017)
6. H. Cherrid, et al., Sliding mode observer based controller for a robot with pneumatic actuators. In: *ECPD, International Conference on Advanced Robotics, Intelligent Automation and Active Systems*. (Moscow, 1998)
7. M.W. Whittle, *Gait Analysis: An Introduction*. (Butterworth-Heinemann, 2014)
8. S.M. Elhafez et al., Percentage contribution of lower limb moments to vertical ground reaction force in normal gait. *J. Chiropr. Med. Chiropr. Med.* **18**(2), 90–96 (2019)
9. Survey results of some anthropometric indicators (static indicators) of Vietnamese people of working age in the current period—institute of occupational safety and health. [http://vnniosh.vn/chitiet\\_NCKH/id/31322/](http://vnniosh.vn/chitiet_NCKH/id/31322/)
10. D.A. Winter, *Bio-mechanics and Motor Control of Human Movement*. (Wiley, 2009)
11. E. Zisser, et al., Position control of a pneumatic actuator under varying external force. **22**(4), 1157–1174 (2018)

# Development of an Automated Electronic Toll Collection System Based on Deep Learning



Thi Thoa Mac

**Abstract** Road toll collection is an indispensable activity of a country, contributing to offset construction costs as well as having more capital to improve road construction. Therefore, the construction of toll stations is mandatory. In order to achieve the highest satisfaction of traffic participants and transport businesses, reduce traffic congestion at toll stations, minimize environmental pollution, we develop a real-time automatic toll collection systems based on deep learning. Our system consists some of advanced technology methods includes: (i) The development of YOLOv5 to detect the car license plate; (ii) The implementation of PaddleOCR to recognize the number license plate; (iii) The development of Web Server to manage the system; (iv) the development of lab-scale express highway used Vietnam Electrical Toll Collection (VETC) to ensure transparency in the toll collection.

**Keywords** Toll collection · YOLOv5 · PaddleOCR · RFID · VETC

## 1 Introduction

Vietnam currently has a total of five expressways, including Cau Gie—Ninh Binh, Noi Bai—Lao Cai, HCM City-Long Thanh—Dau Giay, Ben Luc—Long Thanh, Da Nang—Quang Ngai expressways. Along the five highways mentioned above, there are 206 tollgates managed by Vietnam Expressway Development Investment Corporation (VEC) and 88 BOT toll stations are being located. Vehicles are required to pay tolls when passing through these stations. In Vietnam, tolls are collected by both methods: manual toll collections and automatic toll collections. However, manual toll collections are high time consuming and labor cost. As consequence, transparency in toll payment is necessary to increase efficiency; reduce errors; boost productivity; speed up processes. Therefore, the demand for intelligent toll collection in Vietnam increase dramatically.

---

T. T. Mac (✉)

School of Mechanical Engineering, Hanoi University of Science and Technology, Hanoi, Vietnam  
e-mail: [thoa.macthi@hust.edu.vn](mailto:thoa.macthi@hust.edu.vn)

Recently, Automated Electronic Toll Collection System (AETCS) are developed based on RFID technology [1], computer vision [2], machine learning [3, 4]. In [5], Yolov3 and Yolov3 tinc are implemented to deal with realtime car detection in tolling system with a perpendicular camera angle. In the similar approach, YOLOv3 is investigated to detect and classify the vehicles at toll plazas, on highways and in urban areas. Vision-based approach is developed in [6] to decrease the fuel consumption, vehicle waiting time at the toll plaza. The disadvantage of mentioned studies is the lack of vehicle information such as license plates, customers, user account balance. In this study, we have developed a real-time automated electronic toll collection system based on deep learning techniques which includes:

- The development of YOLOv5 to detect the car license plate.
- The development of PaddleOCR to recognize the number license plate.
- The development of Web Server to manage the system.
- The development of a prototype that imitate the express highway which used ETC for charging transporter.

The advantages of the proposed approaches are high accuracy of detection, linking of the car license and the user money account, increasing speed detection, easy accessing via web system.

The remainder of the paper is organized as follows: Sect. 2 introduces the proposed approach of an automatic detection and recognize member license plate algorithms. Detailed workflow of the designed system and deep learning techniques are illustrated in this section. In Sect. 3, electronic system design and comprehensive results of the proposed approach are presented and discussion. Finally, the conclusion and further study are presented in Sect. 4.

## 2 Automatic Detection and Recognize Number License Plate

### 2.1 Implementing YOLOv5 Algorithm

Based on previous Yolo versions, YOLOv5 is developed by Glenn Jocher [7]. In this study, we focus on identifying the part of the car that is predicted to be the license plate based in Yolov5. The input is the image of car with license plate and the output of the detection is the license plate area with the bounding box. For YOLOv5 parameters in this study, we chose image size  $416 \times 416$ , epochs: 200, config model: yolov5n, 702 train images, 66 validation images with the following environment.

- GPU: NVIDIA GeForce RTX 2070
- Python 3.6, CUDA: 11.2 cuDNN: 8.0
- Tensorflow: 2.1.3.

The 5th steps are implemented for our developed approach.



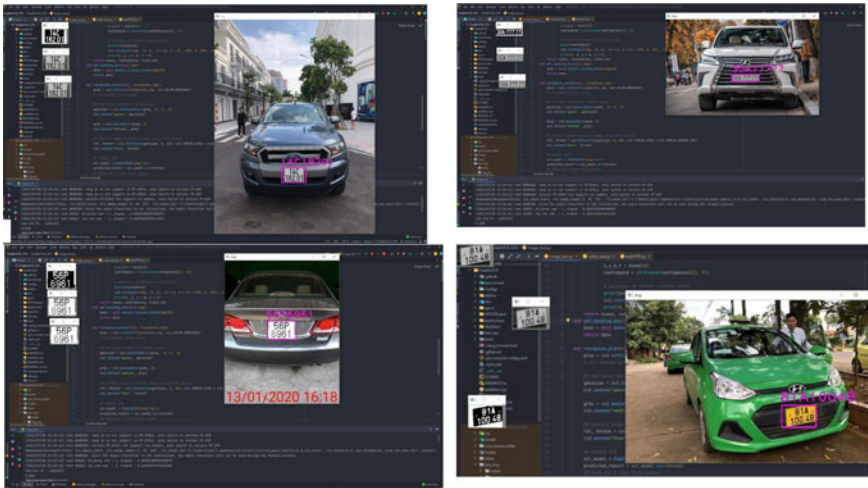


Fig. 1 Detection result with different color license plate

**Step 1:** Upload dataset contain picture and bounding box annotation to Roboflow working space and then split dataset to Training dataset, Validation Dataset (Optional) and Test Dataset with some aspect ratio. In this study, Training Dataset (95%) and Test Dataset (5%).

**Step 2:** Preprocessing for decrease training time and increasing performance by applying image transformations to all images in this dataset. All images are resized to  $416 \times 416$ .

**Step 3:** Implementing augmentation process by adding rotation angel from  $-15^\circ$  to  $15^\circ$ , and gGrayscale images (25%).

**Step 4:** Generate version with custom version size. Version size correspond to the number of training datasets. It can be (xN) times to the original training dataset.

**Step 5:** Export to format of YOLOv5 PyTorch.

Dataset from Kaggle, Car License Plate Detection are used for training in this study [7]. The real-time testing experiment results are presented in Fig. 1 with different color and shape of car license plates.

## 2.2 Web Server and Client Management

In this study, a web server is designed to serve employee control the and add new, edit and delete any car or customer information. Figure 2 presents a basic diagram of the designed web server and database work.

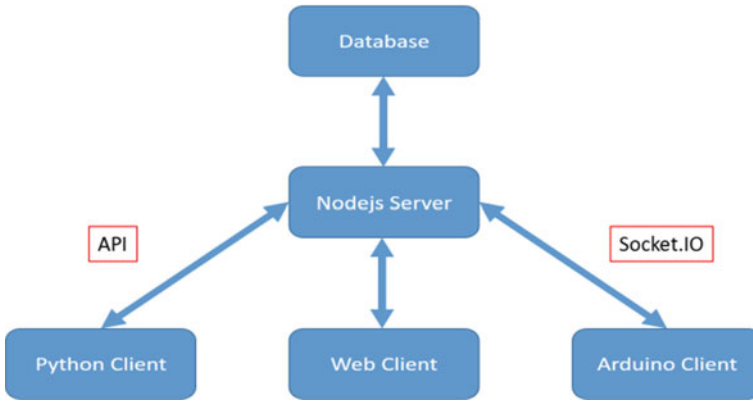


Fig. 2 Connection between the server and client

The client and server communicate via HTTP request, which is made by a client, to a named host, which is located on a server. The aim of the request is to access a resource on the server. The most commonly used HTTP method are POST (create), GET (read), PATCH (update) and DELETE (delete) the data stored in database as mentioned. The Client have three sub-pages: home page, bill history page and car/customer page. Server will receive the signal from Camera and RFID stimulate. The server send those value to Web client and compare those value to data which store in database as shown in Fig. 3.

After recognizing the number plate, Python client will send value of license plate to NodeJS Server by SocketIO method. SocketIO respond for sending data between three clients: Arduino client, Python client and Web JavaScript client. Server plays

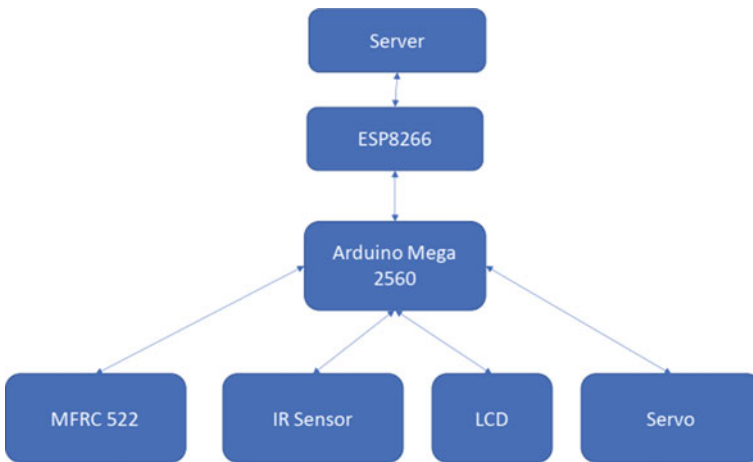


Fig. 3 The workflow of the designed system

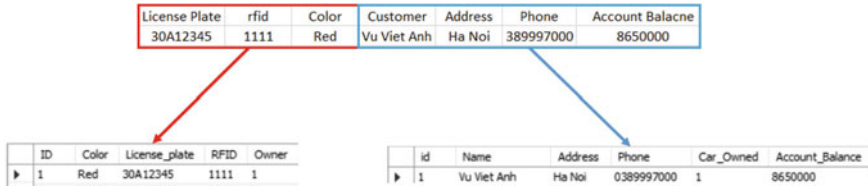


Fig. 4 The customer data on the designed web management system

a role as a transit station data. The customer data is stored on the databased with ID, car color, RFID, name, address, phone and account balance as shown in Fig. 4. The server send the signal to open the barrier incase the necessary condition are satisfied.

### 3 Electronic System Design and Experiment Results

The proposed model can predict the license plate number with the high accuracy, it approximately 89.6% with the best result after 174 epochs. The object loss reaches the lowest value of 0.0058 as shown in Fig. 5.

To validate the algorithm, a lab-scale automatic electronic toll collection is designed which includes a server, a camera, IR sensors, barrier, LCD as shown in Fig. 6. The testing process has shown that our system can work perfectly when the car enter the toll then camera can recognize the license plate number and send value to the server. Then, the server handle the data and compared to the database. If the account has enough money to purchase, the barrier open until the car pass through the barrier. It will automatic close by receive the signal from IR sensors. For Web management, the information of driver, manage the history of car entering and out

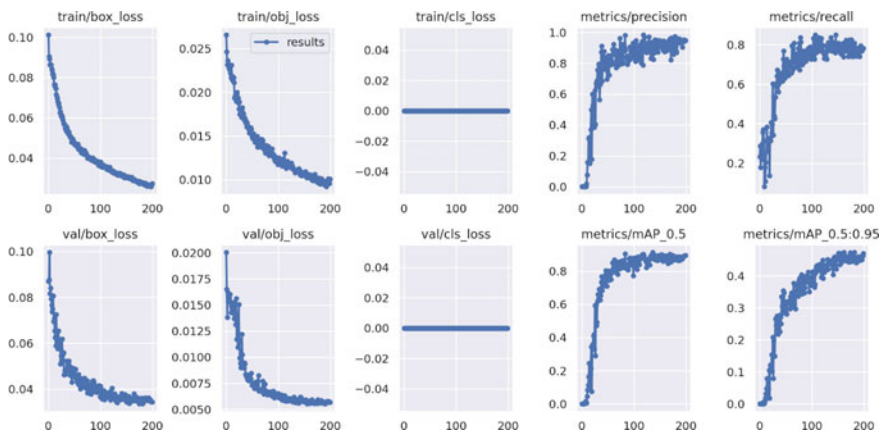
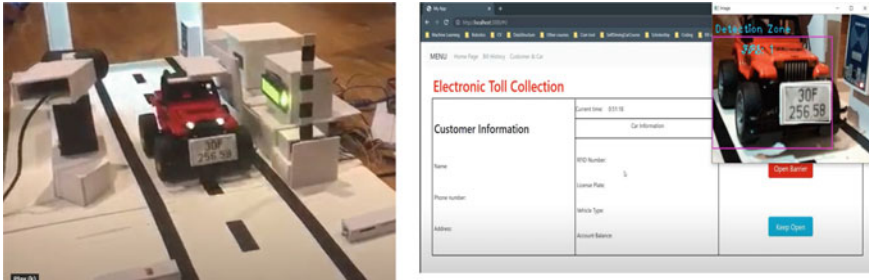


Fig. 5 mAP, loss, accuracy, precision, recall value of the proposed model



**Fig. 6** The experiment design and realtime ETC results

per day and as shown it on the LCD (Fig. 6). In order to develop the system, we enhance the model of detection and recognition license plate, upgrade our devices to meet the requirements of algorithms.

## 4 Conclusion

In this study, an automatic toll collection system is developed based on Yolov5, PaddleOCR via web server. The proposed toll collection system can solve traffic problem, corruption in the toll plaza. Our system consists some of advanced technology methods includes: (i) The development of YOLOv5 to detect the car license plate; (ii) The implementation of PaddleOCR to recognize the number license plate. (iii) The development of Web Server to manage the system; (iv) the development of lab-scale express highway used Vietnam Electrical Toll Collection (VETC) to ensure transparency in the toll collection. The proposed model can detect the license plate number with the high accuracy (approximately 89.6%).

In summary, the benefits of the proposed approaches include a high accuracy of car license plate detection, a linking of the car license and the user account, a increasing speed detection, an easy accessing via web system.

**Acknowledgements** This research is funded by Hanoi University of Science and Technology (HUST) under project number T2022-PC-023.

## References

1. S. Ahmed, T. Tan, A. Mondol, Z. Alam, N. Nawal, J. Uddin, Automated toll collection system based on RFID sensor 1–3 (2019). <https://doi.org/10.1109/CCST.2019.8888429>
2. P. Prommool, S. Auephanwiryakul, N. Theera-Umpon, Vision-based automatic vehicle counting system using motion estimation with Taylor series approximation. In: *6th IEEE International Conference on Control System, Computing and Engineering (ICCSC)*, pp. 485–489. (Penang, Malaysia, 2016)

3. S. Awang, N. Azmi, Automated toll collection system based on vehicle type classification using sparse-filtered convolutional neural networks with layer-skipping strategy (SF-CNNLS). *J. Phys.: Conf. Ser.* (2018)
4. H. Song, H. Liang, H. Li et al., Vision-based vehicle detection and counting system using deep learning in highway scenes. *Eur. Transp. Res. Rev.* **11**, 51 (2019)
5. D. Chattopadhyay, S. Rasheed, L. Yan, *Machine Learning for Real-Time Vehicle Detection in All-Electronic Tolling System, Systems and Information Engineering Design Symposium (SIEDS)*. (Charlottesville, VA, USA, 2020)
6. K. Rajeev, C. Kalpana, Intelligent toll collection system for moving vehicles in India. *Intell. Syst. Appl.* 15 (2022)
7. <https://www.kaggle.com/datasets/andrewmvd/car-plate-detection>

# 6 DOF Robot Control with Object Detection Based on Deep Learning



Hoang Hong Hai, Nguyen Thanh Hung, Le Sy Dung, and Nguyen Huu Long

**Abstract** Computer vision is an area of artificial intelligence that enables computers and systems to extract meaningful information from digital photos, videos, visual inputs and conduct actions or make suggestions based on that information. Robotics with applied computer vision method spans a wide range of fields. In the manufacturing, systems in production lines are continuously being upgraded to increase work efficiency. An ABB IRB1200 5–0.9 robot was chosen for product selection. With the task of controlling the actuator to carry out the task of picking the products in the tray and placing them on the conveyor belt, so as to ensure accuracy, and optimizing time. The article proposes a solution using computer vision algorithm integrated on the robot system, performing object detection, synchronizing camera and robot coordinate systems, and through the Robot Operating System (ROS) platform, controlling the robot to perform the task of picking and dropping objects.

**Keywords** Robot operating system · Object detection · Calibration

## 1 Introduction

The document [1] does a good job of explaining how computer vision functions similarly to human eyesight. Human vision has an edge over machine vision, though, because it has access to lifetimes of context to teach how to distinguish objects, gauge distances between objects, spot a subject's state of motion, and assess if a picture is accurate. Computers train robots to quickly complete these tasks using cameras, data, and algorithms rather than retinas, optic nerves, or a visual brain. Since it can examine hundreds of items or processes in a matter of minutes and can carry out defective object analysis [2], a trained system in product examination or product asset monitoring can outperform human talents.

---

H. H. Hai (✉) · N. T. Hung · L. S. Dung · N. H. Long  
Department of Mechatronics, School of Mechanical Engineering, Hanoi University of Science and Technology, No. 1 Dai Co Viet, Hai Ba Trung, Hanoi, Vietnam  
e-mail: [hai.hoanghong@hust.edu.vn](mailto:hai.hoanghong@hust.edu.vn)

© The Author(s), under exclusive license to Springer Nature Switzerland AG 2024  
B. T. Long et al. (eds.), *Proceedings of the 3rd Annual International Conference on Material, Machines and Methods for Sustainable Development (MMMS2022)*, Lecture Notes in Mechanical Engineering, [https://doi.org/10.1007/978-3-031-57460-3\\_52](https://doi.org/10.1007/978-3-031-57460-3_52)

473

While robotics is defined as the fusion of science, engineering, and technology that creates robots, or machines that mimic or replace human behaviors. It grows from being used in simple tasks such as pick and place to being able to perform more complex applications like welding, grinding, deburring and assembly. In general, robots are widely utilized to cut expenses, boost output, enhance product quality, and remove dangerous duties. Therefore, a combination between robotics and computer vision is being researched for better self-operation, fewer mistakes, more efficient motions and ultimately better process and product quality.

In this paper, we apply object detection, one of the computer vision problems, to the ABB IRB1200 5–0.9 robot [3]. According to this study [4], detecting instances of specific visual object kinds (such people, animals, or automobiles) in digital images is an essential computer vision job.

This paper is organized in the following context: The method of applying object detection is presented in Sect. 2. Section 3 shows the experiments and analysts the result of our approach. The discussion, conclusion and further work are detailed in the last section.

## 2 Methodology

In this work we aim to design and conduct a specific robot grasping application that integrates object detection models into the ROS environment to facilitate effective robot manipulation. Our pipeline contains four key sections of image acquisition, object detection, calibration, and robot controlling as summarized in Fig. 1. The first section captures images for data preparation for training and detection processes. The next section outputs the object classes and object locations in camera coordinate space as well. The calibration step allows the system perceiving the real-world location by converting the information in camera space into the robot one. Final section manipulates the real robot to finish the grasping mission. All sections are conducted by the support of the ROS environment, which allows the robot to communicate with the real world effortlessly.

In the first section, our pipeline acquires both color images and depth maps with the help of 3D depth camera Intel Realsense. The RGB images are fed into a 2D data-driven object detection model. In this work, we investigate two architectures of VGG16 and EfficientNet to figure out the best choice for our application. To improve the performance of object detection, our pipeline submits captured images to the augmentation process to enrich the diversity of the training dataset.

Manipulating robot to correctly grasp objects requires both object recognition and object localization. The object class is accomplished by an object detection model. Exact object location, on the other hand, requires a further process of calibration, which maps the object coordinates to robot perception. This calibration process finds the transformation rules from camera coordinates to robot manipulation. In other words, it needs to figure out the homogeneous matrix, which consists of a rotation matrix  $R$  ( $3 \times 3$ ) and a translation matrix  $T$  ( $3 \times 1$ ) as depicted in Fig. 2.

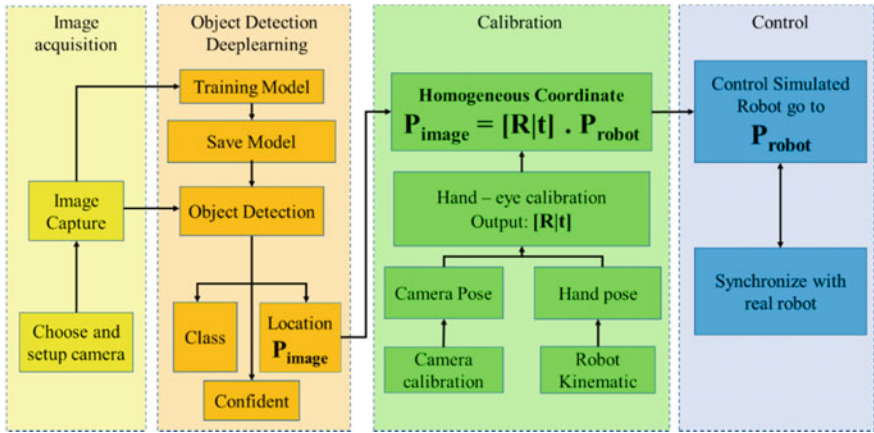


Fig. 1 Our proposal pipeline diagram

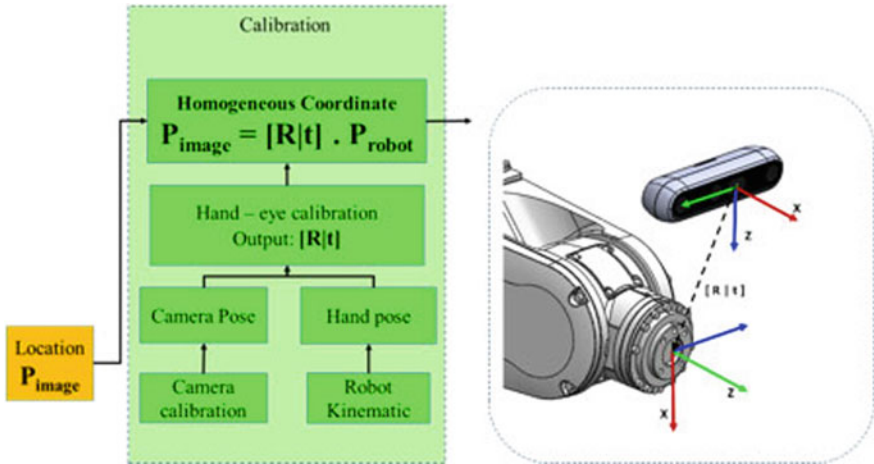


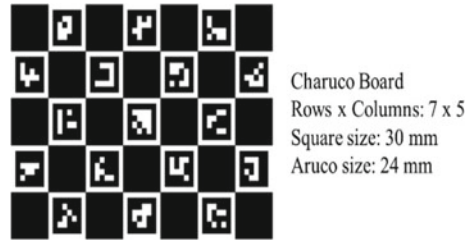
Fig. 2 Illustration of image calibration

Solving the question of R and T requires the process of calibration. In more detail, the system is commanded to sequentially move to different locations of joints in the work space. However, the robot does is not allowed to move randomly, it needs to guarantee that sample calibrator remains in the frame of view (FOV) of the camera. Calibration sample in our work is the Charuco Board (Fig. 3).

$$AX = XB \tag{1}$$

To show the Hand eye calibration’s problem in robotic field, which is illustrated as in (1), [5] and [6] find the rotation matrix by require coordinates of the camera



**Fig. 3** Charuco board

relative to the sample calibrator during each movement of the robot. Whereas, [7] needs the coordinates of the last impact stage relative to the robot's base coordinate system in each movement of the robot in order to analysis and parallel calculation of rotation and translation matrices. By receiving the outputs of the previous steps and using ROS environment, robots can receive command and under control while working.

### 3 Experiment Results

#### 3.1 Experiment Preparation

The robot was simulated on Robot Operating System (ROS) to reduce the time, cost and hazards of operating a real robot. In ROS, the robot model is represented in the Universal Robots Description Format (URDF). We use TCP/IP protocol via Ethernet port as communication between real robot controller and PC.

Figure 4 shows the operation of the system. At the beginning, the robot arm moves back to the Home position, which is already set. After that, the system collects images from the camera and identifies the objects of the operation. When the list of objects is set, the gripper starts to pick object to desire location and place it by using pneumatic method.

#### 3.2 Experiment Results

##### 3.2.1 Training Result

Training is tracked and visualized through TensorFlow's Tensor Board engine. The results below show the training process through 173,000 steps (Fig. 5).

The results show that, after 173,000 steps, the Loss function decreases to about 0.03. The accuracy value evaluated on the test set reached 0.96, equivalent to 96%. The recognition time on the frame is evaluated through 550 frames. The average recognition time reached 0.17 s/frame, equivalent to 5.8 FPS (Fig. 6).

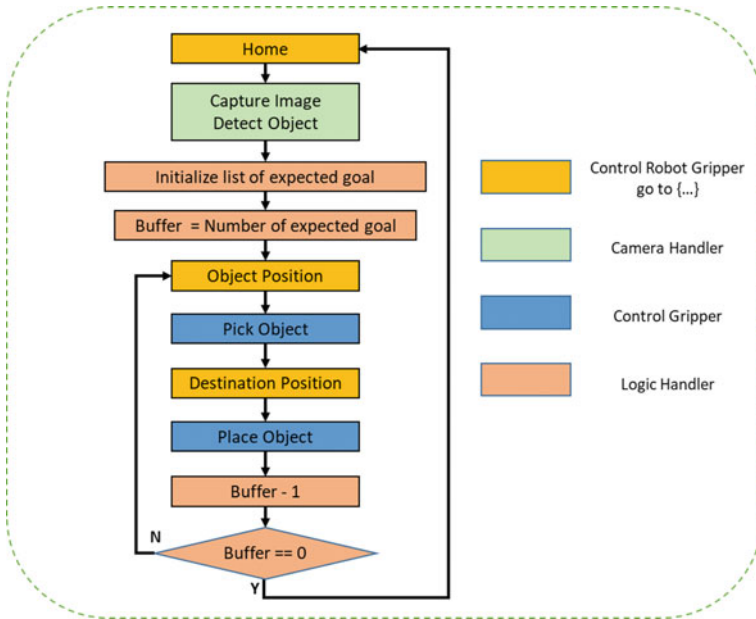


Fig. 4 The operating cycle of the system

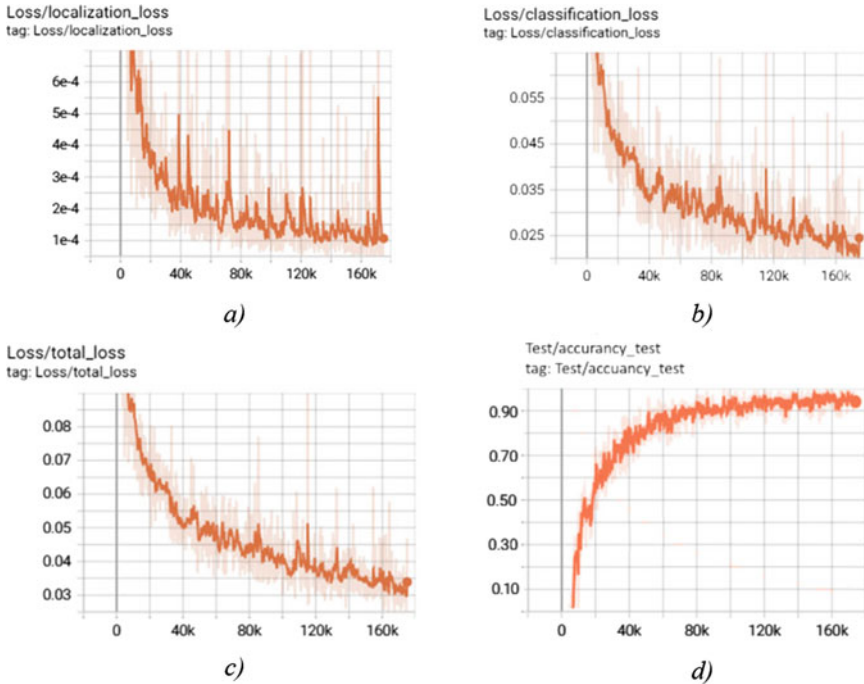
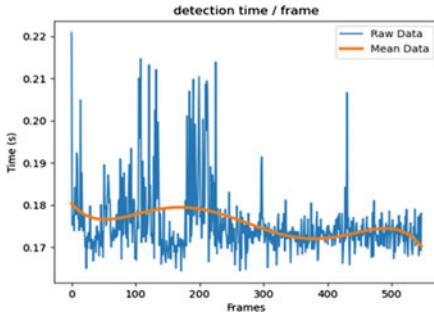


Fig. 5 The training results



Detection time	s/frame
Maximum	0.2209
Minimum	0.1644
Average	0.1757

Fig. 6 Detection result

$$D = \{-0.059, 0.073, 0, 0, -0.023\}$$

$$K = \begin{bmatrix} 631.366 & 0 & 640.753 \\ 0 & 630.637 & 362.701 \\ 0 & 0 & 1 \end{bmatrix}$$

Fig. 7 Camera calibration result as the distortion coefficient  $D$  and the camera matrix  $K$

$$X_{\text{Direct}} = \begin{bmatrix} 0.0477 & 0.999 & -0.0025 & -0.1725 \\ -0.999 & 0.0477 & 0.0212 & -0.022 \\ 0.0212 & 0.0014 & 0.999 & 0.0486 \\ 0 & 0 & 0 & 1 \end{bmatrix}$$

$$X_{\text{PnP}} = \begin{bmatrix} 0.0479 & 0.999 & -0.0027 & -0.1724 \\ -0.999 & 0.0479 & 0.0213 & -0.0217 \\ 0.0214 & 0.0016 & 0.999 & 0.0484 \\ 0 & 0 & 0 & 1 \end{bmatrix}$$

$$X_{\text{FastLoc}} = \begin{bmatrix} 0.048 & 0.999 & -0.0024 & -0.1724 \\ -0.999 & 0.048 & 0.0212 & -0.0217 \\ 0.0213 & 0.0014 & 0.999 & 0.0484 \\ 0 & 0 & 0 & 1 \end{bmatrix}$$

Fig. 8 Calibration result of different methods

### 3.2.2 Calibration Result

Through the camera calibration process, it is found that the Intel Realsense D455 camera has no tangential distortion, because  $p_1, p_2$  are all zero (Figs. 7 and 8).

Figure 9 is the error transformation of each method after over 50 samples. The evaluation results show that the method of Daniilidis [3] has the lowest error.

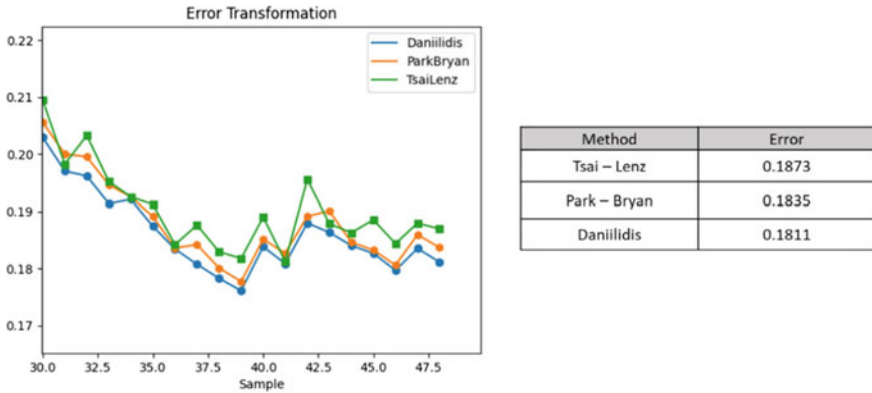


Fig. 9 Error Transformation

### 4 Conclusion

Our research is successful in integrating object detection model SSD into real computer vision system to finish the task of grasping objects. Our work examines different techniques of answering calibration matrix and provides insights into image calibration. Besides, our pipeline manipulates the ABB robot in real-world practice with the support of ROS that allows controlling and commanding robots precisely. Experiments on real applications prove our pipeline’s capability and possibility to be applied widen in the future work.

### References

1. R. Szeliski, *Computer Vision Algorithms and Applications*. (Springer, 2011)
2. M. Radhakrishnan, Application of computer vision technique on sorting and grading of fruits and vegetables. *J. Food Proc. Technol.* 1–7 (2012)
3. J. Gotlih, T. Karner, M. Ficko, M. Brezočnik, Robot-robot cooperation for efficient drilling of soft materials. In: *Automation, Robotics and Communications for Industry 4.0*. (IFSA, 2021) pp. 14–19
4. Z. Zou, Z. Shi, Y. Guo, J. Ye, *Object Detection in 20 Years: A Survey*. (2019)
5. R. Horaud, F. Dornaika, Hand-eye calibration. *Int. J. Rob. Res.* **14**(3), 195–210 (1995)
6. F.C. Park, B.J. Martin, Robot sensor calibration: solving  $AX = XB$  on the Euclidean group. *IEEE Trans. Robot. Autom.* **10**(5), 717–721 (1994)
7. K. Daniilidis, Hand-eye calibration using dual quaternions. *Int. J. Robot. Res.* **18**(3), 286–298 (1999)

# Generative Adversarial Network for Building Large Custom Dataset



Hoang Hong Hai

**Abstract** Acquiring new and clean data is a crucial part of building a good machine learning model, especially in industrial fields, where the dataset is usually small and highly imbalance. In this study, we leverage Generative adversarial network (GAN) to extend and enhance our specific dataset by automatically generating and labeling new images. Our pipeline guarantees the success of the synthesis data by turning and stabilizing the model's parameters. Experimental results prove the extraordinary of our dataset in terms of quantitative and qualitative assessment.

**Keywords** Generative adversarial network · Custom dataset · Synthesis images

## 1 Introduction

Deep Learning Network have nearly achieved human performance level on many tasks if given sufficient and wealthy data. They have been demonstrated in variety of domains, including vision-based tasks (image classification [1–4], segmentation [5], object detection, [6] etc.) and natural language processing applications. Nevertheless, in many realistic cases the deep neural networks perform undesired when dealing with limited datasets. Techniques have been developed over the years to help combat overfitting such as dropout [7], batch normalization [8], batch renormalization [9] or layer normalization [10]. However, these methods are not able to capitalise on known input invariances that might form good prior knowledge for informing the parameter learning. It is also possible to generate additional data from initial data by applying various transformations [1]. These augmentation process includes random translations, rotations, inversions, and the addition of Gaussian noise. This technique seems to be important for datasets of all sizes due to improving the dataset quality in terms

---

H. H. Hai (✉)

School of Mechanical Engineering, Hanoi University of Science and Technology, No. 1, Dai Co Viet, Hanoi, Vietnam

e-mail: [hai.hoanghong@hust.edu.vn](mailto:hai.hoanghong@hust.edu.vn)

of quality and balance. However, these traditional data augmentation procedures use a very limited set of known invariances and can be ineffective to small datasets.

Generative Adversarial Network (GAN) [11] shows potential ways of acquiring new and clear data by discovering and learning the regularities or patterns in input data in such a way that the model can be used to generate or output new examples that could have been drawn from the original dataset. GAN consists of 2 sub-models, the generator model trained to generate new examples, and the discriminator model that tries to classify examples as either real (from the domain) or fake (generated). In this paper, we apply GAN to learn representation of our custom dataset and generate large example images. Secondly, we fine tune model parameters for stabilizing at training and generating results.

## 2 Understand GAN

### *GAN in General*

GAN architectures contains two sub-models: a generator and a discriminator. While the generator (Fig. 2a) creates new images, the discriminator (Fig. 2b) infers whether generated examples are real, from the domain, or fake as described in Fig. 1.

### *GANs and Convolutional Neural Network*

Deep convolution Generative adversarial network (DCGAN) [12] is one of the most popular variants of GAN, with the two basic components of the network being replaced by two separate Convolutional Neural Networks (CNNs). The internal structure of the CNNs is also changed to increase the consistency in the training process by replacing the upsampling layer and the fully connected layer with two convolution layers. Using a CNN structure makes DCGAN better in abstract ability in comparison to other variants. The pooling layer in a basic CNN is adapted with stride CNNs to implement the Generator and the Discriminator. DCGANs have quickly answered the instability problem and the need for additional adjustments in the training phase.

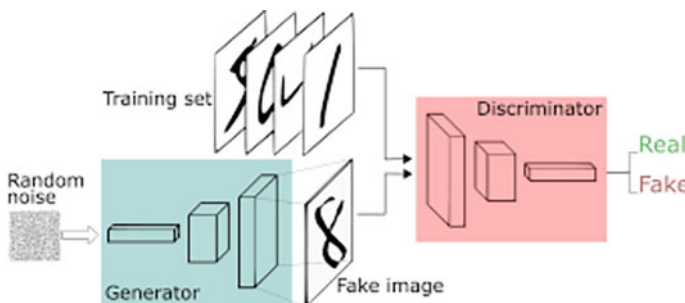
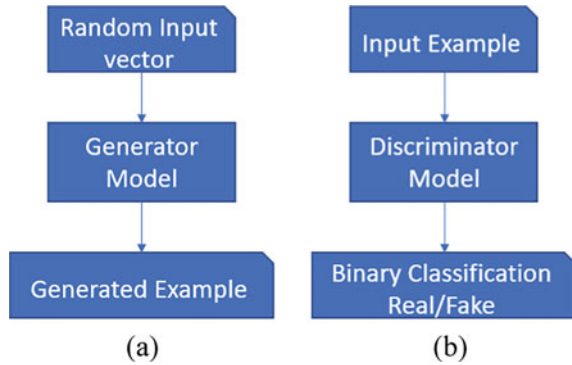


Fig. 1 GAN architecture

**Fig. 2** **a** Generator model (left) and **b** Discriminator model (right)



Therefore, it is considered one of the most reliable yet most straightforward variants of GANs available today, increasing interest in the research field.

**BIGGAN**

The size of image generated by GAN or DCGAN are relatively small, about  $64 \times 64$  or  $128 \times 128$  pixels. And merit of the enhancement to the training have focused on changes to the objective function or constraining the discriminator model during the training process. BIGGAN [13] focuses on both high-quality and larger images by scaling up the model. Specifically, the BigGAN is designed for class-conditional image generation.

– *Self-Attention Module and Hinge Loss*

The most significance is the appearance of Self-Attention GAN [14]. This module passes the feature map to extract the attention map, which can tell the model what significance the model should pay more attention to. Therefore, it can capture the most informative parts of the image as well as neglect the redundant parts.

– *Update Discriminator more than Generator*

The another difference between the discriminator and generator is that the earlier updates twice before the later in each training iteration.

**3 Implementation**

***Building BIGGAN***

In the DCGAN paper, the authors’ implementation is for image of size  $64 \times 64$ , when applying it to larger size, the problem of memory leak regularly happen because of the very large size of last layer in generation model, making it extremely difficult to train the model. Instead, BIGGAN is applied with detail of implementation below:

Discriminator model		Generator model	
Layer name	Shape	Layer name	Shape
Input*	(256, 256, 3)	Input	128
CONV $f = 8, k = 3, s = 2$	(128, 128, 8)	Dense	(4096)
LeakyReLU (0.2)		Reshape	(4, 4, 256)
Dropout (0.25)		T-CONV $f = 128, k = 4, s = 2$	(8, 8, 128)
CONV $f = 16, k = 3, s = 2$	(64, 64, 16)	BN (0.7)	
BN (0.7)		ReLU (0.2)	
LeakyReLU (0.2)		T-CONV $f = 64, k = 4, s = 2$	(16, 16, 64)
Dropout (0.25)		BN (0.7)	
CONV $f = 32, k = 3, s = 2$	(32, 32, 32)	ReLU (0.2)	
BN (0.7)		T-CONV $f = 32, k = 4, s = 2$	(32, 32, 32)
LeakyReLU (0.2)		BN (0.7)	
Dropout (0.25)		ReLU (0.2)	
CONV $f = 64, k = 3, s = 2$	(16, 16, 64)	T-CONV $f = 16, k = 4, s = 2$	(64, 64, 16)
BN (0.7)		BN (0.7)	
LeakyReLU (0.2)		ReLU (0.2)	
Dropout (0.25)		T-CONV $f = 8, k = 4, s = 2$	(128, 128, 8)
CONV $f = 128, k = 3, s = 2$	(8, 8, 128)	BN (0.7)	
BN (0.7)		ReLU (0.2)	
LeakyReLU (0.2)		T-CONV $f = 3, k = 4, s = 2$	(256, 256, 3)
Dropout (0.25)		BN (0.7)	
CONV $f = 256, k = 3, s = 2$	(4, 4, 256)	ReLU (0.2)	
BN (0.7)		CONV ( $f = 3, k = 5, \tanh$ )	(256, 256, 3)
LeakyReLU (0.2)			
Dropout (0.25)			
Flatten ()	(256)		
Dense (128)	(128)		
Dense (1)	(1)		

*f* is number of output channel, *k* is kernel size, *s* is number of convolution stride. T-CONV is transposed convolution. BN is batch normalization with momentum specified in the parentheses. The value inside parentheses next to LeakyReLU is the alpha number

Some of the GAN architecture improvements for stabilize training are explained:

– *Use Strided Convolutions*

We replace pooling layers and upsampling layers by convolution and transposed convolution with stride equal 2. This may increase the computation, but the model is able to learn its own spatial downsampling and upsampling while learning.

– *Remove fully connected layer*



Fully-connected layers are commonly used after the feature extraction layers, while they are removed in GAN. Concretely, the convolution layers in discriminator are flattened and directly convey to the output.

– *Use ReLU and LeakyReLU*

In GAN, the generator part should accompany the ReLU activation function, while the discriminator should be applied with LeakyReLU.

– *Label smoothing*

GAN model is trained with labels to improve image quality. Moreover, we expect better result by changing labels for the discriminator model by stochastic range [0.9,1.0] and for generation model by stochastic range [0.0, 0.1].

### ***Training***

We use dataset from [15], which contain roughly 25,000 images of bamboo strips that is labelled into 7 classes. Both the generator and discriminator are trained with Adam optimizer, learning rate is 0.0001 with decay rate of 0.85 after each 10,000 steps (for both models) and batch size is 16. We train model using GPU NVIDIA 2060 with 6 GB VRAM. The training takes about 3 days to finish.

## **4 Result and Discussion**

Figure 3 shows original images while Fig. 4 shows examples of 48 images generated by the generator model. From the images generated, we can see the images are at good quality (through still have some noise) in comparison to original images, but they are quite reparative. More generation will create different images.

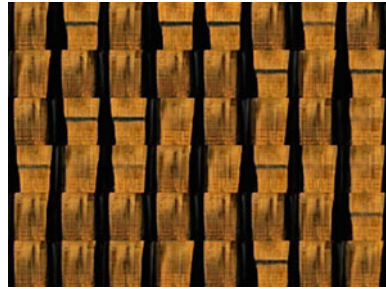
### ***Qualitative GAN Evaluation***

We use L2 distance to compare between synthesis images and original images after each 5000 steps, the result is:

**Fig. 3** Image original



**Fig. 4** Images generated



We select examples of real images from the domain and locating one or more most similar generated images for comparison in pixels. Another evaluation metric we use is Frechet Inception Distance (FID). FID score is meant to show the similar of statistics of a collection of synthetic images compared to the statistics of a collection of real images from the target domain. From Figs. 5 and 6, we can see the downward trend of scores, meaning that the generator model performs better given more training steps. However, FID score in later steps is not stable, this situation needs more investigation. The lowest FID score we get is 329.887.

**Fig. 5** Nearest neighbor score

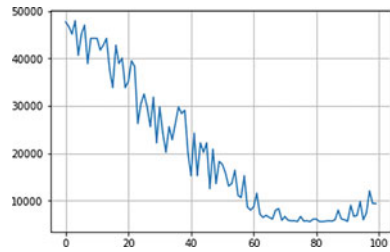
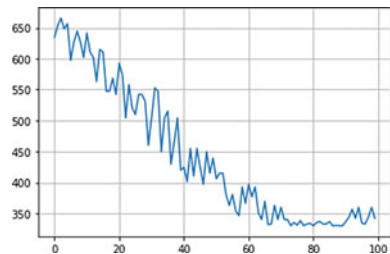


**Fig. 6** FID score



## 5 Conclusion and Future Work

In this study, we have shown a way to apply Generative Adversarial Network for generating large image size, together with some tricks to stabilize and strengthen GAN model. The results in Chap. 4 show that the images generated are quite visually similar to the original one. We also show two metrics that also indicate the similar of the pixels and statistics of the 2 datasets to prove the effective of the generator model. However, there are still noise in the images generated and the FID scores are unstable in later steps, that are still in question. We will find the answer for that and improve the quality and stability of the GAN model in the future.

**Acknowledgements** This work was funded by Vietnam Ministry of Education and Training under project number B2020-BKA-02.

## References

1. A. Krizhevsky, I. Sutskever, G.E. Hinton, *ImageNet Classification with Deep Convolutional Neural Networks* (NIPS, 2012)
2. K. Simonyan, A. Zisserman, *Very Deep Convolutional Networks for Large-Scale Image Recognition*. [arXiv:1409.1556](https://arxiv.org/abs/1409.1556), [cs.CV] (2014)
3. K. He, X. Zhang, S. Ren, J. Sun, *Deep Residual Learning for Image Recognition*. [arXiv:1512.03385](https://arxiv.org/abs/1512.03385), [cs.CV] (2015)
4. G. Huang, Z. Liu, L. Van Der Maaten, K.Q. Weinberger, *Densely Connected Convolutional Networks*. [arXiv:1608.06993](https://arxiv.org/abs/1608.06993), [cs.CV]
5. O. Ronneberger, P. Fischer, T. Brox, *U-Net: Convolutional Networks for Biomedical Image Segmentation*. [arXiv:1505.04597](https://arxiv.org/abs/1505.04597), [cs.CV] (2015)
6. K. He, G. Gkioxari, P. Dollár, R. Girshick, *Mask R-CNN*. [arXiv:1703.06870](https://arxiv.org/abs/1703.06870), [cs.CV] (2017)
7. N. Srivastava, G. Hinton, A. Krizhevsky, I. Sutskever, R. Salakhutdinov, Dropout: a simple way to prevent neural networks from overfitting. *J. Mach. Learn. Res.* **15**, 1929–1958 (2014)
8. S. Ioffe, C. Szegedy, *Batch Normalization: Accelerating Deep Network Training by Reducing Internal Covariate Shift*. [arXiv:1502.03167](https://arxiv.org/abs/1502.03167), [cs.LG] (2015)
9. S. Ioffe, *Batch Renormalization: Towards Reducing Minibatch Dependence in Batch-Normalized Models*. [arXiv:1702.03275](https://arxiv.org/abs/1702.03275), [cs.LG] (2017)
10. J.L. Ba, J.R. Kiros, G.E. Hinton, *Layer Normalization*. [arXiv:1607.06450](https://arxiv.org/abs/1607.06450), [stat.ML] (2016)
11. I. Goodfellow, J. Pouget-Abadie, M. Mirza, B. Xu, D. Warde-Farley, S. Ozair, A. Courville, Y. Bengio, *Generative Adversarial Networks*. [arXiv:1406.2661](https://arxiv.org/abs/1406.2661), [stat.ML] (2014)
12. A. Radford, L. Metz, S. Chintala, *Unsupervised Representation Learning with Deep Convolutional Generative Adversarial Networks*. [arXiv:1511.06434](https://arxiv.org/abs/1511.06434), [cs.LG] (2016)
13. A. Brock, J. Donahue, K. Simonyan, *Large Scale GAN Training for High Fidelity Natural Image Synthesis*. [arXiv:1809.11096](https://arxiv.org/abs/1809.11096), [cs.LG] (2018)
14. H. Zhang, I. Goodfellow, D. Metaxas, A. Odena, *Self-Attention Generative Adversarial Networks*. [arXiv:1805.08318](https://arxiv.org/abs/1805.08318), [stat.ML] (2018)
15. H.H. Hai, *Improvement for Convolution Neural Networks in Image Classification*. *Appl. Sci.* (2021)

# A Robust Robot Correction System Using 6-Axis Force/Torque Sensor



Chi-Cuong Tran, Syed Humayoon Shah, Chyi-Yeu Lin,  
and Anton Royanto Ahmad

**Abstract** Normal trajectory plays a vital role to enhance the quality of robotic-based surface finishing. This paper presents a novel and robust solution for real-time robot (manipulator) pose correction employing a 6-axis force sensor. The proposed scheme enables the robot to automatically correct postures in real-time on the curved surface. This approach does not depend on any prior geometric information of the workpieces, such as a CAD model or a 3D point cloud. The system depends only on the feedback data of a 6-axis force/torque sensor, positioned between the robot flange and a tool. The pose adjustment algorithm determines the normal relationship between the contact tool and the workpiece's surface using the feedback information from the sensor. The experimental results show that the proposed study has great potential to automate surface finishing operations such as robotic-based polishing, particularly on challenging curved surfaces.

**Keywords** Normal estimation · Force/torque sensor · Complex surface

## 1 Introduction

The demand for robotic-based automatic correction is growing substantially, particularly in deburring and polishing [1, 2]. Most industrial sectors still use manual methods for performing these expensive, time-consuming, and highly skilled machining procedures that ensure uniformity in surface finishing [3]. To achieve the desired outcomes in such applications, constant force monitoring must be maintained across the surface, which is a physically demanding process if carried out manually by human labor. Due to the aforementioned circumstance, more advanced machining techniques are required in order to completely automate and maintain a consistent

---

C.-C. Tran · S. H. Shah · C.-Y. Lin (✉) · A. R. Ahmad

Department of Mechanical Engineering, National Taiwan University of Science and Technology, Taipei 106, Taiwan

e-mail: [Chyi-YeuLind10803817@mail.ntust.edu.tw](mailto:Chyi-YeuLind10803817@mail.ntust.edu.tw)

force on complicated geometric surfaces, improving the quality of polishing and deburring [4, 5].

Recently, many studies have used robot arms and advanced control algorithms, which have the ability to offer complete assistance in industrial manufacturing [2, 6, 7]. However, using a robot arm to correct a curved surface in a workpiece with maintaining constant force is extremely difficult. In addition, to maintain a consistent force throughout the tracking of curved surfaces, a reinforcement learning-based control technique was presented by Zhang et al [8]. To calculate the tangential angle between the tool and the workpiece, an artificial neural network (ANN) was employed. For robotic deburring applications, Li et al [9] suggested a 3-D shape-matching approach to correct the real and target trajectory inaccuracy. However, this method must know in advance the 3D model of the object to be machined. Thus, it takes a lot of time to collect information about the machined object.

To solve the problems mentioned above, we proposed a method using a 6-axis force sensor to correct the pose of the curved surface. The method of estimating the surface posture by applying a certain force to the surface of an object. After that, based on the force feedback through the 6-axis force sensor calculate the position and angle of the robot. In addition, the disturbances caused by surface friction are suppressed by a compensator. The experimental results show the potential of the research and can be applied in the industrial environment.

## 2 System Overview

Geometric description of a complicated surface plays a significant role in industrial tasks, such as robotic polishing, deburring, and chamfering. This research proposes a technique for curved surface trajectory tracking correction in real-time. The system employs the force control algorithm to ensure a surface normal between the robot end-effector and the contact environment. The major components of the system include an industrial robot, a correction tool, and a 6-axis force/torque sensor.

### 2.1 ATI Force/torque Sensor

The 6-axis F/T (force/torque) sensor employed in this study was developed by the ATI company, as shown in Fig. 1b. A 6-axis F/T sensor was used to measure force and torque for each of the six components ( $F_X$ ,  $F_Y$ ,  $F_Z$ ,  $T_X$ ,  $T_Y$ , and  $T_Z$ ) individually (Fig. 1a). The  $F_X$ ,  $F_Y$ , and  $F_Z$  axes in this research measured lifting-thrusting motions, respectively, based on the direction of movement. An ATI F/T axia80-m20 sensor has a full-scale force (z-axis) of 360 N, force resolution of 1/10 N, full-scale torque of 8 Nm, and torque resolution of 1/200 Nm [10].

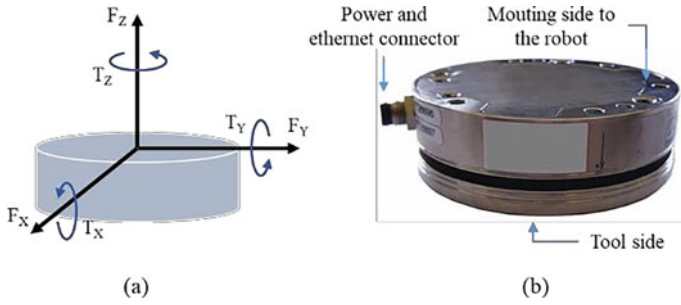


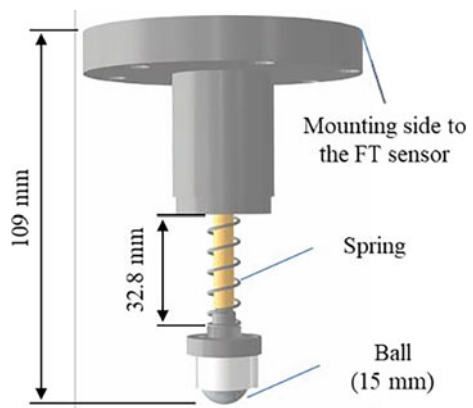
Fig. 1 a The direction of the 6-axis F/T sensor, b ATI 6-axis F/T sensor

## 2.2 Correction Tool

To contact the workpiece surface, a tool has been employed in this study, as shown in Fig. 2 [11]. The physical forces received by the surface through the tool are transmitted to the F/T sensor. Measured sensor information is sent to the computer for analysis and surface posture estimation through the 3-axis ( $F_x$ ,  $F_y$ , and  $F_z$ ). The tool includes three main components: a spring, ball, and tool frame. When the force of contact shifts, depth compensation was handled by a linear spring. The spring stiffness is selected based on the desired amount of force. In addition, the ball is designed to handle major of the friction along the tangent of the surface, and allow it to slide smoothly across the surface. A tool frame that enables the solid rod used within the spring to move along the z-axis and allows the tool to be mounted to the F/T sensor.

The specifications of the tool are as follows: the weight of the tool is 0.92 kg, and the stiffness of the spring employed is 2.0. In addition, the total length of the spring is 40 mm. However, the spring after compression (in the tool in normal mode) is 32.8 mm. Moreover, the weight of the ball is 0.07 kg.

Fig. 2 Correction tool



### 3 Robot Pose Correction with Force-Based Approach

The real-time robot curved surface tracking process modifies the contact relationship between the end-effector and the workpiece by rectifying its displacement and orientation. Consequently, to keep the robot end-effector normal to the surface, it is vital to establish the robot angles ( $R_X, R_Y$ ) and displacement relationship with the force data ( $F_X, F_Y, F_Z$ ) obtained from the 6-axis force/torque sensor. This relationship is beneficial to maintain a constant contact force by adjusting the angles and displacement of the end-effector. The trajectory realized by constant force tracking reduces the actual and desired trajectory error. Furthermore, this trajectory can be employed for direct machining. To avoid damage to the force sensor and the workpiece that may be brought on by force overload, the contact condition between the robot and the workpiece can be guaranteed.

In Fig. 3a, when a force sensor module is positioned perpendicular to a flat surface, the  $f_X$  and  $f_Z$  measurements obtained at the force frame of the force sensor match up with the  $F_N$  and  $F_T$  values measured at the surface contact. The rotating frames do not align as the force sensor module moves over a curved surface, which changes the position of the contact point on the tip of the tool. Thus, a conceptual diagram of the proposed system is described in Fig. 3b, which demonstrates that by employing the force sensor information and pose correction technique, the position and orientation of the robot utilizing the correction tool can be adjusted.

The precise contact surface angle of the object in reference to the range of the sensor frame is provided by the pose estimation technique. The rotation matrix required to adjust the robot end-effector coordinates based on the robot base coordinate is given in Eq. (1).

$${}^R_S T = {}^R_E T {}^E_T T {}^T_S T \tag{1}$$

The transformation of the robot end to the tool coordinate system is determined by Eq. (2). In this case, the length of the tool is not fixed due to the change of the force acting on the tool's z-axis. Thus, the transformation matrix is updated based

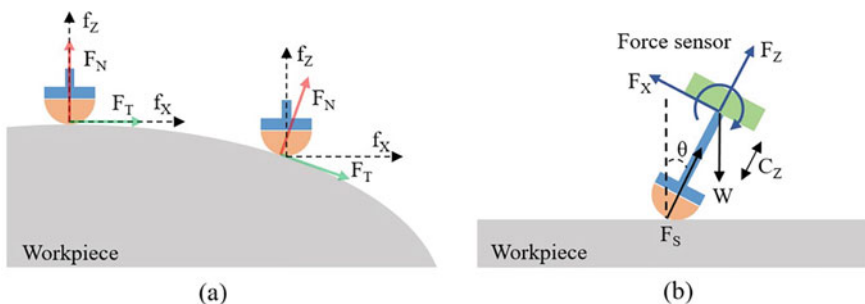


Fig. 3 a Force frame alignment and b Conceptual of surface correction

on the current length of the tool.

$${}^E_T = \begin{bmatrix} 1 & 0 & 0 & 0 \\ 0 & 1 & 0 & 0 \\ 0 & 0 & 1 & L_s \\ 0 & 0 & 0 & 1 \end{bmatrix} \quad (2)$$

In addition,  $LO$  is the base length of the tool without springs, and  $LS$  is the total length including the current springs length and the length of a robotic tool holder. To estimate the current length of the tool, which can be calculated through Eq. (3).

$$L_s = L_o + \frac{F_z}{k} \quad (3)$$

The homogeneous matrix  ${}^T_S T$ , which reflects the rotation of the contact surface to the tool frame is used to represent the contact surface angles.

$${}^T_S T = R_z(\gamma)R_y(\beta)R_x(\alpha)|t \quad (4)$$

$$\begin{cases} \alpha = \tan^{-1}\left(\frac{F_y}{F_z}\right) \\ \beta = \tan^{-1}\left(\frac{F_x}{F_z}\right) \\ \gamma = 0 \end{cases} \quad (5)$$

where,  $\alpha$ ,  $\beta$ , and  $\gamma$  are the actual robot angles. A translation matrix  $t = [0 \ 0 \ 0 \ 1]^T$  is the distance between the end of the tool and the contact surface.

## 4 Experimental Results and Discussions

In Fig. 4, the process of the proposed system is explained. Firstly, linear frictional force compensation is used to reduce errors caused by friction between the tool end and the contact surface. Frictional force arises when the tool slides on the contact surface during pose correction. The linear compensator is estimated based on the roughness of the contact surface and the force applied by the robot. Secondly, the current length of the tool is estimated based on the force ( $FZ$ ) feedback and the spring stiffness. This parameter is used to calculate the displacement when the force is applied. Additionally, the feedback forces of the 3-axis ( $FX$ ,  $FY$ ,  $FZ$ ) are used to estimate the robot's pose relative to the contact surface. We design the end tip of the tool is used the ball to contact the object surface, thus, the z-axis rotation is ignored. Finally, a linear motion function in the robot is used to ensure the robot moves smoothly along the corrected trajectory.



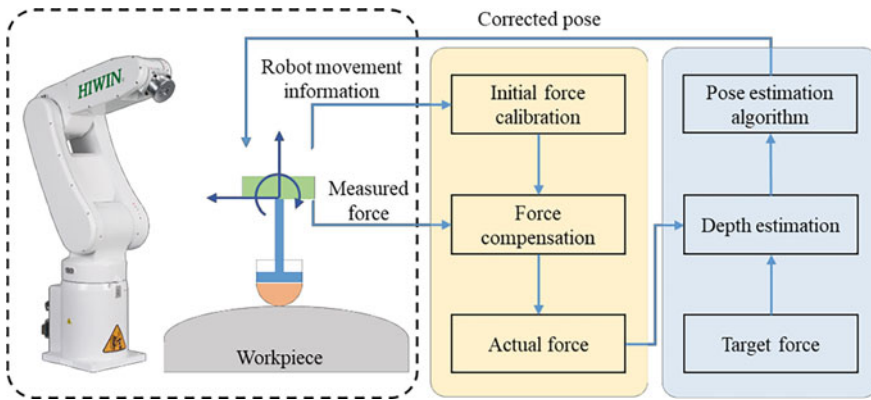


**Fig. 4** Block diagram of the trajectory correction system. In the yellow block, to eliminate impact load from the sensor measurement, a frictional force compensation framework is designed. The blue block contains the pose correction algorithm

Two different paths are established for each workpiece, and the mean absolute error (MAE) of the two paths is applied to evaluate the proposed method’s accuracy in both translation and rotation. A definition of the MAE is:

$$MAE = \frac{\sum_{i=1}^n |y_i - x_i|}{n}$$

where,  $y_i$  represent the estimated angle,  $x_i$  is the ground truth of the angle, and  $n$  denotes the number of test points. Table 1, which presents the MAE results for the two workpieces, demonstrates satisfactory accuracy for both translation and rotation.

For the flat surface, we design the robot moving along the x-direction which the depth (z-axis) and angle ( $RX$  and  $RY$ ) are random within a given range. The experiment results show that the mean absolute and maximum error are 1.7 mm, 4 mm for translation, and 0.7°, 1.6° for rotation. Figure 5 depicts the posture of the robot before and after correction. On a curved surface, Fig. 6 demonstrates the random error pose and corrected pose of the robot. The mean absolute and maximum errors are 1.7 mm and 4 mm for translation. This result is similar to the flat surface. Therefore, the mean absolute error is 0.8°, and the maximum error is 2.5°.

**Table 1** Comparison of performance in robot surface correction

Surface type	Translation (mm)		Rotation (°)	
	MAE	Maximum error	MAE	Maximum error
Flat surface	1.7	4	0.7	1.6
Curved surface	1.7	4	0.8	2.5

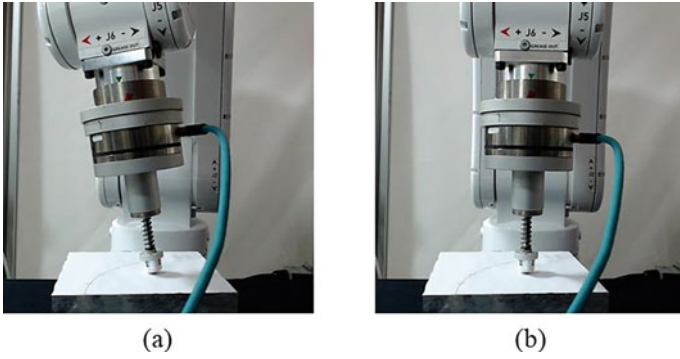


Fig. 5 Results of the **a** random error pose and **b** corrected pose of the robot for a flat surface

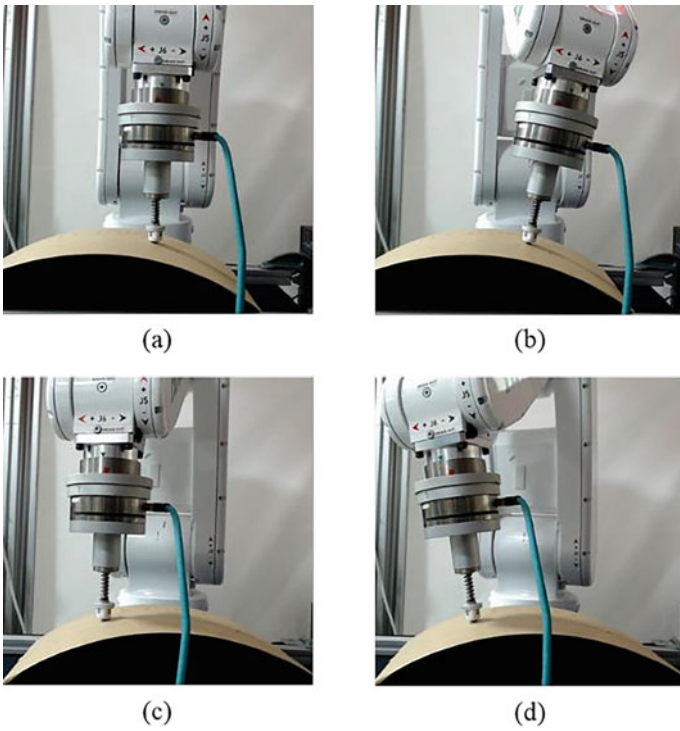


Fig. 6 Results of the **a**, **c** initial pose of the robot and **b**, **d** corrected pose of the robot for curved surface

## 5 Conclusion

This study aims to quantitatively evaluate the ability to estimate posture based on feedback from the 6-axis force/torque sensor. The correction adjustment algorithm is used to calculate and automatically adjust the depth (z-axis) and angles ( $R_X$  and  $R_Y$ ) of a 6-DOF robot manipulator. A compensation method is applied to remove unexpected noise caused by frictional force during the trajectory correction. Experimental results are conducted on two different types of objects such as a flat and curved surface. The mean absolute error of translation is 1.7 mm for both object's surface. For rotation, the mean absolute error is  $1.6^\circ$  and  $2.5^\circ$  for both flat and curved surface, respectively. The system developed has the potential to be widely used in the manufacturing industries for machining operations such as surface finishing. In future work, a variable stiffness spring can be employed in the tool to widen its application for a variety of material workpieces.

## References

1. I. Mohsin, K. He, Z. Li, R. Du, Path planning under force control in robotic polishing of the complex curved surfaces. *Appl. Sci.* **9**(24), (2019). <https://doi.org/10.3390/app9245489>
2. J. Li, T. Zhang, X. Liu, Y. Guan, D. Wang, A survey of robotic polishing. In *2018 IEEE International Conference Robot*, no. June 2019. (Biomimetics, ROBIO 2018, 2018), pp. 2125–2132. <https://doi.org/10.1109/ROBIO.2018.8664890>
3. A.E.K. Mohammad, D. Wang, Electrochemical mechanical polishing technology: recent developments and future research and industrial needs. *Int. J. Adv. Manuf. Technol.* **86**(5), 1909–1924 (2016). <https://doi.org/10.1007/s00170-015-8119-6>
4. M.J. Tsai, J.F. Huang, W.L. Kao, Robotic polishing of precision molds with uniform material removal control. *Int. J. Mach. Tools Manuf* **49**(11), 885–895 (2009). <https://doi.org/10.1016/j.ijmactools.2009.05.002>
5. L. Liao, F. (Jeff) Xi, K. Liu, Modeling and control of automated polishing/deburring process using a dual-purpose compliant toolhead. *Int. J. Mach. Tools Manuf.* **48**(12), 1454–1463 (2008). <https://doi.org/10.1016/j.ijmactools.2008.04.009>
6. C.-H. Shih, Y.-C. Lo, H.-Y. Yang, F.-L. Lian, Key ingredients for improving process quality at high-level cyber-physical robot grinding systems. In *2020 IEEE/ASME International Conference on Advanced Intelligent Mechatronics (AIM)* (2020), pp. 1184–1189. <https://doi.org/10.1109/AIM43001.2020.9159031>
7. W. Ji, L. Wang, Industrial robotic machining: a review. *Int. J. Adv. Manuf. Technol.* **103**(1), 1239–1255 (2019). <https://doi.org/10.1007/s00170-019-03403-z>
8. T. Zhang, M. Xiao, Y. Zou, J. Xiao, S. Chen, Robotic curved surface tracking with a neural network for angle identification and constant force control based on reinforcement learning. *Int. J. Precis. Eng. Manuf.* **21**(5), 869–882 (2020). <https://doi.org/10.1007/s12541-020-00315-x>
9. W. Li, H. Xie, G. Zhang, S. Yan, Z. Yin, 3-D shape matching of a blade surface in robotic grinding applications. *IEEE/ASME Trans. Mechatronics* **21**(5), 2294–2306 (2016). <https://doi.org/10.1109/TMECH.2016.2574813>
10. A. T. I. I. Automation, 6-axis F/T sensor axia80-M20. *ATI Industrial Automation*. [Online]. Available: <https://www.ati-ia.com/>
11. C.-Y. Lin, C.-C. Tran, S.H. Shah, A.R. Ahmad, Real-time robot pose correction on curved surface employing 6-axis force/torque sensor. *IEEE Access* **10**, 90149–90162 (2022). <https://doi.org/10.1109/ACCESS.2022.3201233>

# A Study on YOLOv4 Algorithm for Harvesting Agriculture Robot



Sy-Tai Nguyen, Hong-Ky Dang, Tien Duc Nguyen, Hai-Le Bui,  
and Thi Thoa Mac

**Abstract** Smart agriculture is understood as agriculture applying high technology, production technology, product safety protection, management technology, product identification in series associated with artificial intelligence system. Key technologies used in smart agriculture applications such as: IoT technology with sensors that collect accurate data on climate, growing conditions, and health of crops/animals; intelligent automation technology with robots and unmanned aerial vehicles gradually replacing humans in farming activities; image processing, artificial intelligence (AI). This paper proposes an improved YOLOv4 algorithm to real-time detect tomato for harvesting agriculture robot in Robot Operating System (ROS). The advantage of this model is the use of the combination of data tomato detection and real experiment system to increase the accuracy. To verify the effectiveness of this method, an actual applications, tomato with different ripeness of tomato in the same area can be detected with the accuracy of 89%.

**Keywords** YOLOv4 · Harvesting · AI · Smart agriculture · Detection

## 1 Introduction

Agriculture is an economic sector that contributes 8.7% of Vietnam's GDP but creates jobs for 30.6% of our population, and brings a surplus of 10.7 billion USD to the economy. Even though the share of the economy is on the decline, it will give way to economic sectors with high surplus value in the service industry [1]. However,

---

S.-T. Nguyen · H.-K. Dang · T. D. Nguyen · H.-L. Bui · T. T. Mac (✉)

School of Mechanical Engineering, Hanoi University of Science and Technology, Hanoi, Vietnam

e-mail: [Thoa.macthi@hust.edu.vn](mailto:Thoa.macthi@hust.edu.vn)

S.-T. Nguyen

Vietnam National Institute of Occupational Safety and Health, Hanoi, Vietnam

T. D. Nguyen

Nam Dinh University of Technology Education, Nam Dinh, Vietnam

the agricultural potential of Vietnam is very large with 27.3 million hectares of fertile agricultural land, available agriculture on that land with crops that bring high consumption value and demand. As agricultural industrialization takes place, the scale of agriculture will expand rapidly. Tasks previously performed by humans will have to be replaced by automated processes, otherwise the demand for workers at all levels will not keep pace with demand. Based on this need, it is inevitable that machine learning based on computer vision algorithms are applied [1, 2].

Machine learning based on computer vision algorithms have made significant progress in solving the fruit detection challenges [3]. YOLOFruit was implemented in [4] with the average detection accuracy of 86.2%. In [3], YOLOv4, YOLOv4-tiny, YOLOv3, and YOLOv3-tiny were studied for coffee fruits detection with the mean average precision (mAP) of 81%, 79%, 78%, and 77% respectively. It is noted that in general, the YOLOv4 algorithm is more effective in detecting unripe fruit and is less affected by the density of objects in the image. A novel approach for kiwifruit detection with RGB and NIR images fusion and VGG16 was presented in [4] with the highest AP of 90.7% and the fastest detection speed of 0.134 s per image. The comparison among VGG16, ResNet50 and InceptionV2 methods for fruit recognition was discussed in [5]. YOLOMuskmelon model which integrated was developed in [6] to achieved an average precision AP of 89.6% for fruit detection in complicated environment. In order to fast detect apples in natural environment, a Des-YOLOv4 algorithm is investigated and implemented in the real robot system with the successful harvesting rate of the robot of 92.9%. The kiwi detection and classification based on YOLOv4 is studied in [7] with five classes (NO, OL, OF, OB, and OW). Overall, the highest mAP of 91.9% was achieved by YOLOv4 for 5 mentioned classes which cost 25.5 ms.

In order to implement fast and precisely recognize tomato for harvesting robot based on low-cost camera, this paper investigate Yolov4 algorithm to solve the problems experienced by tomato detection based on ROS framework. The ablation studies on YOLOv4 showed that this approach can achieve an improved real-time detection accuracy and speed.

The remainder of this paper is organized as follows: Sect. 2 introduces Harvesting tomato based on Yolov4 algorithm. Experiment results and Discussion are presented in Sect. 3, the conclusions are drawn in Sect. 4.

## 2 Harvesting Tomato Based on Yolov4 Algorithm

This study investigate the use of Yolov4 for ripe and unripe tomato for real-time harvesting purpose. Yolov4 consist of features: detection, extraction, enhancement. In which, A cross-stage partial (CSP) Darknet53 is implemented for extraction purpose; CSPResNet\_1, CSPResNet\_2; CSPResNet\_4, CSPResNet\_8 are used for improving the learning ability as shown in Fig. 1. All components of Yolov4 structure contribute to improving the inference speed (FPS) and accuracy of recognition (mAP) [8, 9].

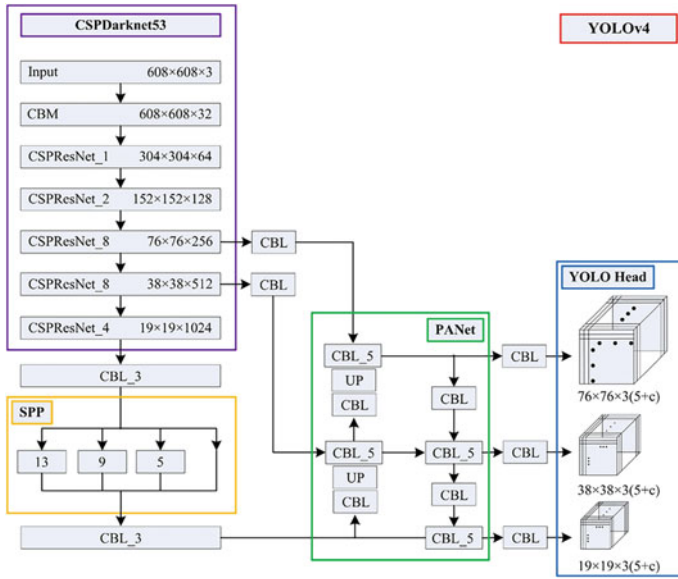


Fig. 1 Block diagram of YOLOv4 object detection [10]

The loss function ( $J$ ) of YOLOv4 model includes three components such as object localization offset loss ( $J_1$ ), confidence loss ( $J_2$ ), classification loss ( $J_3$ ) as follows:

$$J = J_1 + J_2 + J_3$$

$J_1$ : The localization loss measures the errors of the predicted boundary box in term of locations and sizes.  $J_1$  is calculated as follows:

$$J_1 = \lambda_1 \sum_{i=0}^{S^2} \sum_{j=0}^B 1_{ij}^{obj} [(x_i - \hat{x}_i)^2 + (y_i - \hat{y}_i)^2] + \lambda_1 \sum_{i=0}^{S^2} \sum_{j=0}^B 1_{ij}^{obj} [(w_i - \hat{w}_i)^2 + (h_i - \hat{h}_i)^2]$$

where:

$$1_{ij}^{obj} = \begin{cases} 1 & \text{if the } j\text{th boundary box in cell } i \\ 0 & \text{otherwise} \end{cases}$$

$$\lambda_1 = 5$$

( $\hat{x}_i, \hat{y}_i$ ): the center of the predicted box.

$(x_i, y_i)$ : the center of the ground truth box.

$B$ : box predictions for each grid cells.

$J_2$ : the confidence loss measures the objectness of the box.  $J_2$  is calculated as follows:

$$J_2 = \lambda_2 \sum_{i=0}^{S^2} \sum_{j=0}^B 1_{ij}^{noobj} [(C_i - \hat{C}_i)^2]$$

where:

$$1_{ij}^{noobj} = \begin{cases} 1 & \text{if the } j\text{th boundary box in cell } i \\ 0 & \text{otherwise} \end{cases}$$

$$\lambda_2 = 0.5$$

$C_i, \hat{C}_i$ : The box confidence score of the predicted box and ground truth box.

$J_3$ : the classification loss at each:

$$J_3 = \sum_{i=0}^{S^2} 1_{ij}^{obj} \sum_{c \in \text{classes}} [(p_i(c) - \hat{p}_i(c))^2]$$

$p_i(c), \hat{p}_i(c)$ : the conditional class probability of predicted and the truth for class  $c$  in cell  $i$ .

### 3 Experiment Results and Discussion

The used data for this study is a combination of data tomato detection in [10] and [11] and real-time image to increase the accuracy of the training and validation compare to the previous study [1]. The dataset has 2 classes including ripen and unripeness tomato, respectively. The total data set consist of 1015 images for training, 101 images for validation as shown in Table 1. Figure 2 present the original image and the resulted image using Yolov4 to detect ripe and unripe tomato.

Training is implemented with 6000 iterations on Google colab platform. The Loss function and mAP are preented in Fig. 3

**Table 1** Number of images and number of framed cells of each class in the dataset

	Train data		Validation data	
	Ripen	Unripeness	Ripen	Unripeness
Class	4142	3236	336	332
Number of image	1015		101	

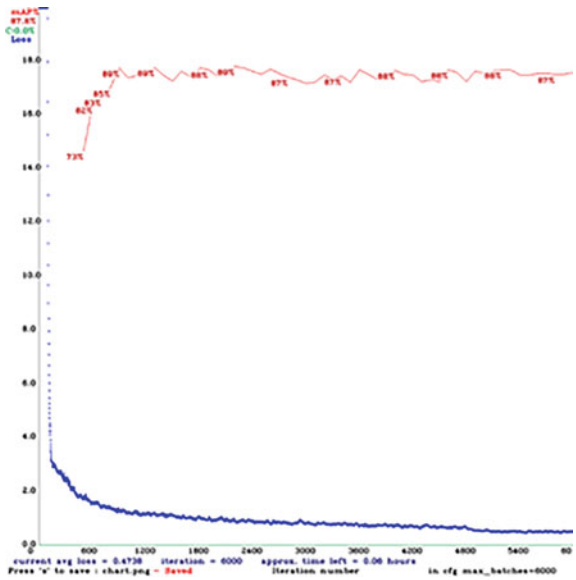


a. Original Image

b. Predicted Image

Fig. 2 The outputs of ripe and unripe tomato detection

Fig. 3 Train loss and mAP of the training process



The real experiment is implemented on the Robot Operating System (ROS) [12] with camera with 30 fps and computer Intel core i7-m4800MQ. The results are shown in Fig. 4 with the accuracy of 89%.



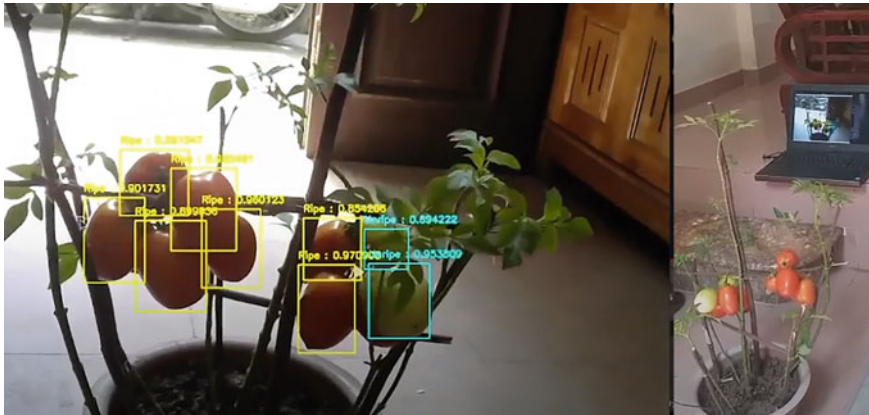


Fig. 4 The real experiment implemented on ROS

## 4 Conclusion

In this study, we have proposed the approach based on YOLOv4 algorithm for tomato harvesting agriculture robot. The training and validation images are the combination of data tomato detection in [13] and [10] and real experiment system to increase the accuracy. The experiment results verify the advantage of the method with an average accuracy of 89%. This proposed method is implemented on ROS system that available for agriculture robot system. Regarding applications in detecting ripe fruit, serving fruit picking robots, the detection algorithm shows that it works quickly, efficiently and accurately. However, other new algorithms can be studied and applied like newer versions of YOLO such as YOLOv5 and YOLOv7, although the actual application shows that these architectures are not really stable, they promise to be more stable. faster and more accurate. RCNN and Unet architectures can also be applied for tomato harvesting agriculture robot applications.

**Acknowledgements** This research is funded by National Foundation for Science and Technology Development of Vietnam NAFOSTED, Vietnam, under Grant 107.01-2018.331.

## References

1. T.T. Mac, V.T. Hoang, H.L. Bui, T.N. Sy, H.H. Hoang, Design of agriculture robot for tomato plants in green house. In: A.T. Le, V.S. Pham, M.Q. Le, H.L. Pham, (eds.) *The AUN/SEED-Net Joint Regional Conference in Transportation, Energy, and Mechanical Manufacturing Engineering. RCTEMME 2021*. Lecture Notes in Mechanical Engineering. (Springer, Singapore, 2022). [https://doi.org/10.1007/978-981-19-1968-8\\_113](https://doi.org/10.1007/978-981-19-1968-8_113)
2. A. Koirala, K.B. Walsh, Z. Wang, C. McCarthy, Deep learning—method overview and review of use for fruit detection and yield estimation. *Comput. Electron. Agric. Electron. Agric.* **162**, 219–234 (2019)
3. O.M. Lawal, et al., Ablation studies on YOLOFruit detection algorithm for fruit harvesting robot using deep learning. *IOP Conf. Ser.: Earth Environ. Sci.* **922**, 012001 (2021)
4. H.C. Bazame, et al., Detection of coffee fruits on tree branches using computer vision. *Sci. Agricola* **80**, (2023)
5. Z. Liu et al., Improved kiwifruit detection using pre-trained VGG16 with RGB and NIR information fusion. *IEEE Access* **8**, 2327–2336 (2020). <https://doi.org/10.1109/ACCESS.2019.2962513>
6. S.C.K. Jagan Mohan, M. Arulalan, Real time riped fruit detection using faster R-CNN deep neural network models. In: *2022 International Conference on Smart Technologies and Systems for Next Generation Computing (ICSTSN)* (2022), pp. 1–4. <https://doi.org/10.1109/ICSTSN53084.2022.9761356>.
7. W. Chen, J. Zhang, B. Guo, Q. Wei, Z. Zhu, An apple detection method based on des-YOLOv4 algorithm for harvesting robots. *Complex Environ., Math. Probl. Eng.* **2021**. <https://doi.org/10.1155/2021/7351470>
8. R. Suo, F. Gao, Z. Zhou, L. Fu, Z. Song, J. Dhupia, R. Li, Y. Cui, Improved multi-classes kiwifruit detection in orchard to avoid collisions during robotic picking. *Comput. Electron. Agric.* **182** (2021)
9. S. Wang, J. Zhao, N. Ta, X. Zhao, M. Xiao, H. Wei (2021). A real-time deep learning forest fire monitoring algorithm based on an improved Pruned + KD model. *J. Real-Time Image Process.* <https://doi.org/10.1007/s11554-021-01124-9>
10. V. Tsironis, S. Bourou, C. Stentoumis, Tomatod: evaluation of object detection algorithms on a new real-world tomato dataset. In: *ISPRS—International Archives of the Photogrammetry, Remote Sensing and Spatial Information Sciences* (2020)
11. <https://www.kaggle.com/datasets/andrewmvd/tomato-detection>
12. T.T. Mac, C. Y. Lin, N.G. Huan, L. Duc, P.C.H. Nhat, H.H. Hai, Hybrid SLAM-based exploration of a mobile robot for 3D scenario reconstruction and autonomous navigation. *Acta Polytech. Hung* **18**, 197–212 (2021)
13. Y. Li et al., A deep learning-based hybrid framework for object detection and recognition in autonomous driving. *IEEE Access* **8**, 194228–194239 (2020). <https://doi.org/10.1109/ACCESS.2020.3033289>
14. O.M. Lawal, YOLOMuskmelon: quest for fruit detection speed and accuracy using deep learning. *IEEE Access* **9**, 15221–15227 (2021). <https://doi.org/10.1109/ACCESS.2021.3053167>

# Design and Simulation of a Scaled Motion Platform System Based Parallel Robot



Van-Quy Hoang, Do Van, Hoang Manh Hung, Pham Kim Mung,  
Le Van Khanh, and Duc An Pham

**Abstract** Driving simulation systems with 6-degree-of-freedom motion platforms based on parallel robots that support motion perception are used in driver training and human sensory research. The article focuses on calculating and building a scaled model of the 6-dof motion platform for both researching motion cueing algorithms in recreating the motion sensation and adjusting their parameters accordingly. Then, the motion platform model is integrated with other devices including the motion control system, the virtual 3D environment to construct a scaled simulation driving system. The simulation results and testing of basic movements of the simulation platform show the accuracy of the position and angle of inclination, in addition, the motion platform responds quickly that is suitable for the study of movements during driving tasks.

**Keywords** Driving simulator · Motion platform · 3D environment

## 1 Introduction

Due to the development of science and technology, driving simulation applications not only satisfy the high standards of the entertainment sector but also the growing demands for training and coaching in both military and civilian settings, in a variety of industries including the automotive, and aerospace. Applications in simulation games, research and development of steering systems, evaluation and analysis of human behavior in hazardous driving scenarios, and training pilots to fly aircraft to help cut training times are some examples of typical applications [1]. Various developed motion cueing algorithms were developed to improve simulation fidelity and

---

V.-Q. Hoang

Faculty of Electric-Mechanical Engineering, Hai Phong University, Haiphong, Vietnam

D. Van · H. M. Hung · P. K. Mung · L. Van Khanh · D. A. Pham (✉)

School Mechanical Engineering, Hanoi University of Science and Technology, Hanoi, Vietnam

e-mail: [an.phamduc@hust.edu.vn](mailto:an.phamduc@hust.edu.vn)

reduce motion sickness [2–5]. However, most of the research related to these algorithms is usually only simulation cases, the actual validation is still difficult due to the high cost of the simulation system and the complicated integration process with the simulation system such as a 3D environment, as well as depending on human judgment [6, 7]. The scaled model of the motion platform system is developed to support the research process related to the driving simulation system, especially for those related to the motion cueing algorithms. The model makes the investigation easier for the quantitative evaluation process to follow more explicit criteria. In addition, the model also is helpful for the integration process between the 3D environment. The article will first present the structure of the scale model of the motion platform system, then present the working space and dynamic computation for the simulation platform, and finally implement the comparison of the workspace of the actual working of the system with that of simulated models.

## 2 Scaled Motion Platform

### 2.1 Mechanical Structure and Operating Workspace of the Motion Platform

The Hexapod motion platform is design to carry maximum 3 kg, the six main components are manufactured as Fig. 1. The calculation of the working space of the simulation platform is implemented through the solving inverse kinematics and the monitoring of the force from the spherical joints. Therefore, inverse kinematic is solved with the support of the mutibody system tools with 12 spherical joints, 6 cylindrical joints and several assumption of fix components. For example, when the upper base of motion platform has both surge and pitch movement that are popular in the simulating the accelerating and deaccelarting tasks in driving situation, the joint angles generated by 6 dc motor (dc\_1–6) are shown in Fig. 1 with the largerest angle of the third joint.

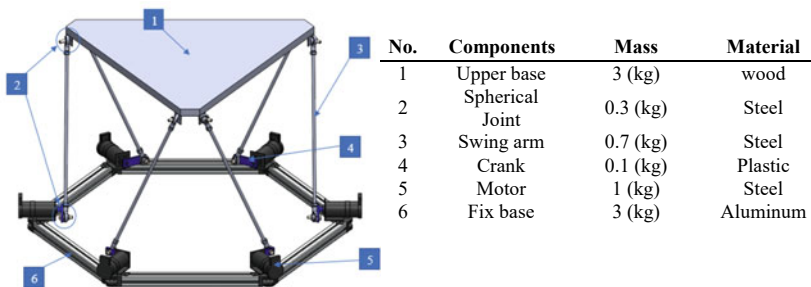


Fig. 1 Components of motion platform

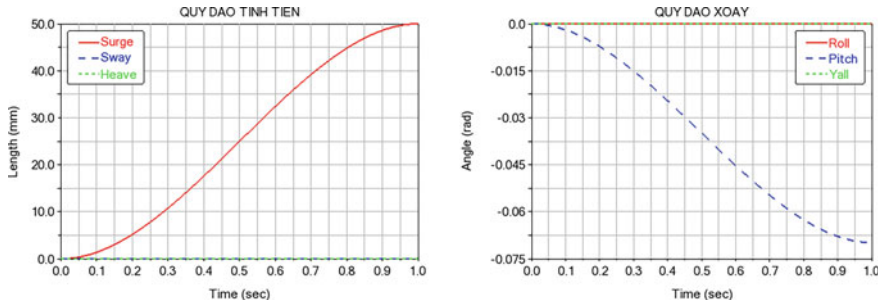


Fig. 2 Translational and rotational trajectory of motion platform

No	Components	Mass (kg)	Material
1	Upper base	3	Wood
2	Spherical Joint	0.3	Steel
3	Swing arm	0.7	Steel
4	Crank	0.1	Plastic
5	Motor	1	Steel
6	Fix base	3	Aluminum

The calculation of the working space of the simulation platform is implemented through the solving inverse kinematics and the monitoring of the force from the spherical joints. Therefore, inverse kinematic is solved with the support of the multi-body system tools with 12 spherical joints, 6 cylindrical joints and several assumption of fix components. For example, when the upper base of motion platform has both surge and pitch movement (Fig. 2) that are popular in the simulating the accelerating and deaccelarting tasks in driving situation, the joint angles generated by 6 dc motor (dc\_1–6) are shown in Fig. 3 with the largerest angle of the third joint.

The mechanical limit is found by placing the contacts between two blocks on the 3D model, then plotting the contact force and evaluating the limit (Fig. 4). During the movement of motion platform, the earliest spherical joint affected by the force value is investigated to find the limitation of the movement. The joints are numbers as Fig. 4a and the force of the joint at the limited position expressed by the abrupt change of amplitude (Fig. 4b and Fig. 5) for only y-axis movement. For example, the upper base moving towards the positive y-axis has a limit of 69 mm and the 11 and 12 spherical joints are affected the earliest (Fig. 5). Similar to the remaining moves, the limit of remain degree of freedom are obtained as in Table 1.

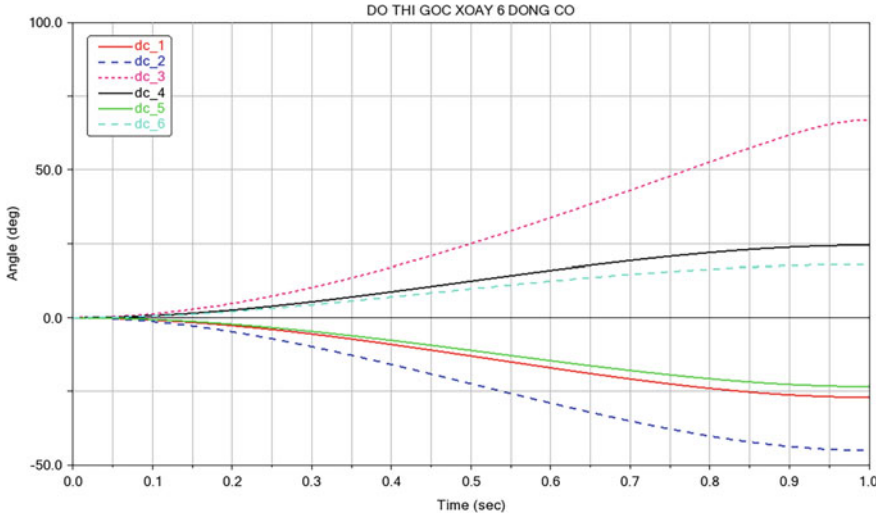


Fig. 3 Joint angles of motion platform according to surge and pitch movements

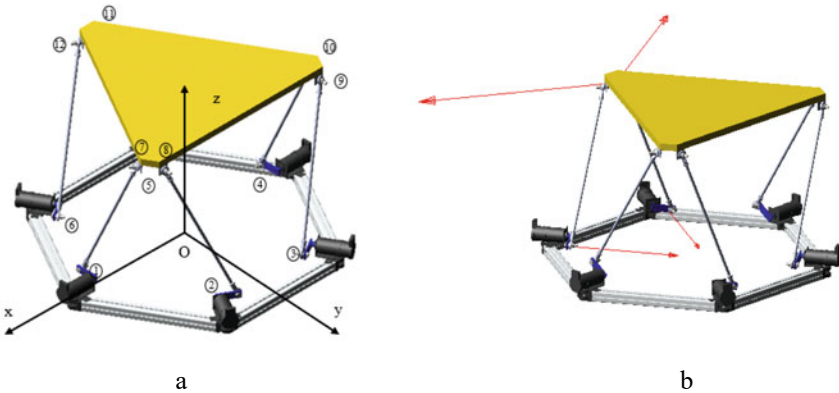


Fig. 4 a Theo coordinate and the joint number of the motion platform, b The force at the limitation of the joint

### 2.2 Compute Require Torque at the Joints

For the engine meets the working requirements, it is necessary to solve the problem of inverse dynamics with the maximum load. The inverse dynamics problem is similar to the inverse kinematics problem done in the previous section, the multibody system tool provides a very powerful tool that allows to simulate inverse dynamics without writing complex computational expressions. With a load placed on the robot of 3 kg

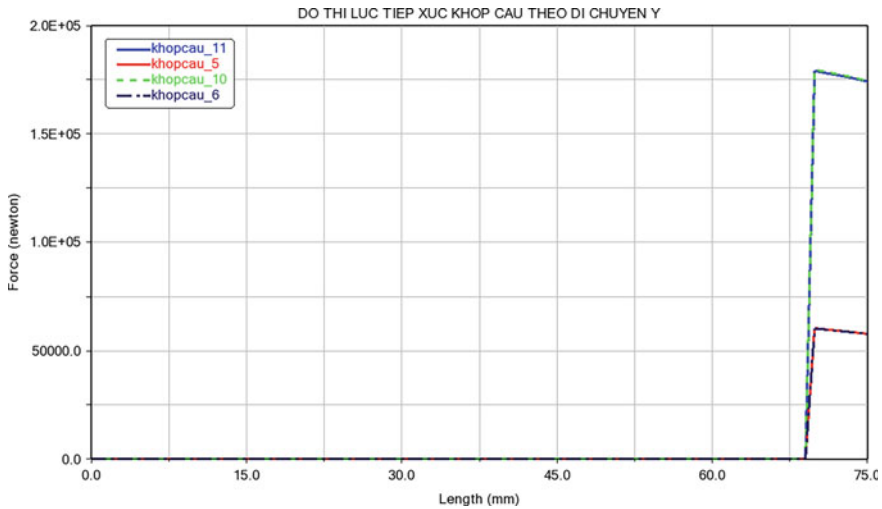


Fig. 5 Contact force at spherical joints corresponding to movement

Table 1 Robot limitation according to joint

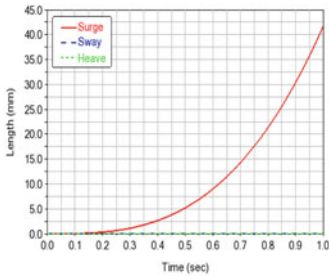
Dof	Upper limit	Joint number over limit	Lower limit	Joint number over limit
Surge	68 (mm)	10	- 52 (mm)	7
Sway	69 (mm)	11, 12	- 52 (mm)	8, 9
Heave	70 (mm)	-	- 32 (mm)	-
Roll	4.4°	6	- 4.3°	9
Pitch	4.8°	1	- 4.9°	9
Yall	5.0°	8, 10, 12	- 5.3°	7, 9, 11

and increased from 0 to 0.25 m/s<sup>2</sup>, the simulation of moving with an acceleration increasing from 0 to 0.25 m/s<sup>2</sup> along the x-axis.

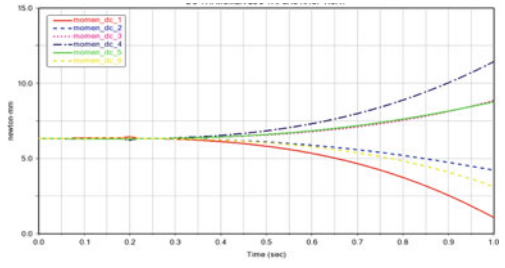
According to Fig. 6b, the motor 1, 4 is subjected to the maximum absolute of torque with an approximate value of 11.45 N mm. Due to the symmetric arrangement of the motor, the result moment of 6 joints of the moving in y axis will be similar.

### 3 Validation with the Real Scaled Model

The driving simulation system model is built with a DC motor which is controlled for position accuracy by a PID controller implemented in an Arduino board. The operating workspace is measured, as shown in Fig. 7, with the laser measurement system. The operating workspace measured in simulation and the real scaled motion platform are shown in Table 2. The measured position deviation is due to the following factors:



a) Motion of the upper base



b) Moment of the 6 joints

**Fig. 6** Investigate the required moment at 6 dofs

(1) Dimension accuracy of the 3D model and the real model when simulating to calculate the reverse kinematics of the motors; (2) The mechanical structure is not accurate enough for simulation data, and not enough rigidity. This is the main cause of the deviation; (3) the deviation when measuring movements includes measuring instrument inaccuracy; however, these small deviations are acceptable for the scale motion platform, and could not generate effect on the investigation of motion sensation.

**Fig. 7** Measurement of the pitch angle in real scaled motion platform

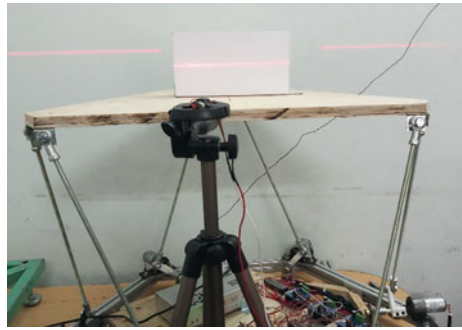


**Table 2** Comparison of operating workspace between some movements between real model and simulation

Sway		Heave		Yaw	
Simulation (mm)	Measure (mm)	Simulation (mm)	Measure (mm)	Simulation	Measure
20	21	30	32	3.0°	3.5°
25	28	35	33	3.5°	4°
30	33	40	44	4.0°	4°



## 4 Conclusion

This paper presents the process of designing, calculating, and simulating a motion reconstruction system for the driving simulation system. The multibody system method is used to help calculate the forces at the joints and to support the calculation of the working space of the motion platform system. Then, the workspace of the scaled model after manufactured is measured to find the actual workspace. The similar workspace found in the simulation and in real measure proves the reliability of the simulated model. In addition, the scale motion platform can be used in studies related to the movement of the platform and the motion cueing algorithm, as well as to demonstrate drivers' perceptions during the driving simulation tasks.

## References

1. D. Stewart, A platform with six degrees of freedom. *Proc. Inst. Mech. Eng.* **180**(1), 371–386 (1965)
2. B. Conrad, S. Schmidt, Motion drive signals for piloted flight simulators (1970)
3. L. Reid, M.A. Nahon, *Flight Simulation Motion-base Drive Algorithms: Part 1. Developing and Testing Equations*. (University of Toronto, 1985)
4. T.-S. Hwang, S.-K. Yeh, J.-R. Lin, W.-P. Su, Adaptive motion washout filter design by using self-tuning fuzzy control. In *IEEE/ASME International Conference on Advanced Intelligent Mechatronics, 2009*. AIM 2009. (IEEE, 2009), pp. 811–815
5. S.-H. Chen, L.-C. Fu, An optimal washout filter design with fuzzy compensation for a motion platform. *IFAC Proc. Volumes* **44**(1), 8433–8438 (2011)
6. L. Reid, M.A. Nahon, *Flight Simulation Motion-Base Drive Algorithms.: Part 2, Selecting The System Parameters*. UTIAS report, no. N307 (1986)
7. D.-A. Pham, D.-T. Nguyen, False cue influence on motion cue quality for 10 motion cueing algorithms. *Sci. Prog.* **104**(3), 00368504211036857 (2021)

# A Multi-Floor Elevator Control Based on Oriented-Object Programming by Using Function Block



Si-Tuan Hoang and Duc An Pham

**Abstract** In this article we have presented a method of object-oriented programming for Siemens S7-1200 PLC to control a multi-floor elevator, using Function Block (FB). The Function Blocks are built based on the behavior of the same functional objects, in which output signals are changed corresponding to input signals in priority. The control method has been implemented with priority control rule for the 4-floor elevator model. Note that, the elevator runs with high stability and ensure all defined functions.

**Keywords** Object-oriented programming · Multi-floor elevators · Function block (FB) · Grafcet

## 1 Introduction

In modern life, with the appearance of a large number of high-rise apartment buildings and supermarkets, elevators have become more and more important means of transportation of people and goods. Elevators help reduce human labor, especially helping the elderly and children easily move up or down between floors in high-rise buildings.

The design of the control system for the elevator can use a relay system or a microprocessor circuit [1], but due to the inconvenience of system scalability as well as the influence of noise or interference, the effect of electromagnetic waves on the signal transmission line, which in practice is also rarely used.

In the studies [2–5], the advantages and disadvantages of replacing the relay system with a PLC controller to control the operation of the elevator system were analyzed, but the control options using the new LADDER programming language only applies to elevators with a small number of floors. Therefore, upgrading or

---

S.-T. Hoang · D. A. Pham (✉)

School Mechanical Engineering, Hanoi University of Science and Technology, Hanoi, Vietnam

e-mail: [an.phamduc@hust.edu.vn](mailto:an.phamduc@hust.edu.vn)

expanding the elevator system with many floors is a real problem if the control program is not organized and arranged scientifically.

In this study, the design option using Siemens S7-1200 PLC was selected with a control program programmed using function blocks (FB) combined with data blocks [6], allowing deploy control program applicable to elevators with multiple floors.

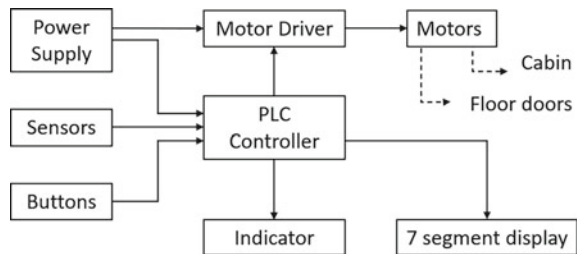
## 2 Design of Oriented Control System

Normally, elevator control system consists of 3 main components: input signal, output signal and controller. Input signals are usually received from sensors, push buttons, control keys, and on-off switches of the control system. While the output signals provide control of output devices such as actuators (electric motor for lifting the elevator and motor for opening and closing doors), bells, display screens, lights, etc. Here the controller of the elevator uses PLC Siemens S7-1200, the diagram of connecting the control elements in the elevator control system is as shown in Fig. 1.

An elevator system consisting of N floors is taken into consider. If only interested in the basic elements of the control system in terms of output control signals, the system will include two types of objects. main statue:

Control the door opening/closing of n floors with input signals from  $2x(N-1)$  floor call buttons located outside the floor doors and N floor selector buttons inside the control panel of the elevator room, In addition, the input signal also has a signal to close and hold the door when the elevator is stopping at floors. To generalize and aim at object-oriented programming to control the opening/closing of the door of each floor without affecting the control rules of the system, we can consider the input signal of each floor to include: the signal of the 2 up/down cascade call buttons (note that the descending call signal of the lowest layer and the upstream call signal of the top layer are always zero), the signal of the floor selector, and the signal of the 2 buttons to close and hold the floor door. In addition, based on the operating status and current position of the elevator, we also determine the priority signal for the up-and-down movement of the corresponding elevator on each floor. The rule to control the opening/closing of the floor door and keeping

Fig. 1 Block diagram of a elevator control system



the priority state of the elevator’s up/down movement on each floor is built by the function block for floor control (FB\_FLOOR\_CONTROL)

Up/Down moving control: The input signal to perform Up/Down moving control is extracted from the motion priority signal (up or down) and set by the function block for floor control (FB\_CABIN\_CONTROL). where the function and data type of the variables are described in Tables 1 and 2.

**Table 1** Input, output variables and global variables of floor control

Input	Data type	Comment
UP BUTTON	BOOL	Push button signal for moving elevator up
DOWN BUTTON	BOOL	Push button signal for moving elevator down
FLOOR BUTTON	BOOL	Push button signal for selecting floor
OPEN BUTTON	BOOL	Push button signal for holding door open
CLOSE BUTTON	BOOL	Push button signal for closing door
HUMAN SENSOR	BOOL	Sensor for detecting obstacle object at door
CALLED FLOOR	INT	Push button for Calling floor (1, 2, ..., N)
Output	-	-
UP SIGNAL	BOOL	Signal for the elevator to go up
DOWN SIGNAL	BOOL	Signal for the elevator to go down
OPEN DOOR	BOOL	Signal for opening door
CLOSE DOOR	BOOL	Signal for closing door
Memory	-	-
PRIORITY UP	BOOL	Priority state for going up
PRIORITY DOWN	BOOL	Priority state for going down
PRESENT FLOOR	INT	Current floor (1, 2, ..., N)

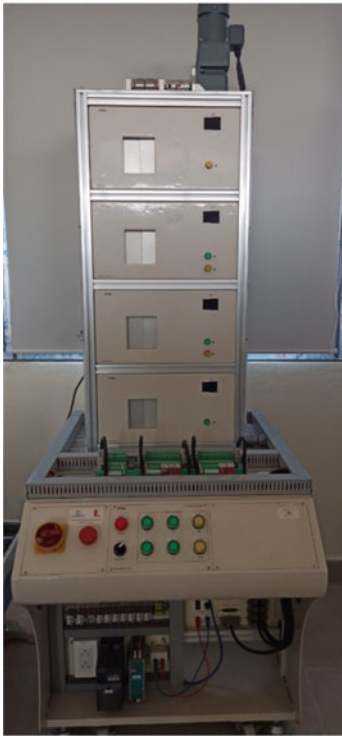
**Table 2** Input, output variables and global variables of cabin control

Input	Data type	Comment
F1_UP_SIGNAL	BOOL	Signal requesting elevator to go up of 1st floor
F1_DOWN_SIGNAL	BOOL	Signal requesting elevator to go down of 1st floor
...	...	...
FN_UP_SIGNAL	BOOL	Signal requesting elevator to go up of Nst floor
FN_DOWN_SIGNAL	BOOL	Signal requesting elevator to go down of Nst floor
Output	-	-
UP	BOOL	Control the cabin going up
DOWN	BOOL	Control the cabin going down

### 3 Implementation the Controller for Scaled Model of 4-floor Elevator

To demonstrate the suitability of the multi-storey elevator control plan using function blocks as mentioned above, the oriented-controller is implemented for the scaled model of 4-floor elevator model ( $N = 4$ ), Fig. 2a.

The I/O variables of the digital devices connected to the PLC are defined as shown in Fig. 2b. The control rule for opening/closing the landing door and setting the motion control state for the cabin is defined in the function block FB\_FLOOR\_CONTROL through input/output control signals, shown in the Grafcet flow chart [7] as shown in Fig. 3a and can be explained as follows: Initially, the system is stopping at STEP 0. Suppose when the floor under consideration has the control signal IN1 (call button goes up), the system switches to STEP 1 (comparison test). The value



a)

Input			
	Name	Data type	Address
1	PC/AUTO	Bool	%I0.0
2	Call F1	Bool	%I0.1
3	Call F2	Bool	%I0.2
4	Call F3	Bool	%I0.3
5	Call F4	Bool	%I0.4
6	Open Button	Bool	%I0.5
7	Close Button	Bool	%I0.6
8	F1 UP	Bool	%I0.7
9	F2 DOWN	Bool	%I1.0
10	F2 UP	Bool	%I1.1
11	F3 DOWN	Bool	%I1.2
12	F3 UP	Bool	%I1.3
13	F4 DOWN	Bool	%I1.4
14	F1 Sensor	Bool	%I1.5
15	F2 Sensor	Bool	%I8.0
16	F3 Sensor	Bool	%I8.1
17	F4 Sensor	Bool	%I8.2
18	L5_LOWEST	Bool	%I8.3
19	L5_HIGHEST	Bool	%I8.4
20	L5_DoorClose	Bool	%I8.5
21	L5_DoorOpen	Bool	%I8.6
22	Obstacle Sensor	Bool	%I8.7

Output			
	Name	Data type	Address
1	Close_F1_Door	Bool	%Q0.0
2	Close_F2_Door	Bool	%Q0.1
3	Close_F3_Door	Bool	%Q0.2
4	Close_F4_Door	Bool	%Q0.3
5	Open_F1_Door	Bool	%Q0.4
6	Open_F2_Door	Bool	%Q0.5
7	Open_F3_Door	Bool	%Q0.6
8	Open_F4_Door	Bool	%Q0.7
9	Arrow_DOWN	Bool	%Q1.0
10	Arrow_UP	Bool	%Q1.1
11	F1 LCD	Bool	%Q8.0
12	F2 LCD	Bool	%Q8.1
13	F3 LCD	Bool	%Q8.2
14	F4 LCD	Bool	%Q8.3
15	Up LED	Bool	%Q8.4
16	Down LED	Bool	%Q8.5
17	Buzzer	Bool	%Q8.6
18	Out lamp button	Bool	%Q8.7

b)

Fig. 2 The 4-floor elevator model and input and output signals

of M3, M4 is the called floor position and current elevator position). If  $M3 > M4$  (the called floor is higher than the current car position), the system switches to STEP 4 (upward motion priority signal is activated). When  $M3 = M4$  (cabin reaches call location), the system switches to STEP 6 (waiting for priority status check). Here, because the IN1 signal is being called, it will need to prioritize going up, the system switches to STEP 7, saves the up-priority state, and simultaneously executes the door opening. When the door opening time is over, the system switches to STEP 9 to close the door, and still maintain the right of way up, while waiting for the door to close if there is 1 of 3 signals (door open button, call button move at if the floor is in the same direction as the movement priority direction), it will return to STEP 7, and if the time runs out, it will return to STEP 0. The remaining cases are implemented similarly.

While the function block FB\_CABIN\_CONTROL is built to control lifting/lowering of the elevator with the control rules shown in the Grafset diagram as shown in Fig. 3b The control cycle of raising/lowering the car can be presented as follows: When the cabin standing still, the system is at STEP 0. If there is any signal

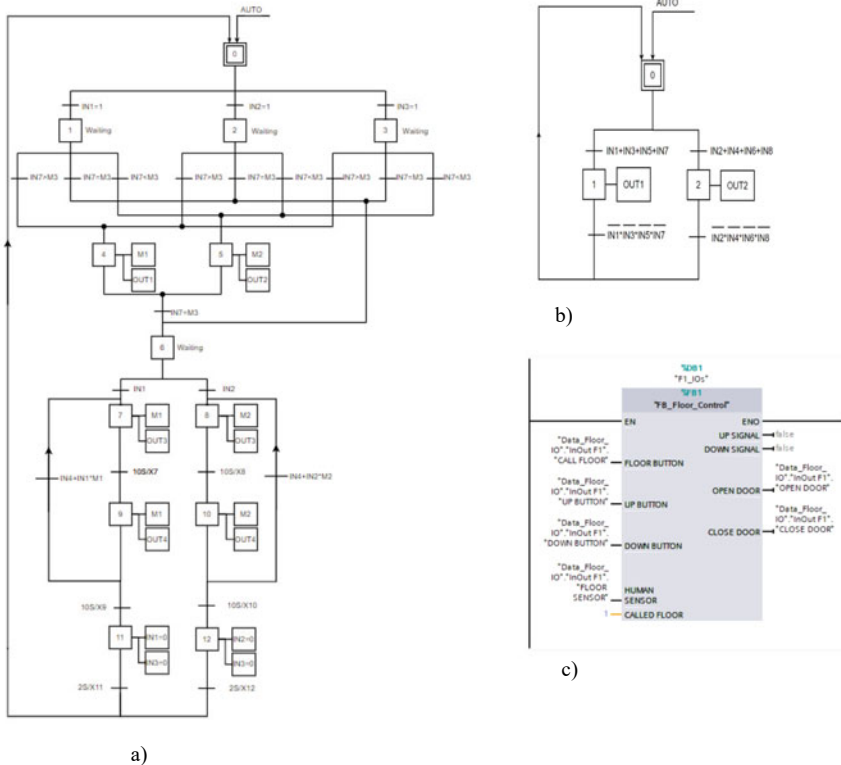


**Fig. 3** a Flow chart of Grafset for opening/closing the floor door, b Fig. 5. Flow chart of Grafset for moving the cabin up/down, c Using FB for opening/closing the floor doors

that requires the elevator to move from the floors, the system will switch to STEP 1 or STEP 2, outputting the signal to control the elevator to go up or down. down, after the end of the up or down request signal, the system returns to STEP 0 and switches to a new cycle.

Following the operating rules of opening/closing the door and lifting/lowering the elevator as described by the Grafset diagrams as presented, the function blocks for floor control (FB\_FLOOR\_CONTROL), and cabin control (FB\_CABIN\_CONTROL) were used to build the subroutines Fig. 3b. To control the opening/closing of doors at 4 floors will be done in the main program (MAIN) with calling 4 times the function block FB\_FLOOR\_CONTROL along with input variables and output variables respectively, like Fig. 3c illustrates the call to open/close control function of the 1st floor. The elevator control operation shows that it completely meets the requirements set out with the priority order of calling the elevator considering the direction of movement of the elevator.

## 4 Conclusions

The application of the function block to the construction of the output control signal for the opening/closing of the floor door and the lifting/lowering of the elevator cabin helps the design engineer to easily build the control program, as well as control the signal. signal or error/failure if any occurs during operation. In addition, the use of function block programming to control the opening / closing of each floor is also easy to expand and improve the elevator control system when the number of floors or input and output signals change.. The results have been verified with the application of the control method to the 4-storey elevator model, the operation of the elevator is assessed to be completely satisfactory in terms of technology requirements.

Future development will continue to develop control methods to be applied to parallel control, taking into account the priority of two or more elevators operating at the same time, for example, for use in apartments or buildings. high-rise buildings, etc. through the communication connection between PLC controllers.

## References

1. H. Qin. Elevator drive control system based on single chip microcomputer. In *8th International Conference on Mechatronics, Computer and Education Informationization (MCEI 2018), Advances in Computer Science Research (ACSR)*, vol. 83, (2018), pp. 137–143
2. K. Tharani, S. Gupta, A. Puri, R. Khera, A. Kumar, PLC based multi-floor elevator control system. *Int. J. Rob. Autom. (IJRA)* **4**(3), 202–208 (2015)
3. A.M. Anusha, A.V. Sutagundar, Design of a PLC based elevator control system. *Int. J. Emer. Technol. (Special Issue on NCRIET-2015)* 32–36 (2015)
4. O.M. Shete, M.A.A. Vitkar, M.A.N. Patil, Design and control of an elevator control system using PLC. *Int. J. Innovative Res. Electr. Electron. Instrum. Control Eng.* **5**(4), 142–147 (2017)

5. P. Wang, A control system design for hand elevator based on PLC. *Fourth International Symposium on Computational Intelligence and Design, 2011* (2011), pp. 71–74
6. Siemens, *Programming Guideline for S7-1200/1500*. Entry ID: 81318674, V1.6, 12/2018 (2018)
7. International Electrotechnical Commission, *Specification Language GRAFCET for Sequential Function Charts*. IEC 60848 Ed. 2.0 (2007)



# Real-Time Deep Learning-Based Automatic Pill Classification



Thi Thoa Mac and Minh-Huy Nguyen

**Abstract** This paper proposes a method of combining pill image processing with a convolution neural network modified VGG16 based on Adam optimization that ensures the high accuracy of defect detection and classification. The novelty lies in: (i) the development of real-time deep learning-based automatic pill defect detection; (ii) the proposed training structure: modified VGG16 structure and Adam optimization algorithms to find the optimal solution and (ii) the design and implementation of a model construction and training based on VGG16. For the training stage, qualified pill images in the real manufacturing system are collected as samples. In the prediction stage, the proposed method is implemented to validate pills and categorize them into three different categories (contamination, good, crack). The results validate the effectiveness of the real-time. It provided a high accuracy on real-time systems. High accuracy and fast processing time make the proposed method highly potential to apply to industrial systems.

**Keywords** Deep learning · Adam · Quality inspection · VGG · Machine vision · Optimization

## 1 Introduction

Production quality control is an essential requirement for the success in the market. The automatic defect-detection system has superiority over manual detection. The requirement for real-time defect detection on an intelligent manufacturing system has increased with deep learning and vision based technique in industrial 4.0. As a consequence, defect-detection-related technologies have attracted many scholars in the last decades such as the laser [1], ultrasound [2], thermal [3], machine vision [4–6] and deep learning [7] detection methods. As pharmaceutical pill manufacture has a board market and the precise pill defect detection in manufacturing line is an essential

---

T. T. Mac (✉) · M.-H. Nguyen  
Hanoi University of Science and Technology, Hanoi, Vietnam  
e-mail: [thoa.macthi@hust.edu.vn](mailto:thoa.macthi@hust.edu.vn)

© The Author(s), under exclusive license to Springer Nature Switzerland AG 2024  
B. T. Long et al. (eds.), *Proceedings of the 3rd Annual International Conference on Material, Machines and Methods for Sustainable Development (MMMS2022)*, Lecture Notes in Mechanical Engineering, [https://doi.org/10.1007/978-3-031-57460-3\\_58](https://doi.org/10.1007/978-3-031-57460-3_58)

521

issue [8]. Artificial techniques are more and more popular in image processing based applications [9]. Several noticeable approaches have been attempted for the pill identification purpose based on computer vision techniques [10–13]. In [14], Ling et al. provides a new pill image database—CURE which includes 8973 images of 196 categories (each image is taken with different background, illumination, focus, and orientation). In [15], an approach based on a convolution neural network (CNN) algorithm is developed for identifying capsule defection. In [16], Zeng et al. introduce the design and evaluation pill image recognition using mobile system. Recurrent attention convolutional neural network (RA-CNN) algorithm is developed in [17] to solve the overfitting problem.

The latest research in the deep learning field has revealed that most difficulties of the pure vision-based approaches were solved by using CNNs [18]. Recent studies indicate that VGG is more advantageous than other approaches. Compared to previous our work in [19, 20], this paper presents the design, implementation, and evaluation a real-time deep learning-based automatic pill defect detection in a manufacturing system. Our study includes three key innovations. The novelty lies in: (i) the development of real-time deep learning-based automatic pill classification; (ii) the design and implementation of a model construction and training based on VGG16. For the training stage, qualified pill images in the real manufacturing system are collected as samples.

This paper is structured as follows: Sect. 2 proposes the deep learning-based image classification approach. Section 3 describes the results and analysis. The discussion, conclusion and further work are provided in Sect. 4.

## 2 Deep Learning-Based Image Classification Approach

First, VGG architecture is introduced in Sect. 2.1. Then, Adam optimization method is introduced in Sect. 2.2.

### 2.1 VGG Architecture

In this study, we leveraged transfer learning to initialize the weights of the VGG16 network. The architecture of the proposed VGG16 in our study is presented in Fig. 1. For real-time pill classification purpose, we used 2500 images in training/validation dataset.

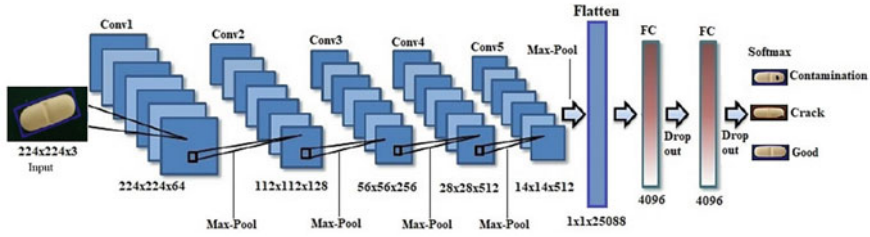


Fig. 1 VGG structure

### 2.2 Adam Optimization Algorithm

Ba [21] is developed Adam optimization algorithm. This method is a combination of the advantages of two other extensions of stochastic gradient descent Adadelata and RMSProp [22, 23].

$$J(w, b) = \frac{1}{m} \sum_{i=1}^m y^i * \log(\hat{y}^i) + (1 - y^i) * \log(1 - y^i) \tag{1}$$

The following objective function in Eq. (1) is calculated as follows.

Where:

$\hat{y}_i$ : predict value.

$y^i$ : real value.

$i$ : 1 ...  $n_{val}$ .

$w, b$ : designed parameters.

## 3 Experiment Results

The system design and its flowchart are shown in Fig. 2, Fig. 3, respectively.

The system has two stations. First, the camera station is used to obtained the image. Second, the package station is designed to pack qualified pills. The camera is mounted perpendicular to the conveyor surface. To process the system, pill images (inputs) are collected by using a CCD camera 30fps, 1920 × 1080 pixels. The conveyor background was excluded. The system uses 2500 image samples for qualified and unqualified pill samples. Based on the pill qualities, the PLC executes different control process. If the pills are unqualified, they are rejected. Otherwise, the qualified pills move to the packaged station as shown in Fig. 2.

To validate the qualification of the inspection system, The accuracy and loss functions results are shown in Figs. 4 and 5, with different batch size and stap per epoch respectively. Figure 4 shows accuracy function with Adam had accuracy of

**Fig. 2** The lab-scale system

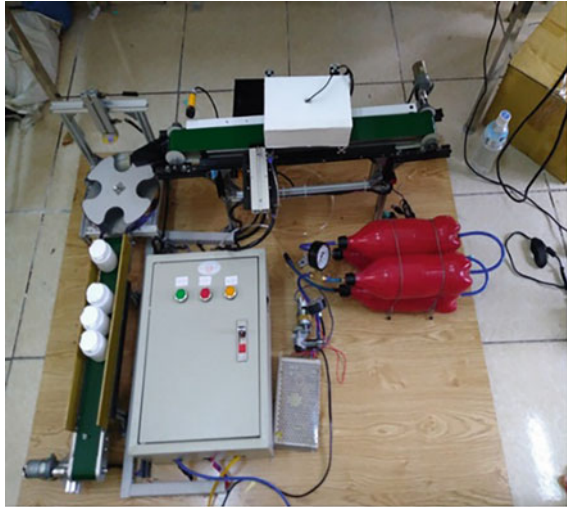
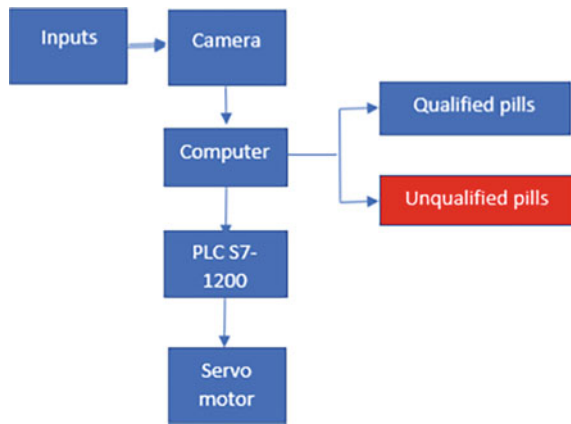


**Fig. 3** Flowchart of the designed system



95%. In Fig. 5, it can be realized that the loss function for a precise classification process.

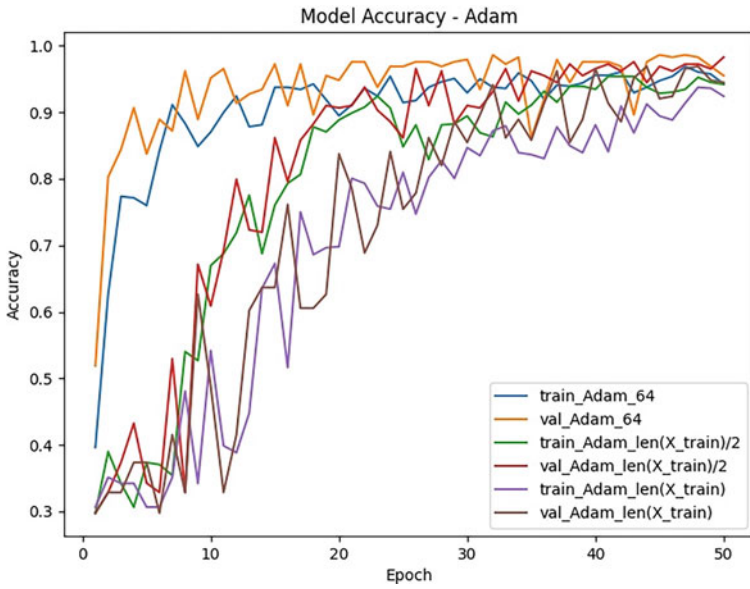


Fig. 4 The accuracy function with different batch size and step per epoch

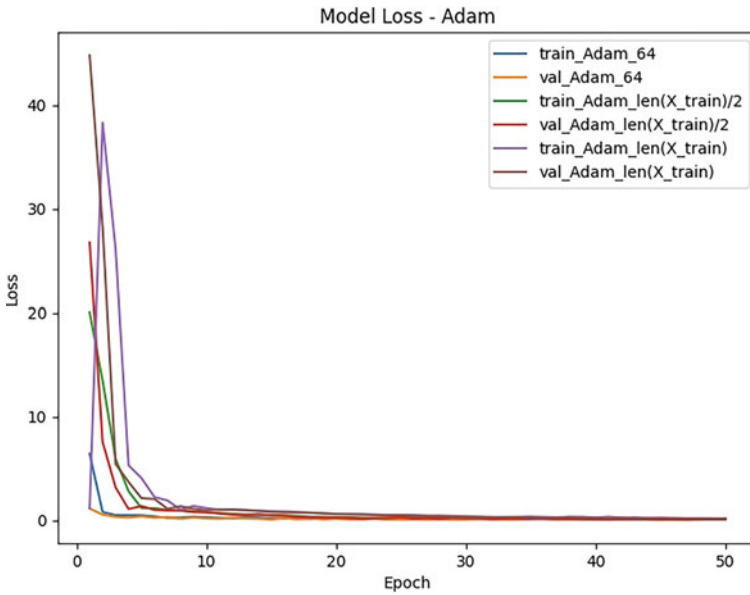


Fig. 5 Loss function with different batch size and step per epoch

## 4 Conclusion

In this paper, we have developed a real-time deep learning-based automatic pill defect detection. The main achievements for this work are: The novelty lies in: (i) the development of a real-time deep-learning based automatic pill defect detection; (ii) the design and implementation of a model construction and training based on VGG16. The training and validation images are collected in the real manufacturing system as the dataset. The experiment results verify the advantages of the integrated model with an average accuracy of 95%. The results showed that our approach can meet actual production requirements. In future work, this approach will be extended in a industrial scale pill manufacturing inspection in term of decreasing the production time and production cost.

## References

1. I. Frosio, P. Tirelli, G. Venturino, G. Rotondo, N.A. Borghese, Flexible and low cost laser scanner for 195 automatic tyre inspection. *IEEE Int. Instrum Meas. Technol. Conf.* 260–264 (2011)
2. R. Vogel, L. Pollard, R. Yates, M. Beller, Ultrasound tool can combine metal loss and crack inspection of gas pipelines. *Pipeline Gas J.* **234**(8), 112–118 (2007)
3. K. Yildiza, A. Buldub, M. Demetgulc, Z. Yildiz, A novel thermal-based fabric defect detection technique. *J. Text. Inst.* **106**(3), 275–283 (2015)
4. Ç. Aytekin, Y. Rezaeitabar, S. Dogru, I. Ulusoy, Railway fastener inspection by real-time machine vision. *IEEE Trans. Syst. Man Cybern. Syst.* **45**, 1101–1107 (2015)
5. H. Lin, H. Chen, Automated visual fault inspection of optical elements using machine vision technologies. *J. Appl. Eng. Sci.* **16**, 447–453 (2018)
6. R. Shanmugamani, M. Sadique, B. Ramamoorthy, Detection and classification of surface defects of gun barrels using computer vision and machine learning. *Measurement* **60**, 222–230 (2015)
7. T. Wuest, D. Weimer, C. Irgens, K. Thoben, Machine learning in manufacturing: advantages, challenges, and applications. *Prod. Manuf. Res.* **4**(1), 23–45 (2016)
8. J. Yang, S. Li, Z. Wang, H. Dong, J. Wang, S. Tang, Using deep learning to detect defects in manufacturing: a comprehensive survey and current challenges. *Mater. (Basel)*. **13**(24), 5755 (2020)
9. T. Zimmermann, G. Ciuti, M. Milazzo, M. Chiurazzi, S. Roccella, C.M. Oddo, P. Dario, Visual-based defect detection and classification approaches for industrial applications—a survey. *Sensors* 20–1459 (2020)
10. J. Yu, Z. Chen, S. Kamata, Pill recognition using imprint information by two-step sampling distance sets. *Int. Conf. Pattern Recogn.* 3156–3161 (2014)
11. N.A. Borghese, M. Fomasi, Automatic defect classification on a production line. *Intell. Ind. Syst.* **1**, 373–393 (2015)
12. D.G. Lowe, Distinctive image features from scale-invariant keypoints. *Int. J. Comput. VisionComput. Vision* **60**(2), 91–110 (2004)
13. T. Ojala, M. Pietikäinen, T. Mäenpää, Multiresolution gray-scale and rotation invariant texture classification with local binary patterns. *IEEE Trans. Pattern Anal. Mach. Intell.* **24**(7), 971–987 (2002)
14. S. Ling, A. Pastor, J. Li, Z. Che, J. Wang, J. Kim, P. Callet, Few-shot pill recognition. *IEEE/CVF Conference on Computer Vision and Pattern Recognition (CVPR)*, (2020), pp. 9789–9798

15. X. Zeng, K. Cao, M. Zhang, MobileDeepPill: a small-footprint mobile deep learning system for recognizing unconstrained pill images. In: *15th Annual International Conference on Mobile Systems, Applications, and Services*, (2017), pp. 56–67. <https://doi.org/10.1145/3081333.3081336>
16. J. Zhou, J. He, G. Li, Y. Liu, *Identifying Capsule Defect Based on an Improved Convolutional Neural Network*, *Shock and Vibration*, vol. 2020, Article ID 8887723, 9 pages, 2020. <https://doi.org/10.1155/2020/8887723>
17. V. Podgorelec, Š Pečnik, G. Vrbančič, Classification of similar sports images using convolutional neural network with hyper-parameter optimization. *Appl. Sci.* **10**, 8494 (2020). <https://doi.org/10.3390/app10238494>
18. S. Lee, J. Kim, H. Kang, D.-Y. Kang, J. Park, Genetic algorithm based deep learning neural network structure and hyperparameter optimization. *Appl. Sci.* **11**, 744 (2021). <https://doi.org/10.3390/app11020744>
19. T.T. Mac, Application of improved Yolov3 for pill manufacturing system. *IFAC-PapersOnLine* **54**(15), 544–549 (2021)
20. T.T. Mac, N.T. Hung, Automated pill quality inspection using deep learning. *Int. J. Modern Phys. B.* **35**(14n16), 2140050
21. D.P. Kingma, J. Ba, Adam: a method for stochastic optimization. [arXiv:1412.6980](https://arxiv.org/abs/1412.6980) (2014)
22. H. Yang, S. Mei, K. Song, B. Tao, Z. Yin, Transfer-learning-based online mura defect classification. *IEEE Trans. Semicond. Manuf.* **31**, 116–123 (2017)
23. K. Simonyan, A. Zisserman, Very deep convolutional networks for large-scale image recognition. *ICLR* (2015)

# Design and Simulation of a Self-Tuning Fuzzy PID Controller for One Axis bar Model



Truong Minh Thong and Pham Duc An

**Abstract** Proportional—Integral—Derivative (PID) controllers are the most widely used controllers in the industry. Despite having been existent for almost a century, the PID controller still demonstrates its efficiency in various systems. Choosing suitable parameters for the PID controller is a crucial problem that needs a huge bunch of time tuning and testing. There are many methods proposed for the tuning of the PID controller. In this paper, a self-tuning PID controller is obtained using fuzzy logic controllers. The method used here is using fuzzy logic to force the PID controller to follow a preselected position track by changing the parameters of PID controllers as the rules set in advance. This Fuzzy PID is designed, optimized, and implemented on the one-axis bar model in this paper, which is a simple case of a quadcopter. The mathematical model of it is considered and simulated with MATLAB toolboxes. Then, the controller is validated on a real model by implementing it in a microcontroller programmed on Arduino IDE. The results have shown that the Fuzzy PID controller performs much better than the classical one, which is evident as a more adaptive, faster response, smaller rise, and settling time.

**Keywords** Fuzzy controller · Fuzzy PID · MATLAB

## 1 Introduction

The conventional Proportional—Integral—Derivative (PID) controller is the most popular controller in the industrial automation and controlling process due to its simplicity of operation, ease of design, low cost, effectiveness, and robust performance for most linear systems [1, 2]. However, the conventional PID controllers cannot satisfy the requirement of considering the nonlinearity of the systems. Hence, other control schemes are necessary to apply for nonlinear systems, time-delayed

---

T. M. Thong · P. D. An (✉)

School of Mechanical Engineering, Hanoi University of Science and Technology, 1 Dai Co Viet Road, Hanoi, Vietnam

e-mail: [an.phamduc@hust.edu.vn](mailto:an.phamduc@hust.edu.vn)



linear systems, and particularly complex systems that have no accurate mathematical models. To solve these issues, various PID controllers have been introduced, such as auto-tuning and adaptive PID controllers [3, 4]. Recently, motivated by the rapid development of intelligent control such as fuzzy control [5], neural networks [6], and genetic algorithms [7], such control systems evolved from conventional PID by adding these intelligent techniques and their development required interdisciplinary research [8, 9].

Fuzzy control, which is the steppingstone from control engineering to artificial intelligence, can be considered a means of improving the man-machine interface by providing human operators with the rationale for automatic control actions [10]. Also, fuzzy logic control (FLC) has been known as an alternative approach for complex systems and nonlinear dynamic systems [11]. Fuzzy PID is the combination of this set and the classical PID controller. A fuzzy PID controller has also been analyzed and guaranteed stability [2, 12, 13]. Many simulational and practical experiments have been given to prove the superior performance of this controller class over the classical one [2, 14].

This paper aims to equip the fuzzy PID controllers with a one-axis bar, which is a simple case of the full quadcopter. This bar is mathematically modeled and simulated with MATLAB toolboxes. The fuzzy PID controller will be designed and optimized its parameters in simulation first and then validated on the real model.

## 2 One-Axis Bar Model

The mechanical model of the one-axis bar is shown in Fig. 1.

There are two rotors with propellers attached to a straight bar with length  $l$ , which spins around an axis. To control these rotors, two ESCs (Electronic Speed Controllers) are used. And the whole model is embedded in a fixed base. The distance between a rotor, an ESC and the axis is  $d, d_1$  respectively. Due to the opposition of the model, the center of gravity of the model is placed in the center of the bar, which is coincident with the position of the spinning axis. Hence, the forces that affect the angular position of the bar are just the thrust  $F_1$  and  $F_2$  generated by two rotors.

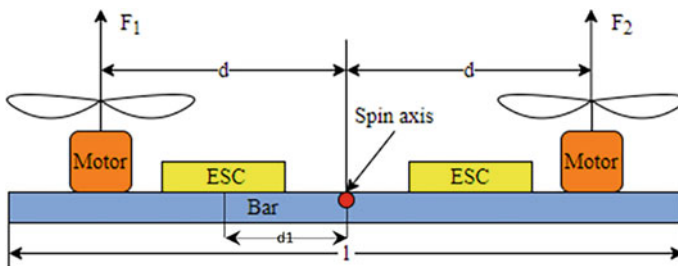


Fig. 1 Mechanic model of one-axis bar

A rotor produces thrust by spinning a propeller which pushes air down causing a reaction force that is up. The force at a distance from the center of gravity produces a torque, which makes the bar spin around the axis. This torque can be calculated in the Eq. (1)

$$\mathbf{M} = \mathbf{F}_1 \mathbf{d} - \mathbf{F}_2 \mathbf{d} = \Delta \mathbf{F} \times \mathbf{d} \quad (1)$$

where  $\Delta F = F_1 - F_2$ , that means when  $\Delta F = 0$  or  $F_1 = F_2$ , the system has no change and in contrast, if  $\Delta F$  does not equal to 0 or the moment  $M$  has affection on the bar. Therefore, the problem can be turned into controlling the speed of two rotors to rotate the bar to the desired angular  $\varphi$ . The parameters of the system are  $l = 0.52$  m,  $d = 0.24$  m,  $d_1 = 0.1$  m,  $m_{bar} = 0.286$  kg,  $m_{motor} = 0.059$  kg,  $m_{ESC} = 0.062$  kg,  $K_T = 1.67511 \times 10^{-6}$  Ns<sup>2</sup>/rad<sup>2</sup>.

Since the control problem is to regulate the speed of two rotors, it is essential to build an equivalent mathematic model for designing and tuning the controllers. The input signal of this model is the PWM signal that is sent to the ESCs and the output is the angle of the bar.

Firstly, according to the Principle of Conservation of momentum [15], only  $F_1$  and  $F_2$  are external forces that have affection on the model, so that the equation of conservation of momentum is presented as:

$$\mathbf{J} \times \ddot{\varphi} = \Delta \mathbf{F} \times \mathbf{d} \quad (2)$$

Or it can be rewritten as:

$$\ddot{\varphi} = \frac{\Delta \mathbf{F} \times \mathbf{d}}{\mathbf{J}} \quad (3)$$

That means the angular acceleration of the bar can be calculated through  $\Delta F$ , the angle position of the bar is the second integrator of the acceleration. Hence, the issue is only figuring out the relationship between the PWM signal and the force of the propeller.

It is well-known that the force generated by the propeller is proportional to the square of angular velocity of the rotor by a drag constant  $K_t$  [16]. The equation between the force and square velocity of rotor is

$$\mathbf{F} = \mathbf{K}_t \times \omega^2 \quad (4)$$

In this paper, the drag constant is determined by an experiment, in which the force is measured by the scale and the velocity is measured by a laser tachometer. The average  $K_t$  is 1.67511E-06.

The other part of the issue is to determine the transfer function from PWM signal to the angular velocity of the rotor. As Sham Seldin proposed in his paper [17], the transfer function has two poles and no zeros, so it can be detected by a toolbox of MATLAB, System Identification Toolbox, in which the data measured about PWM,

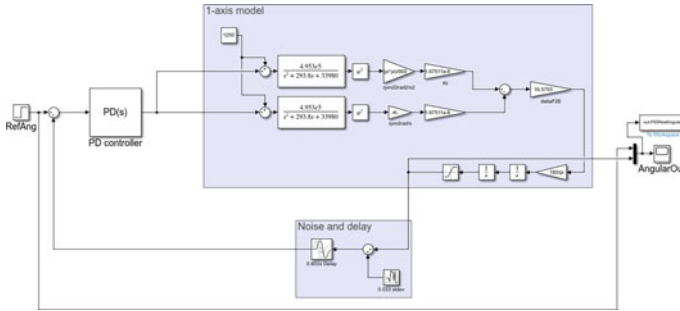


Fig. 2 Structure of PID controller in Simulink MATLAB

and velocity is used for estimation. The transfer function is estimated as:

$$G(s) = \frac{4.953 \times 10^5}{s^2 + 293.8s + 33980} \tag{5}$$

### 3 Fuzzy PID Controller

#### 3.1 PID Controller

The structure of the PID controller for one-axis model is shown in Fig. 2. There is a step signal used for creating the reference angle of the bar, in which the signal changes dramatically from 0° to 50°. The difference between the reference angle and the real angle of the bar is the input for PID controller, and the output of the controller is the subtraction of two PWM signal that will be implemented to two rotors. The output of the one-axis model is added by a noise and delay signal for making the plant closer to the real one. In this paper, the PD controller is used instead of a full PID controller because it has fast response and can reduce the fluctuations in model behavior caused by sensor’s noise. After applying two above methods, the two parameters obtained are  $K_p = 0.9$ ,  $K_d = 0.35$ .

#### 3.2 Fuzzy PID Controller

This self-tuning PID controller includes two parts: the conventional PID and Fuzzy Logic Control (FLC) for self-tuning the PID part. The three parameters  $K_p$ ,  $K_i$ ,  $K_d$  are autotuned to make the system follow the specified reference track while the controller is running due to the capability to track the different set point. Now the

controller with self-tuning can be described as:

$$U^{PID} = K_{pf}e(t) + K_{if} \int e(t) + K_d \frac{de(t)}{dt} \tag{6}$$

This first component converts input data into suitable linguistic values. As show in Fig. 3, there are two inputs to the controller: error and change rate of the error. In this system, both  $e(t)$  and  $\Delta e(t)$  are normalized from  $[-1, 1]$ . The linguistic labels of input are {Negative Big (NB), Negative Small (NS), Zero (ZE), Positive Small (PS), Positive Big (PB)}, and the labels for two outputs  $K_{pf}, K_{df}$  are {Negative Big (NB), Negative Medium (NM), Negative Small (NS), Zero (ZE), Positive Small (PS), Positive Medium (PM), Positive Big (PB)}.

The decision-making logic simulated from human decision process and converted into the rules that interferes control actions from the knowledge of control rules and variable definitions. The rule base of both  $K_{pf}, K_{df}$  is simply shown in the Table 1. The inputs have 5 labels so that there are 25 rules for control actions.

This yields a non-fuzzy control action from inferred fuzzy control action. The most popular method, center of gravity or center of area is used for defuzzification. The output signals  $K_{pf}, K_{df}$  is applied as the parameters for the PID controller. And the controller block which is simulated in Simulink is shown in Fig. 4. It is like the PID structure, but the PID controller is replaced by the self-tuning Fuzzy controller.

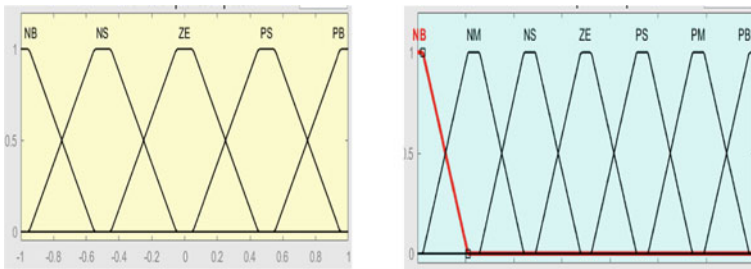


Fig. 3 Memberships function of inputs (e, Δe) and outputs ( $K_{pf}, K_{df}$ )

Table 1 The rule base of  $K_{pf}, K_{df}$

$e/\Delta e$	NB	NS	ZE	PS	PB
NB	NB	NB	NM	NS	ZE
NS	NB	NM	NS	ZE	PS
ZE	NM	NS	ZE	PS	PM
PS	NS	ZE	PS	PM	PB
PB	ZE	PS	PM	PB	PB

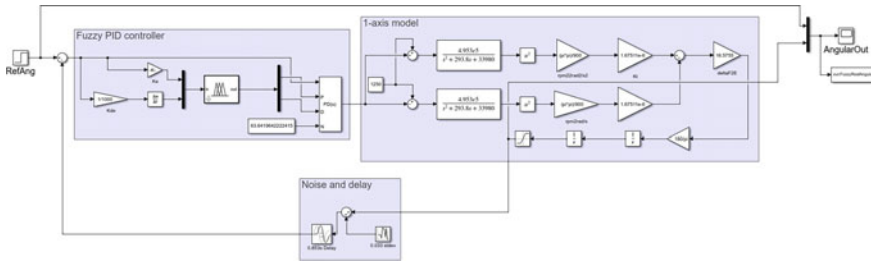


Fig. 4 Structure of fuzzy PID controller in Simulink

### 4 Simulation and Experiment Results

It can be seen in Fig. 5 that the Fuzzy PD controller has a better performance over the classical one. The overshoot of Fuzzy PD controller is 9.03%, which is smaller than 11.34% of the conventional PD. The steady-state error of Fuzzy PD is significantly smaller than the PD’s one, which is 0.095 and 0.807, respectively.

The real model, which is shown in Fig. 6, includes a wood bar, a base made of shaped aluminum, two rotors with propellers, two Electric Speed Controller (ESCs), a sensor MPU6050 for measuring the angle, and an Arduino Nano as the microcontroller. The steel rotation axis is attached to the bar with negative allowance fits and connected to the base through two bearings for reducing the friction while rotating. All the model is powered by a 12V-30A power supply.

It can be easily observed that in Fig. 5, the Fuzzy PD controller shows significant advantages over the conventional PD. The detailed comparison is presented in Table 2. The results show the potential of this proposed controller comparing with the

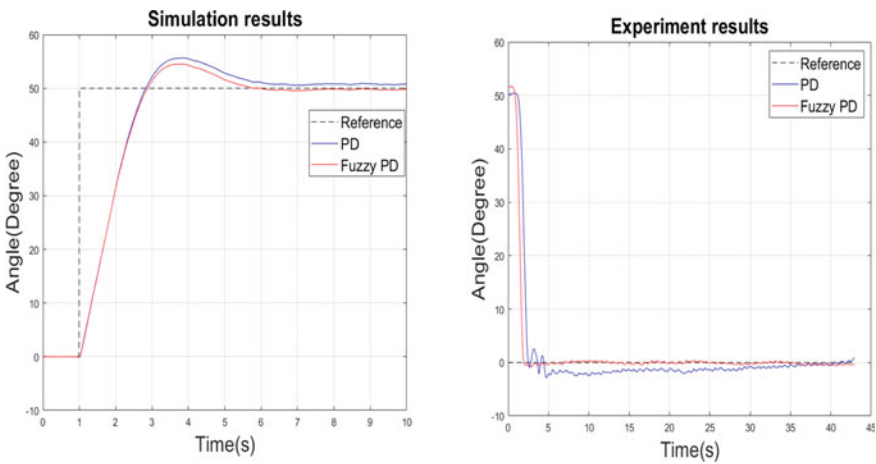
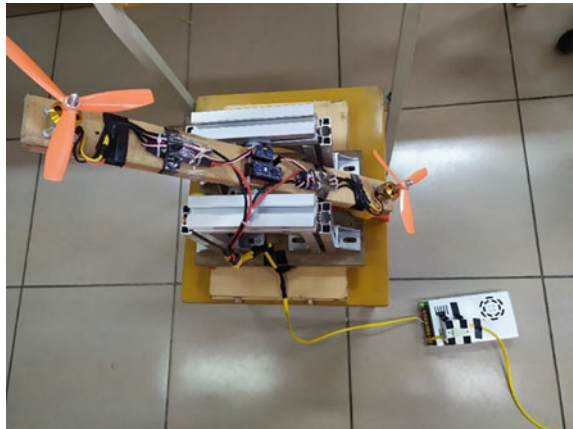


Fig. 5 Simulation and experiment results

**Fig. 6** Real one-axis bar model



**Table 2** Comparison results of fuzzy PD and PD on real model

Type	Overshoot (%)	Rise time	Settling time	Steady-state-error
PD	5.82	2.39	4.92	1.22
Fuzzy PD	1.56	1.84	1.84	0.11

classical one. Moreover, it can be also indicated that the noise of MPU6050 sensor has a severe impact on the model, which makes the controllers harder to reach the reference angles.

## 5 Conclusion

In this paper, a self-tuning Fuzzy PD controller has been designed and validated the performance. The results have clearly emphasized the advantages of the Fuzzy PD controller, in this context. The main benefits in the use of FLC on conventional PID appears when applying controller on a non-linear system as one-axis bar. They are evident as a balance obtained between both rise time and overshoot in the response, smaller steady-state error, and more adaptive with various input signals. The self-tuning feature of the FLC helps the model flexible with the dramatic changes of input and increases or decreases the parameters when it is necessary to make it more suitable for the context. In addition, a comparison between the classical PD and the Fuzzy PD controller has been also made in this paper, which shows that the Fuzzy PD is more stable, faster response, and smaller settling time. However, an issue risen in the process of designing the Fuzzy PID controller is the optimization when choosing the number of membership functions and their shapes that needs an in-depth study in the future.

## References

1. S. Bennett, Development of the PID controller. *IEEE Control. Syst. Mag.* **13**, 58–62 (1993)
2. G. Chen, Conventional and fuzzy PID controllers: an overview. *Int. J. Intell. Control Syst. Intell. Control Syst.* **1**, 235–246 (1996)
3. S.S. Bueno, R.C. de Keyser, G. Favier, Auto-tuning and adaptive tuning of PID controllers. *J. A* **32**, 28–34 (1991)
4. A. Pomerleau, A. Desbiens, D. Hodouin, Development and evaluation of an auto-tuning and adaptive PID controller. *Automatica* **32**, 71–82 (1996)
5. K.M. Passino, S. Yurkovich, M. Reinfrank, *Fuzzy control*. Citeseer (1998)
6. O.I. Abiodun, A. Jantan, A.E. Omolara, K.V. Dada, N.A. Mohamed, H. Arshad, State-of-the-art in artificial neural network applications: a survey. *Heliyon* **4**, e00938 (2018)
7. S. Mirjalili, Genetic algorithm. In *Evolutionary Algorithms and Neural Networks*. (Springer, 2019), pp. 43–55
8. K.M. Passino, Intelligent control for autonomous systems. *IEEE Spectr. Spectr.* **32**, 55–62 (1995)
9. K.J. Åström, T.J. McAvoy, Intelligent control. *J. Process. Control.* **2**, 115–127 (1992)
10. J.A. Bernard, Use of a rule-based system for process control. *IEEE Control. Syst. Mag.* **8**, 3–13 (1988)
11. K. Lamamra, F. Batat, F. Mokhtari, A new technique with improved control quality of nonlinear systems using an optimized fuzzy logic controller. *Expert Syst. Appl.* **145**, 113148 (2020)
12. J. Carvajal, G. Chen, H. Ogmen, Fuzzy PID controller: design, performance evaluation, and stability analysis. *Inf. Sci.* **123**, 249–270 (2000)
13. G. Chen, T.T. Pham, *Introduction to Fuzzy Sets, Fuzzy Logic, and Fuzzy Control Systems* (CRC press, 2000)
14. V. Kumar, B.C. Nakra, A.P. Mittal, A review on classical and fuzzy PID controllers. *Int. J. Intell. Control Syst. Intell. Control Syst.* **16**, 170–181 (2011)
15. M. Brunt, G. Brunt, Introducing conservation of momentum. *Phys. Educ.* **48**, 664 (2013)
16. R. Gill, R. D'andrea, Propeller thrust and drag in forward flight. In *2017 IEEE Conference on Control Technology and Applications (CCTA)*, (2017), pp. 73–79
17. M.A. Shamseldin, A.A. EL-Samahy, Speed control of BLDC motor by using PID control and self-tuning fuzzy PID controller. In *15th International Workshop on Research and Education in Mechatronics (REM)* (2014), pp. 1–9